Geochemistry of Shallow and Deep Water Archean Meta-Iron Formations and their Post-Depositional Alteration in Western Superior Province, Canada

Simon Dolega

A thesis submitted in partial fulfillment of the requirements for the degree of

MASTERS OF SCIENCE

GEOLOGY

Supervisor: Dr. Philip Fralick

August 2018

Department of Geology

Faculty of Graduate Studies

Lakehead University

ABSTRACT

One purpose for studying banded meta-iron formations is to determine the chemical composition of seawater in the Archean ocean and the oxygen content of the Archean oceanic-atmospheric system. Geologists use the geochemistry of meta-iron formations to make interpretations on the chemical conditions in the Archean. However, post-depositional alteration can affect the element geochemistry preserved in the meta-iron formations. This thesis explores the role of post-depositional mechanisms and determines element provenance in four Archean banded meta-iron formations.

The four different locations hosting Archean metamorphosed meta-iron formations chosen for this study are: meta-iron formations from the Beardmore/Geraldton greenstone belt of the Eastern Wabigoon Domain, Lake St. Joseph greenstone belt of the Uchi Domain, North Caribou greenstone belt of the North Caribou Terrane and Shebandowan greenstone belt of the Wawa Subprovince. The meta-iron formations from the Beardmore/Geraldton and Lake St. Joseph greenstone belts are interpreted to have been deposited in a shallow water setting, while meta-iron formations from the North Caribou and Shebandowan greenstone belts are interpreted to be deposited in deeper water environments. This thesis also investigated element and oxygen ocean stratification by comparing the geochemistry of shallow and deep meta-iron formations.

The main source of iron and silica to the oceans was hydrothermal venting fluids. Iron and silica precipitated out of seawater as iron oxyhydroxides and amorphous silica. Elements dissolved in the Archean ocean were adsorbed onto iron oxyhydroxides and silica during deposition. Crystallization of quartz, magnetite and hematite occurred during diagenesis and magnetite continued to grow during progressive metamorphism.

The lack of cerium anomalies, absence of significant Y/Ho anomalies and deficiency of authigenic chromium supplied to the ancient suggests that the oceans were anoxic. Therefore, oxygen stratification did not occur between shallow and deeper water environments in the Archean.

Significantly most of the elements were derived from multiple sources, including the siliciclastic phase, seawater or hydrothermal venting fluids, at various proportions. Al_2O_3, TiO_2, Th, V, Nb, U, REEs and Y were determined immobile during post-depositional alteration.

Mobility during diagenesis is clearly exhibited by sodium and potassium in the meta-iron formation samples from the Beardmore/Geraldton, Lake St. Joseph and North Caribou greenstone belts. Diagenetic modification mobilized sodium in the hematite-, jasper- and chert-dominated samples, while potassium was mobilized in the magnetite-dominated samples.

Element stratification occurred in the Archean due to the source provenance. Deeper oceans were more enriched in Cs, Na_2O, CaO, MnO, Cr and HREEs relative to shallow waters. Shallow oceans were more enriched in K_2O, Rb and LREEs relative to deeper waters. This indicates that the Archean oceans were heterogeneous.

ACKNOWLEDGEMENTS

TABLE OF CONTENTS

LIST OF FIGURES

x

LIST OF TABLES

LIST OF EQUATIONS

ABBREVIATIONS

Regional Geology

BG – Beardmore/Geraldton greenstone belt

LSJ – Lake St. Joseph greenstone belt

NC – North Caribou greenstone belt

SGB – Shebandowan greenstone belt

Minerals

Ap	Apatite	Kfs	K-feldspar
Apy	Arsenopyrite	Mag	Magnetite
Bt	Biotite	Ms	Muscovite
Cb	Carbonate mineral	Pl	Plagioclase
Chl	Chlorite	Py	Pyrite
Chr	Chromite	Qtz	Quartz
Cld	Chloritoid	Rt	Rutile
Cpx	Clinopyroxene	Sch	Scheelite
Ep	Epidote	Stp	Stilpnomelane
Hem	Hematite	Tur	Tourmaline
Ilm	Ilmenite	Zr	Zircon

CHAPTER 1

INTRODUCTION

1.1 Objective

Banded meta-iron formations (meta-BIF) are layered chemical sedimentary rocks that contain a minimum of 15 weight percent iron and are commonly associated with layers of chert (James, 1954). These rocks were formed by the precipitation of iron oxyhydroxides and amorphous silica from seawater. The precipitates sample the water chemistry of their depositional environment and this water chemistry may be recorded in the meta-iron formation. For several decades, scientists have been using the geochemistry of banded meta-iron formations to determine atmospheric and hydrologic conditions in the Precambrian (ex. Cloud, 1973; Garrels et al., 1973; Drever, 1974; Derry and Jacobsen, 1990; Planavsky et al., 2010; Bekker et al., 2014). However, post-depositional mechanisms such as diagenesis, metamorphism and hydrothermal metasomatism can alter the chemistry of meta-iron formations, yielding misinterpretations for the reconstruction of Precambrian history. Despite the fact, there have been very few detailed studies on element mobility during post-depositional alteration in meta-iron formations.

Sedimentological studies have shown that Precambrian meta-iron formations occurred in both deep and shallow water environments (ex. Gross, 1965). In this thesis, shallow water meta-iron formations are discerned from deeper water meta-iron formations by being deposited above wave base, while deeper water meta-iron formations were deposited below wave base. Some scientists believe the oceans may have been stratified due to oxygen-producing photosynthetic bacteria in the shallow water environment, suggesting that a redoxcline occurred between the oxic shallow ocean and the anoxic deep ocean (ex. Cloud, 1973). Scientists have been using this theory to interpret mechanisms for meta-iron formation deposition (ex. Planavsky et al., 2010). This oxygen gradient, as

well as any other element gradients in the Archean oceans may be preserved in the meta-iron

formations.

The purpose of this thesis is to evaluate the role of post-depositional mechanisms and

determine element provenance in Archean shallow and deep water banded oxide-facies meta-iron

formations using petrography and geochemical techniques. Since, major chemical reactions after

deposition were required to produce iron formation, it is hypothesized that some of elements in

Archean meta-iron formations have been mobilized during post-depositional alteration. For the

elements that remined immobile during post-depositional alteration, it is hypothesized that the

meta-iron formations preserve evidence of element stratification in the Archean ocean. To test

these theories, two shallow and two deep water Archean meta-iron formations from the western

Superior Province were investigated. Field observations and petrography were used to categorize

the lithologies, document sedimentary and metamorphic textures and structures, calculate mineral

compositions and determine metamorphic grade. Banded meta-iron formation samples were

separated by their phase-dominated layers to observe the differences occurring during diagenetic

modification. Geochemical analyses were conducted to determine chemical compositions of the

phase-dominated layers. Element mobility and provenance in the meta-iron formations was

ascertained by using graphical techniques to compare immobile element ratios and meta-iron

formations with their associated siliciclastic lithologies. Mineral and element partitioning between

phase dominated layers indicates that some elements were mobilized during diagenesis. Different

immobile element ratio values between shallow and deeper water meta-iron formations indicates

element stratification in the ancient oceans.

In the literature, many scientists have dropped the prefix meta- from meta-iron formations since

all Precambrian iron formations have been subjected to a degree of metamorphism. However,

according to the IUGS Subcommission on the Systematics of Metamorphic Rocks (SCMR), the prefix

"meta" should be used when metamorphosed rocks are named by their protolith (Schmid et al.,

2007). Since this thesis focuses on element mobility during post-depositional alteration and the

correct nomenclature based on SCMR classification scheme is meta-iron formation, all the iron

formation in this thesis will be termed meta-iron formation.

1.2 Field Study Locations

Diverse case study locations hosting Archean banded meta-iron formation were chosen to best

evaluate the objectives of this thesis. These locations differ in age, depositional setting and

metamorphic grade. Study areas include the Beardmore-Geraldton greenstone belt (BG), Lake St.

Joseph greenstone belt (LSJ), North Caribou greenstone belt (NC) and Shebandowan greenstone belt

(SGB) (Figure 1.1). All the greenstone belts are within the western Superior Province in Ontario,

Canada.

BG is located in the municipality of Greenstone, east of Lake Nipigon. Samples of jasper- and

hematite-dominated meta-iron formation were taken from a series of outcrops along Highway 580

towards Poplar Lodge, which is located east of Beardmore near Leitch Mine and Spawn Lake, which

is about 7 km north from the Trans Canada Highway 11 and Windigokan Lake Road junction.

Magnetite-dominated meta-iron formation samples were collected west of Jellicoe at Solomon's

Pillar, and outcrops near the headframe in Geraldton, which is located at the junction of Highway 11

and Hard Rock Road.

LSJ is located about 315 km north of Thunder Bay, Ontario in the Kenora District. All the

magnetite- and hematite-dominated samples were collected from Eagle Island, which is located on

the southwestern side of Lake St. Joseph.
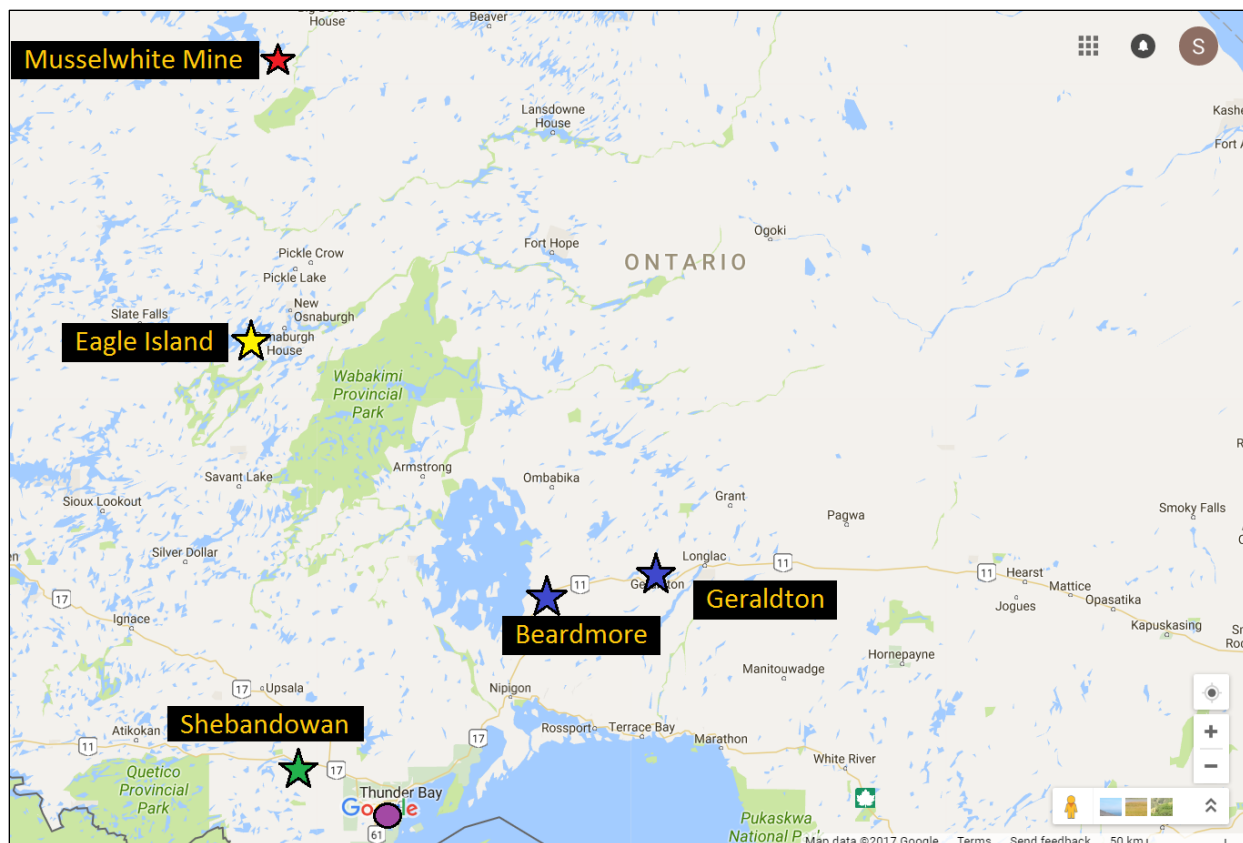
Figure 1.1: A road map of the case study locations in northwestern Ontario. Musselwhite Mine is denoted by a red star, Eagle Island is denoted by a yellow star, Beardmore and Geraldton are denoted by blue stars, Shebandowan is denoted by a green star and Thunder Bay is denoted by a purple circle. Modified from Google Maps (2017). Map of Northwestern Ontario. Retrieved from https://www.google.ca/maps/@50.4229365,-88.001906,7z

Samples from NC were all collected on Musselwhite Mine's property. Musselwhite Mine is located about 480 km north from Thunder Bay on the southern side of Opapimiskan Lake. The samples were chert-grunerite-magnetite meta-iron formation, from the Northern Iron Formation unit.

The final site location for this thesis was an outcrop containing meta-iron formation within the SGB. The town of Shebandowan is located 70 km northwest of Lakehead University, Thunder Bay along Highway 11. The outcrop is situated 12 km from the junction of Highway 11 and Shebandowan Mine Road along Shebandowan Mine Road. Magnetite-jasper-chert meta-iron formation samples were collected from this outcrop, which is located in the southern end of Hagey Township near Lamport Township, just south of Lower Shebandowan Lake.

1.3 Regional Geology

The Superior Province is one the largest stable Archean cratons in the world, spanning about 1 565 000 km^2 (Thurston, 1991). It is bounded to the north, west and south by Paleoproterozic aged provinces and to the southeast by the Grenville Province, which is Mesoproterozoic in age (Percival et al., 2006). The Superior Province is subdivided into several subprovinces, based on their lithologies, metamorphism, deformation structures, isotopic ages and geophysical characteristics (Douglas, 1973; Card and Ciesielski, 1986). These east-west trending subprovinces are classified as granite-greenstone (metavolcanic) assemblages, granitoid-metasedimentary assemblages and high grade metamorphic-granitoid assemblages (Percival et al., 2006). Greenstone assemblages or belts are broadly defined as thick stratigraphic sequences dominated by mafic and ultramafic metavolcanic rock, which have been metamorphosed to the greenschist facies (deWit and Ashwal, 1986). However, within these greenstone belts, the grade of metamorphism can range from subgreenschist to granulite facies (deWit and Ashwal, 1986). Granite-greenstone assemblages are interpreted to be remnants of allochthonous island arc terranes, while granitoid-metasedimentary assemblages are interpreted to be remnants of deep sedimentary basins, where sediment from eroded island arcs accumulated (Langford and Morin, 1976). These arcs and basins were accreted forming the Superior Province by convergent plate tectonics (Langford and Morin, 1976). All the meta-iron formations in this study are located within granite-greenstone assemblages. Case study locations include meta-iron formations from the Beardmore-Geraldton greenstone belt of the Eastern Wabigoon Domain, Lake St Joseph greenstone belt of the Uchi Domain, North Caribou greenstone belt of the North Caribou Terrane and Shebandowan greenstone belt of the Wawa subprovince. Figure 1.2 shows their respective locations within the western Superior Province. Brief descriptions of the regional geology from each case study location is discussed below. Detailed sedimentology and depositional environments from each site location are elaborated in Chapter 3.
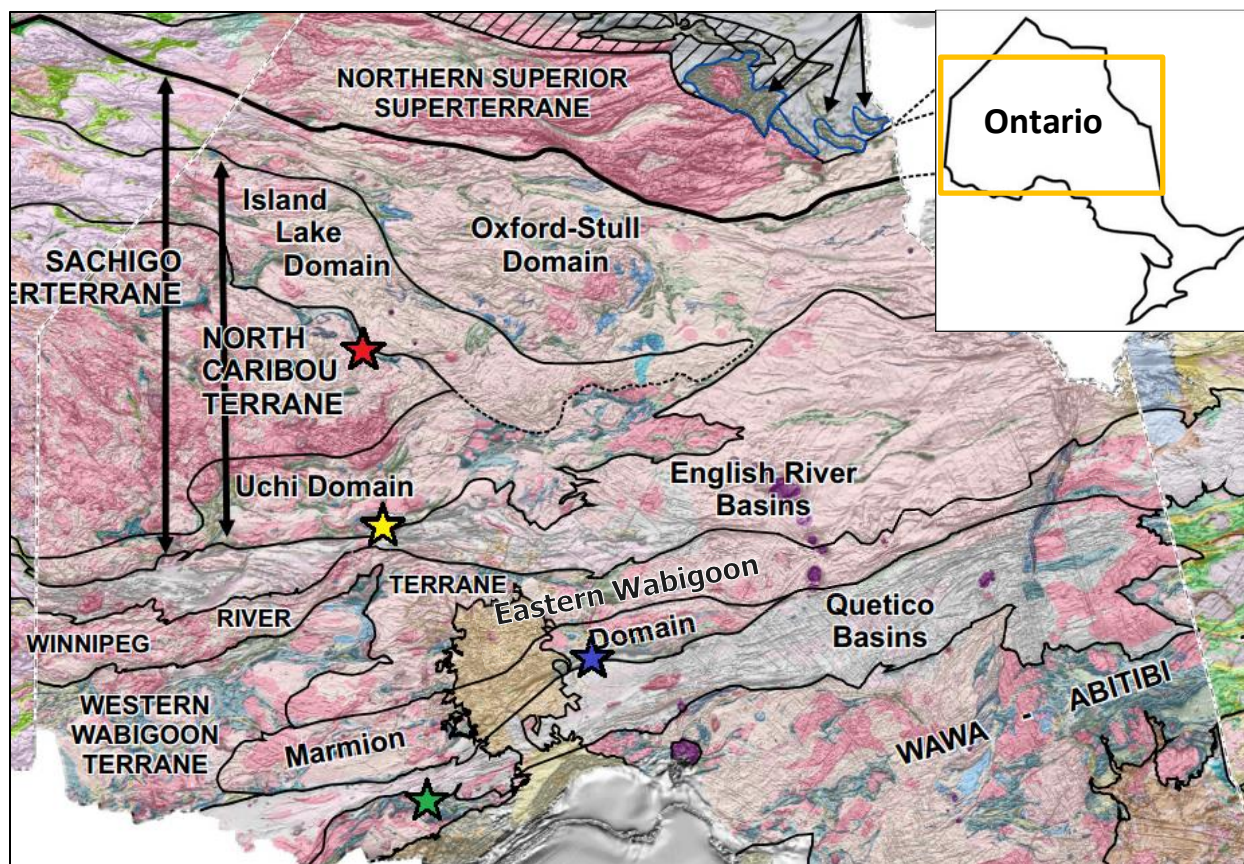
Figure 1.2: Geologic map of the western Superior Province, Ontario, Canada. Coloured stars denote outcrops selected for this study. Blue – Beardmore-Geraldton greenstone belt, Yellow – Lake St. Joseph greenstone belt, Red – North Caribou greenstone belt, Green – Shebandowan greenstone belt. Map modified from Stott (2011).

1.3.1 Beardmore-Geraldton Greenstone Belt

The BG is interpreted to be the transition zone between the Eastern Wabigoon Domain and the Quetico subprovince (Devaney and Williams, 1989; Percival and Easton, 2007). North of the BG is the Onaman-Tashota metavolcanic terrane, which is separated from the BG by the Paint Lake Shear Zone (Devaney and Williams, 1989). Just south of the BG is the Quetico subprovince, which is composed of felsic and mafic turbidites (Fralick et al., 1992) metamorphosed from greenschist to amphibolite facies with localized zones of granulite facies metamorphism (Pan et al., 1994).

The BG consists of six alternating, east-west trending, metavolcanic and metasedimentary sub-belts (Devaney and Williams, 1989; Smyk et al., 2005; Fralick and Pufahl, 2006). These six sub-belts,

from north to south, are divided into the northern metasedimentary belt (NMB), the northern

metavolcanic belt (NVB), central metasedimentary belt (CMB), central metavolcanic belt (CVB),

southern metasedimentary belt (SMB) and the southern metavolcanic belt (SVB) (Figure 1.3)

(Devaney and Williams, 1989; Smyk et al., 2005). Dips of the lithologies are predominantly

subvertical and shear sense indicators show a predominantly dextral sense of movement (Devaney

and Williams, 1989). Stable metamorphic mineral assemblages and microstructures for various

lithologies within the BG suggest a range of metamorphism from lower greenschist to amphibolite

facies (Stinson, 2013).
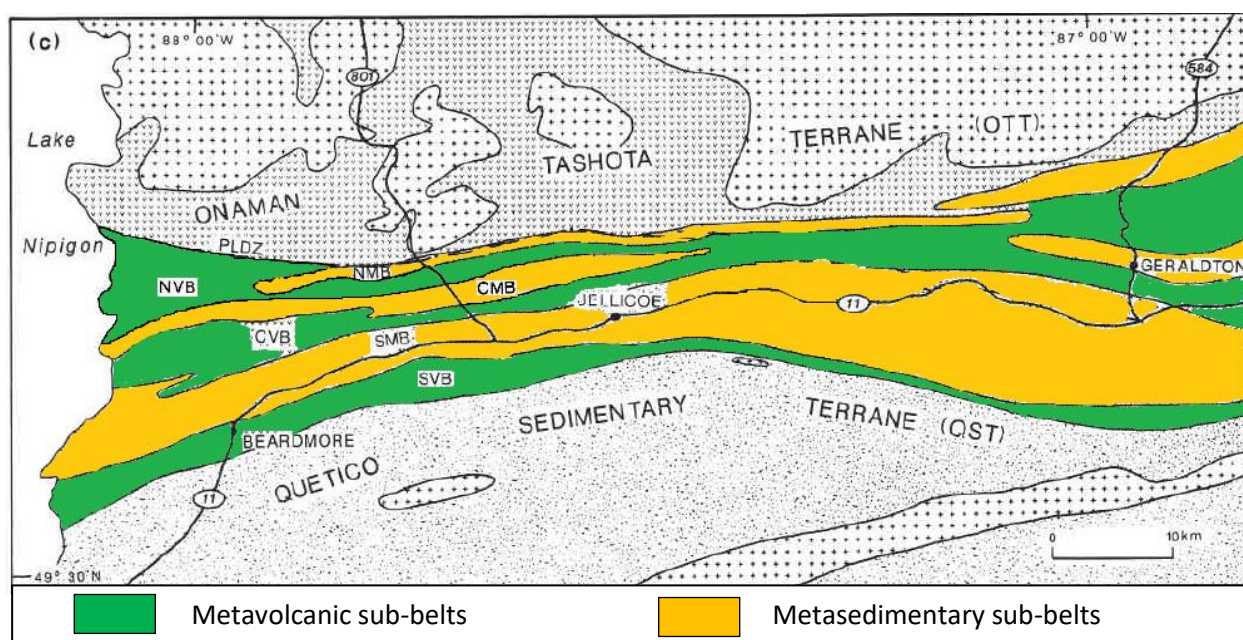
Figure 1.3: Geologic map of the sub-belts in the BG, east of Lake Nipigon. PLDZ – Paint Lake Shear Zone, NMB – Northern Metasedimentary Belt, NVB – Northern Metavolcanic Belt, CMB – Central Metasedimentary Belt, CVB – Central Metavolcanic Belt, SMB – Southern Metasedimentary Belt and SVB – Southern Metavolcanic Belt. Map modified from Devaney and Williams (1989).

The metasedimentary sub-belts have been interpreted to be deposited in a forearc basin

(Barrett and Fralick, 1989). Geochemical evidence strongly suggests that the calc-alkaline volcanic

rocks from the Onaman-Tashota terrane were the sediment source for the metasedimentary rocks

of both the BG and Quetico trench (Fralick and Kronberg, 1997). Tectonic models used to interpret

the formation of the BG are accretionary wedge tectonics (Devaney and Williams, 1989; Smyk et al.,

2005) or backthrusting of the imbricate wedge under the forearc basin (Barrett and Fralick, 1989). Descriptions of the metasedimentary belts from Barrett and Fralick (1989), Devaney and Williams (1989) and Smyk et al. (2005) are summarized below.

The NMB is predominantly composed of massive, clast supported polymictic metaconglomerate interbedded with less than ten percent massive, metasandstone. The compositions of the clasts are dominantly felsic to intermediate metavolcanic rocks, but metamorphosed mafic, granitoid and chert clasts also exist. Deformation is recognized by the flattening of clasts in the direction parallel to foliation. Although there is evidence of deformation and metamorphism in the conglomerate, some primary sedimentary features are preserved, including parallel laminated and cross-bedded pebbly sandstones. This sedimentary lithofacies association is interpreted to be deposited by a gravel-dominated, braided river system either on an alluvial fan or braidplain environment (Devaney and Fralick, 1985). Detrital zircons from metaconglomerates in the NMB, range in age from 2890 Ma to 2710 ± 3 Ma (Hart et al., 2002).

The CMB has a variety of different metasedimentary lithologies and structures. Overall there is a northward-coarsening and northward-younging trend within the CMB. Similar to the NMB, the north part of the CMB is composed of interbedded metaconglomerate and metasandstone layers, which are interpreted to be braided river systems similar to the NMB. Moving south towards the middle of the belt, the lithologies are dominated by metasandstones with well sorted metaconglomerate bands, pebbly metasandstone bands and minor metamudstones. These units are interpreted to be fan and braid deltaic environments (Devaney and Fralick, 1985). The southern part of the CMB is composed of metamudstones, graded metasandstones and meta-iron formations. These lithologies have been interpreted to reflect a subaqueous fan and prodelta environment (Devaney and Williams, 1989). These interpretations indicate a transition between the subaerial lithofacies at the

top of the succession to subaqueous lithofacies lower in the succession (Fralick and Pufahl, 2006). Zircon geochronology on detrital zircons from a metaconglomerate, range in age from 2922 Ma to 2696 ± 2 Ma (Hart et al., 2002).

The northern section of the SMB is composed of polymictic metaconglomerate interbedded with metasandstone and meta-iron formation of varying thicknesses. Detrital zircons in the metasandstones range in age from 2828 Ma to 2703 ± 4 Ma (Hart et al., 2002). The meta-iron formation bearing zone in the SMB is continuous and can be laterally traced for 120 km through aeromagnetic data (Fralick and Pufahl, 2006). The sediments south from this lithofacies are graded, massive and parallel laminated metasiltstones and metasandstones. These are interpreted to be turbidites deposited in a submarine fan and ramp environment (Barrett and Fralick, 1989; Devaney and Williams, 1989). Meta-iron formation from the CMB and SMB were selected for analysis in this study.

1.3.2 Lake St. Joseph Greenstone Belt

The Northern Caribou Superterrane, formerly known as the Sachigo Superterrane, consists of the Oxford-Stull Domain, Island Lake Domain, North Caribou Terrane and the Uchi Domain (Thurston et al., 1991; Percival et al., 2006) (Figure 1.2). The LSJ is located along the southern margin of the Uchi Domain including Lake St. Joseph (Stott and Corfu, 1991). The boundary between the metasedimentary-plutonic sequences of the English River subprovince and the southern end of the LSJ is the Sydney Lake – Lake St Joseph Fault (Stott and Corfu, 1991). The LSJ contains the Confederation and St. Joseph metavolcanic assemblages, the Eagle Island metasedimentary assemblage and two large granitoid batholiths, the Blackstone and Carling batholiths (Stott and Corfu, 1991). The lithologies in the LSJ have been regionally metamorphosed to greenschist facies,

although locally near gabbroic intrusions, the grade of metamorphism is up to hornblende-hornfels facies (Berger, 1981).

Four cycles of volcanic activity are preserved in the LSJ (Stott and Corfu, 1991). These cycles are numbered from 1-4 based on their stratigraphic position within the greenstone belt (Stott and Corfu, 1991) (Figure 1.4). Cycles 1 and 3 are the youngest sequences of the Confederation assemblage and cycles 2 and 4 belong to the youngest sequences of the St. Joseph assemblage (Stott and Corfu, 1991; Corfu and Stott, 1993). Zircons from metamorphosed lapilli tuffs in cycle 1 and metamorphosed rhyodacite tuffs in cycle 3 yielded U-Pb ages of 2733 ± 1.5 Ma and 2730 ± 1 Ma respectively (Corfu and Stott, 1993). Metamorphosed felsic tuffs in cycle 2 and metamorphosed heterolithic tuff breccias in cycle 4 yielded zircon U-Pb ages of 2724 ± 2 Ma and 2713 ± 1.5 Ma, respectively (Corfu and Stott, 1993). Imbricate thrusting of the Confederation and St. Joseph assemblages is the interpretation for why cycle 3 is stacked on top of cycle 2 (Corfu and Stott, 1993).
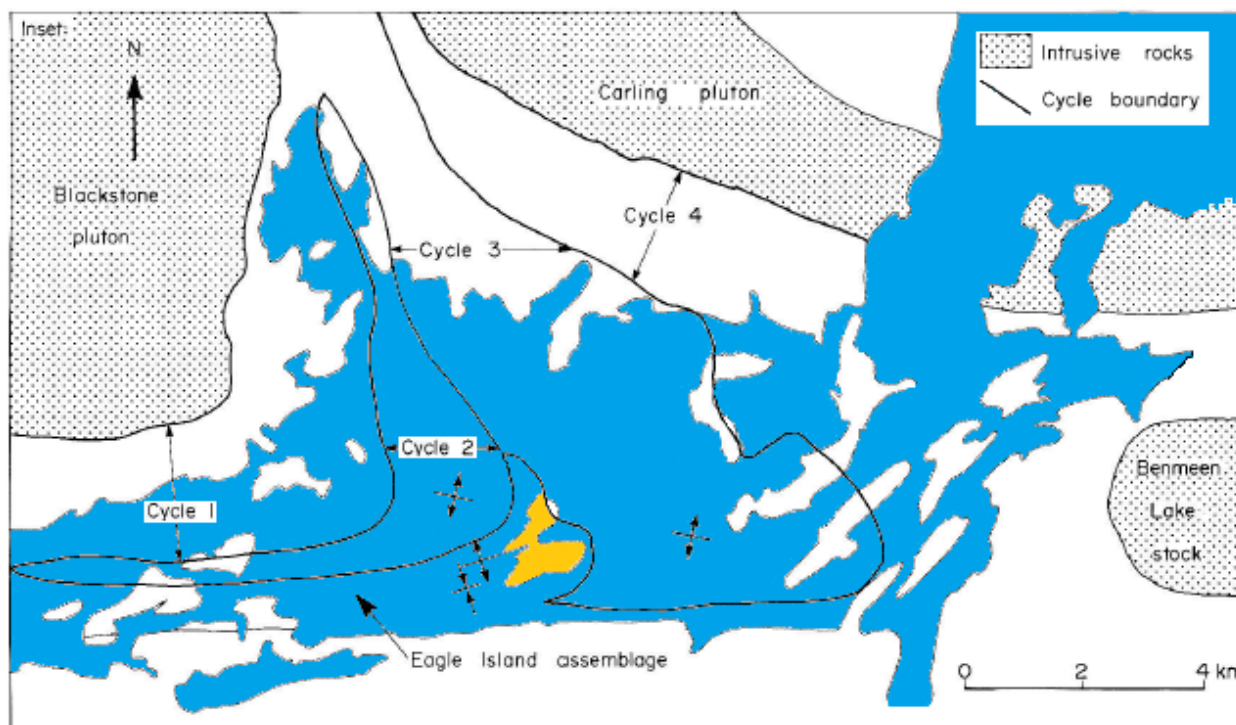
Figure 1.4: Geologic map of the LSJ. Cycle 1 and 3 are part of the Confederation assemblage and Cycle 2 and 4 are part of the Lake St. Joseph assemblage. The Eagle Island assemblage is located south of cycle 2. Eagle island is coloured in yellow and area where meta-iron formation samples were collected. Map modified from Stott and Corfu (1991).

The Eagle Island assemblage is composed of chemical and clastic metasedimentary lithologies. These metasedimentary rocks unconformably overlie metamorphosed pyroclastic rocks from the St. Joseph assemblage (Stott and Corfu, 1991). The Eagle Island assemblage consists of a 500 m thick, stratigraphically coarsening-upward succession from meta-iron formation to graded, medium-grained to coarse-grained metasandstone layers to metasandstones and metaconglomerates (Fralick and Pufahl, 2006). Previously, scientists interpreted the depositional environment for the Eagle Island assemblage to be a deep-water submarine fan environment (Meyn and Palonen, 1980; Berger, 1981; Stott and Corfu, 1991). Recent sedimentology conducted by Fralick and Pufahl (2006) suggests that the Eagle Island assemblage reflects a near shore distributary mouth bar complex.

1.3.3 North Caribou Greenstone Belt

The NC is located within the north-central portion of the North Caribou Terrane (Rayner and Stott, 2005) (Figure 1.2). North of the NC is the Island Lake Domain (Rayner and Stott, 2005). The NC forms a sigmoidal shape around two felsic plutonic complexes, the North Caribou Batholith to the southwest and the Schade Lake Gneissic Complex northeast of the greenstone belt (Breaks et al., 2001) (Figure 1.5). Depending on the author, the NC can be subdivided into four to eight supracrustal assemblages (Breaks et al., 1986; Thurston et al., 1991; Hollings and Kerrich, 1999; Breaks et al., 2001; Moran, 2008; Biczok et al., 2012). In this thesis, five supracrustal assemblages encompass the NC. They include: the Agutua Arm metavolcanic assemblage, Keeyask Lake metasedimentary assemblage, Keeyask Lake metavolcanic assemblages, the McGruer volcanic assemblage and the Eyapamikama Lake metasedimentary assemblage (deKemp, 1987; Thurston et al., 1991). Breaks et al. (1986) identified the North Rim, South Rim, Opapaimiskan-Markop unit and Forester-Neawagank unit as separate assemblages while Thurston et al. (1991) grouped all these metavolcanic units together and named it the McGruer assemblage. Metamorphic grade increases

from greenschist facies in the northeast to upper amphibolite facies in the southwest (Breaks et al., 2001; Biczok et al., 2012).
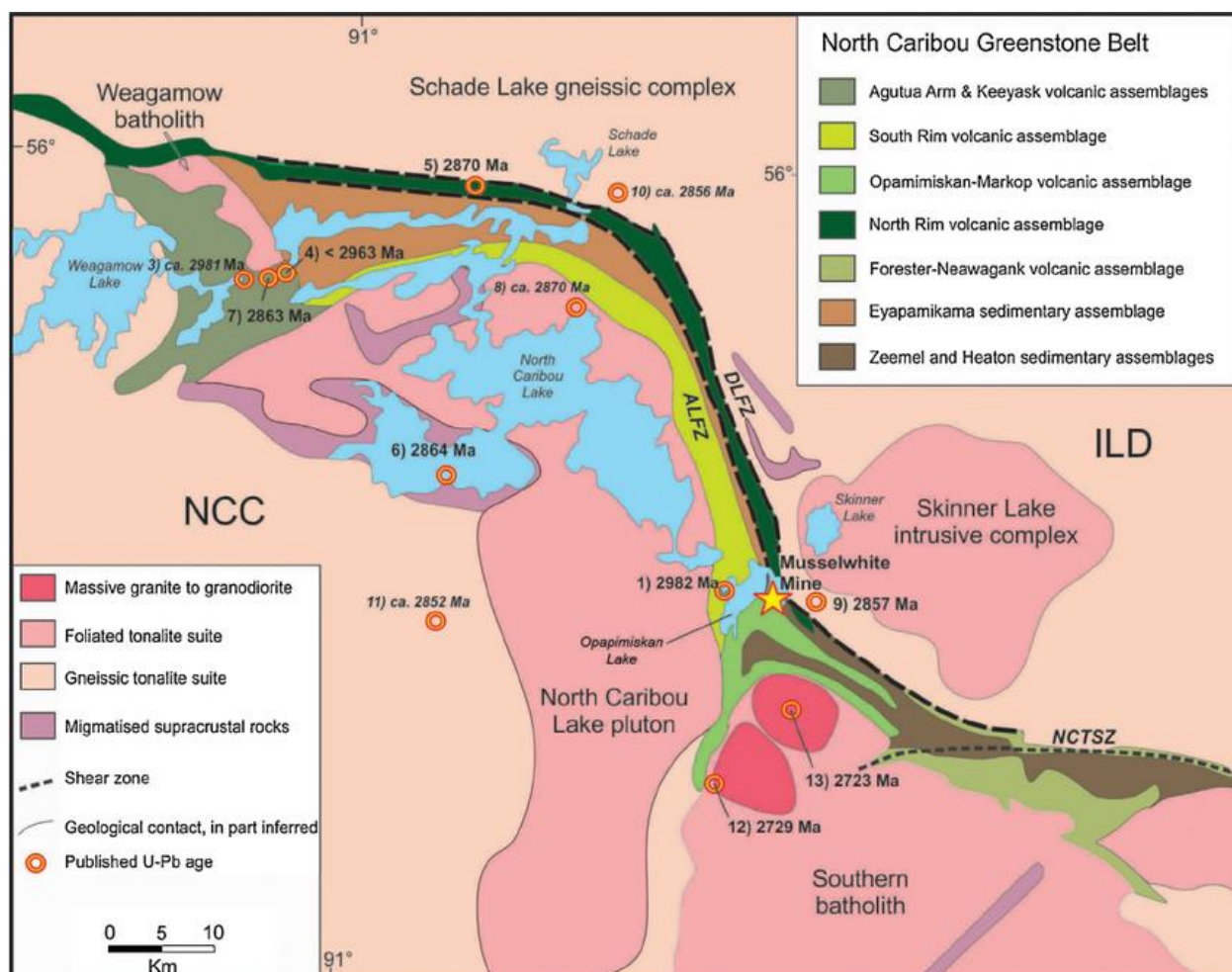
Figure 1.5: Geologic map of the NC. On this map the NC is divided into 8 metavolcanic and metasedimentary assemblages. The South Rim, Opapimiskan-Markop, North-Rim and Forester-Neawagank metavolcanic assemblages are all part of the McGruer assemblage. The Zeemel and Heaton metasedimentary assemblages are grouped with the Eyapamikama metasedimentary assemblages. Map sourced from McNicoll et al. (2016).

The Agutua Arm metavolcanic assemblage is located at the western end of the NC (Figure 1.5). It is bounded to the north by the Weagamow Batholith (deKemp, 1987) (Figure 1.5). The metavolcanic assemblage is dominated by mafic and felsic metavolcanic lithologies (Breaks et al., 2001). U-Pb geochronology of zircon from fragmental felsic metavolcanics had identified the Agutua Arm assemblage as the oldest assemblage in the NC at 2981 ± 1.8 Ma (deKemp, 1987). Thurston et al.

(1991) interpreted the metamafic flows as arc-related subaqueous volcanism and the metamorphosed felsic and intermediate pyroclastic rock as proximal airfall deposits.

Stratigraphically, the Keeyask Lake metasedimentary assemblage overlies the Agutua Arm metavolcanic assemblage (deKemp, 1987). It is composed of quartz meta-arenite, metamudstone, banded meta-iron formations and rare occurrences of quartz metawacke, plagioclase arkosic meta-arenite and metachert (deKemp, 1987). This sequence is interpreted to be a shallow water platform deposit (Thurston and Chivers, 1990; Thurston et al., 1991). Age determination on detrital zircons from the quartz meta-arenite yielded a maximum age of 2980.1 ± 3.0 Ma (deKemp, 1987).

The Keeyask Lake metavolcanic assemblage lies conformably on top of the Keeyask Lake metasedimentary rocks (deKemp, 1987). It consists of ultramafic metavolcanics rock at the bottom of the succession to metamorphosed mafic pillowed basaltic komatiites and tholeiites (deKemp, 1987). The Keeyask Lake metavolcanic assemblage is interpreted to be associated with ocean volcanism (Thurston and Chivers, 1990; Thurston et al., 1991).

The McGruer assemblage stratigraphically overlies the Keeyask Lake metavolcanic assemblage (Thurston et al., 1991). According to U-Pb geochronology conducted by Davis and Stott (2001), zircons in metamorphosed rhyolitic units from the North and South Rim metavolcanic units yielded ages of 2870 ± 2 Ma and 2981.9 ± 0.8 Ma, respectively. This suggests that the South Rim metavolcanic unit is older than the North Rim and they are not directly related to the same volcanic episode (Davis and Stott, 2001).

The South Rim metavolcanic unit is located on the outer and western edge of the NC (Figure 1.5) (Breaks et al., 1986). The bottom of the South Rim metavolcanic unit is tectonically bounded by the Keeyask Lake metavolcanic assemblage (Thurston et al., 1991). The South Rim is composed of Mg-tholeiitic metamafic rocks and felsic to intermediate metavolcanic rocks (Breaks et al., 1986; Breaks

et al., 2001). Metamorphic grade increases towards the contact of the North Caribou Batholith (Breaks et al., 2001). Rare banded meta-iron formation and metaultramafic pillowed flows are interbedded with the mafic metavolcanic rock (Breaks et al., 2001). Trace element geochemistry indicates that the South Rim metavolcanic unit is a result of a plume-related oceanic plateaux interacting with a continental arc (Hollings and Kerrich 1999; Hollings et al., 1999; Smyk, 2013).

The North Rim metavolcanic unit forms the outer north to eastern edge of the NC (Figure 1.5) (Breaks et al., 1986). Like the South Rim unit, the North Rim metavolcanic unit is in tectonic contact with the underlying Keeyask Lake metavolcanic assemblage (Thurston et al., 1991). The North Rim also preserves a gradational contact with the overlying Eyapamikama Lake metasedimentary assemblage (Breaks et al., 2001). The main lithology in the North Rim unit is a massive, mafic tholeiitic metavolcanic rock (Breaks et al., 1986; Thurston et al., 1991). Minor metasedimentary lithologies include grunerite-quartz meta-iron formation, metapelites, feldspathic meta-arenites, garnetiferous metasediments and carbonate metasediments (Breaks et al., 2001).

The Forester-Weaganow metavolcanic unit is located on the eastern part of the NC (Figure 1.5) (Breaks et al., 1986). It is composed of pillowed, massive and amygdaloidal mafic and ultramafic metavolcanic rock (Breaks et al., 2001). Minor felsic metavolcanic units and the grunerite-magnetite-chert meta-iron formation are interbedded with the mafic and ultramafic metavolcanic lithologies (Breaks et al., 2001). This unit is also interpreted to be associated with oceanic volcanism (Thurston et al., 1991).

The Opapimiskan-Markop unit is located in the south-central portion of the NC, just south of Opapimiskan Lake (Figure 1.5). The Au producing Musselwhite property is located within the Opapimiskan-Markop unit and is the site location for the banded meta-iron formations in this thesis. Detailed stratigraphy, sedimentology and petrography of the units located on the Musselwhite

mine's property is presented in Chapter 3.4. Briefly the Opapimiskan-Markop unit is composed of metamorphosed ultramafic to mafic tholeiitic flows, silicate-oxide banded meta-iron formation and clastic metasedimentary lithologies (Breaks et al., 2001). Hollings and Kerrich (1999) used trace element geochemistry from the Opapimiskan-Markop lithologies and interpreted them to be associated with mantle derived, plume magmatism contaminated by impinging continental crust.

The Eyapamikama Lake metasedimentary assemblage displays a fining-upwards sequence starting from clast- to more commonly matrix-supported polymictic metaconglomerates, metasandstones and mudstones (deKemp, 1987). Stratigraphically, the Eyapamikama Lake metasedimentary assemblage overlies all the assemblages in the NC making it the youngest assemblage in the belt (Breaks et al., 2001). The southeast portion of the Eyapamikama metasedimentary assemblage has been termed the Zeemal-Heaton metasedimentary assemblage by various authors (Thurston et al., 1991; Duff, 2014; McNicoll et al., 2016; Bath, 2017) due to the differences in detrital zircon populations and the suggestion that from Nd isotopic work (Duff, 2014), the Zeemal-Heaton metasedimentary detritus was derived from proximal mid- to late-Neoarchean granitoids. The Eyapamikama Lake metasedimentary assemblage is interpreted to be an alluvial fan delta that grades into distal turbiditic deposits (deKemp, 1987). Metamorphic grade of the rocks in the Eyapamikama Lake metasedimentary assemblage ranges from mid-greenschist facies in the central area of the assemblage to mid-amphibolite facies near the margins (deKemp, 1987).

1.3.4 Shebandowan Greenstone Belt

The SGB is located within the north-western portion of the Wawa subprovince of the western Superior Province (Figure 1.2). The belt is bounded by the Quetico Fault and Quetico subprovince to the north and extends south-west towards the Vermilion assemblage in northern Minnesota, USA (Figure 1.6) (Williams et al., 1991; Corfu and Stott, 1998; Lodge, 2016). The Vermilion assemblage is

separated from the SGB by the Saganaga Tonalite (Lodge, 2016). Previously, the SGB was

interpreted to be comprised of three assemblages, the Burchell (metavolcanic) assemblage,

Greenwater (metavolcanic) assemblage and the Shebandowan (metasedimentary) assemblage

(Williams et al., 1991). Extensive mapping and zircon populations from felsic metavolcanic rocks in

the Burchell and Greenwater assemblages yielded U-Pb ages of approximately 2720 Ma (Corfu and

Stott, 1998). However, the north-western portion of the Burchell assemblage yielded an age of

about 2695 Ma, which is 25 m.y. younger than the southern metavolcanic rocks (Corfu and Stott,

1998). Therefore, Corfu and Stott (1998) grouped the southern part of the Burchell assemblage with

the Greenwater assemblage and renamed the younger metavolcanic rocks in the north-west the

Kashabowie assemblage. The metasedimentary rocks of the SGB have been divided into two

assemblages based on detrital zircon ages, the older 2690 Ma Shebandowan assemblage and the

younger ≤2683 ± 3 Ma Auto Road assemblage (Corfu and Stott, 1998). Plutonic rocks occur in the

Northern Light Perching-Gull batholithic complex, just south of the Greenwater assemblage as

isolated pockets distributed within the SGB (Corfu and Stott, 1998). Metamorphic grade ranges

from greenschist facies throughout the greenstone belt to localized lower amphibolite facies near

the contacts of the plutonic rocks (Morin, 1973; Osmani, 1997). Metavolcanic assemblages in the

SGB are interpreted to be subaqueous to subaerial arc-related volcanism (Williams et al., 1991).
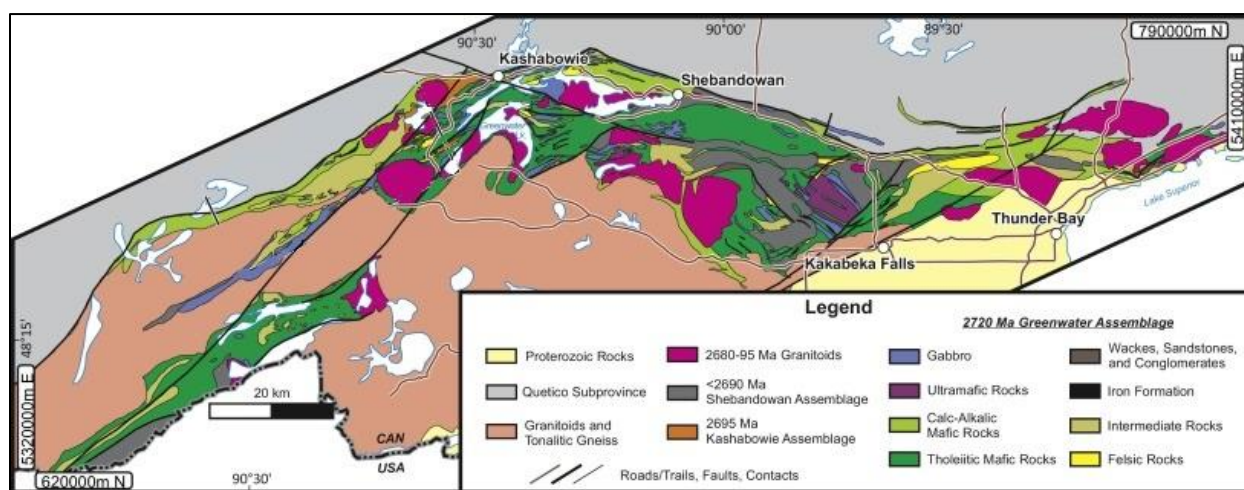
Figure 1.6: Geologic map of the SGB in the Wawa subprovince. Map sourced from Lodge (2016).

Stratigraphically, the basal sequence of the Greenwater assemblage consists of massive to pillowed tholeiitic and calc-alkaline metabasaltic flows (Williams et al., 1991; Osmani, 1997; Corfu and Stott, 1998). Metamorphosed andesite, dacite and rhyolite flows and metapyroclastic rocks occur near the top of the metavolcanic sequence (Williams et al., 1991; Osmani, 1997; Corfu and Stott, 1998). Minor magnetite-quartz meta-iron formation, basaltic metakomatiite and metakomatiitic flows have been reported in the Greenwater assemblage (Williams et al., 1991; Stott and Corfu, 1991; Osmani, 1997). The meta-iron formation in this thesis are from the Greenwater assemblage. Detailed outcrop descriptions, petrography and SEM/EDX mineral compositions of the meta-iron formation and associated meta-igneous rocks are found in Chapter 3.5.

1.4 Previous Work: Genesis of Iron Formations

Sedimentological, geochemical and isotopic research on Precambrian meta-iron formations has been conducted for many decades in order to interpret their provenance, depositional setting and the composition of the ancient atmosphere and ocean. The lack of modern, large-scale banded iron formation analogues in today's oceans makes it difficult to interpret the genesis of meta-iron formations (Bekker et al., 2014). The sheer volume and distribution of Archean banded meta-iron formations suggests that ocean and atmospheric systems operating in the Archean were very different than systems operating in the present. Thus, it is agreed that before 2.45 Ga, the average oxygen content of the atmosphere and ocean was anoxic (ex. Canfield, 1998; Holland, 2002; Bekker et al., 2004; Bekker et al., 2010; Schirrmeister et al., 2015, Ciborowski and Kerr, 2016). Multiple theories for provenance, depositional mechanism and post-depositional modifications of meta-iron formations are currently debated between geoscientists. A brief literature review of these theories will be discussed below.

Gross (1965) classified chemically precipitated meta-iron formation into four types based on lithological features, geologic setting and association with sedimentary facies. These four types have been subdivided into mainly aluminous or siliceous meta-iron formation (Gross, 1965). All the meta-iron formations in this study are siliceous, iron-oxide-chert meta-iron formations. Siliceous meta-iron formations have been subdivided into two groups: (1) Algoma-type and (2) Superior-type (Gross, 1965). Algoma-type meta-iron formations were deposited in deep water environments and locally associated with volcanic activity such as tuffs and flows (Gross, 1965). Precambrian Algoma-type meta-iron formations lack preserved sedimentary features and are several centimetres to tens of metres thick, rarely more than a few kilometers long (Gross, 1965). They are also associated with sedimentary lithologies indicative of deeper water environments, such as turbidites. Superior-type meta-iron formations were deposited on shallow water continental shelves or margins and were mainly Proterozoic in age (Gross, 1965). These meta-iron formations are laterally continuous for several kilometres and are thicker. Since that time, researchers have been using Algoma-type and Superior-type to discern between deep water and shallow water meta-iron formations. In this study meta-iron formations from the NC (Moran, 2008) and SGB have been interpreted to be Algoma-type, while the meta-iron formations from the BG and LSJ have been interpreted to be Archean Superior-type (Fralick and Pufahl, 2006).

Early research suggested that meta-iron formations were the result of limestone replacement (Dimroth, 1977). It was theorized that during early diagenesis, aragonite crystals ($CaCO_3$) were replaced by iron oxides and silica, producing banded meta-iron formation (Dimroth, 1977). However, Dimroth (1977) did not propose a source for the copious amounts of iron and silica required for carbonate replacement. Nevertheless, this research did suggest that element mobility was a major factor during meta-iron formation diagenesis. To date, element mobility during diagenesis has not been investigated extensively.

Another accepted theory is that iron and silica were precipitated out of the ocean as primary amorphous gels (Cloud, 1973; Drever, 1974). Iron was transported from its source, in solution as Fe^{2+} because it is more soluble than Fe^{3+} (Cloud, 1973; Holland, 1973; Bekker et al., 2014; Garcia, 2014). Oxidation of Fe^{2+} to the insoluble Fe^{3+} lead to the precipitation of iron oxyhydroxides onto the ocean floor (Cloud, 1973; Konhauser et al., 2002). However, the source of iron and silica for Archean banded meta-iron formations has been debated in the literature.

Overwhelmingly, the data from rare earth element geochemistry show depleted light rare earth element patterns and positive europium anomalies when normalized to Post Archean Australian Shale (PAAS) compositions (ex. Planavsky et al., 2010). Also, neodymium isotopic signatures on meta-iron formations show positive epsilon neodymium values (ex. Derry and Jacobsen, 1990). This evidence indicates that hydrothermal venting fluids were the provenance for the majority of iron (Cloud, 1973; Holland, 1973; Derry and Jacobsen, 1990; Peter, 2003; Hamade et al., 2003; Bekker et al., 2014). It has been also suggested continental weathering (James, 1954; Garrels et al., 1973) as the source of iron, although this source is considered minor relative to hydrothermal venting.

In modern oceans, organisms such as diatoms, radiolaria and sponges use dissolved silica in the oceans to form their skeletons. When these organisms die, their skeletons settle on the ocean floor and form chert during diagenesis. The lack of preserved silica-secreting fossils in Precambrian rock suggests an inorganic provenance for chert (Siever, 1992; Perry and Lefticariu, 2007). Without biological evidence for the removal of silica from the oceans, it is also theorized that seawater concentrations of silica were higher in the Precambrian (60 ppm silica), than in present-day oceans (<1 - 15 ppm silica) (Siever, 1992).

Two main theories for the inorganic source of silica in the Precambrian include continental runoff and hydrothermal venting. Hamade et al. (2003) used Ge/Si ratios in chert bands from the

Hamersley Group meta-iron formation to determine the provenance for silica. They concluded that low Ge/Si ratio values, similar to modern day values, reflect a dominant continental source for silica. More recent research suggests that fractionation of Ge relative to Si could occur under multiple different geologic processes unrelated to the source of silica (Bekker et al., 2014). Silicon isotope work on chert-dominated meta-iron formation layers have yielded negative to low positive δ^{30}Si values similar to values from present day white smoker hydrothermal venting fluids (ex. Andre et al., 2006; Steinhoefel et al., 2009; Heck et al., 2011; Li et al., 2014). Therefore, it is theorized that like iron, silica is derived from hydrothermal venting fluids.

Although the deposition of iron oxyhydroxides as the primary mode of deposition is accepted by most geoscientists (ex. Cloud, 1973), the mechanism for the iron oxidation reaction is still debated. Three main theories for this oxidation reaction are (1) ultraviolet photooxidation, (2) photosynthetic bacterial oxidation (3) metabolic iron oxidation.

Photooxidation has been proposed as a viable non-biological iron oxidation mechanism for Archean banded meta-iron formations. Cairns-Smith (1978) suggested that high energy ultraviolet rays irradiated Fe^{2+} ions in seawater. This photon energy was absorbed by Fe^{2+} ions causing them to oxidize to Fe^{3+} (Cairns-Smith, 1978). Due to the insolubility of Fe^{3+}, a hydrolysis reaction occurred forming iron oxyhydroxides (Cairns-Smith, 1978). Photooxidation rate calculations indicate that the ultraviolet photooxidation mechanism alone could account for all the Fe^{3+} in Precambrian meta-iron formations (Cairns-Smith, 1978; Braterman et al., 1983; Braterman and Cairns-Smith, 1987). Konhauser et al. (2007) conducted experiments and used thermodynamic models to determine if photooxidation could have been the primary mechanism for meta-iron formation deposition. The experiments showed that Fe^{2+} would react with silica and precipitate as iron silicates faster than photooxidation of Fe^{2+} to Fe^{3+} (Konhauser at al., 2007). Therefore, the mechanism for iron oxidation

needs to be quicker than the formation of Fe^{2+} silicates. Experiments conducted with Fe^{2+} oxidizing

microorganisms indicated that biologic oxidation occurs more rapidly than photooxidation, allowing

iron oxyhydroxides to form faster than the Fe^{2+} silicates (Konhauser et al., 2007). Also, Fralick and

Pufahl (2006) noted, photooxidation should occur at the ocean-atmosphere interface regardless of

ocean depth. There are occurrences within Archean greenstone belts where shallow water

sedimentary facies have abundant meta-iron formations and adjacent deep-water sedimentary

facies lack meta-iron formations (Fralick and Pufahl, 2006). This indicates that the iron oxidation

mechanism for the precipitation of iron oxyhydroxides was dependent on water depth (Fralick and

Pufahl, 2006). Littoral zones associated with river mouths have access to sunlight and a source for

nutrient influx (Fralick and Pufahl, 2006). This environment is ideal for hosting aerobic

photosynthetic bacterial communities capable of iron oxidation either by oxygenic or anoxygenic

processes. Therefore, it is theorized that there is a shallow water biologic mechanism responsible

for some meta-iron formation deposition.

The idea of a biologic iron oxidation mechanism for the deposition of meta-iron formations has

been discussed in the literature for several decades. The presence of possible relict microfossils in

Precambrian meta-iron formations (Cloud and Licaru, 1968; LaBerge, 1973; Dodd et al., 2017) and

the abundance of interpreted stromatolite structures preserved in sedimentary rocks older than

2500 Ma (ex. Schopf et al., 2007) suggests that microorganisms were flourishing in the Archean. The

debate is whether these microorganisms produced biologic oxygen or metabolized iron to oxidize it.

The possibility for biologically generated photosynthetic oxygen before the Great Oxidation

Event ($\sim$2.45 – 2.32 Ga) has been preserved in the Archean rock record (Fru et al., 2016). Geological

biomarker derivatives from fluid inclusion oils in kerogens found in the 2.45 Ga McKim Formation

are almost exclusively produced by photosynthetic cyanobacteria (Buick, 2008). Buick (2008)

suggested that the lack of pyrite relative to kerogens in the 3.2 Ga Gorges Creek Group black shales indicates a photosynthetic oxygen origin. Buick (2008) argues that iron sulphides would be as abundant as the kerogens, if anoxygenic bacteria was the organic material in these shales. If the above evidence represents the production of photosynthetic oxygen via photoautotrophic bacteria in the Archean, then an oxygen redoxcline would have been established between the shallow water and deep-water environment. Due to the lack of bacterial mat structures preserved in meta-iron formations, it is theorized that these organisms were planktonic photosynthesizing bacteria (Fralick and Pufahl, 2006). These organisms thrived in shallow water environments where sunlight and an abundance of nutrients from rivers were accessible. Storm events caused an upwelling of iron-rich deep waters to the oxygenated shallow water environment. These waters flooded the tops of shallow water sedimentary rocks causing iron to precipitate out as iron oxyhydroxides (Cloud, 1973; Fralick and Pufahl, 2006).

Metabolic microbial iron oxidation is also theorized to be a mechanism for meta-iron formation deposition. There are three main mechanisms proposed for metabolic microbial iron oxidation: microaerophilic oxidation, anoxygenic photosynthesis and nitrate dependent oxidation (Bekker et al., 2014). Microaerophilic bacteria, such as *Gallionella ferruginea*, take in CO_2 and Fe^{2+}, use oxygen as their electron acceptor forming organic carbon and Fe^{3+} (Bekker et al., 2014). Significantly, these bacteria can thrive in low oxygenic environments and can oxidize iron 50 times faster than abiotic iron oxidation (Bekker et al., 2014). Anoxygenic photosynthetic bacteria, such as various purple and green bacteria, use Fe^{2+} instead of water as an electron donor as a reductant for CO_2 fixation, producing Fe^{3+} rather than O_2 (Bekker et al., 2014). Lastly, nitrate dependent metabolic iron oxidation, uses nitrate to oxidize Fe^{2+} to Fe^{3+}. However, most nitrate-reducing iron oxidizing bacteria need an organic substrate provided by another bacterial species and laboratory experiments with just nitrate-reducing iron oxidizing bacteria have not yielded iron oxidation without the organic

substrate. Both oxygenic photosynthesis by cyanobacteria and metabolic microbial oxidation are viable iron oxidation mechanisms responsible for the deposition of meta-iron formations.

Many theories for the cyclicity of banded meta-iron formations have been proposed in the literature. These theories include the deposition of hydrothermal muds with iron oxyhydroxides via density currents (ex. Krapež et al., 2003), adsorption of silica during iron oxyhydroxide deposition (ex. Fischer and Knoll, 2009), differences in the physiology of the hydrothermal vent (ex. Fralick et al., 1989) and the evaporative deposition of chert (ex. Drever, 1974).

Krapež et al. (2003) proposed that iron oxyhydroxides were deposited with granular iron-oxide rich hydrothermal muds via density currents driven by density currents or gravity flows, similar to turbidite deposits. Chert replaced the hydrothermal muds before burial compaction and formed silica-dominated layers (Krapež et al., 2003). However, if the precursor minerology for the silica-dominated layers were hydrothermal muds, then the aluminum content for the silica-dominated layers would be much higher than the iron-oxide dominated laminae, which is not seen in many meta-iron formations.

Fischer and Knoll (2009) proposed that during the precipitation of iron oxyhydroxides at the oceans surface, silica adsorbed on the surfaces of the iron oxyhydroxides along with organic matter and both were deposited on the ocean floor. To form the silica-dominated layers, Fe^{3+} respiration occurred causing the iron to re-dissolved into the ocean leaving the chert deposited as chert-dominated layers (Fischer and Knoll, 2009). During iron-oxide diagenesis, silica was liberated from the iron oxyhydroxide surface and deposited in the pore spaces of the iron oxide-dominated layers (Fischer and Knoll, 2009). However, silica-dominated layers are laterally extensive and the efficiency and inefficiency of Fe^{3+} respiration to create cm thick chert-dominated layers followed by a cm-thick iron oxide-dominated layers, respectively seems unlikely. Some believe that the cyclicity is strictly

due to the physiology of the hydrothermal vent. Hydrothermal dormancy and current reorganization is thought to be responsible for the layered bands (Fralick et al., 1989; Konhauser et al., 2005; Moran, 2008). In both cases, it is assumed that the hydrothermal vent supplies the iron and that the oceans are saturated with silica. When hydrothermal venting is active, iron-rich layers are deposited. When the venting stops or the current changes the flow of the venting fluid, silica-rich layers are deposited.

Fralick et al. (1989) and Moran (2008) suggested a temperature dependent factor for the cyclicity of the bands. As iron-rich layers are deposited from high temperature black smokers, the layers clog up the faults which act as conduits for seawater to the magma source. By blocking the flow of seawater, the flow of the whole system is suppressed, and the temperature of the fluids decreases. This causes the formation of lower temperature white smokers which are enriched in Ba, Si and Ca. Reactivation of faults causes the flow to resume increasing the temperature of the fluids and producing black smokers (Fralick et al., 1989). However, Fuchida et al. (2014) sampled black smoker and white smoker hydrothermal fluids that were proximal to each other and recorded similar temperatures (270°C and 243°C) suggesting that black and white smoker activity could be active at the same time at similar temperatures.

Since there is no direct evidence of silica-secreting organisms in the Archean, it is theorized that silica concentrations were higher in the Archean oceans than the present day (Siever, 1992). As dissolved silica concentrations were probably higher in the Archean, some scientists believe that silica might have been precipitating continuously through evaporative processes (ex. Drever, 1974). The chert bands were caused by dormancy of black smoker hydrothermal venting, while the iron oxide-dominated layers were deposited during high amounts of black smoker hydrothermal activity. This theory works well with the studies conducted by Li (2014) on multiple meta-iron formations

across the world, suggesting that the cyclicity of the bands reflects a diurnal precipitation of iron

oxyhydroxide and an annual deposition of silica. Due to the abundance of chert deposits in

Precambrian shallow water deposits (Maliva et al., 1989), it is theorized that the evaporative silica

precipitation theory was the mechanism for deposition in the shallow water meta-iron formations.

It is widely theorized that iron oxide-dominated bands in meta-iron formation are formed during

early diagenesis (ex. Drever, 1974; Klein, 2005; Konhauser et al., 2005; Posth et al., 2013). During

diagenesis, the abundance of organic carbon dictates which iron phase is formed. Iron

oxyhydroxides with low levels of organic carbon will undergo a dehydration reaction forming

hematite ($(Fe^{3+})_2O_3$) and volatiles (Drever, 1974; Konhauser et al., 2005). Higher levels of organic

carbon with iron oxyhydroxides will generate a redox reaction forming magnetite ($(Fe^{3+})_2(Fe^{2+})O_4$)

and volatiles (Drever, 1974). The source of organic carbon in the meta-iron formation is theorized to

be the result of deposition and decomposition of dead microorganisms from the ocean (Posth et al.,

2013). Experimental work on the effects of iron oxyhydroxide diagenesis supports the theory

discussed above (Posth et al., 2013).

CHAPTER 2

METHODOLOGY

2.1 Sample Collection

Samples of meta-iron formation and associated lithologies were gathered from each of the four

site locations for petrography and geochemical analyses. In the BG, samples were taken from

several outcrop locations. Meta-iron formation samples from Solomon's Pillar, Geraldton and Spawn

Lake were collected by Dr. Philip Fralick in 2005. Samples along the Highway 580 outcrops were

gathered by the author during the 2016 summer field season. Meta-iron formation and associated

siliciclastic samples in the LSJ were obtained by Dr. Philip Fralick from Eagle Island in 2003. Samples

of meta-iron formation from Musselwhite Mine were collected by Patrick Moran for his 2008

Master's thesis. Meta-iron formation and associated meta-igneous lithologies from the SGB were

gathered by the author during the summer 2016 field season.

2.2 Geochemical Analysis

Fifty-six meta-iron formation samples were used for geochemical analyses. Samples from the

NC, LSJ and parts of the BG were crushed and powdered earlier by Patrick Moran and Dr. Philip

Fralick. Samples from SGB and the Highway 580 outcrops were cut in a lapidiary facility at Lakehead

University. All the samples were carefully cut along their individual phase-dominated laminae. These

laminae were categorized by their dominant minerology. The classification scheme includes:

magnetite-dominated, hematite-dominated, grunerite-magnetite-dominated, jasper-dominated and

chert-dominated meta-iron formation. A tungsten carbide mallet and plate were used to crush the

individual layers into <1 mm grains. These grains were subsequently crushed into powders in an

agate mill.

All major oxide elements (Al_2O_3, TiO_2, Fe_2O_{3T}, MnO, MgO, CaO, Na_2O, K_2O, P_2O_5), except Si, were

analysed by an Inductively Coupled Plasma Atomic Emission Spectrometer (ICP-AES) at Lakehead

University, Thunder Bay, Ontario. Samples from the NC, LSJ and parts of the BG were sent to OGS

Geoscience Laboratories in Sudbury, Ontario for minor, trace and rare earth element (REE)

concentrations. Minor, trace and REE data for the Highway 580 outcrops and SGB samples were

analysed using an Inductively Coupled Plasma Mass Spectrometer (ICP-MS) at Lakehead University,

Thunder Bay, Ontario. OGS Geoscience Laboratories also determined ferrous and ferric iron content

using potentiometric titration with standardized permanganate. Only samples greater than 5.0

grams of powder were sent to Geoscience Laboratories. All the samples and their corresponding

analysis locations are listed in Table 2.1.

Powdered samples analyzed at Lakehead University were subjected to a hot acid digestion. The

procedure for the acid digestion is described below. The digestion spanned a total of five days. The

standard practice for hot acid digestions at Lakehead University is that on day one, samples are

placed in Teflon beakers and are weighed to 0.5000 grams. However, the iron did not completely

dissolve at a 0.5000-gram sample weight. Therefore, a smaller sample weight (0.0500 grams) was

chosen for all analyzed samples, including the standards, to ensure a complete dissolution. For ICP-

MS a sample weight of 0.0500 grams would be too small, causing most of the concentrations to fall

below detection limits. Therefore, the digestion was performed once again at a sample weight of

0.1500 grams for ICP-MS. Three blanks and two standards were used during the entire dissolution

process to determine precision and accuracy of the analysis. Two USGS standards were chosen for

geochemistry, QLO-1a which is a quartz latite and BHVO-2 which is a Hawaiian basalt. Each Teflon

beaker was filled with 10 mL of double distilled water and 5 mL of nitric acid to eliminate excessive

carbonate. These samples were placed on a hot plate set at a temperature of 90°C until the liquid

was completely evaporated. Once the samples were dry, 5 mL of hydrofluoric acid and 10 ml of

nitric acid was poured into each beaker. Samples were placed back on the hot plate overnight until evaporation was complete. This step was repeated three times to ensure the full dissolution of silica-bearing minerals. On the fifth day, 2 mL of nitric acid was added, and the beakers were placed on the hot plate to simmer for 20 minutes. Next, the beakers were filled with 10 mL of double distilled water and were left to simmer for another 10 minutes. The beakers were then transferred to a 100 mL volumetric flask and placed back on the hot plate for two hours. After the two hours, the beakers were taken off the hot plate, cooled and filled to 100 mL with double distilled water. For ICP-AES, the digest was transferred to 50 mL plastic vials. For ICP-MS, the digest was transferred to a 50 mL plastic vial where it was filled with 10 mL of digest and 40 mL of 2% nitric solution. The dilution factor for the ICP-AES analyses was 2000, while the dilution factor for the ICP-MS analysis was 3333.

Samples sent to Geoscience Laboratories in Sudbury were analyzed on a Perkin-Elmer Elan 9000 ICP-MS following a variation on the protocol described by Burnham and Schweyer (2004) and Tomlinson et al. (1998). A two-stage procedure was used to digest the samples. First, 200 mg of powder was measured. Samples were then digested by a mixture of HF with lesser amounts of HCl and HClO4 in a closed beaker. A secondary mixture of dilute HCl and HClO4 was added to the samples as described by Burnham et al. (2004).

Table 2.1: List of all the samples analyzed for the geochemical analysis. All major element data was analyzed at Lakehead University. Minor, trace and REE data for the samples collected by the author were analyzed at Lakehead University. The rest of the samples were analyzed at OGS Geosciences Laboratories in Sudbury to determine minor, trace and REE data.

Dominant Iron Formation Phase	Sample Number	Lakehead ICP-AES	Lakehead ICP-MS	Geoscience Laboratories ICP-MS	Iron Titrimetry
Beardmore/Geraldton Greenstone Belt					
Magnetite	06-28	Yes	-	Yes	Yes
Magnetite	03-07	Yes	-	Yes	Yes
Magnetite	05-93	Yes	-	Yes	Yes
Magnetite	06-27	Yes	-	Yes	Yes
Magnetite	03-8	Yes	-	Yes	Yes
Magnetite	B0302 M	Yes	Yes	-	-
Magnetite	B0303 M	Yes	Yes	-	-
Magnetite	B0304A M	Yes	Yes	-	Yes
Magnetite	B0304B M	Yes	Yes	-	Yes
Magnetite	B0305 M	Yes	Yes	-	Yes
Magnetite	B0309 M	Yes	Yes	-	Yes
Hematite	B02 S	Yes	Yes	-	-
Hematite	B03 S	Yes	Yes	-	-
Hematite	B04 S	Yes	Yes	-	Yes
Hematite/Jasper	BSL3 HS	Yes	Yes	-	Yes
Jasper	06-25	Yes	-	Yes	Yes
Jasper	06-26	Yes	-	Yes	Yes
Jasper	03-14	Yes	-	Yes	Yes
Jasper	05-91	Yes	-	Yes	Yes
Jasper	03-16	Yes	-	Yes	Yes
Jasper	05-90	Yes	-	Yes	Yes
Jasper	B01 H	Yes	Yes	-	-
Jasper	B02 H	Yes	Yes	-	Yes
Jasper	BIFI H	Yes	Yes	-	Yes
Lake St Joseph Greenstone Belt					
Magnetite	03-118	Yes	-	Yes	Yes
Magnetite	03-85	Yes	-	Yes	Yes
Magnetite	03-83	Yes	-	Yes	Yes
Hematite	03-88A	Yes	-	Yes	Yes
Hematite	03-88B	Yes	-	Yes	Yes
North Caribou Greenstone Belt					
Magnetite	PM05-39	Yes	-	Yes	Yes
Magnetite	PM05-28A	Yes	-	Yes	Yes
Magnetite	PM0540A	Yes	-	Yes	Yes
Magnetite	PM05-31A	Yes	-	Yes	Yes
Magnetite	PM05-21	Yes	-	Yes	Yes
Magnetite	PM05-37	Yes	-	Yes	Yes
Magnetite	PM05-38A	Yes	-	Yes	Yes
Magnetite/Grunerite	PM05-63	Yes	-	Yes	Yes
Magnetite/Grunerite	PM05-64	Yes	-	Yes	Yes
Magnetite/Grunerite	PM05-40B	Yes	-	Yes	Yes
Magnetite/Grunerite	PM05-31B	Yes	-	Yes	Yes
Chert	PM05-06	Yes	-	Yes	Yes
Chert	PM05-38B	Yes	-	Yes	Yes
Chert	PM05-28B	Yes	-	Yes	Yes
Chert	PM05-12	Yes	-	Yes	Yes
Chert	PM05-18	Yes	-	Yes	Yes
Shebandowan Greenstone Belt					
Magnetite	SHO6 M	Yes	Yes	-	Yes
Magnetite	SH07 M	Yes	Yes	-	Yes
Magnetite	SH018 M	Yes	Yes	-	Yes
Magnetite	SH027 M	Yes	Yes	-	Yes
Jasper	SH09 H	Yes	Yes	-	-
Jasper	SH018 H	Yes	Yes	-	-
Jasper	SH022 H	Yes	Yes	-	-
Jasper	SH027 H	Yes	Yes	-	-
Chert	SH07 C	Yes	Yes	-	Yes
Chert	SH010 C	Yes	Yes	-	Yes
Chert	SH016 C	Yes	Yes	-	Yes

2.3 Petrography and SEM/EDX Analysis

Samples of meta-iron formation and associated lithologies were cut for both reflected and transmitted light petrography to examine microstructures, determine the compositions of the mineral phases and determine metamorphic grade. Thin section descriptions are summarized in Chapter 3. Both reflected and transmitted light microscopy was conducted to identify the mineral phases within the meta-iron formation and associated lithologies. Quantitative SEM/EDX point analyses were conducted to determine the end member compositions of each abundant (>30%), common (29% – 10%) and minor (9% - 1%) phases. The compositions for most of the trace (<1%) phases in the samples were calculated semi-quantitively, to determine their relative composition. However, their formulas were not constructed. Unfortunately, rock samples or thin sections from NC were not available. Therefore, petrography and SEM/EDX point analyses were not conducted for the NC samples. Thin section work conducted by Moran (2008) on the meta-iron formations at Musselwhite Mine will be summarized in Chapter 3.4.

Sixteen thin sections were chosen for detailed analysis by standard petrographic methods, back-scattered electron (BSE) imagery and energy dispersive X-ray spectrometry. The Hitachi SU-70 Schottky Field Emission SEM was used to conduct quantitative analyses of the phases, with a 15 mm working distance and an accelerating voltage of 20 kV via the Oxford Aztec 80 mm/124 EV electron dispersive X-ray spectrometer (EDX) equipped on the SEM. All thin sections were coated with a 10 µm thin layer of carbon before use on the SEM. The following well characterized mineral and synthetic standards were used for calibration of the SEM: jadeite (Na, Al); wollastonite (Ca, Si); orthoclase (K); ilmenite (Fe, Ti); periclase (Mg); Mn-hortonolite (Mn) and apatite (P). Point analyses were conducted on cores of mineral phases to determine the major element compositions of each phase within the meta-iron formation and associated lithologies. Several phases within a lithology

were analyzed to get an average composition for the mineral phase. In total, 682 point analyses

were conducted. Raw data was then converted into stoichiometric coefficients to determine mineral

formulas and end member compositions using the Deer et al. (1992) method. Since lithoprobe

analyses calculated all iron as FeO, the Droop (1987) equation was used to estimate the Fe^{3+}

concentrations for magnetite. For hematite, all FeO was assumed to be Fe_2O_3. Stilpnomelane was

calculated by assuming all crystals had 21 oxygens and six hydroxides in their empirical formula.

Refer to Appendix A for SEM data.

CHAPTER 3

DETAILED SEDIMENTOLOGY OF THE META-IRON FORMATIONS

3.1 Introduction

The objective of this chapter was to discuss the similarities and differences between meta-iron

formations from deep and shallow depositional environments. This was achieved by analyzing the

meta-iron formation at the macroscopic and microscopic scales, determining which mineral phases

host each major element and determining the grade of metamorphism. Outcrop descriptions from

BG, LSJ and NC were summarized from work conducted by previous sedimetologists, while a

detailed transect was conducted by the author for SGB. Petrography and SEM/EDX mineral

chemistry calculations from BG, LSJ and SGB were conducted by the author, while petrography

conducted by Moran (2008) for NC was summarized.

3.2 Beardmore-Geraldton Belt

3.2.1 Outcrop Descriptions

BG meta-iron formation samples were collected from the SMB and CMB. Metasedimentary

lithologies in the SMB are subdivided into four main lithofacies associations proposed by Barrett and

Fralick (1989). The first lithofacies is categorized as the meta-iron formation lithofacies association

(IFLA), and is divided into a-type, b-type, c-type and d-type meta-iron formations (Barrett and

Fralick, 1985; 1989) (Figure 3.1, 3.2). These subdivisions are based on the relative thickness of the

meta-iron formation and the associated siliciclastic material. A-type meta-iron formations are

dominated by magnetite-rich, hematite-rich or jasper-rich layers with interbedded mm- to cm-,

graded to ungraded metasiltstone (Figure 3.1B). Graded to sharply bounded metasiltstone with

separated or contiguous mm-thick iron oxide-dominated layers constitute the b-type meta-iron

formation (Figure 3.1C). C-type meta-iron formations are dominated by medium- to coarse-grained metasandstone interbedded with mm- to cm-thick iron oxide-dominated layers (Figure 3.1D). Polymictic metaconglomerates with interbedded metasandstone and meta-iron formation of varying thicknesses dominate the d-type meta-iron formation (Barrett and Fralick, 1985; 1989; Fralick and Barrett, 1991; Smyk et al., 2005; Fralick and Pufahl, 2006).
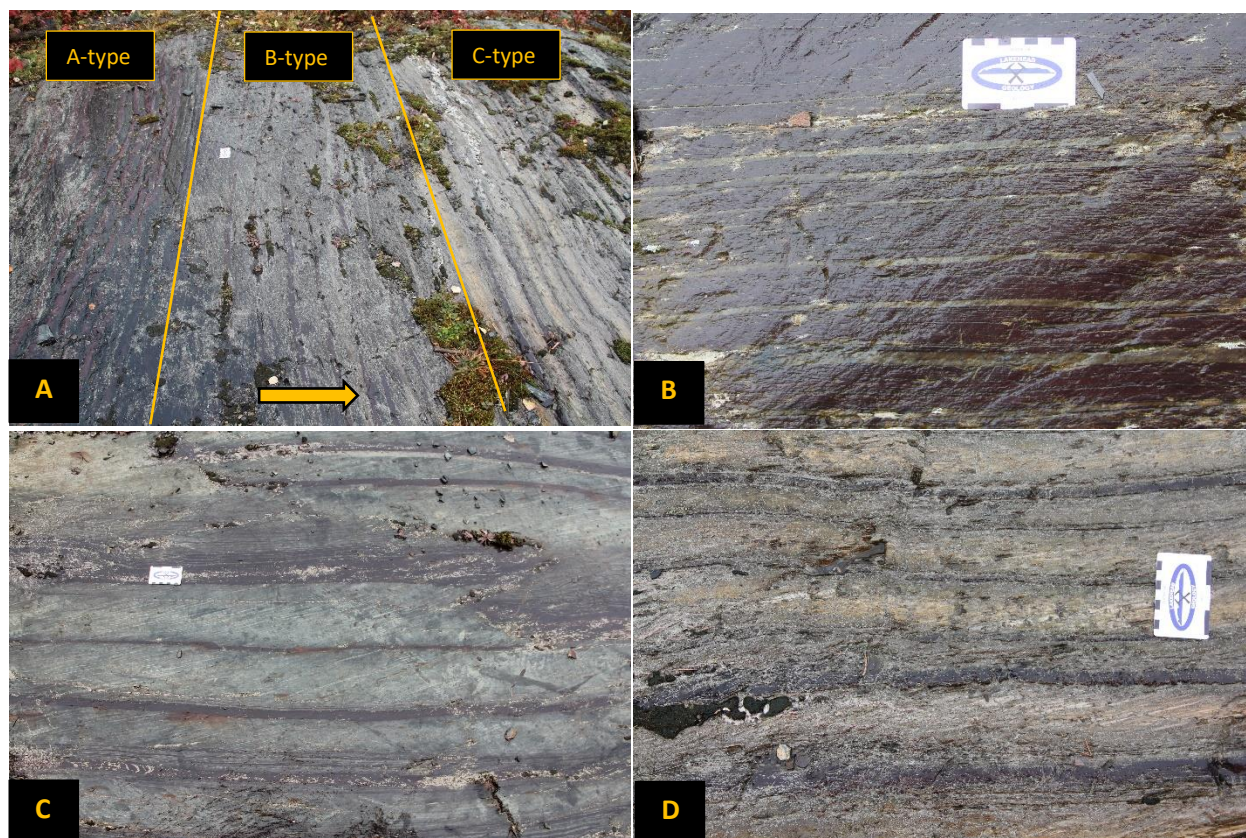
Figure 3.1: Outcrop-scale photographs of IFLA in BG. A) A coarsening-upwards progression from the a-type to c-type meta-iron formation. B) Photograph of the a-type meta-iron formation. Centimetre-thick hematite-jasper meta-iron formation interbedded with mm- to cm-scale metasiltstone layers. C) Photograph of the b-type meta-iron formation. Millimetre- to centimetre-thick hematite-jasper meta-iron formation interbedded with parallel stratified medium- to coarse-grained, mm- to cm-thick metasiltstone. Note the increase of interbedded siliciclastic material relative to the a-type meta-iron formation. D) Photograph of the c-type meta-iron formation. Medium- to coarse-grained, parallel stratified, cm-thick metasandstone beds interbedded with mm- to cm-thick hematite-jasper meta-iron formation.

Lithofacies association 2 (LA2) contains graded metasiltstone and metasandstone beds up to 10 cm thick. The tops of the beds are composed of thinly bedded, alternating bands of metasiltstone and metamudstone. The meta-iron formation occasionally occurs between metasiltstone and metamudstone layers. This lithofacies either thins and fines upwards over several metres or displays

no vertical trend. This lithofacies is interpreted to be graded turbidites deposited on the distal

submarine fan and ramp (Barrett and Fralick, 1989).

Lithofacies association 3 (LA3) is composed of a fining- and thinning-upwards trend of coarse- to

medium-grained metasandstone with flat bases and tops. Centimetre scale couplets of medium-

grained and fine-grained metasandstone occur in this lithofacies association as well as parallel-

laminated metasandstone, which only occurs within tops of the beds. Significantly, there is no meta-

iron formation within LA3. The coarse- to medium-grained metasandstones are interpreted to be

tectonically triggered, sheet-like gravity flows and slumps along a steep and narrow submarine

margin and the metasandstone couplets are interpreted to be turbidites deposited on submarine

fan lobes (Barrett and Fralick, 1989).

The basal portion of the beds in lithofacies association 4 (LA4), is composed of less than 10 – 20

cm thick, coarse-grained to pebble metasandstone. The coarse-grained to pebble metasandstone is

overlain by structureless medium- to coarse-grained metasandstone. This section also includes rip

up clasts of scattered fine-grained metasandstone. The lower parts of these beds show cm-scale

reverse grading and the upper portion has cm-scale normal grading. Although, rare parallel

lamination occurs in the upper portion. The sandy portion of the beds is about 6 – 7 m thick. The

next lithologies are less than 10 – 50 cm thick and contain metasiltstone to fine-grained

metasandstone. The transition from the central lithology to the upper lithology is abrupt. This

lithofacies is interpreted to be thick grain flows filling feeder channels along the mid slope (Barrett

and Fralick, 1989).

Previous studies on the meta-iron formations in the BG have suggested that deposition of iron

formation occurred in a submarine fan, distal-fan ramp and basin plain environments during low

siliciclastic sedimentation rates due to operation of a channel bypass system (Barrett and Fralick,

1989). However, the meta-iron formation occurs stratigraphically high in the SMB and there is evidence of conglomerates erosionally scouring thin layers of iron oxides facies (IFLA d-type meta-iron formation), indicating that subaerial processes were interacting with the meta-iron formation, which cannot happen in a deeper water environment (Fralick and Pufahl, 2006). The metaconglomerates with metasandstone of the IFLA d-type meta-iron formation are interpreted to be a distributary bar complex (Fralick and Pufahl, 2006). During sea level rise and resultant low sedimentation rates on the delta, the shoreline delta was flooded out and meta-iron formation was precipitated on top of siliciclastic units (Fralick and Pufahl, 2006). High siliciclastic sedimentation rates and or a drop in sea level would cause the distributary bar to scour and deposit on top of the meta-iron formation (Fralick and Pufahl, 2006). Therefore, the current model indicates that the meta-iron formation in the BG was deposited in a near shore deltaic environment, which rapidly transitioned offshore to a turbidite ramp/fan.

The grade of metamorphism in BG increases from west to east (Stinson, 2013). Lithologies in Beardmore were subjected to lower greenschist facies metamorphism, while the metamorphic grade ranges from greenschist to amphibolite facies in Geraldton (Stinson, 2013). Lithologies in Longlac were subjected to amphibolite facies metamorphism, while the metamorphic grade
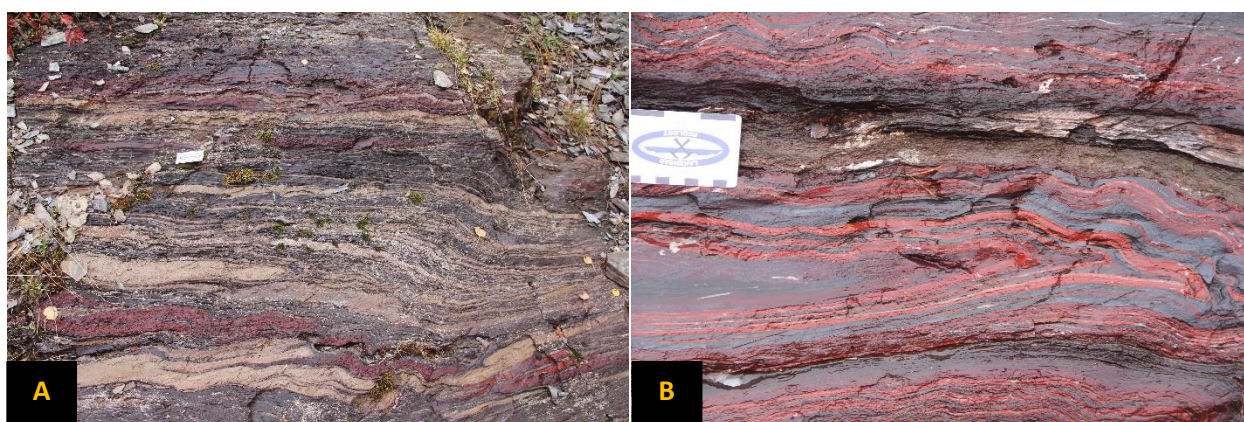
Figure 3.2: Outcrop-scale deformation structures of hematite-jasper meta-iron formation in BG. A) Deformed c-type hematite-jasper meta-iron formation. S- and Z-type fold structures and boudinaged layering can be seen with the metasandstone unit. B) Isoclinal folding of the hematite-jasper meta-iron formation. Purple layers are hematite-dominated meta-iron formation, while bright red layers are jasper-dominated meta-iron formation.

increases to granulite facies in Caramat (Stinson, 2013). Therefore, the meta-iron formations in the

BG have been subjected to different peak temperatures of metamorphism. Outcrop scale

deformation structures present in the meta-iron formation include: S-, Z- and M-type folds, isoclinal

folding and boudinaged lithologies (Figure 3.2).

3.2.2 Petrographic Descriptions and Mineral Compositions

The BG meta-iron formations from the IFLA lithofacies association are composed of two main

units: clastic and chemical metasedimentary units. The clastic metasedimentary lithologies can be

divided into two types: metasandstones and metasiltstones. There are three types of chemical

metasedimentary units in BG: hematite-jasper meta-iron formation, magnetite-quartz meta-iron

formation and iron oxide-quartz meta-iron formation. The iron oxide-quartz meta-iron formation

contains both magnetite and hematite. Detailed descriptions from reflected and transmitted light

petrography for the five main lithologies will be summarized below. SEM/EDX point analyses were

also conducted on several phases within the BG metasedimentary units to determine endmember

mineral compositions. Raw data from the SEM/EDX analysis is provided in Appendix A. Table 3.1

shows the approximate modal abundances of mineral phases in the metasedimentary unit based on

reflected, transmitted light petrography and SEM/EDX point analyses.

Table 3.1: Approximate modal percentages for the phases in the lithologies from BG.

Beardmore/Geraldton Greenstone Belt																				
Lithologies	Ap	Apy	Bt	Brt	Cb	Chl	Chr	Cld	Hem	Ilm	Mag	Ms	Pl	Py	Qtz	Rt	Sch	Stp	Tur	Zr
Metasandstone	T			T	M	M	T					A	C	T	A	T				T
Metasiltstone	T		T			M	T	T	T			A	C	T	C	T			T	T
Hematite-jasper meta-iron formation	M			M	M	T			A			M			C					
Magnetite-quartz meta-iron formation	M	T		T	M	M				T	A		C	T	C	T	T	T		
Iron oxide-quartz meta-iron formation	T				C	C			C	T	A	M	C			C	T			
Modal Percentages: >30% (A - abundant), 10 - 29% (C - common), 1 - 9% (M - minor), <1% (T - trace)																				

Metasandstone

The bulk mineralogy of the metasandstone unit includes abundant quartz, muscovite, with common occurrences of plagioclase, minor amounts of chlorite, carbonate minerals and trace amounts of apatite, rutile, barite, chromite, pyrite and zircon (Table 3.1, Figure 3.3). The main differences between the metasandstone and metasiltstone layers is that the grainsize for the phases in the metasandstone are coarser-grained and the abundance of micas in the metasiltstone is much higher than the metasandstone.

Quartz is anhedral, fine- to medium-grained (<0.1 mm – 1.0 mm) and mostly composed of angular crystals. However, some quartz is lozenge-shaped and their long axes are parallel to the overall foliation. The coarser-grained, lozenge-shaped crystals show deformation structures such as sigma and delta porphyroclasts, subgrain formation and undulatory extinction. Finer-grained quartz occurs along strain shadows of coarser plagioclase and quartz porphyroclasts. Muscovite is fine-grained (<0.1 mm – 0.1 mm), has a lattice and dimension preferred orientation, which defines the foliation of the rock. Muscovite crystals also wrap around quartz and plagioclase porphyroclasts. Plagioclase is fine-grained (<0.1 mm – 0.8 mm) and like quartz, forms angular, subhedral porphyroclasts. Polysynthetic twinning can be seen in the porphyroclasts and many plagioclase crystals show sericite alteration. Chlorite is fine-grained (<0.1 mm – 0.1 mm), defined the foliation with muscovite and occurs in strain shadows of the quartz and plagioclase porphyroclasts. Carbonate minerals are usually fine-grained (<0.1 mm – 0.2 mm), but can form crystals up to 0.5 mm. These minerals occur along grain boundaries of quartz and plagioclase crystals, in strain shadows of quartz and plagioclase porphyroclasts or sporadically throughout the rock, not defining a preferred crystallographic orientation. Like the carbonate minerals, apatite occurs sporadically throughout the rock as fine-grained (<0.1 mm) high relief, clear crystals. Trace amounts of rutile,

barite, zircon, chromite and pyrite are fine-grained (<0.1 mm) and occur sporadically throughout the

metasandstone unit.
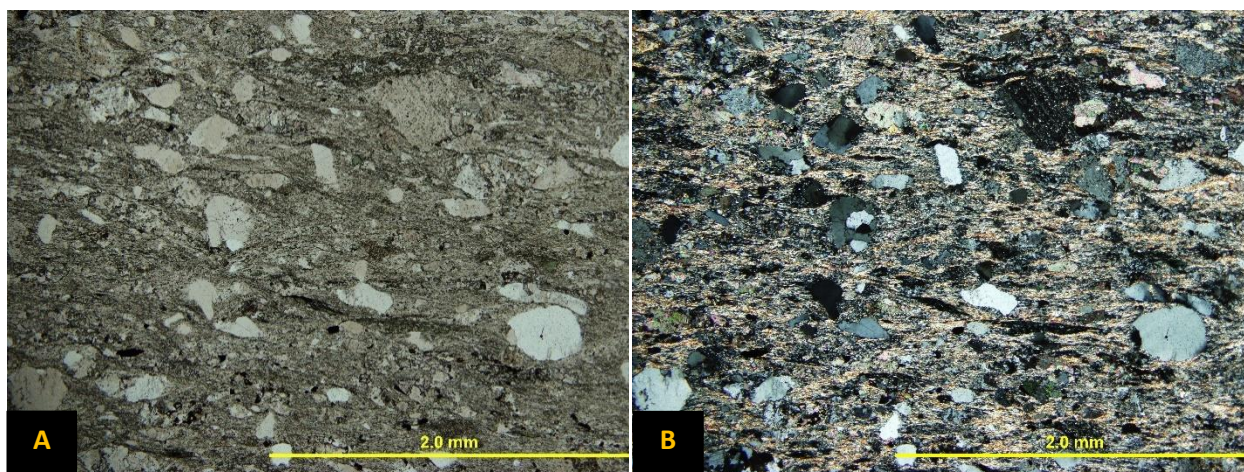
Figure 3.3: Photomicrographs of a metasandstone layer. A) The metasandstone layer in transmitted PPL. Quartz and plagioclase porphyroclasts with a fine-grained matrix of mostly muscovite minerals. B) A transmitted XPL photomicrograph of the metasandstone layer. Fine-grained muscovite is wrapping around quartz and plagioclase crystals. Quartz exhibits undulatory extinction and polysynthetic twinning is preserved in the plagioclase crystals.

Average mineral formulas calculated for most of the phases in the metasandstone are presented

in Table 3.2. Muscovite contains trace amounts of sodium and titanium and is the only potassium-

bearing phase in the metasandstone. The average composition of plagioclase is albite (An0) and it is

the only major sodium-bearing phase in the metasandstone. Due to the higher iron values relative

to magnesium in the chlorite crystal structure, the chlorites are classified as chamosite. Apatite is

the only phosphorous-bearing mineral phase in the metasandstone unit. Trace amounts of sodium

can also be found in apatite. Two types of carbonate minerals occur in the metasandstone layer:

ankerite, which is the magnesium endmember of the dolomite group and siderite, which is an iron

endmember of the calcite group. Siderite also contains trace amounts of manganese. Although the

abundance of rutile is low in the metasandstone, it is the only major titanium-bearing phase.

Table 3.2: Average mineral formulas calculated for the phases in the metasandstone.

Metasandstone		
Mineral	Average Mineral Formula	Samples
Apatite	$(Ca_{4.95}Na_{0.03})_{\Sigma\,4.98}(PO_4)_{2.95}(OH,F,Cl)$	6
Carbonate (Ankerite)	$Ca_{0.97}(Mg_{0.52}Fe_{0.45})_{\Sigma\,0.97}(CO_3)_2$	6
Carbonate (Siderite)	$(Fe_{0.67}Mg_{0.29}Mn_{0.01})_{\Sigma\,0.97}CO_3$	6
Chlorite (Chamosite)	$(Fe_{1.42}Mg_{0.76}Al_{0.73})_{\Sigma\,2.91}(Si_{2.81}Al_{1.19})_{\Sigma\,4.00}O_{10}(OH)_2 \bullet (Fe_{1.42}Mg_{0.76}Al_{0.73})_{\Sigma\,2.91}(OH)_6$	4
Muscovite	$(K_{0.92}Na_{0.02})_{\Sigma\,0.94}(Al_{1.57}Fe_{0.31}Mg_{0.14}Ti_{0.02})_{\Sigma\,2.04}(Si_{3.35}Al_{0.65})_{\Sigma\,4.00}O_{10}(OH)_2$	6
Plagioclase (Albite)	$Na_{1.01}Al_{0.97}Si_{3.01}O_8$	6
Quartz	$Si_{1.00}O_2$	6
Rutile	$(Ti_{0.92}Fe_{0.02})_{\Sigma\,0.94}O_2$	1

Metasiltstone

The bulk composition of the metasiltstones includes an abundance of muscovite, with common occurrences of quartz, plagioclase, minor amounts of chlorite, with trace amounts of apatite, hematite, tourmaline, rutile, pyrite, chloritoid, biotite, zircon and chromite (Table 3.1, Figure 3.4). The foliation is defined by the alternating muscovite-dominated layers and quartz-chlorite-dominated layers. Muscovite-dominated layers contain up to 90% muscovite, while the quartz-chlorite-dominated layers have coarser-grained quartz crystals and contain 40 to 60% quartz, chlorite, and plagioclase. Shear band cleavage is exhibited between the muscovite-dominated layers and chlorite minerals in the quartz-chlorite-dominated layers (Figure 3.4C, D).

Muscovite is fine-grained (<0.1 mm – 0.1 mm), displays a lattice and dimension preferred orientation and defines the C-fabric foliation of the rock. Quartz is anhedral, fine-grained (<0.1 mm – 0.2 mm), while coarser-grained quartz form lozenge-shaped grains and their long axes are parallel to the overall C-foliation. The lozenge-shaped crystals show deformation structures such as undulatory extinction, subgrain formation and sigma porphyroclasts. These coarser-grained quartz and plagioclase crystals have chlorite and muscovite in strain shadows and wrapping around the quartz crystals. Chlorite is fine- to medium-grained (<0.1 mm – 1.0 mm), occurs predominantly with quartz

and defines the overall S-foliation, which is at an angle to the muscovite-dominated layers (Figure

3.4C). Coarser-grained chlorite occurs in quartz-chlorite layers, but the chlorite is anhedral and does

not form the S-foliation as the fine-grained subhedral crystals. Plagioclase is fine-grained (<0.1 mm –

0.2 mm) and forms angular, subhedral porphyroclasts. Apatite occurs sporadically throughout the

rock as fine-grained (<0.1 mm) high relief, clear crystals. The opaque minerals in thin section are

predominantly hematite. Higher concentrations of fine-grained (<0.1 mm – 0.2 mm), platy hematite

crystals are associated with muscovite-dominated layers and in the quartz-chlorite layers they are

more sporadic and less concentrated. Optically in the muscovite-dominated layers, there are brown
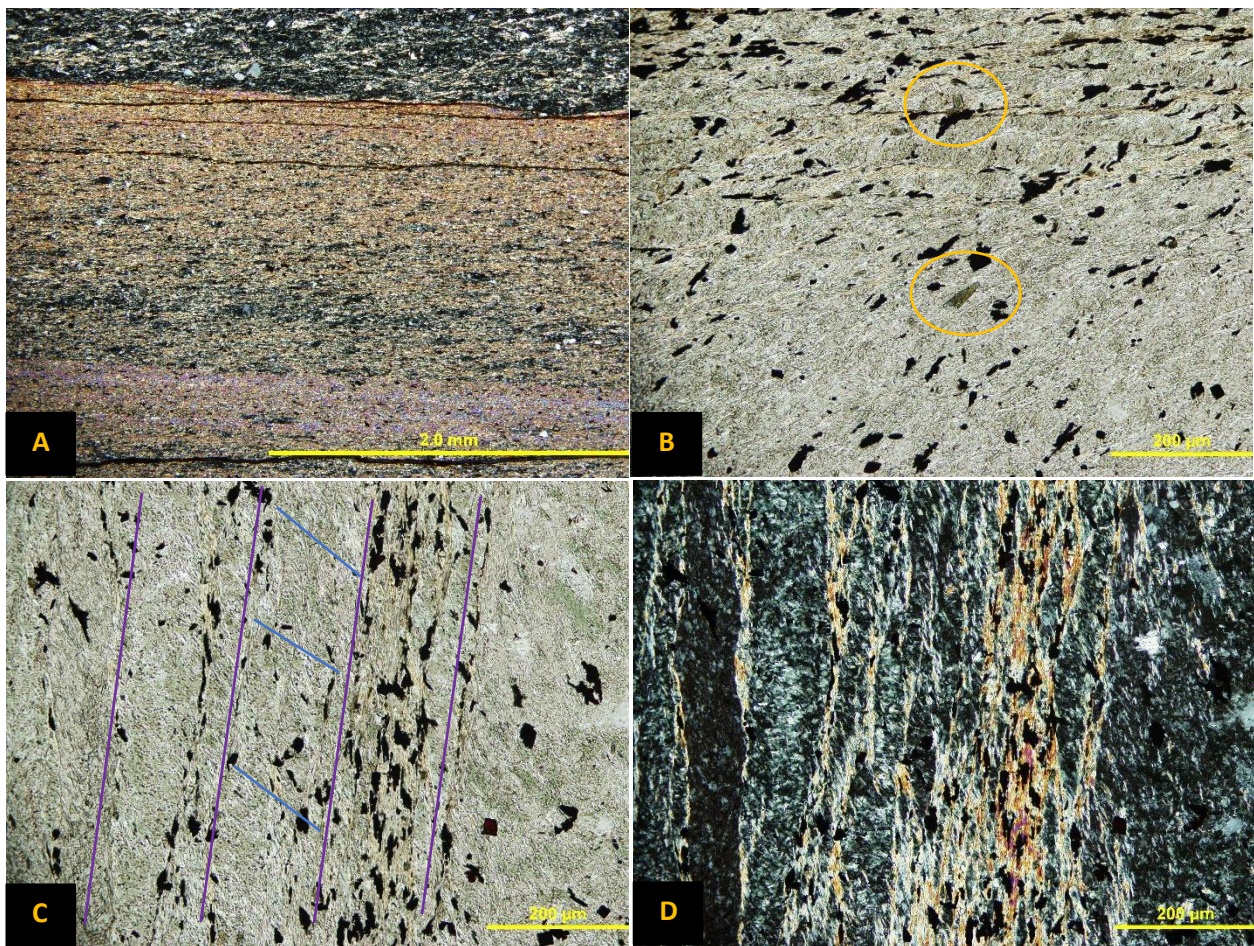
Figure 3.4: Photomicrographs of a metasiltstone layer. A) A transmitted XPL photomicrograph of the metasiltstone layer. The top of the photograph shows a thick muscovite-dominated layer in contact with the quartz-chlorite-dominated layer. The muscovite-dominated layer is mostly composed of muscovite with lesser amounts of quartz, plagioclase and chlorite. B) A transmitted PPL photomicrograph of chloritoid crystals (yellow circles) stable with chlorite, quartz and muscovite. C) Transmitted PPL photograph of shear band cleavage. The purple lines show C-foliation defined by the muscovite crystals and the blue lines show S-foliation defined by chlorite crystals. D) The same photograph as C) showing the shear band cleavage more clearly in transmitted XPL.

pleochroic minerals resembling biotite, but geochemically these crystals are muscovite or chlorite in composition. Therefore, biotite is not a stable phase in the metasiltstone. Tourmaline is fine-grained (<0.1 mm – 0.3 mm), forms high relief elongated minerals parallel to the C-foliation and is mostly fractured. Although in minor amounts, chloritoid forms fine-grained (0.1 mm – 0.2 mm) poikiloblastic, randomly oriented, subhedral crystals (Figure 3.4B). The rest of the minerals, rutile, pyrite, zircon and chromite, are fine-grained (<0.1 mm) and occur in trace amounts.

The compositions of the mineral phases are similar to the metasandstone unit. Average mineral calculations for the phases in the metasiltstone are provided in Table 3.3. Although there are trace amounts of potassium in the plagioclase crystals, muscovite is the only major potassium-bearing phase in the metasiltstone. Muscovite also contains trace amounts of sodium and titanium. Plagioclase and tourmaline are the only major sodium-bearing phase in the metasiltstone unit, however plagioclase occurs more commonly in the unit while tourmaline is less abundant. The average composition of plagioclase is albite (An0). Since there is more iron than magnesium in the chlorite crystal structure, the composition of chlorite is chamosite. The rest of the phases in the metasiltstone are in trace amounts. Apatite is the only major phosphorous-bearing mineral phase, while rutile is the only major titanium-bearing phase in the metasiltstone. Hematite also contains trace amounts of titanium.

Table 3.3: Average mineral formulas calculated for the phases in the metasiltstone.

Metasiltstone		
Mineral	Average Mineral Formula	Samples
Apatite	$Ca_{4.93}(PO_4)_{2.97}(OH,F,Cl)$	6
Chlorite (Chamosite)	$(Fe_{1.27}Mg_{0.93}Al_{0.69})_{\sum 2.89}(Si_{2.91}Al_{1.09})_{\sum 4.00}O_{10}(OH)_2 \bullet (Fe_{1.27}Mg_{0.93}Al_{0.69})_{\sum 2.89}(OH)_6$	6
Hematite	$(Fe_{1.84}Ti_{0.04})_{\sum 1.88}O_3$	6
Muscovite	$(K_{0.87}Na_{0.02})_{\sum 0.89}(Al_{1.40}Fe_{0.42}Mg_{0.25}Ti_{0.03})_{\sum 2.10}(Si_{3.45}Al_{0.55})_{\sum 4.00}O_{10}(OH)_2$	6
Plagioclase (Albite)	$(Na_{0.93}K_{0.02})_{\sum 0.95}Al_{0.96}Si_{3.01}O_8$	6
Quartz	$Si_{0.99}O_2$	6
Rutile	$(Ti_{0.95}Fe_{0.04})_{\sum 0.99}O_2$	5
Tourmaline	$Na_{1.09}(Fe_{2.35}Mg_{1.42})_{\sum 3.77}Al_{6.25}[Si_{7.50}O_{18}](BO_3)_3(O,OH,F)_4$	5

Hematite-jasper Meta-Iron Formation

The bulk composition of the hematite-jasper meta-iron formation is hematite, with common occurrences of quartz, minor amounts of carbonate minerals, apatite, barite, muscovite and trace amounts of chlorite (Table 3.1, Figure 3.5). The banding in the meta-iron formation is defined by alternating hematite-dominated and jasper-dominated layers. Hematite-dominated layers are composed of up to 95% hematite, while the jasper-dominated layers have 40 to 60% quartz. Jasper is defined by fine-grained quartz that contain inclusions of fine-grained iron-oxide minerals and has a red appearance in hand sample. In thin section, both layers range from <0.1 mm to 1.2 mm in thickness.

Hematite is very fine-grained (<0.1 mm) and individual platy, euhedral can only be observed using SEM petrography (Figure 3.5D). Quartz is fine-grained (<0.1 mm) and contains inclusions of iron oxide minerals. Coarser-grained minerals show subgrain formation and deformation tails. Carbonate minerals form as two types: either as anhedral crystals within the jasper-dominated layers or as diamond-shaped crystals with opaque cores. The anhedral carbonate minerals are coarser-grained (up to 0.8 mm) and mostly associated with the jasper-dominated layers, while diamond-shaped carbonate minerals are fine-grained (<0.1 mm – 0.2 mm) and mostly associated with the hematite-dominated layers (Figure 3.5B). Apatite is fine-grained (<0.1 mm – 0.2 mm) and forms euhedral to subhedral dark red crystals that are associated with both jasper- and hematite-dominated layers. They form sporadically throughout the meta-iron formation or as thin (0.1 mm) layers of coarser-grained crystals at the contact between the jasper- and hematite-dominated layers. Chlorite and muscovite are fine-grained (<0.1 mm), long axis oriented parallel to layering and are associated with both layers. Barite is fine-grained, clear and usually forms in the jasper-dominated layer and associated quartz veins.
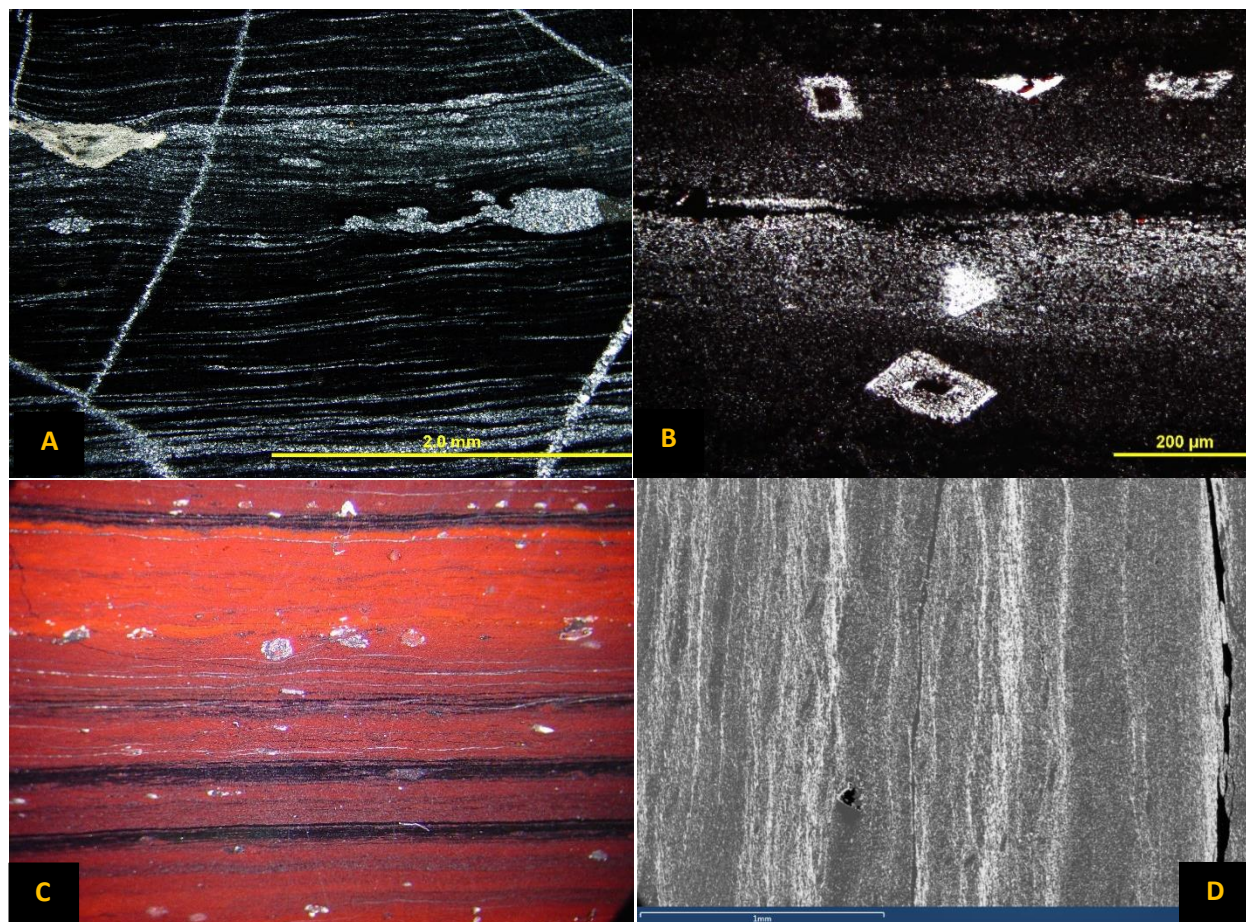
Figure 3.5: Photomicrographs of hematite-jasper meta-iron formation. A) Hematite-dominated (black) and jasper-dominated (grey) microlaminae in transmitted XPL. B) Hematite-jasper meta-iron formation with diamond-shaped carbonate minerals with opaque cores in transmitted PPL. These carbonate minerals are usually associated with the hematite-dominated layers. C) A thin section the hematite-dominated (black) and jasper-dominated (bright red) laminae. Larger quartz porphyroclasts are interpreted to be sand grains deposited with the meta-iron formation D) SEM photomicrograph of the hematite-dominated (white) and jasper-dominated (grey) laminae.

Average mineral calculations for the phases in the hematite-jasper meta-iron formation are presented in Table 3.4. There are two types of carbonate minerals in the hematite-jasper meta-iron formation: ankerite and siderite. The composition of the diamond-shaped carbonates with the opaque cores is siderite, while ankerite forms the sporadic anhedral carbonate minerals. Both carbonate minerals contain trace amounts of manganese. Apatite is the only major phosphorous-bearing phase in the hematite-quartz meta-iron formation. Trace amounts of iron and sodium are also present in apatite crystal structure. Significantly, there is no plagioclase in hematite-jasper meta-iron formation. The abundance of muscovite is minor, but it is the only major potassium-

bearing mineral phase in the hematite-quartz meta-iron formation. Chamosite is the endmember

chlorite phase in the hematite-jasper meta-iron formation. Compared to the chlorites in the clastic

metasedimentary units, there is more aluminum than magnesium in the octahedral sites of the

chlorites, due of the larger amounts of silica in the tetrahedral sites.

Table 3.4: Average mineral calculations for the phases in the hematite-jasper meta-iron formation.

Hematite-jasper Meta-Iron Formation		
Mineral	Average Mineral Formula	Samples
Apatite	$(Ca_{4.86}Fe_{0.17}Na_{0.02})_{\Sigma\,5.05}(PO_4)_{2.85}(OH,F,Cl)$	5
Carbonate (Ankerite)	$Ca_{0.97}(Fe_{0.54}Mg_{0.43}Mn_{0.01})_{\Sigma\,0.98}(CO_3)_2$	7
Carbonate (Siderite)	$(Fe_{0.71}Mg_{0.24}Mn_{0.01})_{\Sigma\,0.96}CO_3$	10
Chlorite (Chamosite)	$(Fe_{1.42}Al_{0.75}Mg_{0.60})_{\Sigma\,2.77}(Si_{3.41}Al_{0.59})_{\Sigma\,4.00}O_{10}(OH)_2 \bullet (Fe_{1.42}Al_{0.75}Mg_{0.60})_{\Sigma\,2.77}(OH)_6$	10
Hematite	$Fe_{1.92}O_3$	11
Muscovite	$(K_{0.75}Na_{0.01})_{\Sigma\,0.76}(Al_{1.44}Fe_{0.50}Mg_{0.12}Ti_{0.01})_{\Sigma\,2.07}(Si_{3.62}Al_{0.38})_{\Sigma\,4.00}O_{10}(OH)_2$	13
Quartz	$Si_{0.99}O_2$	11

Magnetite-quartz Meta-Iron Formation

The bulk composition of the magnetite-quartz meta-iron formation includes an abundance of

magnetite, with common occurrences of quartz and plagioclase, minor amounts of apatite,

carbonate minerals, chlorite and trace amounts of rutile, ilmenite, stilpnomelane, pyrite, barite,

scheelite and arsenopyrite (Table 3.1, Figure 3.6). The magnetite-quartz meta-iron formation is

composed of two layer types: magnetite-dominated and quartz-dominated layers. In most cases,

individual magnetite- and quartz-dominated layers are laterally discontinuous (Figure 3.6B). Due to

this discontinuity, the magnetite-dominated layers are defined by containing mostly magnetite and

the quartz-dominated layers contain mostly quartz. Magnetite-dominated layers can be up to 1.5

mm and quartz-dominated layers can be up to 0.5 mm, however in thin section, their thicknesses

usually range from <0.1 mm – 0.2 mm.

Magnetite is the most dominant mineral phase in the meta-iron formation, composed of fine- to

medium-grained (<0.1 mm to 1.0 mm), subhedral to anhedral poikiloblasts, containing inclusions of

mostly plagioclase and quartz, with lesser abundant inclusions of apatite, chlorite and trace amounts of pyrite, arsenopyrite, scheelite and barite (Figure 3.6C, D). Most magnetite crystals form as clumps with other magnetite crystals and do not have a euhedral cubic crystal structure especially in the magnetite-dominated layers. Quartz is fine-grained (<0.1 mm), anhedral and forms its own layers, but is often associated with fine-grained magnetite crystals. Deformation structures include undulatory extinction and contorted quartz-dominated layers. Plagioclase is fine-grained (<0.1 mm), anhedral and only found in the magnetite-dominated layers, mostly as inclusions in magnetite crystals. When carbonate minerals are not associated with secondary quartz-carbonate veins, they occur as fine-grained (<0.1 mm) minerals sporadically throughout the meta-iron formation without
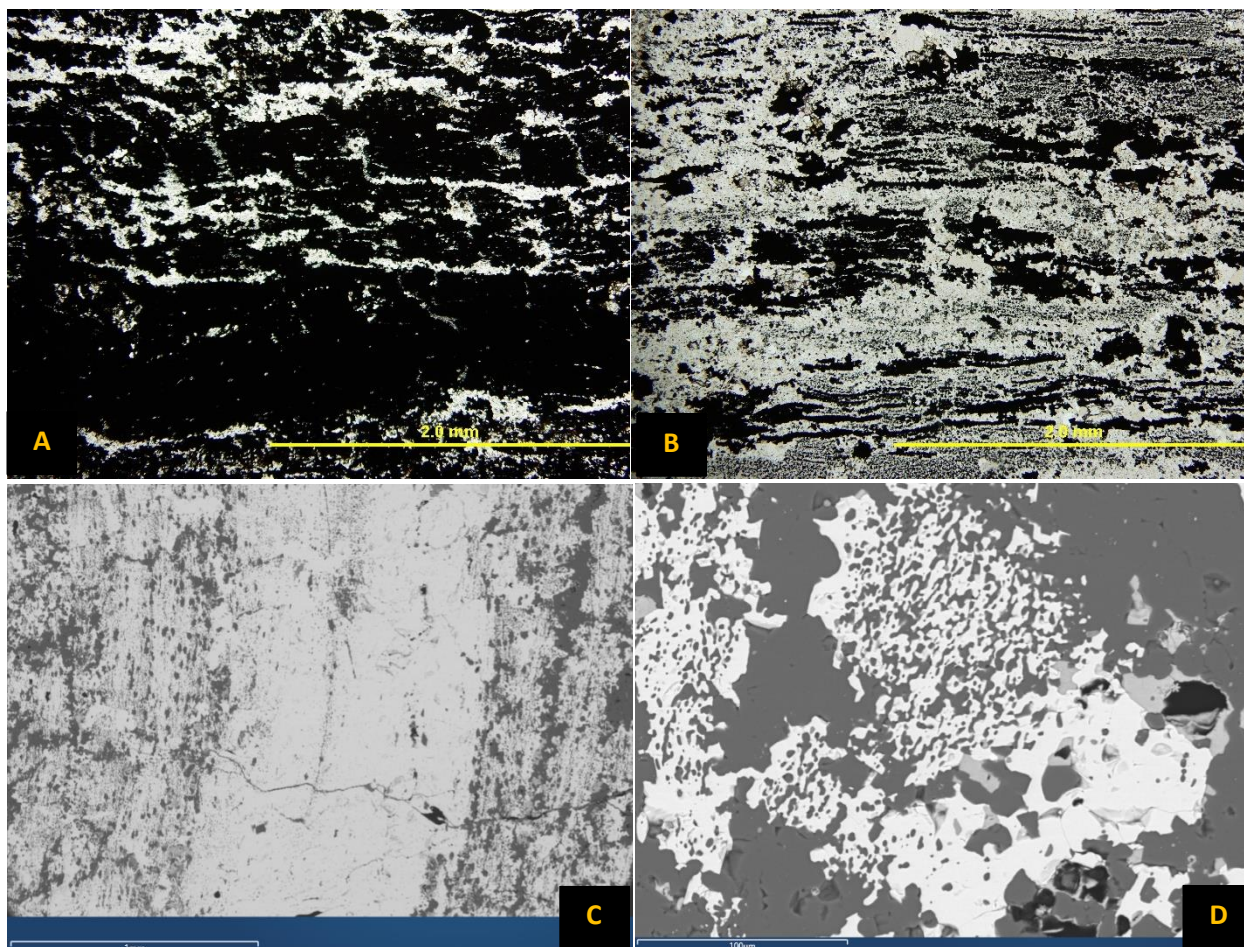
Figure 3.6: Photomicrographs of magnetite-quartz meta-iron formation. A) and B) are transmitted PPL photomicrographs of the magnetite-quartz meta-iron formation. A) is more magnetite-rich, while B) is more quartz-rich. C) Photomicrograph on the SEM of the magnetite-quartz meta-iron formation. Significantly, magnetite does not form euhedral crystals. Instead, magnetite occurs as poikiloblastic crystals and the dominant inclusion inside the magnetite poikiloblasts is quartz and plagioclase. D) A SEM photomicrograph of a poikilitic magnetite crystal, filled with inclusions of apatite, quartz, plagioclase and chlorite.

any direct association with either the magnetite- or quartz-dominated layers. Apatite is fine-grained (<0.1 mm), dark red, euhedral and occurs as inclusions within magnetite or along grain boundaries of magnetite crystals. Chlorite is fine-grained (<0.1 mm) and occurs as inclusions within magnetite crystals and sporadically with magnetite in the quartz-dominated layers. Fine-grained inclusions of magnetite can also be seen in the chlorite crystals. Trace amounts of ilmenite, rutile and stilpnomelane occur sporadically throughout the meta-iron formation.

Average mineral compositions calculated for the magnetite-quartz meta-iron formation is provided in Table 3.5. The average composition of plagioclase is albite (An2). Other than the minor amounts of sodium in the stilpnomelane crystals, albite is the only major sodium-bearing phase in the magnetite-quartz meta-iron formation. Two compositions of carbonate minerals in the meta-iron formation include: ankerite and siderite. Although in trace amounts, ankerite is the only phase in the magnetite-quartz meta-iron formation to contain manganese. Apatite is the only phosphorous-bearing mineral phase in the magnetite-quartz meta-iron formation. The composition of chlorite is chamosite. Stilpnomelane is the only mineral phase to contain potassium, but it also contains minor amounts of sodium. Rutile and ilmenite are the only major titanium-bearing phases in the magnetite-quartz meta-iron formation.

Table 3.5: Average mineral calculations for the phases in the magnetite-quartz meta-iron formation.

Magnetite-quartz Meta-Iron Formation		
Mineral	Average Mineral Formula	Samples
Apatite	$(Ca_{4.91}Fe_{0.05})_{\sum 4.96}(PO_4)_{2.95}(OH,F,Cl)$	7
Carbonate (Ankerite)	$Ca_{0.99}(Mg_{0.59}Fe_{0.38}Mn_{0.02})_{\sum 0.99}(CO_3)_2$	7
Carbonate (Siderite)	$(Fe_{0.74}Mg_{0.22})_{\sum 0.96}CO_3$	3
Chlorite (Chamosite)	$(Fe_{1.51}Mg_{0.91}Al_{0.56})_{\sum 2.98}(Si_{2.82}Al_{1.18})_{\sum 4.00}O_{10}(OH)_2 \bullet (Fe_{1.51}Mg_{0.91}Al_{0.56})_{\sum 2.98}(OH)_6$	7
Illmenite	$Ti_{0.82}Fe_{0.82}O_3$	2
Magnetite	$(Fe^{3+}_{1.96}Fe^{2+}_{1.00})_{\sum 2.96}O_4$	9
Plagioclase (Albite)	$(Na_{0.99}Ca_{0.02})_{\sum 1.01}Al_{1.01}Si_{2.96}O_8$	8
Quartz	$Si_{0.99}O_2$	7
Rutile	$(Ti_{0.83}Fe_{0.05})_{\sum 0.88}O_2$	2
Stilpnomelane	$(K_{0.28}Na_{0.10})_{\sum 0.38}(Fe_{5.56}Mg_{0.56})_{\sum 6.12}Al_{1.29}Si_{7.81}(O,OH)_{27}$	3

Iron oxide-quartz Meta-Iron Formation

The bulk composition of the iron oxide-quartz meta-iron formation is abundant magnetite, with common occurrences of carbonate, chlorite, hematite, plagioclase, quartz, with minor amounts of muscovite, and trace amounts of apatite, ilmenite and rutile (Table 3.1, Figure 3.7). Significantly, the sample analyzed is the only meta-iron formation in the BG to contain significant amounts of both magnetite and hematite crystals. The meta-iron formation contains two different layer types: iron-oxide dominated layers and quartz-dominated layers. Iron oxide-dominated layers are defined by containing 50 – 70% magnetite and hematite, while the quartz-dominated layers are defined by containing 60 – 70% quartz, chlorite and muscovite with smaller abundances of magnetite. Overall, the long axis of the magnetite, hematite and chlorite minerals are not parallel to the foliation (Figure 3.7A). However, this was caused by oblique shearing of the rock at an angle to the foliation.

Magnetite is fine-grained (0.1 mm – 0.5 mm), anhedral and forms lozenge-shaped crystals. Magnetite crystals have the largest grainsize compared to the other minerals in thin section and are poikilitic, containing inclusions of chlorite, plagioclase, quartz, muscovite and apatite. Evidence of deformation is exhibited by magnetite forming sigma poikiloblasts. Hematite crystals are fine-grained (<0.1 mm), euhedral crystals and they are concentrated in the iron oxide-dominated layers. Hematite crystals wrap around magnetite poikiloblasts, however the long axis of most of the hematite crystals is oriented in the same direction as magnetite and chlorite (Figure 3.7). Quartz is mostly fine-grained (<0.1 mm), anhedral and occurs in both types of layers. Coarser-grained quartz crystals (<0.1 mm – 0.1 mm) occur in the strain shadows of magnetite poikiloblasts. When quartz is coarser-grained, deformation structures include undulatory extinction. Quartz also occurs as inclusions in magnetite poikiloblasts. Like hematite in the iron oxide-dominated layers, chlorite

occurs as fine-grained (<0.1 mm) crystals wrapping around magnetite poikiloblasts. Coarser-grained

chlorite minerals occur in strain shadows of magnetite poikiloblasts with quartz and contain

inclusions of quartz and hematite. Plagioclase is fine-grained (<0.1 mm), anhedral and is mostly

associated with the iron oxide-dominated laminae and as inclusions in magnetite poikiloblasts.

When carbonate minerals are not associated with secondary quartz-carbonate veins, they are fine-

grained (<0.1 mm), anhedral crystals found in both phase-dominated layers. Like quartz and chlorite,

coarser-grained carbonate minerals are found within strain shadows of magnetite poikiloblasts.
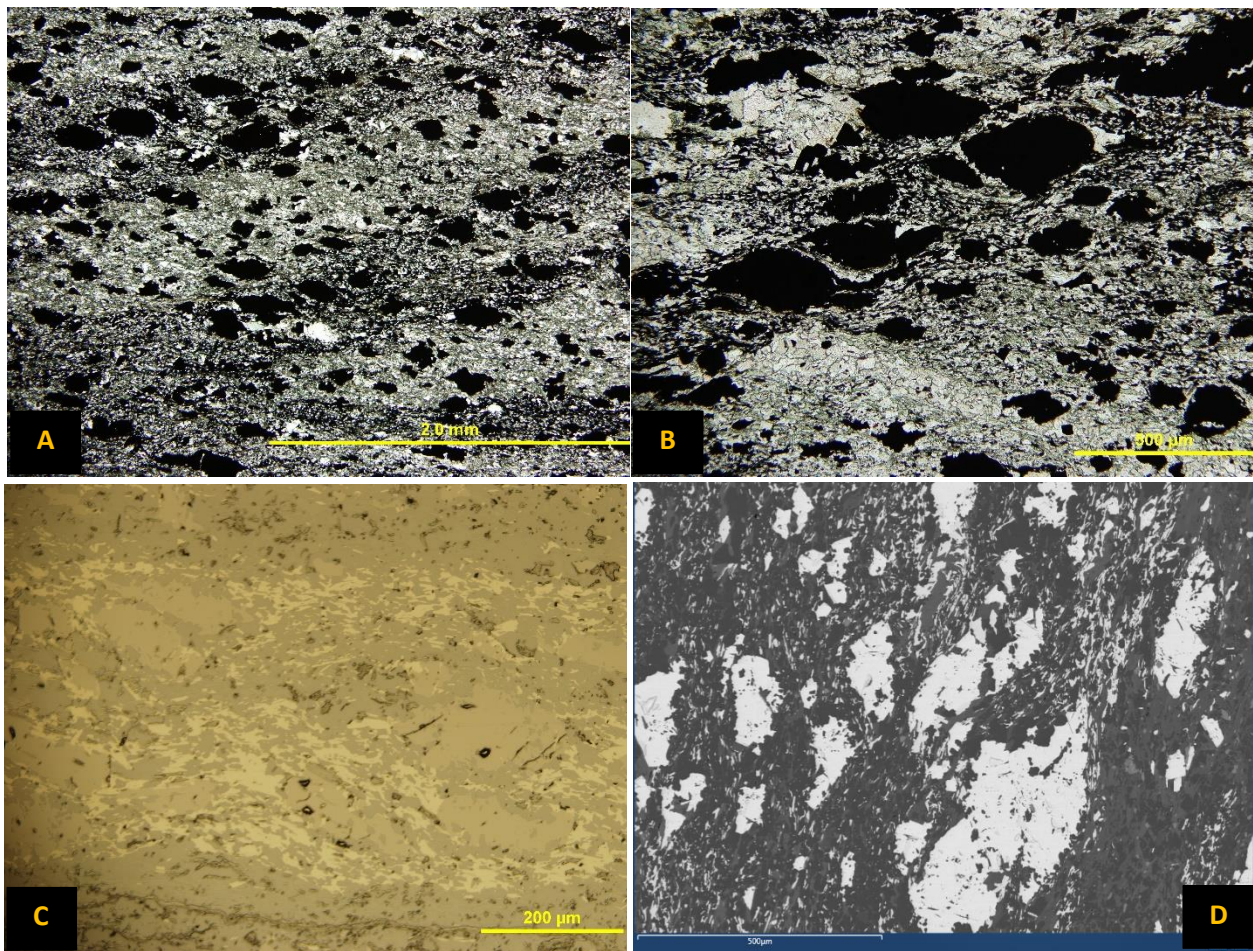
Figure 3.7: Photomicrographs of iron oxide-quartz meta-iron formation. A) and B) are transmitted PPL photomicrographs of the iron oxide-quartz meta-iron formation. A) The long axis of magnetite, hematite and chlorite are not parallel to layering due to oblique shearing. Quartz-dominated layers are mostly chlorite and quartz (green and white layers), while iron-oxide dominated layers contain mostly magnetite and hematite (black and green layers). B) A higher magnification photomicrograph of the magnetite poikiloblasts. Magnetite produces lozenge-shaped crystals which have deformation tails. C) A reflected PPL photograph of the iron oxide-dominated layer. Brown poikiloblastic crystals are magnetite, hematite crystals are the lighter yellow crystals. Significant amounts of hematite wrap around magnetite poikiloblasts. D) SEM photomicrograph of the iron oxide-dominates layer showing the abundant inclusions in magnetite poikiloblasts.

Muscovite is fine-grained (<0.1 mm to 0.1 mm) and occurs with chlorite and hematite crystals, wrapping around magnetite poikiloblasts. Larger muscovite crystals are found as inclusions in magnetite poikiloblasts. Apatite is fine-grained (<0.1 mm), dark red and euhedral. These crystals are mostly associated with magnetite crystals as inclusions or along grain boundaries.

Average mineral formulas calculated for the iron-quartz meta-iron formation are provided in Table 3.6. Hematite contains trace amounts of titanium in its crystal structure. Since there is more magnesium than iron in the chlorite phases, the composition of the chlorite is clinochlore. The composition of the plagioclase in the iron oxide-quartz meta-iron formation ranges from albite to oligoclase (An7 – An14). Other than the minor amounts of sodium in apatite and muscovite, albite and oligoclase are the only major-sodium bearing phases in the iron-oxide-quartz meta-iron formation. The composition of the carbonate minerals is dolomite, which is the only mineral phase to contain manganese, even though it is relatively minor. Again, apatite is the only major phosphorous bearing mineral phase and muscovite is the only major potassium-bearing phase in iron oxide-quartz meta-iron formation.

Table 3.6: Average mineral formulas calculated for the phases in the iron oxide-quartz meta-iron formation.

Iron Oxide-quartz Meta-Iron Formation		
Mineral	Average Mineral Formula	Samples
Apatite	$(Ca_{4.94}Fe_{0.06}Na_{0.01})_{\Sigma 5.01}(PO_4)_{2.88}(OH,F,Cl)$	3
Carbonate (Dolomite)	$Ca_{1.00}(Mg_{0.79}Fe_{0.17}Mn_{0.02})_{\Sigma 0.98}(CO_3)_2$	3
Chlorite (Clinochlore)	$(Mg_{1.34}Fe_{0.93}Al_{0.67})_{\Sigma 2.94}(Si_{2.84}Al_{1.16})_{\Sigma 4.00}O_{10}(OH)_2 \bullet (Mg_{1.34}Fe_{0.93}Al_{0.67})_{\Sigma 2.94}(OH)_6$	3
Hematite	$(Fe_{1.90}Ti_{0.03})_{\Sigma 1.93}O_3$	6
Magnetite	$(Fe^{3+}_{1.97}Fe^{2+}_{0.99})_{\Sigma 2.96}O_4$	3
Muscovite	$(K_{0.86}Na_{0.11})_{\Sigma 0.97}(Al_{1.66}Fe_{0.24}Mg_{0.10}Ti_{0.01})_{\Sigma 2.01}(Si_{3.19}Al_{0.81})_{\Sigma 4.00}O_{10}(OH)_2$	3
Plagioclase (Albite)	$(Na_{0.79}Ca_{0.06})_{\Sigma 0.85}Al_{0.85}Si_{3.12}O_8$	1
Plagioclase (Oligoclase)	$(Na_{0.89}Ca_{0.14})_{\Sigma 1.02}Al_{1.12}Si_{2.85}O_8$	2
Quartz	$Si_{1.00}O_2$	2

3.2.3 Metamorphism

To determine peak metamorphic temperatures for the BG meta-iron formations is essential to establish the stable metamorphic mineral assemblage of the metasiltstone unit. All the metasiltstone samples were gathered from the Highway 580 outcrops near Beardmore. The stable mineral assemblage includes muscovite + quartz + albite + chamosite + chloritoid. For typical pelitic rocks, chloritoid forms at metamorphic temperatures of about 300°C (Bucher and Grapes, 2011). In the metasandstone, the microstructures associated with the coarser-grained quartz crystals, which are interpreted to be detrital sand grains, include undulatory extinction and subgrain formation. This indicates that quartz crystals were deforming plastically, which is at temperatures of at least 250°C (Tullis, 2002). There is no evidence of plastic deformation in the plagioclase crystal, suggesting that metamorphic temperatures did not exceed 400°C (Tullis, 2002). Therefore, the stable mineral assemblage in the metasiltstone, quartz microstructures in the metasandstone and lack of plagioclase microstructures in the metasandstone constrains the peak metamorphic temperatures at lower greenschist facies. Furthermore, these interpretations are consistent with the metamorphic interpretations from Stinson (2013).

It is difficult to determine metamorphic grade solely on the composition of the iron oxide-dominated iron-formation because iron oxides and quartz will not react to form any new mineral phases. This causes these phases to be stable from sub-greenschist facies to granulite facies metamorphism (Klein, 1973). James (1955) had created a classification scheme of determining metamorphic grade using the grainsize of quartz in meta-iron formations. However, regional deformation can cause grainsize reduction of coarser-grained crystals, therefore, yielding misinterpretations in the metamorphic grade. Since the siliciclastic units are interbedded with the meta-iron formation in Beardmore and preserve peak metamorphic temperatures are lower

greenschist facies, the meta-iron formation in Beardmore was also subjected to peak metamorphic temperatures at the lower greenschist facies.

Peak metamorphism of the Geraldton area was determined to range from greenschist to amphibolite facies (Stinson, 2013). Unfortunately, samples of clastic metasedimentary rocks were not collected from the associated meta-iron formation from the Geraldton area. The only lithology obtained from Geraldton were the magnetite-quartz and iron oxide-quartz meta meta-iron formations. Undulatory extinction in the quartz crystals suggests that temperatures were above 250°C (Tullis, 2002). The abundance of chlorite and muscovite in the iron oxide-quartz meta-iron formation indicates that there was a large siliciclastic component deposited with the meta-iron formation. Therefore, as an approximation, this lithology will be regarded as an iron-rich, pelitic rock. The presence of hematite inclusions in the chlorite crystals indicate that chlorite was formed during metamorphism rather than authigenic or detrital grains. According to Winter (2010), chlorite and muscovite are stable at 300°C, which is at lower greenschist facies. Since there is a large component of siliciclastics, the lack of biotite, garnet or staurolite crystals suggests that temperatures of metamorphism did not reach amphibolite facies. Therefore, the quartz microstructures and the stability of muscovite and chlorite suggest peak metamorphic temperatures of at least greenschist facies. The lack of higher temperature stable metamorphic mineral assemblages in the magnetite-quartz and iron oxide-quartz meta-iron formations suggests that peak metamorphic temperatures were below amphibolite facies. However, this conclusion is not definite because diagenesis may have altered the chemistry of the meta-iron formation, which might have been responsible for the lack of higher temperature metamorphic mineral phases.

Interestingly, magnetite occurs as poikiloblasts in the magnetite-quartz and iron oxide-quartz meta-iron formations. Inclusions in the magnetite poikiloblasts include chlorite, albite, oligoclase,

quartz and apatite. Significantly, chlorite contains inclusions of magnetite in the magnetite-quartz meta-iron formation and hematite in the iron oxide-quartz meta-iron formation. Since magnetite poikiloblasts contain inclusions of chlorite and chlorite has inclusions of magnetite and hematite, chlorite and magnetite were growing simultaneously during metamorphism. Therefore, this indicates that magnetite crystals continued to grow during metamorphism, probably at the expense of other magnetite crystals, which formed during diagenesis.

3.2.4 Petrographic Summary

The main sodium-bearing phases in the BG clastic and chemical metasedimentary rocks are albite and oligoclase. Significantly, albite and oligoclase are found in magnetite-quartz and as anhedral inclusions in poikiloblastic magnetite crystals from both magnetite-dominated meta-iron formations (Figure 3.8), while they are absent from the hematite-quartz meta-iron formation. Since both clastic metasedimentary units also contain plagioclase and the magnetite-dominated meta-iron formations contain plagioclase, the lack of plagioclase in the hematite-quartz meta-iron formation suggests that a reaction occurred with the minerals in the hematite-quartz meta-iron formation causing a loss of sodium during post-depositional alteration.

In some of the magnetite-quartz meta-iron formation samples there is an abundance of chlorite crystals with lesser abundances of potassium-bearing phases, such as muscovite and K-feldspar. Since the clastic metasedimentary rocks contain significant amounts of potassium-bearing phases and chlorite, the minor amounts of potassium-bearing phases compared to the abundance of chlorite in the magnetite-quartz meta-iron formation samples suggests a loss of potassium in the magnetite-dominated layers during post-depositional alteration.

The presence of titanium in the crystal lattice of the hematite crystals and the presence of chlorite and plagioclase (both aluminum-bearing silicicates) inclusions in the magnetite crystals

strongly suggests that magnetite and hematite formed after deposition. This supports the theory that iron was deposited as iron oxyhydroxides and then transformed into hematite and magnetite during diagenesis. The poikiloblastic texture of magnetite indicates that these minerals grew during progressive metamorphism by solid state diffusion.
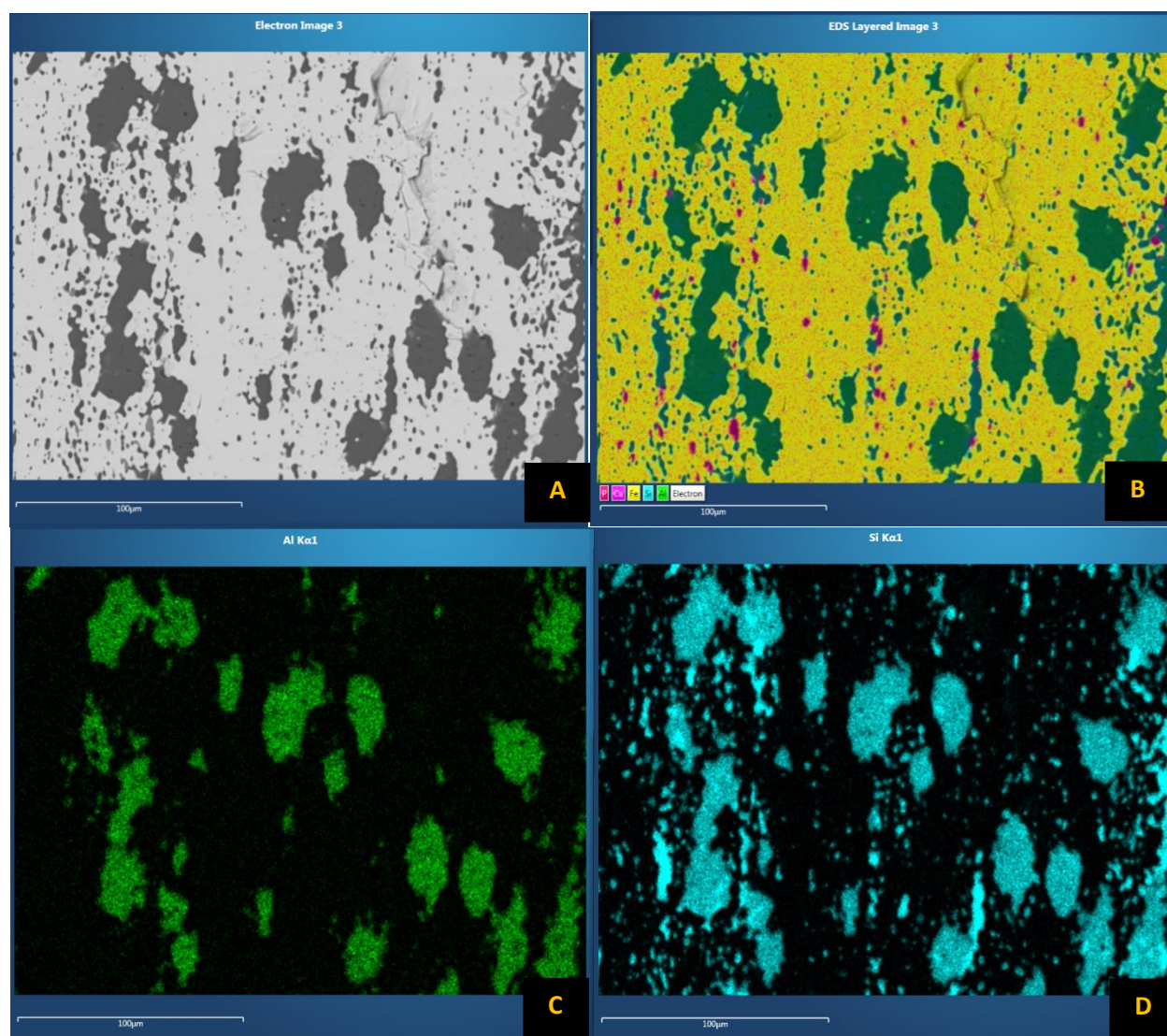
Figure 3.8: SEM backscatter electron false colour geochemical maps of magnetite-quartz meta-iron formation. A) Magnetite-dominated layers with inclusions of apatite, quartz and albite. B) Layered geochemical map of the different phases in the magnetite-dominated layers. Yellow is iron (magnetite), purple is calcium (apatite), pink is phosphorous (apatite), green is aluminum (albite) and blue is silica (quartz and albite). C) and D) are maps of only aluminum and silica, respectively. Most of the inclusions in the magnetite crystals are anhedral albite crystals.

3.3 Lake St. Joseph Greenstone Belt

3.3.1 Outcrop Descriptions

The Eagle Island assemblage of the LSJ forms a depositional system consisting of two coarsening upwards successions, that contain metamorphosed iron oxide-dominated lithofacies associations and metamorphosed siliciclastic-dominated lithofacies associations (Fralick and Pufahl, 2006). The metamorphosed iron oxide lithofacies associations in the Eagle Island assemblage have been categorised based on the amount of the siliciclastic material interbedded within the meta-iron formation and the grainsize of the detritus. These categories are separated into the same a-type, b-type and c-type classification scheme as the BG meta-iron formations (Barrett and Fralick, 1985). Stratigraphically, the two coarsening upward cycles are separated by a 73 m-thick meta-iron formation (Figure 3.9). Detailed sedimentology of the Eagle Island assemblage conducted by Fralick in 2003 will be summarized below, moving up stratigraphy and starting from the base of the assemblage. All the lithologies in the Eagle Island assemblage have been subjected to a degree of metamorphism.

The lowermost 35 m of the Eagle Island assemblage forms one of the coarsening upward cycles (Figure 3.9). This lithofacies association consists of three sequences that coarsen upwards from fine-grained magnetite-dominated meta-iron formation to metamorphosed coarse-grained siliciclastic-dominated lithologies (Fralick and Pufahl, 2006). These three sequences are subdivided into the lower, middle and upper parasequences.
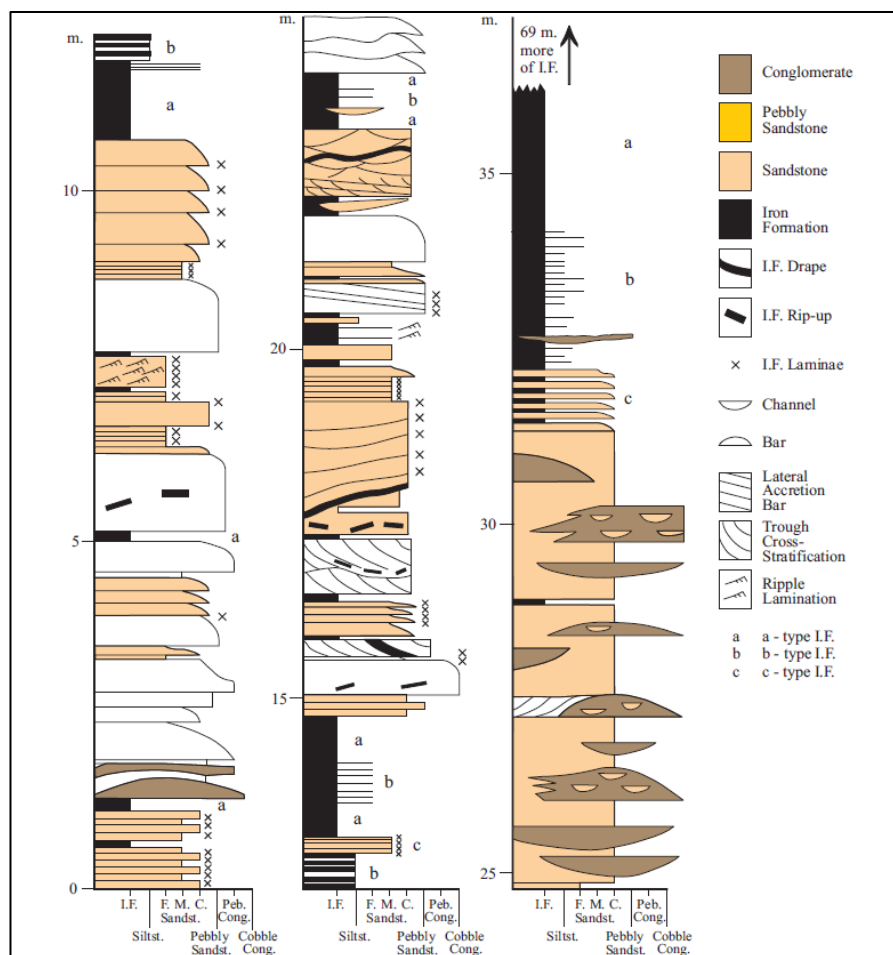
Figure 3.9: A stratigraphic column of the lowermost 35 m coarsening upwards sequence of the Eagle Island assemblage, stratigraphically underneath the 73 m-thick meta-iron formation (P. Fralick personal communication, 2018).

The lower parasequence is a 12 m-thick coarsening upwards succession. The bottom 125 cm of the succession is composed of thinly-laminated, magnetite-dominated, meta-iron formation with interbedded cm-thick, coarse- to medium-grained metasandstone. The amount of siliciclastics increases up stratigraphy (Figure 3.10A). A 65 cm-thick succession of low angle, laterally accreting pebble metaconglomerate and coarse-grained metasandstone is in sharp contact with the underlying meta-iron formation. Magnetite-dominated meta-iron formation occurs along reactivation surfaces of the metaconglomerate and metasandstone layers. The next 304 cm are in sharp contact with the underlying unit and are composed of graded, pebble metaconglomerates to coarse-grained metasandstone and fine-grained metasandstone with thin parallel-laminated,

magnetite-dominated meta-iron formation occurring at the top of these graded sedimentary

packages (Figure 3.10B) (Fralick and Pufahl, 2006). This parasequence is interpreted to be coarse-

grained graded deposits forming on the delta front (Fralick and Pufahl, 2006).

Figure 3.10: The lower parasequence of the basal coarsening upward cycle in the Eagle Island assemblage. A) Outcrop scale photograph of the lower parasequence. Metamorphosed graded siliciclastic units are interbedded with cm-scale, magnetite-dominated meta-iron formation. The stratigraphic younging direction is towards the left. B) A smaller scale photograph of thinly-laminated magnetite-dominated meta-iron formation and metasiltstone overlain by a metasandstone and graded coble-sized to pebbly metaconglomerate.

The middle parasequence is in sharp contact with the top of the underlying lower parasequence.

The first 5 m of the middle parasequence are composed of thinly-laminated, magnetite-dominated,

meta-iron formation interbedded with varying amounts of siliciclastics that range in grainsize from

metasiltstone to coarse-grained metasandstone. The meta-iron formation is overlain by 8 m of

siliciclastic-dominated lithologies that have a variety of preserved sedimentary structures. Low

angle, laterally accreting, coarse-grained metasandstone and metaconglomerate beds form the

bottom of this succession. Magnetite occurs along reactivation surfaces between prograding

metasandstone and metaconglomerate units (Figure 3.11A), draped irregularly over

metaconglomerate clasts (Figure 3.11B) and internally interbedded within the siliciclastics (Fralick

and Pufahl, 2006). The middle part of this succession is dominated by graded, granular- to medium-

grained metasandstone with magnetite-dominated meta-iron formation forming along surfaces

between graded beds. At the top of this parasequence, mm thick magnetite-dominated layers occur

along avalanche surfaces of small-scale, trough cross-stratified and ripple-laminated, medium-

grained metasandstones (Figure 3.11C). Medium-grained metasandstone is also seen loading into

meta-iron formation laminae (Figure 3.11D). This sequence is interpreted to be a distributary mouth

bar complex, which forms the strand-line separating truly sub-aerial and truly sub-aqueous

environments (Fralick and Pufahl, 2006).
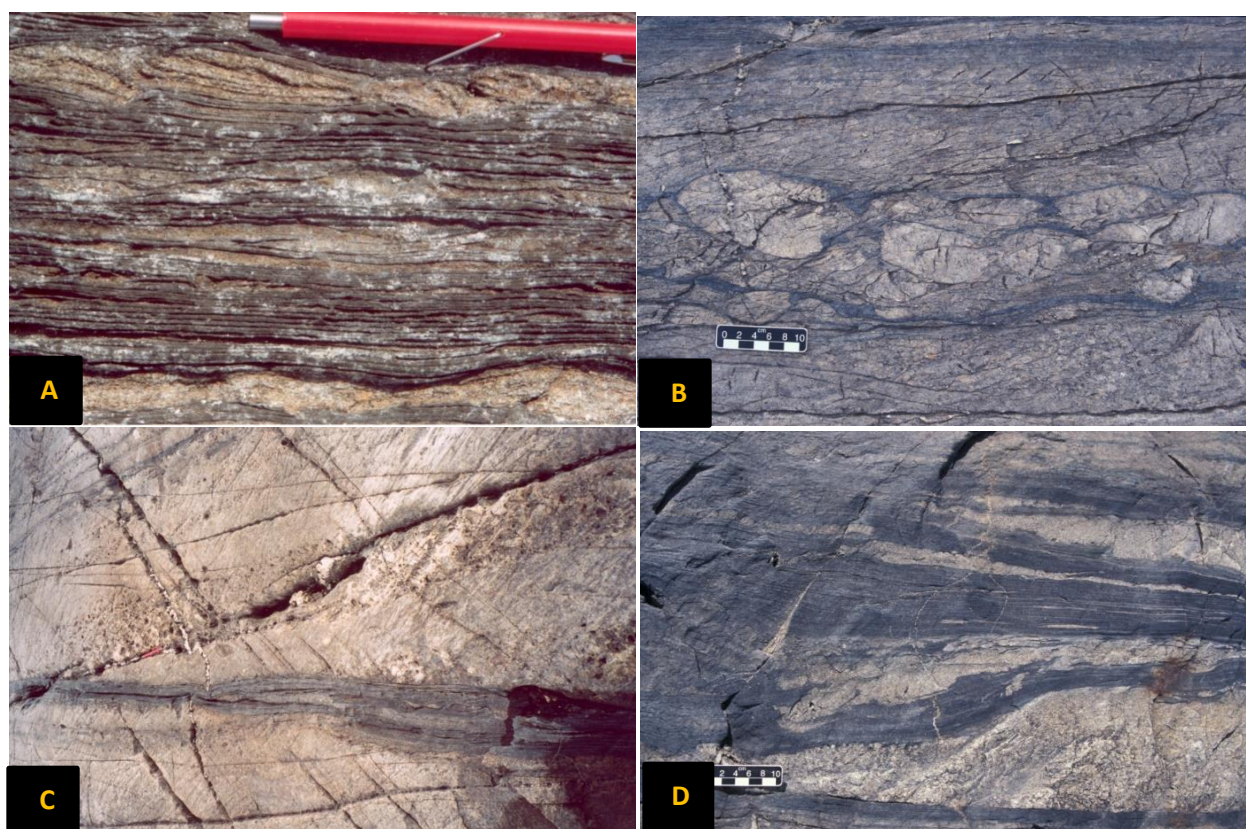
Figure 3.11: Middle parasequence of the lower coarsening-upward succession, Eagle Island assemblage. A) Low angle (10°) dipping metaconglomerate and metasandstone beds. Magnetite-dominated meta-iron formation along surfaces between prograding coarse-grained bars. B) Magnetite-dominated meta-iron formation draping clasts and reactivation surfaces within a metaconglomerate. C) Magnetite-dominated meta-iron formation interbedded with ripple-laminated metasandstone. Magnetite drapes on ripple reactivation surfaces indicate rapid deposition of the chemical sediment. D) Metasandstone loading into meta-iron formation, indicating that the meta-iron formation was low density during deposition and rapid accumulation of siliciclastic sediment created depressions in the amorphous meta-iron formation. Photographs from Fralick and Pufahl (2006).

The upper parasequence is dominated by lenticular metaconglomerates with cross-stratified metasandstone lenses (Figure 3.12A). Adjacent to metaconglomerate lenses are large-scale cross-stratified, coarse-grained metasandstones that contain pebble stringers. Magnetite-dominated meta-iron formation is scarce within this parasequence, but it does occur between two coarse-grained sedimentary assemblages. Ripped up fragments of meta-iron formation also occur as clasts within the metaconglomerate (Figure 3.12B). This parasequence is interpreted to be fluvial, braided river delta top deposits (Fralick and Pufahl, 2006). In summary, the first 40 m of the Eagle Island assemblage represents a progradational parasequence set composed of three parasequences with meta-iron formation deposited on flooding surfaces between parasequences and draped on reactivation surfaces.

The lower coarsening-upward succession described above is sharply overlain by a transgressive systems tract flooding surface. 50 cm of graded, very coarse-grained to medium-grained metasandstone beds with three-centimetre-thick packages of parallel-laminated magnetite lie above this surface and it, in turn, are overlain by a two-metre-thick package of b-type meta-iron formation consisting of fine-grained metasandstone to coarse-grained metasiltstone interbedded with thinly-laminated magnetite. A 71 m-thick a-type meta-iron formation overlies the b-type meta-iron formation. It is composed of thinly-laminated iron oxide layers with rare, thin, fine- to coarse-grained metasiltstone layers. Magnetite dominates the iron oxide layers for the first 30 m of the a-type meta-iron formation. Hematite and jasper dominates 30 m and 44 m above the base of the a-type meta-iron formation respectively. The meta-iron formation forms the basal assemblage of the upper upward-coarsening succession.
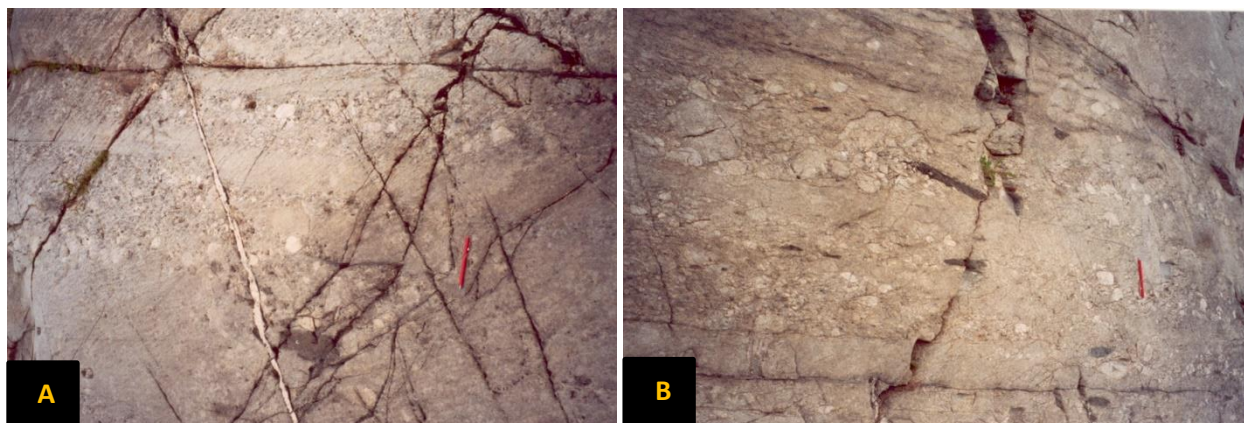
Figure 3.12: The upper parasequence of the lower coarsening upward succession. A) Coble metaconglomerates interbedded with cross-stratified metasandstone lenses. B) Metaconglomerate beds with ripped up fragments of meta-iron formation. This indicates that fluvial channels eroded the meta-iron formation forcing chunks of BIF to be carried by the river. Significantly, this indicates that the meta-iron formation was deposited in proximity to the shoreline.

Another upward-coarsening succession, which is 400 m-thick, caps the Eagle Island assemblage (Figure 3.13). The base of this depositional cycle is the 73 m-thick meta-iron formation described above. This is followed upwards by thick, graded, medium- to fine-grained metasandstone beds rarely separated by parallel-laminated, magnetite-dominated layers. This unit is interpreted to be turbidites deposited in the prodelta (Fralick and Pufahl, 2006). The middle lithofacies association is in sharp erosional contact with the underlying turbiditic lithofacies association. It consists of sedimentary packages that contain trough cross-stratified, coarse-grained metasandstone overlain by ripple-laminated, fine- to medium-grained, clay-rich metasandstone. This unit is interpreted to be a distributary mouth bar complex (Fralick and Pufahl, 2006). The upper lithofacies association is composed of interlayered metaconglomerate and metasandstone, which are also in sharp contact with the middle lithofacies association. The clast population for the metaconglomerate is 50% metamorphosed chert-magnetite clasts and 50% metamorphosed igneous clasts. Small, medium-grained metasandstone lenses are abundant within the metaconglomerate and often show trough cross-stratification. A 50 cm-thick package of parallel-laminated magnetite-dominated meta-iron formation grading to metasiltstone, fills in a broad scour which occurs 9 m from the base of the succession. This succession is interpreted to be fluvial and foreshore deposits (Fralick and Pufahl,

2006). Although meta-iron formation is not as common in the nearshore of the upper coarsening-upward succession as it is in the lower, some meta-iron formation is present (Fralick and Pufahl, 2006). The upper succession is overlain by ten metres of cm-scale, graded coarse- to fine-grained metasandstone. Magnetite-dominated meta-iron formation starts abruptly over this package and is interbedded with coarse-grained metasandstone and metasiltstone. Above that unit are mm-scale, parallel-laminated hematite-dominated and magnetite-dominated meta-iron formation.
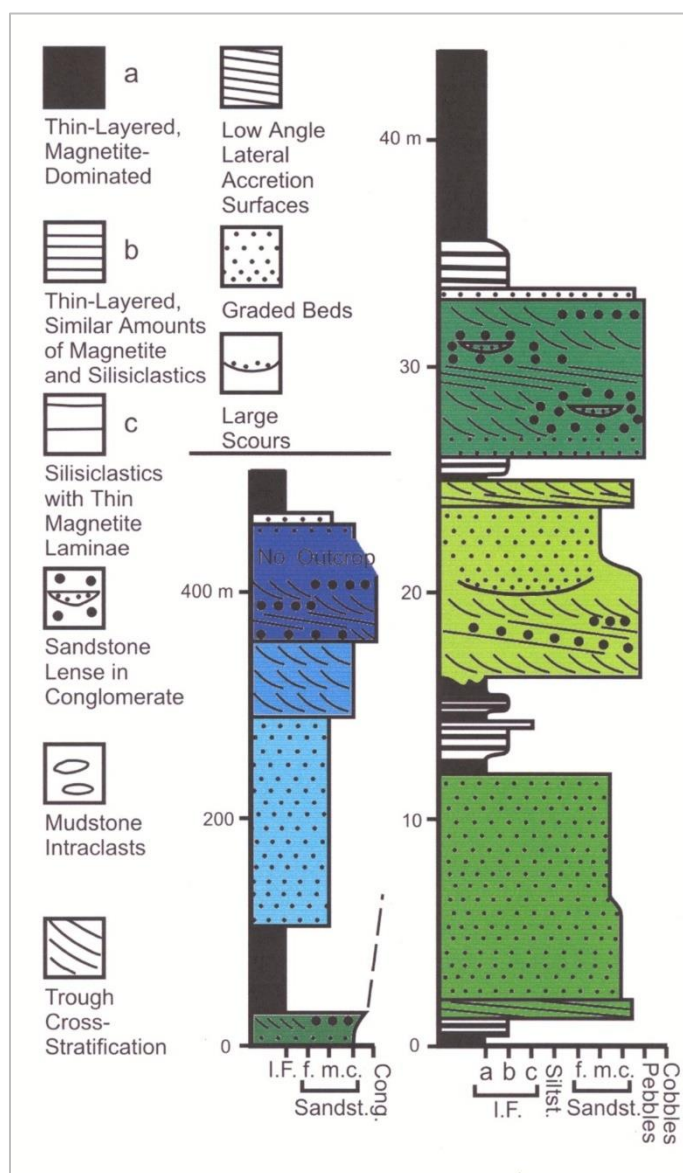
Figure 3.13: A stratigraphic column of the Eagle Island assemblage. The stratigraphic column on the left includes both the lower and upper coarsening-upwards successions. The stratigraphic column on the right is a more detailed column of the lower coarsening-upwards succession. Image from Fralick and Pufahl (2006).

Both coarsening upward cycles represent progradational sequences from the subaqueous environment to transitional strandline to subaerial deposits (Fralick and Pufahl, 2006). The sedimentology leads to the conclusion that the depositional environment for the Eagle Island assemblage was a wave dominated delta (Fralick and Pufahl, 2006). Iron oxyhydroxides were precipitated on top of the distributary mouth bar complex during flooding events and periods of sediment starvation from the subaerial environment (Fralick and Pufahl, 2006). Therefore, the meta-iron formation was deposited in a shallow water environment.

3.3.2 Petrographic Descriptions and Mineral Compositions

Samples were taken from five different locations within the stratigraphic column to accurately represent the mineralogy of the meta-iron formation in the Eagle Island assemblage. These samples include: an a-type magnetite-quartz meta-iron formation from the middle parasequence in the lower coarsening-upward succession (J0383), a b-type magnetite-quartz meta-iron formation from the basal 2 m of the 73 m-thick iron oxide-dominated meta-iron formation (J0385), an a-type hematite-quartz meta-iron formation from the middle of the 73 m iron oxide-dominated meta-iron formation (J0388), a magnetite-quartz meta-iron formation from the graded metasandstone lithofacies association in the prodelta of the upper coarsening-upward succession (J0395) and a magnetite-quartz meta-iron formation from the magnetite-dominated meta-iron formation above the upper depositional cycle (J03118). The lithologies in the Eagle Island assemblage can be grouped into four main units: magnetite-quartz meta-iron formation, hematite-quartz meta-iron formation, metasandstone and metasiltstone. SEM/EDX point analyses were conducted to determine the composition of the mineral phases in each lithology. Raw data from the SEM/EDX analysis can be seen in Appendix A. Table 3.7 shows the approximate modal abundances of the mineral phases from

the four main lithologies based on reflected, transmitted light petrography and SEM/EDX qualitative and quantitative point analyses.

Table 3.7: Approximate modal percentages for the phases in the lithologies from LSJ.

Lake St. Joseph Greenstone Belt														
	AFS	Ap	Bt	Cb	Chl	Ep	Hem	Kfs	Mag	Mus	Pl	Py	Qtz	Rt
Magnetite-quartz meta-iron formation		M	T/M	M	C	T	T		A	T/M	M	T	A	T
Hematite-quartz meta-iron formation	C	M					A	M	C	M			A	
Metasandstone		T	C	M				C	T	C	C	T	C	T
Metasiltstone		T	C	T					T	A	M	T	M	
Modal Percentages: >30% (A - abundant), 10 - 29% (C - common), 1 - 9% (M - minor), <1% (T- trace)														

Magnetite-quartz Meta-Iron Formation (a-type, lower coarsening-upward succession)

The a-type, lower coarsening-upward succession, magnetite-quartz meta-iron formation is composed of magnetite + quartz + chlorite + plagioclase + carbonate minerals + apatite ± biotite ± rutile (Figure 3.14). The meta-iron formation can be divided into two alternating layer types: magnetite-dominated and quartz-dominated laminae, which have both gradational and sharp contacts with each other. Thicknesses for the magnetite-dominated laminae range from <0.1 mm to 1.0 mm thick and <0.1 to 1.2 mm thick for the quartz-dominated laminae. Magnetite-dominated laminae are defined by layers that contain 60 – 80% magnetite, while quartz-dominated laminae are defined by layers that contain 40 – 70% quartz (Figure 3.14A, B).

Magnetite crystals are fine-grained (<0.1 mm – 0.2 mm), euhedral to subhedral and can contain inclusions of quartz, chlorite and carbonate minerals (Figure 3.14C). Quartz is also fine-grained (<0.1 mm – 0.1 mm), anhedral and flattened in the direction parallel to layering. Coarser-grained quartz is found within the quartz-dominated laminae and in lower strain zones associated with coarser-grained minerals such as magnetite, chlorite and carbonates (Figure 3.14D). Undulatory extinction, formation of subgrains and irregular subgrain boundaries are common deformation structures within quartz crystals. Plagioclase crystals are fine-grained (<0.1 mm – 0.1 mm), anhedral and

moderately flattened in the direction parallel to layering. Polysynthetic twinning is sometimes

preserved and when its not, it resembles quartz in thin section. Most of the plagioclase crystals are

restricted to the magnetite-dominated laminae. Chlorite crystals are very fine-grained (<0.1 mm),

display anomalous purple or brown interference colours and exhibit lattice and dimension preferred

orientation parallel to layering. Carbonate minerals are more common within the quartz-dominated

layers than the magnetite-dominated layers. These minerals form lozenge-shaped crystals which are

elongated parallel to layering. Generally, these crystals are coarser-grained compared to the rest of

the minerals, but they are still considered fine-grained (<1 mm – 0.3 mm). Carbonate minerals are

commonly poikiloblastic, and contain inclusions of magnetite, chlorite and quartz. Apatite forms

fine-grained (<0.1 – 1 mm), bright red, euhedral to subhedral hexagonal crystals and is only found

within the magnetite-dominated laminae. Biotite is rare in the meta-iron formation. When present,

it occurs as fine-grained (<0.1 mm) crystals orientated parallel to layering and shows retrograde

metamorphic reactions altering to chlorite. Rutile is found as a fine-grained (<0.1 mm), trace mineral

phase within the meta-iron formation and is associated along the grain boundaries of magnetite

crystals. Average mineral formulas calculated for the phases in the magnetite-quartz meta-iron

formation from the a-type lower coarsening-upwards sequence in Table 3.8.

Table 3.8: Average mineral formulas calculated for the a-type magnetite-quartz meta-iron formation from the lower coarsening upward succession.

Magnetite-quartz Meta-Iron Formation (a-type, lower coarsening upward succession)		
Mineral	Average Mineral Formula	Samples
Apatite	$Ca_{4.93}(PO_4)_{2.96}(OH,F,Cl)$	3
Carbonate (Ankerite)	$Ca_{0.99}(Mg_{0.59}Fe_{0.37}Mn_{0.02})_{\sum 0.98}(CO_3)_2$	4
Chlorite (Chamosite)	$(Fe_{1.39}Mg_{0.89}Al_{0.69})_{\sum 2.97}(Si_{2.68}Al_{1.32})_{\sum 4.00}O_{10}(OH)_2 \bullet (Fe_{1.39}Mg_{0.89}Al_{0.69})_{\sum 2.97}(OH)_6$	4
Magnetite	$(Fe^{3+}_{1.96}Fe^{2+}_{0.99})_{\sum 2.95}O_4$	8
Plagioclase (Albite)	$(Na_{1.02}Ca_{0.02})_{\sum 1.04}Al_{1.00}Si_{2.96}O_8$	4
Quartz	$Si_{1.00}O_2$	2
Rutile	$(Ti_{0.96}Fe_{0.05})_{\sum 1.01}O_2$	1
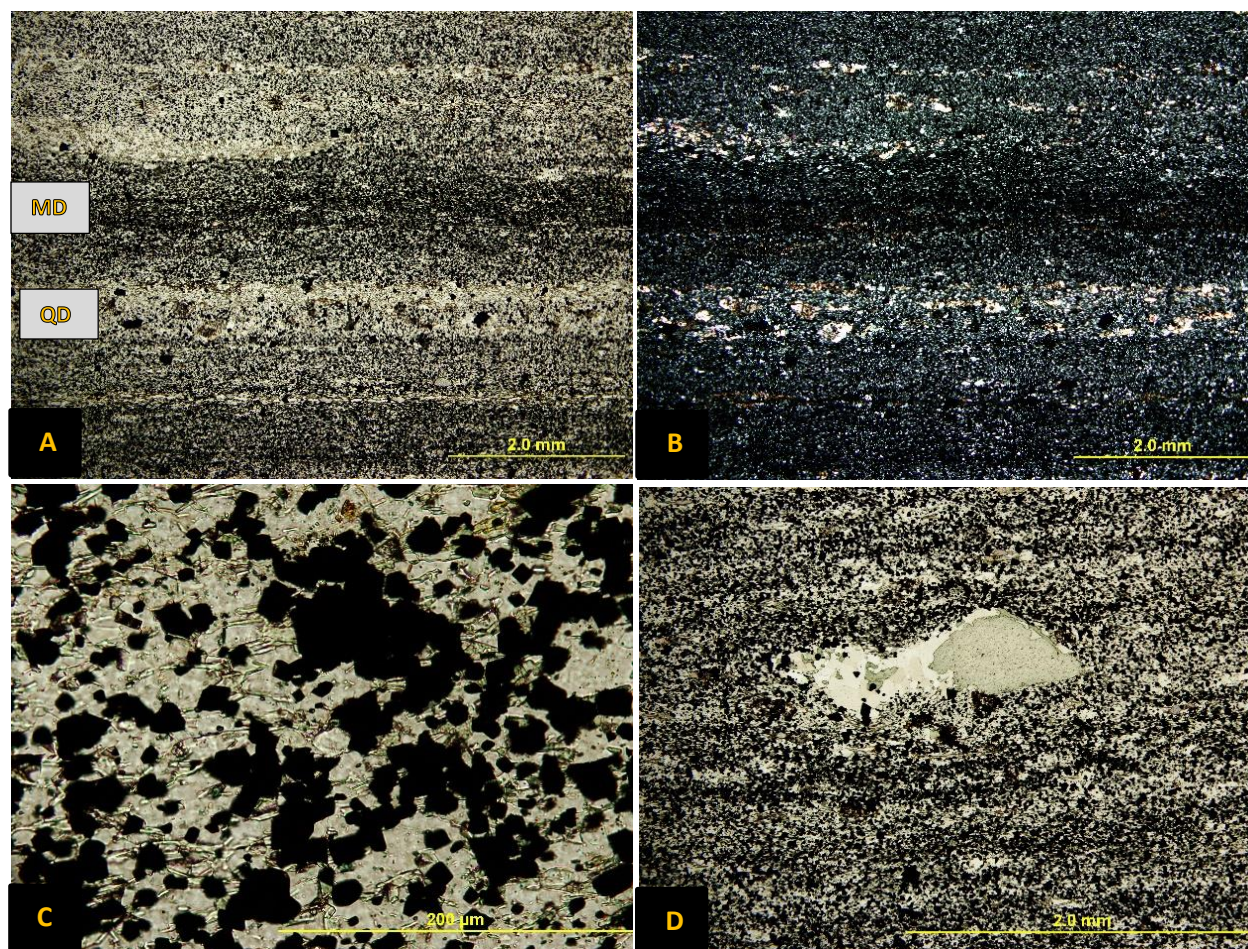
Figure 3.14: Photomicrographs of magnetite-quartz, a-type meta-iron formation. A) A transmitted PPL photomicrograph of the magnetite-quartz, a-type meta-iron formation. MD – magnetite-dominated laminae, QD – quartz-dominated laminae B) A transmitted XPL photomicrograph of the magnetite-quartz, a-type meta-iron formation. C) Poikiloblastic magnetite crystals with inclusions of quartz and chlorite. D) A chlorite crystal with coarser-grained quartz growing in the strain shadow indicating that solid state deformation had occurred.

Magnetite-quartz Meta-Iron Formation (b-type, basal section of the 73 m-thick meta-iron formation)

The composition of the magnetite-quartz, b-type meta-iron formation is magnetite + quartz + chlorite + plagioclase + carbonate minerals + apatite ± muscovite ± hematite ± rutile ± pyrite (Figure 3.15). Similarly, the meta-iron formation is composed of two alternating layer types: magnetite-dominated and quartz-dominated, which have transitional to sharp contacts. Average thicknesses for the quartz-dominated laminae are slightly thicker (<0.1 mm – 1.5 mm) than the previously described a-type meta-iron formation, while the magnetite-dominated laminae have relatively the same thicknesses (<0.1 mm – 1.0 mm).

Magnetite crystals are fine-grained (<0.1 mm – 0.1 mm), euhedral to anhedral and some contain inclusions of quartz and chlorite. Quartz is fine-grained (<0.1 mm – 0.1 mm), anhedral and displays undulatory extinction, flattening in the direction parallel to layering, formation of subgrains and irregular grain boundaries. Coarser-grained quartz is seen in quartz-dominated laminae, as well as in lower stain zones associated with coarser-grained magnetite, chlorite and carbonate minerals. Chlorite is fine-grained (<0.1 mm – 0.3 mm), euhedral to subhedral crystals, with anomalous brown interference and show a dimension preferred orientation parallel to layering. Finer-grained crystals occur throughout the rock, but coarser crystals occur most often in quartz-dominated laminae along the contact between the magnetite-dominated laminae. These crystals are often poikiloblastic containing inclusions of magnetite, quartz and carbonate minerals. Plagioclase is fine-grained (<0.1 mm – 0.1 mm), anhedral, flattened in the direction parallel to layering and most crystals do not preserve their polysynthetic twinning. Most of the plagioclase crystals are restricted in the magnetite-dominated laminae. Carbonate minerals are fine-grained (<0.1 mm), lozenge-shaped crystals oriented parallel to layering and are preferentially associated with the quartz-dominated layers. Apatite occurs as fine-grained (<0.1 mm – 0.3 mm), bright red, high relief crystals that are mostly associated in the magnetite-dominated layers. Muscovite, which consists of less than 1% of the minerology, is fine-grained (<0.1 mm), euhedral to subhedral and displays a lattice preferred and dimension preferred orientation in the direction parallel to layering. Hematite is fine-grained (<0.1 mm – 0.1 mm), and occurs as trace, platy, euhedral crystals associated with the chlorite. Rutile is fine-grained (<0.1 mm – 0.3 mm), euhedral to anhedral crystals that occur along grain boundaries of magnetite crystals. Pyrite is fine-grained (<0.1 mm – 0.5 mm) and occurs as trace minerals in both the magnetite- and quartz-dominated layers and contains inclusions of carbonate minerals and quartz. Average mineral formulas calculated for the phases in the magnetite-quartz meta-iron formation from the b-type, basal section of the 73 m thick meta-iron formation in Table 3.9.

Table 3.9: Average mineral formulas calculated for the phases in the b-type, magnetite-quartz meta-iron formation from the basal section of the 73 m-thick meta-iron formation.

Magnetite-quartz Meta-Iron Formation (b-type, basal section of 73 m thick meta-iron formation)		
Mineral	Average Mineral Formula	Samples
Apatite	$Ca_{4.92}(PO_4)_{2.97}(OH,F,Cl)$	3
Carbonate (Dolomite)	$Ca_{0.97}(Mg_{0.79}Fe_{0.17}Mn_{0.03})_{\Sigma 0.99}(CO_3)_2$	3
Chlorite (Clinochlore)	$(Mg_{1.55}Fe_{0.84}Al_{0.59})_{\Sigma 2.98}(Si_{2.79}Al_{1.21})_{\Sigma 4.00}O_{10}(OH)_2 \bullet (Mg_{1.55}Fe_{0.84}Al_{0.59})_{\Sigma 2.98}(OH)_6$	3
Hematite	$Fe_{1.97}O_3$	3
Magnetite	$(Fe^{3+}_{1.96}Fe^{2+}_{0.99})_{\Sigma 2.95}O_4$	3
Muscovite	$(K_{0.64}Na_{0.39})_{\Sigma 1.03}(Al_{1.50}Fe_{0.28}Mg_{0.15}Ti_{0.01})_{\Sigma 1.94}(Si_{3.54}Al_{0.46})_{\Sigma 4.00}O_{10}(OH)_2$	3
Plagioclase (Albite)	$Na_{0.94}Al_{0.93}Si_{3.05}O_8$	3
Quartz	$Si_{1.00}O_2$	2
Rutile	$(Ti_{0.98}Fe_{0.02})_{\Sigma 1.00}O_2$	3
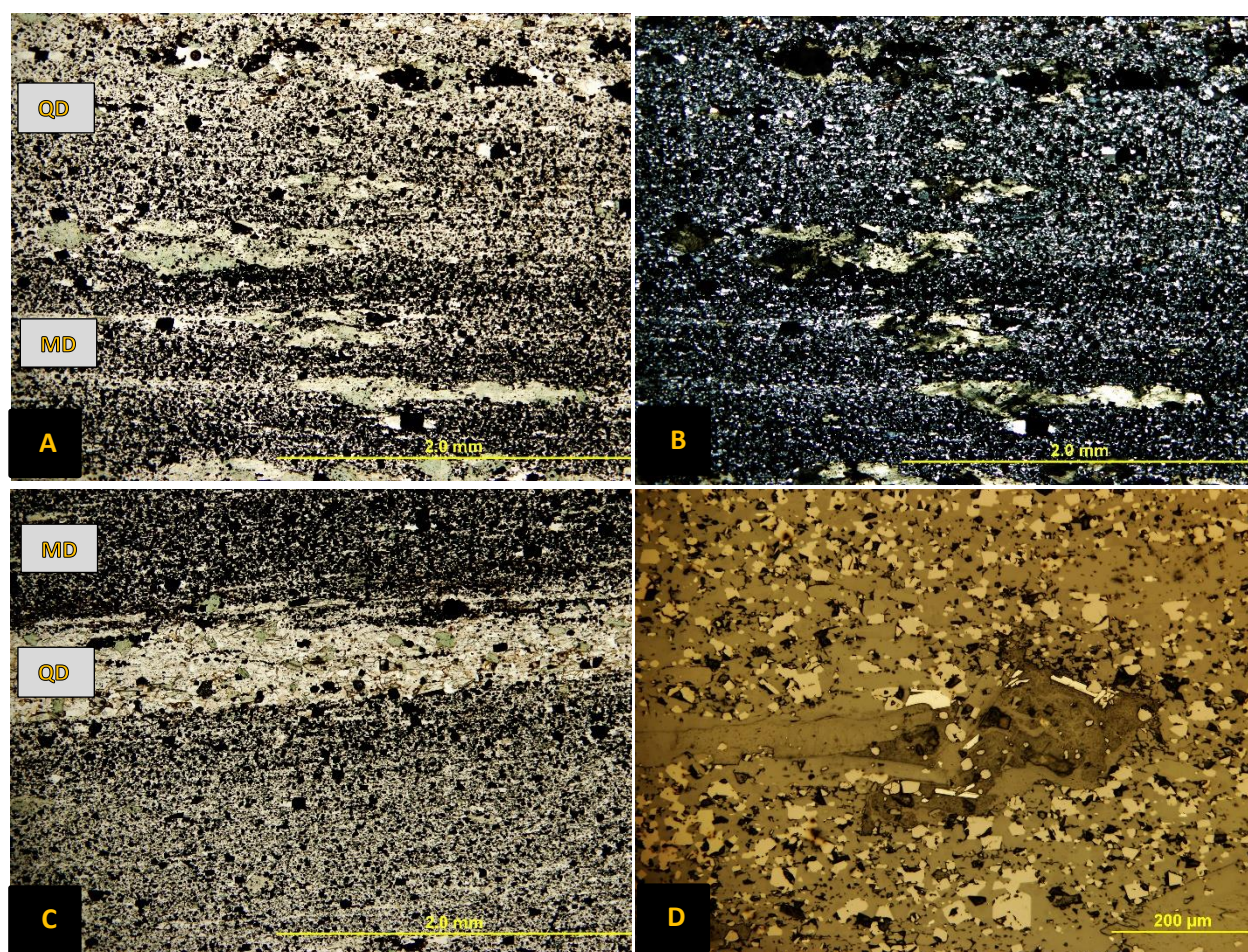
Figure 3.15: Photomicrographs of magnetite-quartz, b-type meta-iron formation. A) A transmitted PPL photomicrograph of the b-type, meta-iron formation. MD – Magnetite-dominated laminae, QD – Quartz-dominated laminae. B) A transmitted XPL photomicrograph of the b-type, meta-iron formation. C) Sharp contacts between the quartz- and magnetite-dominated layers. Coarser-grained chlorite crystals occur in the quartz-dominated layers. D) A reflected PPL photomicrograph of fine-grained hematite crystals (bright sliver crystals) forming as long laths near coarser-grained chlorite (elongated dark grey minerals).

Magnetite-quartz Meta-iron Formation (turbiditic prodelta, upper coarsening-upwards succession)

The composition of the quartz-magnetite meta-iron formation from the turbiditic prodelta is magnetite + quartz + chlorite + plagioclase + muscovite + biotite + epidote + apatite + rutile ± pyrite (Figure 3.16). The laminae are divided into three types of layers: 1) magnetite-rich laminae, 2) quartz-dominated laminae and 3) silicate-dominated layers, which are interpreted to be siliciclastic layers. Rarely preserved in thin section, the magnetite-dominated laminae have sharp bottom contacts and grade to the quartz-magnetite dominated layers (Figure 3.17D). Magnetite-dominated laminae are 0.1 mm – 1.2 mm thick and the bulk mineralogy consists of 50 – 55% magnetite, 35 – 30% chlorite, 5 – 10% muscovite and about 5 – 10 % quartz and plagioclase. The quartz-magnetite layers have relatively similar thicknesses and the same bulk composition as the magnetite-rich laminae except with different proportions: 50 – 45% quartz and plagioclase, 25 – 30% magnetite, 15 – 25% chlorite and 5% muscovite. Silicate-dominated layers are 0.5 mm to more than 10 mm thick, and a bulk mineralogy of 40% plagioclase, 20% quartz, 20% chlorite 10% magnetite and 10% muscovite.

Magnetite is fine-grained (<0.1 mm – 0.2 mm) and has euhedral to subhedral crystals. Coarser-grained crystals are fractured and contain inclusions of quartz, chlorite and pyrite. Quartz occurs as fine-grained (<0.1 mm – 0.2 mm), anhedral crystals and displays undulatory extinction, formation of subgrains and irregular grain boundaries. Crystals are flattened in the direction parallel to layering. Chlorite is fine- to medium-grained (<0.1 mm – 1.3 mm), euhedral to anhedral with anomalous purple interference colours. In all three of the different layer types, chlorite has a strong dimension preferred orientation parallel to layering and a strong lattice preferred orientation. Chlorite also displays anastomosing cleavage around coarser-grained quartz crystals and plagioclase crystals. Coarser-grained chlorite occurs in the low strain zones associate with pyrite and quartz. Plagioclase

is fine-grained (<0.1 mm – 0.2 mm), subhedral to anhedral, and often contains inclusions of sericite

and carbonate minerals. Deformation microstructures such as slight bending and tapering of twins,

subgrain formation are present. However, most coarser-grained minerals preserve their

polysynthetic twins. Plagioclase is coarser-grained in the silicate-dominated layers compared to the

magnetite-and quartz-dominated layers. Muscovite occurs as fine-grained (<0.1 mm) elongated

crystals, strong dimension preferred orientation parallel to layering and a strong lattice preferred

orientation. Both minerals are associated with chlorite and some biotite crystals show retrograde

metamorphic reactions into chlorite. Epidote is fine-grained (<0.1 mm – 0.2 mm), poikilitic,

subhedral to anhedral and is sporadically found in all the layers but especially in the silicate-
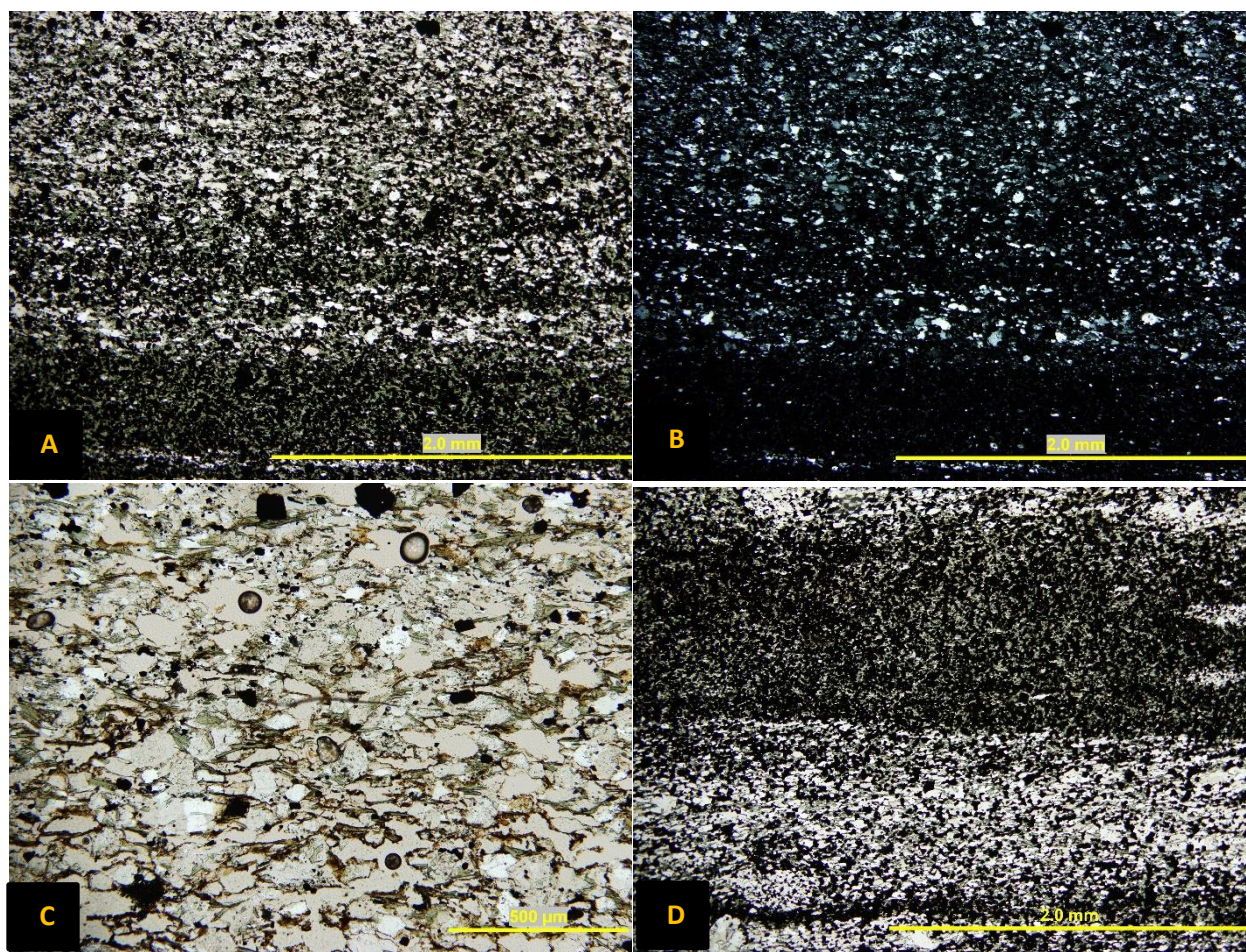
Figure 3.16: Photomicrographs of meta-iron formation from the prodelta. A) Transmitted PPL photomicrograph of magnetite-dominated and quartz dominated layers. B) Transmitted XPL photomicrograph of the magnetite and quartz-dominated layers. C) A transmitted PPL photomicrograph a silicate-dominated layer. D) Sharp contact between the top of the quartz-dominated layer and the bottom of the magnetite-dominated layer.

dominated layers. Rutile is fine-grained (<0.1 mm – 0.5 mm) forming with magnetite and chlorite crystals. Carbonate minerals are fine-grained (<0.1 mm – 0.2 mm), anhedral to subhedral, elongated crystals forming parallel to layering. Coarser-grained carbonate minerals occur along low strain zones of coarser-grained quartz and pyrite crystals. Pyrite occurs as euhedral, fine-grained (0.1 mm – 1.0 mm) crystals. Average mineral formulas calculated for the phases in the magnetite-quartz meta-iron formation from the turbiditic prodelta in Table 3.10.

Table 3.10: Average mineral formulas calculated for the phases in the magnetite-quartz meta-iron formation from the turbiditic prodelta in the upper coarsening-upwards succession.

Magnetite-quartz Meta-Iron Formation (turbiditic prodelta, upper coarsening upwards succession)		
Mineral	Average Mineral Formula	Samples
Apatite	$Ca_{4.93}(PO_4)_{2.93}(OH,F,Cl)$	6
Chlorite (Chamosite)	$(Fe_{1.32}Mg_{1.00}Al_{0.65})_{\sum 2.97}(Si_{2.70}Al_{1.30})_{\sum 4.00}O_{10}(OH)_2 \bullet (Fe_{1.32}Mg_{1.00}Al_{0.65})_{\sum 2.96}(OH)_6$	7
Epidote	$Ca_{1.96}Al_{2.00}(Fe_{0.93}Al_{0.12})_{\sum 1.05}[Si_{2.20}O_7][Si_{1.00}O_4]O(OH)$	5
Ilmenite	$Ti_{1.13}Fe_{0.56}O_3$	6
Magnetite	$(Fe^{3+}_{1.96}Fe^{2+}_{1.00})_{\sum 2.96}O_4$	8
Muscovite	$(K_{0.87}Na_{0.04})_{\sum 0.91}(Al_{1.62}Fe_{0.28}Mg_{0.15}Ti_{0.02})_{\sum 2.07}(Si_{3.25}Al_{0.75})_{\sum 4.00}O_{10}(OH)_2$	5
Plagioclase (Albite)	$(Na_{0.98}Ca_{0.01})_{\sum 0.99}Al_{1.00}Si_{2.98}O_8$	7
Quartz	$Si_{1.00}O_2$	3

Magnetite-quartz Meta-iron Formation (above the upper depositional cycle)

The composition of the magnetite-quartz meta-iron formation from above the upper depositional cycle is magnetite + quartz + muscovite + biotite + plagioclase + carbonate minerals + apatite (Figure 3.17). The meta-iron formation is comprised of two distinct layers: magnetite-quartz laminae, which are defined by 60 – 80% magnetite and quartz-magnetite laminae, which are defined by 40 – 70% quartz. The thickness of both layers ranges from <0.1 mm – 1.0 mm.

Magnetite is fine-grained (<0.1 mm – 0.1 mm), subhedral, porphyroblastic interlocking crystals that contain inclusions of biotite, quartz, muscovite, apatite and plagioclase (Figure 3.17B). Quartz is fine- to medium-grained (<0.1 mm – 1.2 mm), anhedral, and displays undulatory extinction, irregular grain boundaries and subgrain formation. The quartz crystals are flattened with their long axis in the

direction parallel to layering. Quartz also occurs as coarser-grained minerals in folded quartz-carbonate veins that cut through the meta-iron formation. Muscovite and biotite are fine-grained (<0.1 mm – 0.5 mm), elongated parallel to layering and contains inclusions of magnetite. Coarser-grained crystals are associated with magnetite-quartz laminae. Plagioclase is fine-grained (<0.1 mm – 0.5 mm) and anhedral. Carbonate minerals are fine-grained (<0.1 mm – 0.7 mm), subhedral to anhedral and are more common in quartz-magnetite laminae. In the meta-iron formation, they form lozenge-shaped crystals with their long axis parallel to layering. Apatite is fine-grained (<0.1 mm to 0.2 mm) and is associated with poikiloblastic magnetite crystals or as inclusions in biotite. Most of the apatite is in the magnetite-quartz laminae. Average mineral formulas calculated for the phases in the magnetite-quartz meta-iron formation from above the upper depositional cycle in Table 3.11.

Table 3.11: Average minerals formulas calculated for the phases in the magnetite-quartz meta-iron formation above the upper depositional cycle.

Magnetite-quartz Meta-Iron Formation (above the upper depositional cycle, meta-iron formation)		
Mineral	Average Mineral Formula	Samples
Apatite	$Ca_{4.92}(PO_4)_{2.97}(OH,F,Cl)$	3
Biotite (Phlogopite)	$(K_{0.91}Na_{0.01})_{\Sigma\,0.92}(Mg_{1.50}Fe_{1.23}Ti_{0.10})_{\Sigma\,2.83}Al_{1.33}Si_{2.80}O_{10}(OH)_2$	3
Carbonate (Ankerite)	$Ca_{0.99}(Mg_{0.73}Fe_{0.24}Mn_{0.03})_{\Sigma\,1.00}(CO_3)_2$	4
Magnetite	$(Fe^{3+}_{1.96}Fe^{2+}_{1.00})_{\Sigma\,2.96}O_4$	3
Muscovite	$(K_{0.95}Na_{0.02})_{\Sigma\,0.97}(Al_{1.46}Fe_{0.40}Mg_{0.25}Ti_{0.02})_{\Sigma\,2.13}(Si_{3.24}Al_{0.76})_{\Sigma\,4.00}O_{10}(OH)_2$	3
Plagioclase (Albite)	$(Na_{1.01}K_{0.01})_{\Sigma\,1.02}Al_{0.99}Si_{2.98}O_8$	3
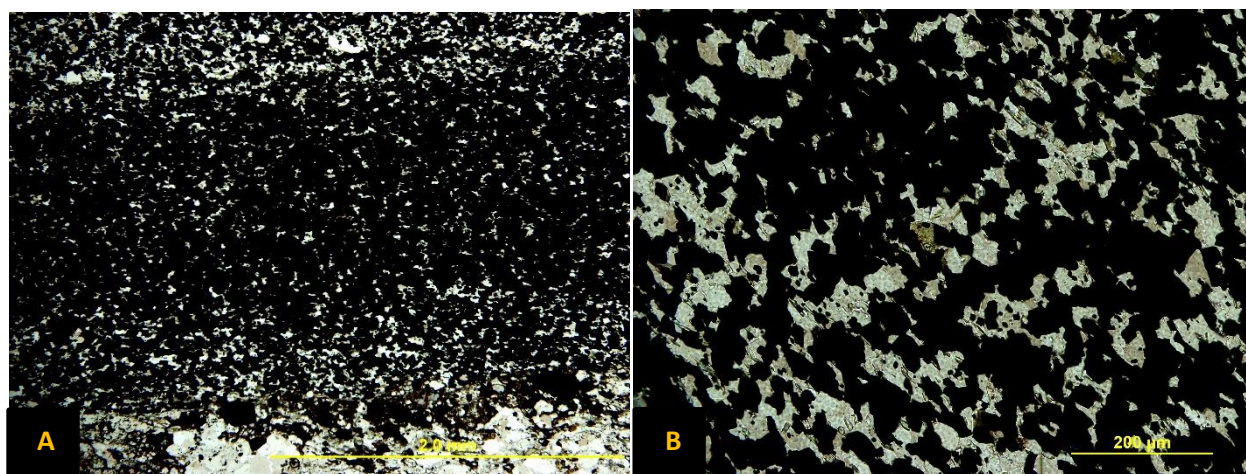
Figure 3.17: Photomicrographs of magnetite-quartz meta-iron formation from above the upper depositional cycle. A) Transmitted PPL photomicrograph of the magnetite-quartz meta-iron formation. B) Photomicrograph of the magnetite-dominated laminae. Subhedral, interlocking porphyroblastic crystals can be seen. They contain inclusions of muscovite, biotite, plagioclase, apatite and quartz.

Magnetite-quartz Meta-Iron Formation Mineral Compositions

Tables 3.8 – 3.11 show the average composition of the mineral phases in the magnetite-quartz meta-iron formations throughout the Eagle Island assemblage. Significantly, the compositions of the phases in the meta-iron formation are consistent throughout the stratigraphic column. Approximate modal percentages for the phases in the magnetite-quartz meta-iron formation include abundant magnetite and quartz, with common occurrences of chlorite, minor amounts of apatite, carbonate minerals, plagioclase and trace amounts of rutile, hematite, epidote and pyrite (Table 3.7). The abundance of muscovite and biotite varies between minor and trace amounts in the magnetite-quartz meta-iron formation within the stratigraphic column.

In the magnetite-quartz meta-iron formation, chlorite ranges in composition from chamosite to clinochlore throughout the Eagle Island assemblage. However, most of the chlorite is chamosite in composition. The composition of the carbonate minerals ranges from ankerite to dolomite in the magnetite-quartz meta-iron formations. However, the majority of the carbonate minerals are ankerite in composition, which is the iron-endmember of the dolomite group carbonates. Although manganese is not abundant in the ankerite and dolomite phases, they are the only phases analyzed that contain manganese above detection limits. The magnetite-quartz meta-iron formation from the turbiditic prodelta is the only magnetite-quartz meta-iron formation that does not contain carbonate minerals. However, it is the only magnetite-quartz meta-iron formation to contain epidote. Plagioclase was determined to be albite (An0 – An2) in composition for all the magnetite-quartz meta-iron formation samples. Significantly, albite is the only major sodium-bearing phase in the meta-iron formation. Although, trace amounts of sodium are present in muscovite and biotite. Apatite is the only phosphorous-bearing mineral phase in the magnetite-quartz meta-iron formation. The abundance of the rest of the phases is less than 5%.

The amount of biotite and muscovite increases with the amount of interbedded siliciclastic layers. In the siliciclastic poor meta-iron formation samples there are <1% muscovite and biotite. The meta-iron formation from the turbiditic prodelta and above the upper depositional succession can have up to 5% biotite and muscovite. Biotite was determined to be phlogopite in composition, which is the magnesium-endmember biotite. The composition of muscovite is fairly consistent throughout the Eagle Island assemblage. Significantly, muscovite and biotite are the only major potassium-bearing phases in the magnetite-quartz meta-iron formation. Rutile is the only major titanium-bearing phase in the meta-iron formation.

Hematite-quartz Meta-Iron Formation (a-type, middle section of the 73 m-thick meta-iron formation)

The mineralogy of the a-type, hematite-quartz meta-iron formation from the 73 m-thick meta-iron formation is composed of abundant hematite and quartz, has common occurrences of magnetite and Al-Fe-silicate, as well as minor amounts of K-feldspar, muscovite and apatite (Table 3.7, Figure 3.18). This meta-iron formation is composed of two types of layers: iron oxide-dominated laminae and quartz-dominated laminae. The iron oxide-dominated laminae are defined by $80 - 95\%$ hematite and magnetite, while the quartz-dominated laminae are defined by $40 - 60\%$ quartz (Figure 3.18A, B). For most of the iron oxide- and quartz-dominated couplets, the iron oxide-dominated laminae grades into the quartz-dominated laminae, with sharp contacts between couplets (Figure 3.18B). The thicknesses of both types of laminae range from <0.1 mm – 1.5 mm.

Hematite is the dominant minerology of the hematite-quartz meta-iron formation. It forms as platy, fine-grained (<0.1 mm – 0.2 mm) crystals that exhibit a moderate to strong lattice and dimension preferred orientation parallel to the direction of layering. Quartz is fine-grained (<0.1 mm – 0.1 mm), anhedral and displays undulatory extinction, irregular grain boundaries and formation of subgrains. The crystals are coarser-grained in the quartz-dominated laminae and along low strain

zones associated with coarser-grained phases. Magnetite crystals are fine-grained (<0.1 mm – 0.2 mm), cubic, euhedral to subhedral and highly fractured (Figure 3.18C). All the euhedral to subhedral magnetite crystals have hematite exsolution laminae, which can be seen in XPL through a reflected light microscope. Muscovite is fine-grained (<0.1 mm), euhedral to subhedral and forms a dimension preferred orientation parallel to layering in both the iron oxide- and quartz-dominated laminae. K-feldspar is fine-grained (<0.1 mm to 0.1 mm), anhedral and optically resembles quartz.
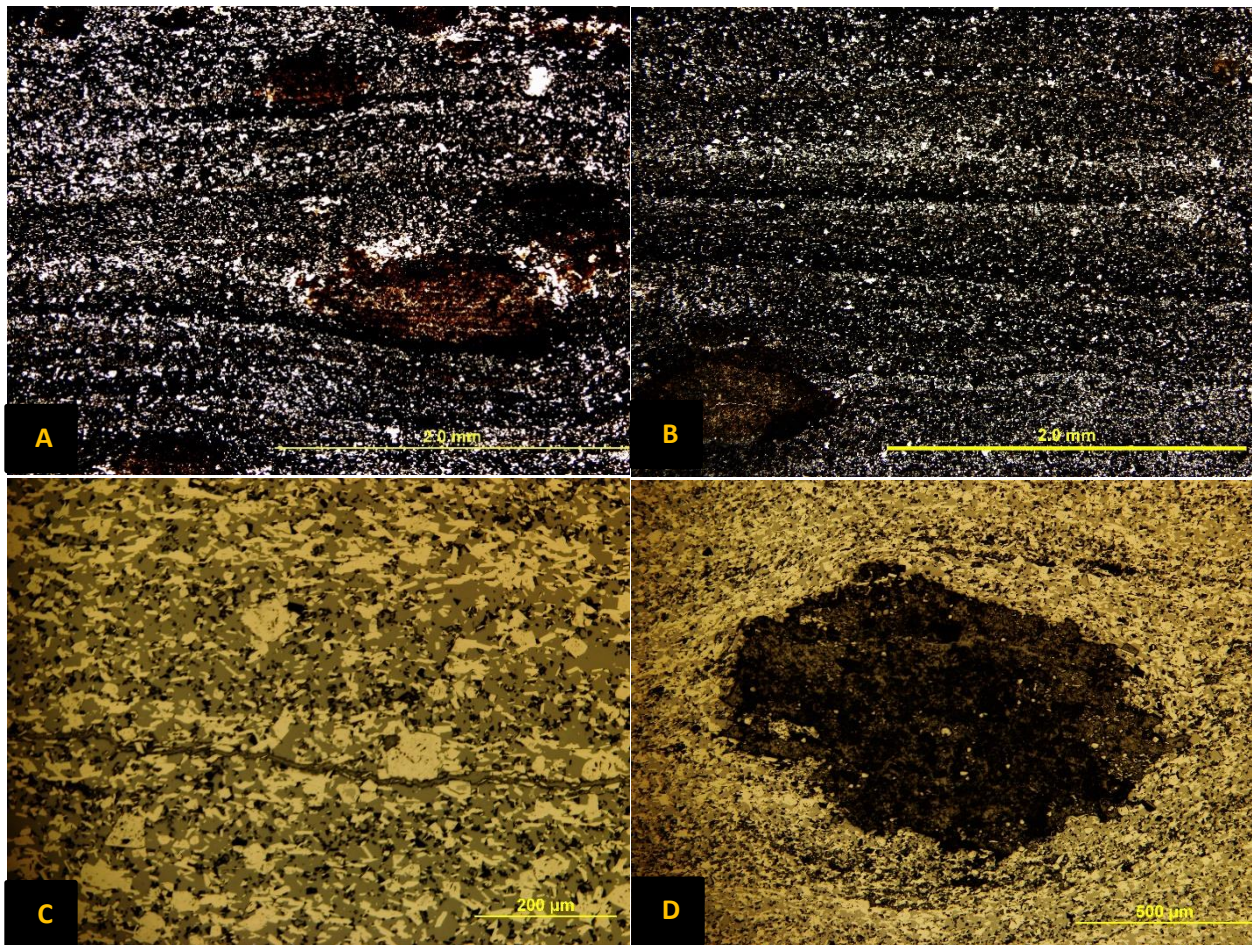
Figure 3.18: Photomicrographs of hematite-quartz meta-iron formation. A) A photomicrograph of the hematite-quartz meta-iron formation in transmitted PPL. The dark (iron oxide) layers are wrapping around the iron rusted, ellipsoidal, Al-Fe-silicate (brown/red) crystals. B) Transmitted light photomicrograph of the gradational contacts between iron oxide- (darker layers) and quartz-dominated (lighter layers) couplets and sharp contacts between couplets. C) Photograph of the magnetite and hematite crystals in reflected light. The cubic magnetite crystals are all fractured. Hematite crystals are platy and display a moderate dimension preferred orientation parallel to layering. D) An Al-Fe-silicate porphyroblast with hematite and magnetite crystals wrapping around the porphyroblast in reflected light.

Al-Fe-silicate occurs as fine- to medium-grained (<0.1 mm – 1.5 mm), iron-rusted, ellipsoidal porphyroblasts (Figure 3.18D). The mineral phase was termed Al-Fe-silicate because the mineral could not be identified based on the SEM/EDX analysis data. The porphyroblasts contain inclusions of magnetite, hematite, muscovite, quartz and apatite. The long axis of the hematite and muscovite grains are slightly rotated inside the Al-Fe-silicate porphyroblasts. Iron oxide-dominated laminae also wrap around the Al-Fe-silicate porphyroblasts. Apatite is more abundant in these lithologies than in the a- and b-type magnetite-quartz meta-iron formations. It is fine-grained (<0.1 mm – 0.1 mm), bright red and forms euhedral to subhedral crystals. Most commonly apatite is in contact with hematite and magnetite crystals, but also occurs in Al-Fe-silicate porphyroblasts.

Mineral formulas calculated for the hematite-quartz meta-iron formation is presented in Table 3.12. Muscovite has a similar composition to the muscovite from the magnetite-quartz meta-iron formation. However, the muscovite from the hematite-quartz meta-iron formation contains no titanium. Muscovite and K-feldspar are the only major potassium-bearing phases in the hematite-quartz meta-iron formation. Al-Fe-silicate contains silicon, iron, aluminum, calcium and magnesium, but the formula for this mineral is unknown. Lastly, apatite has a similar composition to the apatite in the magnetite-quartz meta-iron formation. It is the only phosphorous-bearing mineral phase in the meta-iron formation. Significantly, the hematite-quartz meta-iron formation does not contain carbonate minerals or any major sodium-bearing phases.

Table 3.12: Average mineral formulas calculated for the phases in the hematite-quartz meta-iron formation.

Hematite-quartz Meta-Iron Formation (a-type, middle section of the 73 m thick meta-iron formation)		
Mineral	Average Mineral Formula	Samples
Apatite	$Ca_{4.88}(PO_4)_{2.96}(OH,F,Cl)$	6
Hematite	$Fe_{1.97}O_3$	6
K-Feldspar	$(K_{0.95}Na_{0.02})_{\Sigma\,0.97}Al_{0.95}Si_{3.02}O_8$	4
Magnetite	$(Fe^{3+}_{1.93}Fe^{2+}_{1.01})_{\Sigma\,2.94}O_4$	6
Muscovite	$(K_{0.94}Na_{0.02})_{\Sigma\,0.96}(Al_{1.44}Fe_{0.40}Mg_{0.27})_{\Sigma\,2.11}(Si_{3.34}Al_{0.66})_{\Sigma\,4.00}O_{10}(OH)_2$	5
Quartz	$Si_{0.99}O_2$	2
Al-Fe-silicate	unknown formula	9

Magnetite-quartz Meta-Iron Formation with Clastic Metasedimentary Layers (above the upper

depositional cycle)

The magnetite-quartz meta-iron formation from above the upper depositional cycle contains

interbedded clastic metasedimentary layers: metasandstone and metasiltstone layers. The

metasandstone layers consist of common occurrences of quartz, K-feldspar, plagioclase, muscovite,

biotite, with minor amounts of carbonate minerals and trace amounts of magnetite, apatite and

rutile (Table 3.7). The metasiltstone layers contain abundant muscovite, common occurrences of

biotite, minor amounts of quartz, plagioclase and trace amounts of carbonate minerals, magnetite,

pyrite and apatite (Table 3.7). Metasandstone layers are defined by coarse-grained K-feldspar,

plagioclase and quartz crystals (Figure 3.19A, B), while the metasiltstone layers are defined by 70 –

90% biotite and muscovite (Figure 3.19C, D). Thicknesses of the metasedimentary layers ranges

from 0.1 mm to more than 20 mm.

Magnetite is fine-grained (<0.1 mm – 0.1 mm), subhedral, porphyroblastic interlocking crystals

that contain inclusions of biotite, quartz, muscovite, apatite and plagioclase. Quartz is fine- to

medium-grained (<0.1 mm – 1.2 mm), anhedral and displays undulatory extinction, irregular grain

boundaries and subgrain formation. The quartz crystals are flattened with their long axis in the

direction parallel to layering. In the metasandstone layers, quartz occurs as medium-grained

porphyroclasts with deformation tails. This indicates that these grains were rotated during

metamorphism and deformation. Muscovite and biotite are fine-grained (<0.1 mm – 0.5 mm),

elongated parallel to layering and contains inclusions of magnetite. Coarser-grained crystals and

anastomosing cleavage are associated with the metasedimentary layers. K-feldspar crystals occur as

fine- to medium-grained (<0.1 mm – 1.5 mm), anhedral crystals and are only observed in the

metasandstone layers. The medium-grained porphyroclasts show deformation structures such as
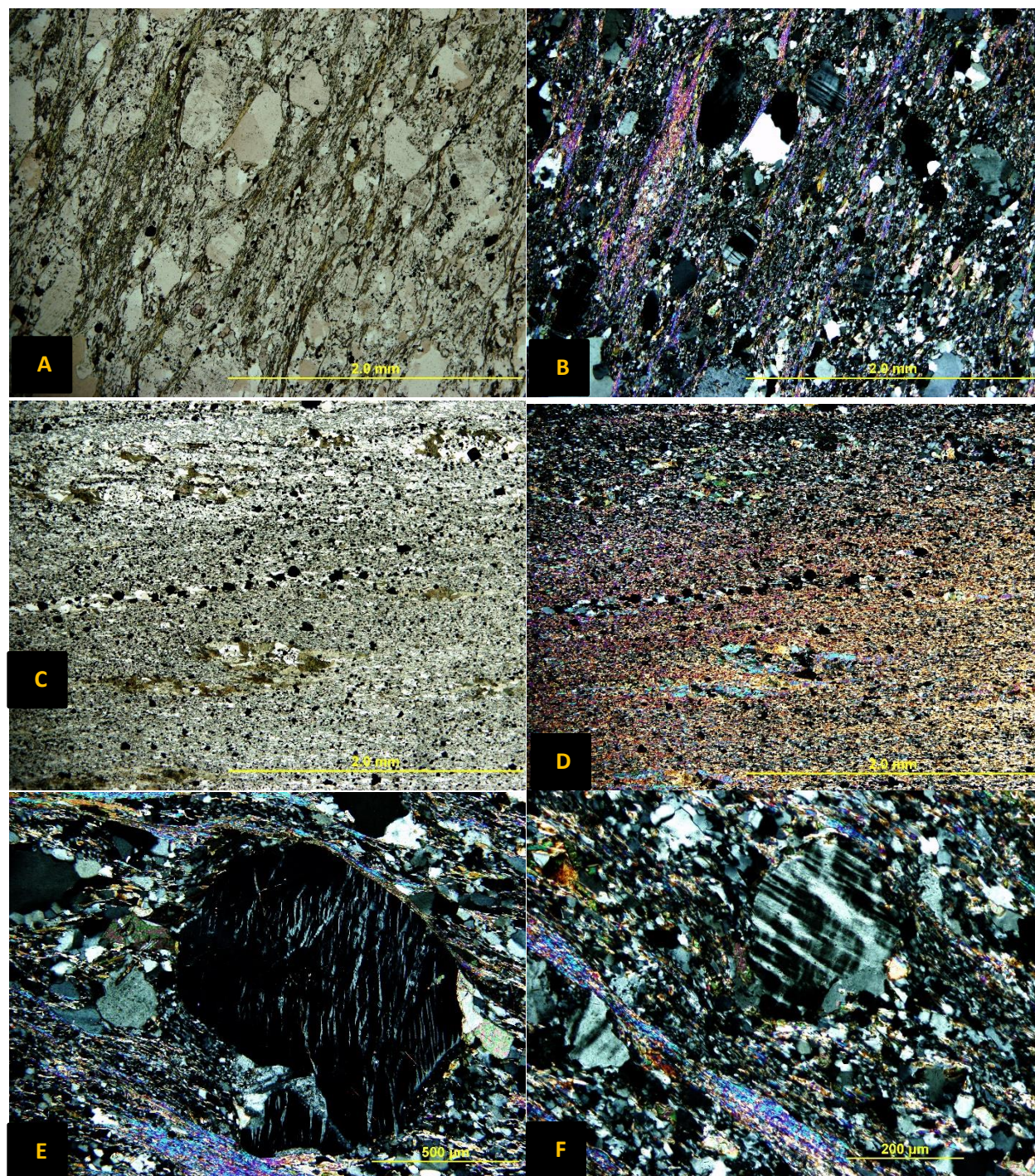
Figure 3.19: Photomicrographs clastic metasedimentary layers above the upper depositional cycle. A) Photograph of the metasandstone layer in PPL. Biotite and muscovite anastomosing around medium-grained K-feldspar, plagioclase and quartz porphyroclasts. B) Photograph of a metasandstone layer in XPL. C) Photograph of a metasiltstone layer in PPL. Biotite crystals display brown pleochroism and are coarser-grained. D) Photograph of the metasiltstone layer in XPL. E) and F) Deformation structures of K-feldspar crystals in the metasandstone layers.

undulatory extinction, subgrain formation, irregular grain boundaries, tapering, bending of twins and formation of wormy-like intergrowths (Figure 3.19E, F). Some K-feldspar grains contain sericite and carbonate inclusions. Plagioclase is fine- to medium-grained (<0.1 mm – 1.5 mm), anhedral and are coarser-grained in the metasandstone layers. Carbonate minerals are fine-grained (<0.1 mm – 0.7 mm), subhedral to anhedral and commonly occur as coarser-grained crystals forming in the low strain zones of the quartz and K-feldspar porphyroclasts of the metasandstone. Apatite is fine-grained (<0.1 mm – 0.2 mm) and is associated with poikiloblastic magnetite crystals or as inclusions in biotite. Most of the apatite is in the magnetite-dominated laminae. Rutile is fine-grained (<0.1 mm – 0.1 mm) and restricted to the metasandstone layers. Pyrite crystals are fine-grained (<0.1 mm – 0.3 mm), euhedral to subhedral crystals. Average mineral formulas calculated for the metasandstone and metasiltstone layers can be seen in Tables 3.13 and 3.14, respectively. Only qualitative analyses were conducted on quartz and pyrite.

Table 3.13: Average mineral formulas calculations for the phases in the metasandstone from above the upper depositional cycle.

Magnetite-quartz Meta-Iron Formation (above the upper depositional cycle, coarse-grained metasandstone)		
Mineral	Average Mineral Formula	Samples
Apatite	$Ca_{4.99}(PO_4)_{2.95}(OH,F,Cl)$	3
Biotite (Phlogopite)	$(K_{0.92}Na_{0.02})_{\sum 0.93}(Mg_{1.44}Fe_{1.24}Ti_{0.13})_{\sum 2.81}Al_{1.31}Si_{2.81}O_{10}(OH)_2$	4
Carbonate (Ankerite)	$Ca_{0.98}(Mg_{0.71}Fe_{0.23}Mn_{0.03})_{\sum 0.97}(CO_3)_2$	3
K-Feldspar	$(K_{0.97}Na_{0.01})_{\sum 0.98}Al_{0.98}Si_{3.02}O_8$	2
Magnetite	$(Fe^{3+}_{1.94}Fe^{2+}_{1.01})_{\sum 2.95}O_4$	3
Muscovite	$(K_{0.92}Na_{0.02})_{\sum 0.94}(Al_{1.46}Fe_{0.34}Mg_{0.23}Ti_{0.04})_{\sum 2.07}(Si_{3.38}Al_{0.62})_{\sum 4.00}O_{10}(OH)_2$	2
Plagioclase (Albite)	$(Na_{0.96}Ca_{0.01})_{\sum 0.97}Al_{0.98}Si_{3.02}O_8$	2
Rutile	$Ti_{0.98}O_2$	1

Table 3.14: Average mineral formulas calculated for the phases in the metasiltstone from above the upper depositional cycle.

Magnetite-quartz Meta-Iron Formation (above the upper depositional cycle, metasiltstone)		
Mineral	Average Mineral Formula	Samples
Apatite	$Ca_{5.00}(PO_4)_{2.93}(OH,F,Cl)$	3
Biotite (Phlogopite)	$(K_{0.86}Na_{0.05})_{\sum 0.91}(Mg_{1.48}Fe_{1.19}Ti_{0.09})_{\sum 2.76}Al_{1.37}Si_{2.82}O_{10}(OH)_2$	3
Magnetite	$(Fe^{3+}_{1.95}Fe^{2+}_{0.99})_{\sum 2.94}O_4$	3
Muscovite	$(K_{0.90}Na_{0.03})_{\sum 0.93}(Al_{1.42}Fe_{0.42}Mg_{0.26}Ti_{0.03})_{\sum 2.13}(Si_{3.31}Al_{0.69})_{\sum 4.00}O_{10}(OH)_2$	3
Plagioclase (Albite)	$(Na_{0.90}K_{0.02})_{\sum 0.92}Al_{0.99}Si_{3.02}O_8$	3

K-feldspar is only found in the metasandstone and has a composition similar to the K-feldspar in the hematite-quartz meta-iron formation. Biotite is phlogopite in composition which is the magnesium-endmember biotite. Muscovite also has a similar composition to the muscovite from both hematite-quartz and magnetite-quartz meta-iron formation. K-feldspar, muscovite and biotite are the main potassium-bearing phases and all these phases contain trace amounts of sodium. Plagioclase is albite (An1 – An2) in composition and is found in both the metasedimentary layers. Albite is the only major sodium-bearing phase in the clastic metasedimentary layers. Carbonate minerals are ankerite in composition and are found in both metasedimentary layers. Although in trace amounts, ankerite is the only phase in the clastic metasedimentary layers that contains manganese above detection limits. Apatite has the same composition as the apatite from the meta-iron formation samples and again is the only major phosphorous-bearing phase in the clastic metasedimentary rocks. The composition of the magnetite is consistent with the magnetite from the meta-iron formation samples, while rutile is pure titanium without a solid solution with iron as observed in the magnetite-quartz meta-iron formation.

3.3.3 Metamorphism

To determine peak metamorphism in the LSJ Eagle Island assemblage, it is imperative to determine the stable metamorphic mineral assemblage of the metasiltstone layer. The metasiltstone units were collected from above the upper depositional cycle. The stable metamorphic mineral assemblage of the metasiltstone is quartz + albite + biotite + muscovite + magnetite. For Al-poor pelitic rocks, biotite and muscovite can be stable at 400°C (Bucher and Grapes, 2011; Winter, 2010). However, since there is an abundance of muscovite and biotite in the metasiltstone and their formulas contain significant amounts of aluminum, the aluminum content for the protolith of the metasiltstone was at least average. Since there are significant amounts of

magnesium in the biotite and muscovite crystals, the peak metamorphic temperature was at least

420°C and most likely closer to 440°C (Bucher and Grapes, 2011). Therefore, the stable metamorphic

mineral assemblage suggests that peak metamorphic temperatures were at least at the mid-

greenschist facies.

Microstructures can constrain the range of metamorphism by looking at the metasandstone

layers, which were collected from above the upper depositional cycle. Quartz shows undulatory

extinction, significant grain size reduction, visible subgrain formation and rotation of subgrains

indicating that dislocation creep had occurred in the metasandstone. This indicates that

temperatures of metamorphism were at least 300°C, which is at greenschist facies (Tullis, 2002).

Visible equant subgrains are not seen in the K-feldspar and plagioclase crystals indicating that

temperatures of metamorphism were not high enough for deformation via dislocation creep in

feldspar crystals, which is about 500 – 600°C (Tullis, 2002). The lack of dislocation creep structures in

the feldspar crystals constrains the upper limit of metamorphism to below amphibolite facies.

Therefore, peak metamorphism in the LSJ Eagle Island assemblage range between mid-greenschist

to lower than amphibolite facies.

As seen in the BG meta-iron formation, there are magnetite poikiloblasts that contain minerals

formed during metamorphism. In the LSJ meta-iron formations, magnetite poikiloblasts contain

inclusions of chlorite, biotite, quartz, muscovite, apatite, carbonate minerals and plagioclase. Biotite,

carbonate minerals and chlorite also contain inclusions of finer-grained magnetite. Since there are

inclusions of metamorphic minerals in magnetite grains and metamorphic minerals have inclusions

of magnetite, this indicates that magnetite crystals grew during progressive metamorphism.

3.3.4 Petrographic Summary

The Na-bearing phase in the magnetite-dominated layers of the magnetite-quartz meta-iron formations and in the metasedimentary layers is albite. Quartz-dominated layers in the magnetite-quartz meta-iron formation contain minor amounts of albite and the hematite-quartz does not contain a significant Na-bearing phase. Since the metasedimentary rocks contain albite, it is believed that the albite in the magnetite-quartz meta-iron formation was derived from the siliciclastic phase. However, the absence of albite or any other Na-bearing mineral phase in the hematite-quartz meta-iron formation and minor amounts of albite in the quartz-dominated layers from the magnetite-quartz meta-iron formation suggests a preferential loss of sodium after deposition.

The main K-bearing phase in the hematite-quartz meta-iron formation and metasandstone is K-feldspar, while muscovite and biotite are present in all the meta-iron formation and clastic metasedimentary layers in varying amounts. K-feldspar grains are present in the hematite-quartz meta-iron formation, but not in the magnetite-quartz meta-iron formation. Also, like in the BG, there is an abundance of chlorite and minor amounts of K-bearing phases in the magnetite-quartz meta-iron formation samples. Therefore, this suggests that there was a preferential loss of potassium in the magnetite-dominated layers after deposition.

Another example of mineral partitioning between the magnetite-quartz meta-iron formation and the hematite-quartz meta-iron formation is the presence of carbonate minerals. Interestingly, there is an abundance of carbonate minerals in the magnetite-quartz meta-iron formation and lack of carbonate minerals in the hematite-quartz meta-iron formation. This may be caused by reactions that occurred during diagenesis. It is believed that iron in iron oxyhydroxides react with organic carbon, producing magnetite along with CO_2 as a by-product. Iron, magnesium, calcium and manganese bonded with CO_2 and forming ankerite and dolomite. Since no CO_2 is produced by the

transformation of iron oxyhydroxides into hematite, there is a lack of carbonate minerals in the hematite-quartz dominated meta-iron formation. The evidence suggests that iron was deposited as iron oxyhydroxides and diagenesis was responsible for the genesis of the phase-dominated layers in the meta-iron formation.
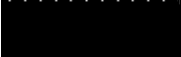
3.4 North Caribou Greenstone Belt

Lithologies on Musselwhite mine's property are part of the Opapimiskan-Markop unit and South Rim metavolcanic assemblages (Moran, 2008; Oswald et al., 2015). The South Rim metavolcanic assemblages on Musselwhite mine's property includes metamorphosed tholeiitic basalts and minor felsic flows. The Opapimiskan-Markop unit includes meta-ultramafic, metamafic, meta-iron formation and clastic metasedimentary lithologies. All the meta-iron formation in this study are drill core samples supplied by Musselwhite mine from the Northern Iron Formation unit of the Opapimiskan-Markop unit. These samples were collected by Patrick Moran for his 2008 MSc thesis.

The stratigraphy of the mine is divided into six main lithological packages categorized by the geology and exploration departments at Musselwhite mine. Starting at the base and moving upwards in order of structural stacking, the packages consist of the 'Lower Basalts', followed by the 'Southern Meta-iron formation' (SIF), 'Basement Basalts', 'Northern Meta-iron formation' (NIF), 'Bvol' and 'Avol' at the top (Moran, 2008; Biczok et al., 2012; Oswald et al., 2015). Currently, there is a discussion on the stratigraphic age relationships for the lithologies on the Musselwhite mine property. The current debate focuses on the age of the 'Lower Sediments', a metasiliciclastic-metavolcaniclastic unit intercalated with minor felsic metavolcanic and metaultramafic rock (McNicoll et al., 2016). This unit is structurally located below the 'Lower Basalts'. Biczok et al. (2012) retrieved zircons from a felsic tuff in the 'Lower Sediments' and determined a weighted average Pb^{207}/Pb^{206} age of 2982 ± 0.8 Ma. This age is older than the 2973.4 ± 1.6 Ma Pb^{207}/Pb^{206} age retrieved

from zircons in a felsic rock that was part of the 'Avol' unit located at the top of Musselwhite mine's

stratigraphy. They concluded that the younging direction is up stratigraphy. Contrary to this theory,

McNicoll et al. (2016) obtained zircons from a felsic ash tuff and detrital zircons from biotite-quartz-

feldspar metasedimentary rock that were both part of the 'Lower Sediments' and determined

maximum Pb^{207}/Pb^{206} ages of <2850 Ma and <2846 Ma respectively. Zircons from metasedimentary

rocks in the Opapimiskan-Markop assemblage, yielded a maximum Pb^{207}/Pb^{206} age of <2967 Ma

(McNicoll et al., 2016). Zircons from a feldspar-phyric felsic dike yielded a Pb^{207}/Pb^{206} age of 2909.4 ±

0.7 Ma. Significantly, this dike crosscuts the NIF, 'Basement Basalts', SIF and the 'Lower Basalts'. This

would indicate that the deposition of the Opapimiskan-Markop assemblage occurred before

2909Ma, which is more than 50 m.y. older than the maximum deposition age for the 'Lower

Sediments' determined by McNicoll et al. (2016). All these ages determined by McNicoll et al. (2016)

are younger than zircons from an 'Avol' felsic ash tuff, which yielded a Pb^{207}/Pb^{206} age of 2978.7 ±

1.0 Ma. Researchers have suggested that the younging direction for the lithologies on Musselwhite

mine's property is down stratigraphy (McNicoll et al., 2016). The main difference between the work

conducted by these geoscientists is the determined age of the felsic ash tuff layer in the 'Lower

Sediments', which has yielded contradictory stratigraphic interpretations. For both authors, the

felsic ash tuff layer in the 'Lower Sediments' had a range of zircon population clusters. McNicoll et

al. (2016) interpreted the younger zircon ages as primary, undisturbed, igneous zircons, yielding

crystallization ages of <2850 Ma, while Biczok et al. (2012) interpreted the younger zircon ages as

loss of Pb post-crystallization. P. Fralick (personal communication, 2018) has noted that in some

areas of the mine, graded beds overlie the biotite-garnet schist giving a reliable up direction away

from the underlying meta-iron formation. Therefore, it is more logical for the sedimentology of the

stratigraphic sequence to be upright rather than inverted. The generalized stratigraphy of

Musselwhite mine is shown in Table 3.15.

Table 3.15: Generalized stratigraphy of the lithologies on Musselwhite mine's property. Modified from Moran (2008).

Musselwhite Mine Generalized Stratigraphy			
Lithology		Mine Terminology	Composition
	Felsic Metavolcanic Flows	Avol	Massive Dacitic to Rhyolitic Metavolcanic Tuffs and Flows
	Meta-Basalt	Bvol	Basaltic to Andesitic Metavolcanic Rock
	Northern Iron Formation	6	Garnet-Quartzite
		4f	Biotite-Garnet Schist
		4e	Hornblende-Garnet Schist
		4ea	Silicicate-Dominated Banded Meta-Iron Formation
		"Clastic 4b"	Transitional Oxide- to Silicate-dominated Meta-iron Formation
		4b	Oxide-Dominated Banded Meta-Iron Formation
		4a	Quartz-Grunerite Banded Meta-Iron Formation
		4h	Meta-Argillite
	Meta-Basalt	"Basement Basalts"	Metaultramafic, Meta-Basaltic Komatiites and Meta-Andesites
	Southern Iron Formation	SIF	Oxide-Dominated Banded Meta-Iron Formation
	Meta-Basalt	"Lower Basalts"	Tholiitic Metabasalts, Komatiitic Metabasalts and Metaultramafic Rocks

3.4.1 Outcrop Descriptions

Structurally situated above the "Basement Basalt" unit is the stratigraphically younger NIF. Moran (2008) completed a detailed log stratigraphy of the NIF and categorized the NIF into five distinct lithofacies associations (LA): LA1 metavolcanic-metavolcaniclastic, LA2 meta-argillite and metamorphosed quartz-grunerite BIF, LA3 metamorphosed thinly- to thickly-laminated oxide-dominant BIF, LA4 metamorphosed oxide/silicate-BIF and silicate-dominant BIF, LA5 hornblende-garnet schist, biotite-garnet schist, and garnet bearing quartzite. Most NIF units have been subsequently deformed after deposition and contain post-depositional quartz veining.

The metavolcanic-metavolcaniclastic LA1 is composed of mafic to intermediate metavolcanic and metavolcaniclastic flows. Metavolcanic units containing biotite porphyroblasts were interpreted to be volcaniclastic material while massive metavolcanic units were interpreted to be eruptive flows or dikes (Moran, 2008). LA1 occurs stratigraphically above and below the NIF assemblage, as well as interbedded with hornblende-garnet schist, silicate-dominated meta-BIF, the biotite-garnet schist and the garnet-bearing quartzite. Minor instances of ultramafic metavolcanic flows and metadikes are also included in LA1. These ultramafic lithologies typically occur lower in the NIF stratigraphy, as well as stratigraphically below the NIF assemblage.

LA2 consists of a metamorphosed quartz-grunerite BIF and meta-argillite. This lithofacies association forms the lowermost metasedimentary unit of the NIF. These lithologies form a discontinuous layer with the underlying metavolcanic lithologies from LA1 (Figure 3.20A). Distinct layers, 1 mm – 20 mm-thick, are preserved in the least deformed sections of the meta-argillite unit. This unit consists of four compositional layers: biotite-grunerite-hornblende-garnet-pyrrhotite ± chlorite layers, quartz-grunerite-carbonate-pyrrhotite layers, quartz-pyrrhotite layers and primary pyrrhotite layers. The biotite-grunerite-hornblende-garnet-pyrrhotite ± chlorite layers represent the bulk minerology of the meta-argillite and are interpreted to reflect the chemistry of the sedimentary protolith (Moran, 2008). The quartz-grunerite-carbonate-pyrrhotite layers are found at contacts between the quartz-dominated layers and the biotite-grunerite-hornblende-garnet-pyrrhotite ± chlorite layers. These quartz-grunerite-carbonate-pyrrhotite layers are interpreted to be the product of contact metasomatism between the two other layers during regional metamorphism (Moran, 2008). Primary pyrrhotite occurs as millimetre-scale laminations or as disseminated crystals throughout the meta-argillite. Lastly, there are instances of small blobs and laminations of carbonaceous material (Figure 3.19A) (Moran, 2008). Folding, brecciation and shear fabrics are observed when deformation is pervasive through the meta-argillite unit. The meta-argillite is

interpreted to be detrital clays deposited during quiescence of hydrothermal black smoker activity and before volcanism (Moran, 2008).

In the least deformed sections, the metamorphosed quartz-grunerite BIF is composed of thinly-laminated, 0.01 – 0.2 cm, fine-grained quartz-dominated and grunerite-dominated bands with minor amounts of magnetite, biotite and garnet. This portion of the meta-iron formation is typically <1 m to 2 m thick, but locally it can be 10 – 20 m thick. Thin, 1 – 2 cm layers of magnetite-dominated laminae are sometimes interlayered with the quartz-grunerite layers (Figure 3.20B). The magnetite-dominated layers resemble the magnetite-dominated layers from the overlying oxide-dominated meta-BIF. Therefore, it is believed that the quartz-grunerite BIF grades into the oxide-dominated meta-BIF (Moran, 2008).
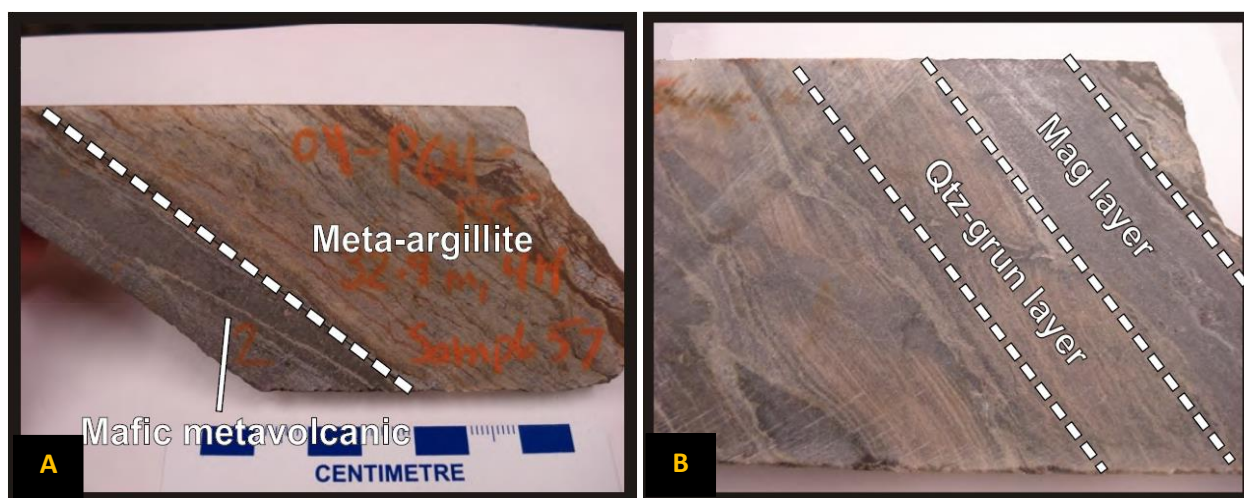
Figure 3.20: Drill core samples from LA2. A) A photograph of the underlying mafic metavolcanic rock from the 'Basement Basalts' in contact with the overlying meta-argillite unit from the NIF. B) Photograph of the quartz-grunerite meta-BIF with alternating magnetite layers. Photographs from Moran (2008).

Moving up stratigraphy, lithofacies 3 comprises thinly- to thickly-laminated oxide-dominated meta-BIF. The oxide-dominated meta-BIF is the most voluminous, extensive and observable metasedimentary unit at Musselwhite mine. On average, this lithofacies is composed of 1.0 cm-thick layers of alternating quartz-dominated and magnetite-dominated laminae. Variability in the oxide-

dominated meta-BIF is caused by changes in layer thickness of the quartz-dominated and magnetite-dominated layers.

The bottom of this lithofacies is composed of thinly-laminated oxide-dominated meta-BIF which forms a discontinuous layer on top of the quartz-grunerite meta-BIF described in the earlier section. This section comprises <50% of the oxide-dominated meta-BIF. The thickly-laminated variety of oxide-dominated meta-iron formation is the dominant lithology in this unit (Figure 3.21A), consisting of >50 – 85% of the unit. All these units have been subsequently deformed, and their primary structures and thicknesses are rarely preserved. Semi-massive, brecciated sulfide veins containing pyrrhotite ± arsenopyrite are seen stratigraphically in the bottom lithofacies association. These veins are restricted to the oxide-dominated meta-iron formation and are believed to represent remobilized sulphides from the meta-argillite during post-depositional alteration (Moran, 2008).
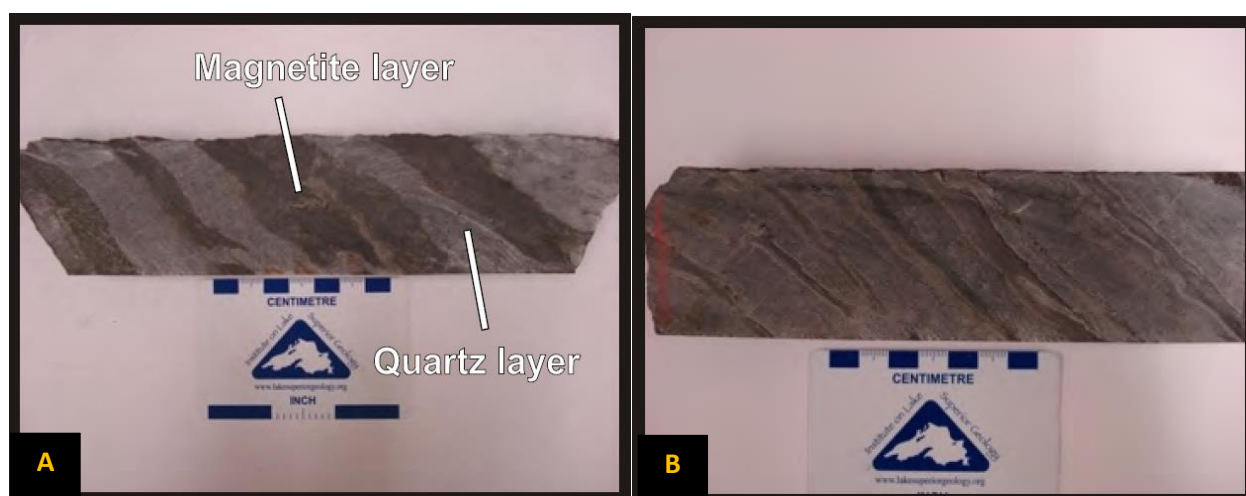
Figure 3.21: Drill core samples from LA3. A) A photograph of the thickly-banded oxide-dominated meta-iron formation showing alternating magnetite- and quartz-dominated laminae. B) A photograph of the banded oxide-dominated meta-iron formation with metasomatic reaction rims of grunerite-dominated layers (tan) between magnetite-dominated (black) and quartz-dominated layers (grey). Photographs from Moran (2008).

The oxide-dominated meta-BIF is composed of three distinct layers: ≈40% magnetite-dominated layers, ≈40% quartz-dominated and <15% grunerite-dominated layers. The last 5% is composed of sulphides. Magnetite-dominated layers are 0.5 – 3cm thick and range from homogeneous magnetite

layers to layers with thin quartz laminations (0.1 – 0.2 cm thick). Quartz-dominated layers are 0.5 –

3.0 cm thick and represent metamorphosed chert crystals. Grunerite-dominated layers are 0.2 – 0.7

cm thick and are found in between quartz- and magnetite-dominated layers (Figure 3.21B). They are

interpreted to be contact metasomatic reaction layers between the quartz and the magnetite

crystals formed during regional metamorphism (Moran, 2008).

LA4 consists of a transitional oxide-silicate meta-BIF and silicate-dominated meta-BIF. The oxide-

silicate meta-BIF is interpreted to be a transitional unit between the stratigraphically overlying

silicate-dominated meta-iron formation and underlying oxide-dominated meta-iron formation from

lithofacies association 3. It is composed of alternating, thinly-banded layers of quartz-dominated

and magnetite-dominated bands intercalated with hornblende-garnet schist layers (Figure 3.22A).

Lithofacies association 4 is in gradational contact with the stratigraphically underlying lithofacies

association 3 lithologies. This gradation is caused by an increase in siliciclastic material up-

stratigraphy. The overlying silicate-dominated meta-iron formation contains alternating garnet +

grunerite ± hornblende ± biotite bands and quartz-rich bands (Figure 3.22B). This meta-iron
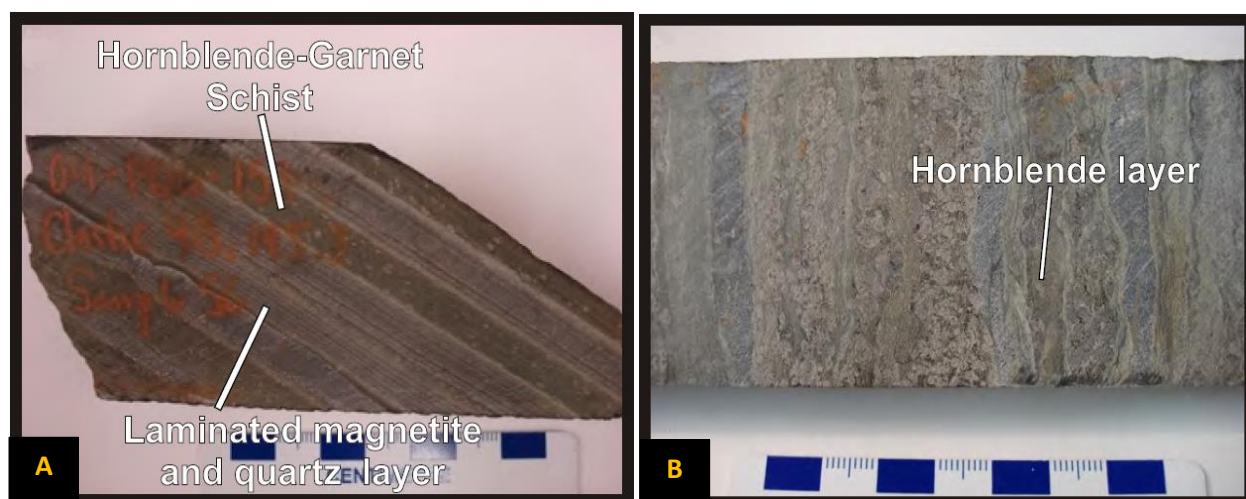
Figure 3.22: Drill core samples of the LA4 lithologies. A) A photograph of the transitional oxide-silicate meta-BIF with thinly-laminated magnetite-dominated and quartz dominated laminae from the oxide-dominated meta-iron formation interbedded with the hornblende-garnet schist layers. B) The silicate-dominated meta-BIF with garnet-dominated layers, hornblende-dominated layers, quartz-dominated layers and grunerite-dominated layers. Photographs from Moran (2008).

formation is in gradational contact with the underlying oxide-silicate meta-BIF. Gradation is

observed by the increase in amphibole-garnet bands up stratigraphy from the oxide-silicate meta-

BIF to the silica-dominated meta-BIF.

Lithofacies association 5 is composed of clastic metasedimentary units and minor amounts of

metavolcaniclastic units (Moran, 2008). Metasedimentary units include hornblende-garnet schist

(Figure 3.23A) and biotite-garnet schist (Figure 3.23B, C). Stratigraphically, the hornblende-garnet

schist forms the bottom of lithofacies association 5. This unit is typically <1 m to 3 m in thickness

and usually is intercalated with the stratigraphically underlying silicate- and oxide-silicate-dominated
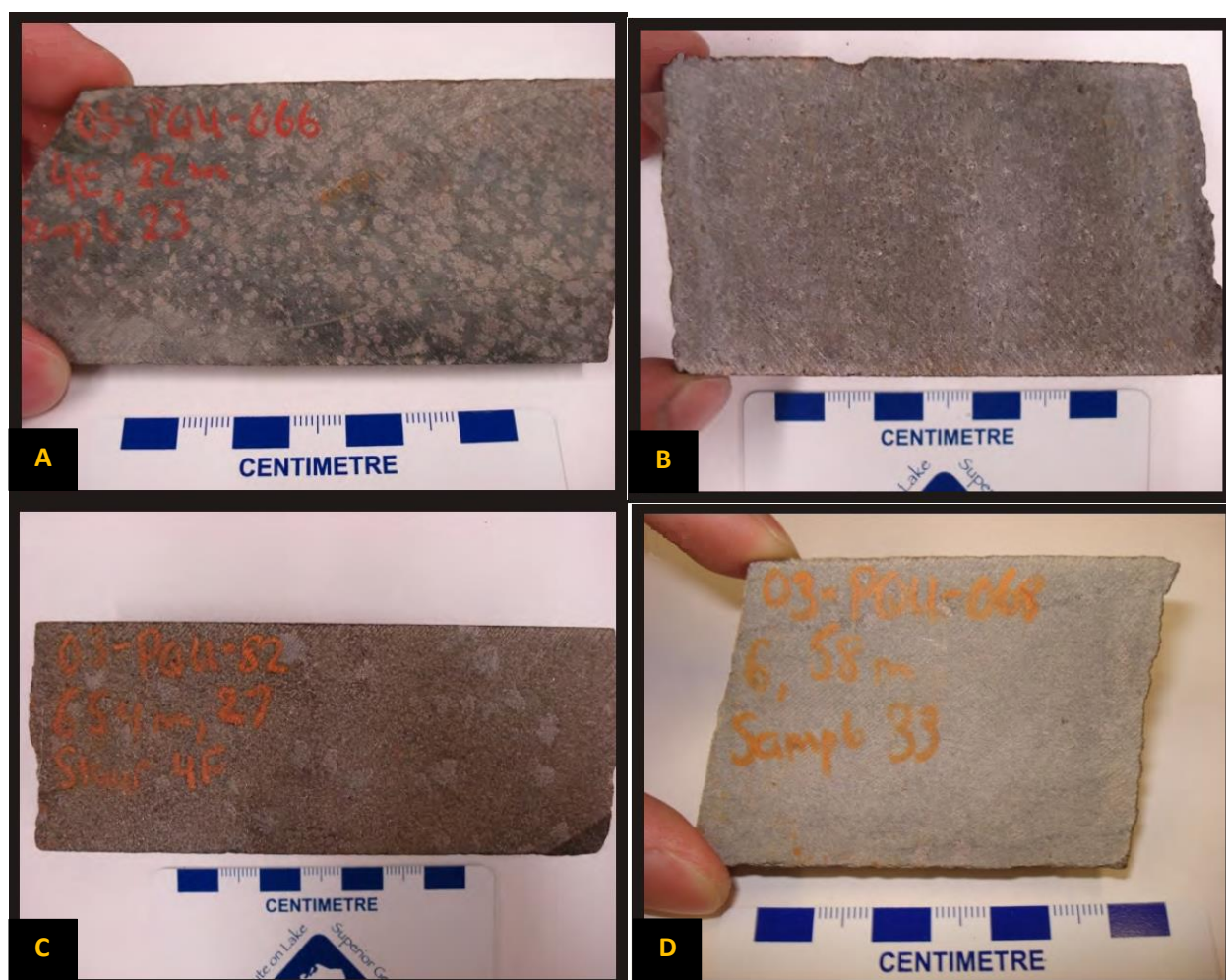
Figure 3.23: Drill core samples from LA5. A) The photograph of the hornblende-garnet schist. B) A photograph of the biotite-garnet schist. C) A photograph of the garnet-biotite schist with porphyroclasts of staurolite. D) A photograph of the garnet-quartzite. Photographs from Moran (2008).

meta-BIF and overlying biotite-garnet schist. The biotite-garnet schist is interbedded with the underlying silicate-dominated meta-iron formation, meta-chert layers, hornblende-garnet schist and overlying garnet quartzite layers (Moran, 2008). The garnet-quartzite (Figure 3.23D) is interpreted to be derived from a volcanic ash deposit with a felsic composition (Moran, 2008). It delineates the stratigraphic uppermost contact of the NIF. Lithologies in this lithofacies are massive and porphyroblastic. The bottom section of garnet quartzite is intercalated with the underlying biotite-garnet schist indicating a gradational contact.

The clastic metasedimentary rocks in the NIF and SIF have an active margin turbiditic geochemical signature (Moran, 2008). This indicates that the meta-iron formations were deposited in deeper water. Therefore, the NC meta-iron formations are classified as Algoma-type meta-iron formations, deposited in a deeper water setting (Moran, 2008).

3.4.2 Petrographic Descriptions

New petrographic descriptions or SEM data was not conducted on the meta-iron formation samples and associated lithologies due to the lack of available materials. SEM data from Moran (2008) was not used since only major phases were analyzed and the SEM data did not contribute to the discussion of this thesis. Petrography will be summarized from Moran (2008) and only the main lithologies that will be discussed in the geochemistry section (Chapter 4) will be mentioned. These lithologies include the metamorphosed thinly to thickly-laminated oxide-dominated BIF from LA3 and the biotite-garnet schist from LA5. The LA3 oxide-dominated meta-iron formations can be grouped into three layer types: magnetite-dominated, quartz-dominated and grunerite-dominated layers.

Magnetite-dominated Layers

The minerology of the magnetite-dominated layers by modal abundance is magnetite + quartz ± grunerite ± apatite ± carbonate minerals ± sulphides (Figure 3.24A). On average, magnetite-dominated layers are 0.5 – 1.0 cm thick. Magnetite-dominated layers appear different in drill core than in the trench samples. In drill core, the magnetite-dominated layers are mostly composed of magnetite (80 – 100%) with minor amounts of quartz (3 – 20%) and have sharp contacts with the grunerite-dominated layers. Magnetite crystals are fine-grained (<0.1 mm) anhedral to subhedral and contain inclusions of grunerite, apatite, calcite and sulphides. Coarser-grained apatite also occurs along grain boundaries of magnetite crystals. Magnetite-dominated layers from the trench samples typically have up to 50% grunerite, with the rest of the mineralogy consisting of magnetite and very minor amounts or lack of quartz. Layers with high amounts of grunerite are commonly zoned with coarser-grained grunerite forming around magnetite cores (Moran, 2008).

Quartz-dominated Layers

The mineralogy of the quartz-dominated layers by modal abundance is quartz ± magnetite ± grunerite ± carbonate minerals ± sulphides (Figure 3.24B). The quartz-dominated layers on average are 0.5 – 3.0 cm thick and are defined by containing >95% quartz and <5% magnetite, grunerite, carbonate minerals and sulphides. Quartz is fine-grained (<0.1mm), forms moderately developed triple junctions, however in sections with pervasive deformation, quartz has sutured grain boundaries due to grainsize reduction. The centres of the quartz-dominated layers have finer-grained quartz, with coarser-grained quartz forming at the margins of the layers. Magnetite grains are fine-grained (<0.1 mm), about 10% of the size of the associated quartz crystals and occur along the grain boundaries of quartz crystals. Fine-grained (<0.1 mm) grunerite and carbonate minerals also form on the grain boundaries of coarser-grained quartz crystals and grunerite forms euhedral

needles, while carbonate minerals are subhedral. Pyrrhotite and minor amounts of chalcopyrite and pyrite are associated with quartz veins that crosscut the quartz-dominated layers (Moran, 2008).

Grunerite-dominated Layers

The minerology of the grunerite-dominated samples by modal abundance is grunerite ± carbonate minerals ± pyroxene (Figure 3.24C, D). Like the magnetite-dominated layers, the grunerite-dominated layers differ between the samples from drill core and samples from the trenches. In drill core, the grunerite-dominated layers occur between magnetite- and quartz-
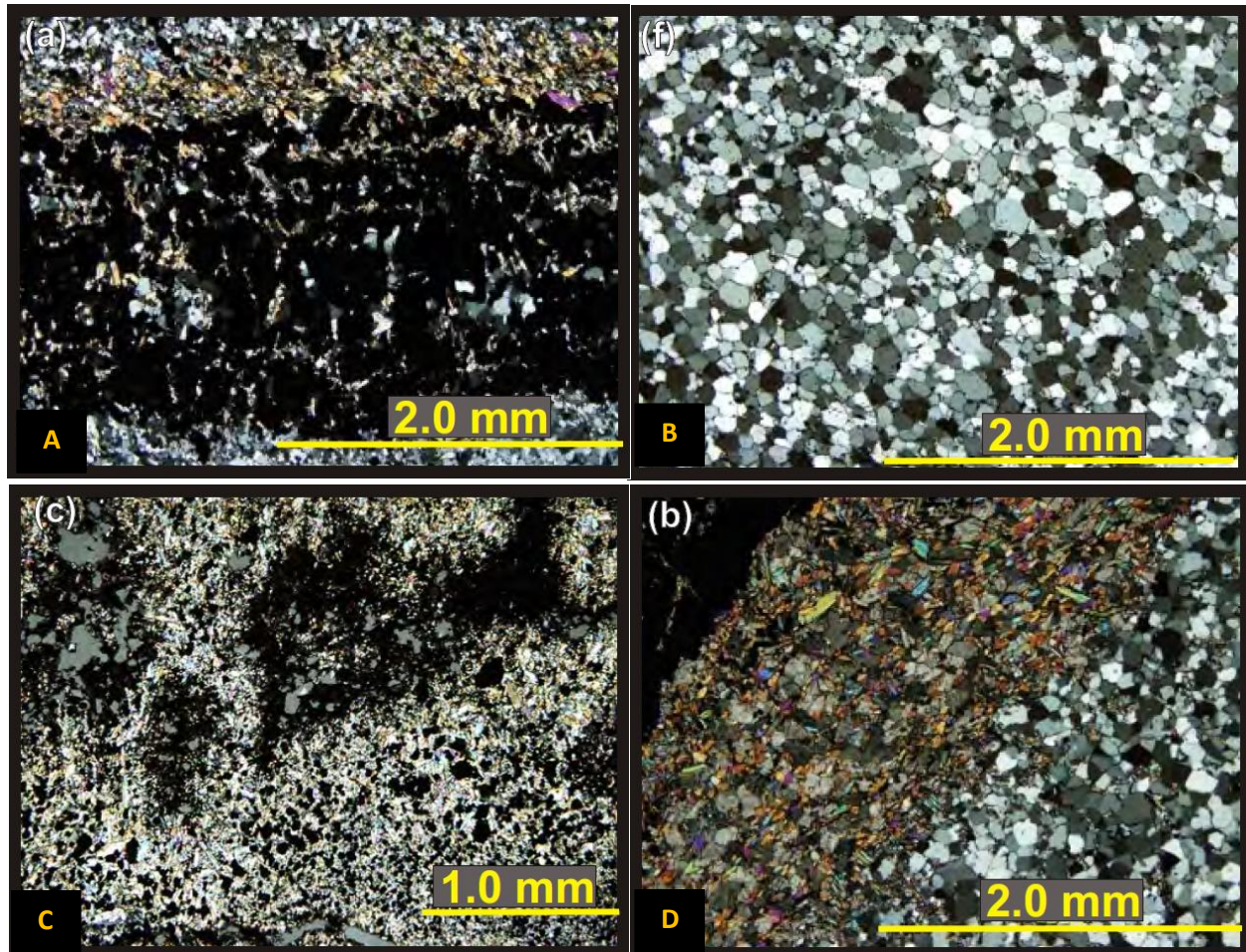
Figure 3.24: Photomicrographs of oxide-dominated banded meta-iron formation from NIF. A) A transmitted XPL photomicrograph of the magnetite-dominate layer with grunerite formed at the contacts between quartz- and magnetite-dominated layers. Some grunerite also forms on grain boundaries of magnetite crystals in the magnetite-dominate layer. B) A transmitted XPL photomicrograph of a quartz-dominated layer with quartz grain boundaries forming well developed triple junctions. C) A transmitted XPL photomicrograph of a grunerite-rich magnetite-dominated layer. D) A transmitted XPL photomicrograph of a 2 mm-thick grunerite-dominated layer forming between a quartz- and magnetite-dominated layers. Photographs from Moran (2008).

dominated layers, they are 0.1 – 0.4 cm thick and can contain up to 10% orthopyroxene and carbonate minerals. Grunerite is fine- to medium-grained and occurs as radiating laths extending towards the quartz-dominated layers or as euhedral 'diamond-shaped' amphiboles. Orthopyroxene and carbonate minerals are fine- to medium-grained, subhedral to anhedral crystals. In the trench samples, the grunerite-dominated layers are not well defined and contain 40 – 100% grunerite with the rest of the mineralogy consisting of magnetite, with little to no quartz and carbonate minerals. Orthopyroxene appears to be absent in the grunerite-dominated samples from the trenches. Grunerite-dominated layers from the trenches have grunerite crystals surrounding relict magnetite grains suggesting that magnetite reacted to form grunerite during progressive metamorphism (Figure 3.24C) (Moran, 2008).

Biotite-garnet schist

The mineralogy of the biotite garnet schist consists of a biotite-rich groundmass + garnet porphyroblasts ± staurolite poikiloblasts (Figure 3.25). The biotite-garnet schist contains 0 – 30% garnet, with the rest of the mineralogy consisting of the biotite-rich groundmass.

The biotite-rich groundmass is composed of mostly biotite, quartz, plagioclase with lesser amounts of K-feldspar, magnetite, pyrrhotite, zircon with trace amounts of zoisite and chalcopyrite. Biotite, quartz and plagioclase define the foliation and in some instances the foliation is crenulated. Biotite is fine-grained (0.3 mm – 0.4 mm), subhedral to euhedral platy minerals that contain inclusions of zircons that display radiation haloes. Quartz is fine-grained (0.05 mm – 0.2 mm) and equidimensional in shape. Plagioclase is also fine-grained (0.05 mm – 0.2 mm) and exhibits polysynthetic twinning. Pyrrhotite is fine-grained (0.1 – 0.4 mm), anhedral and contains inclusions of chalcopyrite. It is disseminated throughout the biotite-rich groundmass or occurs in fractures of garnet porphyroblasts. Garnet porphyroblasts range from medium- to coarse-grained (3.0 mm – 10

mm), anhedral to euhedral and contain inclusions of titanomagnetite, quartz, apatite, magnetite, pyrrhotite ± staurolite, biotite and zoisite. The porphyroblasts are very inclusion-rich exhibiting inclusion trails, which are interpreted to reflect the pervious foliation during garnet growth. In some of the biotite-garnet schist samples there are 5 – 20% staurolite porphyroblasts that contain inclusions of quartz. These porphyroblasts are medium- to coarse-grained (3 mm – 6 mm) and subhedral (Moran, 2008).
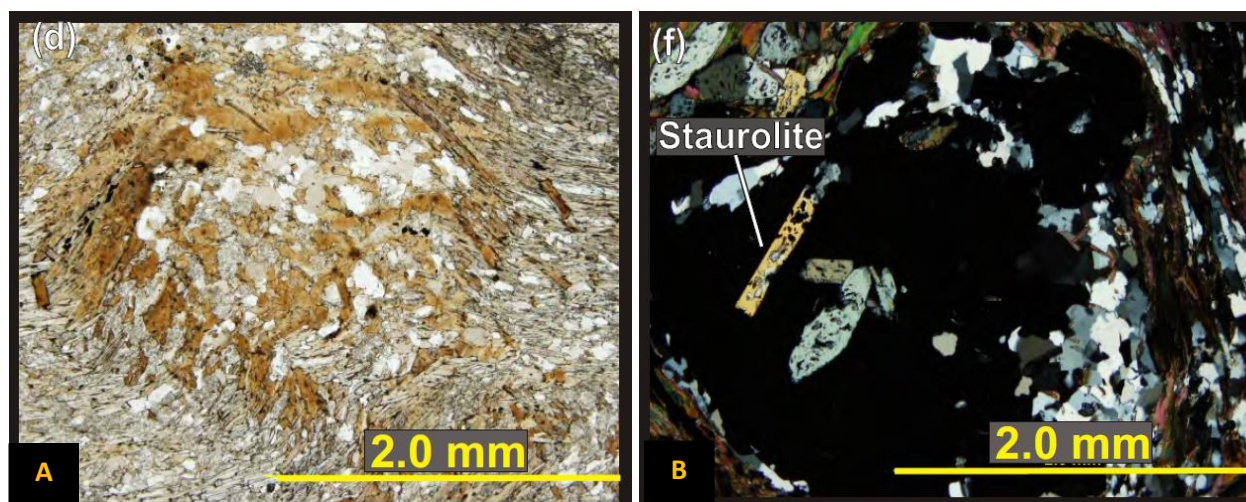
Figure 3.25: Photomicrographs of biotite-garnet schist. A) A transmitted PPL photomicrograph of the biotite-garnet schist with biotite and quartz wrapping around garnet porphyroblasts. B) A transmitted XPL photomicrograph of garnet crystal with inclusions of staurolite. Staurolite also occurs with the biotite and quartz groundmass. Photographs from Moran (2008).

3.4.3 Metamorphism

Peak metamorphic temperatures and pressures have been debated in the NC. Hall and Rigg (1986) conducted arsenopyrite-iron sulphide geothermometry to determine peak metamorphism at Musselwhite mine. Arsenopyrite-iron sulphide geothermometry of the metapelites in Musselwhite mine constrains peak metamorphic temperatures between 530°C – 570°C (Hall and Rigg, 1986), which is at lower amphibolite facies. Otto (2002, from Moran, 2008) conducted garnet-biotite geothermometry on lithologies at Musselwhite mine and determined that peak metamorphic

temperatures occurred between 540°C – 600°C at 5 to 7 kilobars, which is also at lower amphibolite facies.

Stinson (2010) documented the presence of sillimanite in the metapelitic rocks at Musselwhite mine. Since sillimanite is the only aluminosilicate stable at Musselwhite mine, peak metamorphic temperatures must have been above 500°C (Stinson, 2010). The stable peak metamorphic mineral assemblage for the metapeltic rocks at Musselwhite mine is sillimanite + garnet + biotite + quartz + muscovite (Stinson, 2010). For metamorphosed pelitic rocks, this mineral assemblage is stable at the sillimanite zone of upper amphibolite facies metamorphism (Stinson, 2010).

The metamorphic mineral assemblage of the oxide-dominated meta-iron formation can also be used to estimate the peak metamorphic temperatures during regional metamorphism. Interestingly, the mineral assemblage of the grunerite-dominated layers is grunerite, carbonate minerals and orthopyroxene. Since the grunerite-dominated layers are interpreted to be formed by contact metasomatism between two contrasting lithologies, magnetite- and quartz-dominated layers, grunerite and orthopyroxene were formed after deposition. Grunerite can form as a decomposition product of minnesotaite or as reactions between iron-rich carbonates and quartz (Klein, 2005). However, Klein (2005) suggests that without any carbonates or silicate minerals in the quartz-iron oxide meta-iron formation, grunerite will not form. Therefore, in the NC meta-iron formation carbonates and/or silicates must have played a vital role during deposition. The reactions to form grunerite can occur at the biotite zone of greenschist facies (Klein, 2005). Orthopyroxene can form as a result of two reactions: the decomposition of grunerite or the reaction between quartz and iron carbonates (Klein, 2005). Significantly, orthopyroxene forms at the staurolite-kyanite and kyanite zone, which is at metamorphic temperatures of at least amphibolite facies. Based on the mineral

assemblages and geothermometric analyses conducted on the Musselwhite mine lithologies, metamorphic temperatures were in the range of amphibolite facies.

3.4.4 Petrographic Summary

In summary, both magnetite- and quartz-dominated layers contain magnetite, quartz, grunerite, carbonate minerals and sulphides at different abundances. The main difference between the phase-dominated layers is that in the magnetite-dominated layers there is also apatite, suggesting a relationship between phosphorous and the iron oxyhydroxides during deposition and post-depositional alteration. The grunerite-dominated layers formed due to the contact metasomatic reaction between magnetite and quartz. However, it is also proposed that iron-carbonates had a role in the formation of grunerite and orthopyroxene crystals. The presence of grunerite inclusions in magnetite crystals suggests that magnetite grew during progressive metamorphism.

3.5 Shebandowan Greenstone Belt

Meta-iron formations in the Shebandowan area are associated with mafic to intermediate metavolcanic and clastic metasedimentary rocks (Osmani, 1997). Outcrops with meta-iron formation are relatively minor compared to the other lithologies in SGB, but they are widely distributed throughout the greenstone belt (Osmani, 1997). The most dominant meta-iron formation facies are chert ± jasper-magnetite bands, although chert, magnetite and chert with pyrite ± pyrrhotite bands also exist (Osmani, 1997). Minor silicate-facies bands composed of chlorite ± actinolite are also found between contacts of chert and magnetite bands (Osmani, 1997). Chert-magnetite-jasper meta-iron formation is interbedded with metawacke and metasiltstone near Dakota-Peetawa Lake. More commonly, the meta-iron formation is associated with mafic to intermediate metavolcanic flows (Osmani, 1997).

Samples of meta-iron formation were collected from an outcrop mapped by Morin (1973) and

Osmani (1997) along Shebandowan Mine Road, Hagey Township (Figure 3.26). Both scientists

classified the meta-iron formation as a jasper-magnetite ironstone, but Morin (1973) interpreted the

associated volcanic flows to be andesitic in composition, while Osmani (1997) interpreted the flows

to be massive fine- to coarse-grained mafic metavolcanic flows and plagioclase-phyric metavolcanic

flows. Detailed sedimentology and an interpretation of the depositional environment for the meta-

iron formation has not been conducted in the past. Therefore, a detailed transect from east to west

with macroscopic and petrographic descriptions was conducted on the study outcrop (Table 3.16). A

stratigraphic column was not produced due to the lack of primary structures that indicate

stratigraphic up-directions and the abundance of isoclinal fold structures. All the lithologies in the

transect have been subjected to regional metamorphism.

Figure 3.26: The study outcrop along Shebandowan Mine Road. The lighter green lithologies are metavolcanic rock and the darker grey lithologies are iron-oxide facies meta-iron formation. The arrow indicates the direction that the detailed transect will be described.

Shebandowan Transect		
Transect Distance	Thickness	Name of Lithology
0 m	725 cm	Medium-grained chlorite-actinolite-plagioclase granofels
7.25 m	6 cm	Metamorphosed fine-grained mafic intrusion
7.31 m	785 cm	Medium-grained chlorite-actinolite-plagioclase granofels
15.16 m	20cm	Fine-grained chlorite-actinolite-plagioclase granofels/Shear Zone
15.36 m	80 cm	Jasper-magnetite meta-iron formation
16.16 m	54 cm	Chert-magnetite meta-iron formation
16.70 m	62 cm	Jasper-magnetite meta-iron formation
17.32 m	30 cm	Fine-grained chlorite-actinolite-plagioclase granofels
17.62 m	20 cm	Medium-grained chlorite-actinolite-plagioclase granofels
17.82 m	70 cm	Layered metapyroclastic rock
18.52 m	12 cm	Magnetite-jasper meta-iron formation
18.64 m	24 cm	Shear Zone
18.88 m	40 cm	Layered metapyroclastic rock
19.28 m	19 cm	Jasper-magnetite meta-iron formation
19.47 m	7 cm	Chert-magnetite meta-iron formation
19.54 m	16 cm	Jasper-magnetite meta-iron formation
19.70 m	70 cm	Layered metapyroclastic rock
20.40 m	>1 m	Medium-grained chlorite-actinolite-plagioclase granofels

3.5.1 Outcrop Descriptions

The first 15 m of the transect consists of the chlorite-actinolite-plagioclase granofels. It is composed of medium-grained, randomly oriented relict clinopyroxene, plagioclase, chlorite, actinolite and epidote. In the medium-grained chlorite-actinolite-plagioclase granofels, there is a 6 cm intrusion composed of fine-grained mafic minerals and disseminated coarse-grained pyrite grains (Figure 3.27A). The composition of the intrusion is similar to the chlorite-actinolite-plagioclase granofels. The medium-grained chlorite-actinolite-plagioclase granofels is separated from the fine-grained chlorite-actinolite-plagioclase granofels by a shear zone up to 20 cm wide (Figure 3.27B). The mineralogy of the fine-grained chlorite-actinolite-plagioclase granofels is the same mineralogy as the medium-grained chlorite-actinolite-plagioclase granofels, except without any relict clinopyroxene crystals. This lithology is in sharp contact with an oxide-dominated meta-iron formation.
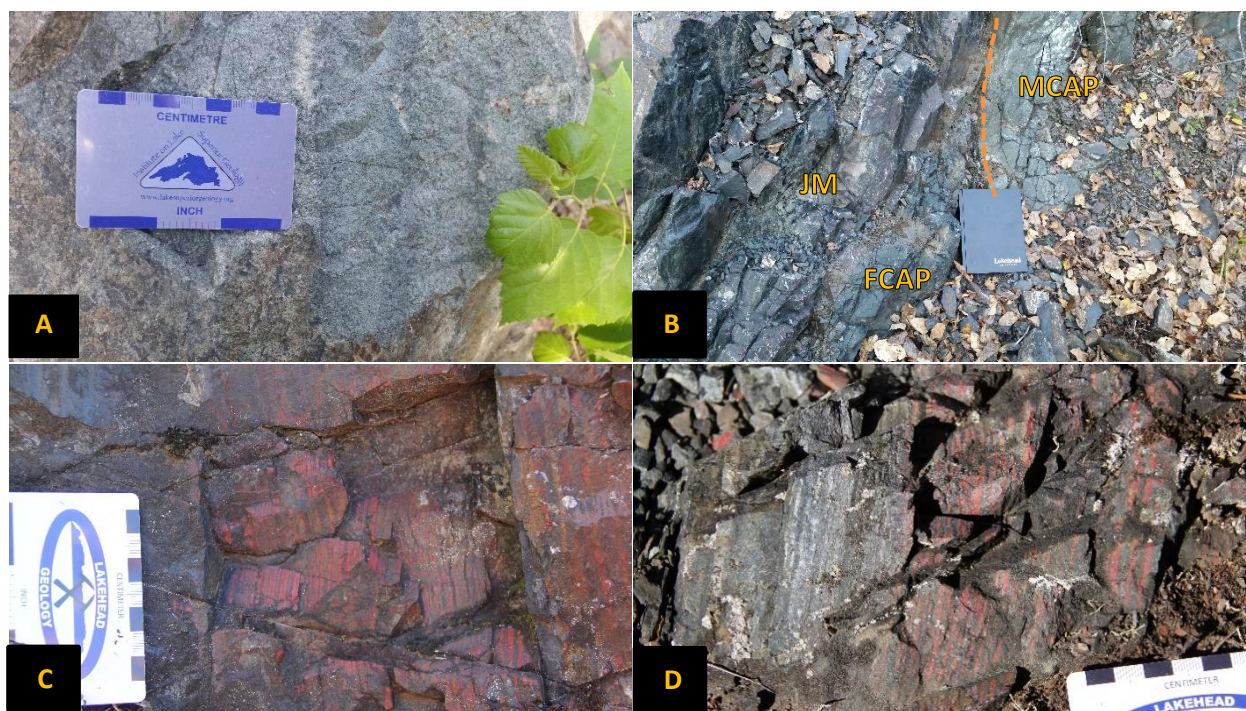
Figure 3.27: Outcrop-scale photographs of SGB meta-iron formation and associated lithologies. A) Photograph of a fine-grained metamafic dike containing disseminated pyrite crystals intruding the medium-grained chlorite-actinolite-plagioclase granofels. B) A shear zone between medium-grained chlorite-actinolite-plagioclase granofels (MCAP), fine-grained chlorite-actinolite-plagioclase granofels (FCAP) and jasper-magnetite meta-iron formation (JM). The orange dotted line is the shear zone. C) Alternating jasper- and magnetite-dominated meta-iron formation. Jasper-dominated bands are generally thicker than magnetite-dominated bands. D) Sharp contact between the chert-magnetite and jasper-magnetite meta-iron formation.

The first 80 cm of the oxide-dominated meta-iron formation are composed of alternating jasper- and magnetite-dominated laminae. On average, the jasper-dominated laminae are 0.5 – 1.0 cm thick, while the thinner magnetite-dominated laminae are commonly 0.1 – 0.5 cm thick (Figure 3.27C). This oxide-facies abruptly shifts to alternating bands of chert- and magnetite-dominated meta-iron formation for the next 54 cm. The chert-dominated layers are thicker, up to 1.2 cm, while the magnetite-dominated laminae are up to 0.6 cm thick (Figure 3.27D). Small jasper blebs can be seen in the chert-dominated laminae (Figure 3.28A). Alternating bands of jasper- and magnetite-dominated meta-iron formation continue for the next 62 cm. These laminae are 0.1 – 0.4 cm thick. Again, the jasper-dominated laminae are on average thicker than the magnetite-dominated laminae. Both contacts between the jasper-magnetite-dominated and chert-magnetite-dominated meta-iron formation are sharp. Isoclinal fold structures are present within the jasper-magnetite-dominated meta-iron formation (Figure 3.28B).

Eastward from the jasper-magnetite meta-iron formation is a 30 cm-thick bed of the fine-grained chlorite-actinolite-plagioclase granofels. The next 20 cm is the medium-grained granofels which grades into the layered metapyroclastic rock. The layered metapyroclastic rock consists of <1 mm to 3 cm layers that grade from a more feldspar-dominated to a more mafic-dominated assemblage (Figure 3.28C). The layered metapyroclastic rock is in contact with a magnetite-jasper-dominated meta-iron formation. This meta-iron formation is 12 cm thick and contains magnetite-dominated layers up to three cm-thick and jasper layers up to two cm-thick. In general, the alternating bands are thicker than the previous jasper-magnetite dominated meta-iron formation. Eastward from the magnetite-jasper-dominated meta-iron formation is another sequence of layered metapyroclastic rock. These two lithologies are separated by a shear zone, which is up to 24 cm wide. In the layered metapyroclastic rock, the stilpnomelane and actinolite content increases toward the shear zone, which gives a redder appearance at outcrop scale (Figure 3.28D). Next is a

package of meta-iron formation, which alternates from jasper-magnetite-dominated to chert-magnetite-dominated and back to jasper-magnetite-dominated meta-iron formation. This meta-iron formation package is in contact with another sequence of layered metapyroclastic rock followed by the medium-grained chlorite-actinolite-plagioclase granofels.
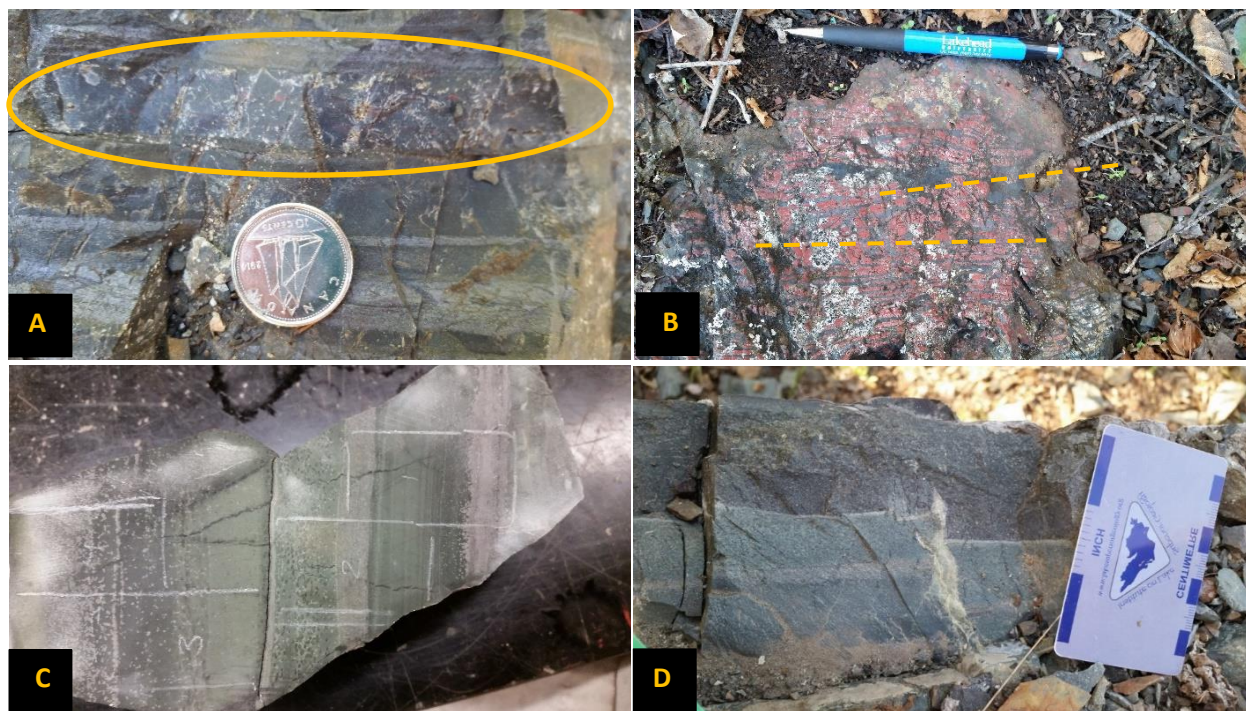
Figure 3.28: Outcrop-scale photographs of SGB meta-iron formation and associated meta-pyroclastic rock. A) Chert-magnetite meta-iron formation with small red blebs of jasper in the chert layers denoted by the yellow circle. B) Jasper-magnetite meta-iron formation showing evidence of deformation and tight folds near a shear zone. C) Sample of the layered metapyroclastic rock cut perpendicular to layering. Plagioclase (silver) crystals grade up to more mafic compositions (green). D) Outcrop of the layered metapyroclastic rock. The shear zone is located just above the dark red layer. Compared to the lighter green layer, the dark red layer has an increased abundance of stilpnomelane and actinolite. For photo A, B and D, east is on the top and west on the bottom of the photo.

In summary, the Shebandowan meta-iron formation is interbedded with chlorite-actinolite-plagioclase granofels and layered metapyroclastic sequences. The evidence of tight folds in the meta-iron formation suggest that all the meta-iron formation might have been deposited during one depositional event and folded during deformation and regional metamorphism. Overall, the thickness of the meta-iron formation is less than a few metres thick even with the evidence of strata-thickening due to tight folding. The meta-iron formation lacks preserved primary siliciclastic sedimentary features and is associated with igneous sequences. Based on the classification scheme

by Gross (1973) and the lack of preserved subaerial structures, the Shebandowan meta-iron
formation was deposited in a deeper water environment.

3.5.2 Petrographic Descriptions and Mineral Compositions

All the samples from SGB were collected from different sections of the transect. There are three
main lithologies along the Shebandowan transect, which include: the chlorite-actinolite-plagioclase
granofels, layered metapyroclastic rock and the jasper-magnetite-chert meta-iron formation. The
jasper-magnetite-chert meta-iron formation can be subdivided into two main lithologies: the jasper-
magnetite meta-iron formation and the magnetite-chert meta-iron formation. Detailed descriptions
from reflected and transmitted light petrography for the main lithologies will be summarized below.
SEM/EDX point analyses were conducted to determine the composition of the mineral phases in the
meta-iron formation and associated meta-igneous rocks. Data from the SEM/EDX point analyses is
presented in the Appendix A. Table 3.17 shows the approximate modal percentages phase for the
main lithologies sampled from SGB based on reflected, transmitted light petrography and SEM/EDX
qualitative and quantitative point analyses.

Table 3.17: Approximate modal percentages of the phases in the lithologies from SGB.

Shebandowan Greenstone Belt												
	Act	Ap	Cb	Chl	Cpx	Ep	Mag	Pl	Py	Qtz	Ttn	Stp
Chlorite-actinolite-plagioclase granofels	C	M		C	C	M		A		M	M	
Layered metapyroclastic rock	C	T	C	C		M		A	T	T	T	C
Jasper-magnetite meta-iron formation	C	T	C	M		T	A			C		C
Magnetite-chert meta-iron formation	C	T	M				A			A		C
Modal Percentages: >30% (A - abundant), 10 - 29% (C - common), 1 - 9% (M - minor), <1% (T- trace)												

Chlorite-actinolite-plagioclase granofels

The composition of the chlorite-actinolite-plagioclase granofels is abundant plagioclase,
common occurrences of clinopyroxene, actinolite, chlorite, with minor amounts of titanite, apatite,

epidote and quartz (Table 3.17, Figure 3.29). This lithology is observed as two different types: the

medium-grained chlorite-actinolite-plagioclase granofels and the fine-grained metavolcanic rock.

Aside from the difference in grainsize, the only differences between these two lithologies is that the

relict clinopyroxene grains in the medium-grained chlorite-actinolite-plagioclase granofels have

been replaced by fine-grained epidote, chlorite and actinolite. This was caused by prograde

reactions during regional metamorphism. The medium-grained variety will be discussed below

because it is a better representation of the original protolith during deposition. Plagioclase is fine- to

medium-grained (0.4 mm – 3.0 mm), randomly oriented, long subhedral to anhedral laths that
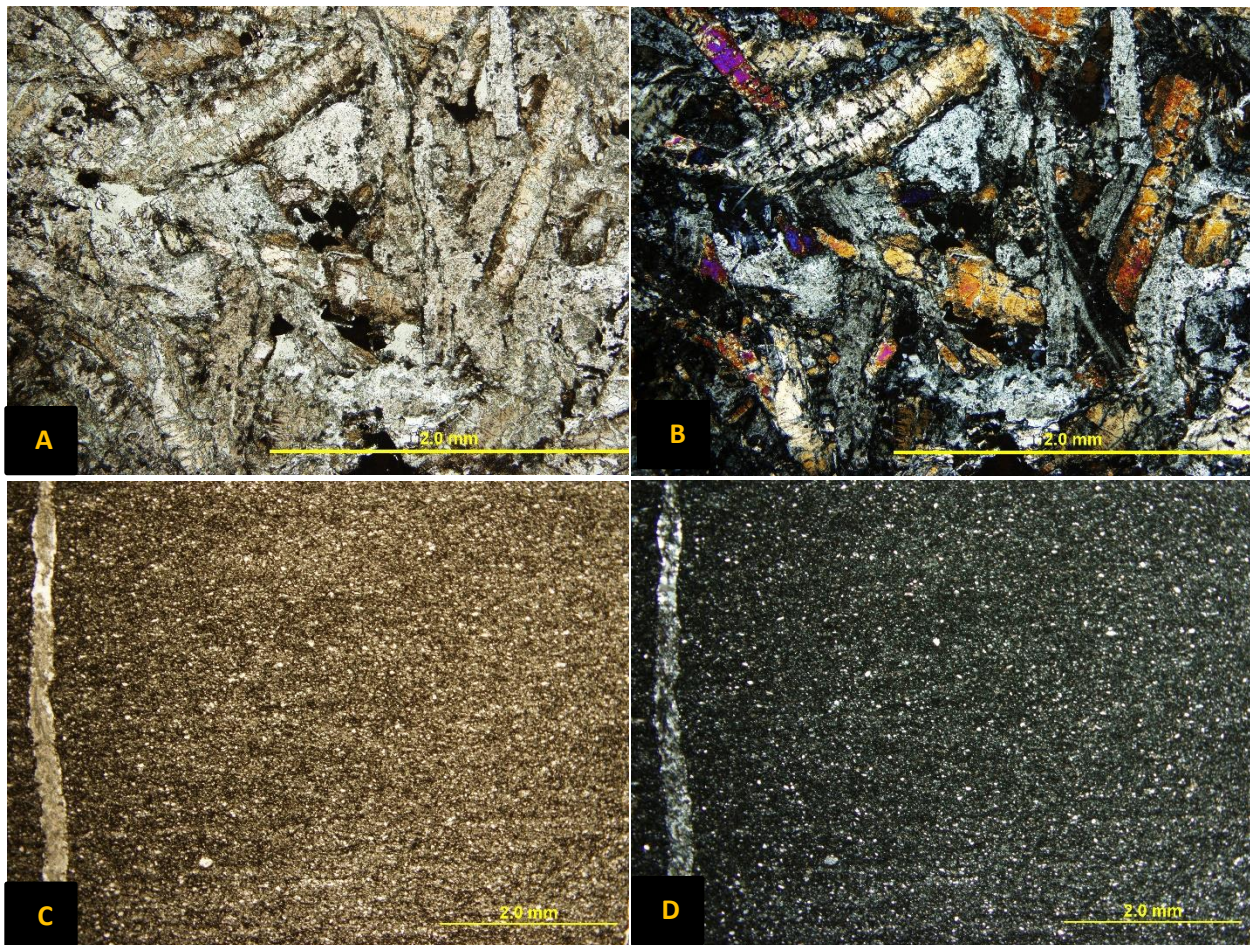
Figure 3.29: Photomicrographs of chlorite-actinolite-plagioclase granofels. A) A transmitted PPL photomicrograph of the medium-grained chlorite-actinolite-plagioclase granofels. The relict clinopyroxene crystals are altering to chlorite, actinolite and epidote. B) A transmitted XPL photomicrograph of the medium-grained chlorite-actinolite-plagioclase granofels. C) A transmitted PPL photomicrograph of the of the fine-grained chlorite-actinolite-plagioclase granofels. Note the lack of relict clinopyroxene crystals and the significantly reduced grainsize compared to the medium-grained chlorite-actinolite-plagioclase granofels. Significantly, the finer-grained chlorite-actinolite-plagioclase granofels are usually associated with shear zones. D) A transmitted XPL photomicrograph of the fine-grained chlorite-actinolite-plagioclase granofels.

contain inclusions of epidote and apatite. Deformation structures include bending of twins, weak undulatory extinction, tapering out twins and irregular grain boundaries. Clinopyroxene is fine- to medium-grained (0.2 mm – 3.0 mm), displays brown pleochroism or is colourless, randomly oriented, long euhedral to subhedral laths. These crystals are most often altered to actinolite, chlorite and epidote. Actinolite is fine-grained (<0.1 mm – 0.7 mm) and in the samples containing clinopyroxene, forms long thin needles replacing clinopyroxene crystals. Chlorite displays weak green pleochroism, is fine- to medium-grained (<0.1 mm – 1.5 mm), anhedral crystals, and it is often seen replacing clinopyroxene crystals. Epidote is fine-grained (<0.1 mm – 0.6 mm), pleochroic pale yellow to deep yellow, euhedral to subhedral and occurs along grain boundaries of clinopyroxene and plagioclase crystals with chlorite and actinolite. Apatite is fine-grained (<0.1 mm – 0.2 mm), euhedral to subhedral hexagonal crystals and usually occurs as inclusions in plagioclase crystals. Titanite is fine- to medium-grained (0.3 mm – 1.0 mm), dark brown, euhedral to anhedral and contains inclusions of plagioclase and epidote. Quartz is anhedral, fine-grained (<0.1 mm – 0.3 mm) and it is associated with chlorite and epidote. Deformation structures include subgrain formation, irregular grain boundaries and undulatory extinction.

Average mineral formulas calculated for the phases from the chlorite-actinolite-plagioclase granofels can be seen in Table 3.18. The composition of plagioclase is fairly consistent throughout the chlorite-actinolite-plagioclase granofels samples. Based on the anorthite content, the composition of plagioclase is albite (An2). Albite is the only major-sodium bearing mineral phase in the chlorite-actinolite-plagioclase granofels. Where clinopyroxene is present, the composition ranges from a high calcium-bearing augite to diopside. The composition of chlorite ranges from chamosite to clinochlore, which are the iron and magnesium endmember chlorite, respectively. Clinochlore is associated with the coarser-grained chlorite-actinolite-plagioclase granofels associated with the relict clinopyroxene crystals, while chamosite is associated with the finer-

grained chlorite-actinolite-plagioclase. Apatite is the only major phosphorous-bearing phase in the chlorite-actinolite-plagioclase granofels. Trace amounts of iron and sodium are also associated with apatite. Titanite is the only major titanium-bearing phase in the chlorite-actinolite-plagioclase granofels.

Table 3.18: Average mineral formulas calculated for the phases in the chlorite-actinolite-plagioclase granofels.

Chlorite-actinolite-plagioclase granofels		
Mineral	Average Mineral Formula	Samples
Actinolite	$(Ca_{1.99}Na_{0.11})_{\Sigma\,2.10}(Mg_{3.08}Fe_{1.76}Al_{0.12})_{\Sigma\,4.96}(Si_{7.79}Al_{0.21})_{\Sigma\,8.00}O_{22}(OH)_2$	6
Apatite	$(Ca_{4.90}Fe_{0.06}Na_{0.01})_{\Sigma\,4.97}(PO_4)_{2.95}(OH,F,Cl)$	4
Chlorite (Chamosite)	$(Fe_{1.25}Mg_{0.97}Al_{0.65})_{\Sigma\,2.87}(Si_{3.11}Al_{0.89})_{\Sigma\,4.00}O_{10}(OH)_2 \bullet (Fe_{1.25}Mg_{0.97}Al_{0.65})_{\Sigma\,2.87}(OH)_6$	3
Chlorite (Clinochlore)	$(Mg_{1.25}Fe_{1.14}Al_{0.58})_{\Sigma\,2.97}(Si_{2.84}Al_{1.16})_{\Sigma\,4.00}O_{10}(OH)_2 \bullet (Mg_{1.25}Fe_{1.14}Al_{0.58})_{\Sigma\,2.97}(OH)_6$	3
Clinopyroxene (Augite)	$(Ca_{0.78}Na_{0.02})_{\Sigma\,0.80}(Mg_{0.62}Fe_{0.58})_{\Sigma\,1.19}Si_{1.93}O_6$	3
Clinopyroxene (Diopside)	$(Ca_{0.91}Na_{0.04})_{\Sigma\,0.95}(Mg_{0.62}Fe_{0.41})_{\Sigma\,1.03}Si_{1.97}O_6$	3
Epidote	$Ca_{1.96}Al_{1.91}(Fe_{0.64}Al_{0.36})_{\Sigma\,1.00}[Si_{2.23}O_7][Si_{1.00}O_4]O(OH)$	10
Plagioclase (Albite)	$(Na_{0.93}Ca_{0.02})_{\Sigma\,0.95}Al_{0.98}Si_{3.01}O_8$	7
Titanite	$Ca_{1.00}(Ti_{0.90}Al_{0.09}Fe_{0.03})_{\Sigma\,1.02}OSi_{1.00}O_4$	2

Layered Metapyroclastic Rock

The bulk composition of the layered metapyroclastic rock is abundant plagioclase, with common occurrences of actinolite, chlorite, stilpnomelane, carbonate minerals, minor amounts of epidote with trace amounts of apatite, quartz, pyrite and titanite (Table 3.17, Figure 3.30, 3.31). The metapyroclastic rock is composed of three distinct layer types: fine-grained chlorite-actinolite-plagioclase layers, poikilitic plagioclase layers and chlorite-actinolite clast layers. The poikilitic plagioclase layer always has a sharp contact with the underlying layer, whether it is with the chlorite-actinolite-plagioclase or chlorite-actinolite clast layers. Poikilitic plagioclase layers grade to the chlorite-actinolite clast and the chlorite-actinolite-plagioclase layers. The order of deposition was the poikilitic plagioclase layer, followed by the chlorite-actinolite clast layer and the chlorite-actinolite-plagioclase layer.

The poikilitic plagioclase layer is predominantly composed of porphyroclastic plagioclase minerals with chlorite, plagioclase, epidote, stilpnomelane, quartz and carbonate minerals making the matrix of the layer (Figure 3.30A, B). Porphyroclastic plagioclase minerals are fine- to medium-grained (<0.1 mm – 2.0 mm), poikilitic, subhedral to anhedral, display hourglass zonation (Figure 3.31A, B) and contain inclusions of plagioclase, epidote and quartz. The porphyroclastic crystals are iron stained and their mineral composition cannot be calculated, however petrographically, the crystals resemble plagioclase. The crystals that make up the matrix around the plagioclase porphyroclasts are fine-grained (<0.1 mm).

The chlorite-actinolite clast layer consists of elliptical clasts (up to 3.0 mm), predominantly composed of chlorite, actinolite and plagioclase, surrounded by a fine-grained matrix of chlorite, actinolite, plagioclase, epidote, quartz, stilpnomelane, carbonate minerals and minor amounts of poikilitic plagioclase porphyroclasts (Figure 3.30D).

The chlorite-actinolite-plagioclase layer is composed of fine-grained (<0.1 mm), randomly oriented chlorite, actinolite, stilpnomelane, quartz, epidote and carbonate minerals. Some layers preserve layering and it is defined by alternating dark and green patches (Figure 3.30C). Chlorite-actinolite clast layers and poikilitic plagioclase porphyroclasts can occur sporadically throughout the layer (Figure 3.30E, F). In the section that is closest to the shear zone, the chlorite-actinolite-plagioclase layer progressively becomes a mylonite (Figure 3.31C, D).
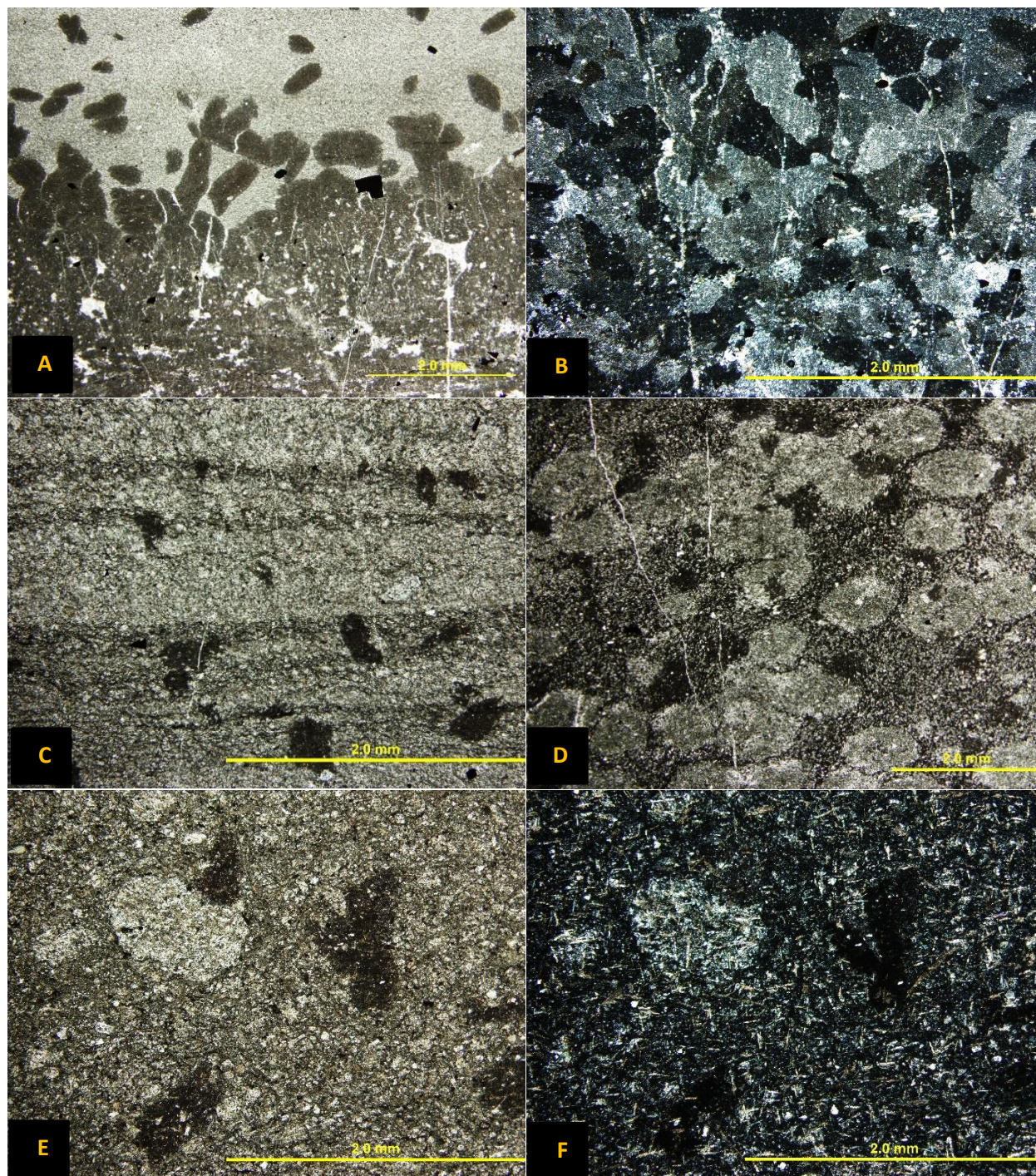
Figure 3.30: Photomicrographs of layered pyroclastic rock. A) A transmitted PPL photomicrograph of the poikilitic plagioclase layer. This layer grades to the fine-grained chlorite-actinolite-plagioclase layers. B) A transmitted XPL photomicrograph of the poikilitic plagioclase layer. Poikilitic plagioclase layers are porphyroclastic, have first order interference and contain inclusions of epidote, plagioclase and quartz. C) A PPL photomicrograph of the fine-grained chlorite-actinolite-plagioclase layer. Chlorite-actinolite-plagioclase layers contain porphyroclasts of poikilitic plagioclase minerals and occasionally shows banding defined by alternating dark and light layers. D) A transmitted PPL photomicrograph of the chlorite-actinolite clast layer. Average size of the elliptical clasts is 1mm. The clasts are composed of fine-grained chlorite, actinolite and plagioclase. E) A transmitted PPL photomicrograph of the chlorite-actinolite-plagioclase layer with both the poikilitic plagioclase porphyroclasts and chlorite-actinolite clasts. F) A transmitted XPL photomicrograph of the same chlorite-actinolite-plagioclase layer as E). Clasts have higher abundances of plagioclase than the matrix.
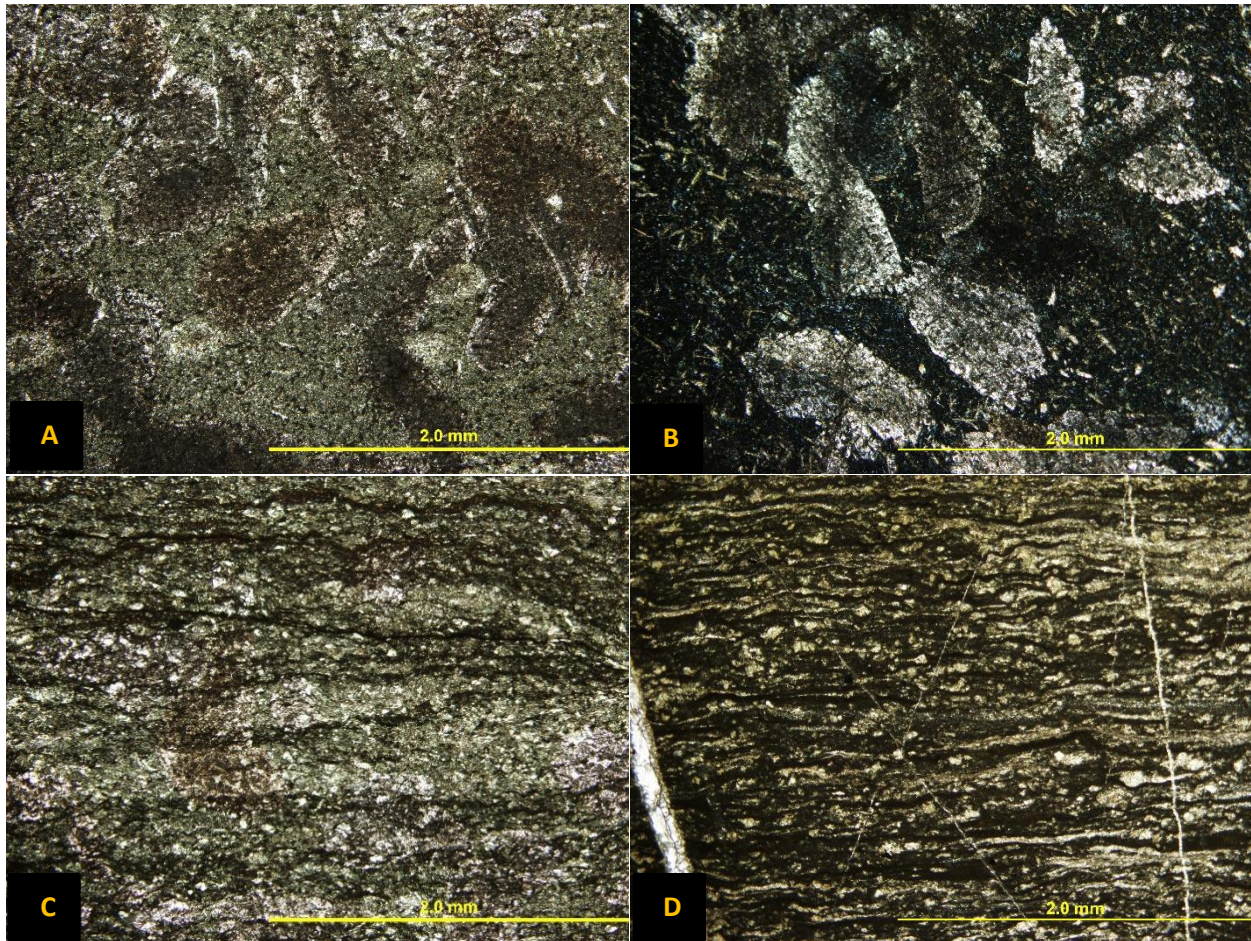
Figure 3.31: Photomicrographs of metapyroclastic rock. A) A transmitted PPL photograph of the poikilitic plagioclase layers showing the medium-grained crystals of randomly oriented poikilitic plagioclase porphyroclasts. B) A transmitted XPL photomicrograph of the poikilitic plagioclase layer. Crystals show radiating extinction zoning. C) A transmitted PPL photomicrograph of the chlorite-actinolite-plagioclase layers close to the shear zone. Layered bands are contorted and rounded quartz and feldspar porphyroclasts are being formed. D) A transmitted PPL photomicrograph of the chlorite-actinolite-plagioclase layer closest to the shear zone. Plagioclase and quartz sigma and delta porphyroclasts are more well defined and layering is finer-grained. This layer is classified as a mylonite.

Average mineral formulas calculated for the phases in the meta-pyroclastic rock are presented in Table 3.19. The composition of the chlorites is chamosite, which is the iron-endmember chlorite. There is a large compositional range for the plagioclase crystals in the metapyroclastic rock. Plagioclase ranges from albite to andesine (An3 – An37) in composition. Andesine and oligoclase crystals occur only as inclusions in poikilitic plagioclase porphyroclasts, while albite is the feldspar phase in the matrix of the metapyroclastic rock. Other than the minor amounts of sodium in stilpnomelane, plagioclase is the only major sodium-bearing phase in the

metapyroclastic rock. In the metapyroclastic rock the stilpnomelane content increases towards to the shear zone. Stilpnomelane is the only major potassium-bearing phase in the metapyroclastic rock. The poikilitic plagioclase porphyroclasts consists of aluminum, calcium, silicon and iron. In thin section it resembles plagioclase, however a formula cannot be constructed. The composition of the carbonate minerals is calcite. Calcite also contains trace amounts of iron. Titanite is the only major titanium-bearing phase in the metapyroclastic rock.

Table 3.19: Average calculated formulas for the phases in the layered metapyroclastic rock.

Layered meta-pyroclastic rock		
Mineral	Average Mineral Formula	Sample
Actinolite	$Ca_{1.91}(Mg_{2.53}Fe_{2.31}Al_{0.35})_{\Sigma 5.19}Si_{7.80}O_{22}(OH)_2$	6
Apatite	$(Ca_{4.86}Na_{0.07}Fe_{0.04})_{\Sigma 4.97}(PO_4)_{2.82}(OH,F,Cl)$	2
Carbonate (Calcite)	$(Ca_{0.89}Fe_{0.01})_{\Sigma 0.90}CO_3$	8
Chlorite (Chamosite)	$(Fe_{1.38}Mg_{0.89}Al_{0.62})_{\Sigma 2.89}(Si_{3.01}Al_{0.99})_{\Sigma 4.00}O_{10}(OH)_2 \bullet (Fe_{1.88}Mg_{0.89}Al_{0.62})_{\Sigma 2.89}(OH)_6$	17
Epidote	$(Ca_{1.86}Na_{0.09})_{\Sigma 1.95}Al_{2.03}Fe_{0.80}[Si_{2.10}O_7][Si_{1.00}O_4]O(OH)$	14
Plagioclase (Albite)	$(Na_{0.95}Ca_{0.03})_{\Sigma 0.98}Al_{0.97}Si_{3.00}O_8$	14
Plagioclase (Andesine)	$(Na_{0.71}Ca_{0.41})_{\Sigma 1.12}Al_{0.98}Si_{2.77}O_8$	8
Plagioclase (Oligoclase)	$(Na_{0.83}Ca_{0.26})_{\Sigma 1.09}Al_{0.98}Si_{2.87}O_8$	1
Quartz	$Si_{1.00}O_2$	1
Stilpnomelane	$(K_{0.58}Na_{0.26})_{\Sigma 0.84}(Fe_{4.06}Mg_{1.51}Al_{030})_{\Sigma 5.81}Al_{1.00}Si_{7.97}(O,OH)_{27}$	17
Titanite	$Ca_{0.85}(Ti_{0.68}Al_{0.16}Fe_{0.11})_{\Sigma 0.95}OSi_{1.19}O_4$	10
Poikilitic Plagioclase	unknown formula	13

Jasper-magnetite-chert Meta-iron formation

The jasper-magnetite-chert meta-iron formation can be divided into two distinct lithofacies: jasper-magnetite meta-iron formation and the magnetite-chert meta-iron formation. The bulk composition of the jasper-magnetite meta-iron formation is abundant magnetite, common occurrences of actinolite, carbonate minerals, quartz, stilpnomelane, minor amounts of chlorite and trace amounts of apatite and epidote (Table 3.20, Figure 3.32). The magnetite-chert meta-iron formation consists of abundant magnetite, quartz, common occurrences of actinolite,

stilpnomelane, minor amounts of carbonate minerals and trace amounts of apatite (Table 3.21, Figure 3.32).

The meta-iron formation as a whole is divided into three distinct layer types: jasper-dominated layers, magnetite-dominated layers and quartz-dominated layers. The jasper-dominated laminae are defined by layers containing 60 – 90% fine-grained (<0.1 mm) quartz with 40 – 85% fine-grained hematite inclusions in the quartz, and the outstanding percent composed of the remaining minerals listed above. The mineralogy of the quartz-dominated layers is similar to the jasper-dominated layers. However, there are less hematite-inclusions in the quartz-dominated layers (<40%). Magnetite-dominated laminae are defined by layers containing 55 – 70% fine-grained magnetite and 20 – 25% fine-grained quartz, with the outstanding percent composed of the remaining minerals listed above. The main morphological difference between the three layers is that the crystal size of magnetite and quartz is significantly coarser-grained in the magnetite-dominated laminae than both the jasper and quartz-dominated laminae (Figure 3.32A). Sharp contacts can be seen between alternating layers. Thicknesses for both phase-dominated layers ranges from 0.1 mm to 1.5 mm. In some of the quartz- and jasper-dominated layers, there are quartz deformation tails, suggesting that localized shearing occurred in the meta-iron formation. It is important to note that in Figure 3.32B, quartz veins cross-cuts the quartz-dominated laminae and are truncated by the magnetite-dominated layers.

Quartz in both the quartz- and jasper-dominated layers is fine-grained (<0.1 mm), anhedral and show undulatory extinction. In the magnetite-dominated layers, where quartz occurs on the grain boundaries of coarser-grained magnetite, quartz is coarser-grained (<0.1 mm – 0.1 mm) and elongated parallel to layering (Figure 3.32A, B, C). Magnetite in the quartz-dominated layers is fine-grained (<0.1 mm) and in the magnetite-dominated layers is coarser-grained (<0.1 mm – 0.3 mm).
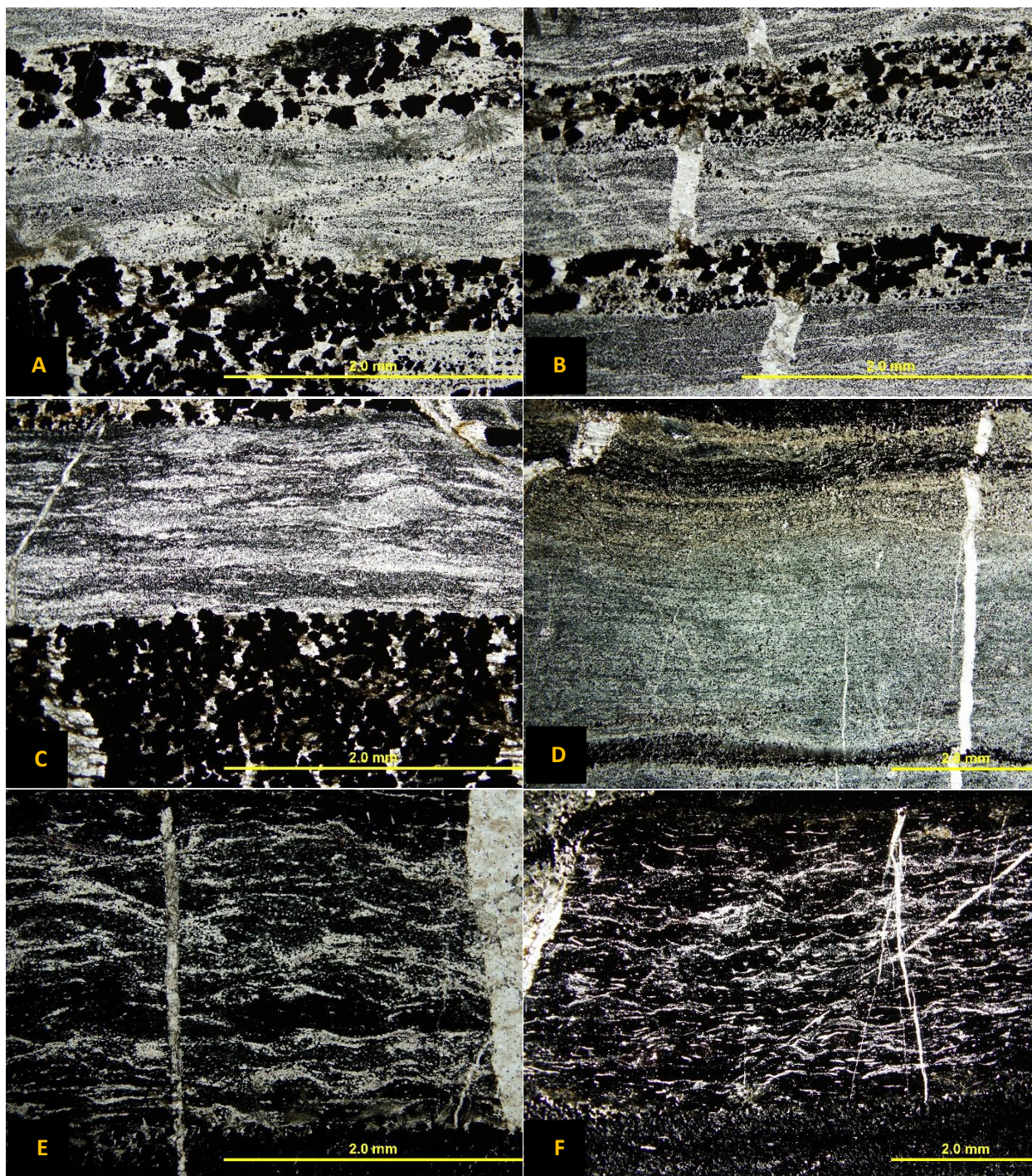
Figure 3.32: Photomicrographs of jasper-magnetite-chert meta-iron formation. A) A transmitted PPL photomicrograph of the magnetite-chert meta-iron formation. Actinolite crystals usually form on the contact between the magnetite- and quartz-dominated laminae and radiate outward towards the quartz-dominated laminae. The grain size of the magnetite crystals in the magnetite-dominated laminae is significantly bigger than the quartz crystals. B) A transmitted PPL photomicrograph of the magnetite-chert met-meta-iron formation. A quartz carbonate vein crosscuts the quartz-dominated layers however, the same vein in the magnetite-dominated layers disappears and is continued in the quartz-dominated layers. C) A transmitted PPL photomicrograph of the magnetite-chert meta-iron formation. Quartz crystals are showing deformation structures such as delta porphyroclasts. D) A transmitted light photomicrograph of the magnetite-chert meta-iron formation. Note the amount of stilpnomelane near the contacts between magnetite- and quartz-dominated layers. E) and F) are transmitted PPL photomicrographs of the jasper-magnetite meta-iron formation. Note the significant increase of hematite inclusions compared to the chert dominated layers. Quartz crystals are wavy indicating that deformation was pervasive in this unit.

Coarser-grained magnetite is euhedral to subhedral and contains inclusions or forms coronas around stilpnomelane, apatite, quartz, actinolite, chlorite and carbonate minerals. Most of the grain boundaries of the magnetite crystals in the magnetite-dominated laminae appear to be in contact with each other. Stilpnomelane is fine-grained (<0.1 mm – 0.3 mm), fibrous, has strong brown pleochroism and the long axis of minerals is parallel to layering, unless it is in a quartz or carbonate vein. Most of the stilpnomelane crystals occur on the contacts between quartz- and magnetite-dominated layers Although, the crystals occur with quartz in magnetite inclusions and coronas, as well as in quartz and carbonate veins. When stilpnomelane is in the magnetite-dominated layers, it grows in the strain shadows of the magnetite grains, parallel to layering. Actinolite is fine-grained (<0.1 mm – 0.3 mm) forming radiating sheaves that usually occur along the contacts between quartz- jasper- and magnetite-dominated laminae. It appears that the actinolite radiating sheaves cluster point start at the magnetite-dominated laminae and the crystals radiate outward in the quartz- and jasper-dominated laminae (Figure 3.32A). Actinolite also occurs as inclusions in magnetite in the magnetite-dominated laminae. Carbonate minerals are fine-grained (<0.1 mm – 0.03 mm), subhedral to anhedral and occur as sporadic crystals within quartz- jasper- and magnetite-dominated layers or as veins crosscutting the meta-iron formation. Apatite is fine-grained (<0.1 mm), and most often is associated with magnetite in the magnetite-dominated layers. Chlorite occurs as fine-grained (<0.1 mm – 0.2 mm), euhedral platy to anhedral crystals along grain boundaries of magnetite crystals or inclusions in magnetite.

Average calculated formulas for the phases in the jasper-magnetite meta-iron formation are in Table 3.20. The composition of actinolite ranges from actinolite to ferro-actinolite. Stilpnomelane is the only major-potassium bearing phase in the magnetite-jasper meta-iron formation. Apatite is the only major phosphorous-bearing mineral phase in the meta-iron formation. It also contains trace amounts of iron and sodium. Carbonate minerals in the meta-iron formation are calcite in

composition, containing trace amounts of iron. The composition of chlorite is chamosite, which is the iron end-member chlorite. Chamosite contains significant amounts of iron, magnesium, aluminum and silica.

Table 3.20: Average calculated formulas for the mineral phases in the magnetite-jasper meta-iron formation.

Magnetite-chert meta-iron formation		
Mineral	Average Mineral Formula	Samples
Actinolite	$(Ca_{1.81}Na_{0.18})_{\Sigma\,1.99}(Mg_{2.61}Fe_{2.41}Al_{0.05})_{\Sigma\,5.07}Si_{7.99}O_{22}(OH)_2$	5
Apatite	$(Ca_{4.81}Na_{0.06})_{\Sigma\,4.87}(PO_4)_{2.72}(OH,F,Cl)$	4
Carbonate (Calcite)	$(Ca_{0.94}Fe_{0.02})_{\Sigma\,0.96}CO_3$	6
Magnetite	$(Fe^{3+}_{1.87}Fe^{2+}_{1.04})_{\Sigma\,2.91}O_4$	8
Quartz	$Si_{1.00}O_2$	4
Stilpnomelane	$(K_{0.37}Na_{0.08})_{\Sigma\,0.45}(Fe_{4.43}Mg_{1.52}Mn_{0.04}Ca_{0.03})_{\Sigma\,6.01}Al_{1.00}Si_{8.12}(O,OH)_{27}$	7

Average calculated formulas for the mineral phases in the magnetite-chert meta-iron formation are presented in Table 3.21. Stilpnomelane is the only mineral phase to have detectible amounts of potassium and manganese in the magnetite-chert meta-iron formation. Apatite is the only phosphorous-bearing mineral phase in the magnetite-chert meta-iron formation. The composition of the carbonate minerals is calcite, which contain trace amounts of iron. Significantly, in both meta-iron formation samples, the composition of the phases is similar.

Table 3.21: Average calculated mineral formulas for the phases in the magnetite-chert meta-iron formation.

Jasper-magnetite meta-iron formation		
Mineral	Average Mineral Formula	Samples
Actinolite	$(Ca_{1.68}Na_{0.28})_{\Sigma\,1.96}(Mg_{3.19}Fe_{1.68}Al_{0.12})_{\Sigma\,4.99}Si_{8.05}O_{22}(OH)_2$	9
Ferro-actinolite	$(Ca_{1.69}Na_{0.20})_{\Sigma\,1.89}(Fe_{3.21}Mg_{1.81}Al_{0.32})_{\Sigma\,5.02}Si_{7.84}O_{22}(OH)_2$	3
Apatite	$(Ca_{4.92}Fe_{0.14}Na_{0.04})_{\Sigma\,5.12}(PO_4)_{2.89}(OH,F,Cl)$	9
Carbonate (Calcite)	$(Ca_{0.96}Fe_{0.01})_{\Sigma\,0.97}CO_3$	7
Chlorite (Chamosite)	$(Fe_{1.48}Mg_{1.06}Al_{0.44})_{\Sigma\,2.98}(Si_{3.12}Al_{0.88})_{\Sigma\,4.00}O_{10}(OH)_2 \bullet (Fe_{1.48}Mg_{1.06}Al_{0.44})_{\Sigma\,2.98}(OH)_6$	4
Epidote	$Ca_{2.09}Al_{2.08}Fe_{1.04}[Si_{2.11}O_7][Si_{1.00}O_4]O(OH)$	6
Magnetite	$(Fe^{3+}_{1.91}Fe^{2+}_{1.01})_{\Sigma\,2.92}O_4$	10
Quartz	$Si_{0.99}O_2$	4
Stilpnomelane	$(K_{0.66}Na_{0.14})_{\Sigma\,0.80}(Fe_{4.80}Mg_{0.92}Al_{0.14}Mn_{0.04}Ca_{0.04})_{\Sigma\,5.94}Al_{1.00}Si_{8.02}(O,OH)_{27}$	18

3.5.3 Metamorphism

To constrain the peak regional metamorphic temperatures for the SGB meta-iron formation and associated meta-igneous lithologies, the stable metamorphic mineral assemblage of the chlorite-actinolite-plagioclase granofels can be used. The stable metamorphic mineral assemblage of the chlorite-actinolite-plagioclase granofels is albite + chlorite + actinolite + epidote + quartz. Therefore, this indicates that peak metamorphic temperatures were at greenschist facies (Bucher and Grapes, 2011). The presence of oligoclase and andesine in the metapyroclastic rock indicates that temperatures might have been up to granulite facies (Bucher and Grapes, 2011). However, these feldspars are only associated as inclusions in the poikilitic plagioclase porphyroclasts minerals, indicating the preservation of relict detrital feldspar crystals rather than metamorphic. Since the stable metamorphic mineral assemblage is albite + chlorite + actinolite + epidote + quartz, this indicates that the protolith for the chlorite-actinolite-plagioclase granofels is a mafic igneous rock, as interpreted by Osmani (1997). The chlorite-actinolite-plagioclase granofels and meta-iron formation are in contact with each other Therefore, the meta-iron formation was also subjected to regional metamorphism at greenschist facies.

3.5.4 Petrographic Summary

The meta-igneous rocks associated with the meta-iron formation include the chlorite-actinolite-plagioclase granofels and the layered metapyroclastic rock. The chlorite-actinolite-plagioclase granofels has similar textures to the pillow lavas from the Chitradurga greenstone belt in South India (Duraiswami et al., 2013) suggesting that the igneous protolith was mafic volcanic flows. Therefore, the meta-iron formation was deposited in the deeper water environment. The layered metapyroclastic rock are interpreted to be pyroclastic fall deposits either setting out subaerially or underwater.

Most of the mineral phases in the magnetite-chert meta-iron formations have similar compositions to the magnetite-jasper meta-iron formations. Therefore, there is no evidence major phase partitioning between the magnetite-jasper and magnetite-chert meta-iron formation as seen in the other studies. Most of the actinolite occurs at the contacts between the magnetite-dominated layer and adjacent jasper- or quartz-dominated layers. This indicates actinolite grew during contact metasomatism between contrasting lithologies. However, since actinolite has calcium in its crystals structure, it is believed that calcium-bearing silicates or carbonates were deposited with the meta-iron formation causing reactions to initiate during regional metamorphism.

Significantly, there are quartz-calcite veins that crosscut the meta-iron formation. These veins cut through the quartz- and jasper-dominated layers but disappear in the magnetite-dominated layers. Also, the magnetite and quartz crystals in the magnetite-dominated layers are significantly larger than the quartz in the quartz- and jasper-dominated layers. Magnetite also has inclusions of actinolite, stilpnomelane and quartz. This evidence suggests that strain partitioning was occurring between the alternating phase-dominated bands. The quartz- and jasper-dominated layers behaved more competent than the magnetite-dominated layers due to reaction softening. The presence of actinolite, stilpnomelane and quartz inclusions in the magnetite crystals indicates that magnetite was growing during progressive metamorphism. Since magnetite was reacting to form larger magnetite crystals through solid state diffusion, the magnetite-dominated layers were more ductile than the quartz crystals in the quartz-dominated layers. A competency contrast between the competent quartz-dominated and the less competent magnetite-dominated layers caused brittle fractures to occur in the quartz-dominated layers. Therefore, all this evidence indicates that magnetite was growing during progressive deformation and metamorphism and reactions were primarily occurring in the magnetite-dominated layers or at the contacts between the quartz- and magnetite-dominated layers.

CHAPTER 4

GEOCHEMISTRY

4.1 Introduction and Geochemical Data

To determine the chemical composition of the Archean ocean-atmospheric system, it is imperative to investigate the provenance and geologic processes responsible for supplying and concentrating each element in the meta-iron formation. Since meta-iron formations are interpreted to be chemical precipitates, they can sample the chemistry of the ocean, which is dictated by provenance from two dominant sources: hydrothermal venting fluids and dissolved load from continental runoff. In addition, the presence of siliciclastic detritus can also affect the overall chemistry of meta-iron formations. Geologic processes such as physical and chemical erosion, deposition, and post-depositional alteration, such as diagenesis, regional metamorphism and late stage hydrothermal metasomatism, can have a profound effect on mobilizing and concentrating some elements in the meta-iron formations. This chapter will focus on determining the provenance and investigating the effects of post-depositional alteration of the elements using geochemical relationships. Once these factors are determined, shallow and deep water meta-iron formations will be compared to investigate evidence of stratification in the ancient Archean ocean. Data from the geochemical analyses can be seen in Tables 4.1 – 4.5.

Table 4.1: Major element geochemical data for the meta-iron formation samples in BG, LSJ, NC and SGB. (*) indicates concentrations below detection limits, (-) indicates that the element was not analyzed.

Dominant Minerology	Sample Number	Al_2O_3	TiO_2	Fe_2O_{3T}	Fe_2O_{3V}	FeO	MnO	CaO	MgO	Na_2O	K_2O	P_2O_5
Major Element Geochemical Data												
Beardmore/Geraldton												
Magnetite	06-28	1.090	0.023	51.305	45.496	14.670	0.037	0.557	0.106	0.705	0.055	0.228
Magnetite	03-07	2.373	0.066	46.198	36.950	15.910	0.030	0.511	0.238	1.402	0.199	0.278
Magnetite	05-93	3.832	0.052	49.458	43.831	12.900	0.071	0.563	0.158	1.608	0.536	0.296
Magnetite	06-27	3.726	0.092	56.441	54.944	13.780	0.029	0.824	0.043	1.778	0.134	0.188
Magnetite	03-8	6.517	0.193	27.932	16.981	11.900	0.062	2.435	0.473	2.318	0.258	0.319
Magnetite	B0302 M	6.785	0.176	33.134	-	-	0.041	1.582	1.819	2.812	0.392	0.218
Magnetite	B0303 M	3.294	0.091	44.997	-	-	0.033	1.207	1.768	1.135	0.289	0.175
Magnetite	B0304A M	2.397	0.056	58.336	38.046	18.280	0.008	0.295	0.514	1.263	0.024	0.116
Magnetite	B0304B M	1.916	0.065	83.385	57.422	23.390	0.010	0.386	0.058	1.052	0.006	0.237
Magnetite	B0305 M	9.566	0.339	19.734	9.843	8.910	0.089	2.313	3.594	3.563	0.104	0.132
Magnetite	B0309 M	3.184	0.118	45.040	30.488	13.110	0.027	1.217	1.090	1.557	0.406	0.339
Hematite	B02 S	0.275	0.019	85.987	-	-	0.002	1.158	0.014	0.022	0.080	0.774
Hematite	B03 S	2.489	0.077	82.242	-	-	0.008	0.121	0.234	0.063	0.691	0.077
Hematite	B04 S	0.868	0.038	68.631	67.221	1.270	*	0.220	0.220	0.009	0.041	0.140
Hematite/Jasper	BSL3 HS	1.282	0.031	56.849	52.920	3.540	0.057	3.405	1.290	0.031	0.194	0.177
Jasper	06-25	0.367	0.008	38.060	46.593	0.430	0.019	0.093	0.715	0.149	0.078	0.139
Jasper	06-26	0.423	0.010	26.290	27.146	0.950	0.006	0.066	0.216	0.083	0.116	0.058
Jasper	03-14	0.632	0.009	21.721	39.253	0.700	0.017	0.213	0.072	0.013	0.173	0.011
Jasper	05-91	0.830	0.019	40.193	52.505	0.860	0.013	0.267	0.115	0.200	0.121	0.146
Jasper	03-16	3.633	0.111	54.611	76.733	1.340	0.015	0.868	0.604	0.248	0.651	0.054
Jasper	05-90	4.959	0.175	40.994	42.607	4.030	0.026	2.067	1.438	0.491	0.129	0.125
Jasper	B01 H	0.178	0.004	12.671	-	-	*	0.086	0.034	0.015	0.058	0.009
Jasper	B02 H	0.181	0.003	13.712	13.445	0.240	0.005	0.224	0.064	0.028	0.058	*
Jasper	BIFI H	0.843	0.017	33.659	32.538	1.010	*	0.061	0.228	0.024	0.076	0.034
Lake St Joseph												
Magnetite	03-118	1.851	0.028	49.138	40.002	15.980	0.035	0.589	0.432	1.008	0.132	0.405
Magnetite	03-85	4.150	0.027	43.750	29.895	14.230	0.040	1.161	0.018	1.994	0.039	0.190
Magnetite	03-83	5.773	0.032	38.952	28.628	15.470	0.033	1.420	0.496	2.301	0.033	0.241
Hematite	03-88A	0.864	0.014	32.701	49.560	0.550	0.006	0.157	2.148	0.103	0.316	0.259
Hematite	03-88B	1.151	0.020	38.946	60.214	0.510	0.006	0.195	1.009	0.228	0.382	0.229
North Caribou												
Magnetite	PM05-39	0.340	0.003	73.191	58.988	27.290	0.242	1.770	0.775	0.481	0.005	0.025
Magnetite	PM05-28A	0.352	0.004	73.649	51.098	31.930	0.085	1.758	0.324	0.451	0.009	0.109
Magnetite	PM0540A	0.198	0.001	62.669	51.745	29.770	0.197	1.476	1.332	0.275	0.003	0.121
Magnetite	PM05-31A	0.424	0.011	66.615	48.835	26.770	0.159	2.430	0.124	0.475	0.009	0.266
Magnetite	PM05-21	0.625	0.019	67.187	49.871	25.450	0.113	3.982	0.252	0.592	0.164	0.095
Magnetite	PM05-37	0.343	0.004	63.469	48.190	24.730	0.185	1.463	0.317	0.475	0.007	0.061
Magnetite	PM05-38A	0.319	0.004	63.755	46.024	25.150	0.156	1.803	0.993	0.418	0.004	0.020
Magnetite/Grunerite	PM05-63	0.322	0.004	42.618	21.008	26.020	0.120	4.275	0.018	0.428	0.005	0.157
Magnetite/Grunerite	PM05-64	0.347	0.006	36.830	13.078	28.110	0.346	3.560	0.052	0.370	0.020	0.147
Magnetite/Grunerite	PM05-40B	0.149	0.001	32.393	2.038	30.560	0.653	7.301	6.840	0.185	0.003	0.177
Magnetite/Grunerite	PM05-31B	0.157	0.002	23.814	2.784	20.420	0.187	3.831	1.053	0.082	0.007	0.054
Chert	PM05-06	0.070	0.003	12.388	5.713	6.610	0.108	1.238	1.200	0.014	0.006	0.072
Chert	PM05-38B	0.012	0.001	8.562	3.184	5.330	0.091	1.199	0.899	*	0.002	0.005
Chert	PM05-28B	0.027	0.001	5.356	0.539	4.100	0.058	0.786	0.095	*	0.003	0.007
Chert	PM05-12	0.017	0.001	1.943	0.434	1.150	0.029	0.276	1.755	*	0.004	0.004
Chert	PM05-18	0.021	0.001	1.867	0.712	0.710	0.018	0.155	1.429	0.000	0.004	0.003
Shebandowan												
Magnetite	SHO6 M	0.719	0.018	53.590	35.475	16.320	0.059	2.269	0.711	0.034	0.220	0.166
Magnetite	SH07 M	0.863	0.027	72.805	46.632	23.580	0.082	1.857	1.081	0.042	0.331	0.268
Magnetite	SH018 M	7.038	0.405	52.589	28.946	21.300	0.040	1.563	4.017	1.689	0.159	0.141
Magnetite	SH027 M	3.244	0.153	58.823	32.227	23.960	0.090	2.921	1.612	0.233	0.669	0.327
Jasper	SH09 H	0.278	0.006	5.551	-	-	0.005	2.279	0.088	0.020	0.042	0.041
Jasper	SH018 H	0.075	0.003	11.536	-	-	0.007	2.315	0.097	0.006	0.020	0.039
Jasper	SH022 H	0.211	0.004	16.622	-	-	0.012	1.063	0.232	0.015	0.078	0.037
Jasper	SH027 H	0.290	0.007	16.502	-	-	0.012	2.044	0.193	0.074	0.096	0.061
Chert	SH07 C	0.738	0.014	14.873	8.146	6.060	0.042	2.803	0.849	0.055	0.262	0.035
Chert	SH010 C	0.443	0.014	12.502	6.996	4.960	0.039	4.451	0.452	0.017	0.168	0.032
Chert	SH016 C	0.416	0.002	9.637	5.452	3.770	0.036	4.211	0.619	0.036	0.136	0.022

Table 4.2: Minor and trace element geochemistry of the meta-iron formation samples from BG. (*) indicates concentrations below detection limits.

| Trace Elements | Beardmore/Geraldton | | | | | | | | | | | | | | | Jasper | | | | | | | | |
| | Magnetite | | | | | | | | | | | Hematite | | | Hematite/Jasper | Jasper | | | | | | | | |
Sample Number	06-28	03-07	05-93	06-27	03-8	B0302 M	B0303 M	B0304A M	B0304B M	B0305 M	B0309 M	B02 S	B03 S	B04 S	BSL3 HS	06-25	06-26	03-14	05-91	03-16	05-90	B01 H	B02 H	BIFI H
Cr	*	30.00	30.00	42.00	79.00	72.89	26.37	11.67	10.87	79.25	13.29	4.17	9.93	6.91	7.65	*	*	*	*	45.00	69.00	2.53	1.25	3.39
Cs	0.22	2.00	3.10	1.20	0.62	2.35	2.56	0.37	0.46	0.58	5.78	0.33	2.87	0.21	0.89	0.27	0.34	0.47	0.39	1.80	0.73	0.59	0.42	0.44
Cu	5.55	132.39	11.15	13.03	7.15	4.71	20.73	2.61	2.71	*	0.24	2.75	1.61	2.85	4.45	4.79	1.31	29.55	5.99	3.03	12.11	3.31	2.95	1.49
Hf	0.20	0.40	0.90	0.50	1.10	2.03	1.63	1.77	0.60	1.35	0.78	0.78	1.10	0.52	0.74	0.20	0.10	*	0.50	0.60	0.80	0.14	0.12	0.33
Mo	*	2.00	*	*	*	0.55	0.79	2.28	2.48	0.10	0.33	0.27	0.09	0.06	0.10	*	*	*	*	*	*	0.09	0.13	0.17
Nb	0.30	1.00	1.60	1.10	2.30	1.03	1.25	0.83	0.53	2.13	0.98	0.21	1.32	0.46	0.37	0.50	0.30	0.30	1.20	2.10	1.70	0.06	0.07	0.30
Ni	24.00	50.00	29.00	47.00	48.00	30.89	13.85	12.57	2.55	43.87	14.27	0.13	10.01	4.09	9.51	17.00	12.00	14.00	16.00	30.00	54.00	0.33	0.15	1.75
Pb	5.00	61.00	24.00	8.00	16.00	14.11	10.64	7.23	6.55	6.76	15.83	1.72	1.38	1.39	2.31	*	*	10.00	*	8.00	*	2.12	1.94	1.65
Rb	3.50	13.00	34.00	8.90	8.70	41.88	35.71	2.75	0.96	3.93	43.37	5.30	55.63	3.48	17.06	6.10	6.30	8.70	11.00	34.00	6.60	5.37	4.43	3.82
Sc	8.00	8.00	8.00	13.00	14.00	8.06	3.74	2.42	1.78	13.24	5.04	0.34	2.00	0.84	2.28	*	*	*	*	*	11.00	0.08	0.14	0.76
Sn	5.00	*	7.00	*	*	0.56	0.46	0.37	0.46	0.20	0.97	0.20	0.56	0.17	0.19	*	*	*	6.00	*	*	0.82	0.45	0.86
Sr	22.41	75.89	46.17	40.85	190.09	74.33	41.89	45.79	40.81	400.60	46.60	105.23	11.23	16.01	192.25	18.05	12.05	3.97	30.17	7.53	17.69	4.67	8.95	6.69
Th	0.33	1.00	1.60	1.20	2.70	3.42	1.61	1.08	0.70	3.14	1.13	0.26	0.94	0.43	0.37	0.15	0.11	0.16	0.33	1.50	1.40	0.05	0.06	0.20
U	0.11	0.46	0.41	0.49	0.68	0.73	0.44	0.40	0.18	0.71	0.29	0.17	0.64	0.14	0.30	0.11	0.09	0.13	0.15	0.96	0.37	0.05	0.05	0.22
V	11.47	22.23	24.59	37.35	52.63	58.63	27.95	25.67	17.33	81.01	37.21	3.63	25.21	7.87	11.23	6.07	4.91	4.47	7.59	37.87	46.27	0.89	0.83	9.85
Y	7.50	9.10	7.90	7.30	14.00	5.09	3.72	3.65	4.61	4.42	6.47	5.63	1.87	2.42	6.71	4.20	1.50	2.20	4.90	7.80	8.30	0.23	0.36	1.15
Zn	21.53	223.97	114.93	47.69	97.37	51.58	51.64	62.02	48.72	92.80	48.72	62.88	59.66	30.92	35.90	22.81	8.85	69.65	16.93	63.41	39.77	8.62	9.50	26.82
Zr	40.88	61.44	49.64	44.44	77.36	73.04	59.92	72.20	31.64	65.87	25.79	40.44	47.12	26.44	32.24	24.96	16.08	7.64	43.84	43.52	62.56	6.50	5.84	15.06
La	3.50	8.74	8.71	6.14	15.60	9.43	6.17	4.80	3.60	9.52	7.55	4.16	5.53	3.96	3.88	2.52	1.35	1.98	3.52	6.41	6.50	0.42	0.47	1.59
Ce	6.14	16.60	15.60	12.60	31.20	19.14	12.30	10.60	7.42	21.50	15.33	7.52	11.25	8.31	7.67	4.58	2.41	3.59	6.90	13.40	13.40	0.70	0.83	3.21
Pr	0.73	1.87	1.76	1.54	3.67	2.28	1.47	1.30	0.94	2.67	1.84	0.91	1.32	1.01	0.94	0.56	0.27	0.41	0.83	1.55	1.61	0.08	0.10	0.40
Nd	3.01	7.43	6.66	6.22	14.50	8.93	5.78	5.13	4.04	10.54	7.45	3.83	5.04	4.08	4.07	2.25	0.98	1.54	3.19	5.76	6.44	0.31	0.40	1.59
Sm	0.63	1.43	1.26	1.32	2.91	1.80	1.14	1.04	0.90	2.11	1.42	0.82	0.95	0.81	0.88	0.45	0.18	0.25	0.61	1.11	1.36	0.06	0.07	0.30
Eu	0.32	0.56	0.51	0.59	0.83	0.58	0.42	0.38	0.42	0.57	0.54	0.62	0.35	0.42	0.58	0.36	0.10	0.11	0.47	0.38	0.48	0.08	0.07	0.15
Gd	0.83	1.50	1.21	1.40	2.76	1.70	1.11	1.07	1.05	1.92	1.63	1.05	0.80	0.82	1.18	0.55	0.21	0.25	0.72	1.10	1.44	0.05	0.08	0.34
Tb	0.13	0.22	0.18	0.21	0.38	0.22	0.14	0.14	0.15	0.24	0.24	0.14	0.09	0.10	0.17	0.09	0.03	0.04	0.11	0.18	0.22	0.01	0.01	0.05
Dy	0.87	1.34	1.09	1.22	2.24	1.01	0.65	0.68	0.75	1.07	1.19	0.75	0.36	0.46	1.01	0.57	0.20	0.30	0.71	1.22	1.40	0.04	0.06	0.24
Ho	0.20	0.29	0.22	0.25	0.46	0.19	0.13	0.13	0.15	0.17	0.22	0.15	0.07	0.09	0.20	0.13	0.05	0.07	0.16	0.28	0.30	0.01	0.01	0.05
Er	0.61	0.84	0.65	0.74	1.36	0.56	0.37	0.36	0.39	0.50	0.59	0.47	0.20	0.23	0.59	0.39	0.14	0.21	0.47	0.85	0.85	0.03	0.04	0.13
Tm	0.09	0.12	0.09	0.11	0.19	0.09	0.06	0.05	0.05	0.08	0.08	0.07	0.03	0.03	0.08	0.06	0.02	0.03	0.07	0.13	0.13	0.00	0.01	0.02
Yb	0.57	0.76	0.59	0.71	1.30	0.66	0.43	0.40	0.33	0.59	0.57	0.41	0.22	0.21	0.55	0.37	0.13	0.22	0.45	0.84	0.84	0.02	0.05	0.10
Lu	0.09	0.12	0.09	0.11	0.20	0.12	0.07	0.06	0.05	0.10	0.09	0.07	0.04	0.03	0.09	0.06	0.02	0.03	0.07	0.13	0.13	0.01	0.01	0.01

Table 4.3: Minor and trace element geochemistry for meta-iron formation samples from LSJ. (*) indicates concentrations below detection limits.

Lake St. Joseph				
Trace Elements	Magnetite			Hematite	
	03-118	03-85	03-83	03-88A	03-88B
Cr	10.00	23.00	61.00	7.00	7.00
Cs	0.71	0.16	0.20	0.44	1.00
Cu	34.43	185.11	23.51	30.75	36.39
Hf	0.40	0.90	1.10	0.20	0.20
Mo	*	2.00	*	*	3.00
Nb	0.70	2.10	2.60	0.50	0.40
Ni	48.00	40.00	49.00	24.00	19.00
Pb	99.00	88.00	50.00	35.00	29.00
Rb	8.20	1.60	1.40	18.00	30.00
Sc	*	8.00	10.00	*	*
Sn	*	5.00	*	*	*
Sr	81.53	28.81	82.41	10.65	9.41
Th	0.93	1.60	3.00	0.41	0.51
U	0.55	0.55	0.58	0.20	0.18
V	27.55	27.99	39.07	5.55	6.67
Y	10.00	6.70	8.10	3.20	4.50
Zn	390.73	267.21	254.21	166.93	83.77
Zr	56.12	79.80	74.48	16.24	31.68
La	8.64	6.40	11.10	3.01	3.53
Ce	15.00	12.90	21.90	5.10	6.11
Pr	1.70	1.53	2.51	0.57	0.68
Nd	6.69	5.82	9.28	2.21	2.61
Sm	1.29	1.05	1.68	0.40	0.44
Eu	0.61	0.28	0.49	0.18	0.19
Gd	1.43	0.98	1.45	0.43	0.47
Tb	0.22	0.15	0.21	0.06	0.07
Dy	1.42	0.94	1.26	0.40	0.47
Ho	0.31	0.21	0.26	0.09	0.11
Er	0.95	0.63	0.74	0.28	0.36
Tm	0.13	0.09	0.10	0.04	0.05
Yb	0.88	0.60	0.66	0.25	0.33
Lu	0.13	0.10	0.10	0.04	0.05

Table 4.4: Minor and trace element geochemistry for meta-iron formation samples from NC. (*) indicates concentrations below detection limits.

| Trace Elements | North Caribou | | | | | | | | | | | | | | | |
| | Magnetite | | | | | | | Magnetite/Grunerite | | | | | Chert | | | |
	PM05-39	PM05-28A	PM0540A	PM05-31A	PM05-21	PM05-37	PM05-38A	PM05-63	PM05-64	PM05-40B	PM05-31B	PM05-06	PM05-38B	PM05-28B	PM05-12	PM05-18
Cr	44.00	58.00	41.00	43.00	44.00	42.00	42.00	30.00	34.00	25.00	16.00	35.00	16.00	14.00	33.00	16.00
Cs	18.00	*	8.00	13.00	11.00	19.00	9.00	7.00	8.00	*	9.00	9.00	9.00	15.00	7.00	11.00
Cu	0.35	1.99	0.47	6.95	1.75	1.19	1.95	0.63	4.59	1.35	20.19	3.91	0.27	1.95	1.03	19.47
Hf	*	*	*	0.20	0.20	*	*	*	*	*	*	0.10	*	0.10	0.10	0.10
Mo	*	*	*	*	*	*	*	*	*	*	*	*	*	*	*	*
Nb	*	0.20	*	*	0.30	*	*	*	*	*	*	*	*	*	*	*
Ni	13.00	25.00	14.00	16.00	17.00	31.00	17.00	14.00	14.00	8.00	10.00	9.00	10.00	3.00	18.00	13.00
Pb	*	7.00	*	5.00	*	*	*	*	*	*	*	*	*	*	*	*
Rb	0.14	0.69	0.10	0.18	11.00	0.14	0.14	0.24	2.61	0.11	0.12	0.28	0.08	0.12	0.09	0.15
Sc	18.00	14.00	18.00	15.00	12.00	14.00	15.00	13.00	23.00	8.00	*	*	*	*	*	*
Sn	12.00	9.00	15.00	13.00	12.00	5.00	11.00	5.00	*	*	*	*	*	*	*	*
Sr	1.49	2.69	1.33	4.69	5.57	1.77	2.05	7.13	8.09	1.57	2.57	0.57	*	3.33	0.09	0.13
Th	*	*	*	0.29	0.55	*	*	*	*	*	*	*	*	*	*	*
U	*	0.01	*	0.03	0.09	*	*	0.01	0.02	0.01	0.01	0.02	*	0.01	0.02	0.02
V	1.39	3.63	1.19	2.55	5.35	3.15	2.71	2.59	3.63	0.55	0.15	0.95	0.19	0.31	0.19	1.27
Y	2.34	3.57	4.26	4.34	5.70	2.81	1.96	12.80	13.50	6.34	1.36	1.82	0.30	2.58	0.48	0.84
Zn	25.41	55.69	22.49	27.53	28.97	22.21	24.89	27.57	25.73	30.61	21.17	19.41	5.21	7.41	6.25	9.53
Zr	61.00	67.72	51.40	42.24	68.28	55.04	44.24	45.36	39.80	20.92	11.92	4.32	2.08	1.36	1.00	1.60
La	2.84	2.46	3.15	1.18	4.96	2.71	2.46	3.49	4.47	2.90	1.02	1.35	0.42	0.90	0.66	0.32
Ce	3.84	4.98	5.53	1.50	9.02	4.11	3.11	6.32	9.22	5.94	1.01	2.60	0.60	1.69	1.14	0.61
Pr	0.33	0.55	0.51	0.17	1.01	0.39	0.26	0.77	1.13	0.58	0.09	0.23	0.05	0.19	0.13	0.08
Nd	1.15	2.36	1.97	0.75	3.91	1.44	0.94	3.36	4.93	2.41	0.31	1.06	0.17	0.82	0.47	0.32
Sm	0.18	0.47	0.36	0.19	0.61	0.26	0.14	0.79	1.22	0.54	0.06	0.22	0.03	0.20	0.07	0.08
Eu	0.14	0.33	0.27	0.19	0.42	0.19	0.10	0.69	0.83	0.42	0.06	0.16	0.01	0.17	0.03	0.05
Gd	0.23	0.59	0.48	0.30	0.64	0.33	0.17	1.19	1.61	0.74	0.09	0.28	0.03	0.27	0.06	0.09
Tb	0.03	0.09	0.07	0.05	0.10	0.05	0.03	0.20	0.26	0.12	0.01	0.05	0.01	0.05	0.01	0.02
Dy	0.25	0.59	0.53	0.34	0.68	0.36	0.21	1.37	1.82	0.82	0.11	0.30	0.04	0.33	0.05	0.12
Ho	0.06	0.13	0.13	0.09	0.17	0.09	0.05	0.34	0.42	0.19	0.03	0.07	0.01	0.08	0.01	0.03
Er	0.19	0.38	0.39	0.30	0.58	0.29	0.17	1.09	1.34	0.61	0.11	0.20	0.03	0.26	0.05	0.09
Tm	0.03	0.06	0.06	0.05	0.10	0.04	0.03	0.16	0.20	0.09	0.02	0.03	0.01	0.04	0.01	0.01
Yb	0.19	0.39	0.40	0.32	0.68	0.30	0.19	1.05	1.30	0.60	0.14	0.20	0.04	0.25	0.05	0.08
Lu	0.03	0.06	0.06	0.06	0.12	0.05	0.03	0.17	0.20	0.10	0.03	0.03	0.01	0.04	0.01	0.01

Table 4.5: Minor and trace element geochemistry for meta-iron formation samples from SGB. (*) indicates concentrations below detection limits.

Trace Elements	Magnetite				Jasper				Chert		
	SHO6 M	SH07 M	SH018 M	SH027 M	SH09 H	SH018 H	SH022 H	SH027 H	SH07 C	SH010 C	SH016 C
Cr	0.53	2.67	16.55	24.15	0.67	21.45	0.11	21.61	1.61	0.71	1.97
Cs	4.82	7.44	4.71	16.67	0.33	0.70	1.49	2.60	2.63	5.58	2.56
Cu	34.39	30.47	272.64	21.13	21.01	35.63	80.48	35.59	40.55	58.68	78.69
Hf	1.43	0.73	2.73	2.47	0.04	0.13	*	0.30	0.46	0.22	0.20
Mo	0.82	1.56	0.28	1.01	0.33	0.26	0.19	1.09	0.38	0.20	0.42
Nb	0.16	0.38	3.57	1.17	0.10	0.07	0.28	0.11	0.18	0.19	0.04
Ni	1.65	3.33	10.27	23.45	0.67	10.85	1.39	9.65	0.97	2.19	1.37
Pb	3.40	4.04	9.54	17.59	0.96	4.32	3.55	16.14	16.92	13.22	7.79
Rb	16.85	26.04	19.83	51.21	2.84	2.12	5.81	7.68	7.87	22.86	8.51
Sc	0.48	0.68	5.60	2.84	0.10	0.08	0.20	0.08	0.20	0.48	0.50
Sn	1.14	1.31	6.07	8.21	0.76	0.79	2.04	2.97	0.71	1.34	1.49
Sr	22.00	13.20	20.20	70.31	11.83	23.71	12.60	23.55	7.89	22.40	10.39
Th	0.11	0.40	2.35	0.90	0.27	0.02	*	0.05	0.10	0.11	0.01
U	0.08	0.14	0.48	0.12	0.06	0.03	0.02	0.03	0.08	0.05	0.04
V	8.13	8.23	49.60	25.49	1.27	0.79	1.64	0.83	2.03	3.28	4.53
Y	11.04	10.43	20.73	7.38	0.62	2.04	1.75	1.58	2.48	2.91	0.58
Zn	177.12	270.46	434.16	497.06	10.52	118.70	58.68	118.78	133.80	309.00	271.86
Zr	57.80	37.10	128.83	87.16	2.04	6.68	4.67	6.42	12.76	6.07	18.44
La	3.35	5.07	10.36	8.91	3.01	1.05	0.90	1.24	2.98	2.36	1.00
Ce	8.21	11.46	27.67	17.82	6.66	2.28	2.24	2.43	5.74	5.73	2.00
Pr	1.17	1.50	3.82	2.14	0.70	0.29	0.28	0.30	0.67	0.70	0.23
Nd	5.56	6.78	16.86	8.66	2.29	1.20	1.13	1.25	2.72	2.74	0.86
Sm	1.57	1.58	3.99	1.67	0.30	0.26	0.22	0.27	0.59	0.57	0.15
Eu	1.76	1.46	3.09	1.21	0.17	0.32	0.24	0.21	0.44	0.50	0.06
Gd	2.03	1.91	4.74	1.84	0.31	0.35	0.33	0.33	0.64	0.65	0.15
Tb	0.31	0.27	0.75	0.26	0.04	0.05	0.06	0.05	0.09	0.10	0.02
Dy	1.85	1.57	4.61	1.36	0.15	0.32	0.34	0.28	0.49	0.51	0.11
Ho	0.37	0.33	0.95	0.27	0.03	0.07	0.06	0.06	0.10	0.11	0.03
Er	1.10	0.93	2.91	0.76	0.07	0.23	0.23	0.19	0.32	0.34	0.08
Tm	0.15	0.13	0.45	0.11	0.01	0.04	0.03	0.03	0.05	0.05	0.01
Yb	0.93	0.81	3.08	0.68	0.06	0.26	0.23	0.18	0.33	0.31	0.09
Lu	0.13	0.13	0.46	0.11	0.01	0.05	0.03	0.03	0.06	0.05	0.02

Shebandowan

4.2 Siliciclastic Endmember Elements

First, it is important to establish which elements in the meta-iron formation were derived from the siliciclastic phase and remained immobile. Elements classified as immobile were resistant to chemical weathering during continental erosion and remained isochemical during post-deposition alteration. If an element is deemed immobile, that element was chemically immobile since its incorporation into minerals during igneous crystallization, and after subaerial erosion, these minerals became the siliciclastic component of the meta-iron formation.

Geochemical bivariate plots can be used to effectively discriminate between mobile and immobile elements. MacLean (1990) used bivariate plots to test which elements were immobile during hydrothermal alteration of igneous rocks. This technique can equally be used to distinguish the immobility of elements for metamorphosed sedimentary rock (MacLean, 1990) and its implementation for metasedimentary rocks has been highly effective (Fralick and Kronberg, 1997; Fralick, 2003). The theoretical premise behind this technique entails that immobile elements will decrease or increase in concentration at a constant rate relative to the mass gain or loss of the mobile elements to/from the system, respectively. Therefore, the data set will form a linear array that goes through the origin, if both elements were chemically immobile (MacLean, 1990; Fralick and Kronberg, 1997; Fralick, 2003). However, elements that share similar chemical properties can produce linear relationships even if both elements were mobile (Fralick, 2003). To remove this effect, elements with different chemical properties were plotted against each other to determine the immobile elements in the siliciclastics.

Each element obtained from the geochemical analysis was plotted against each other to determine which elements were derived from the siliciclastic phase and remained immobile during post-depositional alteration. Figures 4.1 – 4.5 are logarithmic bivariate element plots for Al_2O_3, TiO_2,

Th, V, Nb and U. There is a strong linear correlation between Al_2O_3 and TiO_2 for the meta-iron formation samples (Figure 4.1). Al_2O_3 vs Th (Figures 4.2) and Al_2O_3 vs V (Figure 4.3) also show a strong linear correlation, except at lower values where the correlation is less defined. At these lower levels, the elements are approaching their respective lower detection limits. As analytical techniques reach lower levels of detection, the errors associated with the analysis increase, which decreases the accuracy in measuring the abundance of each element and effects the overall trend of the data. The strong correlations between Al_2O_3 vs TiO_2 (Figure 4.1), TiO_2 vs Th (Figure 4.2), Al_2O_3 vs V (Figure 4.3), TiO_2 vs Nb (Figure 4.4) and TiO_2 vs U (Figure 4.5) demonstrates that all these elements were derived from the siliciclastic phase and remained relatively immobile during post-depositional alteration. The rest of the elements analysed were derived from another source other than the siliciclastic phase, derived from multiple sources and/or mobilized during post-depositional alteration.
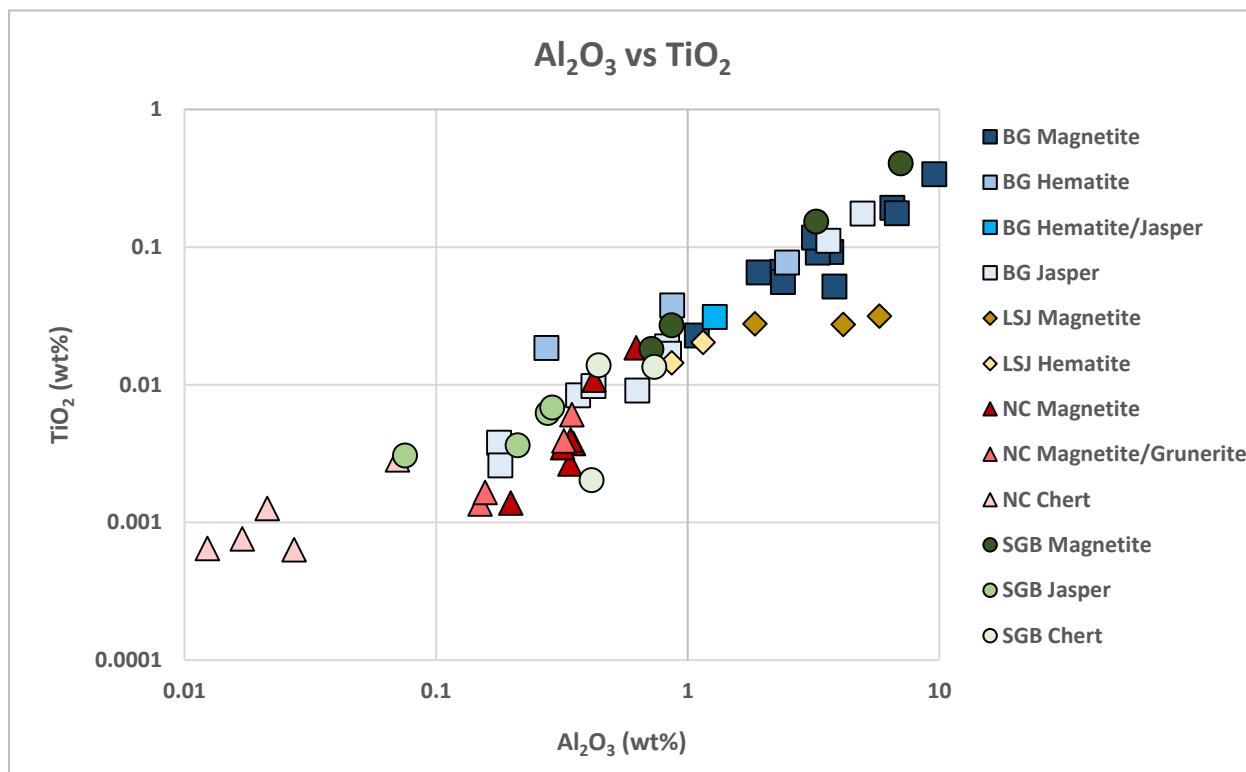
Figure 4.1: A logarithmic bivariate plot of aluminum versus titanium. This graph shows a very strong, positive, linear correlation between titanium and aluminum, indicating that both elements were immobile during erosion and post-depositional alteration. Also, both elements were derived from the siliciclastic phase.
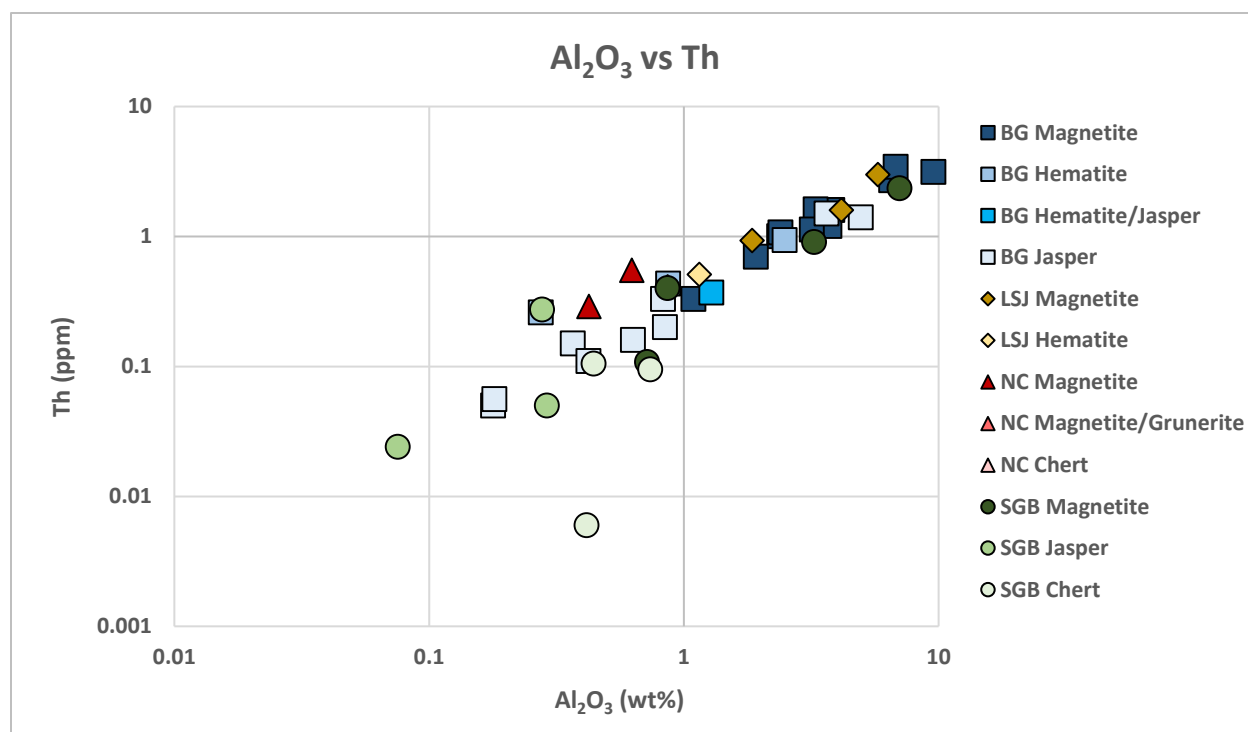
Figure 4.2: A logarithmic bivariate plot of aluminum plotted against thorium. This graph shows a strong, positive, linear trend between aluminum and thorium. The linear relationship between thorium and aluminum indicates that thorium was derived from the siliciclastic phase and was immobile during post-depositional alteration.
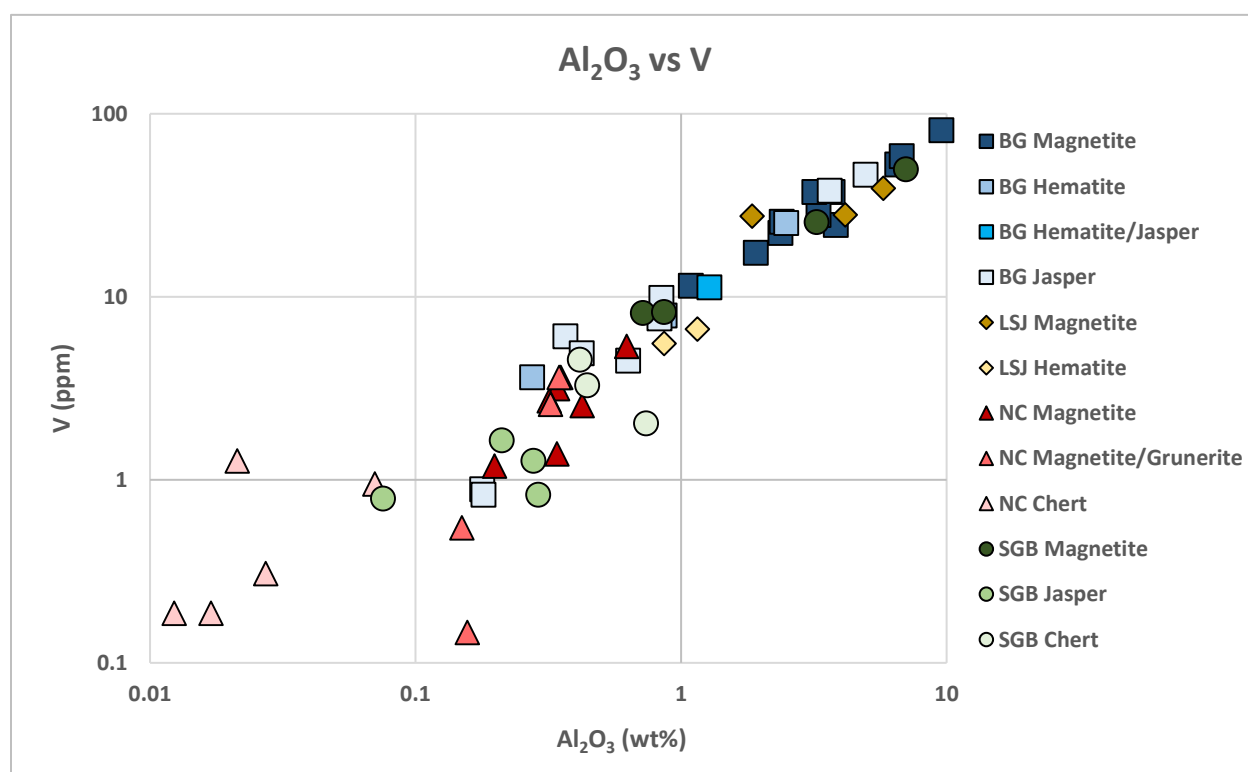
Figure 4.3: A logarithmic bivariate plot of aluminum versus vanadium. This graph shows a strong, positive, linear correlation between aluminum and vanadium. However, at lower concentrations, the data becomes more scattered. The strong linear relationship indicates that vanadium was immobile and derived from the siliciclastic phase.
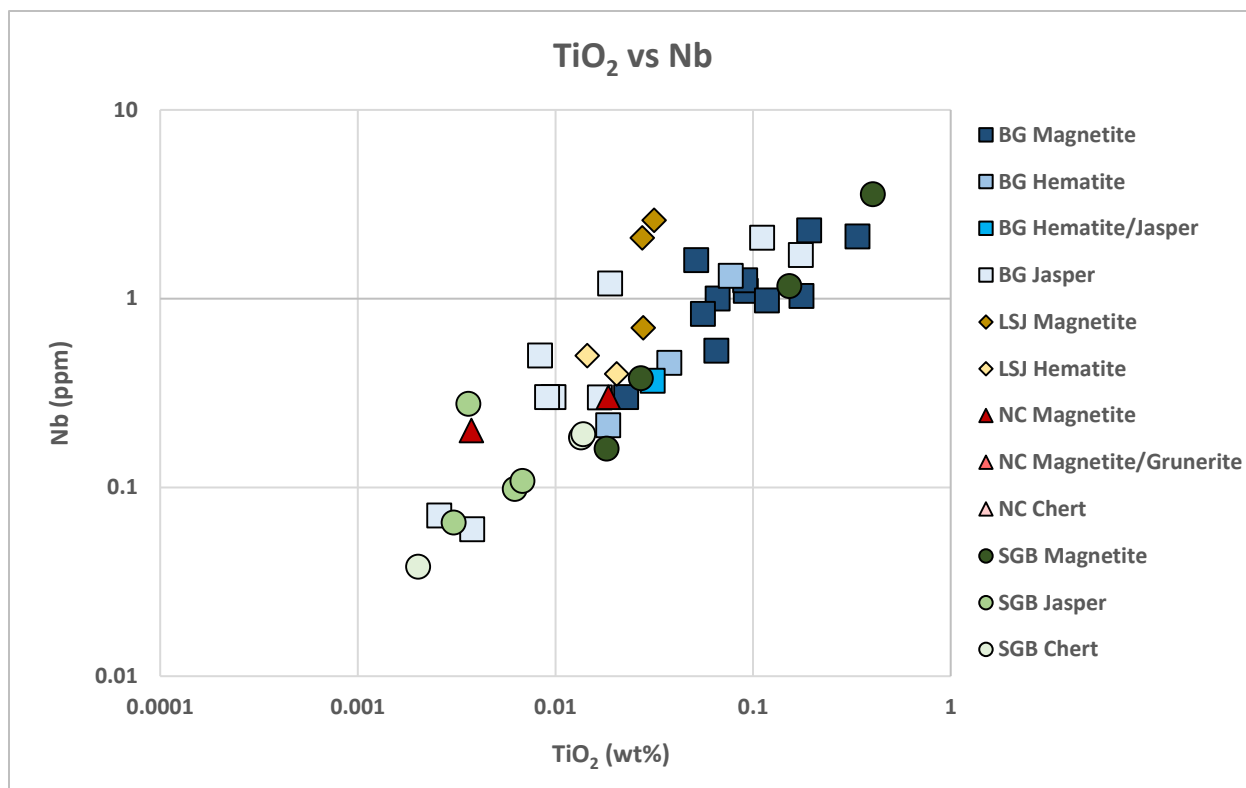
Figure 4.4: A TiO₂ vs Nb logarithmic bivariate plot. This graph shows a strong, positive, linear relationship between titanium and niobium. This means that niobium was derived from the siliciclastic phase and remained immobile during post-depositional alteration.
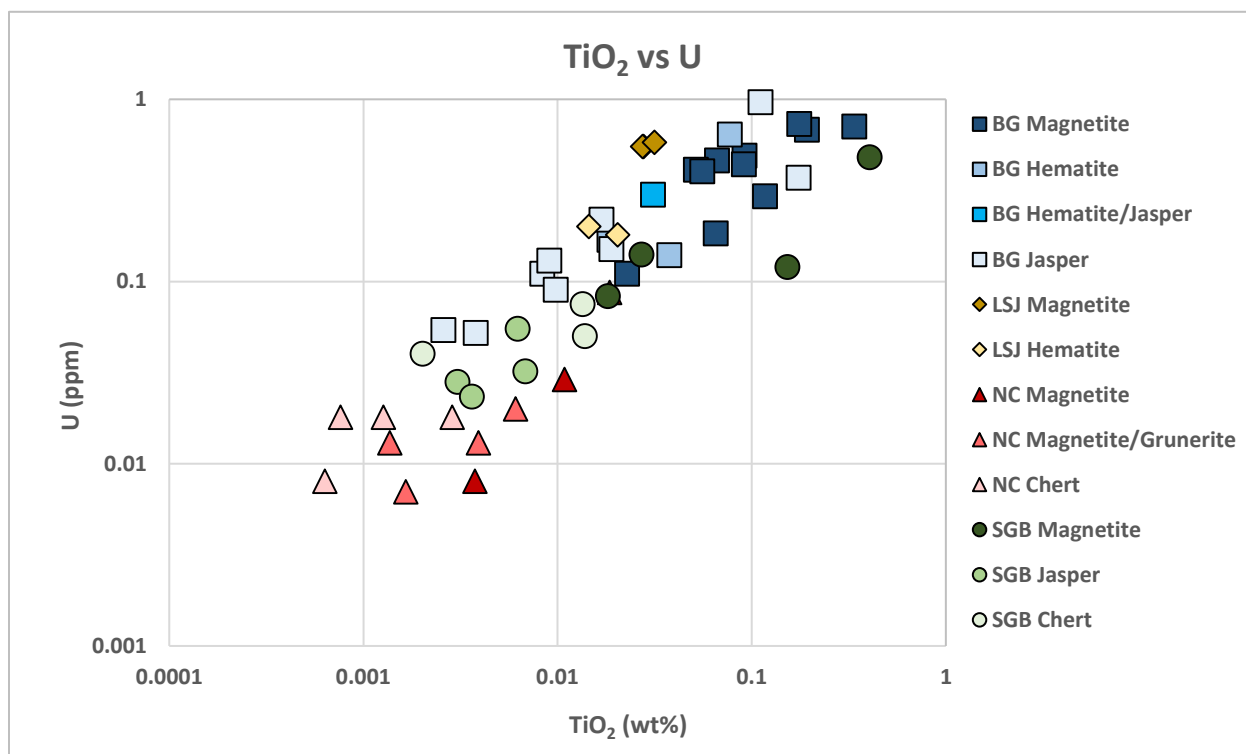
Figure 4.5: A TiO₂ vs U logarithmic bivariate plot. This graph shows a positive, linear relationship between uranium and titanium. This indicates that uranium was derived from the siliciclastic phase and immobile during post-depositional alteration.

4.3 Hydrothermal Endmember Elements

This section will focus on elements in the meta-iron formation derived solely from hydrothermal venting fluids. Hydrothermal venting systems can be subdivided into two main types: black and white smoker hydrothermal systems. Black smokers are higher temperature, hydrothermal venting fluids which predominantly contain dissolved metals, mostly iron. White smokers are commonly lower temperature hydrothermal venting fluids that contain dissolved silica, calcium and barium. However, both black and white smoker hydrothermal systems can occur at similar temperatures (Fuchida et al., 2013). Since black and white smoker hydrothermal systems discharge different elements, each system may have affected the geochemistry of the meta-iron formation differently.

Many geochemical studies have demonstrated that Eu^{2+} has a direct relationship with hydrothermal venting fluids. The oxidation state for all the rare earth elements (REE) is +3, while europium and cerium can also occur as Eu^{2+} and Ce^{4+}. This allows the behaviour of europium and cerium to be chemically different compared to the rest of the REEs. Europium's ability to exist in the Eu^{2+} or Eu^{3+} oxidation states is reliant on the redox conditions of the system (Peter, 2003). The redox conditions for europium are dependent on the temperature and acidity of the hydrothermal fluid, as well as fluid-rock interactions of the system (Douville et al., 1999; Peter, 2003).

Studies from modern day hydrothermal systems show that the REE chemistry of hydrothermal fluids strongly resembles the trace element geochemistry of plagioclase phenocrysts (Klinkhammer et al., 1994a; Douville et al., 1999). Plagioclase crystallization from a reducing magmatic fluid preferentially partitions europium into the crystal lattice due to europium's ability to substitute for calcium during igneous crystallization. The compatibility of Eu^{2+} in the plagioclase crystal lattice causes an enrichment of europium relative to the other REE. This geochemical signature is mimicked by the hydrothermal fluid when the fluid preferentially leaches plagioclase phenocrysts during

hydrothermal alteration at temperatures greater than 250°C (Peter, 2003). Europium along with the other REEs attach to chloride ligands within the hydrothermal fluid and form chloride complexes (Douville et al., 1999). The fluids containing these complexes are carried towards the surface and deposited on the ocean floor (Douville et al., 1999). The strength of the europium anomaly is reflected by the amount of Eu^{2+} leached out of plagioclase compared to the other trivalent REE during hydrothermal alteration. Therefore, a positive europium anomaly indicates that Eu^{2+} was derived from hydrothermal venting fluids at temperatures greater than 250°C.

The europium anomaly is calculated by the following equation:

$$\text{Equation [1]} \quad Eu/Eu^* = \frac{Eu_{PAAS}}{(\frac{2}{3}Sm_{PAAS} + \frac{1}{3}Tb_{PAAS})} \quad \text{(Bau and Dulski, 1996)}$$

where Eu/Eu* is the europium anomaly and Eu_{PAAS}, Sm_{PAAS} and Tb_{PAAS} are raw data values from the geochemical analysis divided by Post Archean Australian Shale (PAAS) normalization constants. Detailed explanation of the PAAS normalization procedure is summarized in section 4.12. Terbium is used in the europium anomaly calculation instead of the neighbouring element gadolinium because seawater can have slightly positive gadolinium anomalies (Bau and Dulski, 1996; Planavsky et al., 2010).

The europium anomaly calculated using Equation [1], was plotted against aluminum in Figure 4.6. BG and LSJ meta-iron formation samples form a negative correlation between the europium anomaly and aluminum at higher than one weight percent aluminum. However, at lower than one weight percent aluminum, the strength of the correlation is weaker and the points are more scattered. This correlation suggests that the amount of siliciclastic contamination dictates the strength of the europium anomaly for the shallow water meta-iron formation. Samples with greater than one weight percent aluminum had their europium anomaly dampened by the influx of REEs

from the siliciclastic phase. At lower than one weight percent aluminum, the siliciclastic derived

REEs have a smaller effect on these samples causing the meta-iron formations to preserve the

europium anomaly of their depositional environment.
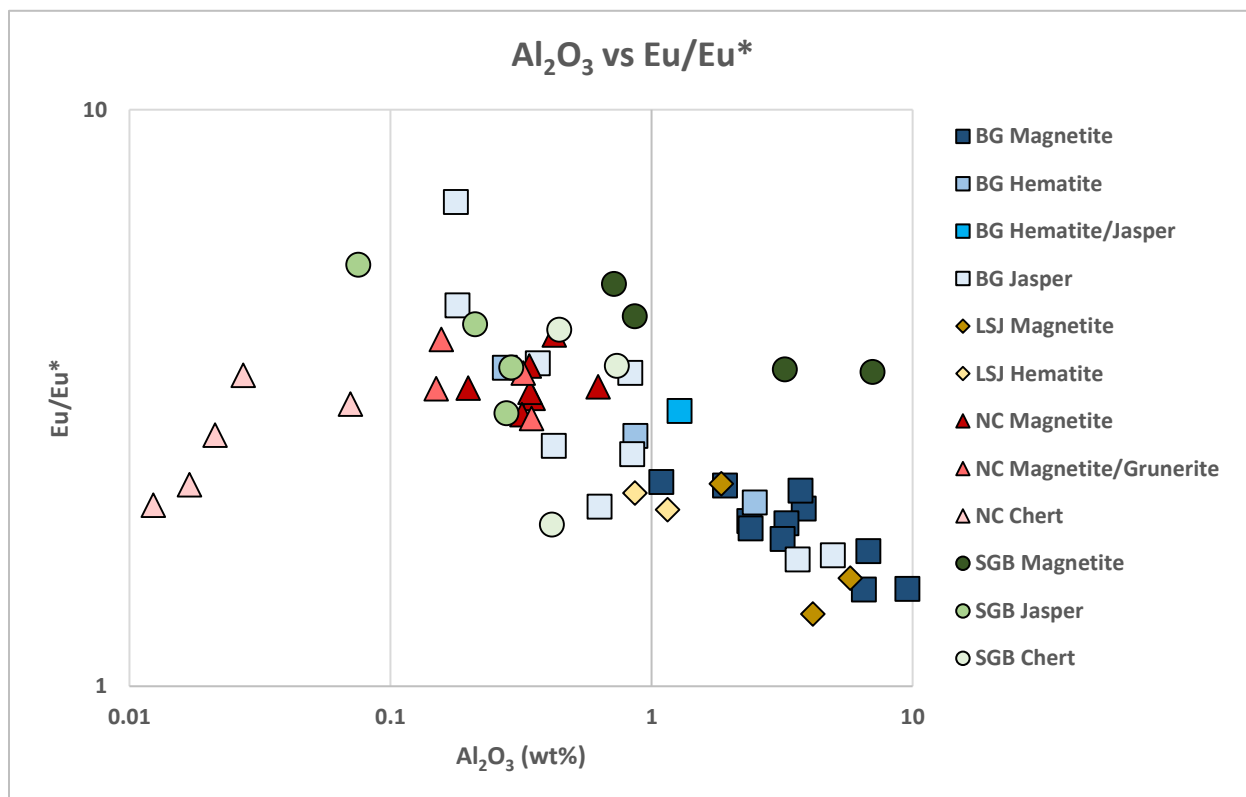
Figure 4.6: A logarithmic bivariate plot of aluminum versus the europium anomaly. The BG and LSJ meta-iron formation samples display a negative trending correlation. However, at lower degrees of siliciclastic contamination, the BG samples are more scattered. The NC and SGB meta-iron formation samples form a scattered horizontal correlation, suggesting that siliciclastic contamination had little to no influence on the strength of the europium anomaly for these samples. Therefore, hydrothermally derived Eu^{2+} was more concentrated in the deeper water setting relative to the shallow ocean.

SGB and NC meta-iron formation samples form a scattered horizontal correlation which does

not follow the trend established by the BG and LSJ meta-iron formation samples. At aluminum

values greater than one weight percent, the SGB magnetite samples plot at much higher europium

anomalies than the BG meta-iron formation samples. Since NC and SGB meta-iron formation

samples generally have higher values than the BG and LSJ samples, the deeper oceans were more

enriched in hydrothermally derived Eu^{2+} than shallow oceans. This also indicates that for the NC and

SGB samples, the strength of the europium anomaly is not dampened by siliciclastic contamination as the shallow water meta-iron formation samples.

All the meta-iron formation samples, except for NC chert, have prominent europium anomalies suggesting that europium was derived from hydrothermal venting fluids at temperatures exceeding 250°C. Most of the NC chert samples have smaller europium anomalies than the NC iron oxide-rich samples, even though the NC chert samples have much lower degrees of siliciclastic contamination. This suggests that hydrothermal venting fluids related to NC chert deposition were less able to leach europium from plagioclase during hydrothermal alteration because they were lower temperature venting fluids.

Since both iron oxide-dominated and silica-dominated samples have positive europium anomalies, most of the iron and silica should also be derived from hydrothermal fluids. To test if iron was derived from hydrothermal fluids, aluminum was plotted against total iron (Figure 4.7). Since aluminum was derived from the siliciclastic phase, total iron should form a negative relationship with aluminum. Interestingly, a parabolic correlation exists between the two elements. The meta-iron formation samples with greater than one weight percent aluminum, have a negative relationship between total iron and aluminum. This indicates that at higher degrees of siliciclastic contamination, total iron content decreases. This would suggest that most, if not all the iron was derived from hydrothermal venting fluids. Contrary to the previous statement, at lower than one weight percent aluminum, the correlation between total iron and aluminum is weakly positive, suggesting that iron was derived from the siliciclastic phase. However, this interpretation is illogical since at higher degrees of siliciclastic contamination the correlation between aluminum and total iron is strongly negative. If total iron was derived from the siliciclastic phase, the correlation between aluminum and total iron at greater than one weight percent aluminum should be strongly

positive. Therefore, another factor was responsible for the positive relationship between aluminum and total iron at lower than one weight percent aluminum.
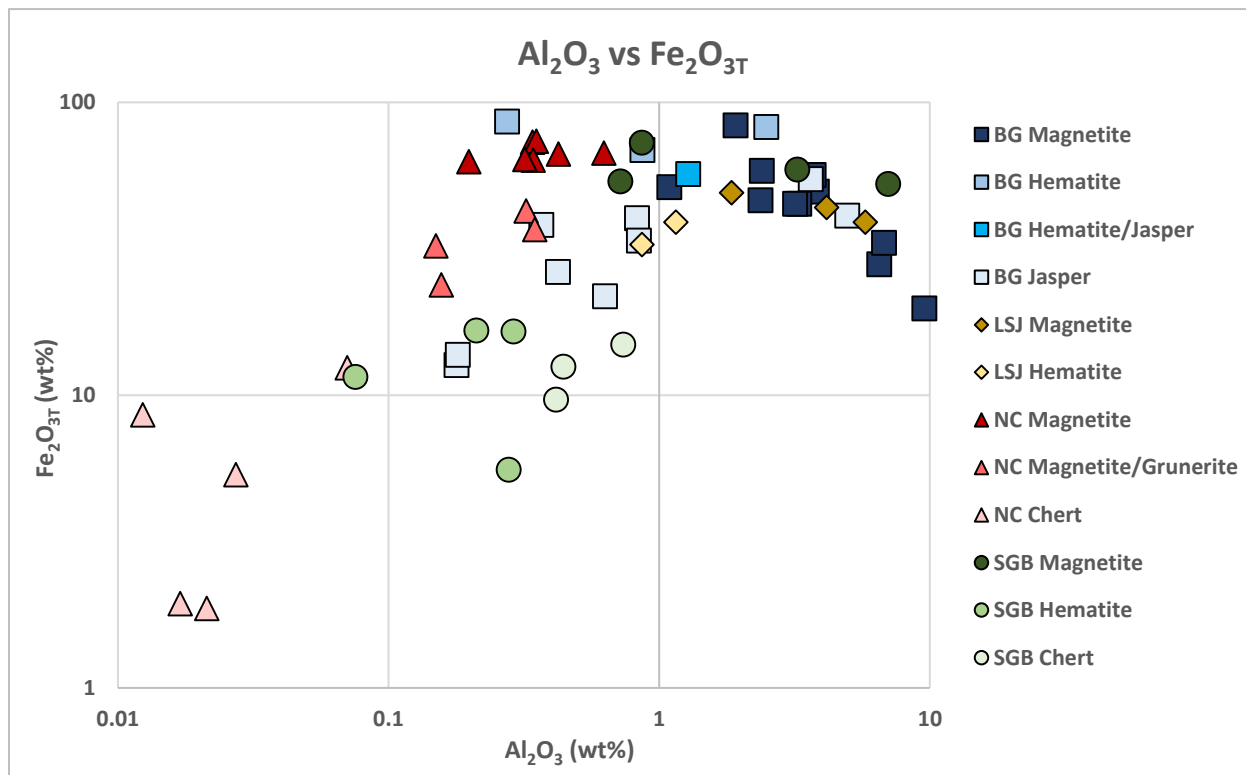
Figure 4.7: A logarithmic bivariate plot of aluminum versus total iron. At greater than one wt% aluminum, the correlation between total iron and aluminum is negative, indicating that iron was derived from the hydrothermal fluid phase. At less than one wt% aluminum, there is a positive correlation between aluminum and total iron. The positive correlation between iron and aluminum was caused by the constant sum problem between iron and silica. Therefore, most of the iron was derived from hydrothermal venting fluids.

Since geochemical data is expressed as percentages at around 100%, a constant sum problem occurs (Rollinson, 1992). When two variables are the dominant constituents in a system, ex. iron and silica in meta-iron formations, as one variable increases, the other variable must decrease (Rollinson, 1992). This causes a statistical negative bias and forces a correlation between two elements that may or may not have any relationship with each other (Rollinson, 1992).

The effects of the constant sum problem can be used to interpret the parabolic relationship between total iron and aluminum (Figure 4.7). Significantly in Figure 4.7, the data points below one weight percent aluminum are silica-dominated meta-iron formation samples. These samples have

high silica content, which causes them to have low concentrations of total iron. Since siliciclastic contamination is low for these samples and total iron is low due to the constant sum problem, a positive correlation occurs between iron and aluminum even though aluminum and total iron are not derived from the same sources. Therefore, below one weight percent aluminum the constant sum problem between silica and iron affects the total iron content more than siliciclastic contamination. For samples greater than one weight percent aluminum, siliciclastic contamination has a progressively stronger effect on the total iron content than silica, which causes the parabolic correlation seen in Figure 4.7.

In summary, total iron is inversely correlated with aluminum, indicating that most of the iron was derived from a non-siliciclastic source. Since all the iron oxide-dominated and silica-dominated samples from both the deep and shallow water meta-iron formations have positive europium anomalies, most of the iron and silica was derived from black and white smoker hydrothermal venting fluids, respectively rather than dissolved load associated with continental runoff.

4.4 Graphical Techniques

Since aluminum, titanium, niobium, uranium, thorium, and vanadium were deemed immobile during chemical weathering and post-depositional alteration, these elements can be used to analyze the behaviour of the mobile elements. Element ratios consisting of a mobile element over an immobile element can be plotted to observe the nature of the mobile element relative to the immobile element. Plotting these ratios will also subtract the effects of the siliciclastic detritus from the meta-iron formation samples, which can assist in the determination of provenance and element mobility during post-depositional processes. These ratios will prove to be essential for determining element provenance because most of the elements were derived from multiple sources. As it will be determined, a component was derived from the siliciclastic phase for almost all the elements. Any

siliciclastic endmember element can be used as the denominator for the element ratios and in this thesis, aluminum was chosen.

Figure 4.8 is a logarithmic bivariate plot of possible correlations that could exist based on the relationship between two elements and aluminum. Numerical values for all the samples are charted below in Table 4.6. If aluminum was correlative with both elements (Case 1, Figure 4.8), the data set would plot as a cluster. This indicates that all three elements behaved similarly, were most likely derived from the siliciclastic phase and remained chemically immobile. If aluminum was correlative with one element but not the other (Case 2 and 3, Figure 4.8), a vertical or horizontal linear trend occurs, depending on the axis position that the correlative element was assigned to. The element that formed this linear trend was chemically immobile like aluminum and most likely was derived from the siliciclastic phase. The other element either behaved differently during post-depositional alteration or was derived from another source. A positive linear correlation between two mobile elements (Case 4, Figure 4.8), indicates that once the siliciclastic contamination was removed (Al_2O_3), both elements were derived from the same source and behave similarly during post-depositional alteration. Lastly, if both elements were not derived from the same source, not related to the siliciclastic phase and behaved differently during post-depositional alteration (Case 5, Figure 4.8), then the data set will be scattered.

Significantly, by normalizing the elements over aluminum and plotting them against each other, the data points were translated relative to the degree of siliciclastic contamination. Higher amounts of siliciclastic material (higher Al_2O_3 content) and lower concentrations of the mobile element drag the points closer to zero. Lower amounts of siliciclastic contamination (lower Al_2O_3 content) and higher concentrations of the mobile elements drag the points towards infinity. Significantly, this

method subtracts the effects of siliciclastic contamination without forcing a positive linear

correlation between the two elements (ex. Case 5, Figure 4.8).

Table 4.6: Numerical values and colours used for points in Figure 4.8. Each case forms a different trend on the logarithmic bivariate plot in Figure 4.8.

Al_2O_3	E1	E2	$E1/Al_2O_3$	$E2/Al_2O_3$	Al_2O_3	E1	E2	$E1/Al_2O_3$	$E2/Al_2O_3$
				Element/Aluminum Table					
Case 1: E1=E2=Al					Case 2: E1=Al≠E2				
1	0.51	0.2	0.51	0.2	1	0.4	4	0.4	4
2	0.96	0.41	0.48	0.205	2	0.8	18	0.4	9
3	1.52	0.62	0.506667	0.206667	3	1.2	1	0.4	0.333333
4	2.1	0.79	0.525	0.1975	4	1.6	2.6	0.4	0.65
5	2.49	0.97	0.498	0.194	5	2	14	0.4	2.8
6	3.2	1.19	0.533333	0.198333	6	2.4	14	0.4	2.333333
Case 3: E1≠Al=E2					Case 4: E1=E2≠Al				
1	3.3	0.5	3.3	0.5	1	80	20	80	20
2	3	1	1.5	0.5	2	40	10	20	5
3	7	1.5	2.333333	0.5	3	120	30	40	10
4	8	2	2	0.5	4	20	5	5	1.25
5	4.5	2.5	0.9	0.5	5	60	15	12	3
6	5	3	0.833333	0.5	6	100	25	16.66667	4.166667
Case 5 and 6: E1≠E2≠Al									
1	4300	4	4300	4					
2	980	27	490	13.5					
3	11000	5	3666.667	1.666667					
4	659	55	164.75	13.75					
5	4300	34	860	6.8					
6	980	34	163.3333	5.666667					
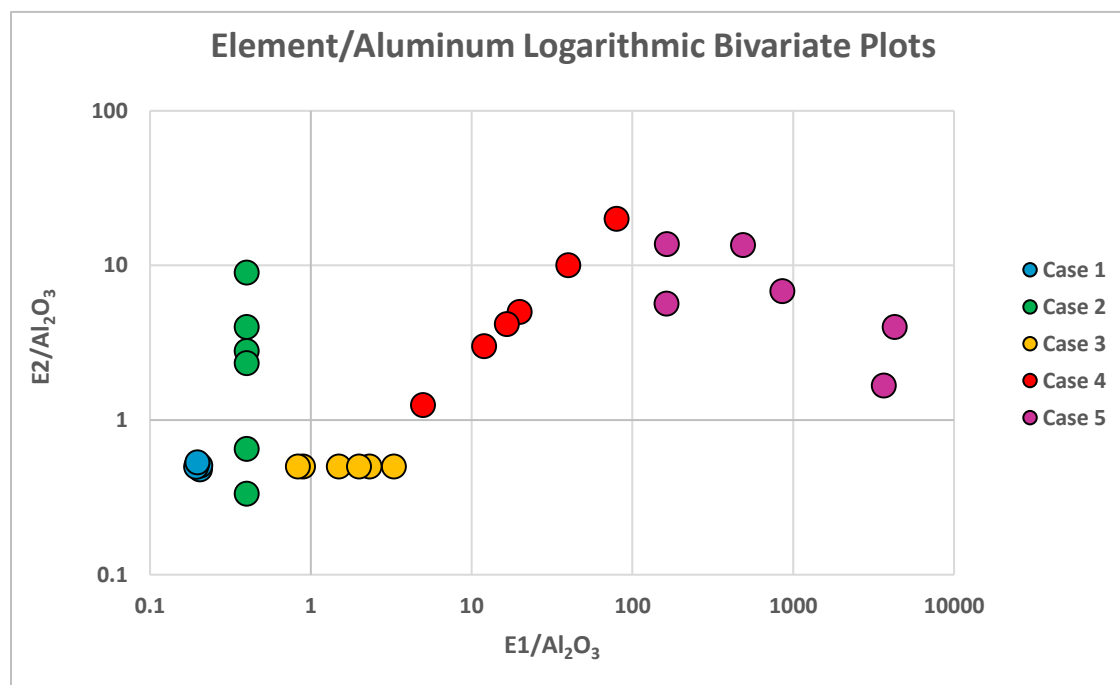
Figure 4.8: A logarithmic bivariate plot of the possible cases for the relationship between two elements and aluminum. Colours correspond to different cases and numerical values from Table 4.6. Normalizing over aluminum subtracts the effects of siliciclastic contamination without forcing positive linear correlations. This normalization can be used to determine the effect of siliciclastic contamination.

Bivariate plots can also be used to observe the effects of diagenesis. During meta-iron formation diagenesis, iron oxyhydroxides transform into magnetite or hematite, depending on the amount of organic carbon deposited. The chemical formula for magnetite is $(Fe^{3+})_2 (Fe^{2+}) O_4$, while the formula for hematite is $(Fe^{3+})_2O_3$. The main difference between magnetite and hematite is that some iron in magnetite occurs in the +2 state, while in hematite it does not. The ratio between Fe_2O_3/FeO can be used to isolate hematite-, magnetite-, magnetite/grunerite-, jasper- and chert-dominated samples. A higher ratio indicates that the meta-iron formation is more hematite-dominated, while ratios around two indicate the meta-iron formation is more magnetite-dominated. Ratios lower than one indicate that Fe^{2+}-bearing silicates dominate the meta-iron formation. Both magnetite- and hematite-dominated layers were deposited as iron oxyhydroxides. Therefore, any partitioning of elements between the magnetite- or hematite-dominated samples must have occurred during diagenesis.

Since all the meta-iron formation samples in this study have a siliciclastic component, the geochemistry of associated siliciclastic lithologies were compared with the geochemistry of the meta-iron formation. This determined the provenance, especially if the elements were derived from multiple sources, and observed the differences element mobility during post-depositional alteration. First, it is important to establish which siliciclastic lithology has the closest composition to the siliciclastic component of the meta-iron formation. Published geochemical data of siliciclastic units from the BG and NC were used to determine the composition of the siliciclastic component of the meta-iron formation.

The metasandstone lithologies in the BG were derived from the calc-alkaline volcanic suites of the Onaman-Tashota terrain that were intermediate to felsic in composition (Fralick and Kronberg, 1997). Since the BG meta-iron formation samples are interbedded with the metagreywacke units,

the metagreywacke rocks are interpreted to be the siliciclastic component of the BG meta-iron

formation. When plotted on a Na_2O/Al_2O_3 versus K_2O/Al_2O_3 diagram (Figure 4.9), the geochemical

data of metagreywacke samples from Fralick and Barrett (1991) plot as a cluster indicating that

potassium and sodium remained chemically immobile during post-depositional alteration.

Therefore, the metagreywacke samples from Fralick and Barrett (1991), were plotted with meta-iron

formation samples to determine if the elements in the BG meta-iron formation were derived from

the siliciclastic phase and their behaviour during post-depositional alteration.
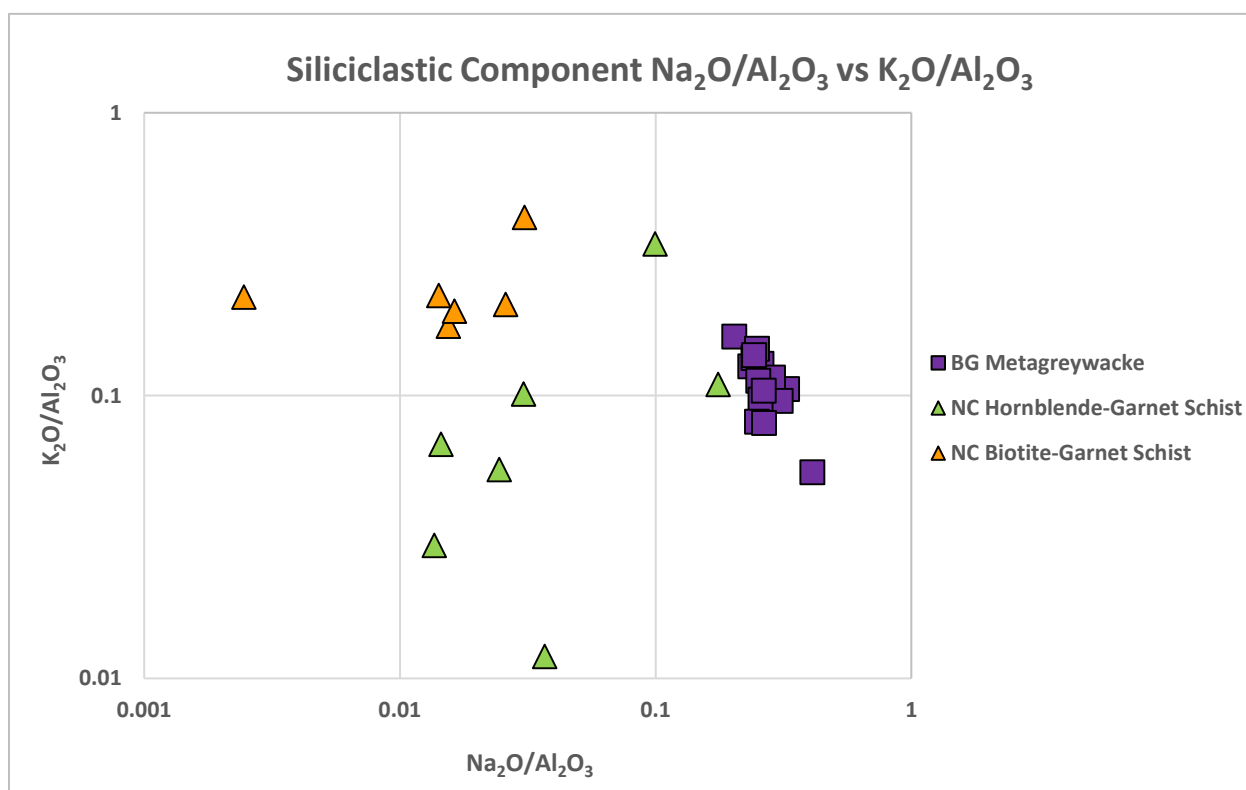
Figure 4.9: A logarithmic bivariate plot of Na_2O/Al_2O_3 versus K_2O/Al_2O_3 of the siliciclastic units deposited with the meta-iron formations from BG and NC. The clustering of the BG metagreywacke samples indicates that potassium and sodium remained immobile during post-depositional alteration. The scattered nature of the NC hornblende-garnet schist samples indicates that potassium and sodium were highly mobile during post-depositional alteration. Although the biotite-garnet schist samples do not cluster like the BG metagreywacke samples, they cluster more than the hornblende-garnet schist samples. This indicates that the NC biotite-garnet schist samples are a better representation of the siliciclastic phase before post-depositional alteration than the NC hornblende-garnet schist. Geochemical data for the BG metagreywacke samples are from Fralick and Barrett (1991) and geochemical data for the NC hornblende-garnet schist and NC biotite-garnet schist samples are from Moran (2008).

In the NC, Moran (2008) identified the hornblende-garnet schist as the siliciclastic component of

the NIF due to its intercalated nature with the silicate-dominated BIF, as well as the similar

geochemical characteristic with the silicate-dominated BIF. The biotite-garnet schist is the thickest

siliciclastic-dominated sedimentary unit stratigraphically above the hornblende-garnet schist and is

interpreted to be metamorphosed ferruginous shales (Moran, 2008). When plotting the

geochemical data from Moran (2008) of the hornblende-garnet schist and biotite-garnet schist on a

Na_2O/Al_2O_3 vs K_2O/Al_2O_3 plot, the hornblende-garnet schist samples plot as a scattered linear array

while the biotite-garnet schist samples cluster at relatively consistent Na_2O/Al_2O_3 and K_2O/Al_2O_3

values (Figure 4.9). The scattered linear array for the hornblende-garnet schist samples indicates

that potassium and sodium were chemically mobile during post-depositional alteration, while in the

biotite-garnet schist, they were relatively more immobile. The geochemistry of the immobile

elements in the hornblende-garnet schist and biotite-garnet schist are quite similar suggesting that

both lithologies were most likely derived from the same source. Moran (2008) suggested that the

higher potassium values for the biotite-garnet schist relative to the hornblende-garnet schist

indicated a felsic to intermediate siliciclastic source. On the Winchester and Floyd (1977) diagrams in

Moran (2008, Fig 15.3), both lithologies plot in the andesite/basalt and subalkaline basalt field. Since

it was established that potassium was mobile in the hornblende-garnet schist, it is assumed that the

primary depositional potassium values in the hornblende garnet schist before post-depositional

alteration were similar to the biotite-garnet schist. Therefore, the hornblende-garnet and biotite-

garnet schist were derived from the same source rock and the biotite-garnet schist is a better

representation of the siliciclastic component of for the NC meta-iron formations due to the evidence

of lower degrees of element mobility during post-depositional alteration.

Most of the elements analysed using geochemical techniques were plotted against each other

and placed into groups based on similar chemical properties and geochemical behaviour. These

eight groups include: 1) group 1 elements: Na, K, Rb and Cs; 2) group 2 elements: Ca, Mg and Sr; 3)

group 4 elements: Zr and Hf; 4) group 3, 5 and 6 elements: Sc, V and Cr; 5) group 5, 7 and 8

elements: Mo, Mn and Fe; 6) group 10, 11 and 12 elements: Ni, Cu and Zn; 7) group 15 elements: P

and 8) group 3 and lanthanoids: Y and REEs.

4.5 Group 1 Elements, Alkali Metals: Na, K, Rb and Cs

Group 1 elements whose data was obtained from the geochemical analysis include sodium,

potassium, rubidium and cesium. Figure 4.10 displays a very strong, positive linear correlation

between K_2O and Rb for the BG, LSJ and SGB samples. The NC samples also plot as a strong,

positively trending linear correlation. However, the K/Rb ratio is slightly higher than the other meta-

iron formation samples. The strong linear relationship between Rb and K_2O indicates that rubidium

and potassium behaved similarly during deposition and post-depositional alteration. It also indicates

that the K/Rb ratio remained isochemical during deposition and post-depositional alteration.
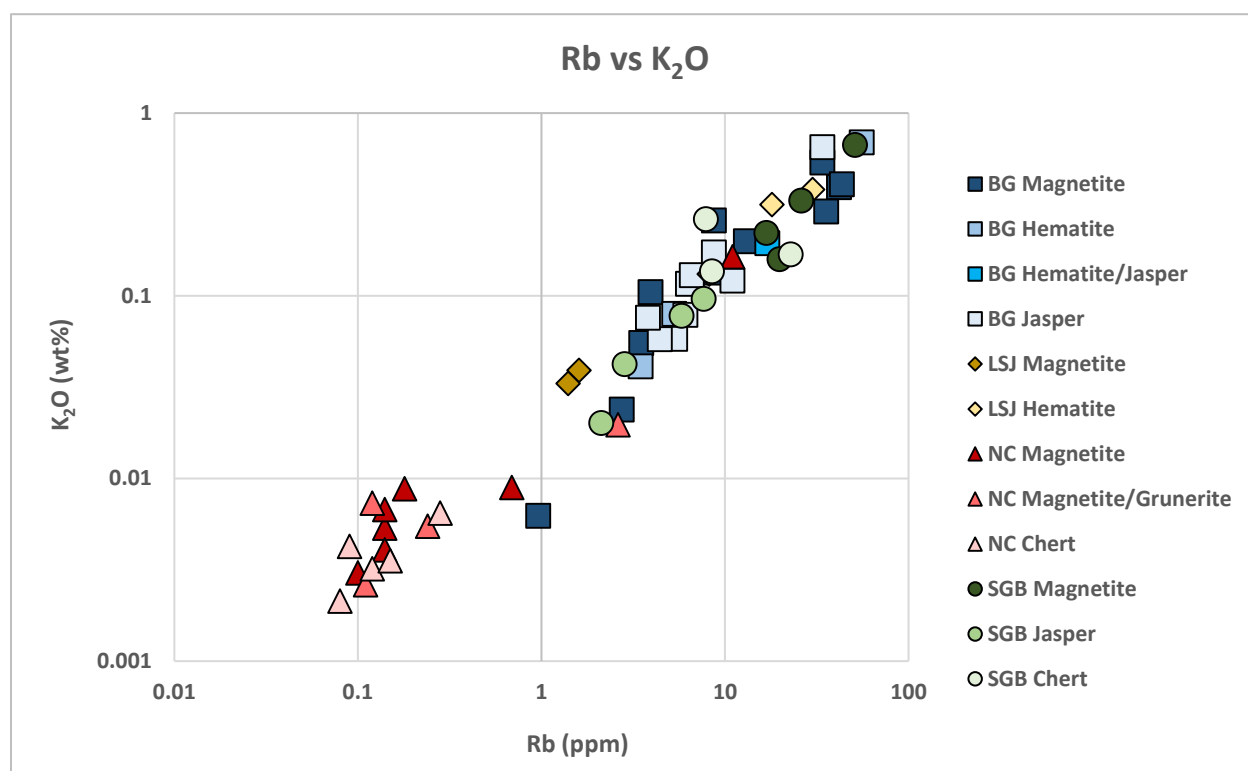
Figure 4.10: A logarithmic bivariate plot of rubidium vs potassium. The strong, positive, linear correlation between potassium and rubidium indicates that both these elements behaved similarly during deposition and post-depositional alteration. The slight deviation of the NC meta-iron formation samples compared to the BG, LSJ and SGB samples suggests that the K/Rb ratio was higher in the NC relative to the other study locations.

Rubidium and potassium were normalized over aluminum to investigate the relationship between the meta-iron formations and the siliciclastic phase (Figure 4.11). Clusters occur for some of the NC chert, LSJ hematite, NC magnetite, BG hematite and BG jasper samples. At first glace, all the SGB samples cluster together. However, when looking at the sample categories individually (magnetite-, jasper- and chert-dominated samples), the SGB magnetite and SGB chert samples form scattered linear trends. The clustering of the NC chert and NC magnetite samples suggests that potassium and rubidium were derived from the siliciclastic phase and remained immobile. However, if potassium and rubidium were derived from the siliciclastic phase and remained immobile during post-depositional alteration, both phase-dominated laminae would plot at similar Rb/Al_2O_3 and K_2O/Al_2O_3 ratios instead of two separate clusters (Figure 4.11).
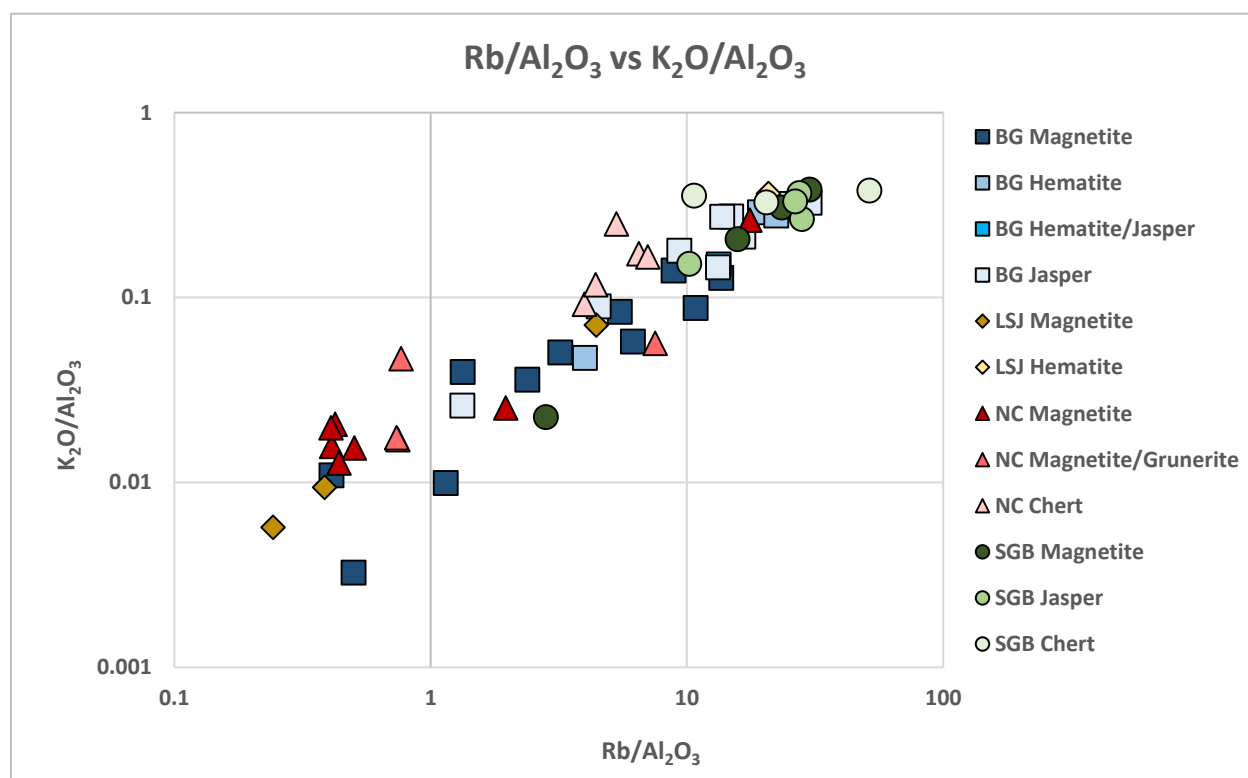
Figure 4.11: A logarithmic bivariate plot of Rb/Al_2O_3 versus K_2O/Al_2O_3. The variability in the correlation between the sample categories and the fact that the NC chert and NC magnetite clusters plot separately indicate that potassium and rubidium were mobile during post-depositional alteration. The lack of clustering for the meta-iron formation samples also suggests that potassium and rubidium were either derived from the siliciclastic phase and were mobile or there was an influx of both elements from a non-siliciclastic source.

The reasoning behind the separate clustering of the NC magnetite and NC chert samples is explained using Figure 4.12, a Rb/Al$_2$O$_3$ versus K$_2$O/Al$_2$O$_3$ graph of the NC meta-iron formation samples plotted with geochemical data of the biotite-garnet schist. The NC biotite-garnet schist plot as scattered points at higher Rb/Al$_2$O$_3$ and K$_2$O/Al$_2$O$_3$ ratios relative to the meta-iron formation samples. The NC chert samples plot close to the NC biotite-garnet schist, while the NC magnetite and NC magnetite/grunerite samples plot at much lower Rb/Al$_2$O$_3$ and K$_2$O/Al$_2$O$_3$ values. Significantly, the K/Rb ratio for the NC meta-iron formation samples is similar to the NC biotite-garnet schist, suggesting that most, if not all the potassium and rubidium was derived from the siliciclastic phase. The lower Rb/Al$_2$O$_3$ and K$_2$O/Al$_2$O$_3$ values for the NC magnetite and NC magnetite/grunerite indicate that there was a loss of rubidium and potassium in the meta-iron formation samples during post-depositional alteration. However, the siliciclastic derived K/Rb ratio remained relatively similar.
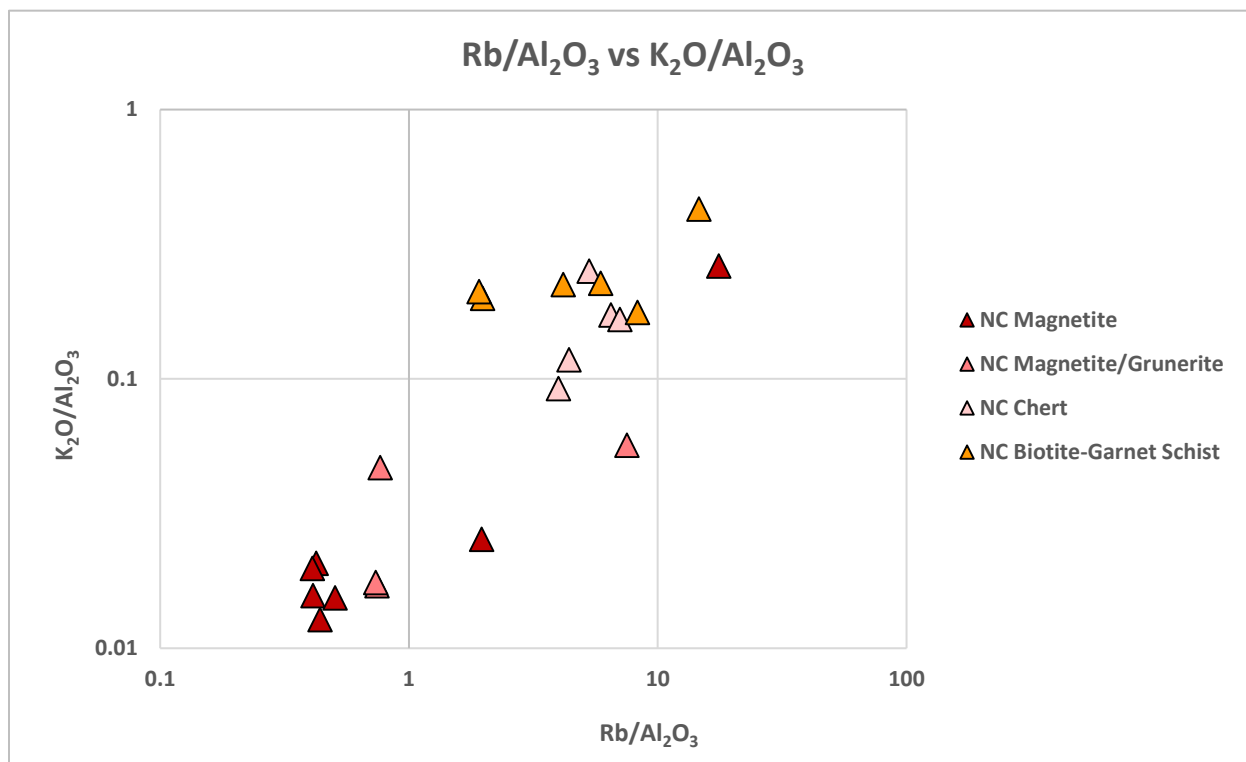
Figure 4.12: A logarithmic bivariate plot of Rb/Al$_2$O$_3$ versus K$_2$O/Al$_2$O$_3$ of the meta-iron formation and biotite-garnet schist samples from NC. The meta-iron formation samples are depleted in rubidium and potassium relative to NC biotite-garnet schist, indicating a loss of potassium and rubidium during post-depositional alteration. Potassium and rubidium in the NC meta-iron formation were derived from the siliciclastic phase.

A non-siliciclastic influx of potassium and rubidium during deposition for the BG meta-iron

formation samples is evident in Figure 4.13, a Rb/Al_2O_3 versus K_2O/Al_2O_3 graph of the meta-iron

formation samples from the BG plotted with the BG metagreywacke. Most of the BG hematite and

BG jasper samples have higher K_2O/Al_2O_3 and Rb/Al_2O_3 values than the BG metagreywacke,

indicating an enrichment of potassium and rubidium relative to the siliciclastic phase. The BG

magnetite samples plot at similar K_2O/Al_2O_3 values compared to the BG metagreywacke. Also, all the

meta-iron formation samples have lower K/Rb ratios compared to the BG metagreywacke. To get an

enrichment of potassium and rubidium in the BG jasper and BG hematite layers, while decreasing

the K/Rb ratio in all the BG meta-iron formation samples, there must have been an external influx of

potassium and rubidium from a non-siliciclastic source that had lower K/Rb ratios than the

siliciclastic phase during deposition. For example, if the K/Rb ratio of the non-siliciclastic phase was

two, while the siliciclastic derived K/Rb ratio was ten, the K/Rb ratio recorded in the meta-iron

formation would reflect the proportion derived from the non-siliciclastic versus the siliciclastic

phase. This would cause the data points to form a scattered correlation based on the proportion

between the siliciclastic and non-siliciclastic sourced potassium and rubidium. This might account for

the very slight deviations between the K/Rb ratios of the BG meta-iron formation samples.

Therefore, potassium and rubidium in the BG were sourced from multiple sources, the siliciclastic

phase and a non-siliciclastic source with a lower K/Rb values than the siliciclastic phase. This lower

K/Rb value and the proportion between the siliciclastic phase and non-siliciclastic phase derived

potassium and rubidium must have been uniform because there are only minor deviations in the

K/Rb ratio for the BG meta-iron formations. Since there was an external influx of potassium and

rubidium for the BG meta-iron formation samples, the lower K_2O/Al_2O_3 and Rb/Al_2O_3 values for the

BG magnetite samples relative to the BG jasper and BG hematite was caused by a preferential loss of

potassium and rubidium in the BG magnetite during post-depositional alteration.
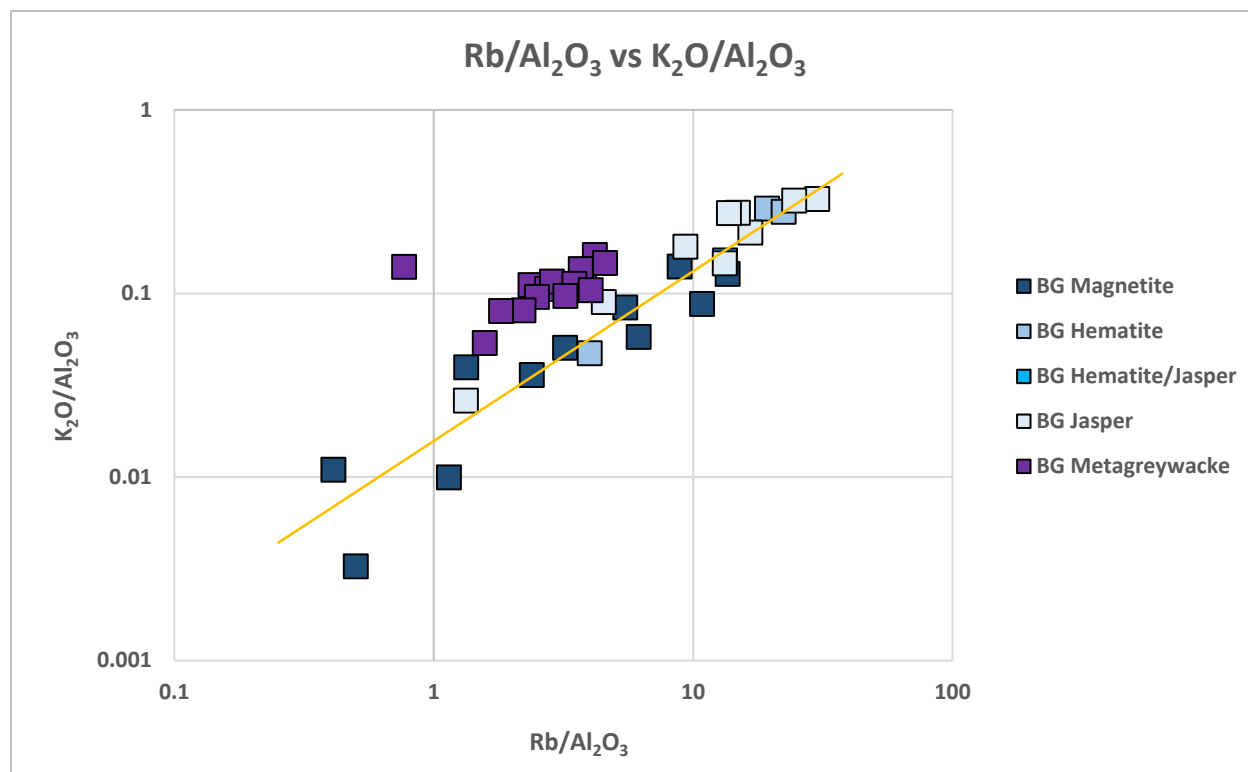
Figure 4.13: A logarithmic bivariate plot of Rb/Al_2O_3 versus K_2O/Al_2O_3 for the BG meta-iron formation samples and associated siliciclastic lithology. The BG meta-iron formation samples plot as a positive linear correlation at lower K/Rb than the BG metagreywacke samples. Since there is an enrichment of potassium and rubidium in the BG jasper and BG hematite relative to the BG metagreywacke, an influx of potassium and rubidium from a non-siliciclastic source occurred during deposition. BG magnetite has similar K/Rb ratios and lower Rb/Al_2O_3 and K_2O/Al_2O_3 values compared to the rest of the meta-iron formation samples suggesting that in the BG magnetite layers there was a loss of rubidium and potassium during post-depositional alteration.

The preservation of an external influx of potassium and rubidium in the BG samples and lack of potassium and rubidium enrichment in the NC samples, suggests that the shallow oceans were more enriched in potassium and rubidium relative to the deeper oceans. Since the BG meta-iron formations were deposited in the shallow water setting closer to land and farther away from hydrothermal venting fluids than the NC meta-iron formation samples, the influx of potassium and rubidium to the shallow oceans was derived from continental runoff.

On the cesium versus rubidium plot (Figure 4.14), meta-iron formation samples from BG, LSJ and SGB display a moderately strong, positive correlation between cesium and rubidium. This indicates that for these locations, cesium and rubidium behaved chemically similar during erosion, deposition

and post-depositional alteration. Interestingly, the samples from NC all cluster away from the main

correlation trends at high cesium and low rubidium values, indicating that cesium and rubidium did

not behave chemically similar in the NC. Moran (2008) suggested that there might have been an

alkali-element (Cs and Rb) metasomatic enrichment associated with gold mineralization. However,

Moran (2008) determined that there were no correlations between cesium and rubidium for both

the exhalative and siliciclastic lithologies. Since it was determined that rubidium in the NC meta-iron

formations was derived from the siliciclastic phase, the late stage alkali-element metasomatic

enrichment was mostly cesium. Therefore, the lack of correlation between cesium and rubidium in

the NC meta-iron formation samples was caused by an enrichment of cesium during hydrothermal

metasomatism after deposition.
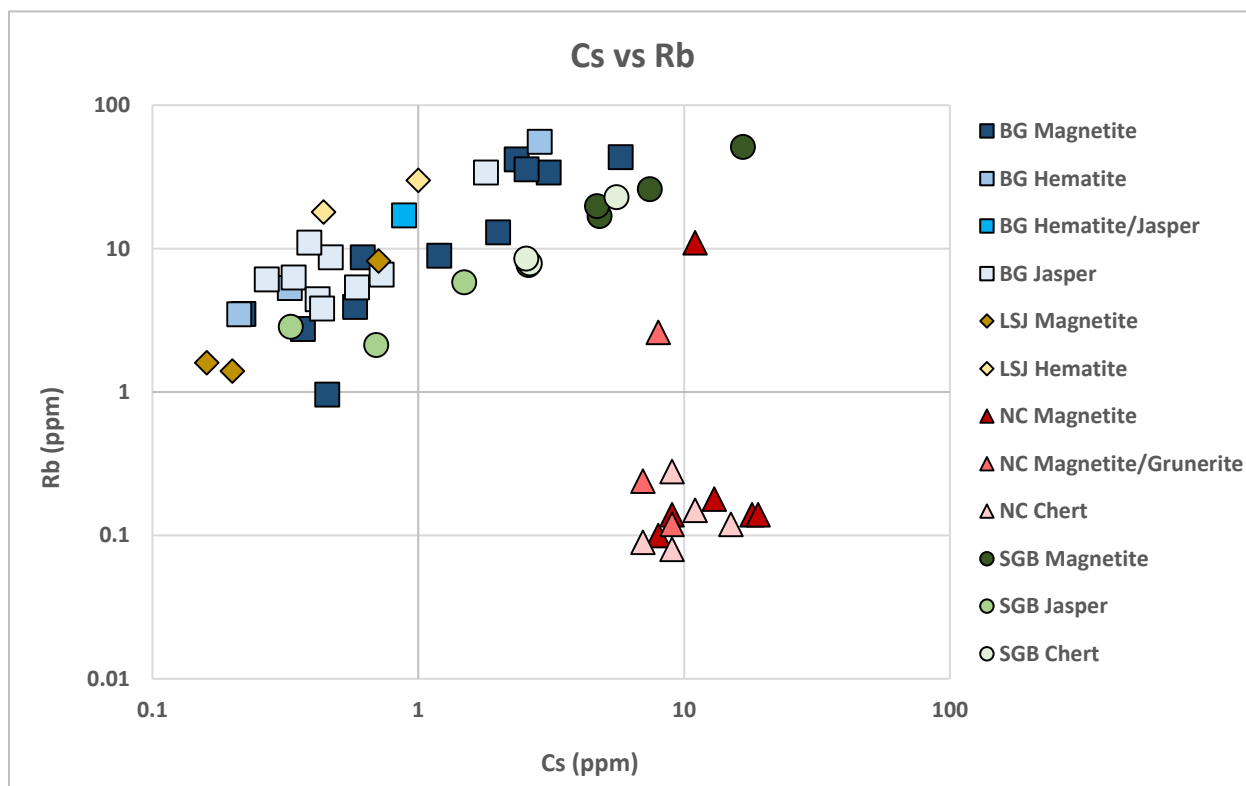
Figure 4.14: A logarithmic bivariate plot of cesium versus rubidium. The BG, LSJ and SGB samples show a moderately strong, positively trending correlation, while most the NC samples cluster at high cesium and low rubidium. This indicates that like rubidium and cesium in the LSJ, BG and SGB behaved similarly during post-depositional alteration. In the NC, there was an enrichment of cesium associated with hydrothermal metasomatism during post-depositional alteration.

As expected, when plotting aluminum against cesium, no definitive correlation exists (Figure 4.15). This indicates that most of the cesium was derived from a non-siliciclastic source for all the meta-iron formation samples. When the iron ratio was plotted against cesium, two clusters occurred (Figure 4.16). Overall, higher cesium values are associated with deeper water meta-iron formations (NC and SGB), while lower cesium values are associated with shallow water meta-iron formations (BG and LSJ). However, there are a few BG magnetite-dominated samples that plot higher with the deeper water meta-iron formations. Significantly, this indicates that for the SGB and possibly the NC meta-iron formation samples, cesium was enriched in the deeper water relative to the shallow water environment. The source of cesium in the deeper water were hydrothermal venting fluids.
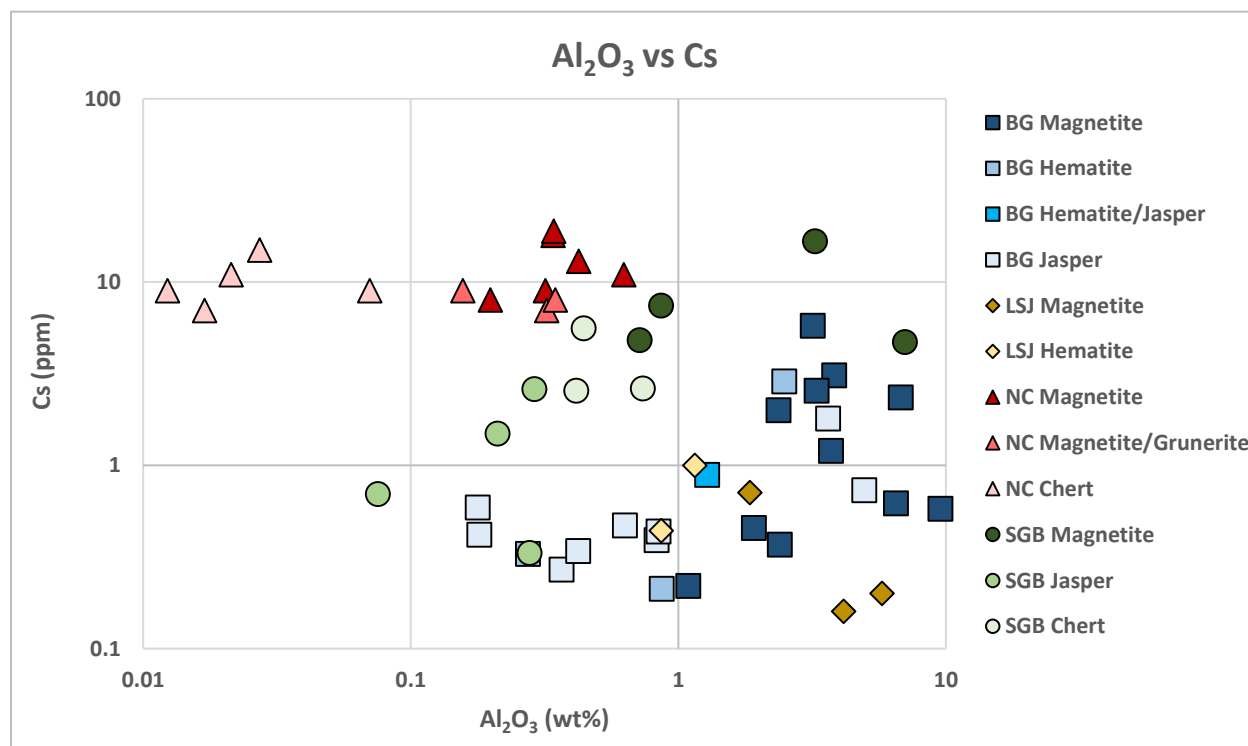
Figure 4.15: A logarithmic bivariate plot of aluminum vs cesium. The data set is scattered without a definite positive correlation. Therefore, most of the cesium is believed to be derived from a non-siliciclastic source.
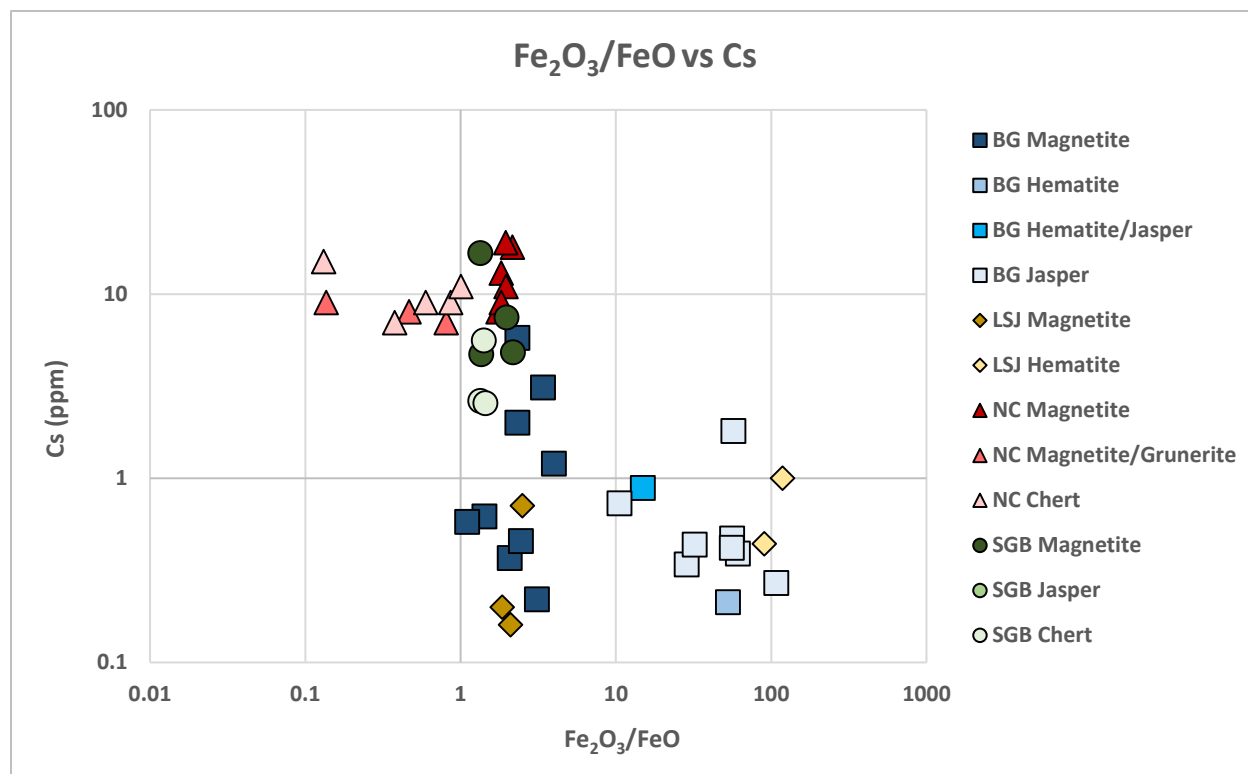
Figure 4.16: A logarithmic plot of the iron ratio vs cesium. Significantly, the SGB meta-iron formation samples plot at higher cesium values compared to the BG and LSJ samples. Therefore, the deeper oceans were more enriched in cesium relative to the shallow water. This also indicates that cesium for the BG, LSJ and SGB was mostly derived from hydrothermal venting fluids.

Interestingly, in Figure 4.14, the Cs/Rb ratio increases towards the deeper water meta-iron formations. Since it was determined that rubidium and potassium were enriched in the shallow water setting and cesium was enriched in the deeper water setting, the progressively higher Cs/Rb and Cs/K ratios recorded in the meta-iron formation samples towards the deeper water setting, possibly reflect ancient Archean seawater compositions. During the precipitation of iron oxyhydroxides, cesium, rubidium and potassium were adsorbed onto the iron oxyhydroxides and amorphous silica, recording the Cs/Rb and Cs/K distribution coefficient of the ancient seawater at their depth of precipitation. This interpretation assumes that the K/Rb ratio for the siliciclastic detritus from the BG, LSJ and SGB were relatively the same. The Cs/Rb and Cs/K distribution coefficient of seawater was not preserved in the NC meta-iron formation samples because they were affected by a metasomatic cesium enrichment during post-deposition alteration.

Sodium was plotted against aluminum to determine the relationship with the siliciclastic phase (Figure 4.17). A strong, positive, linear relationship occurs for BG magnetite, LSJ magnetite, NC magnetite, NC magnetite/grunerite and one SGB magnetite sample at similar Na/Al ratios. This suggests that sodium for these samples was derived from the siliciclastic phase and remained immobile during post-depositional alteration. However, the rest of the samples plot as scattered data sets at lower Na/Al ratios. Since the magnetite-dominated samples from most of the study locations show sodium derived from the siliciclastic phase, sodium in the chert-, jasper- and hematite-dominated samples from all the sample locations was also derived from the siliciclastic phase but was mobilized during post-depositional alteration.
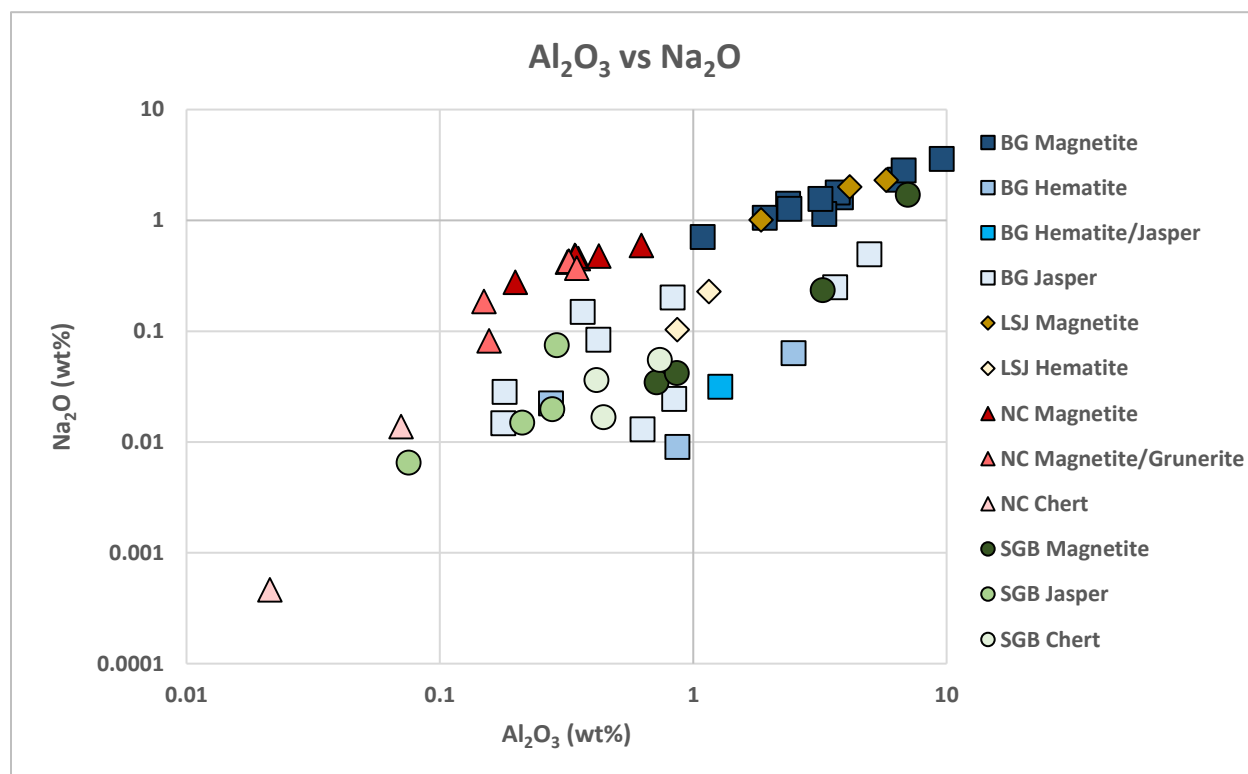
Figure 4.17: A logarithmic bivariate plot of sodium versus aluminum. The magnetite- and magnetite/grunerite-dominated samples from NC, LSJ and BG plot as a strongly, positive linear correlation between sodium and aluminum, suggesting that sodium for these samples was derived from the siliciclastic phase and remained immobile during post-depositional alteration. The chert-, jasper- and hematite-dominated samples plot as scattered correlations, suggesting that sodium for these samples was mobile during post-depositional alteration.

When sodium was plotted against potassium, two linear trends formed (Figure 4.18). Trend 1 contains magnetite- and magnetite/grunerite-dominated samples from BG, LSJ and NC, while trend 2 contains hematite-, jasper-, and chert-dominated samples from all locations. Trend 2 also includes three magnetite-dominated samples from SGB. When Na_2O and K_2O were normalized over Al_2O_3, trends 1 and 2 were further segregated into group 1 and group 2, respectively (Figure 4.19). Group 1 samples have constant Na_2O/Al_2O_3 values with varying K_2O/Al_2O_3 values. The K_2O/Al_2O_3 values for the group 2 samples are reasonably consistent, with most of the values greater than the group 1 samples. Also, most of the Na_2O/Al_2O_3 values are lower in the group 2 samples compared to the group 1 samples (Figure 4.19). These graphs indicate that the phase-dominated samples behaved differently during post-depositional alteration.
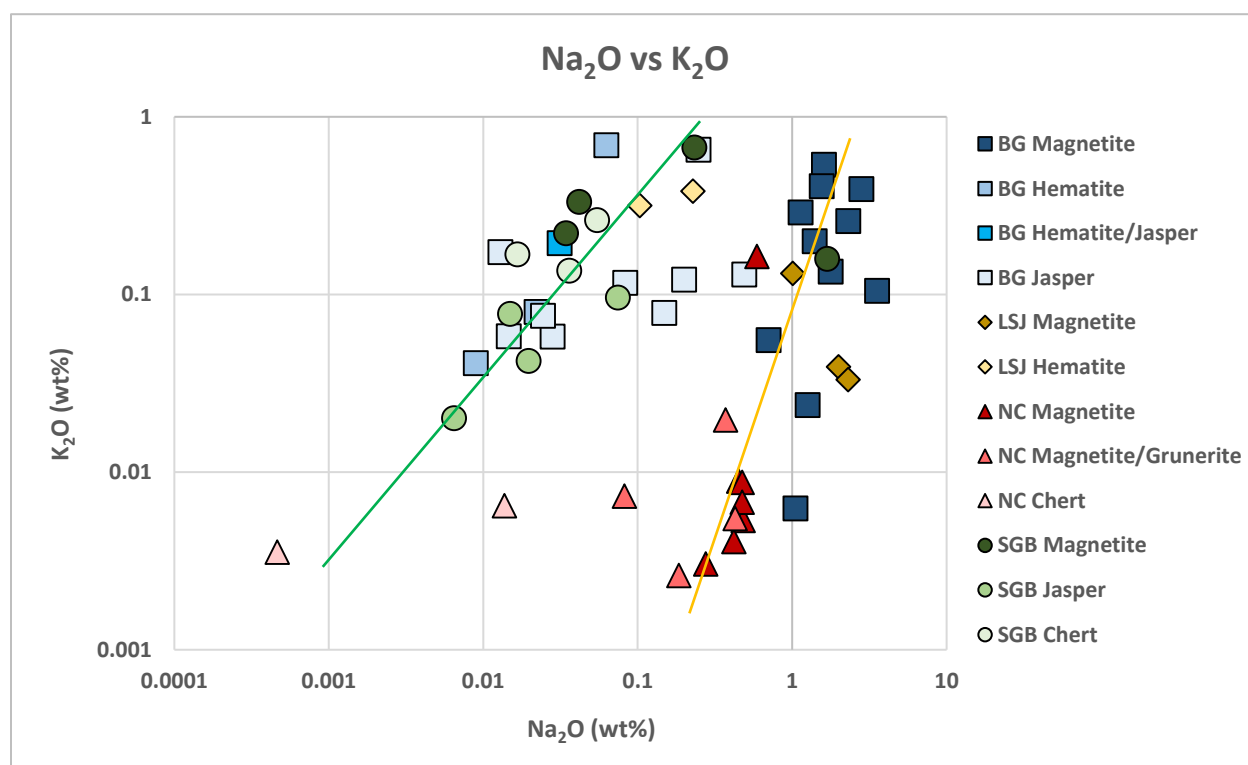
Figure 4.18: A logarithmic bivariate plot between sodium and potassium. Trend 1 is denoted by the yellow line, while trend 2 is denoted by the green line. The BG magnetite, LSJ magnetite, NC magnetite/grunerite and NC magnetite have higher sodium values than the rest of the meta-iron formation samples. This indicates that the magnetite-dominated samples behaved differently than the hematite-, jasper- and chert-dominated samples during post-depositional alteration.
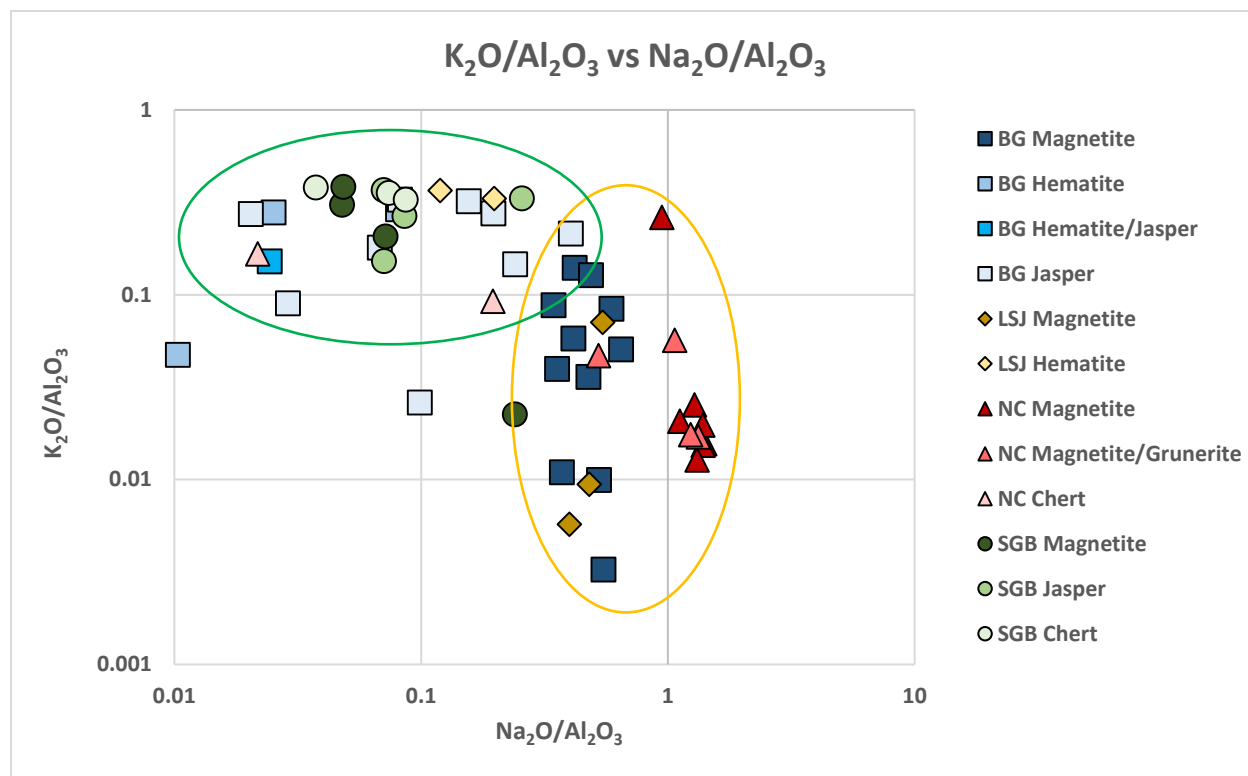
Figure 4.19: A logarithmic bivariate plot between sodium and potassium normalized over aluminum. Group 1 samples are denoted by a yellow oval, while the green oval represents the group 2 samples. This indicates that the magnetite-dominated samples behaved differently than the hematite-, jasper- and chert-dominated samples during post-depositional alteration.

Figure 4.20 is a Na_2O/Al_2O_3 versus K_2O/Al_2O_3 graph of the meta-iron formation samples from BG plotted with the metagreywacke geochemical data from the surrounding area. Compared to the siliciclastics, most of the jasper- and hematite-dominated meta-iron formation samples have higher K_2O/Al_2O_3, while the Na_2O/Al_2O_3 values are mostly much lower. The opposite trend is seen with the magnetite-dominated samples, which have slightly higher Na_2O/Al_2O_3 values and similar to lower K_2O/Al_2O_3 values.

The absence of sodium and potassium partitioning in the BG metagreywacke samples (Figure 4.20), indicates that in the BG metagreywacke, the siliciclastic detritus had a consistent Na/K ratio during deposition and the Na/K ratio remained isochemical during post-depositional alteration. Since hematite- and magnetite-dominated bands are deposited under the same physiochemical parameters, the Na/K ratio for the BG hematite and BG magnetite should record the same Na/K

ratios, which are a reflection of the siliciclastic component in the meta-iron formation. Therefore, the differences in the Na/K ratio between the BG jasper and BG hematite compared to the BG magnetite must have occurred during post-depositional alteration.
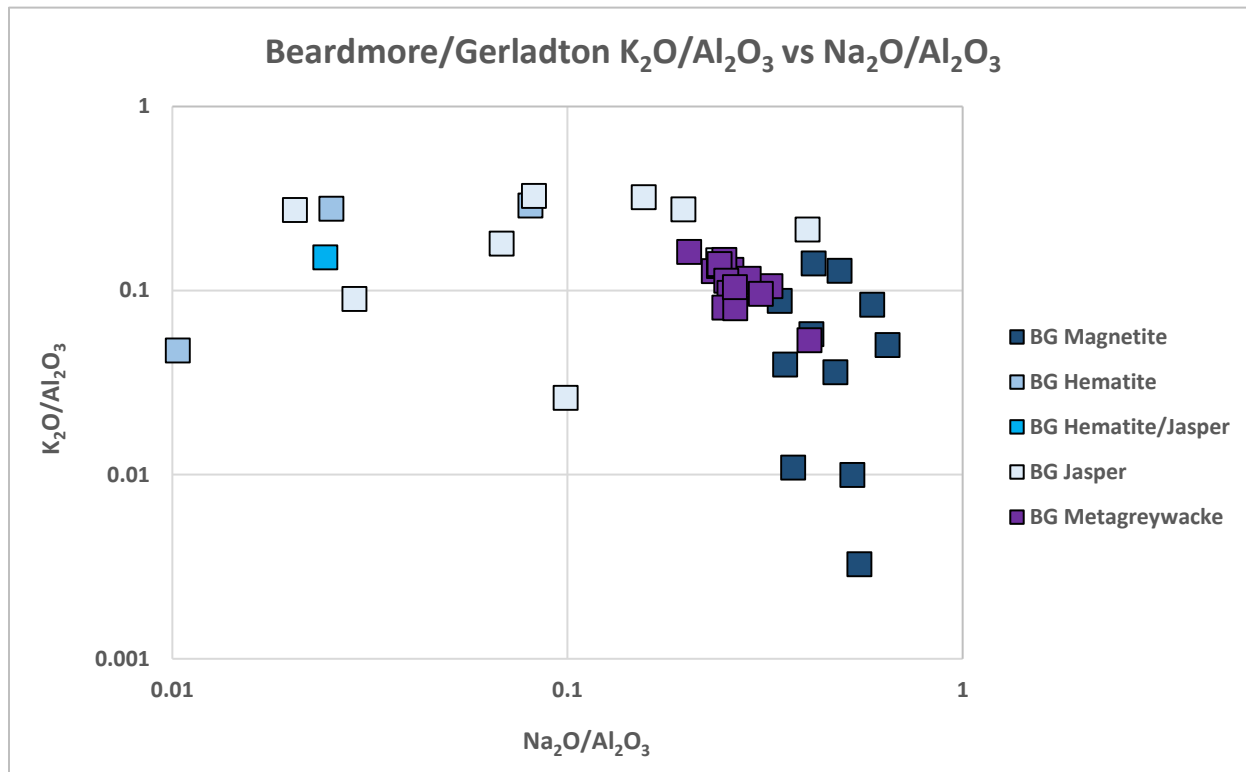
Figure 4.20: A logarithmic bivariate plot between sodium and potassium normalized over aluminum for the BG meta-iron formation samples and associated siliciclastic lithologies. The BG magnetite samples are enriched in sodium compared to the BG metagreywacke, while the BG jasper and BG hematite samples are depleted compared to the BG metagreywacke. The BG jasper and BG hematite are mostly enriched in potassium compared to the BG metagreywacke, while the BG magnetite samples are depleted compared to the BG metagreywacke. The sodium enrichment in the BG magnetite samples was caused by either an influx of sodium during deposition or albitization. As determined earlier, the increase of potassium in the BG hematite and BG jasper samples was probably caused by an influx from seawater during deposition.

Figure 4.21 is a Na_2O/Al_2O_3 versus K_2O/Al_2O_3 graph of the meta-iron formation samples from the NC plotted with the NC biotite-garnet schist samples. The NC chert samples have similar to lower Na_2O/Al_2O_3 values and slightly lower K_2O/Al_2O_3 values compared to the siliciclastics, while the NC magnetite and NC magnetite/grunerite samples have higher Na_2O/Al_2O_3 values and mostly lower K_2O/Al_2O_3 values compared to the siliciclastics.
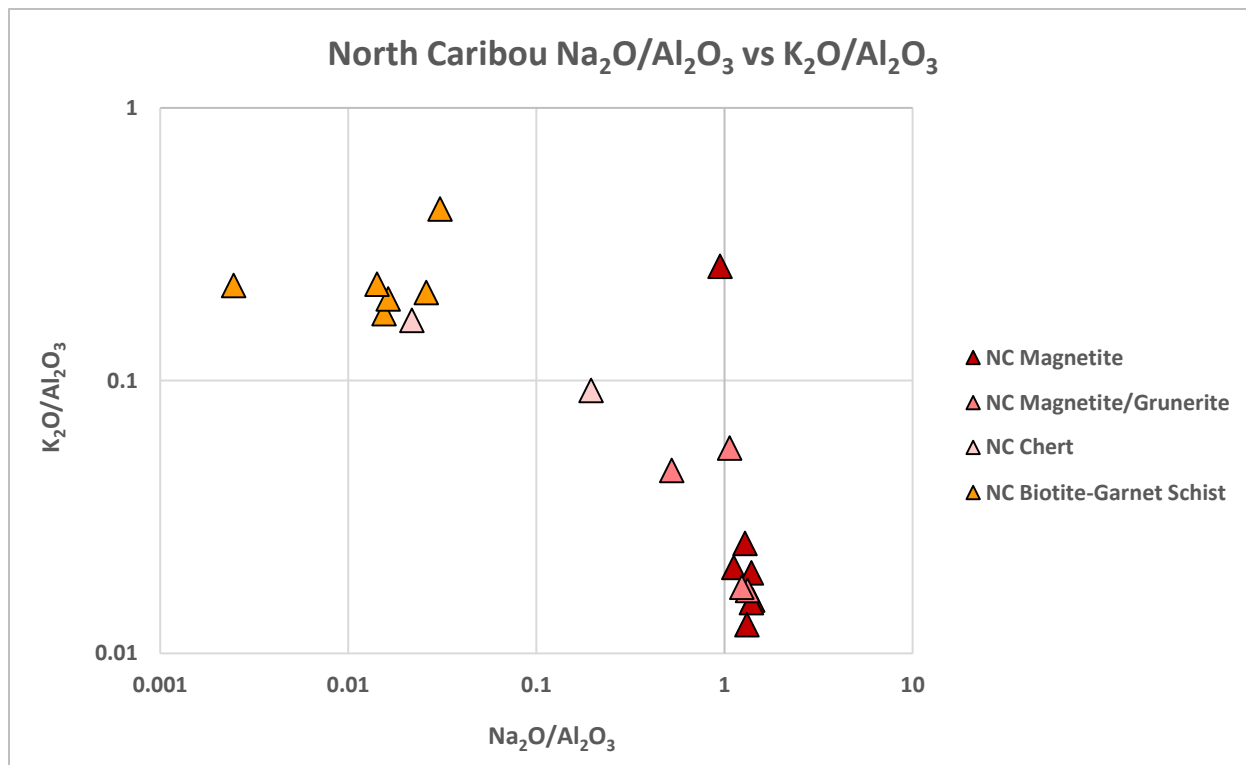
Figure 4.21: A logarithmic bivariate plot of Na_2O/Al_2O_3 versus K_2O/Al_2O_3 of the samples from NC. NC chert samples have similar sodium values as the siliciclastics indicating that the sodium enrichment was derived from a non-siliciclastic source during deposition.

Significantly, both the magnetite-dominated samples from the BG and NC indicate an influx of sodium relative to the siliciclastic phase. However, the strong linear relationship between sodium and aluminum for the BG magnetite-dominated samples in Figure 4.17 and the close Na/K ratios between the BG magnetite and BG metagreywacke samples in Figure 4.20 suggests that most of the sodium in the BG was derived from the siliciclastic phase. The NC magnetite- and magnetite/grunerite-dominated samples also have a strong linear relationship between sodium and aluminum in Figure 4.17, indicating that most of the sodium was derived from the siliciclastic phase. However, the Na/Al ratio for the NC magnetite- and magnetite/grunerite-dominated samples is much larger than the NC biotite-garnet schist in Figure 4.22. This indicates that the sodium enrichment in the NC was significantly greater than in the BG.

The post-depsitional mechanism responsible for the loss of sodium and retention of potassium in the hematite-, jasper- and chert- dominated layers should be different from the retension of sodium and loss of potassium in the magnetite- and magnetite/grunerite-dominated layers. Since the magnetite-, hematite-, jasper- and chert-dominated bands were collected proximal to one another at each study location, regional metamorphism and hydrothermal metasomatism would have affected each phase-dominated layer to the same degree. During diagenesis, dehydration reactions occurred to form hematite-, jasper and chert-dominated bands. Magnetite-dominated bands were formed by the reduction of iron due to the presence of organic carbon which caused dehydration and decarbonization reactions to occur. Therefore, diagenesis was responsible for partitioning sodium in the magnetite- and magnetite/grunerite-dominated samples. It is hypothesized that chemical products released after the formation of magnetite during diagenesis preferrentially retained sodium in the siliciclastic phase, while chemical products produced after the dehydration reaction forming hematite-, jasper- and chert-dominated layers preferrentially mobilized sodium. Although the geochemical data suggests that these processes are occuring, the actual nature of these reactions are unknown.

In the petrographic analysis, the partitioning of sodium and potassium can clearly be observed. Albite, which is the dominant sodium-bearing phase in the LSJ and BG samples is found in the magnetite-dominated samples as inclusions in the magnetite crystals (BG) or as crystals interbedded with magnetite (LSJ). In the hematite and quartz-dominated meta-iron formation samples, albite is completely absent and no other major sodium-bearing phase is present. Significantly, the associated siliciclastic lithologies of the BG and LSJ contain albite. Geochemically, the NC samples preserve the same trends as the BG and LSJ meta-iron formations, suggesting that the same diagnetic processes ocurring in the BG and LSJ, occurred in the NC. In the SGB, there are no traces of albite in either the magnetite-, jasper- or chert-dominated layers. Since this meta-iron formation is deposited between

hypabyssal mafic igneous rocks, the source siliciclastic component of the SGB meta-iron formation is unknown. If the siliciclastic component of the SGB meta-iron formation was plagioclase-poor, albite would not be preserved in the magnetite-dominated samples. However, if the siliciclastic component did contain albite, then sodium was mobilized during post-depositional alteration in all the phase-dominated layers of the SGB meta-iron formation including SGB magnetite. Since the partitioning of sodium is occuring in the other meta-iron formations, it is believed that the lack of sodium-bearing feldspars in the siliciclastic phase is the more viable theory.

The partitioning of potassium is not as evident in petrography as sodium. In the LSJ, the hematite-quartz dominated meta-iron formation contains K-feldspar and muscovite as their dominant potassium-bearing phase, while the magnetite-dominated layers contain biotite and muscovite. The LSJ siliciclastic phase contains K-feldspar, muscovite and biotite. The presence of K-feldspar in the hematite-dominated layers and silciclastic lithologies and lack of K-feldspar in the magnetite-dominated samples suggests potassium mobility in the magnetite-dominated samples during diagenesis. However, the Eagle Island assemblage was subjected to greenschist facies metamorphism at the biotite zone, where chlorite and K-feldspar, with muscovite and quartz in excess, react to form biotite and muscovite. Therefore, the lack of K-feldspar should be refelcted by the enrichement of muscovite and biotite. The magnetite-dominated layers contain significant amounts of chlorite and minor amounts of biotite and muscovite. This suggests that K-feldspar and muscovite were not abundant enough in the magnetite-dominated layers to form biotite crystals during regional metamorphism. Therefore, potassium loss occurred before greenschist facies metamorphism, most likely during diagenesis. The BG meta-iron formations were also subjected to greenschist facies metamorphism and also show an abundance of chlorite and minor amounts of major potassium-bearing minerals in the magnetite-domianted layers, suggesting the same potassium-partitioning processes occurred in the BG meta-iron formations. The NC meta-iron

formation samples also preserve a K/Al depletion relative to the siliciclastic phase, suggesting the same potassium partitioning processes that operated in the LSJ and BG occured in NC. In SGB, there is no obvious partitioning of potassium between the magnetite-dominated layers and the jasper- and chert-dominated layers. However, stilpnomelane is the only major potassium-bearing phase, in the meta-iron formation and contains minor amounts of sodium in the crystal structure. Significantly, the SGB meta-iron formation samples contain quartz, actinolite, epidote and chlorite, which other than albite, is the stable mineral assemblage of the chlorite-actinolite-plagioclase granofels. Therefore, this suggests that the more mafic variety of the meta-pyroclastics may be the siliciclastic component of the SGB meta-iron formations. Since the feldspars deposited as large porphyroclasts in the meta-pyroclastic rock, the rest of the pyroclastic material was more mafic in composition, causing an absence of albite in the SGB meta-iron formation. This conclusion can account for the lack of sodium partitioning in the SGB meta-iron formation.

In summary, potassium and rubidium in the BG, LSJ and SGB were derived from dissolved load caused by continental runoff and the siliciclastic phase. Also, the Rb/K ratio remained isochemical during deposition and post-depositional alteration. Most of the potassium and rubidium in the NC was derived from the siliciclastic phase. Minor amounts of cesium might have been derived from the siliciclastic phase. However, in the BG LSJ and SGB most of the cesium was derived from hydrothermal venting fluids and adsorbed onto iron oxyhydroxides. A significant portion of cesium in the NC was derived from a late stage cesium hydrothermal metasomatism. Although, some cesium was sourced from seawater derived from hydrothermal venting fluids. Overall, deeper waters were enriched in cesium relative to rubidium and potassium, while the shallow water is enriched with potassium and rubidium relative to cesium. This indicates that there was a possible seawater gradient between the potassium- and rubidium-enriched, cesium-depleted shallow waters to the potassium- and rubidium-depleted, cesium enriched deeper waters. If the Rb/K ratio for the

siliciclastic in the BG, LSJ and SGB was the same, then the Cs/Rb and Cs/K was preserved, suggesting that the partitioning distribution coefficient of seawater was recorded by the meta-iron formation during the adsorption onto iron-oxyhydroxides and deposition and the ratios were preserved during post-depositional alteration. For the LSJ, NC and BG samples, diagenetic modification as responsible for partitioning sodium into the magnetite- and magnetite/grunerite dominated layers relative to the loss of sodium in the chert-, jasper- and hematite-dominated layers. Also, for the LSJ, NC and BG samples, diagenesis was responsible for partitioning-potassium into the hematite-, jasper- and chert-dominated layers relative to the loss of potassium in the magnetite- and magnetite/grunerite layers. The source of sodium will be discussed in Chapter 4.6

4.6 Group 2 Elements, Alkali Earth Metals: Ca, Mg and Sr

The group 2 elements whose data were obtained from the geochemical analysis include calcium, magnesium and strontium. Overall, when Sr was plotted against Al_2O_3, the points formed a positive linear correlation (Figure 4.22), suggesting that most strontium may have been derived from the siliciclastic phase. However, when looking at the sample categories individually, all the SGB samples, LSJ hematite, LSJ magnetite and BG jasper plot as nearly horizontal correlation curves. The variability in the correlations between strontium and aluminum indicates that a component of strontium in some samples was either mobile during post-depositional alteration or in part derived from a secondary non-siliciclastic source during deposition.

When calcium was plotted against aluminum, the data sets separated into two distinct regions (Figure 4.23). Region 1 contains samples from BG and LSJ, which display a positive linear correlation that extends towards the origin. This suggests that calcium was derived from the siliciclastic phase and remained immobile during post-depositional alteration. Overall the region 2 samples from NC
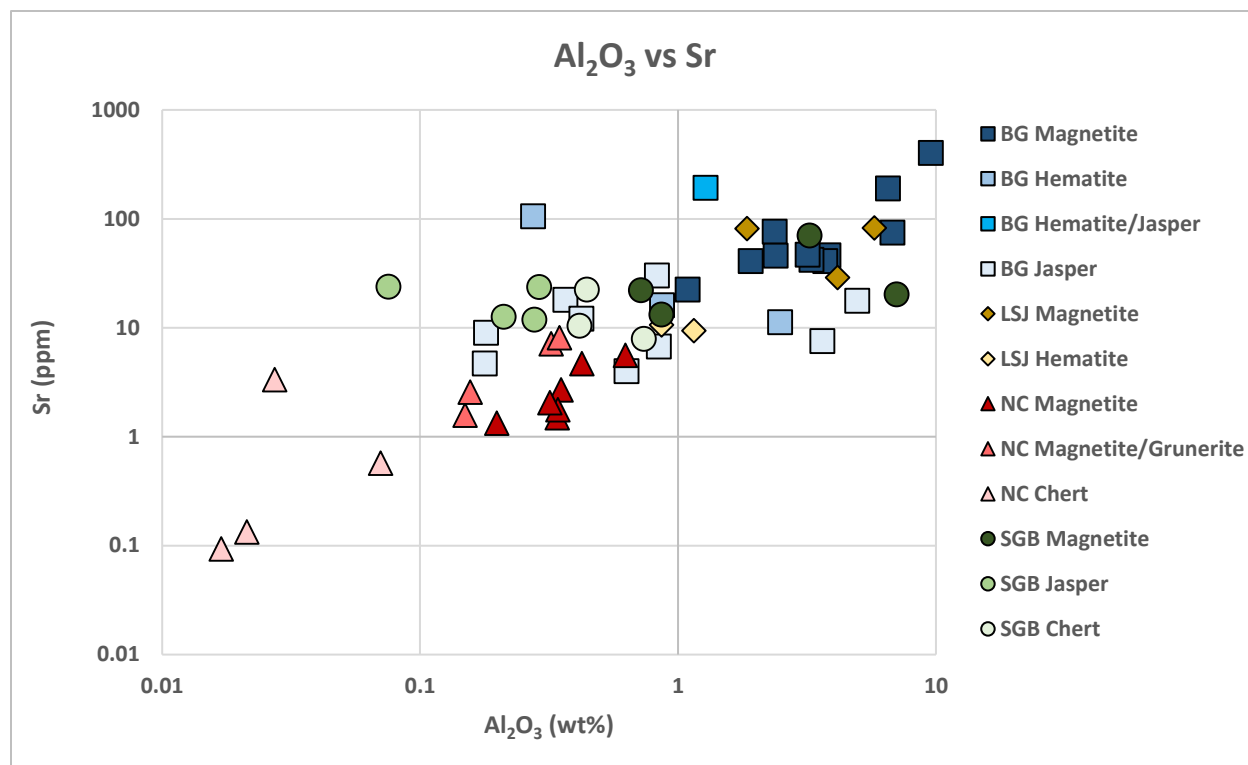
Figure 4.22: A logarithmic bivariate plot of aluminum versus strontium. The overall positively sloping correlation suggests that most of the strontium was derived from the siliciclastic phase.
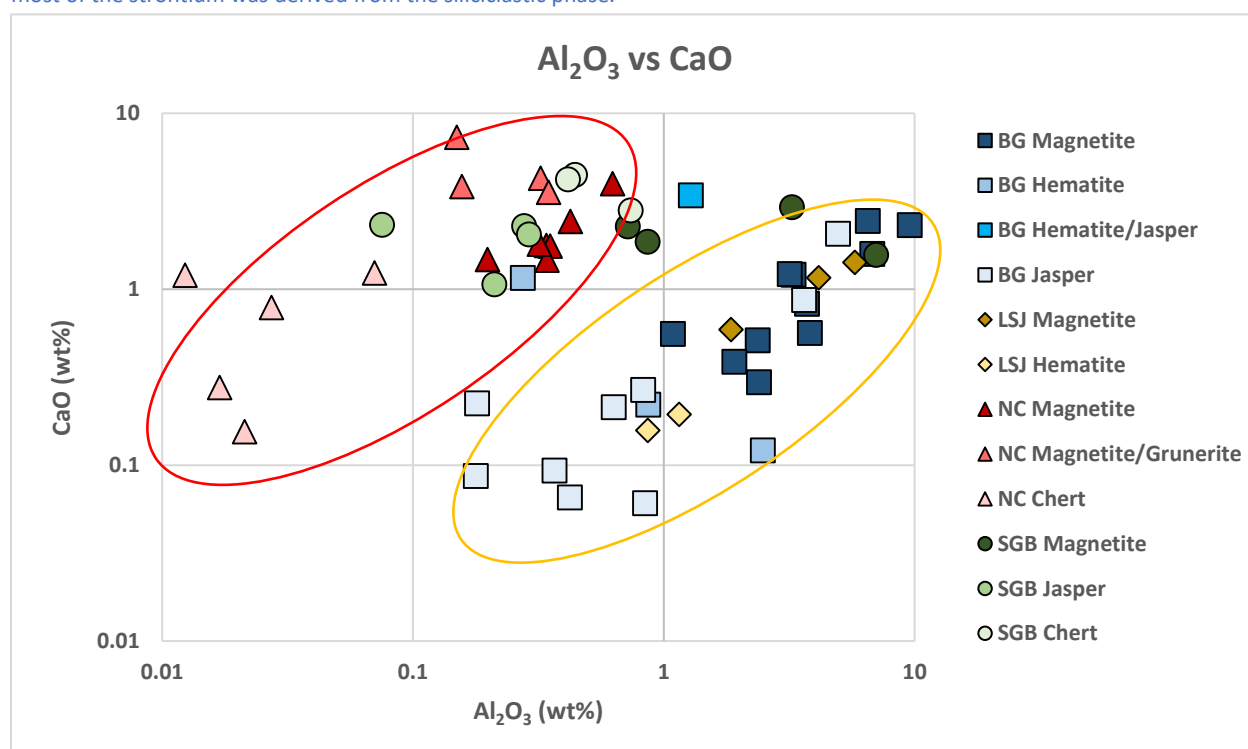
Figure 4.23: A logarithmic bivariate plot of aluminum plotted against calcium. The data sets are divided into two regions: region 1 (yellow) contains samples from the BG and LSJ, while region 2 (red) contains samples from NC and SGB. Calcium from region 1 was derived from the siliciclastic phase and immobile during post-depositional alteration, while calcium from region 2 was either derived from siliciclastic detritus with higher Ca/Al ratios, mobile during post-depositional alteration or in part, derived from a non-siliciclastic source during deposition.

and SGB display an overall scattered, positive linear trend, at higher Ca/Al ratios. This suggests that calcium was either mobile during post-depositional alteration or an influx of calcium from a non-siliciclastic source during deposition. However, the correlation trend for the NC magnetite samples extends close to the origin, suggesting that the higher Ca/Al ratio compared to the region 1 samples might have been inherited from source rocks with higher Ca/Al ratios.

To determine if the higher Ca/Al ratios for the NC magnetite samples were inherited from the siliciclastic phase or from a secondary non-siliciclastic source, the NC meta-iron formation samples were plotted on an aluminum versus calcium plot with the NC biotite-garnet schist (Figure 4.24). The biotite-garnet schists plot at similar calcium values as the NC magnetite samples, but since there is more aluminum in the siliciclastics, the Ca/Al ratio for the NC magnetite samples is higher than the ratio for the siliciclastics. Since aluminum was deemed chemically immobile, the higher calcium values for the meta-iron formation samples was caused by an influx of calcium from a non-
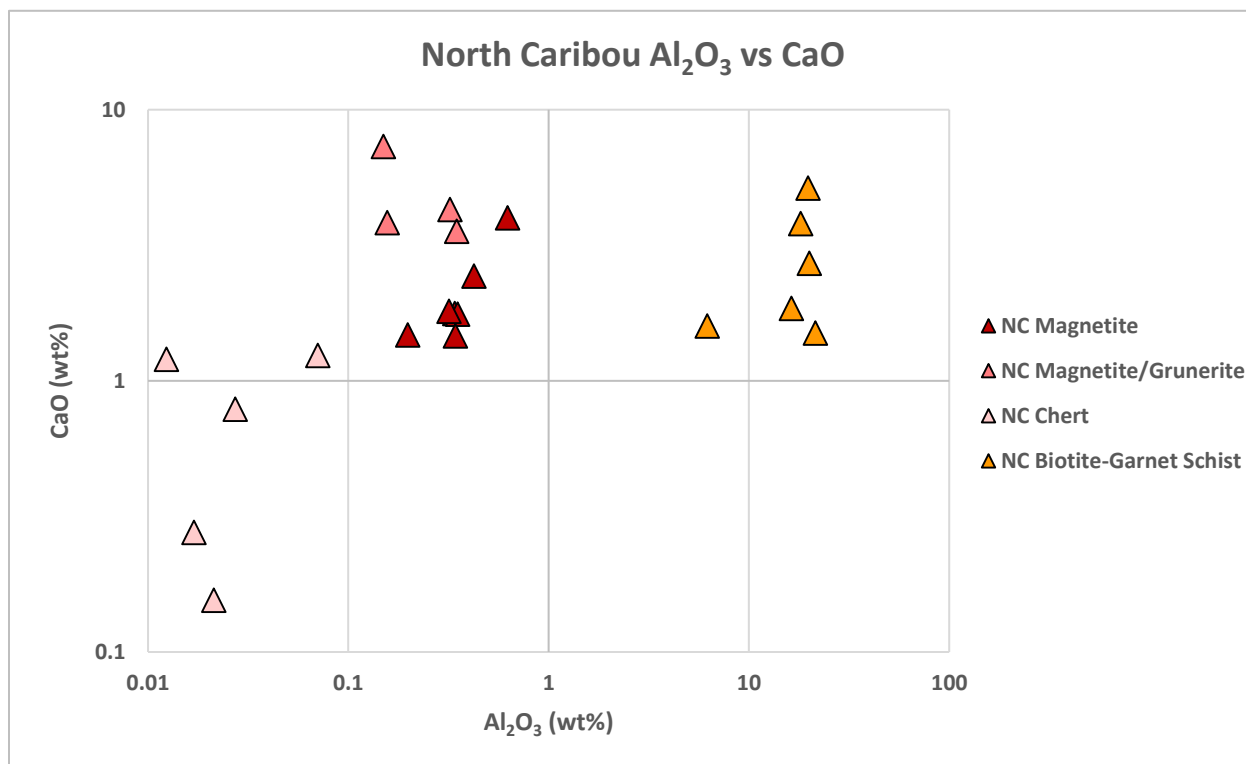
Figure 4.24: A logarithmic bivariate plot of aluminum versus calcium plotted with the meta-iron formation samples and siliciclastics from NC. The NC magnetite samples plot at much higher Ca/Al ratios than the NC biotite-garnet schist, suggesting a major influx of calcium to the meta-iron formation samples during deposition.

siliciclastic source. The positive linear correlation for the NC magnetite samples indicates that the influx of calcium during deposition was uniform. Therefore, calcium in the NC was derived in part from the siliciclastic phase and a non-siliciclastic source during deposition.

When plotting Ca against Sr on a logarithmic bivariate plot, the data sets divided into three distinct regions (Figure 4.25). Region 1 contains samples from BG and LSJ, region 2 contains samples from SGB and regions 3 contains samples from the NC. Interestingly, the Sr/Ca ratio decreases from the shallow water to the deeper water meta-iron formation samples. Scientists studying modern day ocean and river systems have determined that strontium levels in river systems are significantly higher than hydrothermal venting fluids (Graham et al., 1982; Chaudhuri and Clauer, 1986; Veizer, 1989), while calcium abundances are comparable between hydrothermal systems and river systems (Graham et al., 1982). This means that the Sr/Ca values in rivers and shallow water environments should be higher than deeper water environments associated with hydrothermal venting. Most
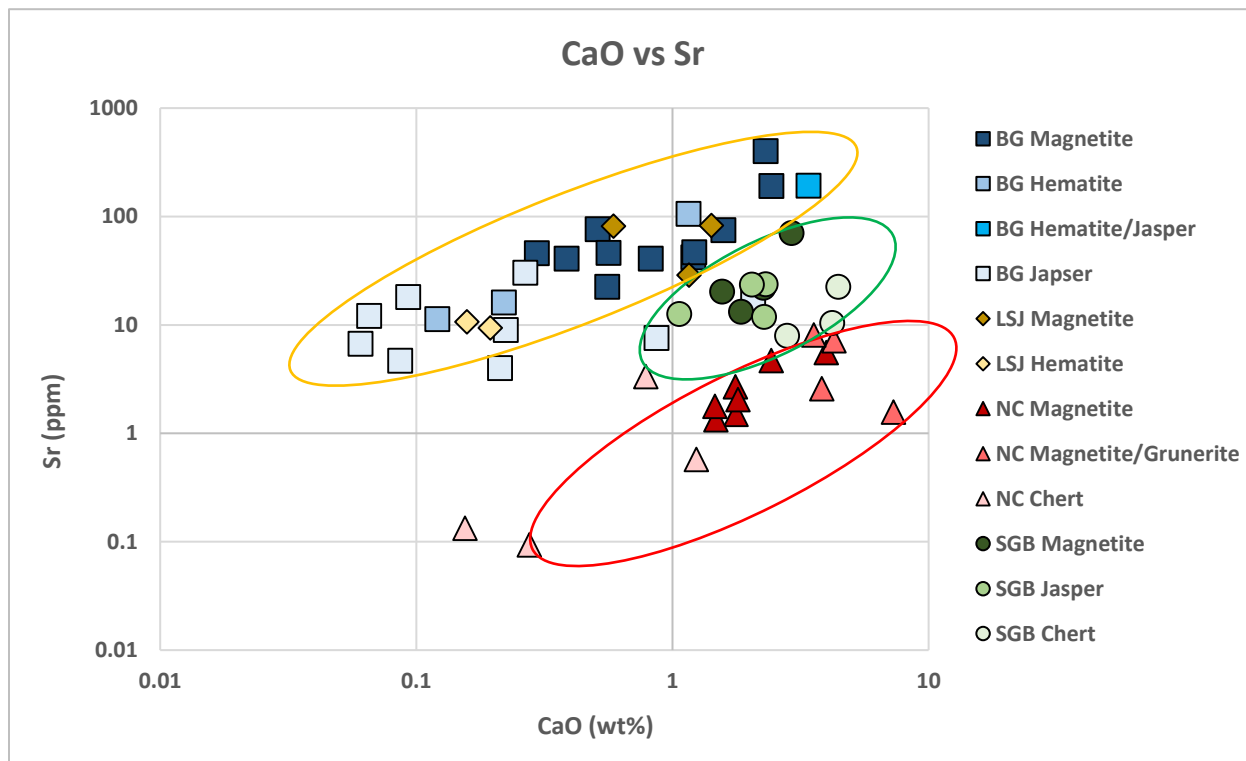
Figure 4.25: A logarithmic bivariate plot of calcium plotted against strontium. Three distinct regions separate the data sets. Region 1 is in yellow, region 2 is in green and region 3 is in red. The meta-iron formations are segregated based on their depositional environment.

Sr/Ca research has focused on recreating oceanic paleotemperatures in the Cenozoic by sampling calcareous fossils (ex. Tripati et al., 2009). Corals build their reef structures by taking calcium and strontium from dissolved seawater, preserving the composition of the ocean in the calcareous fossils. Since meta-iron formations also sample the chemistry of the ocean, the Sr/Ca trends might be preserved in Archean banded meta-iron formations from this study.

To test if the strontium and calcium concentrations are reflecting ocean or siliciclastic detritus concentrations in the BG, calcium and strontium were normalized over aluminum and plotted with the associated siliciclastic lithology (Figure 4.26). Significantly, the BG metagreywacke samples cluster with the BG magnetite samples. Since both axes are element ratios, when points cluster they indicate a mutual geochemical relationship. Therefore, the cluster suggests that calcium and strontium were derived from the siliciclastic phase and remained immobile during post-depositional alteration. However, the scattered points for some of the BG jasper and BG hematite, suggests that calcium and strontium were slightly mobile during post-depositional alteration

The strong relationship between the BG metagreywacke and most of the BG meta-iron formation samples indicates that both calcium and strontium were derived from the siliciclastic phase and most of the samples remained isochemical during post-depositional alteration. Therefore, for BG and possibly LSJ, the Sr/Ca ratio reflects the Sr/Ca ratio of the siliciclastic sourced detritus. However, the influx of calcium and strontium in the NC samples cannot be attributed to the siliciclastic phase, since the NC biotite-garnet schist samples have much lower Ca/Al ratios than the NC meta-iron formations. Since the NC samples are interpreted to be deposited in the deeper water setting, it is suggested that calcium was sourced from hydrothermal venting fluids. These fluids caused an enrichment of calcium in the deeper water relative to the shallow water setting resulting in higher adsorption rates onto iron oxyhydroxides during iron formation deposition. Therefore,

there might have been a seawater gradient in the ancient oceans with higher calcium

concentrations in the deeper ocean relative to the shallow ocean.
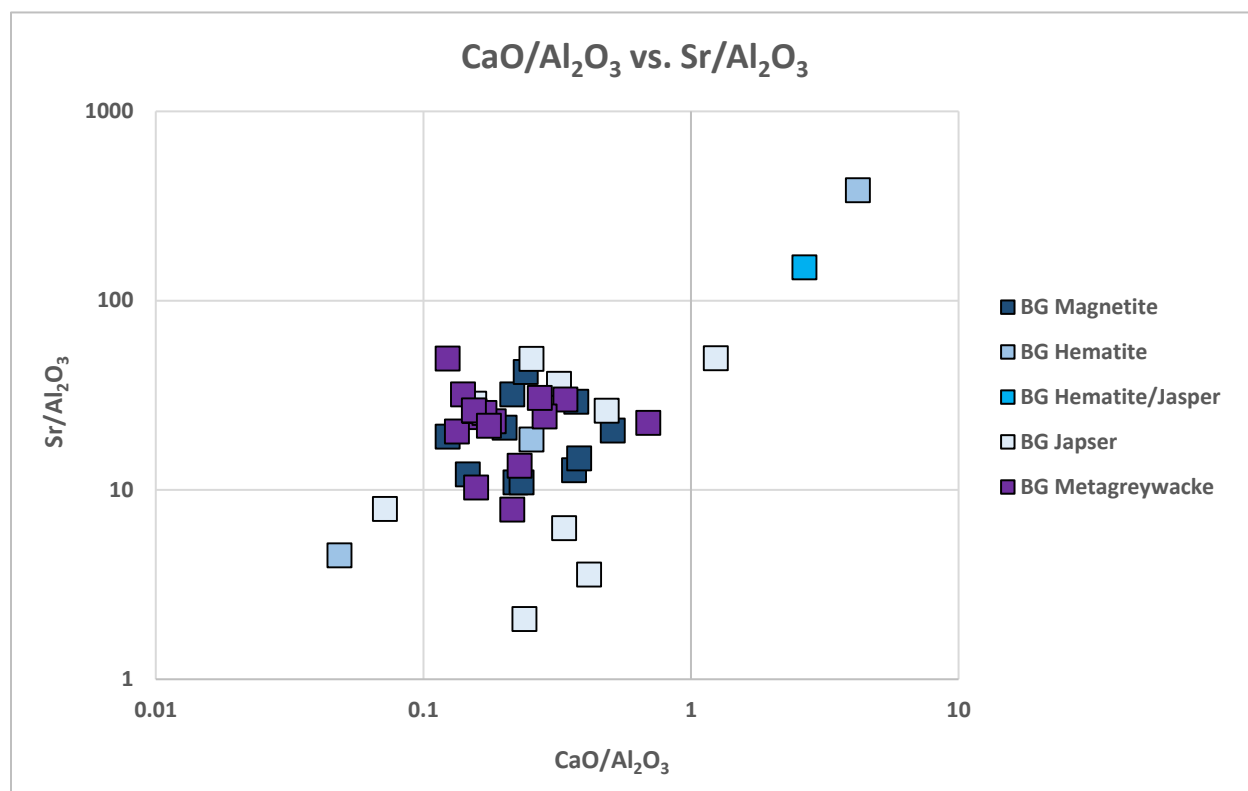
Figure 4.26: A logarithmic bivariate plot between CaO/Al_2O_3 and Sr/Al_2O_3 of the BG meta-iron formations samples plotted with the associated siliciclastics. The BG metagreywacke plot with the BG magnetite samples suggesting that strontium and calcium were derived from the siliciclastic phase. The scattering for some of the BG hematite and BG jasper samples suggests that calcium and strontium may have been slightly mobile during post-depositional alteration.

To determine the source of sodium in the meta-iron formations, CaO/Al_2O_3 was plotted against

Na_2O/Al_2O_3 (Figure 4.27). Significantly, NC magnetite, BG magnetite and LSJ magnetite all form

clusters. However, the NC magnetite samples cluster at higher Na_2O/Al_2O_3 and CaO/Al_2O_3 values

compared to the BG and LSJ samples. Since it was determined earlier that there was a major influx

of calcium and sodium in the NC samples and a minor influx of sodium in the BG samples from a

non-siliciclastic phase, the clustering of these samples indicates that there was no loss of siliciclastic-

derived calcium and sodium during post-depositional alteration and the influx of calcium and

sodium was uniform. If albitization due to late stage hydrothermal metasomatism, was responsible

for the sodium influx in the BG or possibly the NC samples, there would be a loss of calcium with

respect to the sodium influx. The Ca/Al values are relatively similar between meta-iron formations

from the same depositional setting (deep and shallow). Therefore, the lack of calcium depletion

relative to sodium, suggests that albitization was not responsible for the sodium influx for the

magnetite-dominated samples from BG (possibly LSJ and also NC) and the influx occurred during

deposition. Since the influx of sodium in the deeper water setting is greater than in the shallow

water setting, it is suggested that there was a geochemical gradient between sodium-enriched

deeper waters to sodium-depleted shallow waters in the ancient oceans caused by the influx of

sodium from hydrothermal venting fluids.
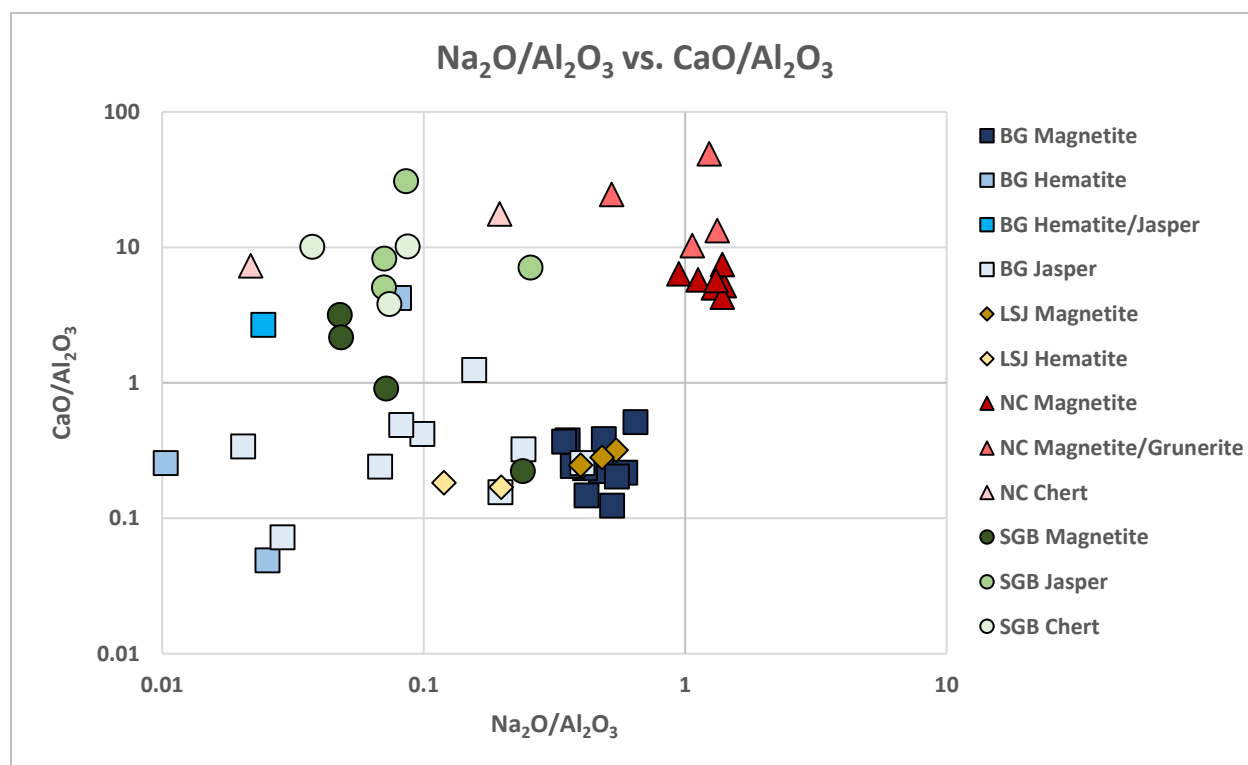
Figure 4.27: A logarithmic bivariate plot of CaO/Al_2O_3 vs Na_2O/Al_2O_3. The higher CaO/Al_2O_3 values for the SGB and NC meta-iron formation samples suggests that calcium was more enriched in the deeper ocean relative to the shallow ocean. Therefore, calcium in the deeper water meta-iron formations was sourced from seawater, derived from hydrothermal venting fluids.

When magnesium was plotted against other elements, no definite positive correlations were

observed. For example, Figure 4.28 is an Al_2O_3 versus MgO graph. For most of the sample locations,

the range for the aluminum values is fairly similar between samples from the same location, while

the magnesium content has large variations, forming vertical trends. The lack of a positive or

negative correlation between magnesium with other elements indicates that magnesium was most

likely mobile during diagenesis, metamorphism and any hydrothermal alteration. Also, the lack of

any correlations suggests that magnesium was possibly derived from multiple sources, such as

hydrothermal fluids, the siliciclastic phase and from seawater.
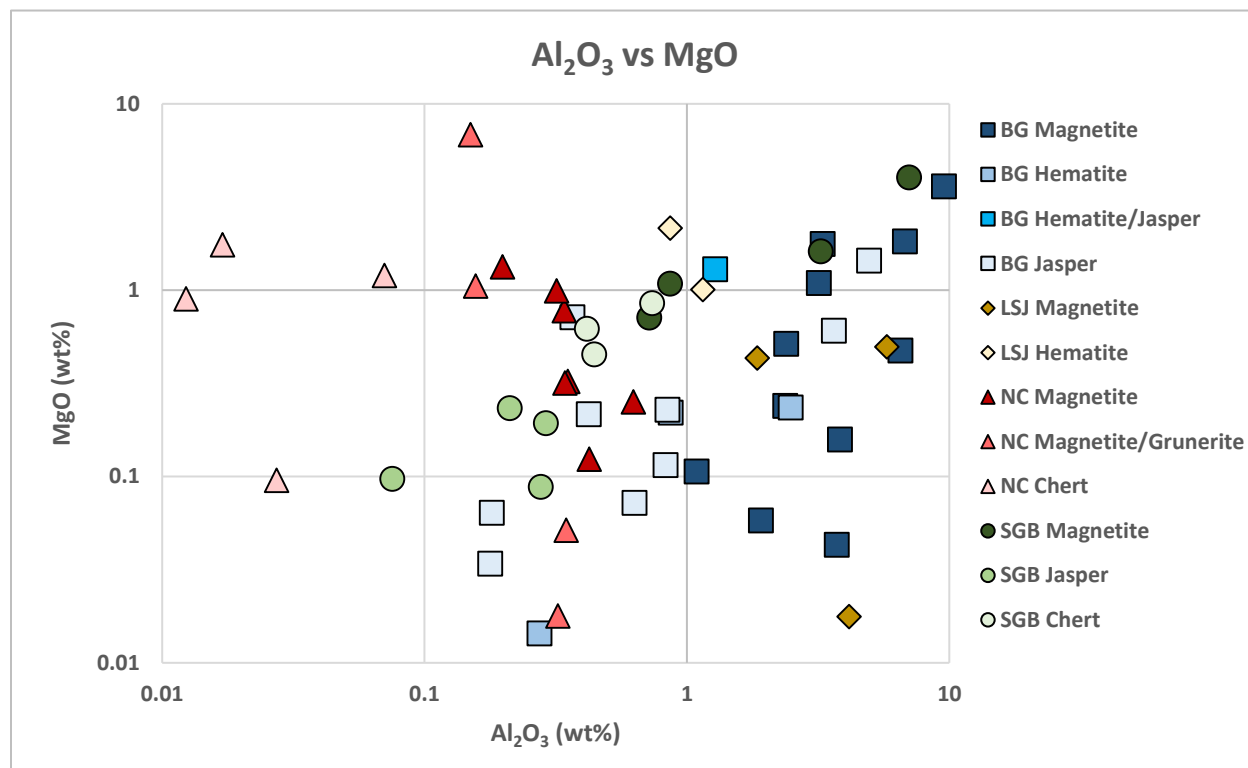
Figure 4.28: A logarithmic bivariate plot of aluminum versus magnesium. The data set is scattered and there is no definite correlation indicating that magnesium was probably mobile during post-depositional alteration and was most likely derived from multiple sources.

In summary, most of the strontium in all the meta-iron formation samples was derived from the

siliciclastic phase. However, the scattering of some of the samples suggests that strontium may have

been slightly mobile during post-depositional alteration. Calcium in the BG and LSJ was derived from

the siliciclastic phase and remained immobile in the magnetite-dominated samples from BG and

possibly LSJ. The scattering of some of the BG and LSJ hematite-, jasper- and chert-dominated

samples suggests that calcium may have been slightly mobile during post-depositional alteration.

For the NC and SGB samples, calcium was derived in part from the siliciclastic phase and seawater.

Since the deeper water meta-iron formation samples record higher Ca/Al and Na/Al ratios than the

shallow water samples, it is suggested that hydrothermal venting fluids were the main source of calcium and sodium to the ancient oceans.

4.7 Group 4 High Field Strength Elements: Zr and Hf

The high field strength elements (HFSE), Zr, Hf, Nb, Ta and TiO_2, have been regarded as immobile elements during post-depositional alteration. In Section 4.2, niobium and titanium were determined to be immobile during post-depositional alteration and associated with the siliciclastic phase. In this section, the relationship between zirconium and hafnium will be tested, as well as their relationship to the siliciclastic phase.

Zirconium was plotted against aluminum to determine the association with the siliciclastic phase (Figure 4.29). At first glance, the overall data appears to be forming a positively sloping linear trend. However, when isolating the samples based on their study location and composition, different
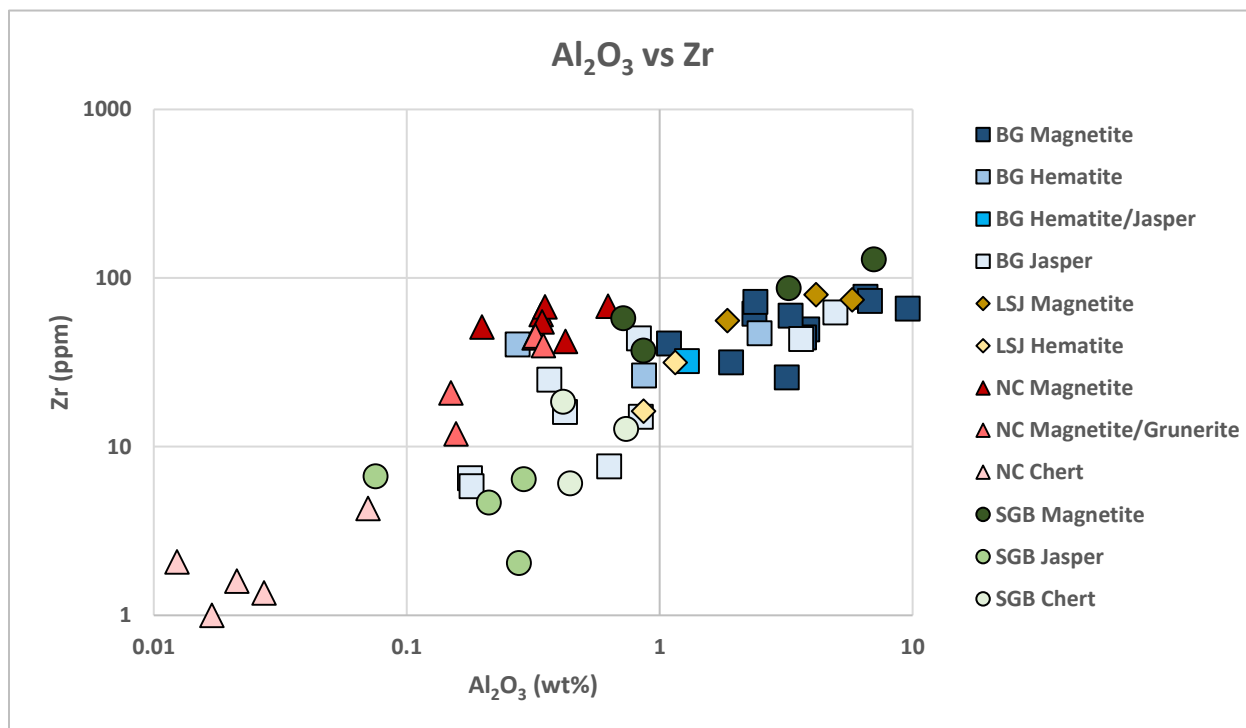
Figure 4.29: A logarithmic bivariate plot of aluminum plotted against zirconium. The BG and NC samples form a positive linear correlation, although the Zr/Al ratio for the NC samples is greater than the BG. For the SGB and LSJ samples, as the aluminum content increases, the slope of the linear correlation trend decreases.

trends occur. The NC meta-iron formation samples display a positive linear trend at slightly higher

Zr/Al ratios than the meta-iron formations from the other study locations. The meta-iron formations

from SGB and LSJ, display a positively sloping correlation at lower aluminum values, although the

points for the SGB samples are scattered. When the aluminum content is higher than one weight

percent, the slope of the correlation for both the LSJ and SGB samples decrease, and the trends are

nearly horizontal. The BG meta-iron formation samples form a relatively shallow-sloping, positive

linear correlation, although the BG jasper samples are scattered.

To determine the source of zirconium, the BG meta-iron formation samples were plotted with

the BG metagreywacke (Figure 4.30). The BG meta-iron formation and metagreywacke samples plot

as a positive, shallowly sloping, linear trend, suggesting that zirconium was possibly derived from

the siliciclastic phase and remained isochemical during post-depositional alteration (Figure 4.30).

However, if this were true, the correlation curve would be steeper and extend towards the origin.
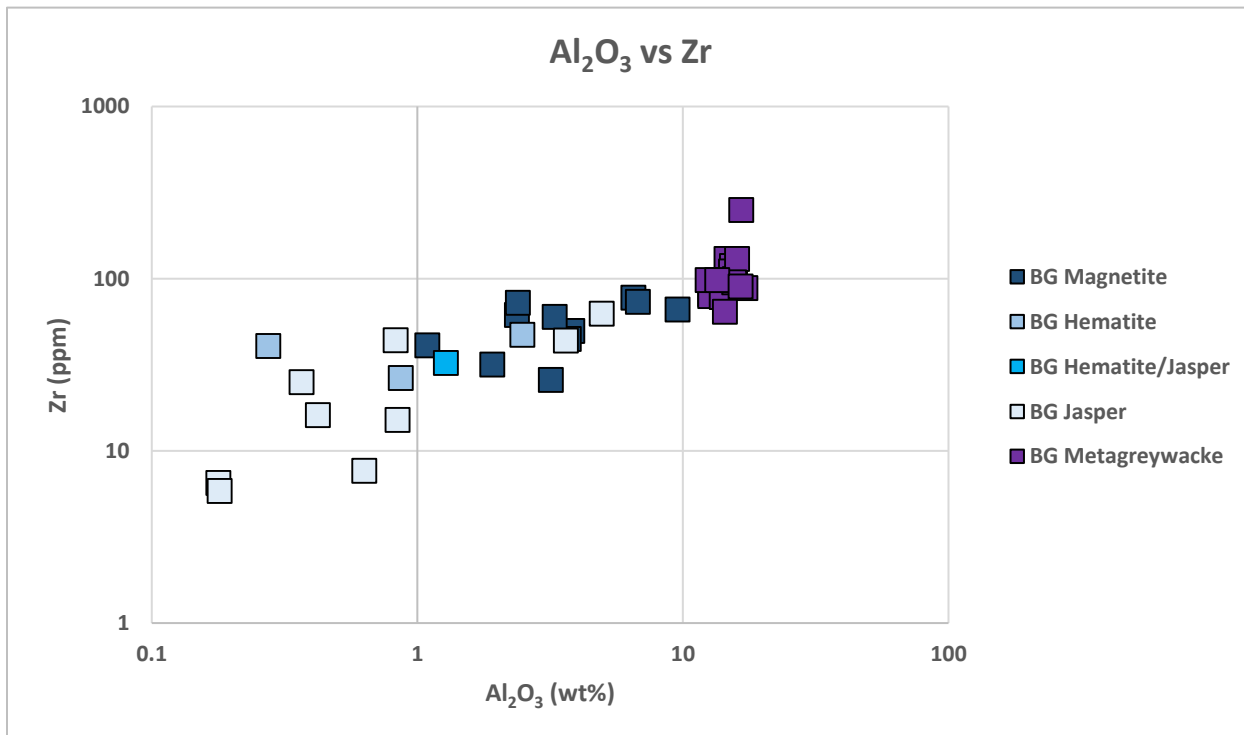
Figure 4.30: A logarithmic bivariate plot of aluminum vs zirconium for the BG meta-iron formation and siliciclastic samples. The BG metagreywacke samples plot along the positive correlation trend with the meta-iron formation samples. However, the trend does not extend towards the origin, suggesting that the Zr/Al_2O_3 ratio for the BG meta-iron formation samples is higher than the BG metagreywacke.

The shallowly sloping correlation indicates that the BG meta-iron formation samples have higher Zr/Al values relative to the BG metagreywacke, suggesting a secondary non-siliciclastic source of zirconium during deposition.

The higher Zr/Al values for the BG meta-iron formation samples compared to the associated siliciclastic lithology can clearly be seen in Figure 4.31, a box and whisker plot of the Zr/Al values for the BG meta-iron formation and BG metagreywacke samples. The BG hematite category also includes the BG hematite/jasper sample. This graph shows that there is a small range between the Zr/Al values for the BG metagreywacke. The Zr/Al values for the BG meta-iron formation are highly variable and are two or more times greater than the Zr/Al values for the BG metagreywacke samples. The higher Zr/Al values for the BG meta-iron formation samples suggests a non-siliciclastic source for some of the zirconium during deposition. Since the Zr/Al ratio for the siliciclastics is
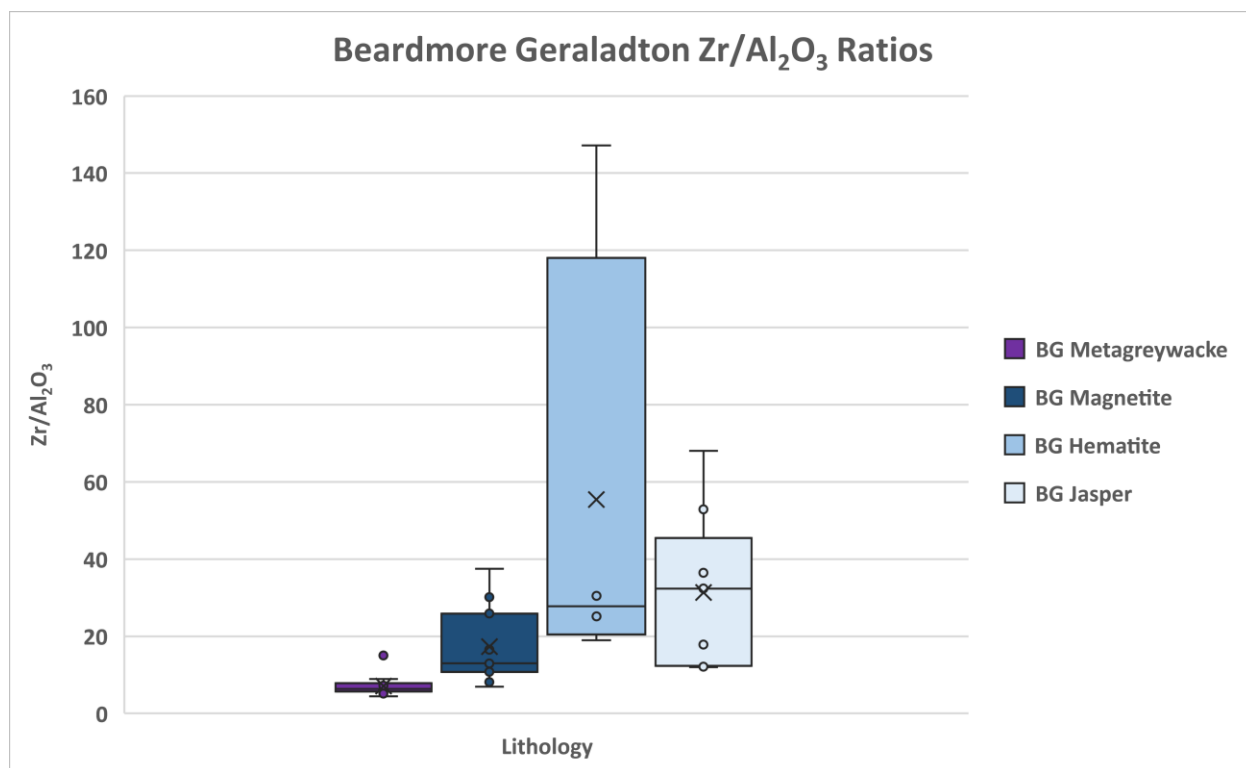
Figure 4.31: A box and whisker plot of the Zr/Al_2O_3 ratios for the BG meta-iron formation samples and associated siliciclastic lithology. The BG metagreywacke samples have lower Zr/Al_2O_3 values and their range is smaller than the BG meta-iron formation samples. This indicates that for the BG meta-iron formation samples there was an influx of zirconium from a non-siliciclastic source during deposition.

consistent for most of the BG metagreywacke samples, the influx of zirconium occurred during deposition and remained immobile during post-depositional alteration.

The NC meta-iron formation samples were plotted with the NC biotite-garnet schist in Figure 4.32. The NC meta-iron formation samples plot as a positive linear correlation, suggesting that zirconium was derived from the siliciclastic phase. However, the biotite-garnet schists plot at much lower Zr/Al ratios than all the NC meta-iron formation samples. Since aluminum was immobile during deposition and post-depositional alteration, the higher Zr/Al ratios for the NC meta-iron formation samples were caused by an influx of zirconium from a non-siliciclastic source during deposition.
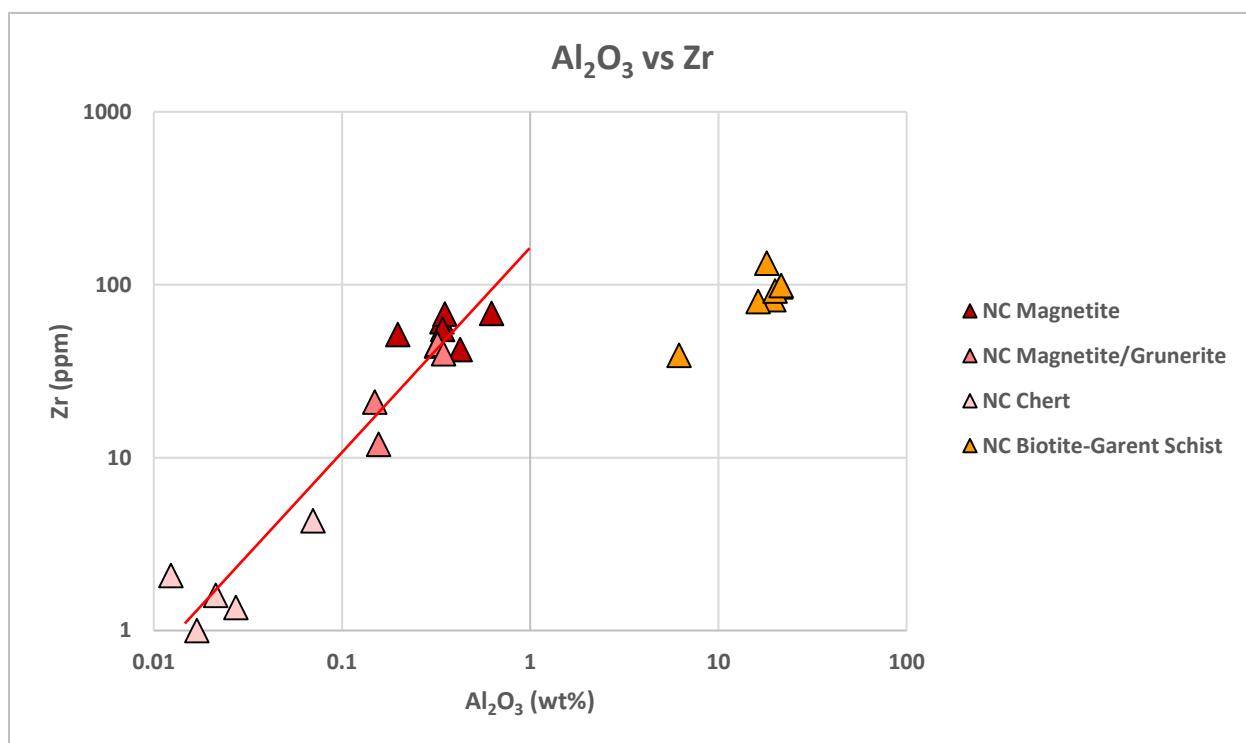
Figure 4.32: A logarithmic bivariate plot of aluminum versus zirconium of the NC meta-iron formation and siliciclastic samples. Significantly, the Zr/Al_2O_3 values for the NC meta-iron formation samples is larger than the Zr/Al_2O_3 values for the NC biotite-garnet schist. Therefore, the higher Zr/Al_2O_3 ratio for the NC meta-iron formation samples was caused by an influx of zirconium from a non-siliciclastic source during deposition.

Figure 4.33 is a logarithmic bivariate plot of aluminium plotted against hafnium. The LSJ magnetite samples are the only data set that displays a very strong positive correlation between

hafnium and aluminum. NC chert, NC magnetite and LSJ hematite samples exhibit flat lying

correlation trends. Increased analytical errors associated with lower values may cause scatter at the

low end of the diagram. However, the rest of the samples form a scattered, positive, linear

correlation. Since hafnium is regarded as immobile during post-depositional alteration, the

scattering of the points suggests that there was an influx of hafnium from a non-siliciclastic source

during deposition. Unfortunately, due to the absence of hafnium geochemical data for the BG

metagreywacke samples from Fralick and Barrett (1991) and most of the hafnium geochemical data

for the NC meta-iron formation samples is below detection limits, the hafnium data for the meta-

iron formation data could not be compared to their respective siliciclastic lithologies.
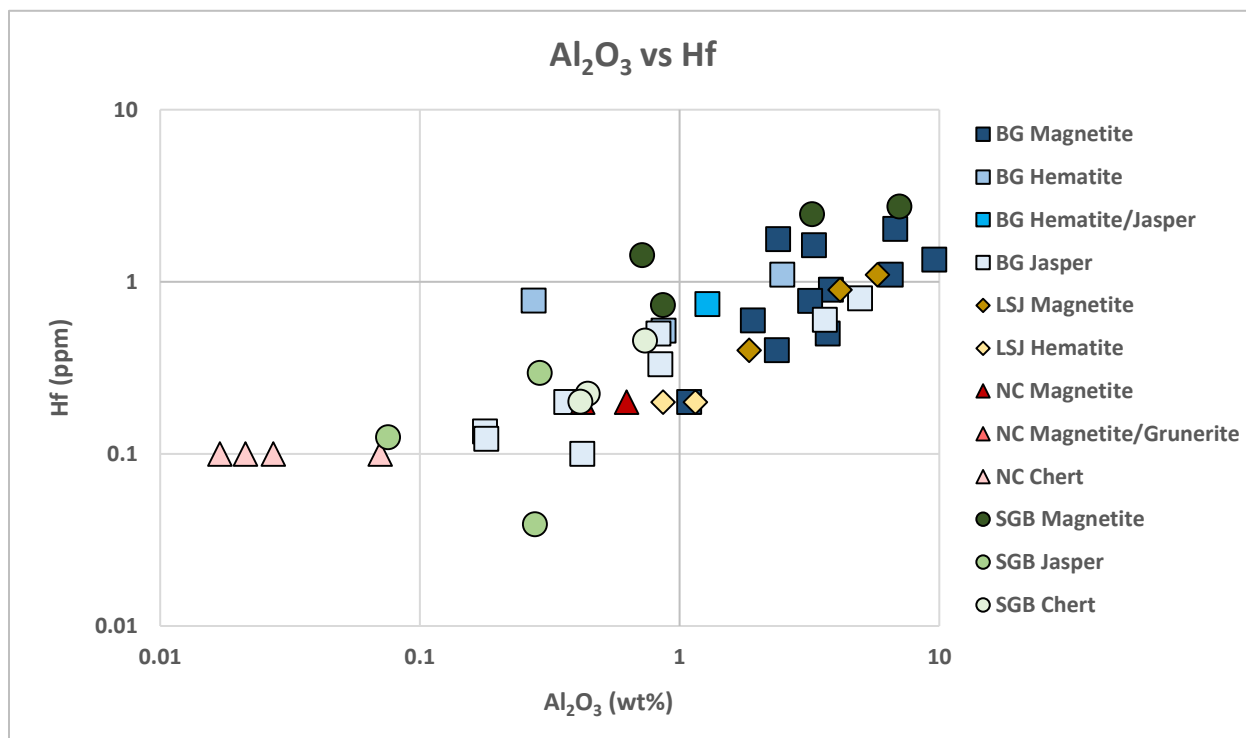
Figure 4.33: A logarithmic bivariate plot between aluminum and hafnium. A moderately strong correlation occurs between these two elements. Hafnium values for NC and LSJ samples were obtained from Geoscience Laboratories in Sudbury and these values are reaching the lower detection limits of their analytical machines. The overall positive correlation suggests hafnium was mostly derived from the siliciclastic phase. However, the scattering suggests an influx of hafnium during deposition.

Since zirconium and hafnium have almost identical atomic radii, both elements should behave

chemically similar during deposition and post-depositional alteration. When plotting zirconium

against hafnium, a positive correlation exists (Figure 4.34). However, at lower levels the data set

becomes scattered because the concentrations are reaching lower detection limits. The positively

trending, linear correlation suggests that zirconium and hafnium were derived from the same

sources and behaved similarly during post-depositional alteration.
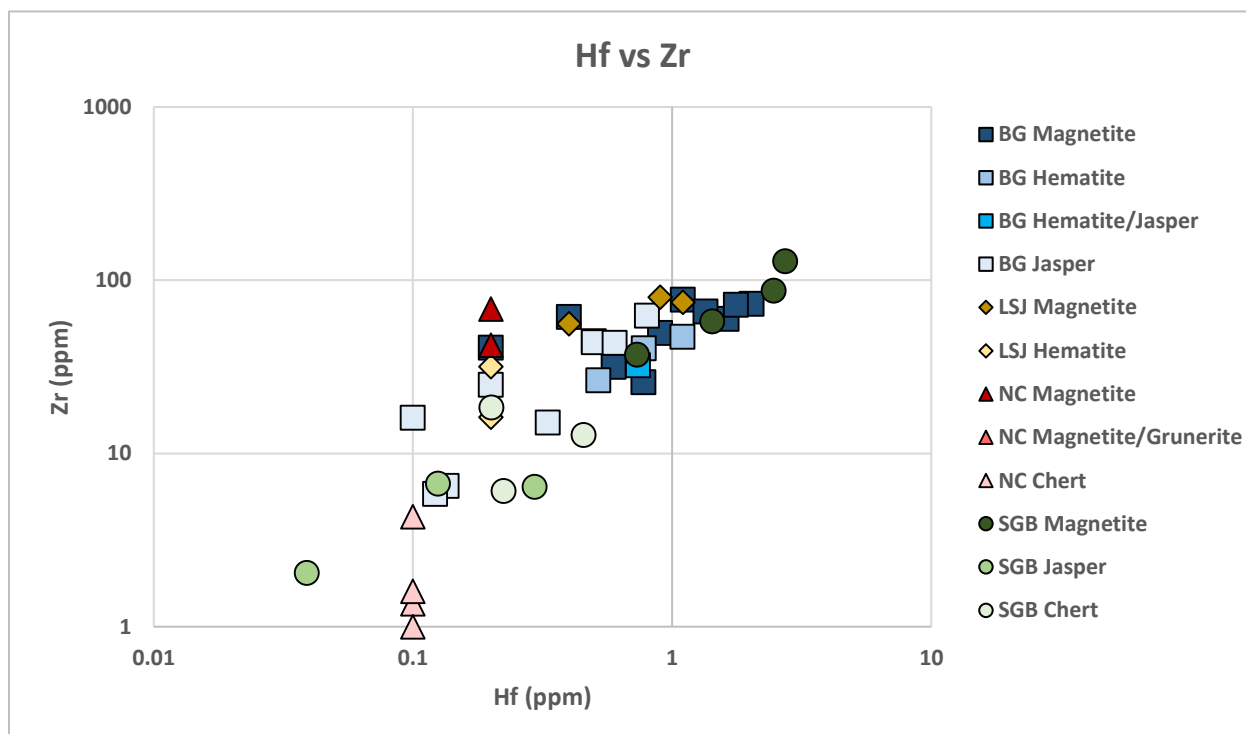
Figure 4.34: A logarithmic bivariate plot between hafnium and zirconium. A positively sloping correlation occurs with these two elements except for the NC and LSJ samples that are reaching the lower detection limits. The positively trending correlation suggests that both elements behaved similarly during post-depositional alteration

Modern oceans have higher Zr/Hf values than chondritic Zr/Hf values, indicating that unlike

igneous systems, zirconium and hafnium fractionation is common in open water systems (Bau and

Alexander, 2009; Censi et al., 2017). When zirconium and hafnium are liberated from detrital

minerals through erosion, Zr^{3+} and Hf^{3+} are able to hydrolyze easily at very low concentrations in

natural waters (Bau and Alexander, 2009). Studies on Zr/Hf ratios indicate that zirconium can

preferentially adsorb onto iron oxyhydroxide mineral surfaces during precipitation, based on the

positive relationship between Eh and Zr/Hf ratio and the positive relationship between the

oversaturation index of iron oxyhydroxides and the Zr/Hf ratio (Censi et al., 2017). Therefore, in

oxidizing environments, where there is an oversaturation of iron oxyhydroxides, zirconium will

preferentially adsorb onto iron oxyhydroxides during deposition, which increases the Zr/Hf relative to chondritic values.

Zirconium and hafnium were plotted against each other on an arithmetic bivariate plot with a line denoting the chondritic Zr/Hf ratio of 34.1 ± 0.3 as determined by Patzer et al. (2010) (Figure 4.35). Significantly, most of the samples plot above the chondritic Zr/Hf ratio indicating that zirconium was fractionated relative to hafnium in the ancient ocean and this fractionation was recorded and preserved in the meta-iron formation samples. This graph strongly suggests that zirconium, in part, from seawater. Zirconium in the seawater was most likely sourced from continental runoff.
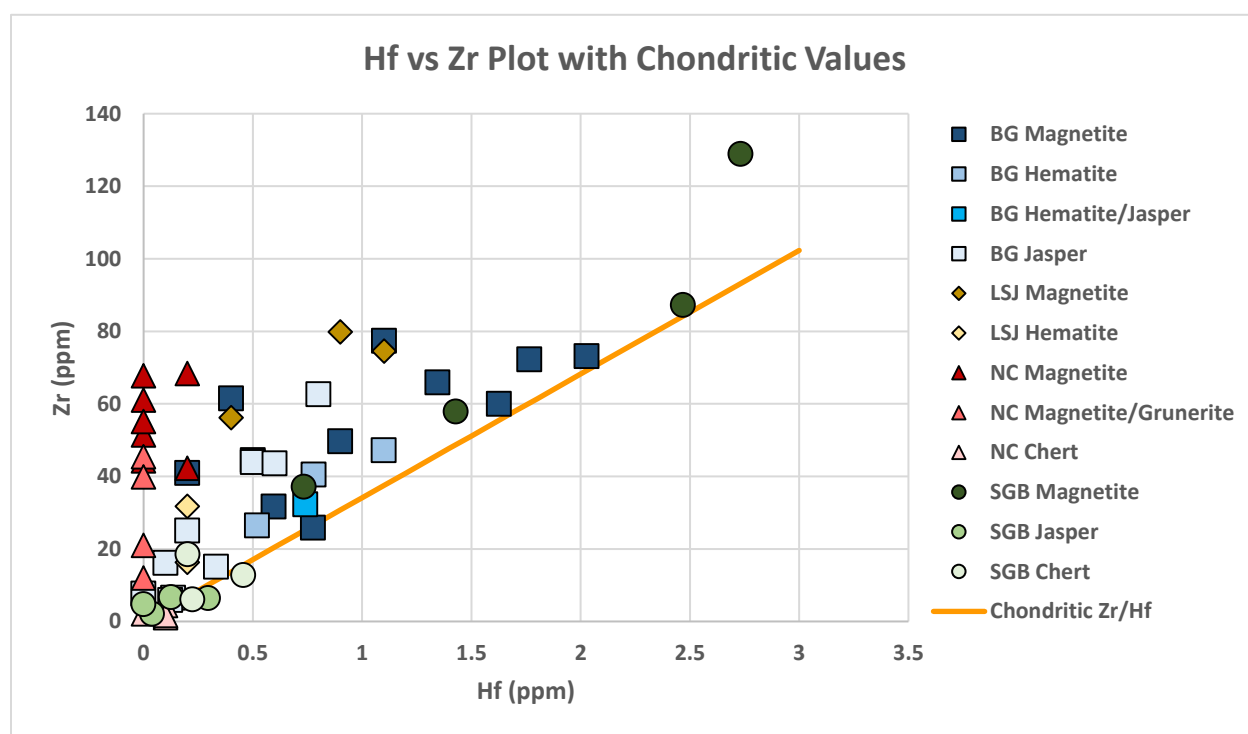
Figure 4.35: An arithmetic bivariate plot of zirconium vs hafnium. The orange line denotes the chondritic Zr/Hf ratio of 34.1. Significantly, most of the meta-iron formation samples plot above the line, suggesting that zirconium in part was derived from a non-siliciclastic phase during deposition.

Since it was determined that a significant amount of the zirconium and possibly hafnium adsorbed onto iron oxyhydroxides during deposition, there should be higher Zr/Hf ratios in the magnetite- and hematite-dominated samples and lower Zr/Hf ratios in the chert- and jasper-

dominated samples. Although the magnetite-dominated samples have higher zirconium values than their associated chert- and jasper-dominated samples, there is no clear significant difference in the Zr/Hf ratio between the phase-dominated layers. This indicates that zirconium can adsorb onto amorphous silica as readily as iron oxyhydroxides. The scattering of the Zr/Hf ratio in Figure 4.35 does suggest that the dissolved zirconium content in the ancient ocean was highly variable.

In summary, zirconium was sourced in part from the siliciclastic phase and seawater, sourced from continental runoff. Zirconium dissolved in seawater adsorbed onto iron oxyhydroxides and amorphous silica during deposition. Hafnium was mostly sourced from the siliciclastic phase, but minor amounts may have been also derived from seawater. Since zirconium in the NC and BG siliciclastic lithologies remained isochemical during post-depositional alteration, it is inferred that zirconium was also isochemical in the meta-iron formation. If both zirconium and hafnium were isochemical during post-depositional alteration, then the Zr/Hf values represent a combination of the siliciclastic-derived Zr/Hf ratio and the dissolved Zr/Hf ratio of the ancient ocean. The scattered Zr/Hf ratio suggests that the zirconium concentrations of the ancient oceans were highly variable.

4.8 Group 3, 5 and 6 Elements, Transition Metals: Sc, V and Cr

Group 3, 5 and 6 elements obtained from the geochemical analysis were scandium, vanadium and chromium. Earlier in Section 4.2, vanadium was deemed immobile and derived from the siliciclastic phase. Since vanadium has a strong, linear relationship with aluminum, the other elements were plotted against vanadium to determine the relationship between these elements and the siliciclastic phase.

When vanadium was plotted against chromium on a logarithmic bivariate plot, the data set is divided into two distinct linear regions (Figure 4.36). Region 1 contains all the BG samples, all the LSJ samples, SGB magnetite, SGB chert and two SGB jasper samples. Interestingly, two trends occur

within this region. Most of the points form a positive linear correlation that extends towards the

origin. However, at around 10 ppm chromium, the BG hematite, BG magnetite, BG jasper and LSJ

hematite samples display a lower sloping correlation, similar to the region 2 samples. For the SGB

samples at lower than 10 ppm vanadium, the data points are scattered. Region 2 is a lower sloping,

near horizontal linear correlation consisting of all the NC samples and two SGB jasper samples at

higher Cr/V ratios relative to region 1.
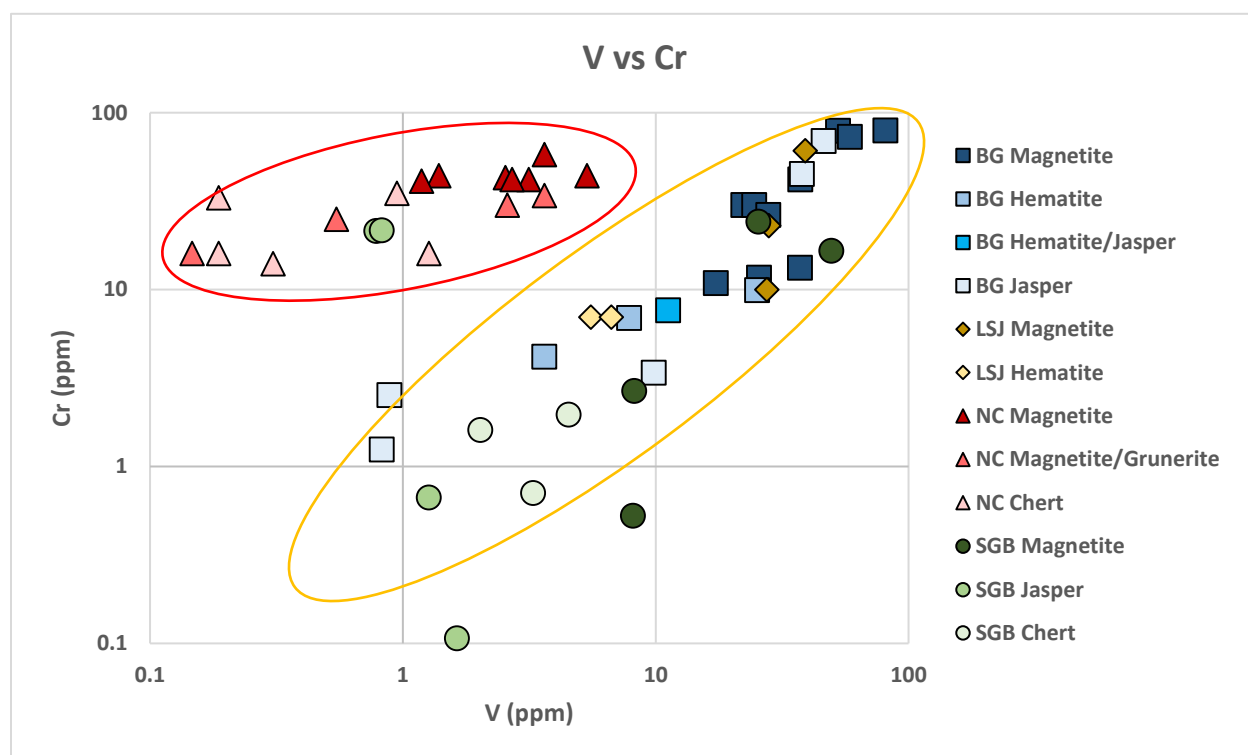
Figure 4.36: A logarithmic bivariate plot of V vs Cr. The data set is separated into two regions on the graph. Region 1 (yellow) contains BG, LSJ and most of the SGB meta-iron formation samples. This region can be extended towards the origin, indicating that most of the chromium for the BG and LSJ samples was probably derived from the siliciclastic phase. Region 2 (red) has higher chromium values than region one and forms a relatively flat-lying trend indicating that the majority of chromium in the NC samples was probably derived from a non-siliciclastic source.

Figure 4.37 is a vanadium versus chromium graph of the BG and NC meta-iron formation

samples are plotted with BG metagreywacke and NC biotite-garnet schist geochemical data. The BG

samples form a relatively positive linear correlation with the BG and NC siliciclastic lithologies at

similar Cr/V ratios. If the siliciclastic lithologies from LSJ has the same Cr/V values as the BG

metagreywacke, then chromium in the BG and LSJ meta-iron formation samples was mostly derived from the siliciclastic phase and remained immobile during post-depositional alteration.

Interestingly, the NC biotite-garnet schist plot with the BG metagreywacke samples indicating that the Cr/V values for the NC meta-iron formation samples are significantly higher than the NC biotite-garnet schist (Figure 4.37). Also, the shallowly sloping, near-horizontal linear relationship between vanadium and chromium for the NC samples indicates that the Cr/V ratio was variable during deposition. Therefore, in the NC, there was an enrichment of chromium from a non-siliciclastic source during deposition.
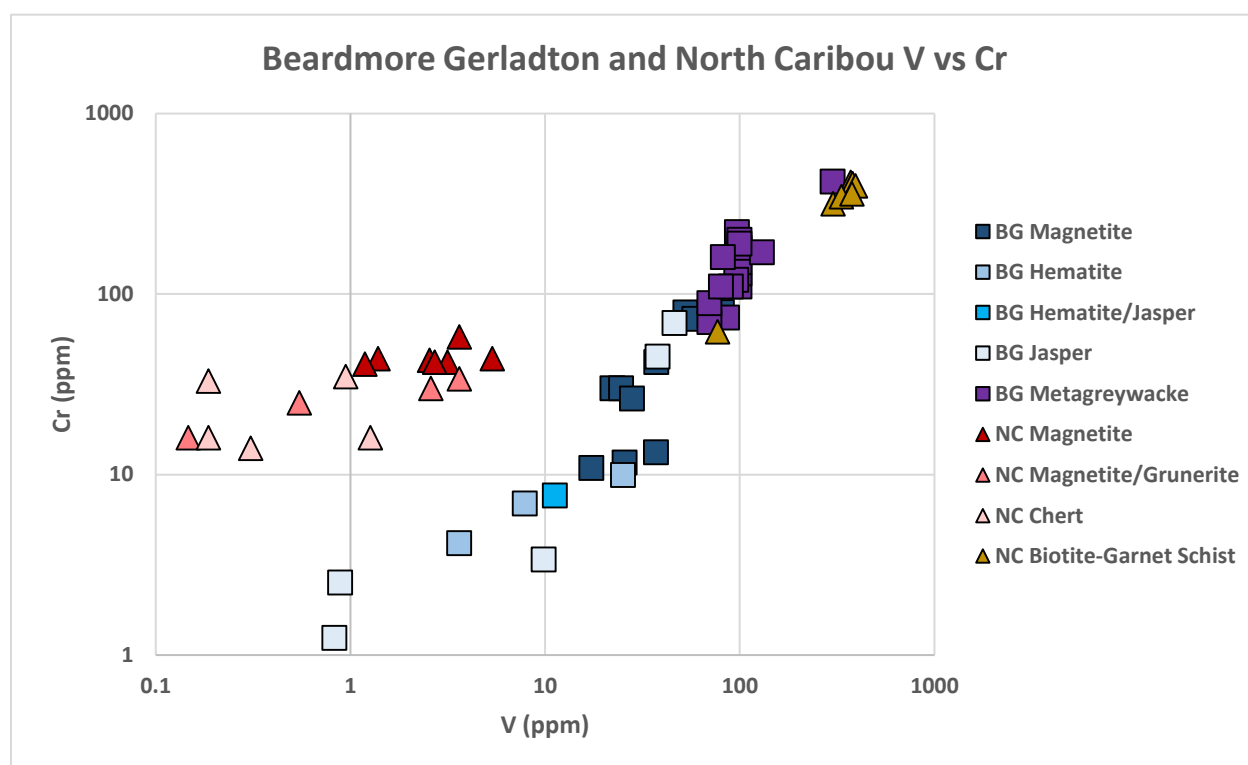
Figure 4.37: A logarithmic bivariate plot of vanadium versus chromium from the NC and BG plotted with their associated siliciclastic lithologies. The positive linear trend for the BG meta-iron formation and siliciclastic samples indicates that chromium was mostly derived from the siliciclastic phase in the BG. The meta-iron formation samples from the NC have higher Cr/V ratios than the siliciclastics, indicating that there was an influx of chromium for the NC samples from a non-siliciclastic source during deposition.

Chromium values for the SGB samples are more scattered than the other study locations, especially at lower concentrations (Figure 4.36). Interestingly, SGB jasper samples plot in both

trends 1 and 2. Since most of the SGB meta-iron formations plot with the BG and LSJ samples along the correlation curve, it is assumed that the Cr/V ratio for the siliciclastic detritus was similar to the BG metagreywacke and NC biotite-garnet schist. Therefore, the higher Cr/V values for the two SGB jasper samples were caused by an influx of chromium during deposition.

A similar relationship can be seen between scandium and vanadium (Figure 4.38). Like chromium, the data sets were separated into two linear trends, although the regression is much stronger. Trend 1 contains all the SGB samples, BG hematite, four BG jasper and five BG magnetite samples. Trend 2 contains all the NC samples and may also contain the LSJ magnetite and five BG magnetite samples. Trend 2 is a linear, slightly negatively sloping correlation and has higher Sc/V ratios than trend 1.
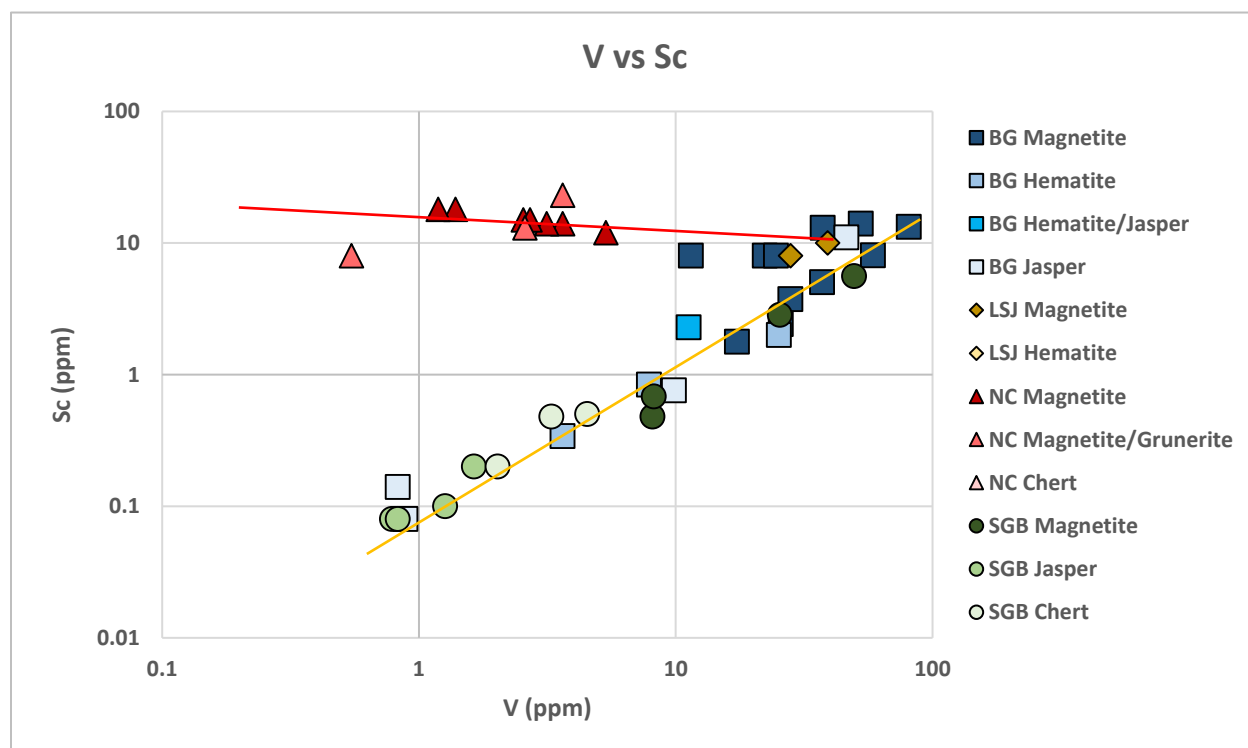
Figure 4.38: A logarithmic bivariate plot of V vs Sc. The strong correlation for trend 1 (yellow) indicates that the scandium for these samples was most likely derived from the siliciclastic phase. The trend 2 (red) samples indicate a non-siliciclastic source for scandium. The strong correlation indicates that Sc was mostly immobile during post-depositional alteration.

The strong relationship between vanadium and scandium indicates that most of the BG, LSJ and

SGB samples were derived from the siliciclastic phase and remained mostly immobile during post-

depositional alteration. However, the slight scandium enrichment in four of the BG magnetite

samples suggests there was a slight influx of scandium from a non-siliciclastic source. The higher

Sc/V ratio for the NC meta-iron formation samples suggests that there was an influx of scandium

from a non-siliciclastic source.

When subtracting the effects of the siliciclastic contamination from both scandium and

chromium, the data set produces two distinct clusters (Figure 4.39). The NC biotite-garnet schist

samples were plotted with the meta-iron formations to determine the scandium's and chromium's

relationship with the siliciclastic phase. Significantly, the NC biotite-garnet schist samples plot with

the LSJ and BG clusters. If the siliciclastic detritus from the BG and LSJ had similar Cr/Al_2O_3 and
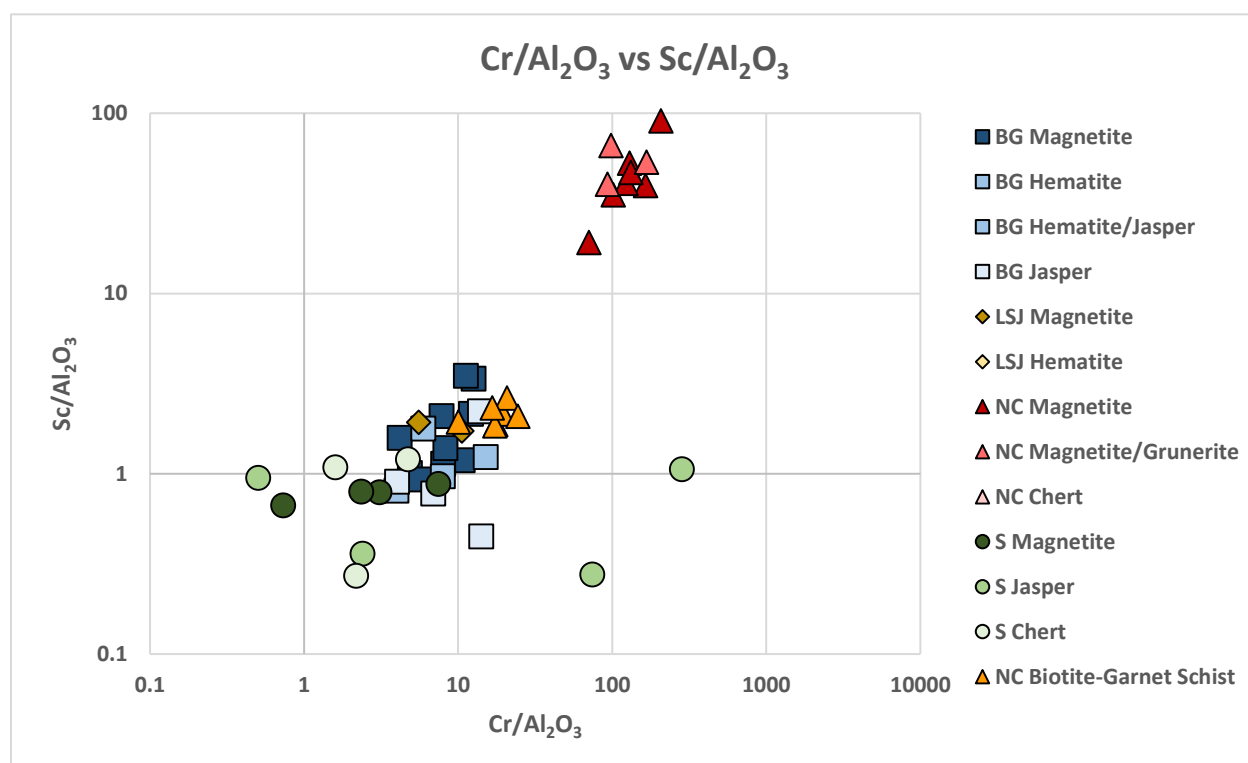
Figure 4.39: A logarithmic bivariate plot of Cr/Al_2O_3 vs Sc/Al_2O_3. The BG and LSJ meta-iron formation samples cluster together with the NC biotite-garnet schist suggesting that scandium and chromium were derived from the siliciclastic phase and remained immobile during post-depositional alteration. NC samples cluster at higher Cr/Al_2O_3 and Sc/Al_2O_3 values compared to the NC biotite-garnet schist suggesting that there was an influx of both elements from seawater, sourced from hydrothermal venting fluids.

Sc/Al_2O_3 ratios as the NC biotite-garnet schist, then chromium and scandium in the BG and LSJ were derived from the siliciclastic phase and remained immobile during post-depositional alteration. The NC meta-iron formation samples cluster at much higher Sc/Al_2O_3 and Cr/Al_2O_3 values than the NC biotite-garnet schist. Therefore, a component of the scandium and chromium in the NC meta-iron formation samples was derived from a non-siliciclastic source during deposition. Since the NC meta-iron formations were deposited in the deeper water setting associated with hydrothermal venting fluids, most of the scandium and chromium in the NC was probably derived from seawater, sourced from hydrothermal venting fluids. Since it was determined that scandium was derived from the siliciclastic phase in SGB and most of the SGB samples vary in chromium values, the differences in the Sc/Cr ratio was most likely caused by an influx of chromium from seawater.

Geologists studying Precambrian meta-iron formations have used chromium isotopes to determine the ancient atmospheric oxygen content. When oxygen is present in the Earth's atmosphere, a catalytic reaction between immobile Cr^{3+} and Mn^{4+}, readily oxidizes Cr^{3+} to Cr^{6+}, which is mobile and can be transported to oceans by continental runoff (Fendorf, 1995; Frei et al., 2009). Cr^{6+} can be reduced back to Cr^{3+} by bacterial microorganism or during oxidation of Fe^{2+} to Fe^{3+} by forming oxyhydroxides (Frei et al., 2009; Konhauser et al., 2011). Due to the insolubility of iron and chromium oxyhydroxides, both phases precipitate out of seawater depositing in meta-iron formation, which causes the ocean to be enriched in Cr^{6+} (Frei et al., 2009; Døssing et al., 2011; Konhauser et al., 2011). Since iron oxyhydroxides can sample the chemistry of the ocean, the Cr^{6+} adsorbs onto iron oxyhydroxides during deposition and records the Cr^{6+} content of the ocean (Døssing et al., 2011). Significantly, Cr^{6+} is enriched up to +7‰ $\delta^{53}Cr$ relative to Cr^{3+}, which means that Cr^{6+} is enriched with the heavier chromium isotope (Frei et al., 2009). However, bacterial microorganisms can metabolically reduce Cr^{6+}, shifting the $\delta^{53}Cr$ to -4.1‰ (Frei et al., 2009). Modern $\delta^{53}Cr$ values for seawater can range from +0.412‰ to +1.505‰, compared to average continental

crust which is -0.124‰ (Bonnand et al., 2013). Therefore, any shift of the δ^{53}Cr value indicates that chromium was oxidized under oxygenic surface condition and recorded in the meta-iron formation.

Studies on chromium isotopes have concluded that there was a minimal supply of authigenic Cr^{6+} to the oceans before 2.48Ga, suggesting an anoxygenic atmosphere (Konhauser et al., 2011). Since chromium in the shallow water meta-iron formations studied were mostly derived from the siliciclastic phase, the lack of chromium enrichment suggests that there was minimal supply of authigenic chromium to the Archean oceans via groundwater and rivers due to the insolubility of Cr^{3+}, indicating an anoxygenic atmosphere. The deeper water meta-iron formation samples show an enrichment of chromium suggesting that chromium was derived from hydrothermal venting fluids. Chromium in the deeper water meta-iron formations was capable of co-precipitating or adsorbing onto iron oxyhydroxides during meta-iron formation deposition.

In summary, scandium and chromium in the BG and LSJ was mostly derived from the siliciclastic detritus, while in the NC, both elements were mostly derived from seawater, most likely sourced from hydrothermal venting fluids. In the SGB, the significant enrichment of chromium in the two SGB jasper samples suggests an influx of chromium derived from hydrothermal venting fluids. For the rest of the SGB samples, most of the chromium was probably derived from the siliciclastic phase with a minor influx from hydrothermal venting fluids. Most of the scandium in the SGB was derived from the siliciclastic phase. The lack of higher Cr/Al values for the shallow water meta-iron formation samples compared to the siliciclastic Cr/Al ratios suggests that there were low values of authigenic chromium supplied to the ancient ocean, indicating an anoxygenic atmosphere.

4.9 Group 6, 7 and 8 Elements, Transition Metals: Mo, Mn and Fe

Manganese is a common element associated with modern hydrothermal venting systems. However, Peter (2003) determined that manganese in the meta-iron formations from the Bathurst

Camp, which are part of the Heath Steele greenstone belt in New Brunswick, was derived from siliciclastic detritus. Therefore, manganese can be derived from both hydrothermal venting fluids and siliciclastic detritus. To determine the source of manganese for the meta-iron formations of this study, manganese was plotted on bivariate plots with different elements.

Figure 4.40 is a geochemical bivariate plot of aluminum versus manganese. The data sets are separated into two distinct regions. Region 1 contains samples from BG and LSJ while region 2, which has higher manganese values than region 1, contains samples from NC. Most of the SGB samples plot in between region 1 and 2. LSJ magnetite, LSJ hematite, SGB magnetite and SGB jasper samples plot at relatively horizontal correlation curves. NC magnetite and NC magnetite/grunerite have negatively sloping correlations, while all the BG and NC chert samples have positive sloping correlations. The higher Mn/Al ratios for the NC samples compared to the region 1 samples and the lack of a positive linear correlation that extends towards the origin suggests that there was a
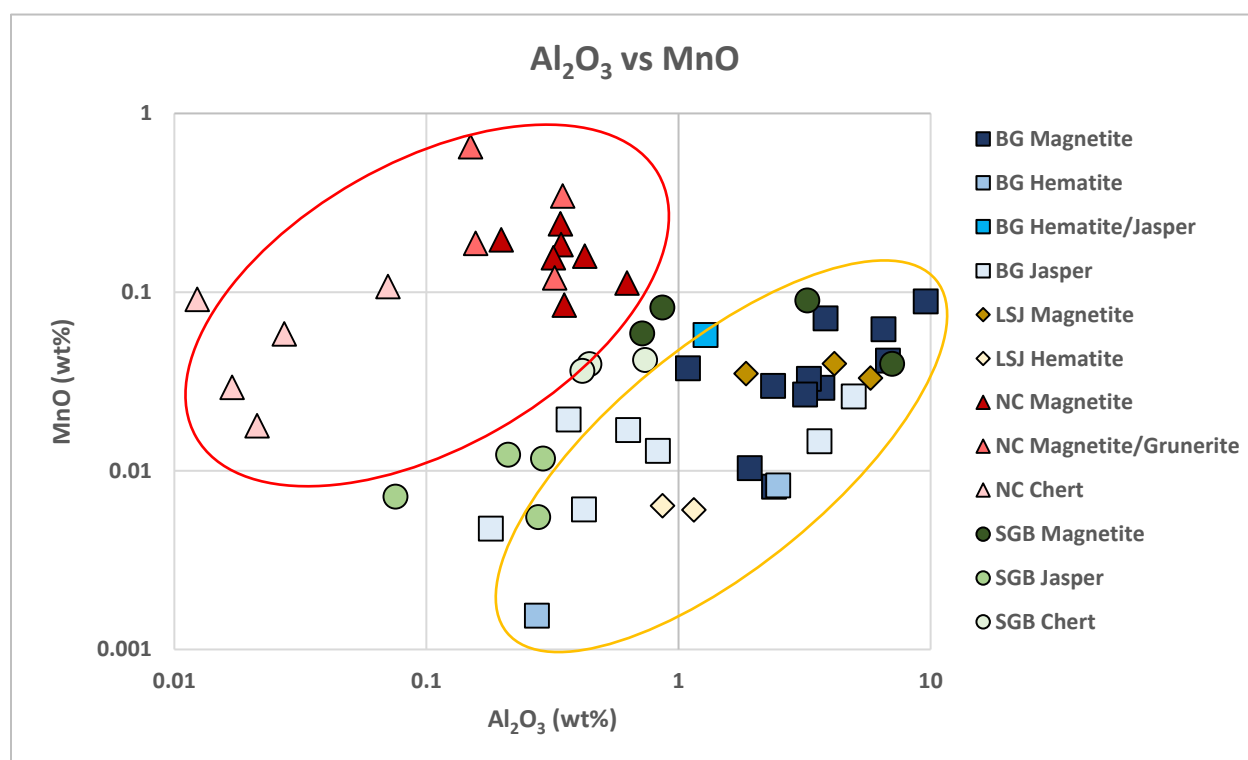
Figure 4.40: A logarithmic bivariate plot of aluminum versus manganese. Region 1 (yellow) contains samples from the BG and LSJ and region 2 contains samples from NC. Most of the SGB samples are plotted in between regions 1 and 2. Significantly, most of the deeper water meta-iron formation samples have higher Mn/Al values than shallow water meta-iron formation samples.

secondary influx of manganese from a non-siliciclastic source. Significantly, the relationship between

manganese and aluminum in Figure 4.40, resembles the relationship between calcium and

aluminum in Figure 4.23. Therefore, manganese and calcium were plotted against each other to

determine the source of manganese and mobility during post-depositional alteration.

Manganese and calcium were normalized over aluminum to subtract the effects of siliciclastic

contamination (Figure 4.41). Overall, there is a positive linear correlation between MnO/Al_2O_3 and

CaO/Al_2O_3, except for one BG hematite, all the SGB jasper and all the SGB chert samples, which

deviate from the overall correlation trend. Looking closer at the sample categories individually, LSJ

magnetite and BG magnetite cluster around similar MnO/Al_2O_3 and CaO/Al_2O_3 values. The clustering

of the BG and LSJ samples suggests manganese and calcium were derived from the siliciclastic

phase. Interestingly, the NC magnetite samples plot as a horizontal trend and the NC chert and NC

magnetite-grunerite plot as a positive linear correlation at higher CaO/Al_2O_3 and MnO/Al_2O_3 values
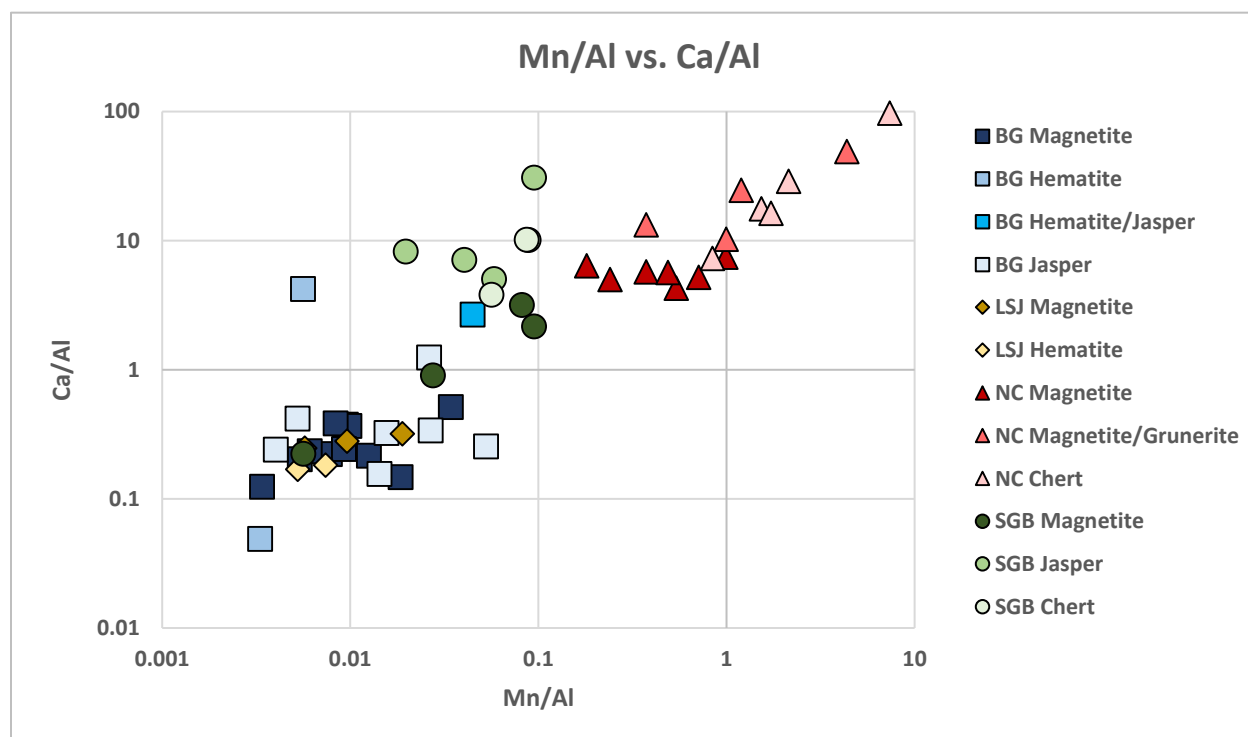
Figure 4.41: A logarithmic bivariate plot of MnO/Al_2O_3 vs CaO/Al_2O_3. Overall, there is a positively sloping correlation between calcium and manganese. BG and LSJ magnetite samples cluster together suggesting that most of the manganese was derived from the siliciclastic phase. The lack of clustering for the NC and SGB meta-iron formation samples suggests that manganese was derived from a non-siliciclastic source.

than the NC magnetite. The SGB magnetite plot at as a positively trending correlation, while the SGB

jasper and SGB chert samples are scattered. The lack of clustering for the deeper water meta-iron

formation samples suggests that manganese was derived from a non-siliciclastic source in the NC

and SGB.

To determine the sources of manganese to the meta-iron formations logarithmic bivariate plots

of MnO/Al_2O_3 versus CaO/Al_2O_3 for the BG and NC were plotted with their associated siliciclastic

lithologies (Figure 4.42, 4.43). In Figure 4.42, the BG metagreywacke samples cluster around the BG

meta-iron formation samples, which strengthens the theory that both calcium and manganese were

derived from the siliciclastic phase. The slight variations of MnO/Al_2O_3 and CaO/Al_2O_3 for the BG

jasper and BG hematite samples might have been caused by mobility during post-depositional

alteration. However, the points that scatter at higher CaO/Al_2O_3 and MnO/Al_2O_3 values than the BG
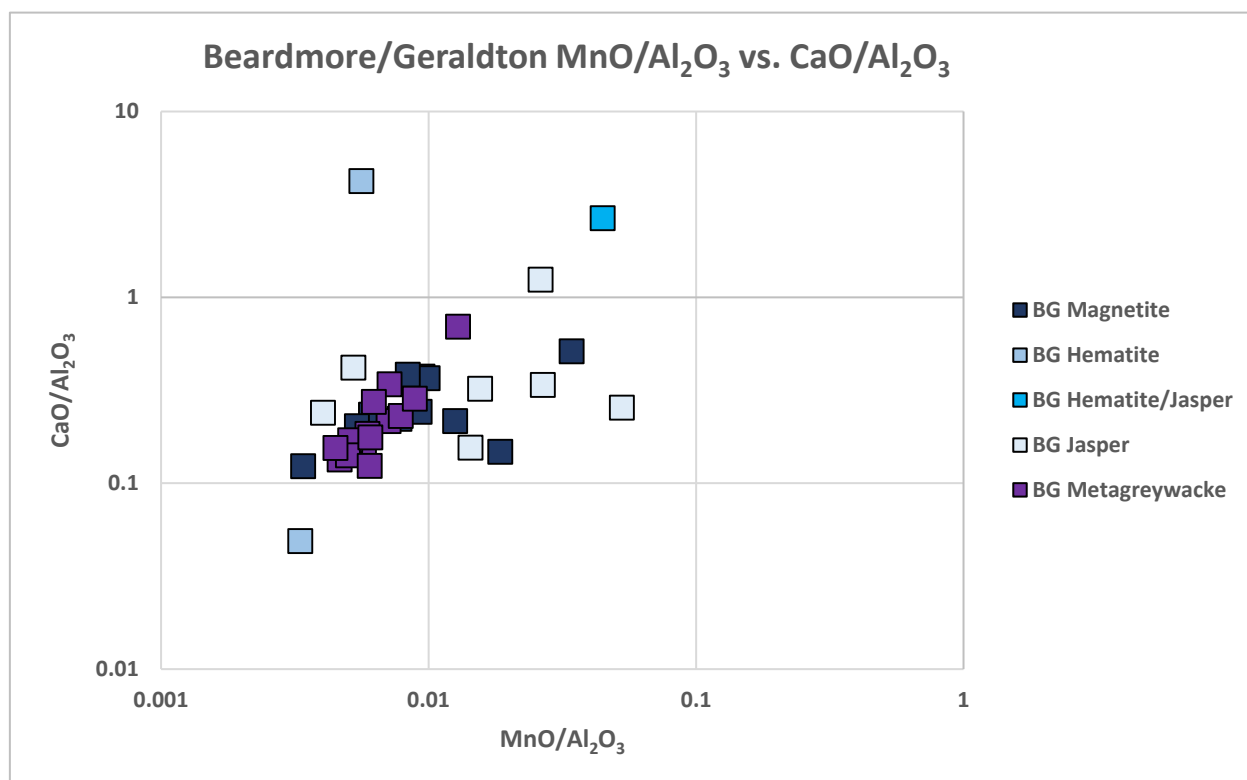
Figure 4.42: A logarithmic bivariate plot of MnO/Al_2O_3 versus CaO/Al_2O_3 for the BG meta-iron formation samples and associated siliciclastic lithologies. The similar values for the BG magnetite and BG metagreywacke indicate that calcium and manganese were mostly derived from the siliciclastic phase. The scattering nature of the BG jasper and BG hematite samples record the presence of a non-siliciclastic influx of manganese and calcium during deposition or indicate that calcium and manganese were slightly mobile during post-depositional alteration.

metagreywacke could have also been subjected to an influx of manganese and calcium from seawater during deposition. Since the BG hematite and BG jasper samples have lower aluminum values compared to the BG magnetite samples and have more scattered MnO/Al_2O_3 and CaO/Al_2O_3 values, these samples may be preserving an influx of manganese from seawater that can only be seen at lower degrees of siliciclastic contamination. The LSJ samples plot at similar MnO/Al_2O_3 and CaO/Al_2O_3 values as the BG magnetite samples (Figure 4.42), strongly suggesting that most of the manganese and calcium was derived from the siliciclastic phase.

In Figure 4.43, the CaO/Al_2O_3 values are similar for both BG metagreywacke and NC biotite-garnet schist, while the MnO/Al_2O_3 values were slightly higher for the NC source rocks. However, the NC meta-iron formation samples plot at much higher MnO/Al_2O_3 and CaO/Al_2O_3 values compared to the NC biotite-garnet schist. Since there is a significant increase in the CaO/Al_2O_3 and MnO/Al_2O_3
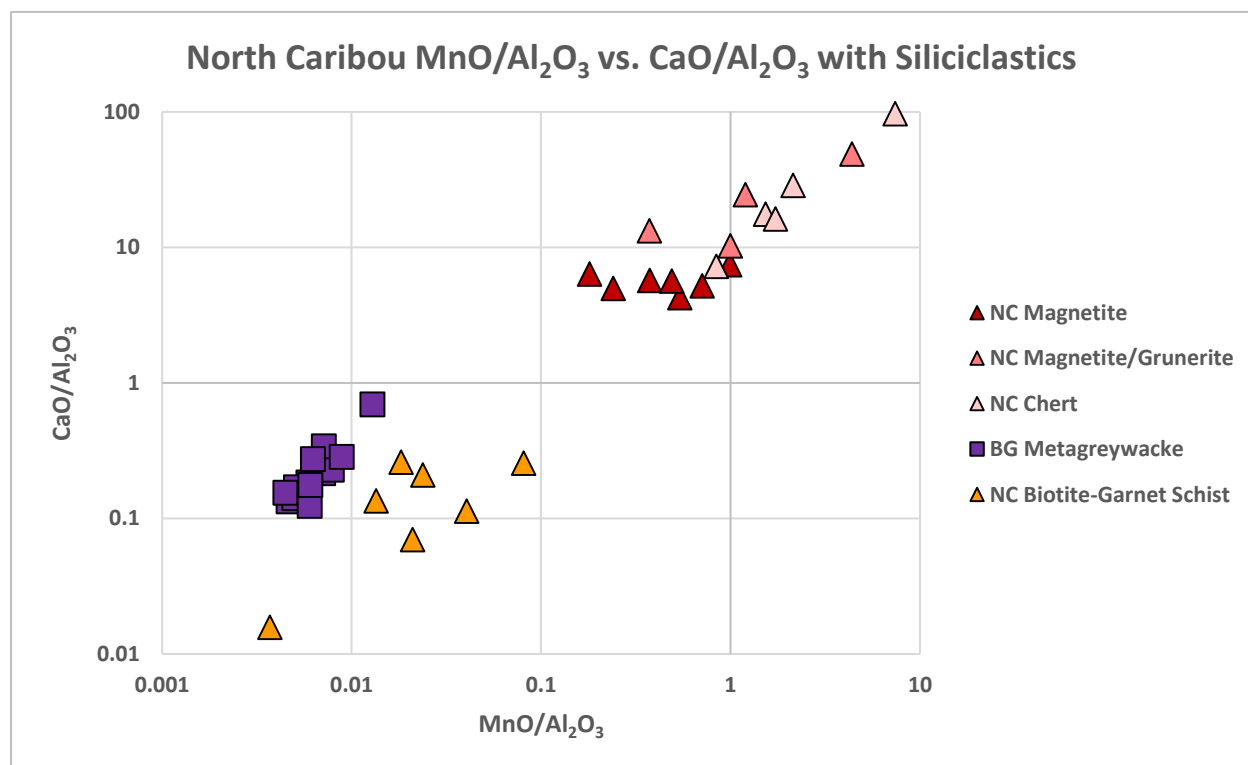
Figure 4.43: A logarithmic bivariate plot of MnO/Al_2O_3 versus CaO/Al_2O_3 for the NC meta-iron formation plotted with the siliciclastic lithologies from the NC and BG. The NC biotite-garnet schist plots at similar CaO/Al_2O_3 values as the BG metagreywacke samples, but at slightly higher MnO/Al_2O_3 values in the NC rocks, indicating that the Mn/Ca ratio was higher for the source rocks in the NC relative to the BG. The enrichment of manganese and calcium in the meta-iron formation relative to the siliciclastic lithologies indicates an influx of both calcium and manganese was sourced from a non-siliciclastic source..

ratios for all the NC meta-iron formation samples relative to the BG biotite-garnet schist, there must have been an influx of calcium and manganese during deposition rather than post-depositional alteration because the NC biotite-garnet schist was not affected by a calcium and manganese influx.

Since it was determined that iron was derived from black smoker hydrothermal venting fluids, manganese and total iron were plotted against each other on a logarithmic bivariate plot to determine if manganese was also derived hydrothermal venting fluids (Figure 4.44). The NC samples, as well as the SGB jasper and SGB magnetite samples display somewhat of a positive, scattered, linear correlation between total iron and manganese indicating that both elements were mainly derived from the same source and behaved relatively similar during post-depositional alteration. Earlier it was determined that most of the manganese in the BG and LSJ meta-iron formations was derived from the siliciclastic phase. The BG magnetite and BG hematite samples show a scattering of points indicating that iron and manganese were derived from different sources. Horizontal correlations for the LSJ samples indicate that iron and manganese were not related to each other. This confirms that manganese in the BG and the LSJ was mostly derived from the siliciclastic phase.

LSJ hematite, LSJ magnetite, NC magnetite, NC magnetite/grunerite, BG hematite, BG jasper, BG magnetite, SGB magnetite have large total iron values, but varying manganese values. Significantly, LSJ hematite and BG hematite have the lowest manganese values; BG magnetite and LSJ magnetite have intermediate manganese values; and SGB magnetite, NC magnetite and NC magnetite/grunerite have the highest manganese values. The higher values for the deeper water meta-iron formation samples suggests that there is an enrichment of manganese in the deeper water setting, mostly likely caused by the influx of manganese from hydrothermal venting fluids. The BG and LSJ magnetite-dominated samples plot at higher manganese values than the hematite-

dominated samples from their respective locations. This is most likely caused by higher degrees of

siliciclastic contamination in the magnetite-dominated samples relative to the hematite-dominated
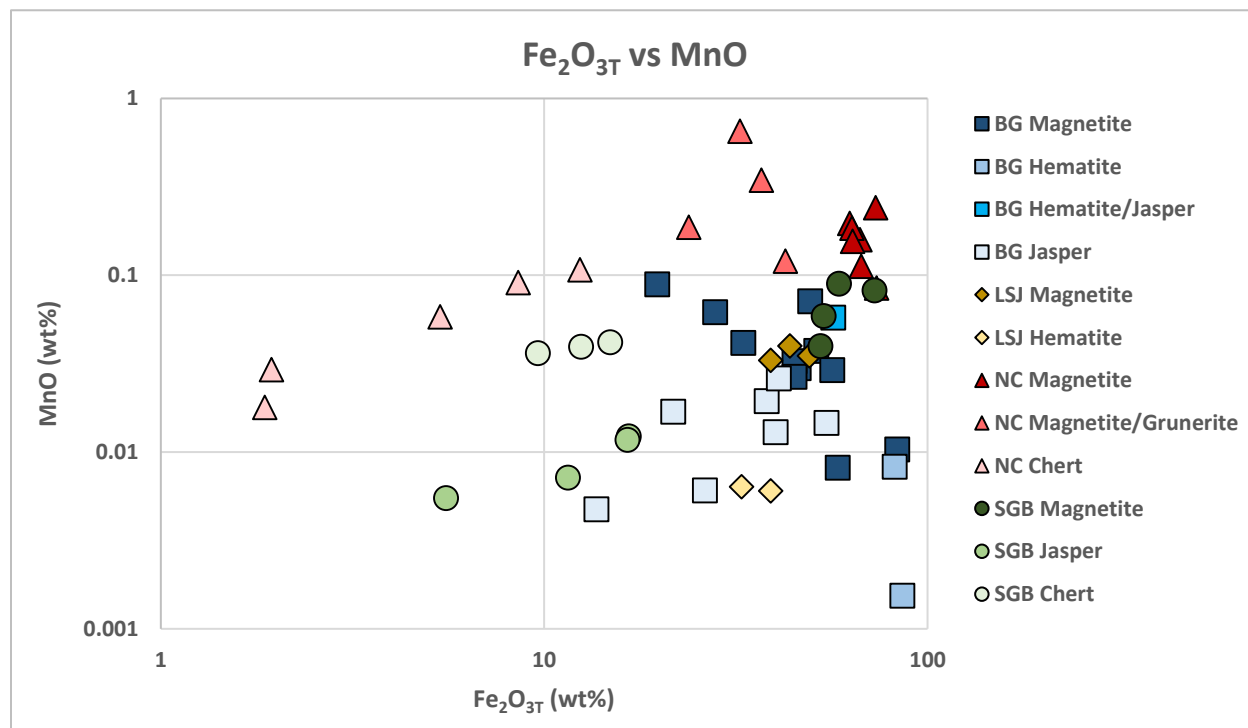
samples.

Figure 4.44: A logarithmic bivariate plot of total iron versus manganese. The NC and SGB samples show a scattered, positive linear correlation. Most of the BG and LSJ samples plot at lower manganese values than the NC and SGB magnetite-dominated samples at relatively similar total iron values. This indicates that the deeper water environment was enriched in manganese relative to the shallow water setting, suggesting that hydrothermal vents were the source for the influx of manganese to the oceans.

To determine the effects of siliciclastic contamination, total iron and manganese were

normalized over aluminum and plotted against each other. Overall, when subtracting the effects of

the siliciclastics on the Fe_2O_{3T}/Al_2O_3 versus MnO/Al_2O_3 plot (Figure 4.45), iron and manganese have a

positive linear relationship. At higher aluminum levels, the correlation curve of the data set

decreases in slope and flattens out. At lower degrees of siliciclastic contamination, the correlation

between Fe_2O_{3T}/Al_2O_3 and MnO/Al_2O_3 is stronger, indicating that manganese and total iron behaved

similarly during post-depositional alteration and were derived from the same sources.

Since, manganese has a stronger relationship with total iron at lower degrees of siliciclastic contamination, iron and manganese for NC and SGB were derived from seawater, affected by black smoker hydrothermal venting fluids. At lower levels of Fe_2O_{3T}/Al_2O_3 and MnO/Al_2O_3, the BG and LSJ samples have fairly similar Mn/Al_2O_3 ratios and varying Fe_2O_{3T}/Al_2O_3 ratios, suggesting that manganese was mainly derived from the siliciclastic phase. The higher manganese values in the deeper water meta-iron formations compared to the shallow water meta-iron formations suggests that the Archean ocean's deeper water environment was more enriched in manganese than the shallow water environment, suggesting a manganese geochemical gradient in the ancient ocean. The positive correlation between total iron and manganese indicates that the manganese enrichment in the deeper water setting was caused by an influx from hydrothermal venting fluids.
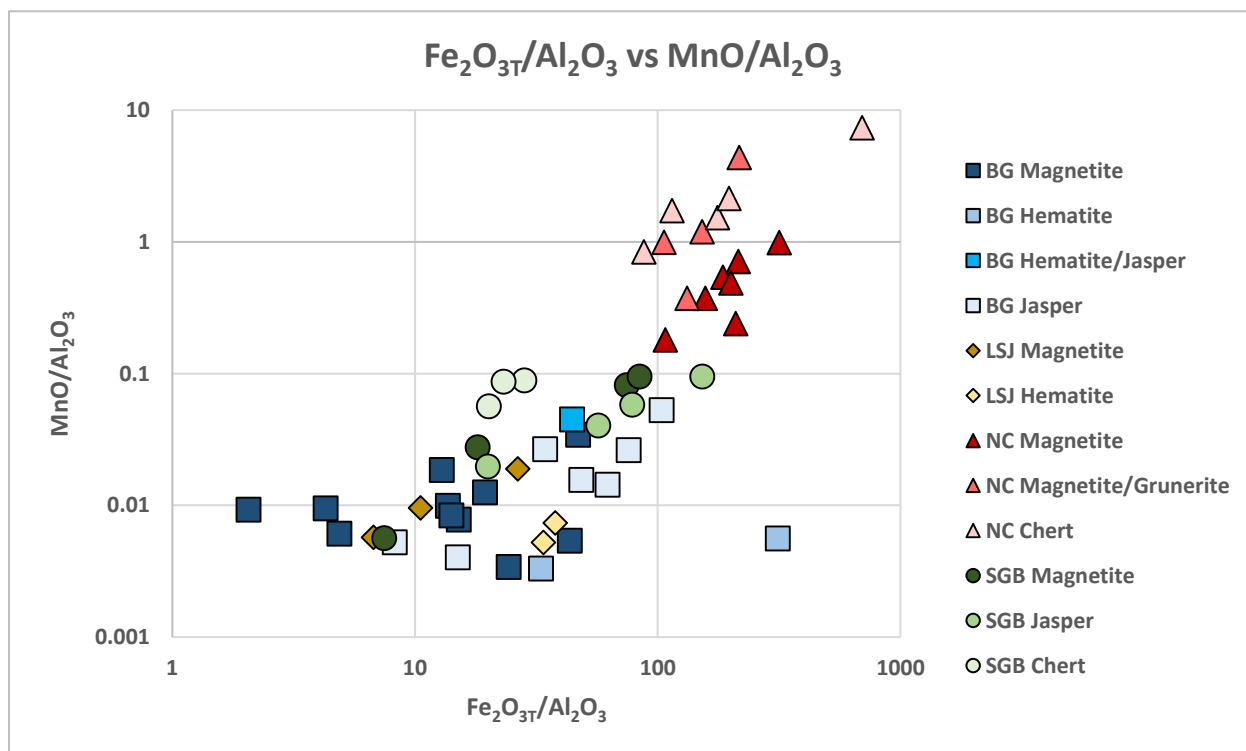
Figure 4.45: A logarithmic bivariate plot of Fe_2O_{3T}/Al_2O_3 vs MnO/Al_2O_3. At lower degrees of siliciclastic contamination (NC and SGB) the slope of the correlation is positively sloping, while at higher degrees of siliciclastic contamination (BG and LSJ), the slope of the correlation curve flattens out. This suggests that the manganese from the BG and LSJ was derived from the siliciclastic phase and the higher manganese values for the deeper water meta-iron formation suggests that manganese was derived from hydrothermal venting fluids.

Molybdenum values for the chemical analysis were very scarce due to the low amounts of this element in the meta-iron formation samples. When plotting molybdenum versus aluminum, an overall definite correlation does not exist (Figure 4.46). Looking at the BG magnetite and SGB magnetite samples, they form a negatively sloping correlation suggesting that molybdenum was derived from a non-siliciclastic source. Although, LSJ hematite and LSJ magnetite only have 1 point each, these samples plot with the BG magnetite samples. There is no overall trend for the BG samples.
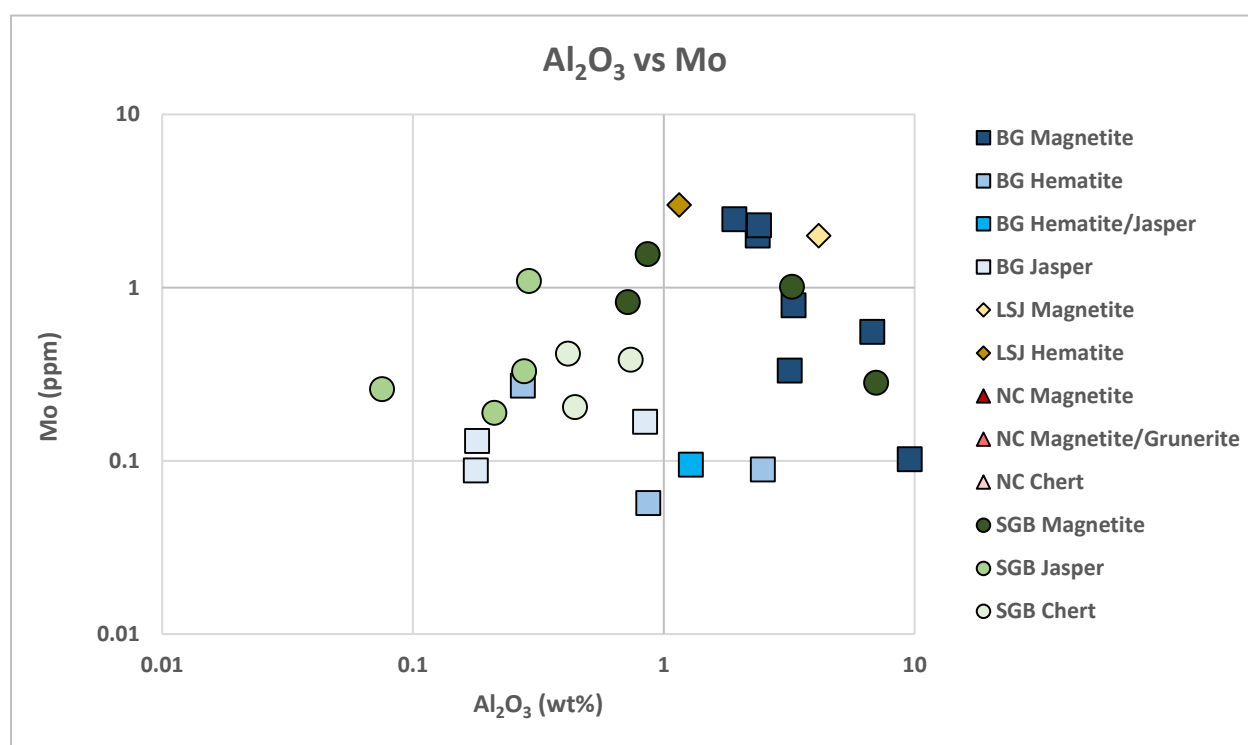
Figure 4.46: A logarithmic bivariate plot of aluminum vs molybdenum. The negative relationship between molybdenum and aluminum for the iron oxide-dominated laminae suggests that molybdenum was derived from a non-siliciclastic source.

Molybdenum isotopes are used to determine the presence of photosynthetic bacteria on ancient Earth (Planavsky et al., 2014). MoO_4^{2-} is highly unreactive in oxygenated waters and has a residence time of 440 ka, indicating that it can be dispersed homogeneously throughout the ocean (Arnold et al., 2004; Kurzweil et al., 2016). Molybdenum can precipitate out of seawater in three different ways: forming H_2S in anoxic, sulphuric conditions and adsorbing onto Fe-oxyhydroxides or

Mn-oxyhydroxides, which can affect the δ^{98}Mo value (Arnold et al., 2004; Planavsky et al., 2014; Kurzweil et al., 2016). When Mo forms with H_2S, there is little net fractionation of the molybdenum isotope so the δ^{98}Mo value is similar to the δ^{98}Mo of the ocean (Arnold et al., 2004). However, preferential sorption of the lighter molybdenum isotope onto Fe- and Mn-oxyhydroxides fractionates the molybdenum isotope by -1.1‰ and -2.7‰, respectively (Planavsky et al., 2014). The large fractionation of the lighter molybdenum isotope is caused by the change from tetrahedral to octahedral coordination during adsorption of Mo onto Mn-oxyhydroxides (Kurzweil et al., 2016). To precipitate out Mn-oxyhydroxides, the water column needs to be undersaturated with iron and sulphide (Planavsky et al., 2014). Also, there requires a presence of dissolved oxygen in the water to oxidize Mn^{2+} (Planavsky et al., 2014). Therefore, if there is evidence of Mn^{2+} oxygenation, then there were oxygen producing photosynthetic bacteria in the ancient oceans (Planavsky et al., 2014).

The iron oxide-dominated samples show a negative correlation with aluminum indicating that molybdenum was derived from a non-siliciclastic source. Since molybdenum can precipitate out by reacting with H_2S or adsorbing onto Fe- and Mn-oxyhydroxides, molybdenum was plotted against manganese and total iron. Since the dominant iron phase in these meta-iron formations are iron oxides not pyrite, a euxinic depositional environment is highly unlikely. Interestingly, when manganese was plotted against molybdenum (Figure 4.47), there is a negative correlative trend for the BG magnetite samples and a very weak positively trending correlation for the SGB magnetite samples. Earlier it was determined that manganese from the BG was derived from the siliciclastic phase while in the SGB it was derived from hydrothermal venting fluids. Therefore, the positive correlation with the SGB samples and negative relationship with the BG samples indicates that molybdenum was derived from hydrothermal fluids and/or continental runoff, contributing to the molybdenum in seawater and precipitated out by adsorbing onto Mn-oxyhydroxides.
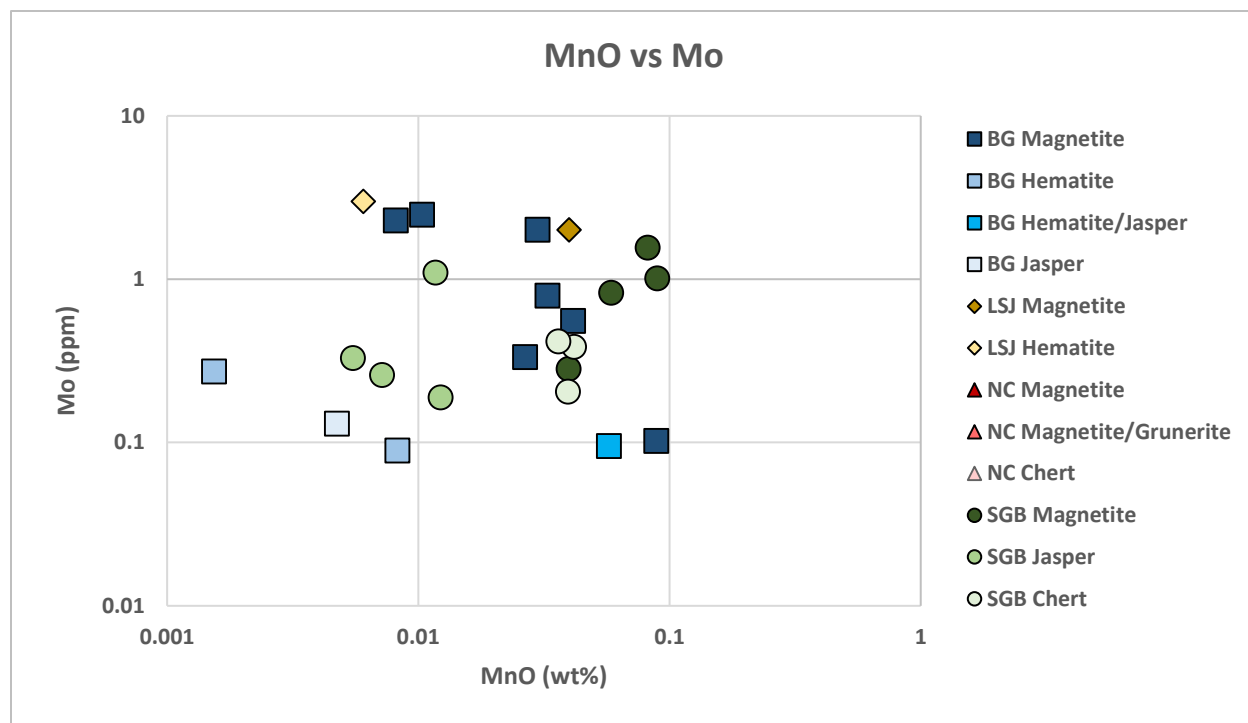
Figure 4.47: A logarithmic bivariate plot of manganese plotted against molybdenum. Since manganese was interpreted to be derived from the siliciclastic phase in the BG, the negative correlation between molybdenum and manganese for the BG magnetite samples indicates that molybdenum was not derived from the siliciclastic phase. Manganese in the SGB was interpreted to be derived from the hydrothermal phase therefore, the positive correlation for the SGB magnetite samples suggests that molybdenum may have been derived from seawater, through the derivation from continental runoff.

In Figure 4.48, total iron was plotted against molybdenum. BG magnetite and SGB magnetite and BG plot as a positively sloping correlation and the LSJ samples again plot with BG magnetite, while the rest of the samples are scattered. Interestingly, the magnetite-dominated samples have a positive relationship between iron and molybdenum, while there is no correlation with the jasper- and chert-dominated samples. If molybdenum was precipitated out of seawater, there should be a positive relationship with iron for all the samples. The positive correlation between molybdenum and total iron for only the magnetite-dominated samples suggests that molybdenum adsorbed onto Fe-oxyhydroxides during deposition. Molybdenum in the oceans was derived from weathered terrestrial molybdenum-bearing sulfides (Arnold et al., 2014).
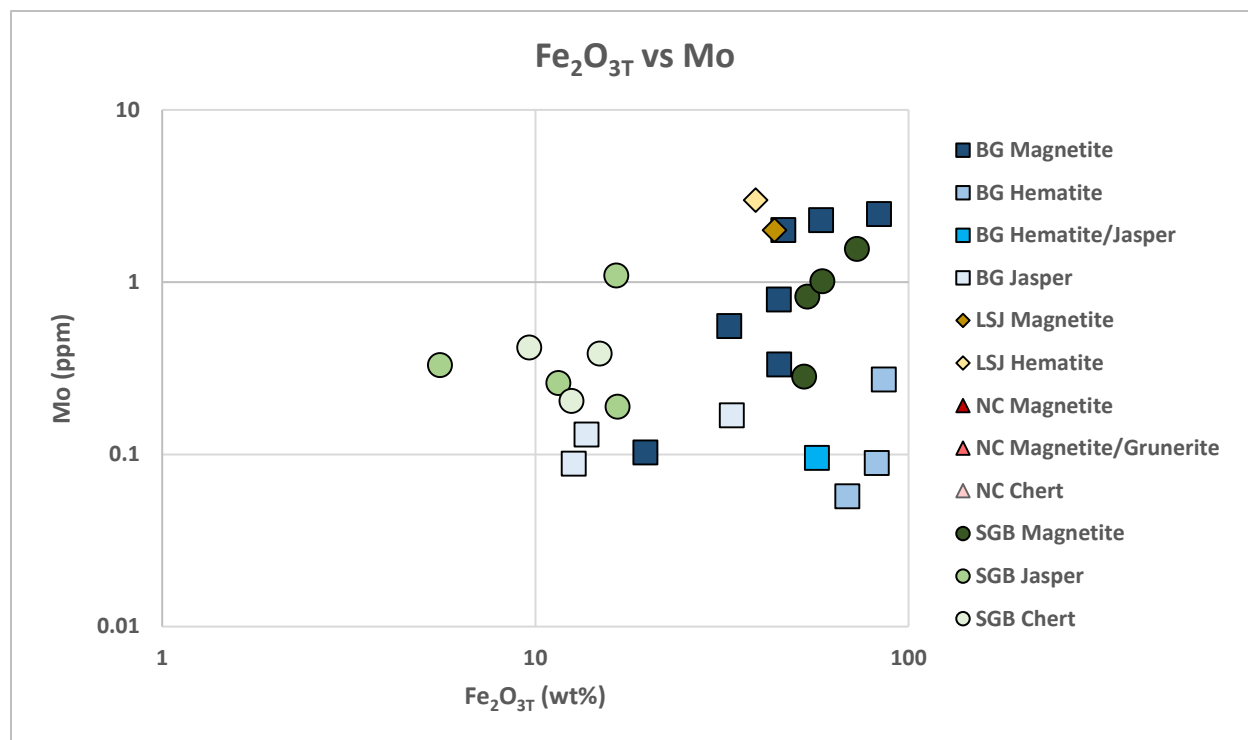
Figure 4.48: A logarithmic bivariate plot of total iron versus molybdenum. The iron oxide-dominated samples (BG magnetite, SGB magnetite) have a positive relationship between total iron and molybdenum. This indicates that molybdenum adsorbed onto Fe-oxyhydroxides during deposition.

In summary, most of the manganese in the shallow water meta-iron formations (BG and LSJ) was derived from siliciclastic detritus. Hydrothermal-derived manganese were major components of the deeper water meta-iron formations (NC and SGB). The lack of significant manganese enrichment in the shallow water meta-iron formations from seawater suggests that there was a manganese geochemical gradient in the ancient ocean. Manganese was enriched in the deeper water setting relative to the shallow water setting due to the proximity with hydrothermal venting fluids, which was the source for manganese to the Archean ocean. Molybdenum was most likely derived from seawater, sourced from continental runoff and adsorbed onto iron or manganese oxyhydroxides during deposition.

When determining mineral composition of the phases in the meta-iron formation samples, manganese only occurred in very trace amounts in carbonates (ankerite, dolomite and siderite) from LSJ and BG. Manganese also occurred in trace amounts in stilpnomelane crystals from SGB. From the

geochemical analysis, manganese did not exceed 0.1 weight percent for the SGB, LSJ and BG

samples and did not exceed one weight percent for the NC samples. This suggests that the

manganese influx in the meta-iron formation was relatively minor compared to the other major

elements.

4.10 Group 10, 11 and 12 Elements, Transition Metals: Ni, Cu and Zn

Nickel, copper and zinc were the group 10, 11 and 12 elements obtained from the geochemical

analysis. Peter (2003) sampled meta-iron formations from the Heath Steele belt and determined

that nickel was derived from the siliciclastic phase, while copper and zinc were derived from

hydrothermal venting fluids. These elements were plotted on bivariate plots to determine the

provenance and investigate their mobility during post-depositional alteration.

Nickel was plotted against aluminum to determine the relationship with the siliciclastic phase

(Figure 4.49). Interestingly, two positively sloping correlations exist, and they are divided into region

1 and region 2. Region 1 contains BG hematite, half of the BG jasper and BG magnetite samples, SGB

magnetite, SGB chert and two of the SGB jasper samples. Overall, the region 1 samples form a

positively sloping correlation curve that extends towards the origin. However, the data points are

more scattered at nickel contents below five ppm nickel. Region 2 contains all the LSJ samples, the

other half of the BG jasper and BG magnetite samples, two SGB jasper and all the samples from NC.

This data set forms a lower sloping, near horizontal positive correlation that does not extend towards

the origin. Overall, the region 2 samples have higher Ni/Al_2O_3 ratios than the region 1 samples. The

higher Ni/Al_2O_3 values for the NC samples could have been inherited from the source siliciclastic

phase or, alternatively, there was an influx of nickel from a non-siliciclastic source.
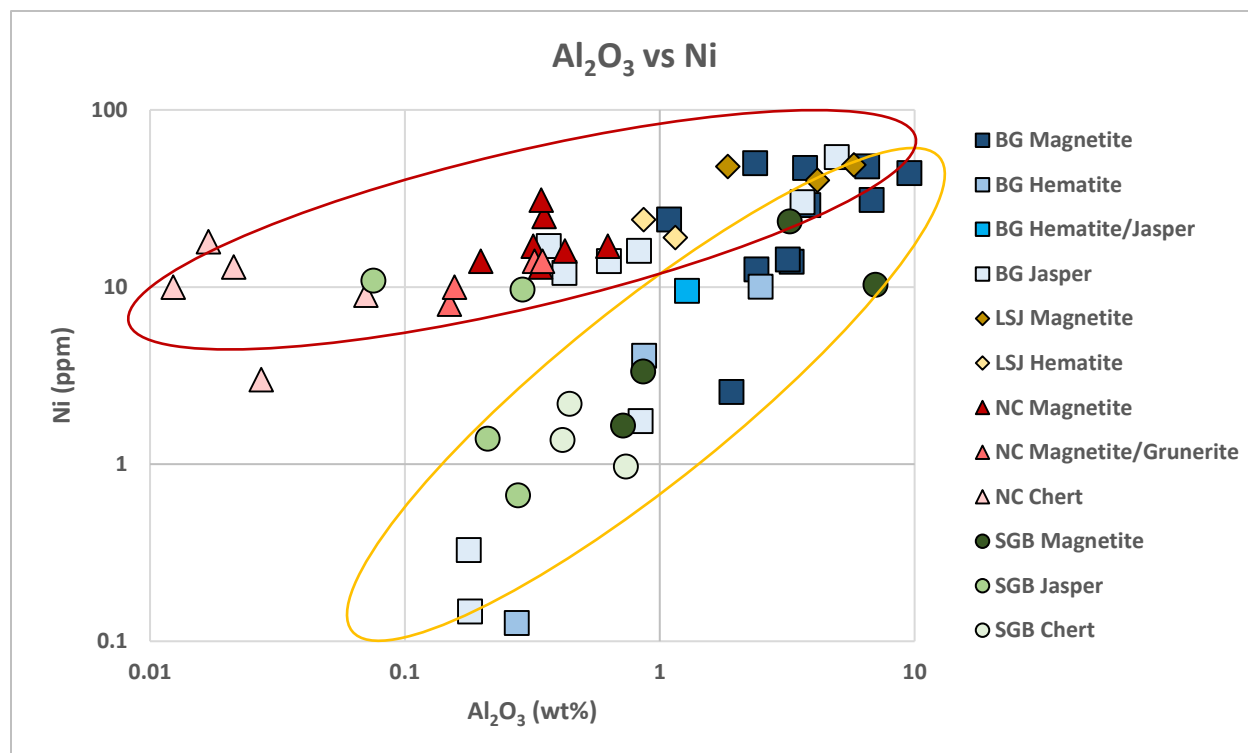
Figure 4.49: A logarithmic bivariate plot of aluminum plotted against nickel. Region 1 (yellow) shows an overall positively sloping correlation that extends towards the origin. The trend of the region 2 samples (red) does not extend towards the origin and the Ni/Al$_2$O$_3$ values are higher than region 1.

Siliciclastic lithologies from the NC were plotted with the NC and BG meta-iron formation samples in Figure 4.50. The BG metagreywacke samples were not plotted because most of the nickel concentrations were below detection limits (Fralick and Barrett, 1991). Significantly, the NC biotite-garnet schist samples plot near the convergence of the two regions at high aluminum values. Since the NC biotite-garnet schist samples cluster, the nickel in the siliciclastics remained immobile during post-depositional alteration. The NC meta-iron formations have a shallower correlation curve which does not extend towards the origin. Also, the Ni/Al ratio for the NC meta-iron formation samples is much higher than the NC biotite-garnet schist. Therefore, there was an influx of nickel from a non-siliciclastic source for the NC samples and possibly the BG, LSJ and SGB samples that plot with the NC meta-iron formations (region 2). The source of nickel was most likely seawater.
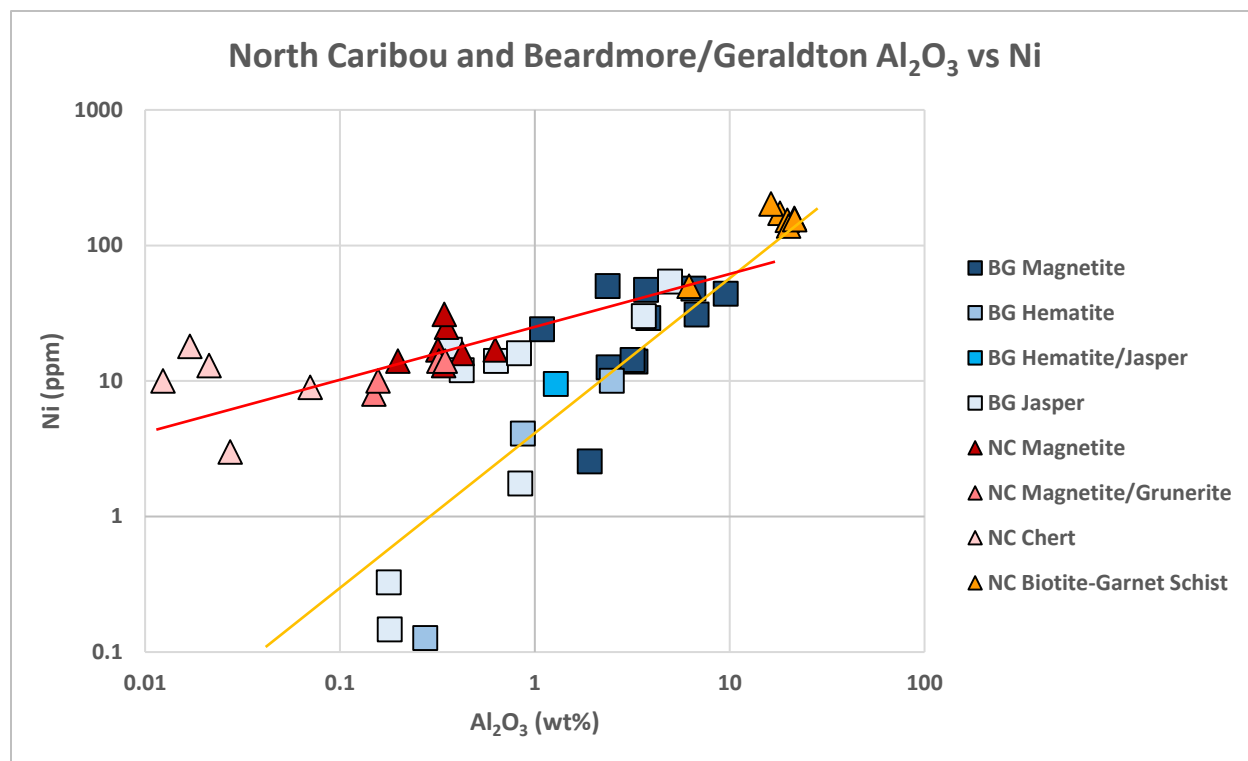
Figure 4.50: A logarithmic bivariate plot of aluminum vs nickel for the BG and NC meta-iron formation samples plotted with the siliciclastics from NC. The NC biotite-garnet schist samples form a linear correlation with most of the BG meta-iron formations samples from region 1 and the correlation curve extends towards close to the origin (yellow), which indicates that the nickel in these rocks was most likely derived from the siliciclastic phase. The correlation curve for the NC meta-iron formation samples and the rest of the region 2 samples (red) has a shallower slope that does not extend towards the origin. Therefore, a significant amount of nickel for the region 2 samples was derived from a non-siliciclastic source during deposition.

Scientists have been studying nickel abundances in meta-iron formation to determine the nickel concentrations of the ancient oceans (Konhauser et al., 2009; Bekker et al., 2014). Nickel can adsorb onto iron-oxyhydroxides during the deposition of meta-iron formation (Bekker et al., 2014). The amount of adsorbed nickel onto the iron-oxyhydroxides is proportional to the amount of dissolved nickel in the ocean (Bekker et al., 2014). Although, if there is high dissolved silica content in the ocean, silica will outcompete nickel for adsorption spots on the iron-oxyhydroxides and yield lower Ni/Fe values that do not reflect the chemistry of the ocean (Konhauser et al., 2009).

Nickel was plotted against total iron to determine if the Ni/Fe ratio from ancient seawater was preserved in the meta-iron formation (Figure 4.51). Significantly, in each study location, there are different trends and the data points are mostly scattered, suggesting that nickel did not adsorb on

the iron oxyhydroxides during deposition. However, it was determined earlier that there is nickel in some of the meta-iron formation samples derived from siliciclastic detritus and some samples were derived from another non-siliciclastic source during deposition.
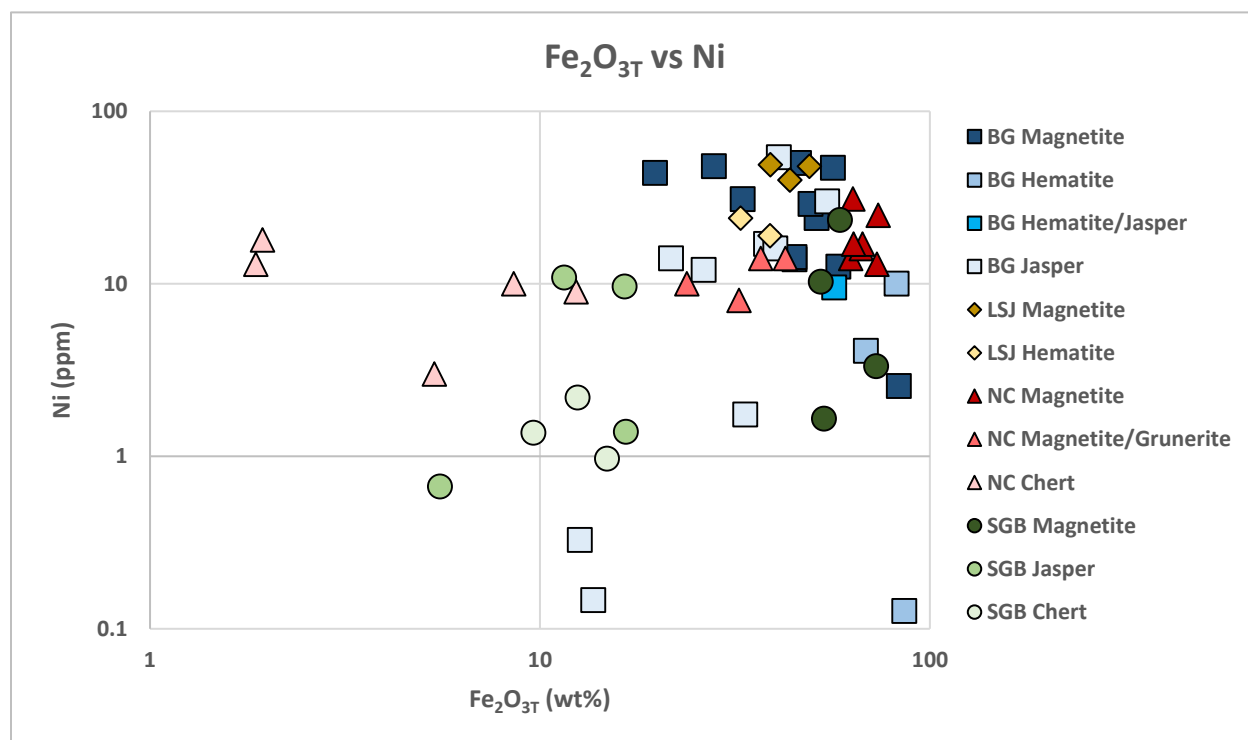
Figure 4.51: A logarithmic bivariate plot of total iron versus nickel. Overall there is no definite correlation between total iron and nickel suggesting that the Ni/Fe ratio of the ancient ocean was not preserved. However, if nickel was derived from different sources, a siliciclastic and non-siliciclastic source during deposition, the lack of correlation might be caused by siliciclastic-derived nickel contamination.

To subtract the effects of siliciclastic contamination, nickel and total iron are normalized over aluminum and plotted against each other (Figure 4.52). The region 2 samples from Figure 4.49, plot as a positive linear correlation, except for the SGB chert samples, while the region 1 samples are scattered at lower Ni/Al_2O_3 values. Significantly, it was determined earlier that there was an influx of nickel from a non-siliciclastic source for the region 2 samples. The positive linear relationship between Ni/Al_2O_3 and Fe_2O_{3T}/Al_2O_3 suggests that the nickel not derived from the siliciclastic phase (region 2), behaved similarly to total iron during deposition and post-depositional alteration. Therefore, this suggests that the influx of nickel for the region 2 samples was caused by the adsorption of nickel onto iron-oxyhydroxides from seawater during the precipitation of iron-

oxyhydroxides, which preserved the dissolved nickel content of the ancient ocean. Significantly, the region 2 jasper- and chert-dominated samples have the same Ni/Fe ratio as the region 2 magnetite- and hematite-dominated samples, except for the NC chert samples, suggesting that dissolved silica probably did not affect the amount of nickel adsorption. Since there is a positive correlation between the Ni/Al_2O_3 and Fe_2O_{3T}/Al_2O_3 for the region 2 meta-iron formation samples, the Ni/Fe ratio composition for the shallow and deep ocean was uniform, suggesting a well mixed ocean at the time-scale of nickel residence time and meta-iron formation deposition.
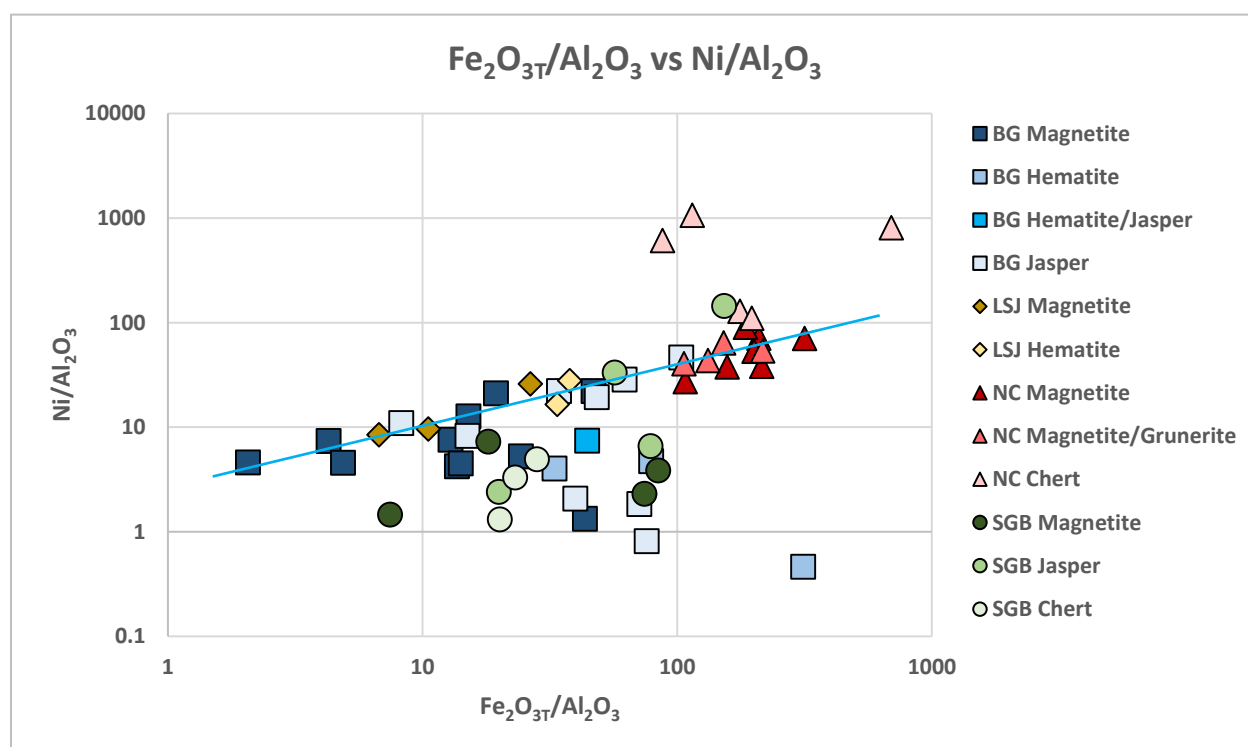
Figure 4.52: A logarithmic bivariate plot of Fe_2O_{3T}/Al_2O_3 versus Ni/Al_2O_3. The positive relationship (blue line) between nickel and total iron for the region 2 samples indicates that nickel adsorbed onto iron oxyhydroxides during deposition. Similar Ni/Fe ratios for the shallow and deep water meta-iron formations indicates that the oceans were very well mixed with nickel. The positive relationship also indicates that total iron and nickel behaved similarly during post-depositional alteration. When subtracting the meta-iron formation samples that have Ni/Al_2O_3 ratios lower than 2.5, the region 1 samples form a horizontal correlation, suggesting that nickel in these samples was mostly derived from the siliciclastic phase and remained isochemical during post-depositional alteration.

Region 1 samples from BG form a negative trending correlation (Figure 4.53). However, the meta-iron formation samples with less than 2.5 Ni/Al_2O_3 have nickel values that are approaching the lower detection limits. When looking at the samples that are above Ni/Al_2O_3 values of 2.5, most of

the samples plot near the same Ni/Al_2O_3 value (4), indicating that the Ni/Al_2O_3 ratio was derived from the siliciclastic phase and remained relatively isochemical during post-depositional alteration.

Zinc and aluminum were plotted against each other to determine the relationship between zinc and the siliciclastic phase (Figure 4.53). Overall, there is a moderate, strong, positive correlation between zinc and aluminum for the meta-iron formation samples. However, the LSJ and SGB samples have higher zinc values than most of the NC and BG samples. Also, the correlation of the NC and BG meta-iron formation samples is stronger than the LSJ and SGB samples, which are more scattered. This suggests that in the SGB and LSJ there was an influx of zinc from a non-siliciclastic source or zinc was mobile during post-depositional alteration.
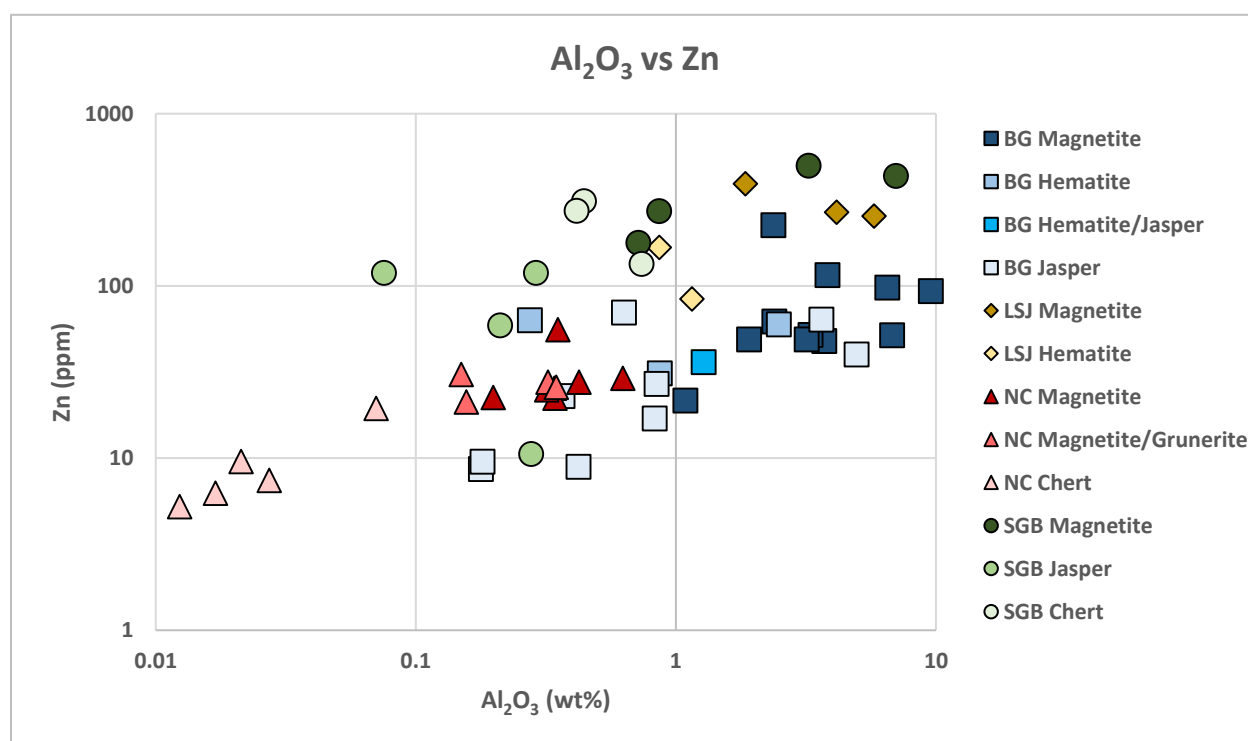
Figure 4.53: A logarithmic bivariate plot of aluminum versus zinc. Overall, there is a moderately strong positive correlation between aluminum and zinc. The scattering of the LSJ and SGB samples suggests and influx of zinc from a non-siliciclastic source during deposition or zinc was mobile during post-depositional alteration.

Figure 4.54 is a logarithmic bivariate plot of zinc plotted against aluminum for the meta-iron formation and siliciclastic lithologies from BG. The BG metagreywacke samples plot at similar zinc concentrations as the meta-iron formation samples. However, the aluminum concentrations for the

meta-iron formations are lower than the siliciclastics. Therefore, the Zn/Al ratio for the siliciclastic lithologies is lower than in the meta-iron formation. This suggests that there was an influx of zinc from a non-siliciclastic source for the BG samples. Also, since the BG metagreywacke cluster, zinc was remained immobile during post-depositional alteration in both metasedimentary lithologies.
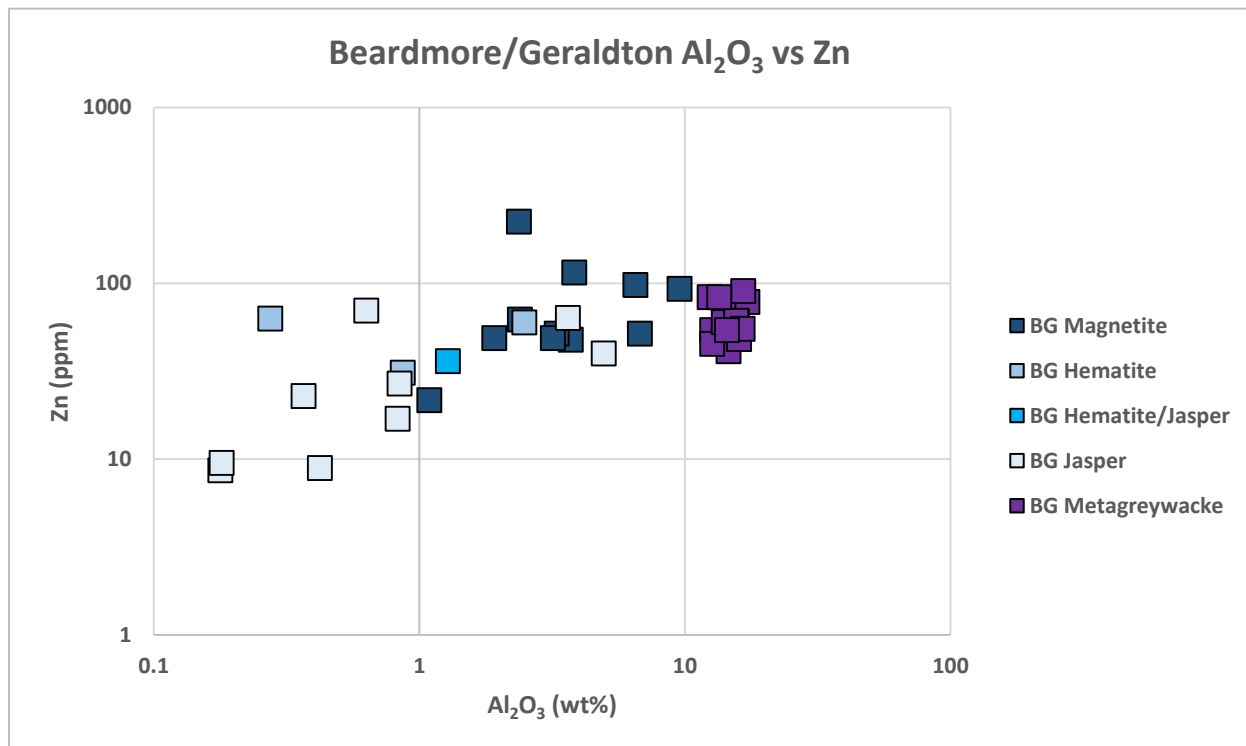
Figure 4.54: A logarithmic bivariate plot of aluminum versus zinc for the meta-iron formation samples and associated siliciclastic lithologies from the BG. The clustering of the NC metagreywacke samples indicates that zinc was immobile during post-depositional alteration. The higher Zn/Al values for the meta-iron formation samples suggests that there was an influx of zinc from a non-siliciclastic source.

Similar relationships can be seen with the NC meta-iron formation samples and the associated siliciclastics (Figure 4.55). The Zn/Al ratios for the NC biotite-garnet schist are much lower than the Zn/Al ratios for the NC meta-iron formation samples. Again, this indicates that there was an influx of zinc from a non-siliciclastic source. Overall, the Zn/Al ratios for the SGB, NC and LSJ are higher than the BG meta-iron formations suggesting that the ocean concentration of zinc was variable. Therefore, it is believed that zinc was sourced from both hydrothermal venting fluids and continental runoff.
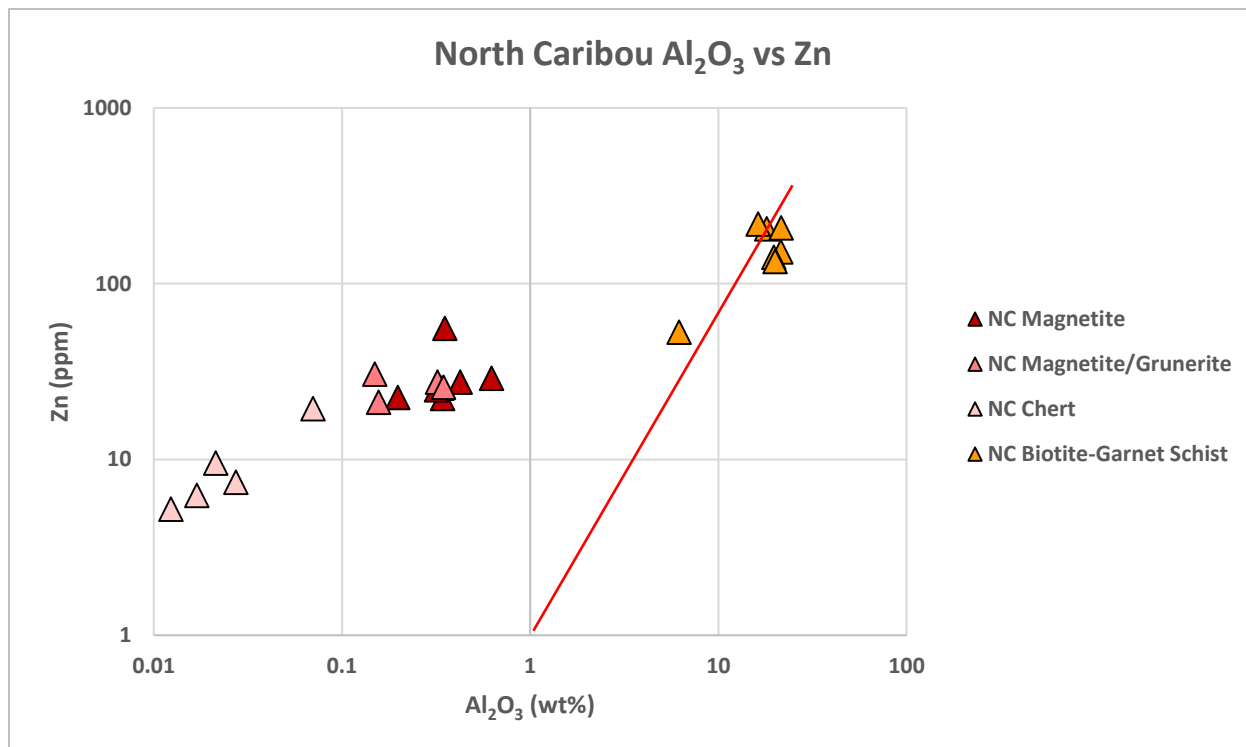
Figure 4.55: A logarithmic bivariate plot of aluminum versus zinc for the NC meta-iron formation samples and the associated siliciclastic lithology. The red line denotes the Zn/Al ratio for the siliciclastic lithologies. Note that the Zn/Al values for the meta-iron formation samples are much higher than the NC biotite-garnet schist samples. This suggests that zinc, in part, was derived from a non-siliciclastic source. The overall clustering of the NC biotite-garnet schist samples suggests that Zn was immobile during post-depositional alteration in the siliciclastics.

When copper was plotted against each element, there was no definite correlation. Figure 4.56 is a logarithmic bivariate plot of aluminum versus copper. However, the meta-iron formations are separated into four loose, overlapping regions. The NC samples plot at low aluminum and low copper values (region 1), most of the BG samples plot at high aluminum, low copper concentrations (region 2), the SGB samples plot at low aluminum high copper concentrations (region 3), while the LSJ samples plot at high aluminum, high copper concentrations (region 4). If copper was derived from seawater, this would indicate that the concentration of dissolved copper in the ancient oceans was highly variable and possibly changing through time. The scattering of the samples could also indicate that copper was mobile during post-depositional alteration.
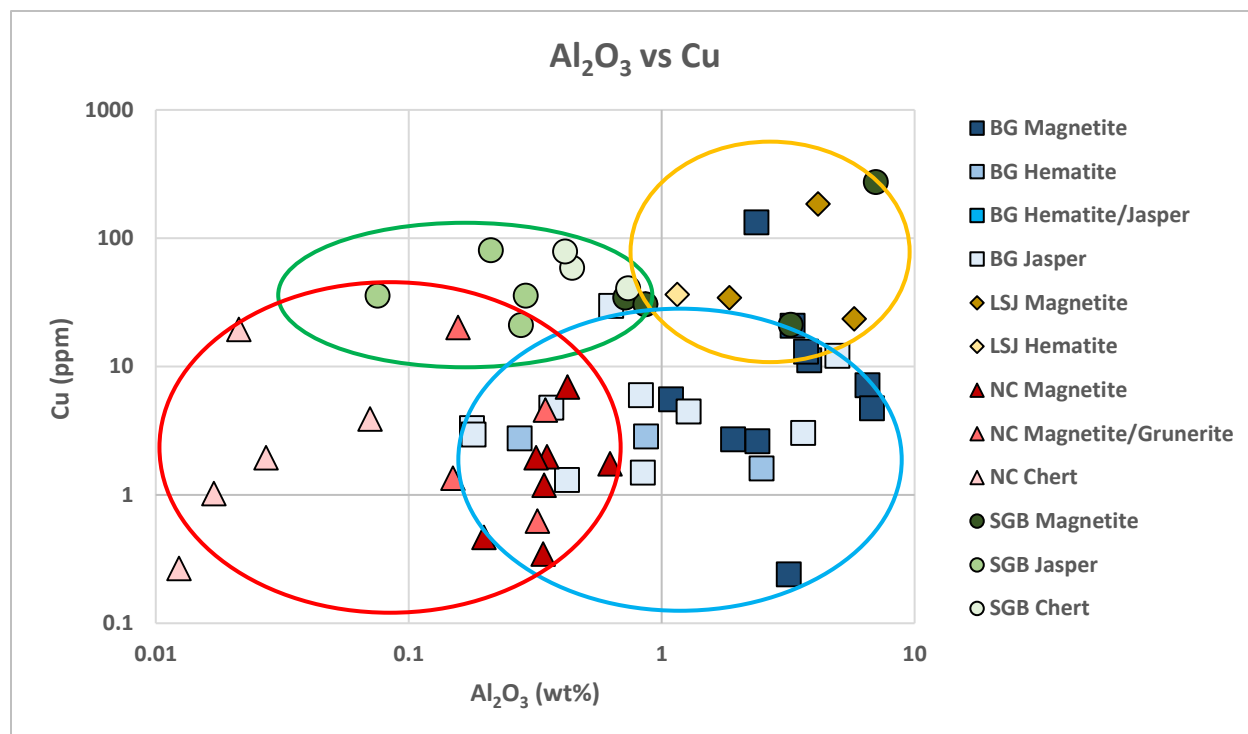
Figure 4.56: A logarithmic bivariate plot of aluminum versus copper. Four loose overlapping regions occur. Region one contains the NC samples (red), region 2 contains the BG samples (blue), region 3 contains the SGB samples (green) and region 4 contains the LSJ samples (yellow). Overall, there is no correlation between copper and aluminum and the points are very scattered. The scattering of the points indicates the copper concentrations in the ancient oceans were highly variable or copper was mobile during post-depositional alteration.

Zinc and copper were normalized over aluminum to subtract the siliciclastic effect and plotted against each other (Figure 4.57). Again, there appears to four areas where loose clusters occur. The BG meta-iron formation samples have generally low Cu/Al_2O_3 and Zn/Al_2O_3 values (region 1), NC magnetite and NC magnetite/grunerite have similar Cu/Al_2O_3 values than the BG meta-iron formation samples, but higher Zn/Al_2O_3 values (region 2), LSJ meta-iron formations have similar Zn/Al_2O_3 values as the region 2 samples, but have higher Cu/Al_2O_3 values (region 3) and the NC chert and SGB meta-iron formation samples have the highest Cu/Al_2O_3 and Zn/Al_2O_3 ratios (region 4). Although these are loose clusters, most of these clusters are site specific. If zinc and copper were derived from seawater, then this would indicate that either the oceans were heterogeneous in relation to its zinc and copper concentration ocean concentrations of zinc and copper have been fluctuating between the Mesoarchean and Neoarchean.
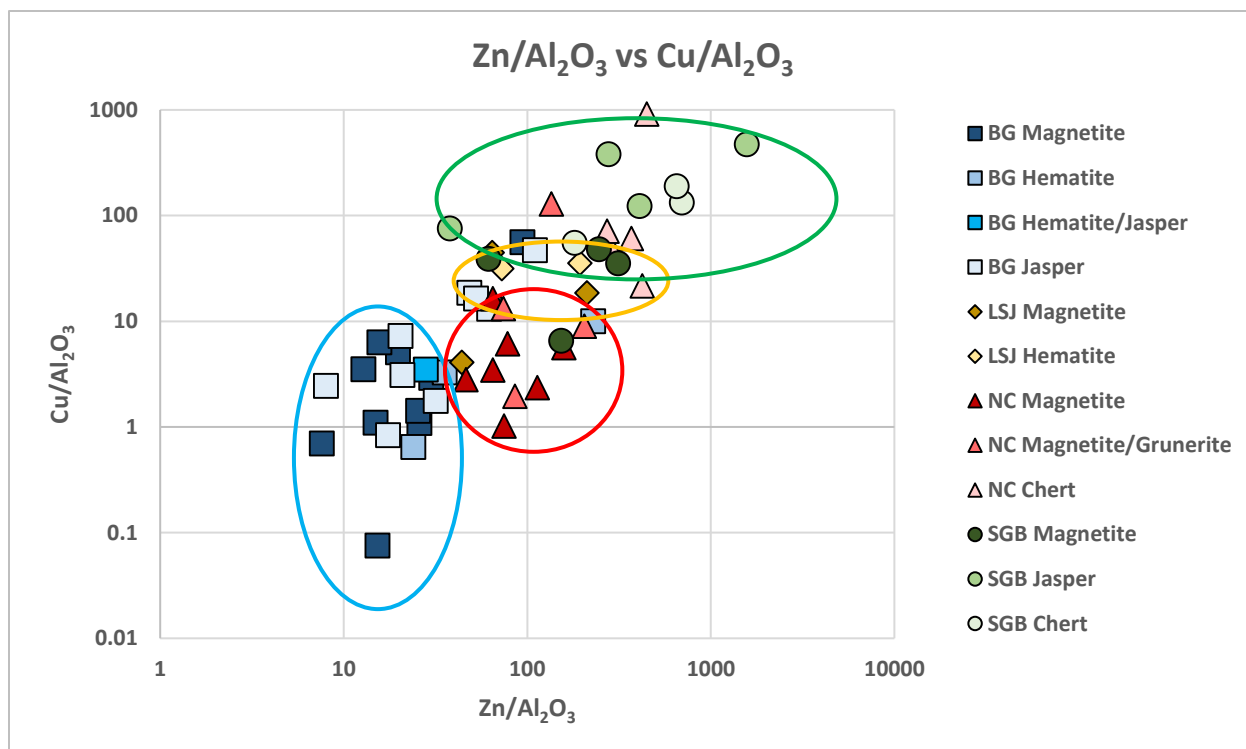
Figure 4.57: A logarithmic bivariate plot of Zn/Al_2O_3 vs Cu/Al_2O_3. Overall the data set shows a moderately strong positive correlation. Although not as predominant, the phase-dominated samples from the same study area plot in similar loose regions. Region 1 contains the BG meta-iron formation samples, region 2 contains the NC magnetite and NC magnetite/grunerite samples, region 3 contains the LSJ meta-iron formation samples and region 4 contains the SGB meta-iron formation samples and the NC chert samples. If copper and zinc were derived from seawater, this would indicate that the ancient oceans were highly heterogeneous.

In summary, nickel for most of the SGB and BG meta-iron formation samples (region 1) was derived from the siliciclastic phase, while the nickel for the rest of the SGB, BG samples and all of the NC and LSJ samples (region 2) was precipitated out of seawater. Most of the zinc in all of the meta-iron formation samples was derived, in part, from the siliciclastic phase and seawater. Zinc in the oceans was sourced from a combination of continental runoff and hydrothermal venting fluids. Copper has weak associations aluminum suggesting that copper was derived from multiple sources and/or mobile during post-depositional alteration. If Figure 4.57 represents copper and zinc concentration of ancient seawater, this would indicate that the copper and zinc concentrations of the Archean ocean was highly variable and heterogeneous.

4.11 Group 15 Elements: P

The group 15 element whose data was obtained from the geochemical analysis was phosphorous. In Peter (2003), phosphorous in the meta-iron formations from the Heath Steele belt was derived from hydrothermal verting fluids. Phosphorous will be plotted against the other elements to determine their provenance and behaviour during post-depositional alteration.

Phosphorous abundances in meta-iron formations have been used to determine the dissolved phosphorous content of the ancient oceans (ex. Bjerrum and Canfield, 2002). Since phosphorous is an essential nutrient for microorganisms, phosphorous abundances in meta-iron formation can indicate the amount of organic productivity in the Archean (Kipp and Stüeken, 2017). Studies show that the Archean oceans had much lower dissolved phosphorous concentrations than modern oceans (ex. Jones et al., 2015; Kipp and Stüeken, 2017). Three mechanisms proposed for phosphorous deposition during meta-iron formation genesis include: adsorption of phosphorous onto iron oxyhydroxides (Bjerrum and Canfield, 2002), coprecipitation of Ca-F-P phases with iron oxyhydroxides (Feely et al., 1998; Edmonds and German, 2004) or the deposition of dead microorganisms that used phosphorous as an essential nutrient (Kipp and Stüeken, 2017).

Studies on Cenozoic rock and modern-day hydrothermal systems suggests that there could be a loss of phosphorous during pyrite oxidation and more importantly diagenesis (Poulton and Canfield, 2006), even up to 50% (Jones et al., 2015). Modern day oceans also show that less than one percent of the phosphorous deposited with biomass is preserved in sediment because phosphorous is liberated back into the ocean during remineralization (Kipp and Stüeken, 2017). However, Kipp and Stüeken (2017) argue that due to the lack of electron acceptors in the Archean oceans, most of the phosphorous in the organic biomass was preserved in the sediment (Kipp and Stüeken, 2017).

To determine the provenance for phosphorous, aluminum was plotted against phosphorous on a logarithmic bivariate plot (Figure 4.58). Overall, below one weight percent aluminum, there is a positive linear correlation between phosphorous and aluminum. However, above one weight percent aluminum, the correlation is near horizontal. Since higher concentrations of aluminum show a weaker correlation between phosphorous and aluminum, it seems illogical that phosphorous was derived solely from the siliciclastic phase. The relationship between aluminum and phosphorous is similar to the relationship observed between total iron and aluminium (Figure 4.7). Since total iron was derived from hydrothermal venting fluids, phosphorous might have also been derived from a non-siliciclastic source. The lack of negative correlation between aluminum and phosphorous at higher degrees of siliciclastic contamination indicates that a minor component of phosphorous was derived from the siliciclastic phase.
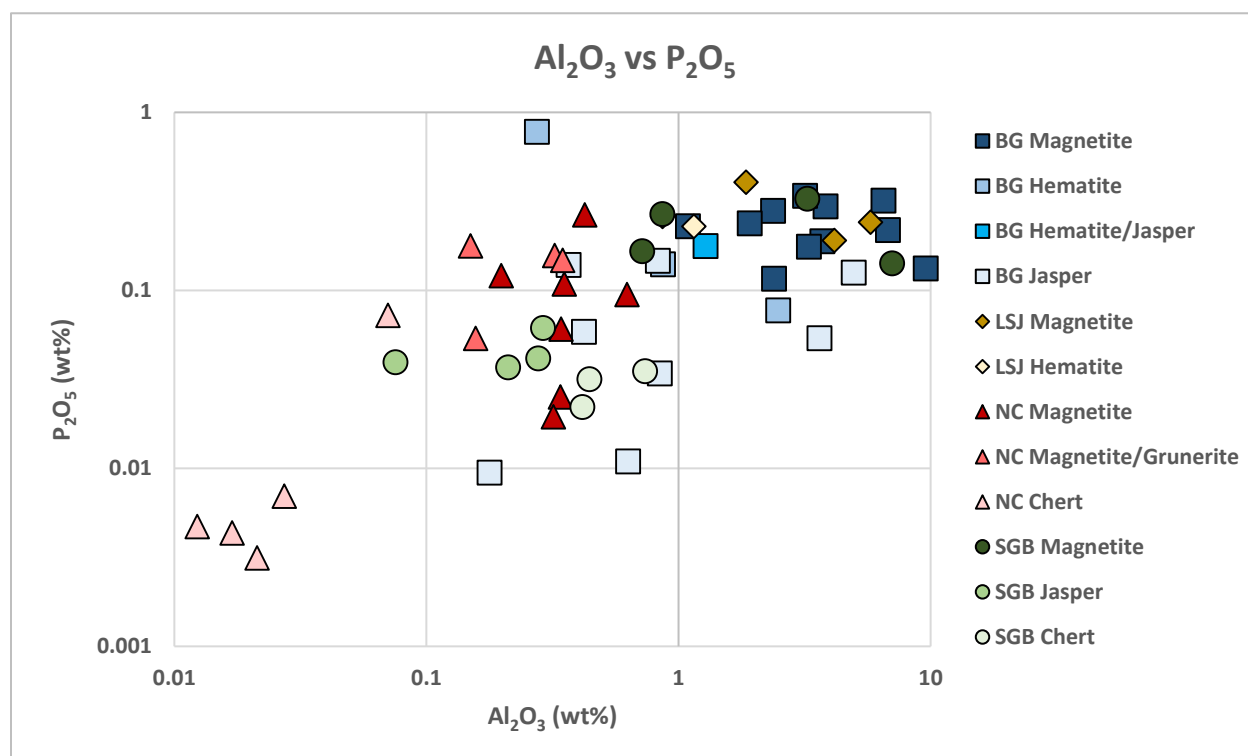
Figure 4.58: A logarithmic bivariate plot of aluminum versus phosphorous. At lower than one weight percent aluminum there is an overall positively trending correlation, although most of the data points are scattered. At higher than one weight percent the data sets show no correlation. Interestingly this resembles the association between total iron and aluminum, suggesting that phosphorous might have been derived from a non-siliciclastic source.

To determine if phosphorous was derived from a non-siliciclastic source during deposition, siliciclastic lithologies from the BG and NC were plotted with the meta-iron formation samples (Figure 4.59). The BG metagreywacke and NC biotite-garnet schist plot as clusters at similar P/Al values. This indicates that phosphorous in the clastic metasedimentary lithologies was immobile during post-depositional alteration. Most of the BG and NC meta-iron formation samples plot at similar phosphorous values, but at lower aluminum values. Therefore, the P/Al values for the NC and BG meta-iron formation samples are higher than the associated NC and BG siliciclastic lithologies. This indicates that for both the NC and BG meta-iron formation samples there was an influx of phosphorous from a non-siliciclastic source during deposition.
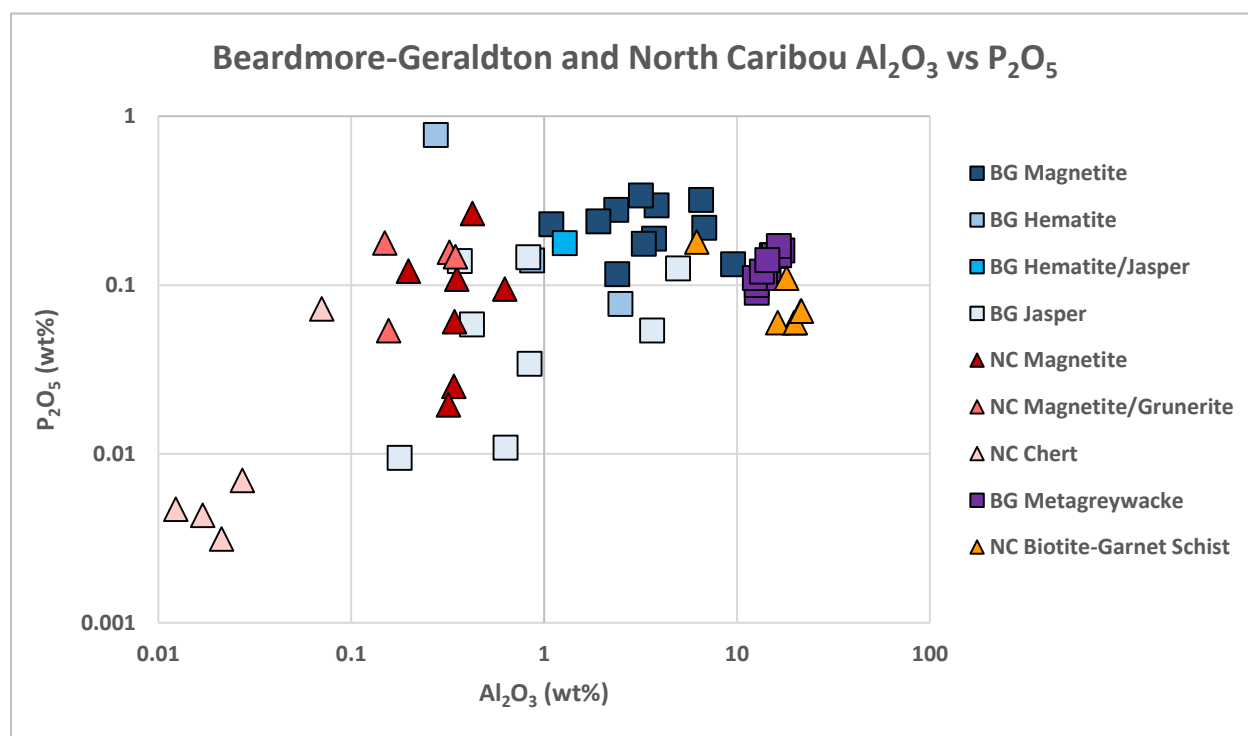
Figure 4.59: A logarithmic bivariate plot of aluminum versus phosphorous of the BG and NC meta-iron formation samples plotted with their associated siliciclastic lithologies. The meta-iron formation samples have higher P/Al values than the NC biotite-garnet schist and BG metagreywacke, indicating an enrichment of phosphorous to the meta-iron formations from a non-siliciclastic source during deposition.

Phosphorous and total iron were normalized over aluminum to subtract the effects of siliciclastic contamination (Figure 4.60). Overall, the BG, LSJ and SGB samples form positive linear

correlations, while the NC meta-iron formation samples plot as a scatter at high P_2O_5/Al_2O_3 and Fe_2O_{3T}/Al_2O_3 ratios. The positive correlation for the BG, LSJ and SGB meta-iron formation samples between P_2O_5/Al_2O_3 and Fe_2O_{3T}/Al_2O_3 indicates that most of the phosphorous was most likely sourced from seawater and adsorbed onto iron oxyhydroxides. However, the meta-iron formation correlations plot at different P/Fe_T (phosphorous and iron total) ratios. The P/Fe_T ratio for the BG magnetite samples is higher than most of the BG jasper samples. This suggests that either the P/Fe ratio of the ancient seawater was fluctuation or phosphorous may have been remobilized after deposition. For these reasons, it is believed that the P/Fe ratio of the ancient seawater was not preserved in the meta-iron formations of this study. Also, since studies show that phosphorous is remobilized during post-depositional alteration (ex. Poulton and Canfield, 2006; Jones et al., 2015), phosphorous abundances in the meta-iron formations do not preserve the phosphorous abundances of the ancient oceans.
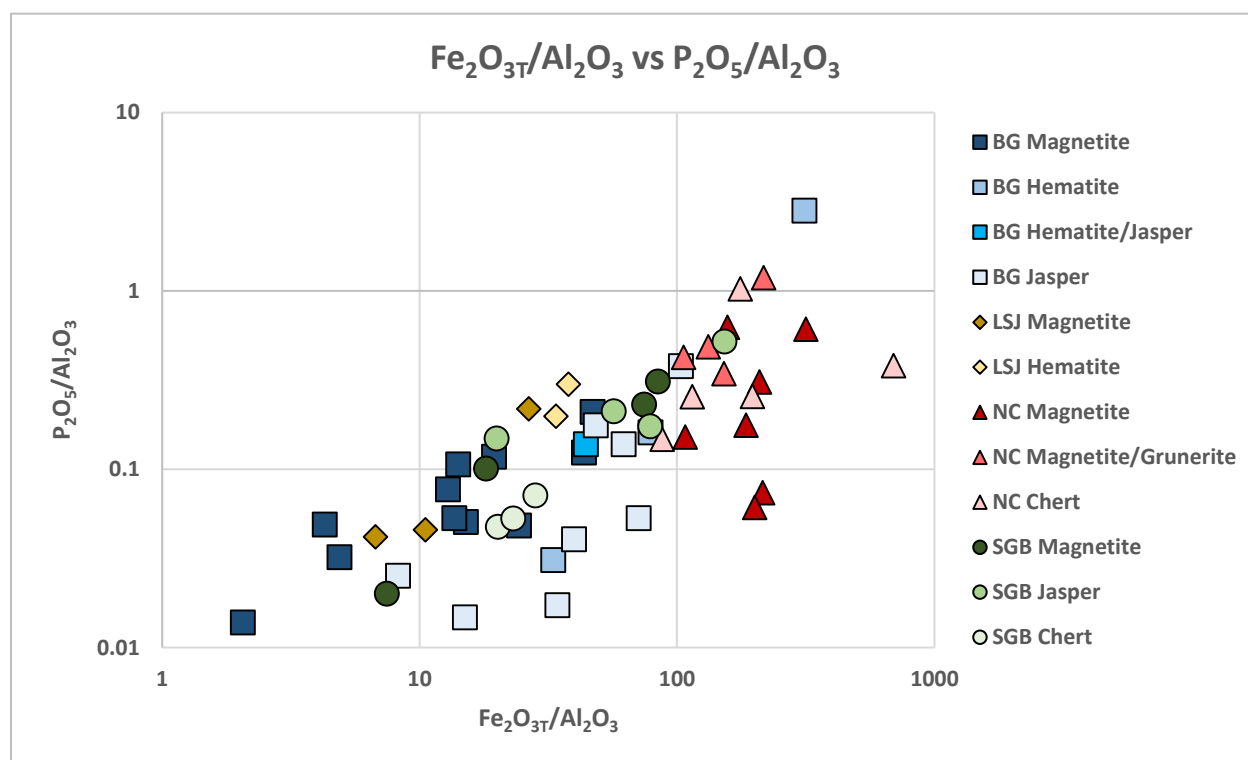
Figure 4.60: A logarithmic bivariate plot of Fe_2O_{3T}/Al_2O_3 vs P_2O_5/Al_2O_3. Significantly, there is an overall positively trending correlation. However, the BG magnetite samples plot at higher P/Fe ratios than the BG jasper samples. Significantly, this means that either there was fluctuating in the P/Fe ratio of the ancient ocean or phosphorous was mobile during post-depositional alteration.

In summary, phosphorous in the BG, LSJ and SGB was mostly derived from adsorption of phosphorous onto iron oxyhydroxide surfaces. A minor component of phosphorous was derived from the siliciclastic phase. However, the scattering of the data sets, suggests that the P/Fe ratio and phosphorous abundances of the ancient seawater were not preserved in the meta-iron formations.

In petrography, the only phosphorous-bearing mineral phase in all the meta-iron formation samples is apatite. Significantly, apatite is mostly associated with magnetite and hematite-dominated layers suggesting that there was a relationship between phosphorous and iron during deposition. Since geochemically phosphorous has a stronger relationship with total iron than with calcium when normalized over aluminum (Figure 4.61), phosphorous was adsorbed onto iron oxyhydroxides rather than forming Ca-F-P phases during meta-iron formation deposition.
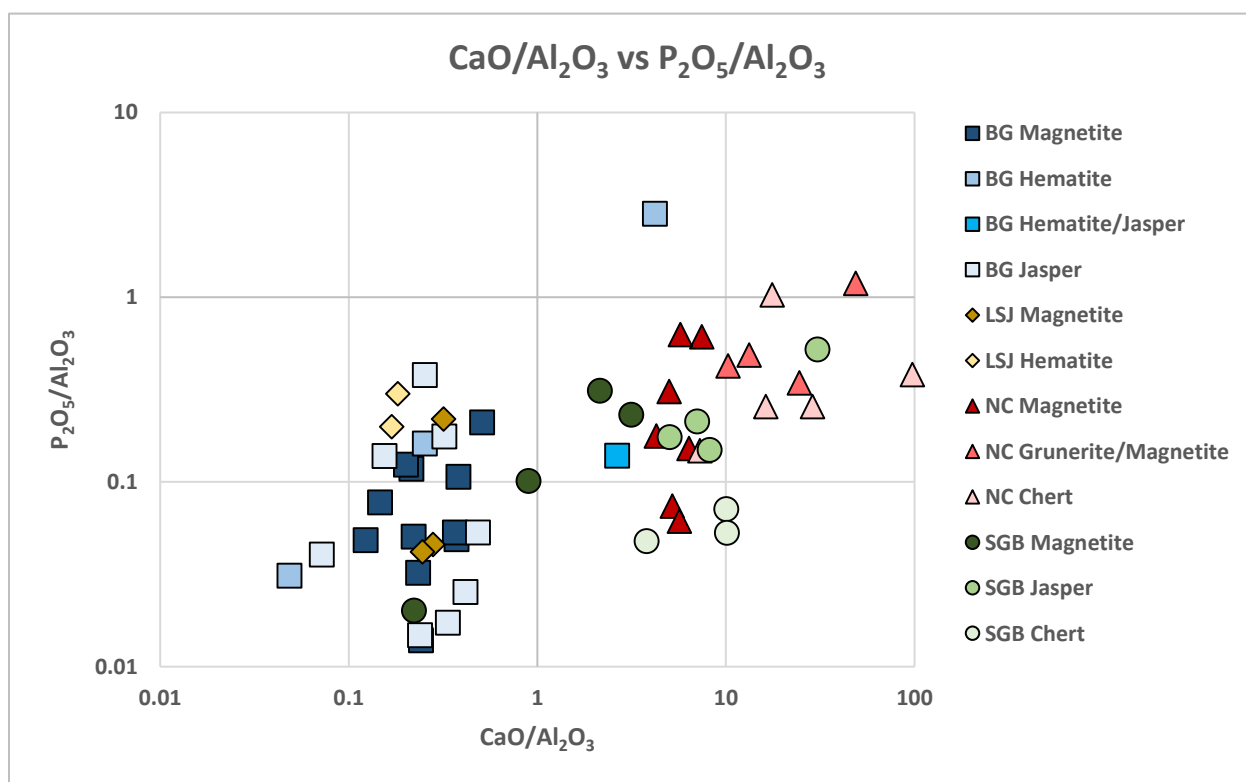
Figure 4.61: A logarithmic bivariate plot of CaO/Al_2O_3 vs. P_2O_5/Al_2O_3. Overall the data points are fairly scattered suggesting that calcium and phosphorous did not behave similarly during deposition or post-depositional alteration. This graph shows that the relationship between total iron and phosphorous normalized over aluminum in Figure 4.60 is stronger than the relationship between calcium and phosphorous. This suggests that phosphorous most likely adsorbed onto iron oxyhydroxides during deposition rather than forming Ca-F-P phases.

4.12 Group 3 Elements, Lanthanides: Y and Rare Earth Elements

Geoscientists have used rare earth element (REE) geochemical data from meta-iron formations to determine the chemical composition and investigate the stratification of the ancient ocean. The REEs consist of 14 lanthanide series elements and are often divided into two groups: light rare earth elements (LREE) and heavy rare earth elements (HREE). The LREE include La, Ce, Pr, Nd, Sm, Eu and Gd, while the HREE comprise of Tb, Dy, Ho, Er, Tm, Yb and Lu. As mentioned in Section 4.3, some of the REE can fractionate related to the redox conditions of seawater during the time of meta-iron formation deposition. A useful chemical property for Precambrian geochemists is that the lanthanides remain immobile under most metamorphic conditions and during late stage hydrothermal metasomatism (Taylor and McLennan, 1988). This suggests that the REE chemistry preserved in the meta-iron formations may reflect the redox conditions and chemical composition of seawater during deposition.

Most geochemists studying meta-iron formations use PAAS normalized spider diagrams to compare the composition of the ancient ocean relative to the average composition of the upper continental crust (shales) (ex. Planavsky et al., 2010). The PAAS normalization procedure, developed by Nance and Taylor (1976), consists of the average rare earth element concentrations of 23 Australian sedimentary shales, ranging in age from middle Proterozoic to Triassic. This technique was used due to three factors: (1) it smooths out the curves, removing the Oddo-Harkins effect, which is the greater stability of the even number nuclides compared to the odd number nuclides, causing the even number nuclides to be more abundant, (2) the normalization to an equal base makes it easy to compare sets of curves, and (3) anomalies can be clearly seen between neighbouring elements (Taylor and McLennan, 1988). Yttrium behaves geochemically similar to the heavy rare earth elements in nature, and it is commonly placed between dysprosium and holmium

on the PAAS normalized diagram due to its similar ionic radius and ionic charge to holmium. PAAS

normalization constants for the REE and Y were obtained from Taylor and McLennan (1988).

PAAS normalized diagrams for the meta-iron formations can be seen in Figures 4.62 – 4.72. All

the meta-iron formation samples display positive europium anomalies at various strengths. Yttrium

anomalies for the meta-iron formations range from positive to negative. The ratio between the LREE

and HREE is predominantly less than one, which is indicated by the positive sloping trends on the

PAAS normalized spider plots. This indicates that the meta-iron formations are mostly recording a

LREE depletion relative to the HREE. Almost all the meta-iron formation samples have values less

than one on the PAAS normalized plot, indicating that REE and yttrium concentrations in the oceans

are depleted relative to shales.
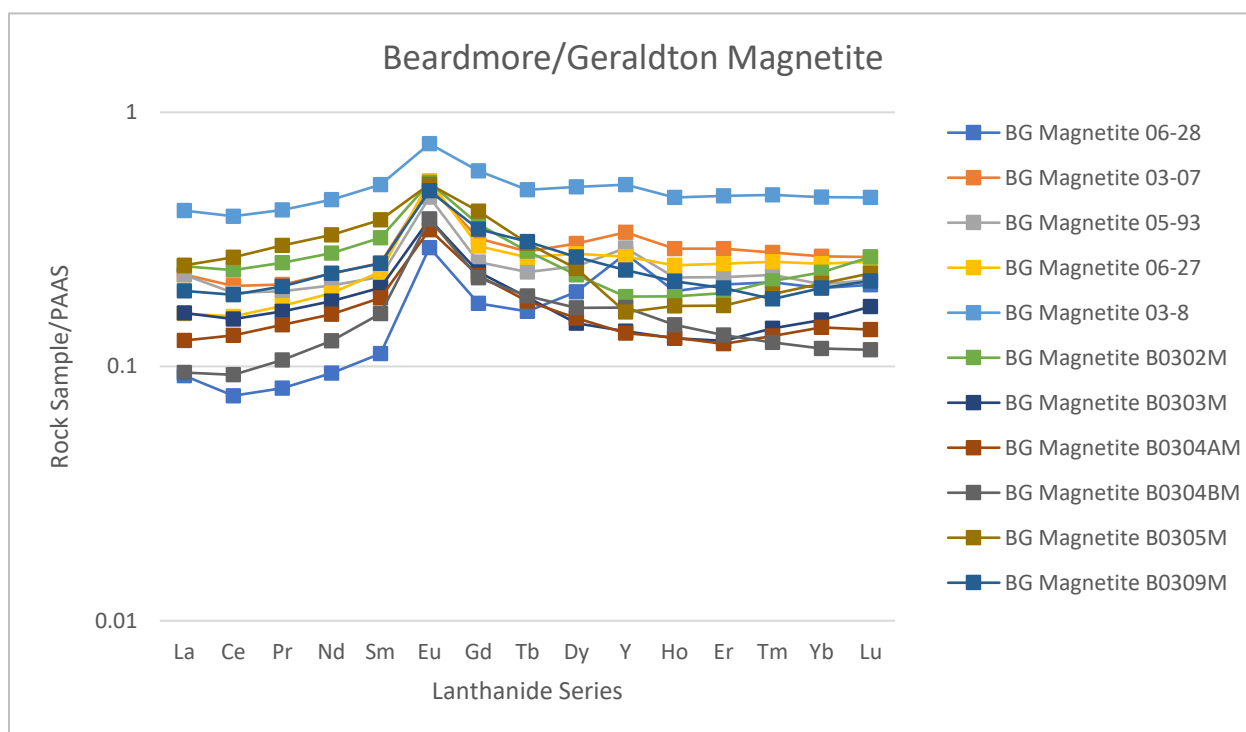
Figure 4.62: A PAAS normalized diagram for the magnetite-dominated meta-iron formation samples from BG. Most of the samples show positive Eu anomalies with various strengths, positive and negative Y anomalies and LREE/HREE slopes that range from positive to negative.
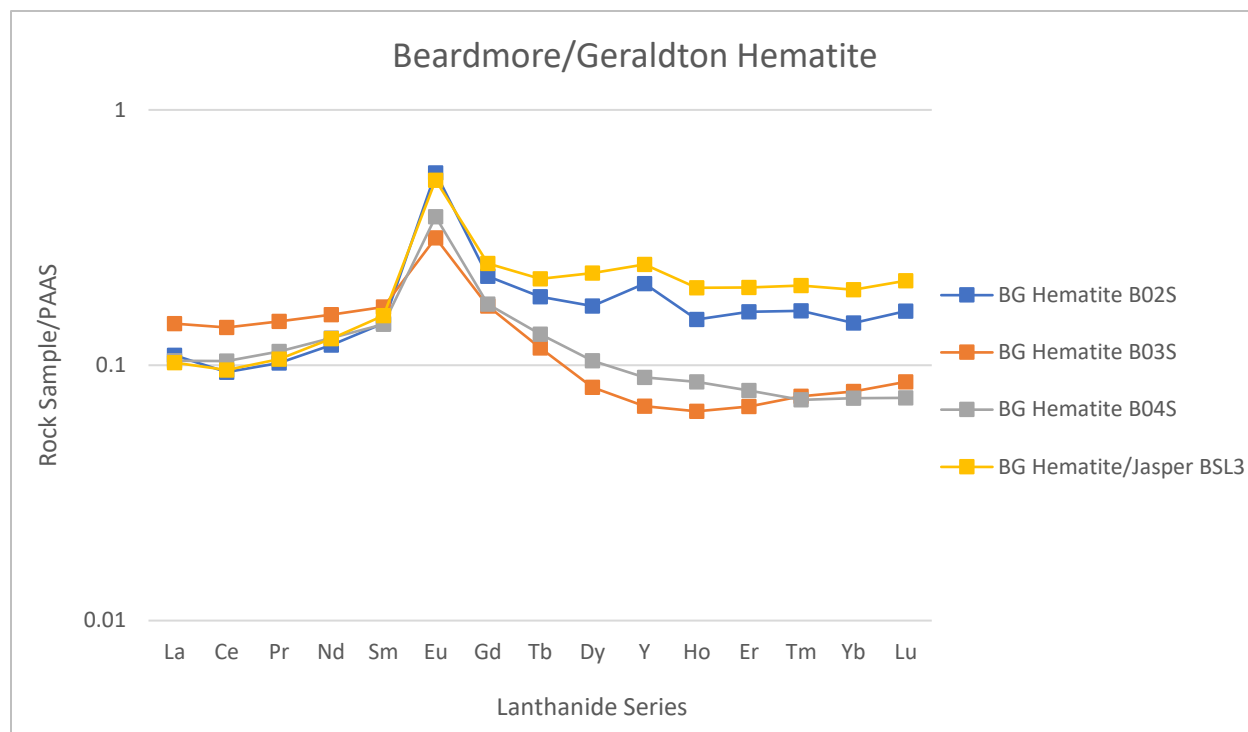
Figure 4.63: A PAAS normalized spider diagram for the hematite-dominated meta-iron formation samples from BG. All the samples show positive europium anomalies at varying strengths, positive and negative yttrium anomalies and the LREE/HREE slopes range from positive to negative.
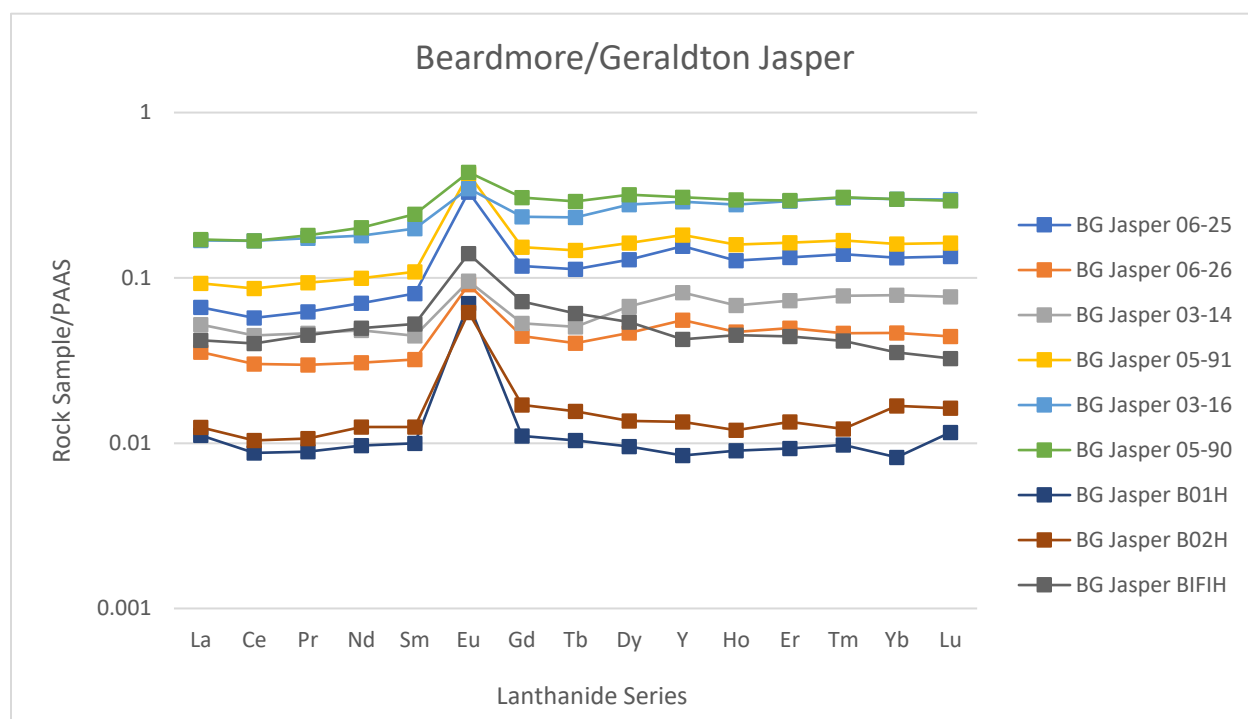
Figure 4.64: A PAAS normalized spider diagram for the jasper-dominated meta-iron formation samples from BG. All of the samples show a positive europium anomaly at varying strengths, slightly negative to slightly positive yttrium anomalies and the LREE/HREE ranges from mostly positive to negative.
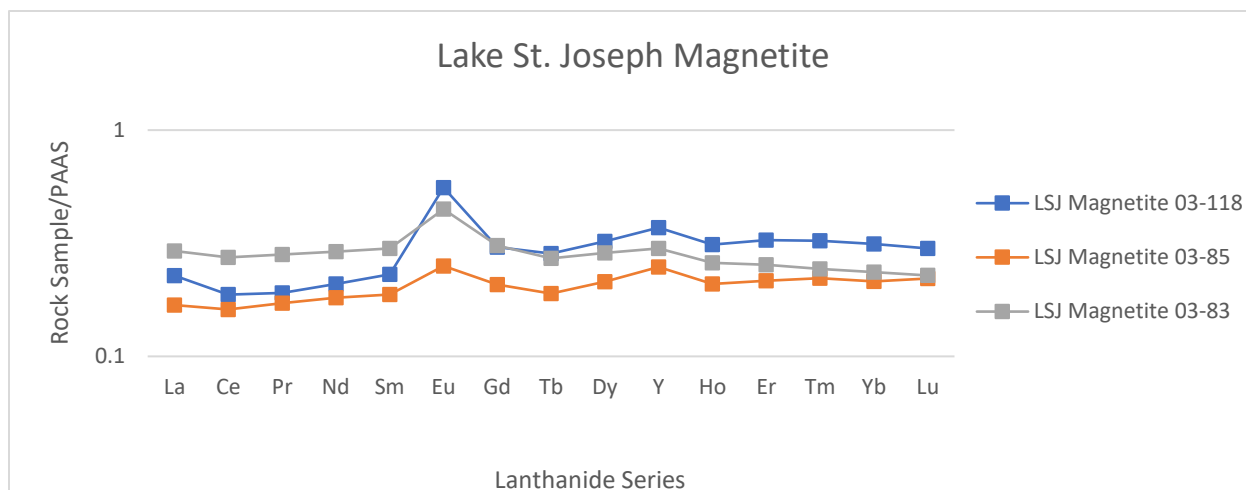
Figure 4.65: A PAAS normalized spider diagram for the magnetite-dominated meta-iron formation samples from LSJ. All the samples show a positive europium anomaly at varying degrees, positive yttrium anomalies and LREE/HREE slopes that are slightly positive to slightly negative.
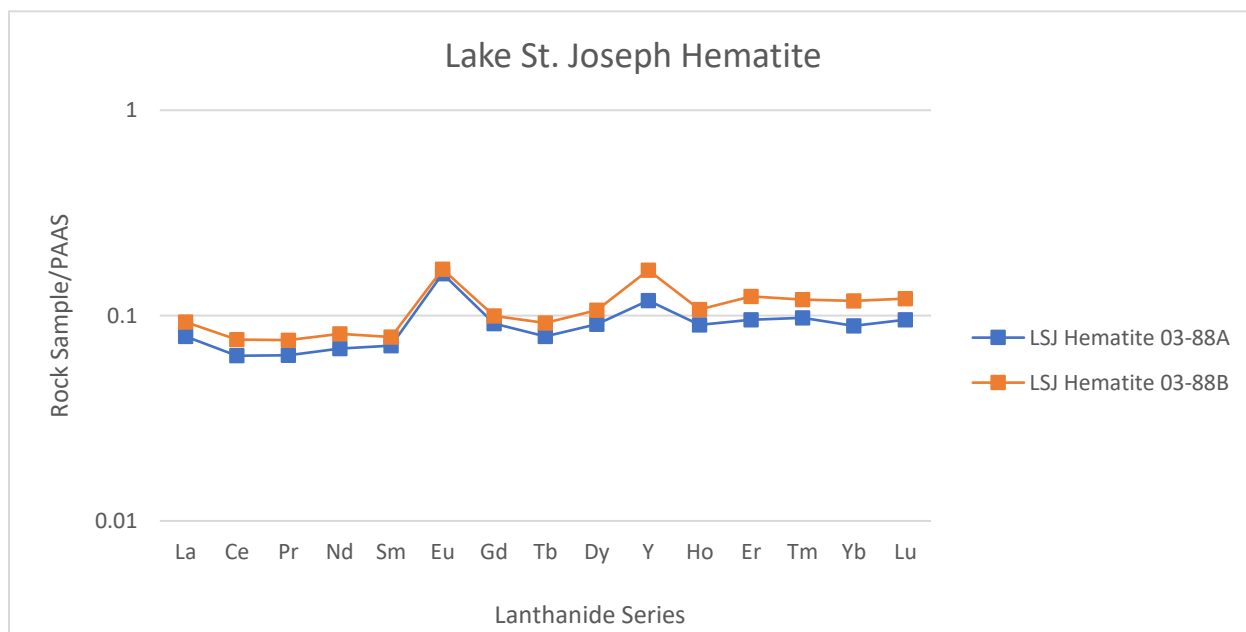
Figure 4.66: A PAAS normalized spider diagraph for the hematite-dominated meta-iron formation samples from LSJ. All the samples show positive europium anomalies, positive yttrium anomalies and all the LREE/HREE slopes are slightly positive.
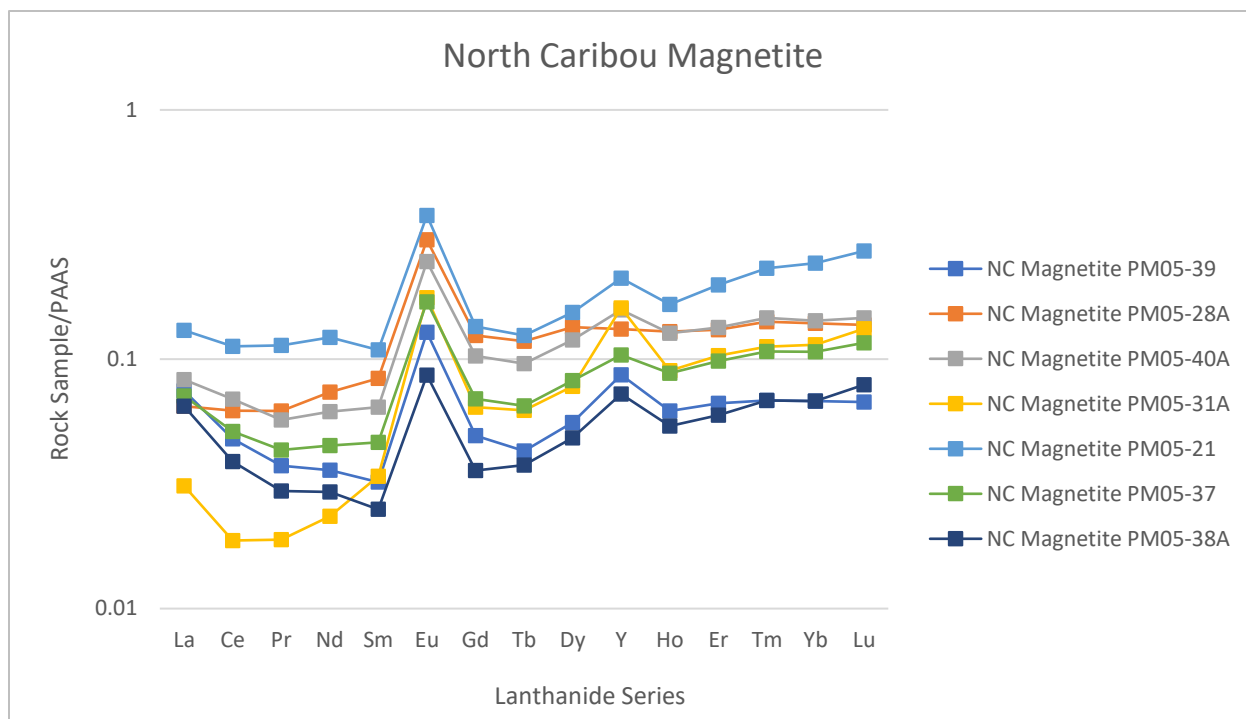
Figure 4.67: A PAAS normalized spider plot for the magnetite-dominated meta-iron formation samples from NC. All the samples display a pronounced europium anomaly, positive to flat lying yttrium anomalies and LREE/HREE slopes which are strongly positive. Most of the NC magnetite samples also have a pronounced positive lanthanum anomaly.
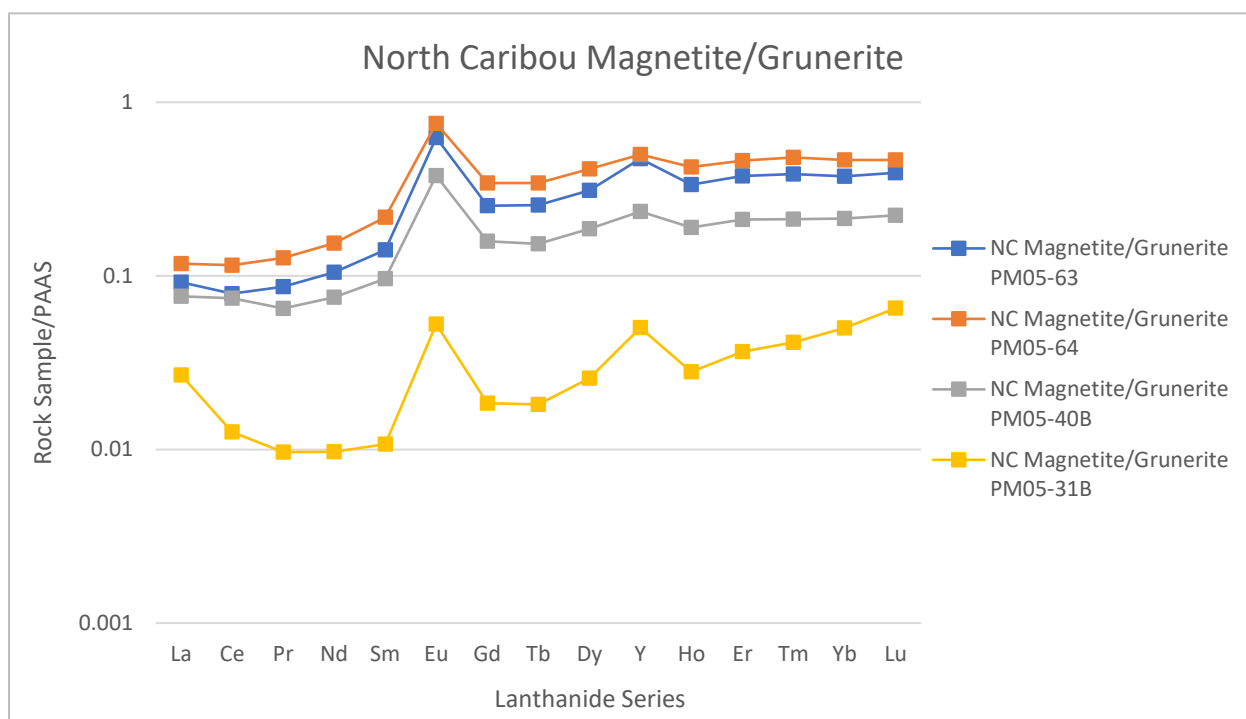
Figure 4.68: A PAAS normalized spider plot for the magnetite/grunerite-dominated meta-iron formation samples from NC. All the samples show a prominent positive europium anomaly, positive yttrium anomalies and LREE/HREE slopes that are positive. Also, for one sample there are positive lanthanum anomalies, while the rest of them are either slightly positive or flat-lying.
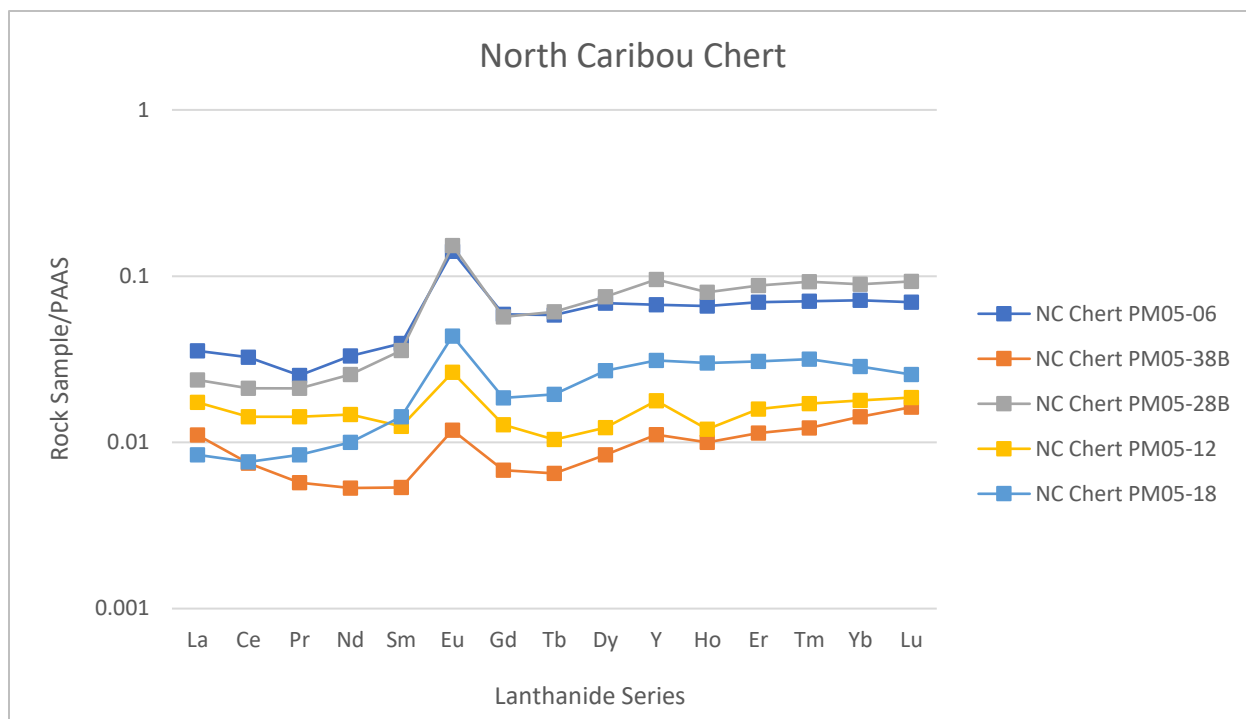
Figure 4.69: A PAAS normalized spider diagram of the chert-dominated meta-iron formation samples from NC. All the samples display a prominent europium anomaly, positive to flat-lying yttrium anomalies and LREE/HREE slopes that range from strongly to slightly positive. All the samples also show a positive lanthanum anomaly at various degrees.
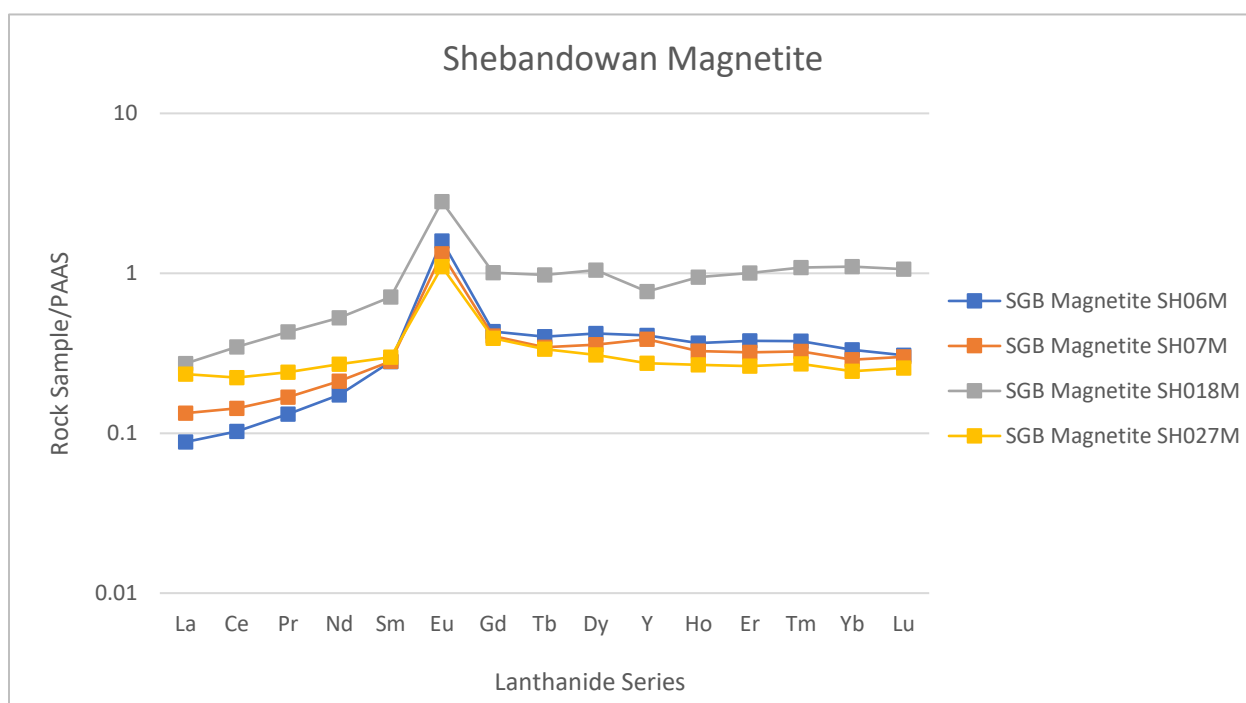
Figure 4.70: A PAAS normalized spider diagram of the magnetite-dominated meta-iron formation samples from SGB. All the samples show a prominent europium anomaly, slightly positive to negative yttrium anomalies and LREE/HREE slopes that are positive or horizontal.
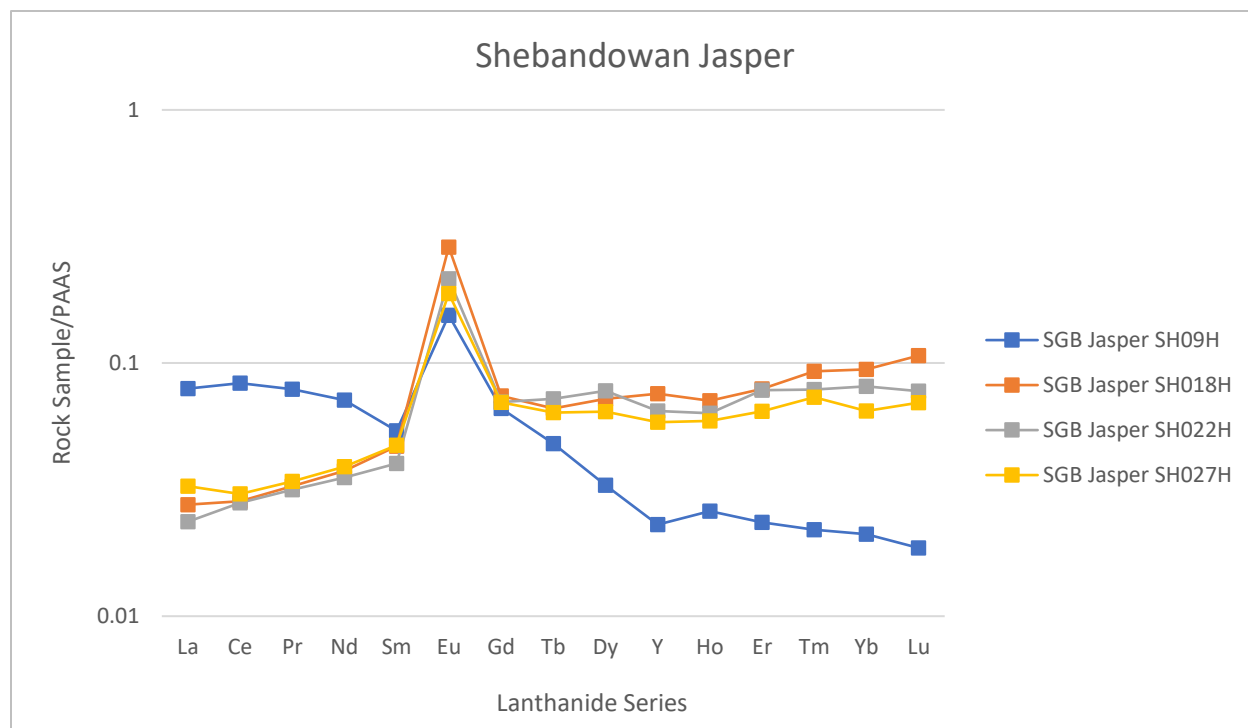
Figure 4.71: A PAAS normalized spider diagram for the jasper-dominated meta-iron formation samples from SGB. All the samples display a prominent positive europium anomaly, negative to slightly positive yttrium anomalies and LREE/HREE slopes that are mostly strongly positive, with one sample that has a strongly negative LREE/HREE slope.
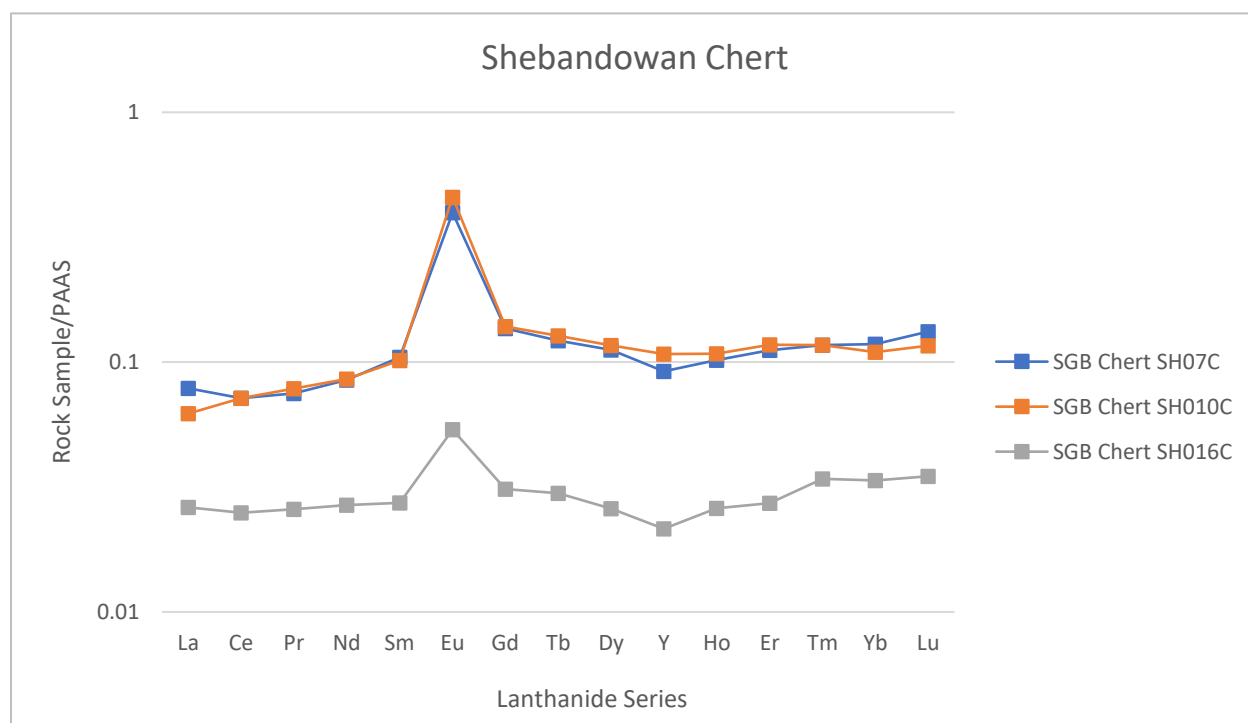
Figure 4.72: A PAAS normalized spider diagram for the chert-dominated meta-iron formation samples from SGB. All the samples show a prominent positive europium anomaly, slightly negative yttrium anomalies and LREE/HREE slopes that range from slightly positive to slightly negative.

The difference in the strength of the anomalies could be caused by the amount of siliciclastic detritus in the meta-iron formation samples. To clearly see the effects of the siliciclastics on the REE chemistry in the meta-iron formation samples, the lanthanides and yttrium values from each sample were divided by the Al_2O_3 content. That value was divided by the PAAS normalization constant for that element. This technique translates the curves up or down the spider plot, relative to the amount of siliciclastic material without changing the strength of the anomalies between neighbouring elements. Samples with higher siliciclastic contamination will plot lower on the spider diagram, while samples with lesser degrees of siliciclastic contamination will plot higher on the spider plot.

Significantly, when the PAAS normalized line plots for the BC magnetite samples were normalized over aluminum (Figure 4.73), many interesting features were observed. First, meta-iron formation samples with greater amounts of siliciclastic contamination, have smaller positive europium anomalies and negative yttrium anomalies. Samples with lower degrees of siliciclastic contamination have higher positive europium and positive yttrium anomalies. When looking at the curves in Figure 4.73, samples with smaller europium anomalies, negative yttrium anomalies and higher aluminum content have LREE/HREE ratios that are higher than one, which display negative sloping curves. Samples with larger europium anomalies, positive yttrium anomalies and lower aluminum content have LREE/HREE ratios lower than one, which display positive trending curves. This indicates that for the BG magnetite samples, the strength of the europium anomaly, yttrium anomaly and the slope of the curve is mostly dependent on the degree of siliciclastic contamination. Therefore, samples with lower siliciclastic contamination reflect ancient seawater concentrations, suggesting that the ancient oceans had high europium anomalies, high yttrium anomalies and were LREE depleted relative to the HREE.
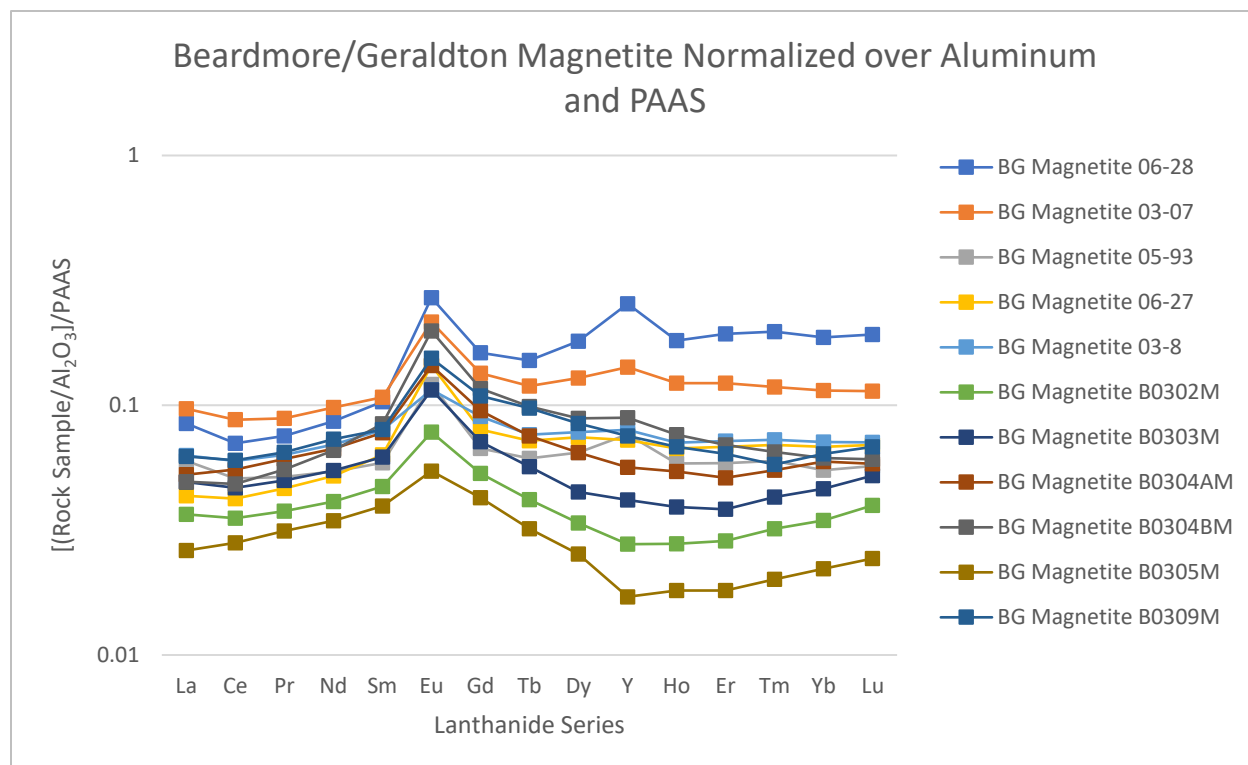
Figure 4.73: An aluminum and PAAS normalized REE + Y spider plot for the magnetite-dominated meta-iron formation samples from BG. Significantly, higher amounts of siliciclastic contamination shows lower positive europium anomalies, negative yttrium anomalies and negative sloping LREE/HREE ratios. Samples with less siliciclastic contamination show more prominent positive europium anomalies, positive yttrium anomalies and positive sloping LREE/HREE ratios. This indicates that siliciclastic contamination has a large effect on the REE chemistry of the meta-iron formation samples.

To determine if the distribution of REE and Y geochemistry was heterogeneous or homogenous throughout the ancient ocean all the meta-iron formation samples were plotted on bivariate plots between aluminum and the main redox and complexation sensitive element anomalies recorded in seawater. Element anomalies and trends of great importance in meta-iron formation and ocean geochemistry include europium anomalies (Eu/Eu*) which were discussed in Section 4.3, cerium anomalies (Ce/Ce*), yttrium anomalies (Y/Ho) and the fractionation trends between the LREEs and HREEs (Pr/Yb). Theories for geologic fractionation processes that generate these anomalies and trends will be discussed below.

As mentioned in Section 4.3, cerium can exist in both the Ce^{3+} and Ce^{4+} oxidation states,

depending on the redox conditions of seawater (Bau et al., 1997; Peter, 2003; Planavsky et al., 2010;

Tostevin et al., 2016). In oxygenic ocean waters, cerium will readily oxidize from Ce^{3+} to Ce^{3+}. Ce^{4+} is

highly insoluble in seawater, therefore, it can partition into octahedral sites of precipitates or can be

scavenged and adsorbed onto Fe-Mn oxyhydroxide surfaces. (deBaar et al., 1988; Peter, 2003;

Tostevin et al., 2016). deBaar et al. (1988) sampled the REE chemistry of modern day oxic and anoxic

ocean waters of the Cariaco Trench off the coast of Venezuela. There they discovered a sharp

increase in the dissolved cerium content at and below the oxic/anoxic redoxcline relative to the

shallow oxic water column (deBaar et al., 1988). deBaar et al. (1988) suggested that the enrichment

of cerium in anoxic waters was caused by the preferential adsorption of cerium relative to the other

REEs onto Mn-Fe oxyhydroxide surfaces in oxic water, which settled through the water column until

it passed the redoxcline. Water below the redoxcline is anoxic and allowed the Mn-Fe oxyhydroxides

to re-dissolved back into the ocean, causing an enrichment of cerium relative to the other REEs

(deBaar et al., 1988; Planavsky et al., 2010; Tostevin et al., 2016). However, the mechanism for the

preservation of ocean chemistry in meta-iron formations is not well understood. The theories used

to interpret the mechanism for partitioning the REE between the oxic and anoxic waters is the same

theory used to preserve the ocean chemistry of their depositional environment in the meta-iron

formation; ex. the adsorption of elements onto Fe-Mn oxyhydroxides. However, REE geochemical

data from natural Archean meta-iron formations from different locations display similar trends,

indicating that the REE geochemistry most likely reflects seawater compositions (ex. Planavsky et al.,

2010).

Lanthanum can have anomalous concentrations in seawater, thus producing false negative

cerium anomalies (Bau and Dulski, 1996). To determine if the meta-iron formations are actually

displaying a cerium anomaly, the praseodymium anomaly is calculated and plotted on a bivariate

plot with the cerium anomaly (Bau and Dulski, 1996).

The cerium and praseodymium anomalies were calculated by the following equations:

$$\text{Equation [2]} \quad Ce/Ce^* = \frac{Ce_{PAAS}}{(\frac{1}{2}La_{PAAS}+\frac{1}{2}Pr_{PAAS})} \quad \text{(Bau and Dulski, 1996)}$$

$$\text{Equation [3]} \quad Pr/Pr^* = \frac{Pr_{PAAS}}{(\frac{1}{2}Ce_{PAAS}+\frac{1}{2}Nd_{PAAS})} \quad \text{(Bau and Dulski, 1996)}$$

where Ce/Ce^* is the cerium anomaly, Pr/Pr^* is the praseodymium anomaly and La_{PAAS}, Ce_{PAAS},

Pr_{PAAS} and Nd_{PAAS} are raw data values from the geochemical analysis divided by PAAS normalization

constants.

The cerium anomaly and praseodymium anomaly were plotted against each other to determine

if there were any true cerium or lanthanum anomalies (Figure 4.74). This graph was first developed

by Bau and Dulski (1996). Samples that plot in the middle of the diagram indicate that there is no

cerium or lanthanum anomalies. Points that plot at Ce/Ce^* values lower than 0.95 in the lower left

quadrant are considered to have positive lanthanum anomalies. True negative cerium anomalies

plot in the lower right quadrant and true positive cerium anomalies plot in the upper left quadrant.

Significantly most of the meta-iron formation samples plot in the no lanthanum or cerium anomaly

field or at slightly positive lanthanum anomalies. Most of the NC meta-iron formation samples plot

in the positive lanthanum field suggesting that the lanthanum anomaly for these samples was higher

for the NC compared to the BG, LSJ and SGB meta-iron formations. One NC chert meta-iron

formation sample plots in the positive cerium anomaly quadrant. Since most of the samples do not

exhibit a positive or negative cerium anomaly in the meta-iron formation samples, it is believed that

there was no redoxcline in the water column responsible for segregating cerium-poor oxygenic

waters and cerium-enriched anoxic waters. Therefore, it is believed that both the shallow and deep oceans were mostly anoxic. Similar conclusions were determined by Planavsky et al. (2010) for the Archean meta-iron formations older than 2.5 Ga.
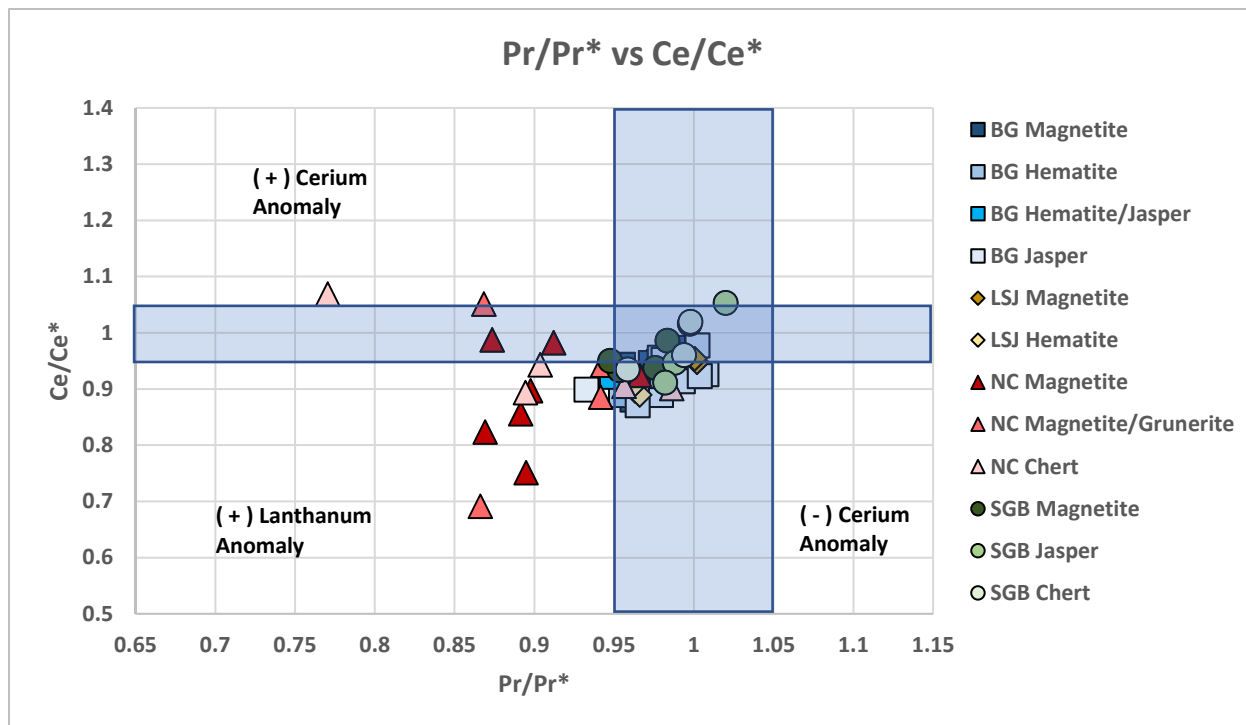
Figure 4.74: An arithmetic bivariate plot of Pr/Pr* versus Ce/Ce*. Most of the meta-iron formation samples plot in the center and lower half of the blue shaded area, which indicates that there is no significant cerium anomaly and a slight lanthanum anomaly. Most of the NC samples plot in the lower left quadrant, which indicates that these samples have a lanthanum anomaly. One NC chert sample plots at a slight cerium anomaly. Overall, most of the samples do not show a significant cerium anomaly, suggesting that there was no redoxcline in the ancient ocean. Graph developed by Bau and Dulski (1996).

The theory behind the partitioning of yttrium is the opposite of the partitioning mechanism for cerium. Holmium preferentially adsorbs onto surfaces of Fe-Mn oxyhydroxides relative to yttrium because holmium is more particle reactive in seawater than yttrium (Bau and Dulski, 1994; Bau et al., 1997). These Fe-Mn oxyhydroxides carry the holmium past the redoxcline where they are re-dissolved, causing the Y/Ho ratio to be higher in shallow oxic water and lower in deep anoxic water (Bau et al., 1997; Planavsky et al., 2010; Tostevin et al., 2016). Therefore, any deviation from the PAAS normalized Y/Ho value for shales (27), indicates a loss or gain of yttrium from seawater. Again,

like for cerium, these trends are observed in modern seawater, but the mechanism for the preservation of the ocean chemistry in meta-iron formations is still unknown.

Figure 4.75 is a bivariate plot of aluminum versus the yttrium anomaly. Since most of the meta-iron formation samples contain less than one weight percent aluminum, the scale of the x-axis is logarithmic to see the trends more clearly. Significantly at higher than one weight percent aluminum, the meta-iron formation samples form a strong negative correlation, suggesting that the siliciclastic phase dictates the strength of the yttrium anomaly. However, samples at lower than one weight percent aluminum do not follow the negative correlation and are fairly scattered. Overall, the NC samples have the highest Y/Ho values while the SGB samples have the lowest Y/Ho values, close to that of shales or slightly lower. Since there is no significant difference in the Y/Ho ratio compared to shales, both shallow and deep oceans were anoxic.
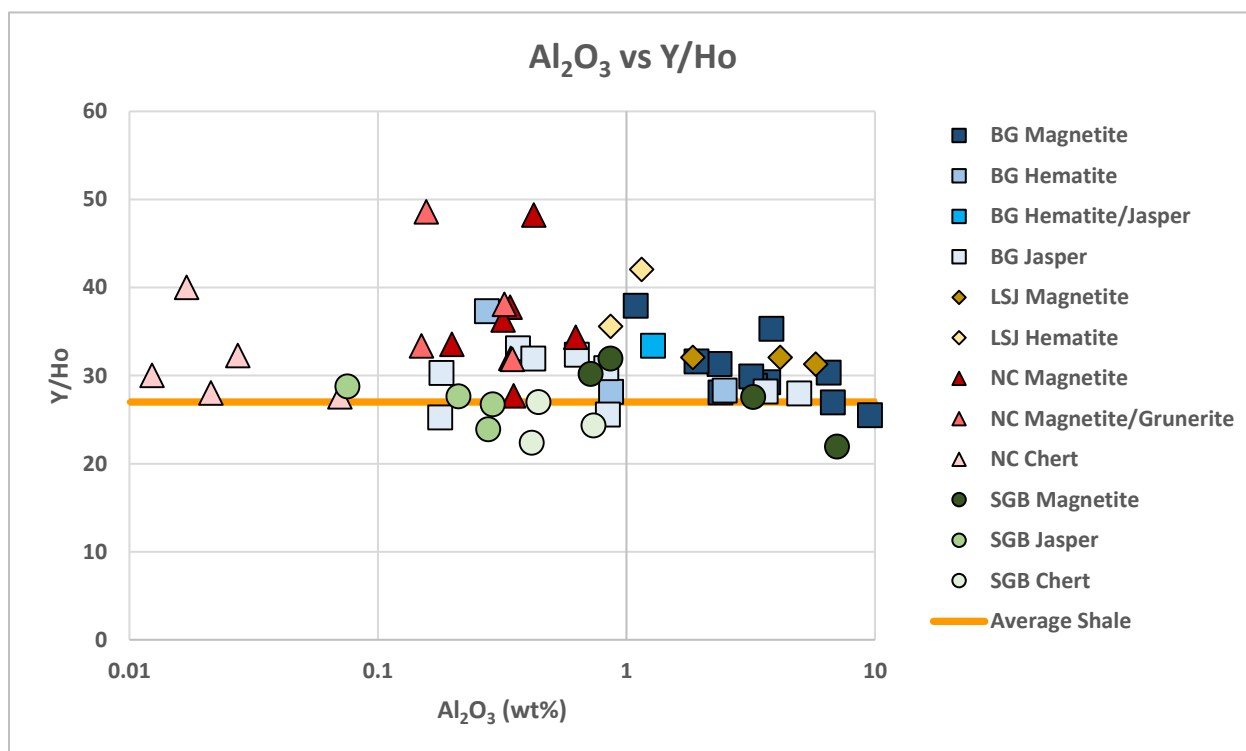
Figure 4.75: A bivariate plot of aluminum versus Y/Ho. The scale of the x-axis is logarithmic, since most of the meta-iron formations have aluminum concentrations lower than one weight percent. The orange line denotes the average PAAS composition (27). At higher than one weight percent aluminum there is a negative correlation between yttrium and aluminum. However, samples with lower than one weight percent aluminum are scattered, plotting mostly around average shale. Since there is no significant different between the Y/Ho ratio and shales, the oceans were anoxic.

It has been stated in the literature that the LREE and HREE fractionate due to the complexation habit of the LREEs relative to the HREEs (Byrne and Kim, 1990; Planavsky et al., 2010). The HREE complex stronger in solution than the LREE causing an enrichment of HREE dissolved in water (Byrne and Kim, 1990). This theory agrees with the work conducted by Goldstein and Jacobsen (1988a), who determined that in modern day rivers, suspended load has HREE-depleted patterns, while dissolved load has HREE-enriched patterns when normalized to shales. As the river reaches the ocean, the suspended load deposits on the delta leaving the dissolved load to enter the ocean, which makes the oceans HREE-enriched relative to shales (Goldstein and Jacobsen, 1988c; Derry and Jacobsen, 1990).

To calculate the slope of the REE curves, the ratio between Pr/Yb normalized to PAAS is used (ex. Planavsky et al., 2010). HREE-depleted and LREE-enriched values will be higher than one, while HREE-enriched and LREE-depleted values are lower than one. Significantly on the aluminum vs Pr/Yb plot (Figure 4.76), most of the samples plot below one, indicating that most of the patterns show a HREE-enrichment or a LREE-depletion. Generally, there is a negative scattered trend between the Pr/Yb ratio and the aluminum content, suggesting that there was a stronger depletion in the LREE with lower degrees of siliciclastic material. Also, at lower degrees of siliciclastic contamination, the Pr/Yb is more scattered. Interestingly, the deeper water meta-iron formations (NC samples) plot at lower Pr/Yb ratios than the BG meta-iron formation samples at the same aluminum levels. This indicates that the HREE are more enriched the deeper water setting compared to the LREE. Significantly, the HREE-enriched pattern compared to the LREEs preserved in the meta-iron formation, suggests that similar LREE and HREE fractionation trends occurring in modern day systems are also occurring in ancient hydrologic systems.
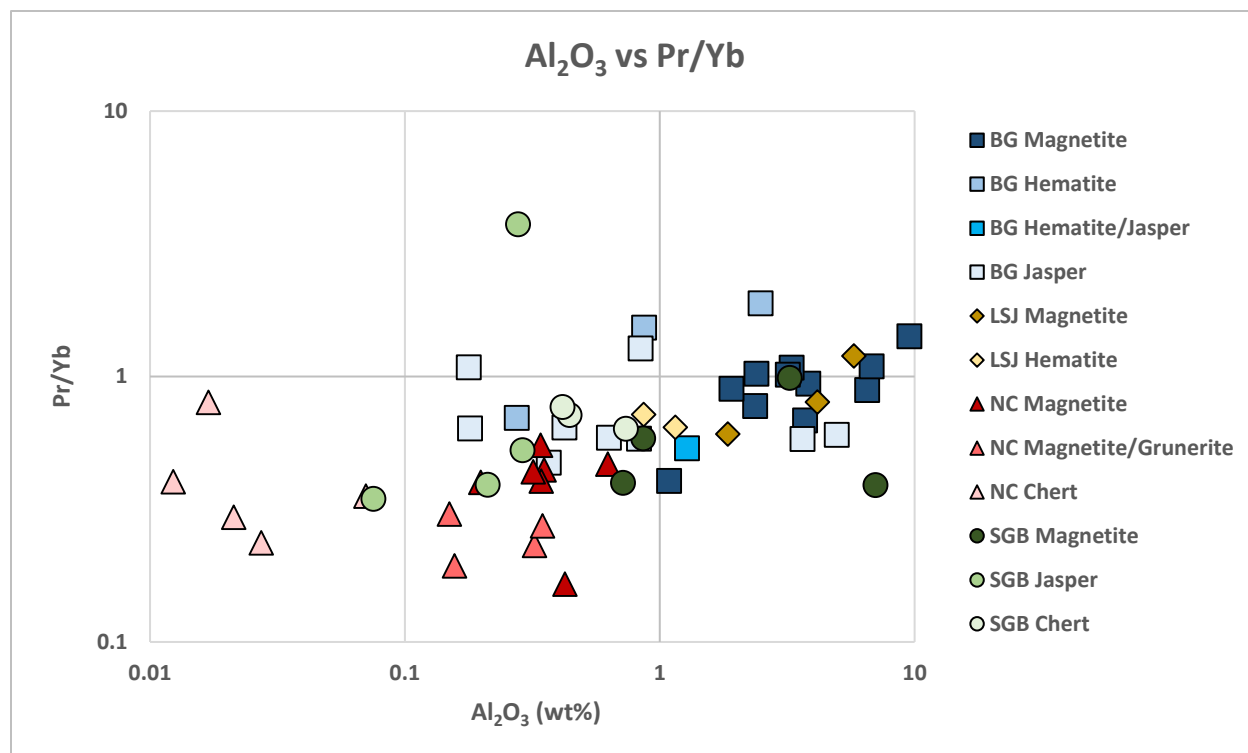
Figure 4.76: A logarithmic bivariate plot of aluminum vs Pr/Yb. Most of the meta-iron formation samples plot below one, indicating that the oceans were HREE-enriched compared to LREE. The lower values for the NC meta-iron formation samples compared to the BG samples at similar aluminum levels suggests that HREE were enriched in the deeper ocean relative to the shallow ocean. This trend is seen in modern day systems, indicating that similar processes were occurring in the Archean oceans.

In summary, at greater than one weight percent aluminum, for most of the shallow water meta-iron formations there is a relationship between the strength of an anomaly and aluminum, suggesting that siliciclastic contamination dampens the strength of anomalies. However, at lower than one weight percent aluminum, the weaker correlation between aluminum and the anomalies suggest the patterns reflect seawater compositions. The deeper water environment has higher hydrothermal europium content and lower Pr/Yb ratios compared to the shallow water environment. This means that the oceans were heterogeneous with respect to the REE chemistry, similar to what is observed in modern day systems. The lack of cerium anomalies and similar Y/Ho ratio between average shales and meta-iron formation samples, suggests that the oceans did not have a redoxcline and were anoxic.

CHAPTER 5

SUMMARY AND CONCLUSIONS

The work conducted in this thesis represents a preliminary study of element provenance in Archean meta-iron formations and the behavior of elements during post-depositional alteration. An outline of the main inferences from this study follows:

1) Based on field observations, petrographic and geochemical work, the SGB meta-iron formation was deposited in the deeper water environment.

2) The metamorphic grade was constrained for all the meta-iron formations in the study. In BG the meta-iron formation the metamorphic grade ranges from lower greenschist to mid-greenschist facies. The metamorphic grade for the LSJ meta-iron formation ranges from mid-greenschist to upper greenschist facies. Metamorphic grade in the NC meta-iron formation was around amphibolite facies, while in the SGB meta-iron formation, the metamorphic grade was at the greenschist facies.

3) Tables 5.1 – 5.4 contain summaries of the provenance and mobility during post-depositional alteration for the major, minor and trace elements in the meta-iron formations. The siliciclastic endmember elements (Al_2O_3, TiO_2, Th, V, Nb, U), rare earth elements and yttrium were immobile during post-depositional alteration. Majority of the iron and silica were most likely sourced from seawater and derived from hydrothermal venting fluids, since all the meta-iron formation samples have positive europium anomalies. The rest of the elements were derived from multiple sources; ex. siliciclastic phase, seawater or hydrothermal venting fluids, in varying proportions.

Table 5.1: Summary of provenance and element mobility for aluminum, titanium, thorium, vanadium, niobium, uranium, total iron, silica, potassium, rubidium and cesium in the meta-iron formation samples.

Al_2O_3, TiO_2, Th, V, Nb, U		
Meta-iron Formation	Provenance	Element Mobility
Beardmore-Gerladton	Derived from the silciclastic phase	Isochemical during post-depositional aletration
Lake St Joseph		
North Caribou		
Shebandowan		
Fe_2O_{3T} and SiO_2		
Meta-iron Formation	Provenance	Element Mobility
Beardmore-Gerladton	Mostly derived from hydrothermal venting fluids	Mostly isochemical during post-depositional aletration
Lake St Joseph		
North Caribou		
Shebandowan		
K_2O and Rb		
Meta-iron Formation	Provenance	Element Mobility
Beardmore-Gerladton	Derived from the siliciclastic phase and seawater, sourced from continental runoff	Immobile in the hematite-, jasper- and chert-dominated layers and mobile in magnetite-dominated layers
Lake St Joseph		
North Caribou	Mostly derived from the siliciclastic phase	
Shebandowan	Derived from the siliciclastic phase and seawater, sourced from continental runoff	Mostly isochemical during post-depositional alteration
Cs		
Meta-iron Formation	Provenance	Element Mobility
Beardmore-Gerladton	Derived from seawater, sourced from hydrothermal venting fluids	Mostly immobile during post depositional alteration
Lake St Joseph		
North Caribou	Late stage hydrothermal metasomatism, and possibly seawater	Mobile during post-depositional alteration
Shebandowan	Mostly derived from seawater, sourced from hydrothermal venting fluids	Mostly immobile during post depositional alteration

Table 5.2: Summary of provenance and element mobility for sodium, calcium, manganese, strontium, zirconium and hafnium in the meta-iron formation samples.

Na$_2$O		
Meta-iron Formation	Provenance	Element Mobility
Beardmore-Gerladton	Mostly derived from the siliciclastic phase, minor amounts derived from seawater, sourced from hydrothermal fluids	Immobile in the magnetite-dominated layers and mobile in the hematite-, jasper- and chert-dominated layers
Lake St Joseph		
North Caribou	Mostly sourced from hydrothermal venting fluids, minor amounts derived from the siliciclastic phase	Unknown, either mobile or immobile
Shebandowan		
CaO and MnO		
Meta-iron Formation	Provenance	Element Mobility
Beardmore-Gerladton	Mostly derived from the siliciclastic phase, minor derived from seawater	Mostly isochemical during post-depositional alteration
Lake St Joseph		
North Caribou	Mostly from seawater, sourced from hydrothermal fluids, minor siliciclastic phase	
Shebandowan	Mostly from seawater, sourced from hydrothermal fluids, minor siliciclastic phase	
Sr		
Meta-iron Formation	Provenance	Element Mobility
Beardmore-Gerladton	Mostly derived from the siliciclastic phase	Slightly mobile during post-depositional alteration
Lake St Joseph		
North Caribou		
Shebandowan		
Zr and Hf		
Meta-iron Formation	Provenance	Element Mobility
Beardmore-Gerladton	Sourced from seawater, minor siliciclastic phase	Mostly isochemical during post-depositional alteration
Lake St Joseph		
North Caribou		
Shebandowan		

Table 5.3: Summary of provenance and element mobility for molybdenum, scandium, chromium, nickel and zinc in the meta-iron formation samples.

Mo		
Meta-iron Formation	Provenance	Element Mobility
Beardmore-Gerladton	Mostly derived from seawater, sourced from continental runoff	Unknown
Lake St Joseph		
North Caribou		
Shebandowan		
Sc and Cr		
Meta-iron Formation	Provenance	Element Mobility
Beardmore-Gerladton	Derived mostly from the siliciclastic phase	Mostly isochemical during post-depositional alteration
Lake St Joseph		
North Caribou	Mostly derived from seawater, sourced from hydrothermal fluids, minor siliciclastic phase	
Shebandowan	Derived mostly from the siliciclastic phase, minor from hydrothermal fluids	
Ni		
Meta-iron Formation	Provenance	Element Mobility
Beardmore-Gerladton	Derived from mostly the siliciclastic phase or seawater	Mostly isochemical during post-depositional alteration, but may have been mobile
Lake St Joseph	Mostly derived from seawater, minor amounts may have been derived from siliciclastic	
North Caribou	Mostly derived from seawater, minor amounts may have been derived from siliciclastic	
Shebandowan	Derived from mostly the siliciclastic phase or seawater	
Zn		
Meta-iron Formation	Provenance	Element Mobility
Beardmore-Gerladton	Mostly derived from the siliciclastic phase, minor influx from continental runoff and hydrothermal venting fluids	Unknown
Lake St Joseph		
North Caribou		
Shebandowan		

Table 5.4: Summary of provenance and element mobility for magnesium, copper, phosphorous, REEs and yttrium in the meta-iron formation samples.

MgO and Cu		
Meta-iron Formation	Provenance	Element Mobility
Beardmore-Gerladton	Source is unknown, could have been derived from multiple sources	Most likely mobile during post-depositional alteration
Lake St Joseph		
North Caribou		
Shebandowan		
P		
Meta-iron Formation	Provenance	Element Mobility
Beardmore-Gerladton	Derived from seawater, sourced from hydrothermal venting, minor from siliciclastics	Most likely mobile during post-depositional alteration
Lake St Joseph		
North Caribou	Unknown, most likely derived from multiple sources	Unknown
Shebandowan	Derived from seawater, sourced from hydrothermal venting minor from siliciclastics	Most likely mobile during post-depositional alteration
REE and Y		
Meta-iron Formation	Provenance	Element Mobility
Beardmore-Gerladton	Siliciclastic phase, hydrothermal venting fluids and seawater	Mostly immobile during post-depositional alteration
Lake St Joseph		
North Caribou		
Shebandowan		

4) The lack of cerium anomaly in most of the meta-iron formation samples, absence of significant yttrium anomalies and deficiency of authigenic chromium supplied to the ancient ocean suggests that a redoxcline did not exist in the Archean ocean. This indicates that most of the ocean was anoxic. Since there was not a major oxygen stratification in the Archean, either metabolic iron oxidation was the primary mechanism for iron oxyhydroxide deposition or the

free oxygen produced by photosynthetic bacterial oxidation was low enough to not generate major oxygen stratification in the Archean ocean.

5) The abundance of carbonate minerals in the magnetite-quartz meta-iron formations relative to hematite-quartz meta-iron formations suggests that diagenetic reactions producing magnetite also produced CO_2 as a by-product.

6) Mobility of elements during diagenetic modification is evidence for sodium and potassium in the BG, LSJ and NC meta-iron formations. Magnetite- and magnetite/grunerite-dominated samples partition sodium and indicate a loss of potassium during diagenesis, while the hematite-, jasper- and chert-dominated samples partition potassium and indicate a loss of sodium during diagenesis. Although it is evident that reactions are partitioning sodium and potassium between layers in the meta-iron formation, the mechanism for the reaction is unknown.

7) Magnetite-dominated meta-iron formation layers from all the study locations contain poikilitic, porphyroblastic magnetite crystals with inclusions of relict detrital siliciclastic-derived phases and mineral phases formed during progressive metamorphism. Porphyroblastic, metamorphic mineral phases also contain significant amounts of fine-grained magnetite crystals. This indicates that magnetite grew during progressive metamorphism.

8) The presence of coarser-grained crystals and metamorphic textures that indicate plastic deformation in the magnetite-dominated samples relative to the quartz-dominated samples, coupled with the evidence of brittle fracturing in the quartz-dominated layers indicates that there are competency contrasts between layers caused by reaction softening. Contact metasomatic reactions were also observed between quartz- and magnetite-dominated layers. These interpretations infer that the layers in the banded meta-iron formation were defined before metamorphism.

Based on the conclusions above, a general depositional model for the banded meta-iron formation follows. Fe^{2+} and silica were derived from hydrothermal venting fluids. Iron oxyhydroxide deposition was caused by metabolic oxidation of microorganism and/or by oxygen-producing photosynthetic cyanobacteria at low levels. Elements dissolved in the water adsorbed onto iron oxyhydroxides and amorphous silica. Deeper oceans were more enriched in Cs, Na_2O, CaO, MnO, Cr and HREEs relative to shallow waters. Shallow oceans were more enriched in K_2O, Rb and LREEs relative to deeper waters. This indicates that the oceans were mostly heterogeneous in composition. Although the mechanism for the cyclicity of the iron-rich and silica-rich layers is unknown, the alternating bands were formed before metamorphism. Magnetite-dominated layers were formed reducing Fe^{3+} to Fe^{2+} in the iron oxyhydroxides by reacting with organic carbon during diagenesis. Dehydration reactions of iron oxyhydroxide during diagenesis formed hematite-dominated layers. Diagenetic modification mobilized sodium in the hematite-, jasper- and chert-dominated samples, while potassium was mobilized in the magnetite-dominated samples. These reactions must have occurred during diagenesis, since metamorphic mineral phases contain inclusions of magnetite and magnetite contains of the metamorphic minerals. Competency contrasts between the less competent magnetite- and more competent quartz-dominated layers was caused by reaction softening in the magnetite-dominated layers during progressive metamorphism. Locally in the meta-iron formation, most of elements were mobile during post-depositional alteration. However, as a whole, the elements in the meta-iron formation deemed mostly immobile during post-depositional alteration were isochemical during post-depositional alteration.

REFERENCES

Andre, L., Cardinal, D., Alleman, L.Y. and Moorbath, S. (2006). Silicon isotopes in ~3.8 Ga West Greenland rocks as clues to the Eoarchaean supracrustal Si cycle. Earth and Planetary Science Letters, 245, 162-173.

Arnold, G.L., Anbar, A.D., Barling, J. and Lyons, T.W. (2004). Molybdenum isotope evidence for widespread anoxia in mid-Proterozoic oceans. Science, 304, p. 87 – 90.

Barrett, T. J. and Fralick, P.W. (1985). Sediment redeposition in Archean iron formation: examples from the Beardmore-Geraldton greenstone belt, Ontario. Journal of Sedimentary Petrology, 55, p. 205 – 212.

Barrett, T. J. and Fralick, P.W. (1989). Turbidites and iron formation, Beardmore–Geraldton, Ontario: application of a combined ramp/fan model to Archean clastic and chemical sedimentation: Sedimentology, 36, p. 221 – 234.

Bath, O. (2017). Provenance of siliciclastic sedimentary rocks in the eastern portion of the North Caribou Greenstone Belt. [M.Sc. Thesis] University of Ottawa, Ottawa, Ontario, 142p.

Bau, M. and Alexander, B.W. (2009). Distribution of high field strength elements (Y, Zr, REE, Hf, Ta, Th, U) in adjacent magnetite and chert bands and in reference standards FeR-3 and FeR-4 from the Temagami iron-formation, Canada, and the redox level of the Neoarchean ocean. Precambrian Research, 174, p. 337 – 346.

Bau, M. and Dulski, P. (1994). Evolution of the yttrium-holmium systematics of seawater through time. Mineralogical Magazine, 58A, p. 61 – 62.

Bau, M. and Dulski, P. (1996). Distribution of yttrium and rare-earth elements in the Penge and Kuruman iron-formations, Transvaal Supergroup, South Africa. Precambrian Research, 79, p. 37 – 55.

Bau, M., Möller, P. and Dulski, P. (1997). Yttrium and lanthanides in eastern Mediterranean seawater and their fractionation during redox-cycling. Marine Chemistry, 56, p. 123 – 131.

Bekker, A., Holland, H.D., Wang, P., Rumble, D., Stein, H.J., Hannah, J.L., Coetzee, L.L. and Beukes, N.J. (2004). Dating the rise of atmospheric oxygen. Nature, 427(6970), p. 117 – 120.

Bekker, A., Planavsky, N., Krapež, B., Rasmussen, B., Hofmann, A., Slack, J.F., Rouxel, O.J. and Konhauser, K.O. (2014). Iron formations: Their origins and implications for ancient seawater chemistry. Treatise on Geochemistry, p. 561 – 628.

Bekker, A., Slack, J.F., Planavsky, N., Krapež, B., Hofmann, A., Konhauser, K.O. and Rouxel, O.J. (2010). Iron formation: The sedimentary product of a complex interplay among mantle, tectonic, oceanic, and biospheric processes. Economic Geology, 105, p. 467 – 508.

Berger, B. (1981). Stratigraphy of the western Lake St. Joseph greenstone terrain, northwestern Ontario. [M.Sc. Thesis] Lakehead University, Thunder Bay, Ontario, 117p.

Biczok, J., Hollings, P., Klipfel, P., Heaman, L., Maas, R., Hamilton, M., Kamo, S. and Friedman, R. (2012). Geochronology of the North Caribou greenstone belt, Superior Province Canada: Implications for tectonic history and gold mineralization at the Musselwhite mine. Precambrian Research, 192-195, p. 209 – 230.

Bjerrum, C.J. and Canfield, D.E. (2002). Ocean productivity before about 1.9 Gyr ago limited by phosphorus adsorption onto iron oxides. Nature, 417, p. 159 – 162.

Bonnand, P., James, R.H., Parkinson, I.J., Connelly, D.P. and Fairchild, I.J. (2013). The chromium isotopic composition of seawater and marine carbonates. Earth and Planetary Science Letters, 382, p. 10 – 20.

Braterman, P.S. and Cairns-Smith, A.G. (1987). Photoprecipitation and the banded iron-formations — Some quantitative aspects. Origins of Life, 17, p. 221 – 228.

Braterman, P.S., Cairns-Smith, A.G. and Sloper, R.W. (1983). Photo-oxidation of hydrated Fe2+ – Significance for banded iron formations. Nature, 303, p. 163 – 164.

Breaks, F.W., Osmani, I.A. and deKemp, E.A. (1986). Opapimiskan Lake Project: Precambrian Geology of the Opapimiskan-Forester Lakes Area, District of Kenora, Patricia Portion; p. 368-378 in Summary of Field Work and Other Activities 1986, by the Ontario Geological Survey, edited by P.C. Thurston, Owen L. White, R.B. Barlow, M.E. Cherry, and A.C. Colvine, Ontario Geological Survey, Miscellaneous Paper 132, 435p.

Breaks, F.W., Osmani, I.A. and deKemp, E.A. (2001). Geology of the North Caribou Lake area, northwestern Ontario; Ontario Geological Survey, Open File Report 6023, 80p.

Bucher, K. and Grapes, R. (2011). Petrogenesis of Metamorphic Rocks (8th ed.). New York: Springer Berlin Heidelberg, 428p.

Buick, R. (2008). When did oxygenic photosynthesis evolve? Philosophical Transactions of the Royal Society B, 363, p. 2731 – 2743.

Burnham, O.M., Hechler, J.H., Semenyna, L. and Schweyer, J. (2004). Mineralogical controls on the determination of trace elements following mixed acid dissolution. Ontario Geological Survey, Open File Report 6100, p. 36.1 – 36.12.

Burnham, O.M. and Schweyer, J. (2004). Trace element analysis of geochemical samples by inductively coupled plasma mass spectrometry at the Geoscience Laboratories: revised capabilities due to improvements to instrumentation. Ontario Geological Survey, Open File Report 6145, p. 54.1 – 54.5.

Byrne, R.H. and Kim, K. (1990). Rare earth element scavenging in seawater. Geochimica et Cosmochimica Acta, 54, p. 2645 – 2656.

Cairns-Smith, A.G., (1978). Precambrian solution photochemistry, inverse segregation, and banded iron formations: Nature, 276, p. 807 – 808.

Canfield, D.E. (1998). A new model for Proterozoic ocean chemistry. Nature, 396, p. 450 – 453.

Card, K.D. and Ciesielski, A. (1986). Subdivisions of the Superior Province of the Canadian Shield. Geoscience Canada, 13(1), p. 5 – 13.

Censi, P., Raso, M., Yechieli, Y., Ginat, H., Saiano, F., Zuddas, P., Brusca, L., D'Alessandro, W. and Inguaggiato, C. (2017). Geochemistry of Zr, Hf, and REE in a wide spectrum of Eh and water composition: The case of Dead Sea Fault system (Israel). Geochemistry, Geophysics, Geosystems, 18, p. 844 – 857.

Chaudhuri, S. and Clauer, N. (1986). Fluctuations of isotopic composition of strontium in seawater during the Phanerozoic Eon. Chemical Geology (Isotope Geoscience Section), 59, p. 293 – 303.

Ciborowski, T.J.R. and Kerr, A.C. (2016). Did mantle plume magmatism help trigger the Great Oxidation Event? Lithos, 246-247, p. 128 – 133.

Cloud, P. (1973). Paleoecological significance of the banded iron-formation. Economic Geology, 68(7), p. 1135 – 1143.

Cloud, P. E. and Licari, G. R. (1968). Microbiotas of the banded iron formations. Proceedings of the National Academy of Sciences, 61(3), p. 779 – 786.

Corfu, F. and Stott, G.M. (1993). U–Pb geochronology of the central Uchi Subprovince, Superior Province. Canadian Journal of Earth Sciences, 30(6), p. 1179 – 1196.

Corfu, F. and Stott, G.M. (1998). Shebandowan greenstone belt, western Superior Province: U-Pb ages, tectonic implications, and correlations. Geological Society of America Bulletin, 110, p. 1467 – 1484.

Davis D.W. and Stott G.M. (2001). Geochronology of several greenstone belts in the Sachigo Subprovince, northwestern Ontario; in Summary of Field Work and Other Activities 2001, Ontario Geological Survey, Open File Report 6070, p. 18-1 to 18-13.

deBaar, H.J.W., German, C.R., Elderfield, H., van Gaans, P. and Bruland, K.W. (Ed.) (1988). Rare earth element distributions in anoxic waters of the Cariaco Trench. Geochimica et Cosmochimica Acta, 52, 1203 – 1219.

Deer, W.A., Howie, R.A. and Zussman, J. (1992). An Introduction to the Rock Forming Minerals, 2nd ed., Longman, London, 696p.

deKemp, E.A. (1987). Stratigraphy, provenance and geochronology of Archean supracrustal rocks of western Eyapamikama Lake area, northwestern Ontario. [M.Sc. Thesis] Carleton University, Ottawa, Ontario, 98p.

Derry, L.A. and Jacobsen, S.B. (1990). The chemical evolution of Precambrian seawater: Evidence for REEs in banded iron formations. Geochimica et Cosochimica Acta, 54, p. 2965 – 2977.

Devaney, J.R. and Fralick, P.W. (1985). Regional sedimentology of the Namewaminikan Group, northern Ontario: Archean fluvial fans, braided rivers, deltas, and an aquabasin. In current research, part B. Geological Survey of Canada, Paper 85-1B, p. 125 – 132.

Devaney, J. R. and Williams, H. R. (1989). Evolution of an Archean subprovince boundary: a sedimentological and structural study of part of the Wabigoon-Quetico boundary in northern Ontario. Canadian Journal of Earth Sciences, 26, p. 1013 – 1026.

deWit, M. J. and Ashwal, L. D. (1986). Workshop on Tectonic Evolution of Greenstone Belts. LPI Tech. Rpt. 86-10. Lunar and Planetary Institute, Houston. 227p.

Dimroth, E. (1977). Facies models 6. Diagenetic facies of iron formation. Geoscience Canada, 4(2), p. 83 – 88.

Dodd, M.S., Papineau, D., Grenne, T., Slack, J.F., Rittner, M., Pirajno, F., O'Neil, J. and Little, C.T.S. (2017). Evidence for early life in Earth's oldest hydrothermal vent precipitates. Nature, 543, p. 60 – 64.

Døssing, L.N., Dideriksen, K., Stipp, S.L.S. and Frei, R. (2011). Reduction of hexavalent chromium by ferrous iron: A process   of chromium isotope fractionation and its relevance to natural environments. Chemical Geology, 285, p. 157 – 166.

Douglas, R.J.W. (1973). Geological Provinces, Map 27-28, National Atlas of Canada, 4th Edition: Surveys and Mapping Branch, Department of Energy, Mines and Resources, Ottawa.

Douville, E., Bienvenu, P., Charlou, J.L., Donval, J.P., Fouquet, Y., Appriou, P. and Gamo, T. (1999). Yttrium and rare earth elements in fluids from various deep-sea hydrothermal systems. Geochimica et Cosmochimica Acta, 63, p. 627 – 643.

Drever, J.I. (1974). Geochemical model for the origin of Precambrian banded iron formations. Geological Society of America Bulletin, 85, p. 1099 – 1106.

Droop, G.T.R. (1987). A general equation for estimating Fe^{3+} concentrations in ferromagnesian silicates and oxides from microprobe analyses, using stoichiometric criteria. Mineralogical Magazine, 51, p. 431 – 435.

Duff, J. (2014) A geochemical and isotope investigation of metasedimentary rocks from the North Caribou greenstone belt, western Superior Province, Canada. [M.Sc. Thesis] University of Ottawa, Ottawa, Canada, 168p.

Duraiswami, R. A., Inamdar, M. M. and Shaikh, T. N. (2013). Emplacement of pillow lavas from the ~ 2.8 Ga Chitradurga Greenstone Belt, South India: A physical volcanological, morphometric and geochemical perspective. Journal of Volcanology and Geothermal Research, 264, p. 134 – 149.

Edmonds, H.N. and German, C.R. (2004). Particle geochemistry in the Rainbow hydrothermal plume, Mid-Atlantic Ridge. Geochimica et Cosmochimica Acta, 68, p. 759 – 772.

Feely, R.A., Trefry, J.H., Lebon, G.T. and German, C.R. (1998). The relationship between P/Fe and V/Fe ratios in hydrothermal precipitates and dissolved phosphate in seawater. Geophysical Research Letters, 25, p. 2253 – 2256.

Fendorf, S.E. (1995). Surface reactions of chromium in soils and waters. Geoderma, 65, p. 55 – 71.

Fischer, W.W. and Knoll, A.H. (2009). An iron shuttle for deepwater silica in Late Archean and early Paleoproterozoic iron formation. Geological Society of America Bulletin, 121(1/2), p. 222 – 235.

Fralick, P.W. (2003). Geochemistry of clastic sedimentary rocks: Ratio techniques, in Lentz, D.R., ed., Geochemistry of Sediments and Sedimentary Rocks: Toronto, Ontario, Canada, Geological Association of Canada, Geotext 4, p. 85 – 104.

Fralick, P.W. and Barret, T.J. (1991). Precambrian depositional systems along the southwestern edge of the Superior craton. Geological Association of Canada, Mineralogical Association of Canada, Society of Economic Geologists, Joint Annual Meeting, Toronto '91, Field Trip A3: Guidebook, 54p.

Fralick, P.W., Barrett, T.J., Jarvis, K.E., Jarvis, I., Schnieders, B.R. and Kemp, R.V. (1989). Sulphide-facies iron formation at the Archean Morley occurrence, northwestern Ontario: contrasts with oceanic hydrothermal deposits. Canadian Mineralogist, 27, p. 601 – 616.

Fralick, P.W. and Kronberg, B.I. (1997). Geochemical discrimination of clastic sedimentary rock sources. Sedimentary Geology, 113(1-2), p. 111 – 124.

Fralick, P.W. and Pufahl, P.K. (2006). Iron Formation in Neoarchean deltaic successions and the microbially mediated deposition of transgressive systems tracts. Journal of Sedimentary Research, 76(9), p. 1057 – 1066.

Fralick, P.W., Wu, J. and Williams, H.R. (1992). Trench and slope basin deposits in an Archean metasedimentary belt, Superior Province, Canadian Shield. Canadian Journal of Earth Sciences, 29, p. 2551 – 2557.

Frei, R., Gaucher, C., Poulton, S.W. and Canfield, D.E. (2009). Fluctuations in Precambrian atmospheric oxygenation recorded by chromium isotopes. Nature, 461, p. 250 – 253.

Fru, E.C., Rodríguez, N.P., Partin, C.A., Lalonde, S.V., Andersson, P., Weiss, D.J., Albani, A.E., Rodushkin, I. and Konhauser, K.O. (2016). Cu isotopes in marine black shales record the Great Oxidation Event. Proceedings of the National Academy of Sciences, 113, p. 4941 – 4946.

Fuchida, S., Mizuno, Y., Masuda, H., Toki, T. and Makita, H. (2014). Concentrations and distributions of amino acids in black and white smoker fluids at temperatures over 200°C. Organic Geochemistry, 66, p. 98 – 106.

Garcia, T.I. (2014). Comparison between the Helen iron formation (Algoma-type) and the Sokoman iron formation (Superior-type): Differences and similarities in their depositional environments, mineralogy and geochemistry [PhD Thesis] University of Toronto, Toronto, Ontario, 176p.

Garrels, R.M., Perry, E.A. and Mackenzie, F.T. (1973). Genesis of Precambrian iron-formations and the development of atmospheric oxygen. Economic Geology, 68, p. 1173 – 1179.

Goldstein, S.J. and Jacobsen, S.B. (1988a). REE in the Great Whale River estuary, northwest Quebec. Earth and Planetary Science Letters, 88, p. 241 – 252.

Goldstein, S.J. and Jacobsen, S.B. (1988c). Rare earth elements in river waters. Earth and Planetary Science Letters, 89, p. 35 – 47.

Graham, D.W., Bender, M.L., Williams, D.F. and Keigwin, L.D. (1982). Strontium-calcium ratios in Cenozoic planktonic foraminifera. Geochimica et Cosmochimica Acta, 46, p. 1281 – 1292.

Gross, G.A. (1965). Geology of iron deposits in Canada: general geology and evaluation of iron deposits: Geological Survey Canada, Economic Geology. Report 22, 1, 181 p.

Hall, R.S. and Rigg, D.M. (1986). Geology of the West Anticline Zone, Musselwhite Prospect, Opapimiskan Lake, Ontario, Canada: in Proceedings of Gold '86 Symposium, Konsult International, Toronto, Ontario, p. 124 – 136.

Hamade, T., Konhauser, K.O., Raiswell, R., Goldsmith, S., & Morris, R.C. (2003). Using Ge/Si ratios to decouple iron and silica fluxes in Precambrian banded iron formations. Geology, 31(1), p. 35–38.

Hart, T.R., terMeer, M. and Jolette, C. (2002). Precambrian geology of Kitto, Eva, Summers, Dorothea and Sandra townships, northwestern Ontario: Phoenix Bedrock Mapping Project; Ontario Geological Survey, Open File Report 6095, 206p.

Heck, P.R., Huberty, J.M., Kita, N.T., Ushikubo, T., Kozdon, R. and Valley, J.W. (2011). SIMS analyses of silicon and oxygen isotope ratios for quartz from Archean and Paleoproterozoic banded iron formations. Geochimica et Cosmochimica Acta, 75, p. 5879 – 5891.

Heier, K.S. (1962). Trace elements in feldspars — a review. Norsk Geol. Tidsskr. 42, p. 415 – 454.

Holland, H.D. (1973). The oceans: A possible source of iron in iron-formations. Economic Geology, 68, p. 1169 – 1172.

Holland, H.D. (2002). Volcanic gases, black smokers, and the great oxidation event. Geochimica et Cosmochimica Acta, 66(21), p. 3811 – 3826.

Hollings, P. and Kerrich, R. (1999). Trace element systematics of ultramafic and mafic volcanic rocks from the 3Ga North Caribou greenstone belt, northwestern Superior Province. Precambrian Research, 93, p. 257 – 279.

Hollings, P., Wyman, D. and Kerrich, R. (1999). Komatiite–basalt–rhyolite volcanic associations in Northern Superior Province greenstone belts: significance of plume-arc interaction in the generation of the proto continental Superior Province. Lithos, 46(1), p. 137 – 161.

James, H.L. (1954). Sedimentary facies of iron-formation. Economic Geology, 49(3), p. 235 – 293.

James, H.L. (1955). Zones of regional metamorphism in the Precambrian of northern Michigan. Bulletin of the Geological Society of America, 66, p. 1455 – 1488.

Jones, C., Nomosatryo, S., Crowe, S.A., Bjerrum, C.J. and Canfield, D.E. (2015). Iron oxides, divalent cations, silica, and the early earth phosphorus crisis. Geology, 43(2), p. 135 – 138.

Kipp M.A. and Stüeken E.E. (2017). Biomass recycling and Earth's early phosphorus cycle. Science Advances, 3, eaao4795, 6p.

Klein, C. (1973). Changes in mineral assemblages with metamorphism of some banded Precambrian iron-formations. Economic Geology, 68, p. 1075 – 1088.

Klein, C. (2005). Some Precambrian banded iron-formations (BIFs) from around the world: Their age, geologic setting, mineralogy, metamorphism, geochemistry, and origins. American Mineralogist, 90, p. 1473 – 1499.

Klinkhammer, G.P., Elderfield, H., Edmond, J.M. and Mitra, A. (1994a). Geochemical implications of rare earth element patterns in hydrothermal fluids from mid-ocean ridges. Geochimica et Cosmochimica Acta, 58, p. 5105 – 5113.

Konhauser, K.O., Amskold, L., Lalonde, S.V., Posth, N.R., Kappler, A. and Anbar, A. (2007). Decoupling photochemical Fe(II) oxidation from shallow-water BIF deposition. Earth and Planetary Science Letters, 258, p. 87 – 100.

Konhauser, K.O., Hamade, T., Raiswell, R., Morris, R.C., Ferris, F.G., Southam, G. and Canfield, D.E. (2002). Could bacteria have formed the Precambrian banded iron formations? Geological Society of America, 30(12), p. 1079 – 1082.

Konhauser, K.O., Lalonde, S.V., Planavsky, N.J., Pecoits, E., Lyons, T.W., Mojzsis, S.J., Rouxel, O.J., Barley, M.E., Rosìere, C., Fralick, P.W., Kump, L.R. and Bekker, A. (2011). Aerobic bacterial pyrite oxidation and acid rock drainage during the Great Oxidation Event. Nature, 478, p. 369 – 373.

Konhauser, K.O., Newman, D.K. and Kappler, A. (2005). The potential significance of microbial Fe(III) reduction during deposition of Precambrian banded iron formations. Geobiology, 3, p. 167 – 177.

Konhauser, K.O., Pecoits, E., Lalonde, S.V., Papineau, D., Nisbet, E.G., Barley, M.E., Arndt, N.T., Zahnle, K. and Kamber, B.S. (2009). Oceanic nickel depletion and a methanogen famine before the Great Oxidation Event. Nature, 458, p. 750 – 753.

Krapež, B., Barley, M.E. and Pickard, A.L. (2003). Hydrothermal and resedimented origins of the precursor sediments to banded iron formation: sedimentological evidence from the Early Palaeoproterozoic Brockman Supersequence of Western Australia. Sedimentology, 50, 979 – 1011.

Kurzweil, F., Wille, M., Gantert, N., Beukes, N.J. and Schoenberg, R. (2016). Manganese oxide shuttling in pre-GOE oceans – evidence from molybdenum and iron isotopes. Earth and Planetary Science Letters, 452, p. 69 – 78.

LaBerge, G.L. (1973). Possible biological origin of Precambrian iron-formations. Economic Geology, 68, p. 1098 – 1109.

Langford, F.F. and Morin, J.A. (1976). The development of the Superior Province of northwestern Ontario by merging island arcs. American Journal of Science, 276, p. 1023 – 1034.

Li, Y.-L. (2014). Micro- and nanobands in late Archean and Palaeoproterozoic banded-iron formations as possible mineral records of annual and diurnal depositions. Earth and Planetary Science Letters, 391, p. 160 – 170.

Li, Y., Hou, K., Wan, D., Zhang, Z. and Yue, G. (2014). Precambrian banded iron formations in the North China Craton: Silicon and oxygen isotopes and genetic implications. Ore Geology Reviews, 57, p. 299 – 307.

Lodge, R.W. (2016). Petrogenesis of intermediate volcanic assemblages from the Shebandowan greenstone belt, Superior Province: Evidence for subduction during the Neoarchean. Precambrian Research, 272, p. 150 – 167.

MacLean, W.H. (1990). Mass change calculations in altered rock series. Mineralium Deposita, 25, p. 44 – 49.

Maliva, R.G., Knoll, A. H. and Siever, R. (1989). Secular change in chert distribution: A reflection of evolving biological participation in the Silica Cycle. Palaios, 4, p. 519 – 532.

McNicoll, V., Dubé, B., Castonguay, S., Oswald, W., Biczok, J., Mercier-Langevin, P., Skulski, T. and Malo, M. (2016). The world-class Musselwhite BIF-hosted gold deposit, Superior Province, Canada: New high-precision U–Pb geochronology and implications for the geological setting of the deposit and gold exploration. Precambrian Research, 272, p. 133 – 149.

Meyn, H.D. and Palonen, P.A. (1980). Stratigraphy of an Archean submarine fan. Precambrian Research, 12, p. 257 – 285.

Moran, P.C. (2008). Lithogeochemistry of the sedimentary stratigraphy and metasomatic alteration in the Musselwhite gold deposit, North Caribou Lake belt, Superior Province, Canada: implications for deposition and mineralization. [M.Sc. Thesis] Lakehead University, Thunder Bay, Ontario, 411p.

Morin, J. A. (1973). Geology of the Lower Shebandowan Lake area, District of Thunder Bay; Ontario Div. Mines, GR110, 45p. Accompanied by Map 2267, scale l inch to 1/2 mile.

Nance, W. B. and Taylor, S. R. (1976). Rare earth element patterns and crustal evolution—I. Australian post-Archean sedimentary rocks. Geochimica et Cosmochimica Acta, 40, p. 1539 – 1551.

Osmani, I.A. (1997). Geology and mineral potential: Greenwater Lake area, West-Central Shebandowan Greenstone Belt; Ontario Geological Survey, Report 296, 135p.

Oswald, W., Castonguay, S., Dubé, B., Malo, M., and Mercier-Langevin, P. and Biczok, J. (2015). New insights on the geological and structural settings of the Musselwhite banded iron-formation-hosted gold deposit, North Caribou greenstone belt, Superior Province, Ontario; Geological Survey of Canada, Current Research 2015-3. 19p.

Otto, A. (2002). Ore forming processes in the BIF-hosted gold deposit Musselwhite Mine, Ontario, Canada. [M.Sc. thesis] Freiberg Institute of Mining and Technology, Freiberg, Germany, 86 pp.

Pan, Y., Fleet, M.E. and Williams, H.R. (1994). Granulite-facies metamorphism in the Quetico Subprovince, north of Manitouwadge, Ontario. Canadian Journal of Earth Sciences, 31(9), p. 1427 – 1439.

Patzer, A., Pack, A. and Gerdes, A. (2010). Zirconium and hafnium in meteorites. Meteoritics and Planetary Science, 45, p. 1136 – 1151.

Percival, J.A. and Easton, R.M. (2007). Geology of the Canadian Shield in Ontario: an update; Ontario Geological Survey, Open File Report 6196, Geological Survey of Canada, Open File 5511, Ontario Power Generation, Report 06819-REP-01200-10158-R00, 65p.

Percival, J.A., Sanborn-Barrie, M., Skulski, T., Scott, G.M., Helmstaedt, H. and White, D.J. (2006). Tectonic evolution of the western Superior Province from NATMAP and lithoprobe studies. Canadian Journal of Earth Sciences, 43(7), p. 1085-1117.

Perry, E. C., Lefticariu, L. (2007). Formation and geochemistry of Precambrian cherts. In: Treatise on Geochemistry; H. Holland and K. Turekian (eds.), 7, Sediments, Diagenesis, and Sedimentary Rocks; F.T. MacKenzie (Ed.), p. 99 – 113.

Peter, J.M. (2003). Ancient iron formations: their genesis and use in exploration of stratiform base metal sulphide deposits, with examples from the Bathurst Mining Camp, in Lentz, D.R., ed., Geochemistry of Sediments and Sedimentary Rocks: Evolutionary Considerations to Mineral Deposit-Forming Environments: Geological Association of Canada, GeoText 4, p. 145 – 176.

Planavsky, N.J., Asael, D., Hofmann, A., Reinhard, C.T., Lalonde, S.V., Knudsen, A., Wang, X., Ossa Ossa, F., Pecoits, E., Smith, A.J.B., Beukes, N.J., Bekker, A., Johnson, T.M., Konhauser, K.O., Lyons, T.W. and Rouxel, O.J. (2014). Evidence for oxygenic photosynthesis half a billion years before the Great Oxidation Event. Nature Geoscience, 7, p. 283 – 286.

Planavsky, N.J., Bekker, A., Rouxel, O. J., Kamber, B., Hofmann, A., Knudsen, A. and Lyons, T. W. (2010). Rare Earth Element and yttrium compositions of Archean and Paleoproterozoic Fe formations revisited: New perspectives on the significance and mechanisms of deposition. Geochimica et Cosmochimica Acta, 74, p. 6387 – 6405.

Posth, N.R., Köhler, I., Swanner, E.D., Schröder, C., Wellmann, E., Binder, B., Konhauser, K.O., Neumann, U., Berthold, C., Nowak, M. and Kappler, A. (2013). Simulating Precambrian banded iron formation diagenesis. Chemical Geology, 362, p. 66 – 73.

Poulton, S.W. and Canfield, D.E. (2006). Co-diagenesis of iron and phosphorus in hydrothermal sediments from the southern East Pacific Rise: Implications for the evaluation of paleoseawater phosphate concentrations. Geochimica et Cosmochimica Acta, 70, p. 5883 – 5898.

Rayner, N. and Stott, G.M. (2005). Discrimination of Archean domains in the Sachigo Subprovince: A progress report on the geochronology; in Summary of Field Work and Other Activities 2005, Ontario Geologic Survey, Open File Report 6172, p. 10-1 to 10-21.

Rollinson, H. R. (1992). Another look at the constant sum problem in geochemistry. Mineralogical Magazine, 56, p. 469 – 475.

Schirrmeister, B.E., Gugger, M. and Donoghue, P.C.J. (2015). Cyanobacteria and the great oxidation event: evidence from genes and fossils. Palaeontology, 58, Part 5, p. 769 – 785.

Schopf, J.W., Kudryavtsev, A.B., Czaja, A.D. and Tripathi, A.B. (2007). Evidence of Archean life: Stromatolites and microfossils. Precambrian Research, 158, p. 141 – 155.

Schmid, R., Fettes, D., Harte, B., Davis E. and Desmons, J. (2007). A systematic nomenclature for metamorphic rocks: 1. How to name a metamorphic rock. Recommendations by the IUGS Subcommission on the Systematics of Metamorphic Rocks. Recommendations, 22p.

Siever, R. (1992). The silica cycle in the Precambrian. Geochimica et Cosmochimica Acta, 56, p. 3265 – 3272.

Smyk, E. (2013). Geochemistry and petrography study of a Mesoarchean felsic metavolcanic unit near Musselwhite Mine, North Caribou greenstone belt. [HBSc. Thesis] Lakehead University, Thunder Bay, Ontario, 106p.

Smyk, M., Fralick, P.W. and Hart T.R. (2005). Field trip 1 – Geology and gold mineralisation of the Beardmore-Geraldton greenstone belt. In; Hollings, P. (Ed.), Institute on Lake Superior Geology Proceedings, 51st Annual Meeting, Nipigon, Ontario, Part 2 – Field trip guidebook, v.51, part 2, p. 3 – 40.

Steinhoefel, G., Horn, I. and Blanckenburg, F.V. (2009). Micro-scale tracing of Fe and Si isotope signatures in banded iron formation using femtosecond laser ablation. Geochimica et Cosmochimica Acta, 73, p. 5343 – 5360.

Stinson, V. (2013). An investigation on the control of gold mineralization in the Beardmore-Geraldton greenstone belt and surrounding Quetico-Wabigoon subprovince boundary area. [M.Sc. Thesis] Lakehead University, Thunder Bay, Ontario, 152p.

Stott, G.M. (2011) A revised terrane subdivision of the Superior Province in Ontario: Ontario Geological Survey, Ministry of Northern Development and Mines, Government of Ontario Miscellaneous Release—Data 278.

Stott, G.M. and Corfu, F. (1991). Uchi Subprovince; in Geology of Ontario, Ontario Geological Survey, Special Volume 4, Part 1, p. 145-237.

Taylor, S.R. and McLennan, S.M. (1988). Significance of the rare earth elements in geochemistry and cosmochemistry. In; Gschniedner K.A. and Eyring L. (Ed.), Handbook on the Physics and Chemistry of Rare Earths, 11, p. 485 – 578.

Thurston, P.C. (1991). Archean geology in Ontario: introduction; in Geology of Ontario, Ontario Geological Survey, Special Volume 4, Part 1, p. 73 – 79.

Thurston, P. and Chivers, K. (1990). Secular variation in greenstone sequence development emphasizing Superior Province, Canada. Precambrian Research, 46(1-2), p. 21 – 58.

Thurston, P.C., Osmani L.A. and Stone, D. (1991). Northwestern Superior Province: review and terrane analysis; in Geology of Ontario, Ontario Geological Survey, Special Volume 4, Part 1, p. 81 – 143.

Tomlinson, K.Y., Bowins, R. and Heshler, J. (1998). Refinement of hafnium (Hf) and zirconium (Zr) analysis by improvement in the sample digestion procedure. Ontario Geological Survey, Miscellaneous Paper 169, p. 189 – 192.

Tostevin, R., Shields, G.A., Tarbuck, G.M., He, T., Clarkson, M.O. and Wood, R.A. (2016). Effective use of cerium anomalies as a redox proxy in carbonate-dominated marine settings. Chemical Geology, 438, p. 146 – 162.

Tripati, A. K., Allmon, W. D. and Sampson, D. E. (2009). Possible evidence for a large decrease in seawater strontium/calcium ratios and strontium concentrations during the Cenozoic. Earth and Planetary Science Letters, 282, p. 122 – 130.

Tullis, J. (2002). Deformation of granitic rocks: Experimental studies and natural examples. Reviews in Mineralogy and Geochemistry, 51, p. 51 – 95.

Veizer, J. (1989). Strontium isotopes in seawater through time. Annual Review of Earth and Planetary Sciences, 17, p. 141 – 167.

Williams, H.R., Stott G.M., Heather K.B., Muir, T.L. and Sage R.P. (1991). Wawa Subprovince; in Geology of Ontario, Ontario Geological Survey, Special Volume 4, Part 1, p. 485 – 540.

Winchester, J.A. and Floyd, P.A. (1977). Geochemical discrimination of different magma series and their differentiation products using immobile elements. Chemical Geology, 20, p. 325 – 343.

Winter, J.D. (2010). An Introduction to Igneous and Metamorphic Petrology (2nd ed.). New York: Prentice Hall, 702p.

APPENDIX A

SEM Data

Beardmore/Geraldton Greenstone Belt

Metasandstone Pt.1

Mineral Phase	Albite 14.1	Albite 14.2	Albite 14.3	Albite 14.4	Albite 14.5	Albite 14.6	Ankerite 14.1	Ankerite 14.2	Ankerite 14.3	Ankerite 14.4	Ankerite 14.5	Ankerite 14.6	Apatite 14.1
Major Element	wt%	wt%	wt%	wt%	wt%	wt%	wt%	wt%	wt%	wt%	wt%	wt%	wt%
SiO_2	66.61	68.13	67.94	68.94	68.69	67.69	0.22	0.37	0.30	1.18	0.46	0.52	0.81
Al_2O_3	18.56	17.14	18.18	19.55	19.55	19.01	0.18	0.04	0.11	0.30	0.09	0.26	0.12
TiO_2	0.00	B.D.	B.D.	0.03	0.01	0.01	0.03	0.00	0.00	0.05	0.01	0.02	0.00
FeO	0.07	0.09	0.06	0.13	0.10	0.26	14.88	15.21	16.12	17.24	18.03	16.23	0.11
MnO	B.D.	0.01	0.00	0.03	0.02	0.02	0.41	0.45	0.74	0.78	0.90	0.75	0.05
CaO	0.02	0.03	0.06	0.13	0.10	0.26	25.50	27.59	27.18	28.08	28.04	27.70	55.10
MgO	0.04	B.D.	0.04	B.D.	0.00	0.01	10.90	11.38	10.64	10.12	9.14	10.87	0.02
Na_2O	11.64	11.34	11.46	12.13	12.24	12.04	0.13	B.D.	0.02	0.06	0.05	0.13	0.07
K_2O	0.05	0.04	0.12	0.06	0.09	0.04	0.07	0.01	0.03	0.08	0.05	0.11	0.17
P_2O_5	0.00	0.00	0.02	B.D.	0.00	0.14	B.D.	0.00	0.04	B.D.	B.D.	B.D.	41.17
Total	96.99	96.78	97.88	101.00	100.80	99.48	52.32	55.05	55.18	57.89	56.77	56.59	97.62
Cation Sum	3.76	3.73	3.74	3.77	3.77	3.77	5.99	5.96	5.96	5.88	5.96	5.96	3.55

Mineral Phase	Apatite 14.2	Apatite 14.3	Apatite 14.4	Apatite 14.5	Apatite 14.6	Chlorite 14.2	Chlorite 14.3	Chlorite 14.5	Chlorite 14.6	Muscovite 14.1	Muscovite 14.2	Muscovite 14.3	Muscovite 14.4
Major Element	wt%	wt%	wt%	wt%	wt%	wt%	wt%	wt%	wt%	wt%	wt%	wt%	wt%
SiO_2	0.84	0.62	0.60	0.40	0.96	25.92	24.41	25.13	29.08	46.73	44.93	50.08	50.49
Al_2O_3	0.09	0.02	0.07	0.13	0.02	20.23	20.34	21.47	21.52	29.58	26.10	28.59	23.50
TiO_2	B.D.	B.D.	0.06	0.04	B.D.	0.04	0.02	0.04	0.12	0.42	0.51	0.21	0.60
FeO	0.33	0.10	0.24	0.12	0.02	31.39	32.36	32.29	30.23	4.66	5.56	3.15	6.79
MnO	B.D.	B.D.	0.04	0.10	0.01	0.09	0.08	0.03	0.04	0.01	0.02	0.05	B.D.
CaO	53.48	53.87	55.57	56.58	55.84	0.03	0.07	0.04	0.04	0.03	0.12	0.09	0.09
MgO	0.13	0.01	0.20	0.04	0.05	8.56	9.39	9.84	9.93	1.18	1.51	0.47	1.64
Na_2O	0.19	0.19	0.18	B.D.	0.30	0.17	0.09	0.19	0.17	0.19	0.09	0.39	0.13
K_2O	0.05	0.04	0.10	0.07	0.08	0.28	0.05	0.08	0.88	10.65	10.43	9.56	9.44
P_2O_5	40.52	40.70	42.73	43.20	40.86	0.11	B.D.	0.00	0.05	0.03	0.01	B.D.	B.D.
Total	95.63	95.55	99.79	100.68	98.14	86.82	86.81	89.11	92.06	93.48	89.28	92.59	92.68
Cation Sum	3.54	3.58	3.54	3.57	3.55	4.22	4.27	4.27	4.20	3.83	3.85	3.74	3.77

Metasandstone Pt. 2

Mineral Phase	Muscovite 14.5	Muscovite 14.6	Quartz 14.1	Quartz 14.2	Quartz 14.3	Quartz 14.4	Quartz 14.5	Quartz 14.6	Rutile 14.1	Siderite 14.1	Siderite 14.2	Siderite 14.3	Siderite 14.4
Major Element	wt%	wt%	wt%	wt%	wt%	wt%	wt%	wt%	wt%	wt%	wt%	wt%	wt%
SiO_2	49.20	46.66	99.05	95.94	99.44	102.85	102	101.83	4.13	0.38	0.4	0.42	0.54
Al_2O_3	26.26	28.13	0.13	0.23	0.33	0.04	0.09	0.04	1.35	0.08	0.10	0.17	0.05
TiO_2	0.21	0.45	B.D.	B.D.	0.01	0.03	B.D.	0.02	93.17	0.01	0.08	B.D.	B.D.
FeO	6.32	5.18	0.16	0.1	0.45	0.06	B.D.	0.12	1.42	45.67	45.50	45.36	46.24
MnO	B.D.	0.04	B.D.	0.07	0.01	B.D.	B.D.	0.03	B.D.	0.67	0.77	0.85	0.67
CaO	0.08	0.09	B.D.	0	0	0.05	0.02	0.01	0.06	0.28	0.19	0.36	0.32
MgO	2.01	1.52	0.05	0.01	0.1	B.D.	B.D.	0.02	0.13	10.67	10.94	10.29	11.72
Na_2O	0.09	0.16	0.08	0.08	0.08	0.09	B.D.	0.03	0.01	0.07	0.18	0.16	0.29
K_2O	10.92	10.94	0.04	0.11	0.03	0.01	B.D.	0.07	0.56	0.01	0.03	0.09	0.03
P_2O_5	B.D.	0.05	0.05	0.05	B.D.	B.D.	0.02	0.00	0.01	0.02	B.D.	0.04	B.D.
Total	95.09	93.22	99.56	96.59	100.45	103.13	102.13	102.17	100.84	57.86	58.19	57.74	59.86
Cation Sum	3.84	3.85	3.01	3.01	3.02	3.01	3.00	3.01	3.07	5.96	5.97	5.97	5.98

Mineral Phase	Siderite 14.5	Siderite 14.6
Major Element	wt%	wt%
SiO_2	0.45	0.43
Al_2O_3	0.09	0.11
TiO_2	B.D.	0.03
FeO	46.28	46.19
MnO	0.96	0.75
CaO	0.53	0.7
MgO	11.12	10.99
Na_2O	0.2	0.21
K_2O	0.03	0
P_2O_5	0	0.03
Total	59.66	59.44
Cation Sum	5.97	5.96

Metasiltstone Pt.1

Mineral Phase	Albite 15.1	Albite 15.2	Albite 15.3	Albite 15.4	Albite 15.5	Albite 15.6	Apatite 15.1	Apatite 15.2	Apatite 15.3	Apatite 15.4	Apatite 15.5	Apatite 15.6	Chlorite 15.1
Major Element	wt%	wt%	wt%	wt%	wt%	wt%	wt%	wt%	wt%	wt%	wt%	wt%	wt%
SiO_2	64.17	69.39	62.45	70.9	65.8	68.29	0.52	0.41	0.19	0.5	0.26	0.88	35.22
Al_2O_3	18.4	15.99	19.04	16.67	19.2	19.15	0.08	0.22	0.16	0.18	0.09	0.05	18.64
TiO_2	0.15	0.01	0.08	0	0.07	0.02	0.02	B.D.	0.04	0.05	B.D.	0.06	0.11
FeO	1.92	0.25	1.14	0.58	0.76	0.28	0.11	0.37	0.25	0.46	0.54	0.59	27.41
MnO	B.D.	0.05	0.01	0.01	0	0.01	B.D.	0.01	0.07	0.02	0.10	0.22	0.07
CaO	B.D.	B.D.	0.19	0.03	0.01	0.06	54.80	54.71	55.33	54.92	55.46	55.02	0.02
MgO	0.39	0.06	0.26	0.12	0.34	0.06	0.07	0.08	0.07	0.02	0.03	0.04	11.64
Na_2O	10.55	9.84	10.15	10.42	10.78	12.06	B.D.	0.04	0.05	0.14	0.05	B.D.	0.17
K_2O	0.14	0.12	0.93	0.08	0.53	0.14	0.07	0.28	0.26	0.32	0.16	0.09	0.02
P_2O_5	0.07	B.D.	0.11	B.D.	0.03	B.D.	41.89	41.49	42.31	41.25	42.68	42.21	0.00
Total	95.79	95.71	94.36	98.81	97.52	100.07	97.56	97.61	98.73	97.86	99.37	99.16	93.30
Cation Sum	3.76	3.65	3.77	3.68	3.76	3.77	3.53	3.51	3.56	3.53	3.54	3.58	4.08

Mineral Phase	Chlorite 15.2	Chlorite 15.3	Chlorite 15.4	Chlorite 15.5	Chlorite 15.6	Hematite 15.1	Hematite 15.2	Hematite 15.3	Hematite 15.4	Hematite 15.5	Hematite 15.6	Muscovite 15.1	Muscovite 15.2
Major Element	wt%	wt%	wt%	wt%	wt%	wt%	wt%	wt%	wt%	wt%	wt%	wt%	wt%
SiO_2	24.76	28.54	24.94	25.83	25.33	4.35	1.44	2.75	0.53	1.28	0.61	48.52	56.76
Al_2O_3	19.61	21.41	18.97	20.49	19.67	1.90	0.68	0.97	0.11	0.33	0.17	24.50	21.72
TiO_2	0.08	0.06	0.15	0.09	0.02	1.58	2.00	1.82	1.47	1.30	2.06	0.71	0.67
FeO	29.73	27.37	28.95	29.5	28.99	82.94	85.89	83.75	87.14	88.72	86.99	8.05	6.49
MnO	0.13	0.17	0.15	0.10	0.16	B.D.	0.04	0.02	0.06	B.D.	0.05	0.07	0.01
CaO	B.D.	0.03	0.00	0.00	0.01	0.11	0.02	0.00	0.03	0.03	0.00	0.05	0.00
MgO	12.06	11.01	12.46	12.28	11.08	0.82	0.15	0.32	B.D.	0.03	B.D.	3.34	2.23
Na_2O	0.13	0.09	0.12	0.12	0.1	0.12	0.50	0.09	0.08	0.21	0.02	0.10	0.09
K_2O	0.06	1.24	0.17	0.31	0.6	0.26	0.10	0.31	0.03	0.06	0.02	9.56	8.91
P_2O_5	0.01	0.12	0.15	B.D.	0.01	B.D.	0.01	B.D.	0.07	0.05	B.D.	B.D.	0.04
Total	86.57	90.04	86.06	88.72	85.97	92.08	90.83	90.03	89.52	92.01	89.92	94.90	96.92
Cation Sum	4.29	4.21	4.29	4.28	4.28	5.56	5.79	5.68	5.87	5.79	5.83	3.84	3.7

Metasiltstone Pt.2

Mineral Phase	Muscovite 15.3	Muscovite 15.5	Muscovite 15.6	Muscovite 15.7	Quartz 15.1	Quartz 15.2	Quartz 15.3	Quartz 15.4	Quartz 15.5	Quartz 15.6	Rutile 15.1	Rutile 15.2	Rutile 15.3
Major Element	wt%	wt%	wt%	wt%	wt%	wt%	wt%	wt%	wt%	wt%	wt%	wt%	wt%
SiO_2	47.05	44.76	54.11	48.58	98.58	97.07	95.24	99.22	97.85	97.68	2.08	1.25	0.90
Al_2O_3	24.77	25.27	25.21	22.66	0.31	1.40	1.05	0.57	1.28	0.63	0.49	0.17	0.25
TiO_2	0.50	0.44	0.42	0.14	0.00	0.17	0.06	0.03	0.06	0.04	95.58	96.72	98.62
FeO	6.27	8.22	6.19	7.91	0.48	0.46	0.45	0.39	0.70	0.35	4.53	4.54	2.30
MnO	0.30	0.00	B.D.	0.03	B.D.	0.01	0.07	B.D.	0.04	B.D.	0.03	B.D.	B.D.
CaO	B.D.	0.08	0.07	0.04	0.03	0.00	B.D.	0.00	B.D.	0.03	B.D.	0.03	0.05
MgO	1.66	2.53	2.00	2.99	0.11	0.13	0.20	0.04	0.09	0.10	0.33	0.04	0.13
Na_2O	0.03	0.13	0.23	0.09	B.D.	0.05	0.03	0.04	0.06	0.29	0.01	B.D.	0.13
K_2O	9.67	10.28	9.82	10.82	0.06	0.61	0.26	0.19	0.69	0.10	0.15	0.09	0.05
P_2O_5	0.14	0.07	0.00	0.07	B.D.	0.00	B.D.	B.D.	B.D.	B.D.	0.02	0.06	B.D.
Total	90.39	91.78	98.05	93.33	99.57	99.90	97.36	100.48	100.77	99.22	103.22	102.90	102.43
Cation Sum	3.80	3.90	3.76	3.88	3.01	3.04	3.03	3.02	3.05	3.03	3.10	3.08	3.05

Mineral Phase	Rutile 15.4	Rutile 15.5	Tourmaline 15.1	Tourmaline 15.2	Tourmaline 15.3	Tourmaline 15.5	Tourmaline 15.6
Major Element	wt%	wt%	wt%	wt%	wt%	wt%	wt%
SiO_2	1.85	2.20	42.14	42.43	36.81	36.40	34.45
Al_2O_3	0.75	0.54	27.27	30.83	28.65	24.81	24.34
TiO_2	96.06	96.72	0.64	0.55	0.54	0.23	2.28
FeO	3.46	1.86	13.72	13.51	12.54	15.80	16.41
MnO	0.02	B.D.	B.D.	0.01	0.02	B.D.	0.02
CaO	B.D.	0.07	0.06	0.09	0.04	0.09	0.09
MgO	0.46	0.28	5.86	6.05	5.23	2.81	4.4
Na_2O	0.09	B.D.	2.94	3.19	2.82	2.71	2.68
K_2O	0.07	0.11	0.18	0.59	0.05	0.16	0.12
P_2O_5	0.05	B.D.	0.10	0.11	0.04	0.04	0.01
Total	102.81	101.78	92.91	97.36	86.74	83.05	84.80
Cation Sum	3.09	3.05	3.84	3.89	3.89	3.93	3.93

Hematite-jasper Meta-iron formation Pt.1

Mineral Phase	Apatite 16.1	Apatite 16.2	Apatite 16.3	Apatite 16.6	Apatite 17.1	Ankerite 16.1	Ankerite 16.2	Ankerite 16.3	Ankerite 16.4	Ankerite 16.5	Ankerite 17.1	Ankerite 17.2	Chamosite 16.1
Major Element	wt%	wt%	wt%	wt%	wt%	wt%	wt%	wt%	wt%	wt%	wt%	wt%	wt%
SiO_2	0.53	1.40	1.43	0.91	3.42	0.62	0.52	0.48	0.43	0.21	0.65	0.65	40.89
Al_2O_3	0.00	0.74	0.00	0.26	0.12	0.00	B.D.	0.03	0.08	0.01	B.D.	0.00	17.48
TiO_2	0.05	B.D.	0.06	B.D.	B.D.	B.D.	0.03	B.D.	0.00	B.D.	0.06	B.D.	0.00
FeO	0.99	0.88	1.95	5.27	2.43	18.14	22.16	19.56	19.49	20.10	17.33	19.48	30.58
MnO	0.00	0.07	B.D.	B.D.	0.01	0.43	0.15	0.74	0.69	0.71	0.32	0.26	0.03
CaO	54.12	51.11	54.82	50.99	51.56	28.13	27.43	26.81	27.53	27.48	27.02	26.50	B.D.
MgO	0.04	0.12	0.04	0.11	0.04	10.09	7.67	7.10	8.87	7.99	9.74	9.48	7.93
Na_2O	0.04	0.31	0.14	0.10	0.13	0.05	0.09	0.03	0.08	0.05	0.02	0.09	0.12
K_2O	0.05	0.51	0.02	0.06	0.05	B.D.	0.07	0.04	0.01	0.01	0.01	0.02	B.D.
P_2O_5	41.17	38.51	42.19	36.01	37.01	B.D.	0.08	B.D.	B.D.	B.D.	B.D.	0.02	0.05
Total	96.99	93.65	100.65	93.71	94.77	57.46	58.20	54.79	57.18	56.56	55.15	56.50	97.08
Cation Sum	3.54	3.62	3.54	3.57	3.66	5.95	5.95	5.92	5.97	6.00	5.94	5.94	3.96

Mineral Phase	Chamosite 16.3	Chamosite 16.4	Chamosite 16.5	Chamosite 16.6	Chamosite 17.1	Chamosite 17.2	Chamosite 17.6	Chamosite 17.7	Chamosite 17.8	Hematite 16.1	Hematite 16.2	Hematite 16.3	Hematite 16.4
Major Element	wt%	wt%	wt%	wt%	wt%	wt%	wt%	wt%	wt%	wt%	wt%	wt%	wt%
SiO_2	36.84	23.71	24.26	25.24	39.99	38.69	33.43	26.68	36.94	0.70	1.03	0.43	0.84
Al_2O_3	16.64	19.91	19.81	19.67	18.42	17.54	15.45	18.63	16.38	0.03	0.06	0.06	0.19
TiO_2	0.02	0.02	0.02	0.01	B.D.	B.D.	0.05	0.02	0.05	B.D.	B.D.	0.07	0.02
FeO	34.47	36.19	37.47	36.70	30.78	30.07	29.82	32.68	32.68	88.42	87.95	87.19	86.53
MnO	0.00	0.09	0.03	0.04	0.00	0.04	0.02	B.D.	B.D.	B.D.	0.01	0.03	0.02
CaO	0.00	0.10	0.04	0.28	0.03	0.00	B.D.	B.D.	0.01	0.00	0.03	0.04	0.06
MgO	7.23	6.60	7.45	6.86	8.42	8.58	7.77	9.42	8.15	B.D.	0.02	B.D.	0.00
Na_2O	0.09	0.16	0.21	0.08	0.06	0.17	0.10	0.13	0.13	0.16	0.15	0.07	0.16
K_2O	0.38	0.29	0.01	B.D.	0.00	0.09	B.D.	B.D.	0.02	0.02	0.02	0.03	0.02
P_2O_5	0.08	0.00	0.01	B.D.	0.04	0.07	0.00	0.06	0.03	0.01	B.D.	0.02	0.02
Total	95.75	87.07	89.31	88.88	97.74	95.25	86.64	87.62	94.39	89.34	89.27	87.94	87.86
Cation Sum	4.05	4.29	4.30	4.26	3.98	4.00	4.05	4.23	4.04	5.96	5.93	5.96	5.93

Hematite-jasper Meta-iron formation Pt.2

Mineral Phase	Hematite 16.5	Hematite 16.6	Hematite 17.1	Hematite 17.2	Hematite 17.3	Hematite 17.4	Hematite 17.5	Muscovite 16.1	Muscovite 16.2	Muscovite 16.3	Muscovite 16.4	Muscovite 16.5	Muscovite 16.6
Major Element	wt%	wt%	wt%	wt%	wt%	wt%	wt%	wt%	wt%	wt%	wt%	wt%	wt%
SiO_2	7.80	1.27	2.30	0.74	1.33	0.88	0.70	53.82	50.37	58.97	45.10	47.27	45.65
Al_2O_3	0.20	0.35	0.09	0.06	0.14	0.02	0.14	18.78	20.75	18.42	27.42	29.41	28.33
TiO_2	0.02	0.06	0.01	B.D.	0.01	0.00	0.00	0.04	0.02	0.05	0.07	0.14	0.17
FeO	82.77	87.88	86.71	86.87	86.66	86.94	87.54	13.27	18.17	11.46	5.80	5.65	6.30
MnO	0.03	0.04	B.D.	B.D.	0.00	B.D.	0.07	B.D.	B.D.	0.03	0.01	B.D.	0.00
CaO	0.05	0.06	0.05	0.03	0.07	B.D.	0.00	0.02	0.02	0.03	0.00	0.06	0.14
MgO	0.18	B.D.	0.07	B.D.	B.D.	0.01	B.D.	0.93	0.76	1.39	1.38	1.21	1.18
Na_2O	0.13	0.05	0.15	0.13	0.07	0.12	0.20	0.13	0.11	0.08	0.13	0.13	0.13
K_2O	0.01	0.02	0.00	B.D.	B.D.	B.D.	0.02	6.55	6.73	7.30	10.49	10.94	10.68
P_2O_5	0.05	0.10	0.15	B.D.	B.D.	B.D.	0.05	0.04	B.D.	0.04	0.07	0.06	0.10
Total	91.24	89.83	89.53	87.83	88.28	87.97	88.72	93.58	96.93	97.77	90.47	94.87	92.68
Cation Sum	5.45	5.88	5.81	5.96	5.89	5.94	5.95	3.69	3.79	3.66	3.85	3.84	3.86

Mineral Phase	Muscovite 16.7	Muscovite 17.1	Muscovite 17.2	Muscovite 17.3	Muscovite 17.4	Muscovite 17.6	Muscovite 17.7	Quartz 16.1	Quartz 16.2	Quartz 16.3	Quartz 16.4	Quartz 16.5	Quartz 16.6
Major Element	wt%	wt%	wt%	wt%	wt%	wt%	wt%	wt%	wt%	wt%	wt%	wt%	wt%
SiO_2	51.84	55.18	61.88	58.62	59.93	54.30	50.01	97.34	94.77	96.38	98.78	94.42	100.70
Al_2O_3	27.13	23.74	20.02	19.91	18.45	20.07	23.23	B.D.	B.D.	B.D.	0.03	0.16	0.58
TiO_2	0.13	0.14	0.16	0.08	0.14	0.13	0.20	B.D.	B.D.	0.01	0.02	0.03	0.02
FeO	5.98	6.36	8.00	11.13	7.97	9.46	5.49	2.52	2.23	3.57	0.64	0.21	1.39
MnO	0.06	B.D.	0.06	0.04	B.D.	0.01	B.D.	0.05	B.D.	0.00	B.D.	B.D.	B.D.
CaO	0.20	0.04	0.02	0.01	B.D.	0.00	0.01	0.01	B.D.	B.D.	0.05	0.01	0.09
MgO	1.15	1.57	1.71	0.04	1.03	1.17	1.86	0.07	0.04	0.01	0.05	0.02	0.18
Na_2O	0.10	0.16	0.06	0.06	0.10	0.05	0.09	0.05	0.09	0.01	0.03	0.03	0.09
K_2O	10.02	9.66	7.93	7.92	7.13	7.97	9.48	0.02	0.04	0.00	B.D.	0.03	0.02
P_2O_5	0.09	0.01	B.D.	B.D.	0.00	B.D.	0.03	0.02	0.04	B.D.	0.05	0.06	B.D.
Total	96.70	96.86	99.84	97.81	94.75	93.16	90.40	100.08	97.21	99.98	99.65	94.97	103.07
Cation Sum	3.77	3.73	3.63	3.68	3.60	3.70	3.76	3.04	3.03	3.05	3.01	3.01	3.03

Hematite-jasper Meta-iron formation Pt.3

Mineral Phase	Quartz 17.1	Quartz 17.2	Quartz 17.3	Quartz 17.5	Quartz 17.6	Siderite 16.1	Siderite 16.2	Siderite 16.3	Siderite 17.1	Siderite 17.2	Siderite 17.3	Siderite 17.4	Siderite 17.5
Major Element	wt%	wt%	wt%	wt%	wt%	wt%	wt%	wt%	wt%	wt%	wt%	wt%	wt%
SiO_2	98.99	97.53	98.37	98.06	93.41	0.49	0.35	0.32	0.55	0.80	0.38	0.37	0.56
Al_2O_3	B.D.	0.02	B.D.	0.02	B.D.	0.00	0.01	0.07	0.02	B.D.	0.00	0	B.D.
TiO_2	0.02	0.02	B.D.	0.01	0.03	B.D.	B.D.	B.D.	B.D.	B.D.	0.00	B.D.	B.D.
FeO	0.26	1.21	0.40	1.22	7.60	46.40	48.89	46.76	48.42	47.09	46.73	45.71	42.51
MnO	B.D.	B.D.	0.06	0.02	B.D.	0.48	0.59	1.31	0.44	0.60	0.68	1.21	0.62
CaO	0.02	B.D.	B.D.	B.D.	B.D.	0.20	0.19	0.16	0.11	0.36	0.22	0.31	0.25
MgO	0.03	0.03	B.D.	B.D.	0.02	9.84	8.64	8.67	8.37	9.37	9.77	10.2	6.35
Na_2O	0.05	0.00	0.08	0.03	0.04	0.20	0.15	0.13	0.06	0.07	0.09	0.18	0.22
K_2O	0.02	0.00	B.D.	0.03	B.D.	0.02	0.03	0.01	0.03	0.01	0.00	B.D.	B.D.
P_2O_5	B.D.	0.00	B.D.	B.D.	0.00	B.D.	0.01	B.D.	0.05	0.05	B.D.	0.01	0.09
Total	99.39	98.81	98.91	99.39	101.10	57.63	58.86	57.43	58.05	58.35	57.87	57.99	50.60
Cation Sum	3.01	3.02	3.01	3.02	3.10	5.97	5.98	5.99	5.94	5.92	5.98	5.98	5.95

Mineral Phase	Siderite 17.6	Siderite 17.7
Major Element	wt%	wt%
SiO_2	0.60	2.05
Al_2O_3	0.02	0.05
TiO_2	0.00	B.D.
FeO	47.15	47.13
MnO	0.64	0.39
CaO	0.36	0.19
MgO	9.26	8.94
Na_2O	0.24	0.18
K_2O	B.D.	0.01
P_2O_5	B.D.	0.09
Total	58.27	59.03
Cation Sum	5.97	5.80

Magnetite-quartz Meta-iron formation Pt.1

Mineral Phase	Albite 18.1	Albite 18.2	Albite 18.3	Albite 18.4	Albite 18.5	Albite 19.1	Albite 19.2	Albite 19.3	Ankerite 18.1	Ankerite 18.2	Ankerite 18.3	Ankerite 18.4	Ankerite 19.1	Ankerite 19.2
Major Element														
SiO_2	wt%	wt%	wt%	wt%	wt%	wt%	wt%	wt%	wt%	wt%	wt%	wt%	wt%	wt%
SiO_2	65.92	65.86	65.80	66.71	65.45	65.39	65.78	66.41	0.22	0.33	0.25	0.22	0.32	0.29
Al_2O_3	18.36	18.05	18.29	18.72	18.74	20.50	20.26	19.21	0.01	0.00	0.03	B.D.	0.06	0.1
TiO_2	B.D.	0.04	B.D.	0.17	0.01	B.D.	0.00	0.02	0.03	0.02	0.01	B.D.	0.02	0.01
FeO	0.36	0.99	1.21	1.64	4.45	0.58	0.46	0.50	16.06	15.35	18.50	15.82	10.69	9.89
MnO	0.02	0.00	0.01	0.01	0.01	B.D.	0.00	0.01	0.47	0.47	0.40	0.19	1.14	1.12
CaO	0.01	0.02	0.04	0.03	0.01	1.69	1.62	0.49	28.05	27.45	27.29	27.55	28.62	28.69
MgO	0.00	0.05	0.03	0.01	0.02	0.01	B.D.	0.07	10.07	11.45	9.09	11.91	13.71	14.17
Na_2O	11.10	11.34	11.64	10.85	12.21	11.10	11.20	11.59	0.08	0.01	B.D.	0.02	0.01	0.05
K_2O	0.03	0.07	0.05	0.05	0.06	0.06	0.03	0.09	0.01	0.02	0.03	0.04	0.02	0.02
P_2O_5	0.02	0.03	0.01	B.D.	0.08	0.11	B.D.	0.08	B.D.	B.D.	B.D.	B.D.	B.D.	B.D.
Total	95.82	96.45	97.08	98.19	101.04	99.44	99.35	98.47	55.00	55.10	55.60	55.75	54.59	54.34
Cation Sum	3.74	3.76	3.78	3.74	3.84	3.78	3.78	3.77	5.99	5.97	5.98	5.99	5.97	5.98

Mineral Phase	Ankerite 19.3	Apatite 18.1	Apatite 18.2	Apatite 18.3	Apatite 18.4	Apatite 19.1	Apatite 19.2	Apatite 19.3	Chamosite 18.1	Chamosite 18.2	Chamosite 18.3	Chamosite 18.4	Chamosite 19.1	Chamosite 19.2
Major Element														
SiO_2	wt%	wt%	wt%	wt%	wt%	wt%	wt%	wt%	wt%	wt%	wt%	wt%	wt%	wt%
SiO_2	0.36	0.50	0.46	0.41	0.62	0.42	1.09	1.04	22.59	23.37	24.74	24.41	27.05	25.62
Al_2O_3	0.1	0.04	0.06	0.06	0.03	0.06	0.35	0.07	17.16	14.02	15.19	14.37	19.62	20.07
TiO_2	0.04	0.03	0.09	B.D.	B.D.	0.01	B.D.	0.02	0.05	0.02	0.06	0.04	B.D.	0.06
FeO	10.41	0.63	1.92	2.45	1.56	0.50	0.94	0.41	40.78	40.41	31.54	34.59	25.33	24.90
MnO	1.01	B.D.	0.00	0.01	0.04	B.D.	B.D.	B.D.	0.02	B.D.	B.D.	B.D.	0.06	0.12
CaO	28.56	54.77	53.04	53.67	54.35	55.86	54.76	54.96	0.03	0.10	0.03	0.03	B.D.	0.00
MgO	14.35	B.D.	0.06	0.00	0.02	0.00	0.21	0.04	3.85	4.61	12.12	7.48	15.47	15.86
Na_2O	B.D.	0.15	0.16	0.02	B.D.	0.07	0.07	0.08	0.13	0.07	0.12	0.12	0.21	0.16
K_2O	0.05	0.06	0.03	0.04	0.05	0.01	0.04	0	0.04	0.12	0.00	0.01	0.00	B.D.
P_2O_5	B.D.	41.48	40.63	41.21	41.39	42.51	41.01	41.64	0.05	B.D.	B.D.	0.01	0.05	B.D.
Total	54.88	97.66	96.45	97.87	98.06	99.44	98.47	98.26	84.70	82.72	83.80	81.06	87.79	86.79
Cation Sum	5.97	3.54	3.47	3.54	3.57	3.58	3.56	3.54	4.31	4.32	4.33	4.28	4.27	4.30

Magnetite-quartz Meta-iron formation Pt.2

Mineral Phase	Chamosite 19.3	Ilmenite 19.2	Ilmenite 19.3	Magnetite 18.1	Magnetite 18.2	Magnetite 18.3	Magnetite 18.4	Magnetite 18.5	Magnetite 18.6	Magnetite 19.1	Magnetite 19.2	Magnetite 19.3	Quartz 18.1	Quartz 18.2
Major Element	wt%	wt%	wt%	wt%	wt%	wt%	wt%	wt%	wt%	wt%	wt%	wt%	wt%	wt%
SiO_2	25.86	9.16	6.46	0.64	0.61	0.52	0.57	0.47	0.55	0.52	0.35	0.56	98.89	98.52
Al_2O_3	19.99	3.37	2.50	0.03	0.08	0.16	0.11	0.04	0.08	0.11	0.04	0.05	B.D.	B.D.
TiO_2	0.06	47.58	51.17	B.D.	B.D.	0.04	B.D.	B.D.	B.D.	B.D.	B.D.	B.D.	B.D.	0.05
FeO	25.29	44.27	45.02	89.83	91.47	91.48	92.76	92.12	90.93	91.75	92.02	91.97	0.38	0.53
MnO	0.11	0.90	1.08	0.03	0.04	B.D.	B.D.	0.05	0.03	0.03	0.08	0.03	B.D.	0.02
CaO	0.03	0.05	0.01	0.05	0.02	0.02	B.D.	B.D.	B.D.	0.05	0.03	B.D.	0	0.00
MgO	15.67	1.08	0.62	0.02	B.D.	0.09	0.01	0.07	0.02	0.05	B.D.	0.11	B.D.	B.D.
Na_2O	0.19	2.06	1.89	0.02	0.21	0.13	0.16	0.16	0.06	0.15	0.19	0.1	0.01	B.D.
K_2O	0.01	B.D.	0.02	0.02	B.F.	0.00	B.D.	B.D.	0.02	0.04	0.02	B.D.	0.01	0.02
P_2O_5	0.07	B.D.	B.D.	B.D.	0.06	0.03	B.D.	0.03	B.D.	0.06	0	B.D.	B.D.	0.04
Total	87.28	108.47	108.77	90.64	92.49	92.47	93.61	92.94	91.69	92.76	92.73	92.82	99.29	99.18
Cation Sum	4.29	4.04	4.03	5.96	5.96	5.96	5.97	5.97	5.97	5.96	5.99	5.97	3.01	3.01

Mineral Phase	Quartz 18.3	Quartz 18.4	Quartz 19.1	Quartz 19.2	Quartz 19.3	Rutile 19.1	Rutile 19.3	Siderite 18.1	Siderite 18.5	Siderite 18.6	Stilpnomelane 18.1	Stilpnomelane 18.3	Stilpnomelane 18.4
Major Element	wt%	wt%	wt%	wt%	wt%	wt%	wt%	wt%	wt%	wt%	wt%	wt%	wt%
SiO_2	99.20	98.7	99.87	98.72	100.86	5.41	8.27	1.35	0.30	0.43	42.28	39.67	41.34
Al_2O_3	0.04	B.D.	0.02	0.65	0.07	2.45	4.34	B.D.	B.D.	0.02	5.96	5.68	5.67
TiO_2	0.00	B.D.	0.03	0.02	0.03	88.01	87.89	B.D.	0.04	B.D.	0.16	0.15	0.09
FeO	0.77	0.89	0.57	1.22	0.68	6.87	2.69	56.78	41.55	49.32	35.09	35.52	34.33
MnO	0.01	0.03	0.01	B.D.	0.01	0.1	0.05	0.03	0.30	0.3	0.11	0.02	0.10
CaO	0.00	0.12	B.D.	0	0.02	0.06	0.06	0.53	0.41	0.4	0.16	0.25	0.04
MgO	B.D.	0	0.04	0.43	0.01	2.32	0.96	0.47	15.73	8.98	2.09	1.98	1.87
Na_2O	0.03	0.03	0.05	0.07	0.07	B.D.	1.47	0.25	0.18	0.03	0.28	0.25	0.28
K_2O	0.00	B.D.	0.02	0.02	0.02	B.D.	0.01	B.D.	0.02	B.D.	1.12	0.98	1.32
P_2O_5	0.11	0.03	0.06	0.07	0.05	0.05	0.04	0.03	0.01	0.04	B.D.	0.11	B.D.
Total	100.16	99.80	100.67	101.20	101.77	105.27	105.78	59.44	58.54	59.52	87.25	84.61	85.04
Cation Sum	3.01	3.01	3.01	3.03	3.01	3.21	3.2	5.88	5.99	5.96	3.91	3.94	3.91

Iron oxide-quartz Meta-iron formation

Mineral Phase	Albite 19.5	Apatite 19.4	Apatite 19.5	Apatite 19.6	Clinochlore 19.4	Clinochlore 19.5	Clinochlore 19.6	Dolomite 19.4	Dolomite 19.5	Dolomite 19.6	Hematite 19.1	Hematite 19.2	Hematite 19.3	Hematite 19.4
Major Element	wt%	wt%	wt%	wt%	wt%	wt%	wt%	wt%	wt%	wt%	wt%	wt%	wt%	wt%
SiO_2	71.76	0.87	3.08	0.73	25.15	30.30	25.14	0.31	0.44	0.35	0.84	0.62	2.86	0.92
Al_2O_3	16.54	0.15	0.04	0.06	20.60	19.07	20.70	0.00	0.00	0.03	0.18	0.09	0.24	0.10
TiO_2	B.D.	0.03	0.02	B.D.	0.11	B.D.	0.00	B.D.	0.07	0.02	0.76	1.19	1.42	1.28
FeO	0.67	1.00	0.92	0.44	22.09	19.77	20.93	6.02	6.79	6.57	86.73	87.78	85.76	86.48
MnO	B.D.	0.12	0.05	0.03	0.01	0.05	0.06	0.77	0.68	0.67	0.01	0.09	B.D.	B.D.
CaO	1.23	54.47	52.53	55.13	0.00	0.02	0.01	29.75	29.52	29.59	0.06	0.10	0.01	0.06
MgO	B.D.	0.02	0.11	0.05	16.81	16.63	17.44	16.89	16.69	16.64	B.D.	B.D.	0.01	0.00
Na_2O	9.36	0.12	0.08	0.06	0.29	0.11	0.16	0.03	0.07	0.08	0.07	0.20	0.30	0.08
K_2O	0.06	0.07	0.07	0.11	0.03	0.01	B.D.	0.07	0.00	0.04	B.D.	0.01	B.D.	0.02
P_2O_5	0.07	39.03	38.72	41.77	0.09	0.05	0.03	B.D.	B.D.	0.00	B.D.	0.00	0.08	0.08
Total	99.69	95.88	95.62	98.38	85.18	86.01	84.47	53.84	54.26	53.99	88.65	90.08	90.68	89.02
Cation Sum	3.63	3.61	3.59	3.56	4.30	4.17	4.29	5.98	5.96	5.97	5.89	5.89	5.71	5.85

Mineral Phase	Hematite 19.5	Hematite 19.6	Magnetite 19.4	Magnetite 19.5	Magnetite 19.6	Muscovite 19.1	Muscovite 19.2	Muscovite 19.3	Oligoclase 19.4	Oligoclase 19.6	Quartz 19.4	Quartz 19.5	Quartz 19.6
Major Element	wt%	wt%	wt%	wt%	wt%	wt%	wt%	wt%	wt%	wt%	wt%	wt%	wt%
SiO_2	0.88	0.59	0.47	0.58	0.32	47.34	46.03	44.33	64.30	63.43	98.28	98.81	99.11
Al_2O_3	0.16	0.18	0.06	0.05	B.D.	28.60	30.28	31.67	21.10	21.54	0.03	0.03	0.09
TiO_2	0.97	1.39	B.D.	B.D.	B.D.	0.22	0.29	0.24	0.06	0.02	B.D.	0.00	0.03
FeO	86.59	86.78	92.60	92.40	92.11	4.25	4.69	3.55	0.64	0.63	0.39	0.44	0.22
MnO	0.01	0.00	0.08	0.00	0.04	B.D.	0.04	0.02	B.D.	0.01	0.01	0.00	0.03
CaO	0.16	0.04	0.04	0.08	0.05	1.03	0.05	0.07	2.56	3.17	0.02	B.D.	0.02
MgO	0.07	0.05	0.05	0.01	B.D.	1.24	0.96	0.73	0.09	0.01	0.02	0.01	0.02
Na_2O	0.19	B.D.	0.12	0.19	0.22	1.08	0.55	0.72	10.48	10.02	0.05	0.07	0.01
K_2O	0.05	0.01	B.D.	0.03	0.00	9.70	9.78	9.71	0.03	0.22	0.01	0.04	0.06
P_2O_5	0.02	B.D.	B.D.	B.D.	0.02	0.45	0.09	0.08	0.07	B.D.	0.00	B.D.	B.D.
Total	89.10	89.04	93.42	93.34	92.76	93.91	92.76	91.12	99.33	99.05	98.81	99.40	99.59
Cation Sum	5.88	5.86	5.98	5.98	5.99	3.84	3.82	3.83	3.77	3.78	3.01	3.01	3.01

Lake St. Joseph Meta-Iron Formations

Magnetite-quartz Meta-Iron Formation (a-type, lower coarsening upward succession)

Mineral Phase	Albite 1.1	Albite 1.2	Albite 1.3	Albite 1.4	Apatite 1.1	Apatite 1.2	Apatite 1.3	Carbonate 1.1	Carbonate 1.2	Carbonate 1.3	Carbonate 1.4	Chamosite 1.1	Chamosite 1.2
Major Element	wt%	wt%	wt%	wt%	wt%	wt%	wt%	wt%	wt%	wt%	wt%	wt%	wt%
SiO_2	67.23	67.64	67.31	66.92	0.44	0.50	0.38	0.41	0.30	0.25	0.28	23.93	24.93
Al_2O_3	19.45	19.57	19.02	19.00	0.02	0.10	0.10	0.01	0.03	0.09	0.06	20.68	22.34
TiO_2	0.06	B.D.	B.D.	0.07	B.D.	0.03	0.05	0.01	0.01	B.D.	B.D.	0.03	0.05
FeO	0.94	0.87	0.68	1.07	1.03	0.68	0.60	14.32	11.67	14.29	14.29	30.39	31.30
MnO	0.00	0.00	0.04	0.01	B.D.	B.D.	0.08	1.07	0.75	0.72	0.74	0.10	0.06
CaO	0.35	0.46	0.14	0.73	55.91	55.39	56.40	27.98	28.42	27.97	27.97	0.03	0.06
MgO	B.D.	B.D.	0.07	B.D.	0.07	B.D.	0.01	11.43	13.37	11.89	11.80	11.09	11.67
Na_2O	12.30	11.98	12.03	11.48	B.D.	0.11	0.11	0.05	0.04	0.04	0.14	0.19	0.13
K_2O	0.02	0.03	0.03	0.01	0.04	0.03	0.07	0.02	0.01	0.02	0.02	0.00	0.00
P_2O_5	B.D.	B.D.	B.D.	0.04	42.44	42.19	42.94	0.01	B.D.	B.D.	B.D.	0.04	0.05
Total	100.35	100.55	99.32	99.33	99.95	99.03	100.74	55.31	54.60	55.27	55.30	86.48	90.59
Cation Sum	3.80	3.78	3.78	3.77	3.52	3.51	3.53	5.96	5.97	5.98	5.99	4.30	4.29

Mineral Phase	Chamosite 1.3	Chamosite 1.4	Magnetite 1.1	Magnetite 1.2	Magnetite 1.3	Magnetite 1.4	Magnetite 1.5	Magnetite 1.6	Magnetite 1.7	Magnetite 1.8	Quartz 1.1	Quartz 1.2	Rutile 1.1
Major Element	wt%	wt%	wt%	wt%	wt%	wt%	wt%	wt%	wt%	wt%	wt%	wt%	wt%
SiO_2	23.81	26.64	0.41	0.59	0.59	0.49	0.37	0.42	0.67	0.77	100.85	101.18	0.89
Al_2O_3	21.18	20.47	0.12	0.15	0.19	0.20	0.13	0.10	0.16	0.10	0.06	0.04	0.19
TiO_2	0.09	0.03	B.D	B.D.	0.07	0.03	0.01	0.02	0.03	B.D.	0.03	0.00	95.72
FeO	30.41	30.61	90.89	89.10	90.31	89.76	90.73	91.58	91.59	91.08	0.52	0.85	4.90
MnO	0.03	0.07	0.02	0.00	0.09	0.00	B.D.	0.01	0.06	0.09	0.02	0.00	B.D.
CaO	0.05	B.D.	0.01	0.04	0.10	0.00	0.04	0.04	0.07	0.05	0.00	0.03	0.00
MgO	11.11	10.30	0.12	0.07	B.D.	0.02	B.D.	B.D.	0.08	0.11	0.01	B.D.	B.D.
Na_2O	0.23	0.19	0.13	0.13	0.16	0.22	0.03	0.10	0.16	0.13	0.05	0.06	0.17
K_2O	B.D.	0.00	0.04	0.00	B.D.	B.D.	0.05	B.D.	0.00	0.13	0.04	0.03	0.03
P_2O_5	0.06	0.06	B.D.	0.08	0.01	0.00	0.04	0.06	0.06	B.D.	0.04	B.D.	0.03
Total	86.97	88.37	91.74	90.16	91.52	90.72	91.40	92.33	92.88	92.33	101.62	102.19	101.93
Cation Sum	4.30	4.23	5.98	5.95	5.95	5.97	5.96	5.96	5.95	5.95	3.01	3.01	3.09

Magnetite-quartz Meta-Iron Formation (b-type, basal section of 73m thick meta-iron formation)

Mineral Phase	Albite 2.1	Albite 2.2	Albite 2.3	Apatite 2.1	Apatite 2.2	Apatite 2.3	Carbonate 2.1	Carbonate 2.2	Carbonate 2.3	Clinochlore 2.1	Clinochlore 2.2	Clinochlore 2.3	Hematite 2.1
Major Element	wt%	wt%	wt%	wt%	wt%	wt%	wt%	wt%	wt%	wt%	wt%	wt%	wt%
SiO_2	71.24	68.05	71.81	0.60	0.34	0.33	0.28	0.57	0.29	26.49	27.19	26.36	0.56
Al_2O_3	16.85	18.74	18.79	0.09	0.05	0.08	0.03	0.02	0.07	19.05	19.76	19.57	0.09
TiO_2	B.D.	0.00	B.D.	B.D.	0.00	0.02	0.00	0.03	0.03	B.D.	0.17	0.02	0.05
FeO	0.56	0.82	0.73	0.66	0.71	0.57	6.39	6.80	5.74	18.97	19.36	19.33	87.38
MnO	B.D.	B.D.	B.D.	0.16	0.04	0.07	0.34	2.57	0.89	0.23	0.25	0.22	0.01
CaO	0.11	0.00	0.00	55.00	54.92	55.56	28.46	27.83	28.71	B.D.	0.00	B.D.	B.D.
MgO	B.D.	B.D.	B.D.	0.03	0.06	0.02	16.86	15.95	16.82	19.80	20.27	19.64	0.07
Na_2O	10.38	11.84	11.42	0.01	0.08	0.06	0.04	0.05	0.01	0.14	0.23	0.10	0.12
K_2O	0.05	0.02	0.03	0.05	0.09	0.01	0.00	0.05	0.02	0.00	0.02	B.D.	0.02
P_2O_5	0.01	0.04	B.D.	41.86	41.92	42.74	0.05	B.D.	0.00	B.D.	0.04	0.04	0.05
Total	99.20	99.51	102.78	98.46	98.21	99.46	52.45	53.87	52.58	84.68	87.29	85.28	88.35
Cation Sum	3.67	3.76	3.72	3.62	3.62	3.62	5.97	5.96	5.97	4.30	4.30	4.29	5.95

Mineral Phase	Hematite 2.2	Hematite 2.3	Magnetite 2.1	Magnetite 2.2	Magnetite 2.3	Muscovite 2.1	Muscovite 2.2	Muscovite 2.3	Quartz 2.1	Quartz 2.2	Rutile 2.1	Rutile 2.2	Rutile 2.3
Major Element	wt%	wt%	wt%	wt%	wt%	wt%	wt%	wt%	wt%	wt%	wt%	wt%	wt%
SiO_2	0.50	0.34	0.72	0.47	0.62	47.71	57.18	55.86	99.70	98.92	0.74	1.02	0.44
Al_2O_3	0.08	0.08	0.02	B.D.	0.10	27.42	22.85	25.15	0.04	0.01	0.10	0.16	0.08
TiO_2	B.D.	0.01	B.D.	B.D.	B.D.	0.36	0.13	0.18	0.00	0.05	101.88	98.11	101.45
FeO	86.61	88.36	89.99	91.75	90.86	6.14	4.09	4.86	0.40	0.47	1.38	2.20	1.82
MnO	0.07	0.08	B.D.	0.04	0.04	B.D.	0.04	B.D.	0.04	B.D	B.D.	B.D.	0.05
CaO	0.00	0.04	0.04	0.03	0.01	B.D.	0.03	0.08	0.20	0.30	B.D.	B.D.	B.D.
MgO	0.02	0.06	0.04	B.D.	B.D.	1.69	1.51	1.24	B.D.	B.D.	B.D.	0.02	B.D.
Na_2O	0.20	0.27	0.01	0.18	0.19	1.51	2.69	4.92	0.09	0.05	0.12	B.D.	0.11
K_2O	B.D.	B.D.	B.D.	0.01	0.02	9.89	6.55	6.24	0.03	0.02	0.01	0.02	B.D.
P_2O_5	0.05	B.D.	0.10	0.01	0.08	0.09	B.D.	0.05	B.D.	0.09	B.D.	0.11	0.07
Total	87.53	89.24	91.07	92.49	91.92	94.81	95.00	98.57	100.50	99.91	104.23	101.64	104.02
Cation Sum	5.97	5.99	5.95	5.98	5.96	3.88	3.71	3.82	3.01	3.01	3.03	3.04	3.03

Hematite-quartz Meta-iron Formation (a-type, middle section of the 73m thick meta-iron formation) Pt. 1

Mineral Phase	Apatite 3.1	Apatite 3.2	Apatite 3.3	Apatite 3.4	Apatite 3.5	Apatite 3.6	Hematite 3.1	Hematite 3.2	Hematite 3.3	Hematite 3.4	Hematite 3.5	Hematite 3.6	KFeldspar 3.2
Major Element	wt%	wt%	wt%	wt%	wt%	wt%	wt%	wt%	wt%	wt%	wt%	wt%	wt%
SiO_2	0.67	0.38	0.50	0.43	0.55	1.22	0.52	0.50	0.57	0.49	0.42	0.74	62.34
Al_2O_3	0.06	0.13	B.D.	B.D.	0.06	0.01	0.16	0.11	0.07	0.13	0.05	0.04	17.43
TiO_2	0.04	0.02	0.00	0.06	B.D.	0.02	0.14	0.07	0.15	0.00	0.09	B.D.	0.10
FeO	0.85	1.09	2.38	1.36	0.92	0.97	88.73	89.05	88.47	86.73	87.43	86.96	0.77
MnO	0.01	B.D.	0.00	B.D.	0.06	0.02	0.06	0.00	B.D.	0.05	B.D.	0.04	B.D.
CaO	55.12	54.97	54.30	54.34	53.85	53.93	0.03	0.01	0.08	0.07	0.02	0.02	0.05
MgO	0.03	0.02	B.D.	0.04	0.02	0.03	0.03	0.03	0.06	0.01	0.08	0.07	0.01
Na_2O	0.04	0.06	0.02	0.08	0.12	0.04	0.14	0.19	0.03	0.06	0.10	0.13	0.23
K_2O	0.10	0.09	0.03	0.07	0.08	0.07	0.00	0.00	0.02	0.04	0.05	0.03	15.88
P_2O_5	41.86	41.78	42.81	41.91	41.00	41.29	0.04	B.D.	0.05	B.D.	0.08	0.01	0.02
Total	98.78	98.54	100.04	98.29	96.66	97.60	89.85	89.96	89.50	87.58	88.32	88.04	96.83
Cation Sum	3.72	3.74	3.71	3.72	3.74	3.71	5.95	5.97	5.94	5.96	5.96	5.95	3.76

Mineral Phase	KFeldspar 3.3	KFeldspar 3.4	KFeldspar 3.5	Magnetite 3.1	Magnetite 3.2	Magnetite 3.3	Magnetite 3.4	Magnetite 3.5	Magnetite 3.6	Muscovite 3.1	Muscovite 3.3	Muscovite 3.4	Muscovite 3.5
Major Element	wt%	wt%	wt%	wt%	wt%	wt%	wt%	wt%	wt%	wt%	wt%	wt%	wt%
SiO_2	64.42	63.38	64.50	0.42	0.62	0.95	0.95	0.87	0.45	47.26	47.35	47.13	45.01
Al_2O_3	16.81	17.47	16.43	0.27	0.19	0.18	0.02	0.10	0.11	24.16	26.15	25.70	24.93
TiO_2	0.12	0.01	0.08	B.D.	0.01	0.06	B.D.	B.D.	0.02	B.D.	B.D.	0.03	0.07
FeO	0.52	0.84	0.61	87.74	91.35	87.29	85.02	85.34	87.52	6.73	6.62	6.39	6.36
MnO	B.D.	0.02	B.D.	0.08	B.D.	0.04	0.02	B.D.	B.D.	0.01	0.01	B.D.	B.D.
CaO	0.07	B.D.	B.D.	0.04	0.01	0.05	0.03	0.09	0.05	0.04	0.06	0.02	0.06
MgO	0.02	0.01	0.00	0.08	0.00	B.D.	0.02	B.D.	B.D.	2.64	2.56	2.28	2.48
Na_2O	0.16	0.18	0.18	0.13	0.12	0.08	0.14	0.20	B.D.	0.13	0.17	0.11	0.22
K_2O	15.47	15.89	15.15	0.02	B.D.	0.00	0.04	B.D.	0.01	10.39	10.51	10.55	10.61
P_2O_5	0.05	B.D.	B.D.	0.06	B.D.	0.13	0.14	0.19	0.13	0.03	0.03	B.D.	0.00
Total	97.64	97.80	96.95	88.84	92.30	88.78	86.38	86.79	88.29	91.39	93.46	92.21	89.74
Cation Sum	3.72	3.75	3.71	5.96	5.95	5.91	5.93	5.92	5.94	3.86	3.87	3.86	3.89

Hematite-quartz Meta-iron Formation (a-type, middle section of the 73m thick meta-iron formation) Pt.2

Mineral Phase	Muscovite 3.6	Quartz 3.1	Quartz 3.2	Al-Fe Silicate 3.1	Al-Fe Silicate 3.2	Al-Fe Silicate 3.3	Al-Fe Silicate 3.4	Al-Fe Silicate 3.5	Al-Fe Silicate 3.6	Al-Fe Silicate 3.8	Al-Fe Silicate 3.9	Al-Fe Silicate 3.10	Al-Fe Silicate 3.11
Major Element	wt%	wt%	wt%	wt%	wt%	wt%	wt%	wt%	wt%	wt%	wt%	wt%	wt%
SiO_2	49.90	99.82	99.57	32.13	39.42	40.62	33.01	32.52	40.21	30.00	38.99	33.46	31.26
Al_2O_3	25.33	0.01	0.00	11.43	11.01	10.35	11.34	11.32	10.86	10.38	10.36	9.62	9.63
TiO_2	B.D.	B.D.	0.00	B.D.	B.D.	0.00	B.D.	B.D.	0.01	0.01	B.D.	B.D.	B.D.
FeO	7.75	1.12	1.29	33.83	25.69	23.90	30.95	37.06	28.19	35.24	28.00	24.49	24.77
MnO	B.D.	B.D.	0.06	0.03	0.05	B.D.	0.05	0.02	B.D.	0.05	0.05	0.09	0.06
CaO	0.12	B.D.	B.D.	1.30	1.45	1.75	1.12	1.54	2.38	1.35	1.54	1.49	1.19
MgO	2.97	0.00	0.00	4.67	4.50	2.49	5.12	5.89	3.14	4.24	2.51	5.86	4.93
Na_2O	0.16	0.09	0.05	0.12	0.10	0.12	0.17	0.22	0.07	0.06	0.10	0.13	0.11
K_2O	9.86	0.01	0.02	0.09	0.18	0.30	0.07	0.11	0.27	0.06	0.64	0.36	0.29
P_2O_5	0.15	0.00	0.01	0.38	0.36	0.27	1.14	0.29	1.13	0.34	0.30	0.64	1.02
Total	96.24	101.05	101.00	83.98	82.76	79.80	82.97	88.97	86.26	81.73	82.49	76.14	73.26
Cation Sum	3.84	3.02	3.02	4.08	3.85	3.77	4.01	4.15	3.84	4.12	3.86	3.96	3.94

Magnetite-quartz Meta-Iron Formation (turbiditic prodelta, upper coarsening upwards succession) Pt. 1

Mineral Phase	Albite 4.1	Albite 4.2	Albite 4.3	Albite 4.4	Albite 4.5	Albite 4.6	Albite 4.7	Apatite 4.1	Apatite 4.2	Apatite 4.3	Apatite 4.4	Apatite 4.5	Apatite 4.6
Major Element	wt%	wt%	wt%	wt%	wt%	wt%	wt%	wt%	wt%	wt%	wt%	wt%	wt%
SiO_2	66.07	65.79	65.19	66.89	66.48	66.94	65.99	0.65	0.53	0.39	1.00	2.10	0.48
Al_2O_3	18.57	18.65	18.39	19.16	18.92	18.88	18.60	0.09	0.03	0.08	0.33	0.46	0.10
TiO_2	B.D.	0.00	0.01	0.00	0.02	0.12	B.D.	B.D.	0.02	0.04	0.01	0.09	0.04
FeO	0.62	0.99	0.51	0.45	0.75	1.10	0.29	0.71	0.73	0.86	0.76	0.87	0.95
MnO	B.D.	0.01	B.D.	B.D.	0.03	0.03	0.00	0.01	B.D.	0.04	0.01	B.D.	0.01
CaO	0.60	0.24	0.17	0.27	0.23	0.38	0.08	53.32	53.84	55.43	53.48	52.28	54.73
MgO	0.03	0.01	0.01	0.00	0.01	0.08	0.04	0.21	B.D.	B.D.	0.06	0.03	0.04
Na_2O	10.56	10.96	11.28	11.59	11.57	11.11	11.40	0.16	0.13	0.03	0.10	0.23	0.04
K_2O	0.03	0.00	0.04	0.00	0.04	0.01	0.02	0.04	0.08	B.D.	0.05	0.05	0.05
P_2O_5	0.06	0.04	B.D.	B.D.	B.D.	B.D.	B.D.	40.71	40.42	42.69	37.61	39.84	41.56
Total	96.54	96.69	95.60	98.36	98.05	98.65	96.42	95.90	95.78	99.56	93.41	95.95	98.00
Cation Sum	3.73	3.75	3.76	3.76	3.77	3.75	3.76	3.57	3.58	3.52	3.53	3.52	3.54

Mineral Phase	Chamosite 4.1	Chamosite 4.2	Chamosite 4.3	Chamosite 4.4	Chamosite 4.5	Chamosite 4.6	Chamosite 4.7	Epidote 4.1	Epidote 4.2	Epidote 4.4	Epidote 4.6	Epidote 4.8	Ilmenite 4.1
Major Element	wt%	wt%	wt%	wt%	wt%	wt%	wt%	wt%	wt%	wt%	wt%	wt%	wt%
SiO_2	23.99	26.81	24.07	24.20	24.92	23.90	23.10	36.37	41.13	35.61	38.77	37.40	0.69
Al_2O_3	20.17	19.90	19.78	20.57	19.73	20.51	18.61	21.78	21.63	20.99	20.36	21.87	0.14
TiO_2	B.D.	0.03	0.11	0.08	0.01	0.03	B.D.	0.05	0.23	0.01	B.D.	0.01	51.14
FeO	28.28	27.66	28.61	29.04	28.46	29.36	28.10	12.96	12.98	13.29	13.22	13.53	41.01
MnO	0.21	0.26	0.22	0.33	0.33	0.24	0.27	0.11	0.14	0.12	0.02	0.12	4.26
CaO	B.D.	0.00	B.D.	0.00	0.04	0.01	0.01	22.92	21.29	22.41	18.63	22.89	0.56
MgO	12.28	11.80	11.88	12.35	11.71	12.32	12.04	0.01	0.13	0.02	0.11	0.07	0.02
Na_2O	0.09	0.44	0.10	0.13	0.24	0.18	0.11	0.04	0.02	0.09	0.01	0.10	0.15
K_2O	0.00	0.02	0.00	B.D.	0.02	B.D.	B.D.	0.00	0.05	0.05	0.03	0.00	0.00
P_2O_5	0.06	0.01	B.D.	B.D.	0.10	B.D.	0.06	B.D.	B.D.	B.D.	0.01	B.D.	0.08
Total	85.08	86.93	84.77	86.70	85.56	86.55	82.30	94.24	97.60	92.59	91.16	95.99	98.05
Cation Sum	4.29	4.24	4.29	4.30	4.28	4.31	4.31	3.99	3.91	4.00	3.90	3.99	4.00

Magnetite-quartz Meta-Iron Formation (turbiditic prodelta, upper coarsening upwards succession) Pt. 2

Mineral Phase	Ilmenite 4.2	Ilmenite 4.3	Ilmenite 4.4	Ilmenite 4.5	Ilmenite 4.6	Magnetite 4.1	Magnetite 4.2	Magnetite 4.3	Magnetite 4.4	Magnetite 4.5	Magnetite 4.6	Magnetite 4.7	Magnetite 4.8	Muscovite 4.1
Major Element	wt%	wt%	wt%	wt%	wt%	wt%	wt%	wt%	wt%	wt%	wt%	wt%	wt%	wt%
SiO_2	0.25	1.87	3.68	2.93	1.55	0.38	0.37	0.37	0.32	0.45	0.61	0.45	0.38	45.13
Al_2O_3	0.14	0.75	1.57	1.08	0.74	0.18	0.06	0.11	0.17	0.09	0.08	0.08	0.11	29.44
TiO_2	49.51	60.55	70.86	77.12	67.96	0.00	0.03	B.D.	B.D.	0.05	0.09	B.D.	B.D.	0.43
FeO	41.92	31.87	17.64	11.76	25.36	91.16	89.95	91.35	90.08	92.22	91.30	92.02	90.13	3.98
MnO	4.64	0.95	0.16	0.07	0.41	0.02	B.D.	0.00	B.D.	0.03	B.D.	B.D.	B.D.	0.08
CaO	B.D.	0.17	0.56	0.28	0.14	0.00	0.06	0.01	0.06	0.01	0.03	0.02	B.D.	0.00
MgO	0.16	0.38	0.87	0.53	0.29	B.D.	0.06	B.D.	B.D.	0.03	0.01	B.D.	0.01	1.12
Na_2O	0.02	0.15	0.00	0.11	0.06	0.17	0.08	0.16	0.05	0.10	0.14	0.21	0.13	0.27
K_2O	B.D.	B.D.	B.D.	B.D.	0.03	0.03	B.D.	B.D.	0.00	B.D.	0.02	0.00	B.D.	9.71
P_2O_5	0.08	0.04	0.10	0.08	0.02	0.10	B.D.	0.11	0.07	0.06	B.D.	0.00	0.02	0.05
Total	96.72	96.73	95.44	93.96	96.56	92.04	90.61	92.11	90.75	93.04	92.28	92.78	90.78	90.21
Cation Sum	4.03	3.70	3.40	3.26	3.53	5.97	5.98	5.97	5.96	5.96	5.97	5.98	5.97	3.80

Mineral Phase	Muscovite 4.3	Muscovite 4.4	Muscovite 4.5	Muscovite 4.6	Muscovite 4.7	Quartz 4.1	Quartz 4.2	Quartz 4.3
Major Element	wt%	wt%	wt%	wt%	wt%	wt%	wt%	wt%
SiO_2	44.06	45.63	43.84	44.13	49.13	97.44	98.13	98.15
Al_2O_3	28.85	27.73	28.47	28.38	24.98	0.02	0.02	0.10
TiO_2	0.44	0.31	0.35	0.46	0.36	B.D.	0.04	B.D.
FeO	4.13	4.38	4.40	4.54	6.78	0.43	0.67	0.41
MnO	0.06	0.01	B.D.	0.00	0.02	B.D.	B.D.	0.03
CaO	0.05	0.57	0.02	0.08	0.06	0.03	B.D.	0.00
MgO	1.22	1.44	1.11	1.28	2.05	0.01	0.01	0.04
Na_2O	0.28	0.68	0.21	0.26	0.20	0.07	0.05	0.11
K_2O	10.09	9.94	9.63	9.67	7.83	0.04	0.04	0.00
P_2O_5	B.D.	0.03	0.01	0.08	0.00	0.02	B.D.	0.04
Total	89.18	90.72	88.04	88.88	91.41	98.06	98.96	98.88
Cation Sum	3.83	3.84	3.82	3.83	3.75	3.01	3.01	3.01

Magnetite-quartz Meta-Iron Formation (above the upper depositional cycle, coarse-grained metasandstone)

Mineral Phase	Albite 5.1	Albite 5.3	Apatite 5.1	Apatite 5.2	Apatite 5.3	Biotite 5.1	Biotite 5.2	Biotite 5.3	Biotite 5.5	Carbonate 5.1	Carbonate 5.2
Major Element	wt%	wt%	wt%	wt%	wt%	wt%	wt%	wt%	wt%	wt%	wt%
SiO_2	66.95	67.38	0.76	0.47	0.54	35.61	34.86	36.18	36.59	0.48	0.34
Al_2O_3	18.42	18.44	0.06	0.08	0.08	14.50	14.53	13.50	14.35	0.06	0.10
TiO_2	0.03	0.05	B.D.	B.D.	0.04	2.37	2.05	2.31	1.98	B.D.	B.D.
FeO	0.03	0.07	0.09	0.09	0.09	19.06	19.18	18.24	19.10	9.42	7.71
MnO	0.04	B.D.	B.D.	B.D.	0.01	0.07	0.02	0.10	0.03	1.19	1.11
CaO	0.08	0.19	55.43	55.32	54.71	0.00	B.D.	0.02	0.07	28.30	28.49
MgO	0.00	0.03	0.04	B.D.	B.D.	11.66	12.68	11.95	12.98	14.41	15.22
Na_2O	10.98	11.02	0.04	0.00	0.13	0.15	0.08	0.07	0.13	0.01	B.D.
K_2O	0.07	0.09	0.05	0.09	0.06	9.43	8.37	9.47	9.33	0.05	0.04
P_2O_5	0.00	B.D.	41.38	41.10	41.35	B.D.	B.D.	0.04	0.06	B.D.	0.00
Total	96.60	97.27	97.85	97.15	97.01	92.85	91.77	91.88	94.62	53.92	53.01
Cation Sum	3.73	3.73	3.65	3.61	3.65	4.30	4.29	4.28	4.30	5.96	5.96

Mineral Phase	Carbonate 5.3	KFeldspar 5.2	KFeldspar 5.3	Magnetite 5.1	Magnetite 5.2	Magnetite 5.3	Muscovite 5.3	Muscovite 5.4	Muscovite 5.5	Rutile 5.3	
Major Element	wt%	wt%	wt%	wt%	wt%	wt%	wt%	wt%	wt%	wt%	
SiO_2	0.46	63.77	63.24	0.57	0.78	0.75	45.80	50.08	46.35	0.93	
Al_2O_3	0.08	17.32	17.53	0.14	0.12	0.17	25.34	22.75	26.22	0.08	
TiO_2	0.05	0.00	0.03	0.00	B.D.	B.D.	0.61	0.70	0.79	100.02	
FeO	8.81	0.01	0.06	92.22	89.98	90.07	5.61	5.34	6.05	0.79	
MnO	1.30	0.05	0.00	0.06	B.D.	0.06	0.01	0.04	0.04	0.03	
CaO	28.28	0.03	0.03	0.03	0.04	B.D.	0.03	0.04	0.01	B.D.	
MgO	14.61	0.02	0.02	B.D.	B.D.	0.03	2.06	2.11	2.25	0.04	
Na_2O	0.01	0.09	0.20	0.14	0.02	0.15	0.14	0.10	0.14	0.02	
K_2O	0.07	15.69	16.14	0.01	0.03	0.04	10.07	9.42	10.84	0.10	
P_2O_5	0.01	0.05	B.D.	B.D.	0.15	0.01	0.12	0.05	0.04	B.D.	
Total	53.68	97.03	97.25	93.17	91.12	91.28	89.79	90.63	92.73	102.01	
Cation Sum	5.95	3.72	3.75	5.96	5.92	5.95	3.84	3.76	3.87	3.02	

Magnetite-quartz Meta-Iron Formation (above the upper depositional cycle, metasiltstone)

Mineral Phase	Albite 5.4	Albite 5.5	Albite 5.6	Apatite 5.4	Apatite 5.5	Apatite 5.6	Biotite 5.6	Biotite 5.7	Biotite 5.8	Magnetite 5.4	Magnetite 5.5	Magnetite 5.6
Major Element	wt%	wt%	wt%	wt%	wt%	wt%	wt%	wt%	wt%	wt%	wt%	wt%
SiO_2	66.77	66.07	65.42	1.05	0.29	0.31	37.58	34.97	33.90	0.74	0.44	0.92
Al_2O_3	18.41	18.46	18.12	0.41	0.07	0.06	14.96	14.02	14.78	0.13	0.19	0.40
TiO_2	B.D.	B.D.	0.01	0.03	B.D.	0.02	1.46	1.68	1.28	0.01	0.01	0.02
FeO	0.25	0.42	0.49	0.52	0.28	0.26	17.76	18.09	17.79	90.62	90.40	90.33
MnO	0.00	0.01	0.02	0.03	0.05	0.03	0.05	0.05	0.06	0.04	0.00	B.D.
CaO	0.07	0.14	0.00	54.08	55.49	55.41	0.00	0.06	0.05	0.03	B.D.	0.01
MgO	B.D.	0.03	0.08	0.03	0.08	B.D.	11.11	12.78	13.62	0.16	B.D.	0.08
Na_2O	10.55	10.21	9.62	0.11	0.11	0.11	0.63	0.17	0.14	0.16	0.14	0.15
K_2O	0.12	0.19	0.52	0.34	0.10	0.10	8.69	8.90	7.95	0.11	0.10	0.19
P_2O_5	0.03	0.03	0.00	39.25	41.71	41.36	B.D.	B.D.	0.06	0.02	0.06	0.05
Total	96.20	95.56	94.28	95.85	98.18	97.66	92.24	90.72	89.63	92.02	91.34	92.15
Cation Sum	3.71	3.71	3.70	3.69	3.71	3.65	4.25	4.31	4.31	5.95	5.97	5.93

Mineral Phase	Muscovite 5.6	Muscovite 5.7	Muscovite 5.8
Major Element	wt%	wt%	wt%
SiO_2	46.45	44.93	48.08
Al_2O_3	25.04	26.22	24.39
TiO_2	0.55	0.55	0.57
FeO	9.05	5.94	6.18
MnO	0.02	B.D.	0.00
CaO	0.03	B.D.	0.00
MgO	2.51	2.21	2.72
Na_2O	0.32	0.23	0.11
K_2O	9.84	10.14	9.93
P_2O_5	0.00	0.05	0.02
Total	93.81	90.27	92.00
Cation Sum	3.88	3.86	3.83

Magnetite-quartz Meta-Iron Formation (above the upper depositional cycle, meta-iron formation)

Mineral Phase	Albite 5.7	Albite 5.8	Albite 5.9	Apatite 5.7	Apatite 5.8	Apatite 5.9	Biotite 5.9	Biotite 5.10	Biotite 5.11	Carbonate 5.4	Carbonate 5.5	Carbonate 5.6	Carbonate 5.7
Major Element	wt%	wt%	wt%	wt%	wt%	wt%	wt%	wt%	wt%	wt%	wt%	wt%	wt%
SiO_2	67.18	66.73	67.10	0.60	0.39	0.48	36.77	36.15	35.58	0.27	0.27	0.25	0.33
Al_2O_3	18.92	18.60	18.88	0.00	0.08	B.D.	13.97	14.96	14.78	0.00	0.03	0.06	0.05
TiO_2	0.02	0.00	0.02	0.05	0.03	0.02	1.78	1.65	1.69	B.D.	0.03	0.05	0.03
FeO	0.61	0.88	0.58	0.47	1.01	0.45	18.34	19.17	19.34	8.90	8.80	8.63	9.35
MnO	B.D.	B.D.	B.D.	0.02	0.03	B.D.	0.06	0.06	0.04	1.05	0.81	1.03	1.17
CaO	0.11	0.06	0.16	55.93	55.42	55.88	0.03	0.03	0.03	28.82	29.36	28.88	28.99
MgO	0.00	0.26	0.04	B.D.	0.00	0.03	13.00	12.97	13.06	15.44	15.63	15.37	15.03
Na_2O	11.80	11.71	11.75	0.01	0.05	0.02	0.10	0.11	0.06	0.07	0.04	0.00	0.06
K_2O	0.13	0.46	0.07	0.11	0.03	0.04	9.35	9.33	8.81	0.03	0.04	0.04	0.05
P_2O_5	B.D.	B.D.	0.04	42.93	42.21	42.79	B.D.	0.00	0.06	B.D.	B.D.	B.D.	B.D.
Total	98.77	98.70	98.64	100.12	99.25	99.71	93.40	94.43	93.45	54.58	55.01	54.31	55.06
Cation Sum	3.77	3.79	3.77	3.63	3.60	3.61	4.30	4.31	4.30	5.99	5.98	5.98	5.98

Mineral Phase	Magnetite 5.7	Magnetite 5.8	Magnetite 5.9	Muscovite 5.9	Muscovite 5.10	Muscovite 5.11
Major Element	wt%	wt%	wt%	wt%	wt%	wt%
SiO_2	0.65	0.45	0.67	46.78	45.91	45.61
Al_2O_3	0.13	0.03	0.07	26.45	27.07	26.65
TiO_2	0.02	0.00	0.02	0.41	0.42	0.49
FeO	92.96	93.03	93.05	6.04	7.12	7.29
MnO	0.02	0.05	B.D.	B.D.	0.01	0.03
CaO	0.02	B.D.	0.06	0.02	0.01	0.00
MgO	0.12	B.D.	B.D.	2.35	2.39	2.36
Na_2O	0.13	0.07	0.13	0.12	0.21	0.15
K_2O	0.03	0.02	0.04	10.59	10.72	10.55
P_2O_5	0.06	0.00	B.D.	0.03	0.04	0.06
Total	94.14	93.65	94.04	92.79	93.90	93.19
Cation Sum	5.95	5.97	5.96	3.86	3.89	3.88

Shebandowan Greenstone Belt

Chlorite-actinolite-plagioclase granofels Pt.1

Mineral Phase	Actinolite 7.1	Actinolite 7.2	Actinolite 7.3	Actinolite 7.4	Actinolite 7.5	Actinolite 7.6	Albite 7.1	Albite 7.2	Albite 7.3	Albite 11.1	Albite 11.2	Albite 11.3	Albite 11.4
Major Element	wt%	wt%	wt%	wt%	wt%	wt%	wt%	wt%	wt%	wt%	wt%	wt%	wt%
SiO_2	53.68	54.64	53.87	54.2	53.78	52.87	66.11	66.89	65.88	66.53	66.69	67.00	65.87
Al_2O_3	1.28	1.72	2.65	2.27	1.43	2.36	18.75	18.87	18.96	18.80	18.25	17.24	18.01
TiO_2	0.05	0.07	0.04	0.00	0.02	B.D.	0.02	0.00	B.D.	0.08	B.D.	0.01	B.D.
FeO	14.20	13.97	14.93	13.87	14.35	16.07	0.23	0.25	0.48	0.21	0.47	0.49	0.47
MnO	0.19	0.25	0.18	0.17	0.19	0.23	B.D.	0.01	B.D.	B.D.	0.05	0.02	0.02
CaO	12.77	12.72	12.81	12.82	12.91	12.88	0.55	0.32	0.55	0.28	0.14	0.14	0.74
MgO	14.49	14.66	14.05	14.34	14.57	13.46	0.03	0.04	0.13	0.08	0.21	0.01	0.01
Na_2O	0.19	0.51	0.68	0.55	0.26	0.20	10.43	10.71	11.36	11.38	10.49	9.97	9.86
K_2O	0.07	0.11	0.08	0.12	0.06	0.09	0.09	0.09	0.12	0.09	0.08	0.03	0.06
P_2O_5	B.D.	B.D.	B.D.	B.D.	B.D.	B.D.	0.00	B.D.	B.D.	0.02	0.00	0.03	B.D.
Total	96.92	98.65	99.29	98.34	97.57	98.16	96.21	97.18	97.48	97.47	96.38	94.94	95.04
Cation Sum	3.93	3.94	3.96	3.94	3.94	3.95	3.72	3.73	3.77	3.76	3.72	3.68	3.70

Mineral Phase	Apatite 7.1	Apatite 7.2	Apatite 7.3	Apatite 11.2	Augite 7.1	Augite 7.4	Augite 7.5	Chamosite 7.4	Chamosite 11.1	Chamosite 11.3	Clinochlore 7.1	Clinochlore 7.2	Clinochlore 7.3
Major Element	wt%	wt%	wt%	wt%	wt%	wt%	wt%	wt%	wt%	wt%	wt%	wt%	wt%
SiO_2	0.71	0.61	0.77	0.89	50.3	49.91	49.38	25.99	31.88	30.64	26.24	26.28	25.81
Al_2O_3	0.11	0.09	0.10	0.07	1.89	1.55	1.16	18.13	17.97	16.90	18.18	17.7	18.58
TiO_2	B.D.	0.04	0.00	B.D.	0.65	0.64	0.38	0.05	0.06	0.04	0.02	B.D.	B.D.
FeO	0.72	0.81	0.93	0.66	16.46	17.56	19.32	25.47	30.10	29.75	24.83	24.86	25.21
MnO	0.06	0.00	0.02	0.12	0.38	0.42	0.65	0.33	0.15	0.14	0.29	0.29	0.32
CaO	53.63	54.33	54.13	53.65	17.74	18.75	19.94	0.12	0.18	0.06	0.12	0.26	B.D.
MgO	0.15	0.09	0.13	0.13	12.44	11.07	8.02	14.10	11.40	11.53	15.71	15.34	15.06
Na_2O	0.04	0.00	0.07	0.23	0.28	0.23	0.39	0.07	0.16	0.15	0.11	0.19	0.09
K_2O	0.02	0.04	0.01	0.06	0.02	0.03	0.02	0.00	0.03	B.D.	0.01	0	B.D.
P_2O_5	41.02	41.48	40.75	41.29	0.01	B.D.	B.D.	B.D.	B.D.	B.D.	B.D.	B.D.	B.D.
Total	96.46	97.49	96.91	97.10	100.17	100.16	99.26	84.26	91.93	89.21	85.51	84.92	85.07
Cation Sum	3.63	3.61	3.62	3.67	4.03	4.03	4.03	4.27	4.16	4.18	4.29	4.29	4.29

Chlorite-actinolite-plagioclase granofels Pt.2

Mineral Phase	Diopside 7.2	Diopside 7.3	Diopside 7.6	Epidote 7.1	Epidote 7.2	Epidote 7.3	Epidote 7.4	Epidote 7.5	Epidote 7.6	Epidote 11.1	Epidote 11.2	Epidote 11.3	Epidote 11.4
Major Element	wt%	wt%	wt%	wt%	wt%	wt%	wt%	wt%	wt%	wt%	wt%	wt%	wt%
SiO_2	51.2	50.2	51.18	37.16	37.62	36.76	39.42	39.54	37.52	41.35	43.8	41.63	44.86
Al_2O_3	0.06	1.95	1.16	26.31	26.68	25.6	23.70	26.10	26.62	21.49	19.81	21.97	19.98
TiO_2	0.06	0.14	0.22	0.06	0.12	0.08	B.D.	0.08	0.07	0.12	B.D.	0.10	0.03
FeO	13.01	11.49	13.52	7.03	6.95	7.55	10.32	7.38	7.26	12.62	11.66	11.98	12.57
MnO	0.49	0.57	0.76	0.06	0.04	0.03	B.D.	0.04	0.04	0.05	0.03	0.02	0.12
CaO	22.81	20.89	21.85	23.40	24.15	23.72	23.25	23.23	24.13	22.42	20.60	22.20	19.56
MgO	10.75	11.28	10.26	0.13	0.10	0.12	0.16	0.06	0.03	0.12	0.16	0.03	0.21
Na_2O	0.40	0.46	0.64	0.00	0.07	0.07	B.D.	B.D.	B.D.	0.04	0.10	0.06	0.08
K_2O	0.06	0.02	0.04	0.00	0.01	0.01	0.04	0.02	0.05	0.05	0.02	0.04	0.03
P_2O_5	B.D.	B.D.	B.D.	B.D.	B.D.	0.00	0.01	0.00	B.D.	0.02	0.02	B.D.	0.00
Total	98.84	97.00	99.63	94.15	95.74	93.94	96.90	96.45	95.72	98.28	96.20	98.03	97.44
Cation Sum	4.03	4.01	4.02	3.92	3.93	3.94	3.93	3.89	3.93	3.92	3.85	3.91	3.84

Mineral Phase	Titanite 7.1	Titanite 7.2
Major Element	wt%	wt%
SiO_2	29.47	30.48
Al_2O_3	2.5	2.18
TiO_2	34.82	37.39
FeO	1.83	0.78
MnO	B.D.	B.D.
CaO	27.78	28.52
MgO	0.26	0.26
Na_2O	B.D.	B.D.
K_2O	0.01	0.03
P_2O_5	B.D.	B.D.
Total	96.67	99.64
Cation Sum	3.67	3.63

Layered meta-pyroclastic rock Pt.1

Mineral Phase	Actinolite 8.1	Actinolite 8.2	Actinolite 8.3	Actinolite 8.4	Actinolite 8.5	Actinolite 9.1	Albite 8.1	Albite 8.2	Albite 8.3	Albite 8.4	Albite 8.7	Albite 8.8	Albite 8.9
Major Element	wt%	wt%	wt%	wt%	wt%	wt%	wt%	wt%	wt%	wt%	wt%	wt%	wt%
SiO_2	55.95	52.97	52.73	50.23	52.08	53.47	66.68	65.69	66.89	68.43	67.97	71.59	66.95
Al_2O_3	1.99	1.43	1.37	3.01	1.52	2.89	18.94	19.25	18.81	18.47	18.79	16.67	20.00
TiO_2	0.01	0.01	0.05	0.06	0.05	0.04	0.00	0.02	0	B.D.	0.03	B.D.	B.D.
FeO	17.22	18.76	19.37	19.73	17.54	19.86	0.23	0.52	0.33	0.08	0.28	0.41	0.23
MnO	0.09	0.03	0.06	0.16	0.00	0.06	B.D.	0.05	0.06	B.D.	0.03	B.D.	0.01
CaO	11.61	12.56	12.48	12.12	12.02	11.81	0.40	1.51	0.52	0.13	0.28	0.28	1.16
MgO	11.68	11.94	11.62	10.58	12.48	10.62	B.D.	0.05	0.12	0.01	0.17	0.08	B.D.
Na_2O	0.71	0.35	0.35	0.49	0.52	0.97	11.45	11.08	11.50	10.74	11.24	10.62	11.36
K_2O	0.05	0.13	0.04	0.18	0.10	0.13	0.09	0.09	0.07	0.05	0.00	0.07	0.08
P_2O_5	B.D.	0.06	B.D.	0.02	0.02	0.01	0.10	0.08	B.D.	0.00	B.D.	B.D.	0.11
Total	99.31	98.24	98.07	96.58	96.33	99.86	97.89	98.34	98.30	97.91	98.79	99.72	99.90
Cation Sum	3.89	3.94	3.94	3.97	3.95	3.95	3.76	3.77	3.77	3.71	3.74	3.68	3.76

Mineral Phase	Albite 8.10	Albite 8.11	Albite 9.1	Albite 9.3	Albite 9.4	Albite 9.5	Albite 9.6	Andesine 8.1	Andesine 8.2	Andesine 8.3	Andesine 8.5	Andesine 8.11	Andesine 9.1
Major Element	wt%	wt%	wt%	wt%	wt%	wt%	wt%	wt%	wt%	wt%	wt%	wt%	wt%
SiO_2	69.13	67.25	66.74	68.86	66.68	66.71	66.42	53.94	55.87	53.25	58.09	57.26	55.26
Al_2O_3	17.10	17.93	19.08	19.38	18.85	18.26	17.99	16.49	17.07	16.81	16.05	16.79	17.3
TiO_2	0.54	0.09	B.D.	B.D.	0.03	0.03	0.00	B.D.	0.82	0.01	0.00	0.42	0.01
FeO	1.13	0.87	0.63	0.16	1.13	0.31	0.21	2.78	2.88	4.31	2.60	3.19	4.90
MnO	0.00	0.01	B.D.	B.D.	B.D.	0.04	0.00	0.33	0.33	0.10	0.09	0.11	0.22
CaO	1.96	1.04	0.41	0.39	0.36	0.28	0.39	7.34	8.29	8.66	5.91	6.52	10.20
MgO	0.10	0.13	0.30	B.D.	0.15	0.04	0.04	0.32	0.33	0.51	0.33	0.36	0.51
Na_2O	9.93	11.08	11.65	11.37	11.08	10.67	10.22	7.16	5.65	6.90	6.73	9.38	8.13
K_2O	0.06	0.08	0.06	0.13	0.03	0.03	0.06	0.02	0.07	0.00	0.04	0.21	0.04
P_2O_5	B.D.	0.21	0.21	0.03	B.D.	0.02	B.D.	0.64	0.57	0.13	B.D.	0.01	0.04
Total	99.95	98.69	99.08	100.32	98.31	96.39	95.33	89.02	91.88	90.68	89.84	94.25	96.61
Cation Sum	3.70	3.75	3.77	3.74	3.75	3.72	3.70	3.79	3.86	3.83	3.72	3.87	3.91

Layered meta-pyroclastic rock Pt.2

Mineral Phase	Andesine 9.2	Andesine 9.5	Apatite 8.2	Apatite 8.3	Chamosite 8.5	Carbonate 8.1	Carbonate 8.2	Carbonate 8.3	Carbonate 8.4	Carbonate 9.1	Carbonate 9.2	Carbonate 9.3	Carbonate 9.4	Chamosite 8.1
Major Element	wt%	wt%	wt%	wt%	wt%	wt%	wt%	wt%	wt%	wt%	wt%	wt%	wt%	wt%
SiO_2	59.02	54.07	4.17	0.58	26.62	0.66	0.26	8.04	0.25	1.13	0.63	1.8	2.29	27.98
Al_2O_3	16.41	16.83	0.88	0.15	16.46	0.33	0.05	2.22	0.06	0.42	0.19	0.36	0.73	17.48
TiO_2	0.10	0.05	0.02	B.D.	0.09	0.07	B.D.	0.09	0.09	0.32	0.1	0.07	0.07	0.1
FeO	3.06	4.06	0.73	0.35	35.49	1.23	0.41	0.4	0.24	0.62	0.59	0.93	2.41	30.64
MnO	0.05	0.08	B.D.	0.12	0.08	0.13	0.01	0.01	0.01	0.01	0.06	0.07	0.09	0.08
CaO	6.30	8.46	52.18	54.68	0.20	52.87	51.27	48.73	53.31	53.74	52.97	51.91	48.83	0.16
MgO	0.29	0.56	0.18	0.21	9.97	0.31	B.D.	0.16	0.05	0.34	0.11	0.21	0.58	11.52
Na_2O	7.92	7.19	0.68	0.17	0.15	0.05	0.03	1.57	B.D.	0	0.03	0.23	0.02	0.47
K_2O	0.04	0.04	0.07	0.00	0.01	0.04	0.25	0.01	0.04	0.01	0.05	0.05	0.05	0.01
P_2O_5	0.05	B.D.	36.66	41.84	0.11	B.D.	B.D.	B.D.	B.D.	0.02	B.D.	B.D.	0.2	B.D.
Total	93.24	91.34	95.57	98.10	89.18	55.69	52.28	61.23	54.05	56.61	54.73	55.63	55.27	88.44
Cation Sum	3.78	3.84	3.62	3.64	4.29	5.92	6	5.37	5.97	5.84	5.94	5.83	5.71	4.26

Mineral Phase	Chamosite 8.2	Chamosite 8.3	Chamosite 8.4	Chamosite 8.5	Chamosite 8.6	Chamosite 8.7	Chamosite 8.8	Chamosite 8.9	Chamosite 8.10	Chamosite 8.11	Chamosite 9.2	Chamosite 9.3	Chamosite 9.4
Major Element	wt%	wt%	wt%	wt%	wt%	wt%	wt%	wt%	wt%	wt%	wt%	wt%	wt%
SiO_2	29.04	27.37	24.45	26.62	27.8	28.3	28.76	26.62	29.3	28.58	35.37	35.68	25.53
Al_2O_3	19.76	18.09	18.08	16.46	18.28	18.13	18.95	17.19	17.37	18.81	17.62	18.11	17.58
TiO_2	0.03	0.01	0.03	0.09	0.02	0.01	0.06	0.01	0.06	B.D.	0.06	0.02	B.D.
FeO	31.37	31.68	36.19	35.49	35.89	31.55	31.47	30.78	30.66	31.6	26.04	27.66	30.72
MnO	0.09	0.09	0.09	0.08	0.07	0.08	0.02	0.05	0.03	0.07	0.02	B.D.	0.1
CaO	0.52	0.27	0.16	0.20	0.20	0.09	0.03	0.04	0.07	0.09	0.07	0.06	0.05
MgO	11.22	11.49	8.52	9.97	7.67	12.69	13.30	12.22	10.15	10.65	11.53	10.55	12.47
Na_2O	0.83	0.26	0.17	0.15	0.07	0.29	0.42	0.28	0.7	0.8	1.41	2.91	0.14
K_2O	0.04	0.04	B.D.	0.01	0.00	0.01	B.D.	0.01	0.02	0.01	0.03	0.01	0.01
P_2O_5	B.D.	0.05	0.02	0.11	B.D.	0.08	0.10	0.02	B.D.	0.02	0.08	0.01	0.04
Total	92.90	89.35	87.71	89.18	90.00	91.23	93.11	87.22	88.36	90.63	92.23	95.01	86.64
Cation Sum	4.26	4.27	4.31	4.29	4.22	4.27	4.27	4.29	4.22	4.25	4.13	4.2	4.31

Layered meta-pyroclastic rock Pt.3

Mineral Phase	Chamosite 9.5	Chamosite 9.6	Chamosite 9.7	Epidote 8.1	Epidote 8.2	Epidote 8.3	Epidote 8.4	Epidote 8.5	Epidote 8.6	Epidote 8.7	Epidote 8.9	Epidote 8.10	Epidote 9.1
Major Element	wt%	wt%	wt%	wt%	wt%	wt%	wt%	wt%	wt%	wt%	wt%	wt%	wt%
SiO_2	26.75	30.29	26.37	36.73	36.56	36.84	36.99	39.27	41.81	45.73	37.17	45.02	41.37
Al_2O_3	18.18	16.88	17.40	22.17	22.54	21.65	22.10	21.29	22.30	24.70	22.22	22.31	24.07
TiO_2	0.01	0.12	0.02	0.10	0.11	0.12	0.18	0.20	0.07	0.06	0.04	0.15	0.04
FeO	29.96	29.46	30.47	12.07	11.14	12.24	12.64	13.62	12.24	11.67	12.54	10.59	11.09
MnO	0.01	0.07	0.03	0.21	0.12	0.06	0.14	0.01	0.18	0.10	0.19	0.09	0.06
CaO	0.09	0.46	0.10	22.45	22.93	23.25	23.65	22.62	20.53	21.29	23.47	20.45	22.24
MgO	12.68	13.04	12.43	0.07	B.D.	0.04	B.D.	0.14	0.18	0.00	B.D.	0.01	B.D.
Na_2O	0.43	0.13	0.13	0.15	0.11	0.11	0.18	0.23	1.14	2.36	0.08	1.94	1.54
K_2O	0.08	0.04	B.D.	0.03	0.06	0.01	0.02	0.24	0.04	B.D.	0.03	0.02	0.02
P_2O_5	0.01	0.05	B.D.	0.02	B.D.	0.43	0.01	B.D.	B.D.	B.D.	B.D.	0.21	0.00
Total	88.20	90.54	86.95	94.00	93.57	94.75	95.91	97.62	98.49	105.91	95.74	100.79	100.43
Cation Sum	4.29	4.22	4.29	3.98	3.97	3.97	3.99	3.97	3.94	3.95	3.99	3.91	3.97

Mineral Phase	Epidote 9.2	Epidote 9.3	Epidote 9.4	Epidote 9.5	Oligoclase 8.4	Poikilitic Plag 8.1	Poikilitic Plag 8.2	Poikilitic Plag 8.3	Poikilitic Plag 8.4	Poikilitic Plag 8.5	Poikilitic Plag 8.6	Poikilitic Plag 8.7	Poikilitic Plag 8.8
Major Element	wt%	wt%	wt%	wt%	wt%	wt%	wt%	wt%	wt%	wt%	wt%	wt%	wt%
SiO_2	41.02	36.12	40.79	37.45	60.18	42.65	46.92	42.02	43.22	43.34	42.58	42.46	42.73
Al_2O_3	20.63	21.37	20.36	19.47	17.36	17.29	17.96	16.68	17.76	16.27	17.23	17.42	17.07
TiO_2	B.D.	B.D.	B.D.	0.15	0.02	0.03	0.00	0.09	0.09	0.46	B.D.	0.08	0.07
FeO	13.57	12.05	13.22	13.17	2.33	10.04	10.18	10.19	10.40	12.84	9.53	9.72	9.94
MnO	0.03	0.05	0.04	0.01	0.08	0.76	1.05	1.66	0.15	0.60	0.20	0.12	0.10
CaO	22.06	22.17	21.3	21.18	5.16	20.37	18.61	19.84	19.38	13.71	20.28	20.14	20.19
MgO	B.D.	B.D.	0.01	0.39	0.27	1.48	1.56	1.04	1.71	2.69	1.94	1.79	1.93
Na_2O	0.43	0.07	0.14	0.18	8.97	0.03	0.47	0.05	0.26	1.53	0.02	0.11	0.07
K_2O	0.03	0.04	0.12	0.11	0.06	0.03	0.26	0.06	0.06	0.80	0.00	0.00	0.00
P_2O_5	0.02	B.D.	B.D.	0.12	0.05	B.D.	B.D.	0.02	B.D.	0.21	0.00	0.01	B.D.
Total	97.79	91.87	95.98	92.23	94.48	92.68	97.01	91.65	93.03	92.45	91.78	91.85	92.10
Cation Sum	3.94	3.97	3.92	3.97	3.79	3.88	3.84	3.88	3.87	3.92	3.87	3.87	3.87

Layered meta-pyroclastic rock Pt.4

Mineral Phase	Poikilitic Plag 8.9	Poikilitic Plag 8.10	Poikilitic Plag 8.11	Poikiliti Plag 8.13	Poikiliti Plag 8.14	Quartz 8.1	Stilp 8.1	Stilp 8.2	Stilp 8.3	Stilp 8.6	Stilp 8.7	Stilp 8.8	Stilp 9.1
Major Element	wt%	wt%	wt%	wt%	wt%	wt%	wt%	wt%	wt%	wt%	wt%	wt%	wt%
SiO_2	42.28	43.20	42.28	42.46	41.77	99.94	45.82	45.37	42.58	46.09	45.00	43.92	45.97
Al_2O_3	17.09	17.18	17.10	17.14	16.64	0.08	5.49	5.69	6.58	6.13	6.16	7.05	5.67
TiO_2	0.00	0.08	0.01	0.04	0.07	B.D.	0.01	B.D.	0.05	0.00	0.18	0.11	B.D.
FeO	10.38	10.20	10.08	10.51	8.81	0.15	28.98	28.24	29.41	29.22	28.10	28.59	26.99
MnO	0.21	B.D.	0.76	0.30	1.44	0.03	0.22	0.30	0.22	0.18	0.21	0.23	0.18
CaO	20.12	20.02	20.06	20.06	20.15	0.15	0.19	0.26	0.37	0.14	0.64	0.59	0.14
MgO	1.64	1.67	1.46	1.48	1.66	B.D.	6.18	6.18	6.36	5.91	6.24	6.28	6.67
Na_2O	0.10	0.10	0.11	0.12	0.14	0.09	0.24	0.22	0.17	0.22	0.37	0.35	0.76
K_2O	0.03	0.02	0.01	0.00	0.04	0.01	1.73	2.55	1.65	2.16	3.17	1.97	4.27
P_2O_5	B.D.	0.01	0.00	B.D.	B.D.	0.06	0.04	B.D.	0.12	B.D.	0.05	B.D.	B.D.
Total	91.85	92.48	91.87	92.11	90.72	100.51	88.90	88.81	87.51	90.05	90.12	89.09	90.65
Cation Sum	3.88	3.86	3.88	3.88	3.88	3.01	3.90	3.93	3.95	3.91	3.97	3.95	4.01

Mineral Phase	Stilp 9.2	Stilp 9.3	Stilp 9.4	Stilp 9.5	Stilp 9.6	Stilp 9.7	Stilp 9.8	Stilp 9.9	Stilp 9.10	Stilp 9.11	Titanite 8.1	Titanite 8.2	Titanite 8.3
Major Element	wt%	wt%	wt%	wt%	wt%	wt%	wt%	wt%	wt%	wt%	wt%	wt%	wt%
SiO_2	46.41	46.45	46.85	46.86	48.53	48.09	47.61	44.54	45.97	47.89	34.21	32.79	31.55
Al_2O_3	6.04	5.82	6.33	7.07	7.59	7.39	6.76	5.68	6.70	6.29	4.65	3.81	5.71
TiO_2	0.06	0.01	B.D.	0.06	0.02	0.01	0.02	0.08	0.07	0.00	29.34	32.39	28.61
FeO	27.08	27.41	27.65	28.53	27.47	27.02	28.15	28.91	27.39	27.96	3.50	3.55	8.17
MnO	0.26	0.26	0.20	0.22	0.14	0.20	0.20	0.14	0.19	0.22	0.05	0.00	0.03
CaO	0.06	0.08	0.04	0.17	0.05	0.27	0.05	0.16	0.17	0.29	24.85	27.00	20.61
MgO	6.65	6.48	6.68	5.52	5.58	4.63	5.18	5.29	5.16	4.97	0.50	0.72	3.56
Na_2O	0.65	0.77	1.23	1.10	1.81	2.06	1.22	0.54	0.93	0.55	0.07	0.31	0.02
K_2O	3.49	3.57	4.38	2.14	2.25	1.75	2.15	3.13	2.21	2.03	1.28	0.55	0.02
P_2O_5	B.D.	0.04	0.02	0.03	0.05	0.08	0.04	0.20	0.15	0.11	0.27	0.20	B.D.
Total	90.70	90.89	93.38	91.70	93.49	91.50	91.38	88.67	88.94	90.31	98.72	101.32	98.28
Cation Sum	3.97	3.98	4.03	3.93	3.94	3.92	3.92	3.96	3.91	3.87	3.70	3.71	3.75

Layered meta-pyroclastic rock Pt.5

Mineral Phase	Titanite 8.4	Titanite 8.5	Titanite 8.6	Titanite 9.1	Titanite 9.2	Titanite 9.3	Titanite 9.4
Major Element	wt%	wt%	wt%	wt%	wt%	wt%	wt%
SiO_2	47.65	39.78	35.31	30.38	50.48	36.29	30.03
Al_2O_3	3.99	2.88	2.67	2.24	3.23	8.78	3.08
TiO_2	26.23	31.17	32.23	28.75	19.60	18.26	32.66
FeO	2.72	2.18	3.30	2.83	4.02	6.42	4.06
MnO	B.D.	0.03	B.D.	B.D.	0.01	0.53	0.03
CaO	21.54	24.60	27.10	31.66	16.58	23.84	27.31
MgO	0.04	0.07	0.06	0.24	1.00	0.37	0.48
Na_2O	1.37	0.66	0.18	0.04	0.36	0.21	0.17
K_2O	0.05	0.15	0.03	0.05	0.05	0.04	0.03
P_2O_5	0.17	B.D.	0.08	0.14	0.04	B.D.	0.04
Total	103.76	101.52	100.96	96.33	95.37	94.74	97.89
Cation Sum	3.56	3.60	3.65	3.79	3.40	3.77	3.72

Jasper-magnetite meta-iron formation Pt. 1

Mineral Phase	Actinolite 10.1	Actinolite 10.2	Actinolite 10.3	Actinolite 10.4	Actinolite 10.5	Actinolite 6.4	Actinolite 6.8	Actinolite 6.9	Actinolite 10.6	Fe-Actinolite 6.1	Fe-Actinolite 6.2	Fe-actinolite 6.3	Apatite 6.2
Major Element	wt%	wt%	wt%	wt%	wt%	wt%	wt%	wt%	wt%	wt%	wt%	wt%	wt%
SiO_2	54.32	55.2	55.47	55.3	63.55	54.19	53.67	58.36	54.85	51.04	54.51	49.83	0.55
Al_2O_3	1.04	1.24	0.62	0.56	0.58	0.64	0.57	0.58	0.45	1.84	1.50	2.10	0.05
TiO_2	0.02	B.D.	0.01	B.D.	0.04	0.06	0.03	0.01	B.D.	0.03	0.02	0.02	0.01
FeO	14.94	14.06	14.50	14.08	12.66	12.70	11.96	11.64	19.19	25.26	24.92	25.84	1.49
MnO	0.08	0.06	0.09	0.05	0.07	0.04	0.01	0.05	0.06	0.12	0.11	0.08	B.D.
CaO	11.25	11.57	11.37	11.25	10.66	9.99	10.32	10.23	11.59	9.85	11.04	10.40	55.26
MgO	15.75	15.77	15.57	15.41	12.23	15.43	16.13	15.67	12.08	8.17	7.84	8.11	0.01
Na_2O	0.92	0.87	1.06	0.98	0.75	1.58	1.21	1.12	0.52	0.93	0.52	0.55	0.10
K_2O	0.06	0.08	0.06	0.00	0.06	0.12	0.09	0.07	0.09	0.27	0.19	0.09	0.05
P_2O_5	0.01	0.06	0.05	B.D.	B.D.	B.D.	B.D.	B.D.	B.D.	B.D.	B.D.	B.D.	41.46
Total	98.39	98.91	98.80	97.63	100.60	94.75	93.99	97.73	98.83	97.51	100.65	97.02	98.98
Cation Sum	3.97	3.95	3.95	3.94	3.76	3.96	3.95	3.88	3.92	3.96	3.90	3.97	3.70

Mineral Phase	Apatite 6.3	Apatite 6.4	Apatite 6.5	Apatite 6.6	Apatite 10.1	Apatite 10.2	Apatite 10.3	Apatite 10.4	Carbonate 6.1	Carbonate 6.2	Carbonate 6.3	Carbonate 6.4	Carbonate 6.5
Major Element	wt%	wt%	wt%	wt%	wt%	wt%	wt%	wt%	wt%	wt%	wt%	wt%	wt%
SiO_2	0.64	0.77	1.56	2.18	1.16	1.41	1.02	0.55	0.53	0.33	0.89	0.82	0.47
Al_2O_3	0.09	0.03	0.00	0.00	B.D.	0.02	0.00	0.00	0.08	0.05	0.05	0.01	B.D.
TiO_2	0.04	B.D.	B.D.	B.D.	0.08	0.04	B.D.	0.01	B.D.	0.03	0.00	0.03	B.D.
FeO	1.98	1.69	4.36	1.69	1.32	1.66	1.57	1.53	0.84	1.09	0.90	0.41	0.41
MnO	B.D.	B.D.	B.D.	0.03	0.04	0.03	B.D.	B.D.	0.07	B.D.	0.04	0.11	0.09
CaO	54.51	54.40	51.25	52.35	54.36	54.57	54.81	54.94	52.66	48.80	46.10	53.09	51.70
MgO	0.04	B.D.	0.04	0.11	0.03	0.07	0.01	0.03	0.02	0.00	0.00	0.06	0.06
Na_2O	0.37	0.02	0.10	0.44	0.48	0.40	0.11	0.26	0.03	0.02	0.01	0.01	B.D.
K_2O	0.04	0.07	0.04	0.04	0.04	0.07	0.04	0.01	0.07	0.04	0.16	0.03	0.01
P_2O_5	40.66	41.35	38.05	39.65	40.62	38.40	40.70	40.98	B.D.	B.D.	B.D.	B.D.	B.D.
Total	98.37	98.33	95.40	96.49	98.13	96.67	98.26	98.31	54.30	50.36	48.15	54.57	52.74
Cation Sum	3.70	3.71	3.73	3.73	3.69	3.74	3.68	3.73	5.96	5.98	5.92	5.92	5.96

Jasper-magnetite meta-iron formation Pt. 2

Mineral Phase	Carbonate 10.1	Carbonate 10.2	Chlorite 6.2	Chlorite 10.1	Chlorite 10.2	Chlorite 10.3	Epidote 6.1	Epidote 6.2	Epidote 6.3	Epidote 6.4	Epidote 6.5	Epidote 6.6	Magnetite 6.1
Major Element	wt%	wt%	wt%	wt%	wt%	wt%	wt%	wt%	wt%	wt%	wt%	wt%	wt%
SiO_2	0.44	0.31	26.88	29.25	27.46	26.81	36.72	36.59	36.93	39.16	36.59	36.71	2.49
Al_2O_3	0.06	B.D.	13.13	12.45	13.86	13.13	21.00	19.90	21.09	21.45	21.23	21.43	0.20
TiO_2	B.D.	0.01	0.01	B.D.	B.D.	B.D.	0.04	0.02	0.02	0.06	0.13	0.09	B.D.
FeO	1.31	0.95	27.73	32.08	33.38	31.99	14.63	15.95	14.63	14.74	14.52	14.18	89.13
MnO	0.09	0.05	0.10	0.09	0.09	0.01	0.17	0.04	0.12	0.22	0.29	0.13	0.01
CaO	53.71	52.96	0.00	0.14	0.09	0.24	23.48	23.35	23.38	22.82	22.93	23.49	0.07
MgO	0.11	0.00	14.78	10.56	13.06	11.83	0.00	0.07	0.04	0.06	0.06	0.01	0.08
Na_2O	0.01	B.D.	0.23	0.20	0.22	0.13	0.04	0.05	0.03	0.07	0.04	0.05	0.16
K_2O	0.00	0.05	0.14	0.03	0.02	0.04	0.02	0.04	0.03	0.07	0.05	0.02	0.04
P_2O_5	B.D.	B.D.	0.01	B.D.	B.D.	0.09	B.D.	B.D.	0.01	B.D.	0.04	0.00	0.00
Total	55.73	54.33	83.01	84.80	88.18	84.27	96.10	96.01	96.28	98.65	95.88	96.11	92.18
Cation Sum	5.96	5.98	4.32	4.24	4.33	4.30	4.02	4.03	4.01	3.98	4.01	4.01	5.82

Mineral Phase	Magnetite 6.2	Magnetite 6.3	Magnetite 6.4	Magnetite 6.5	Magnetite 6.6	Magnetite 10.1	Magnetite 10.2	Magnetite 10.3	Magnetite 10.4	Quartz 6.1	Quartz 6.2	Quartz 6.4	Quartz 10.2
Major Element	wt%	wt%	wt%	wt%	wt%	wt%	wt%	wt%	wt%	wt%	wt%	wt%	wt%
SiO_2	1.21	2.04	0.71	0.64	0.31	1.04	1.61	0.66	1.08	100.41	94.68	98.58	100.42
Al_2O_3	0.33	0.46	B.D.	0.01	0.13	0.16	0.06	B.D.	0.23	0.06	0.03	B.D.	0.02
TiO_2	0.02	B.D.	B.D.	0.04	B.D.	0.02	B.D.	B.D.	B.D.	0.01	0.02	0.02	0.02
FeO	90.84	90.03	92.06	90.80	92.02	91.05	91.89	92.11	91.15	0.76	9.26	0.55	0.37
MnO	B.D.	0.03	B.D.	B.D.	B.D.	0.01	B.D.	0.00	0.03	B.D.	0.01	0.01	0.06
CaO	0.04	0.15	0.01	0.03	0.02	0.10	0.17	0.10	0.06	B.D.	0.12	B.D.	0.04
MgO	0.03	B.D.	0.03	0.03	B.D.	0.03	0.12	0.30	0.02	B.D.	0.04	0.04	B.D.
Na_2O	0.16	0.21	0.16	0.12	B.D.	B.D.	0.13	0.50	0.08	0.08	0.04	0.07	0.05
K_2O	0.11	0.10	B.D.	0.01	B.D.	0.03	0.05	B.D.	0.11	0.03	0.03	B.D.	0.01
P_2O_5	0.02	0.00	B.D.	B.D.	0.01	0.03	0.15	0.03	B.D.	B.D.	0.08	B.D.	B.D.
Total	92.76	93.02	92.97	91.68	92.49	92.47	94.18	93.70	92.76	101.35	104.31	99.27	100.99
Cation Sum	5.91	5.85	5.96	5.96	5.96	5.91	5.88	5.95	5.92	3.01	3.12	3.01	3.01

Jasper-magnetite meta-iron formation Pt. 3

Mineral Phase	Stilpnomelane 6.1	Stilpnomelane 6.2	Stilpnomelane 6.3	Stilpnomelane 6.4	Stilpnomelane 6.5	Stilpnomelane 6.6	Stilpnomelane 6.7	Stilpnomelane 6.8	Stilpnomelane 6.9	Stilpnomelane 6.10	Stilpnomelane 6.11	Stilpnomelane 6.12	Stilpnomelane 6.13
Major Element	wt%	wt%	wt%	wt%	wt%	wt%	wt%	wt%	wt%	wt%	wt%	wt%	wt%
SiO_2	44.73	42.59	42.6	44.85	53.74	45.31	47.41	42.95	44.55	48.33	52.26	52.43	44.83
Al_2O_3	4.76	5.53	6.16	5.82	5.05	5.40	5.42	5.87	5.71	5.18	4.31	4.28	4.67
TiO_2	B.D.	0.29	B.D.	0.03	B.D.	0.03	B.D.	B.D.	B.D.	B.D.	0.00	0.05	0.03
FeO	32.60	33.69	32.82	33.40	30.45	32.72	33.07	32.79	33.42	31.86	28.72	30.56	32.19
MnO	0.32	0.30	0.26	0.31	0.23	0.32	0.21	0.30	0.30	0.26	0.38	0.33	0.36
CaO	1.32	0.03	0.27	0.15	0.03	0.03	0.00	0.13	0.07	0.06	0.12	0.10	0.20
MgO	3.59	3.24	3.76	3.36	3.24	3.21	3.78	3.81	3.69	3.38	4.37	4.50	4.08
Na_2O	0.23	0.39	0.25	0.49	0.33	0.32	0.48	0.45	0.61	0.69	0.13	0.18	B.D.
K_2O	1.64	2.38	2.14	3.22	2.64	2.99	3.26	3.71	3.60	3.96	1.51	1.49	1.65
P_2O_5	0.15	B.D.	0.06	0.04	B.D.	0.00	0.02	0.00	0.05	0.01	0.03	B.D.	B.D.
Total	89.34	88.44	88.32	91.67	95.71	90.33	93.65	90.01	92.00	93.73	91.83	93.92	88.01
Cation Sum	3.92	3.96	3.96	3.98	3.80	3.94	3.95	4.03	4.01	3.95	3.76	3.79	3.89

Mineral Phase	Stilpnomelane 10.1	Stilpnomelane 10.2	Stilpnomelane 10.3	Stilpnomelane 10.4	Stilpnomelane 10.5
Major Element	wt%	wt%	wt%	wt%	wt%
SiO_2	57.98	54.76	57.78	54.72	59.85
Al_2O_3	4.24	4.39	3.67	4.36	3.56
TiO_2	B.D.	B.D.	B.D.	B.D.	B.D.
FeO	28.06	29.09	25.53	26.14	25.53
MnO	0.29	0.28	0.29	0.31	0.23
CaO	0.06	0.06	0.08	0.12	0.07
MgO	4.14	4.51	3.53	3.92	3.98
Na_2O	0.2	0.26	0.25	0.26	0.09
K_2O	1.37	1.64	1.89	1.97	1.42
P_2O_5	0.03	0.09	B.D.	B.D.	B.D.
Total	96.37	95.08	93.02	91.8	94.73
Cation Sum	3.69	3.76	3.67	3.72	3.63

Magnetite-chert meta-iron formation Pt.1

Mineral Phase	Actinolite 7.7	Actinolite 7.8	Actinolite 7.9	Actinolite 7.10	Actinolite 7.11	Apatite 7.4	Apatite 7.5	Apatite 7.6	Apatite 10.5	Carbonate 7.1	Carbonate 7.2	Carbonate 7.3	Carbonate 10.3
Major Element	wt%	wt%	wt%	wt%	wt%	wt%	wt%	wt%	wt%	wt%	wt%	wt%	wt%
SiO_2	56.11	53.43	53.07	53.69	54.02	4.02	0.6	2.31	0.65	1.12	1.85	0.37	0.6
Al_2O_3	0.31	0.41	0.18	0.46	0.19	0.29	0.02	0.00	0.02	0.06	0.02	B.D.	B.D.
TiO_2	0.04	B.D.	0.03	0	0	0.01	B.D.	0.04	B.D.	B.D.	0.06	0.00	0.02
FeO	19.78	20.33	19.53	19.85	17.94	4.65	3.45	6.70	10.22	1.48	1.61	1.39	1.11
MnO	0.14	0.04	0.10	0.11	0.13	0.07	B.D.	0.08	0.04	0.30	0.29	0.27	0.11
CaO	11.23	11.33	11.32	11.01	12.10	51.61	53.64	48.97	48.03	51.15	51.85	51.95	49.17
MgO	11.30	11.54	11.98	11.32	13.05	0.48	B.D.	0.15	0.09	0.31	0.07	0.11	0.07
Na_2O	0.71	0.75	0.57	0.62	0.42	0.23	0.09	0.55	0.57	0.03	B.D.	B.D.	0.01
K_2O	0.02	0.01	0.04	0.04	0.05	0.12	0.05	0.00	0.03	0.02	0.05	0.01	0.02
P_2O_5	0.01	0.00	0.02	0.01	B.D.	37.94	37.69	34.78	34.14	B.D.	0.03	0.00	B.D.
Total	99.65	97.84	96.84	97.11	97.90	99.42	95.54	93.58	93.79	54.47	55.83	54.10	51.11
Cation Sum	3.90	3.95	3.94	3.92	3.94	3.75	3.80	3.81	3.83	5.90	5.81	5.96	5.94

Mineral Phase	Carbonate10.4	Carbonate 10.5	Magnetite 7.1	Magnetite 7.2	Magnetite 7.3	Magnetite 10.6	Magnetite 10.7	Magnetite 10.8	Magnetite 10.9	Magnetite 10.10	Quartz 7.1	Quartz 7.2	Quartz 7.3
Major Element	wt%	wt%	wt%	wt%	wt%	wt%	wt%	wt%	wt%	wt%	wt%	wt%	wt%
SiO_2	0.34	0.42	1.88	1.86	1.64	1.55	1.44	1.91	1.25	2.37	100.66	101.39	100.2
Al_2O_3	0	0.03	0.06	0.06	B.D.	0.04	0.05	0.03	0.08	0.07	B.D.	0.04	0.03
TiO_2	B.D.	0	0.00	0.04	B.D.	0.03	0.00	0.06	0.06	0.02	0.04	0.06	0.04
FeO	1.49	1.05	90.87	89.91	88.56	90.93	91.56	91.54	92.45	89.00	0.38	0.91	0.29
MnO	0.17	0.16	0.08	B.D.	B.D.	B.D.	0.00	B.D.	0.06	0.05	B.D.	B.D.	0.01
CaO	52.17	52.9	0.01	0.05	0.01	0.06	0.20	0.22	0.06	0.05	0.07	0.03	0.3
MgO	0.13	0.2	0.07	0.18	0.14	0.06	0.03	0.13	0.04	0.04	0.05	0	B.D.
Na_2O	0.05	B.D.	0.15	B.D.	0.11	0.07	0.19	0.04	0.07	0.20	0.01	0.06	0.04
K_2O	0	0.05	0.02	0.00	0.04	0.00	0.01	0.03	0.06	0.04	B.D.	B.D.	B.D.
P_2O_5	B.D.	B.D.	0.02	0.07	B.D.	0.02	B.D.	B.D.	B.D.	B.D.	0.05	B.D.	B.D.
Total	54.35	54.81	93.16	92.17	90.50	92.76	93.48	93.96	94.13	91.84	101.26	102.49	100.91
Cation Sum	5.98	5.96	5.87	5.85	5.89	5.88	5.91	5.89	5.91	5.84	3.01	3.01	3.01

Magnetite-chert meta-iron formation Pt.2

Mineral Phase	Quartz 1.3	Quartz 1.4	Stilp 7.1	Stilp 7.2	Stilp 7.3	Stilp 7.5	Stilp 10.6	Stilp 10.8	Stilp 10.9	Stilp 10.10
Major Element	wt%	wt%	wt%	wt%	wt%	wt%	wt%	wt%	wt%	wt%
SiO_2	101.2	99.8	46.99	47.99	47.02	46.43	46.74	46.41	48.45	48.45
Al_2O_3	0.01	0.04	4.69	4.87	4.88	4.67	5.06	5.15	5.28	4.87
TiO_2	0.05	B.D.	B.D.	0.03	B.D.	0.06	B.D.	B.D.	0.03	0.00
FeO	0.69	0.33	31.68	31.82	32.12	32.53	30.16	29.27	29.69	29.41
MnO	0.02	B.D.	0.28	0.36	0.42	0.32	0.30	0.19	0.27	0.28
CaO	0.11	0.01	0.18	0.12	0.20	0.17	0.13	0.18	0.39	0.06
MgO	B.D.	0.03	5.15	5.68	5.65	5.53	5.81	6.19	6.81	6.47
Na_2O	0.06	B.D.	0.27	0.31	0.26	0.25	0.19	0.23	0.21	0.16
K_2O	B.D.	0.02	1.88	1.65	1.89	1.86	1.84	1.60	1.28	1.49
P_2O_5	0.03	B.D.	0.04	0.05	B.D.	0.07	0.02	0.01	0.03	0.09
Total	102.17	100.23	91.16	92.88	92.44	91.89	90.25	89.23	92.44	91.28
Cation Sum	3.01	3.01	3.90	3.90	3.92	3.93	3.90	3.89	3.88	3.86